REPORT DOCUMENTATION PAGE

Public reporting burden for this collection of information is estimated to average 1 hour per response, including the time for reviewing instructions, searching existing data sources, gathering and maintaining the data needed, and completing and reviewing the collection of information. Send comments regarding this burden estimate or any other aspect of this collection of information, including suggestions for reducing this burden, to Washington Headquarters Services, Directorate for Information Operations and Reports, 1215 Jefferson Davis Highway, Suite 1204, Arlington, VA 22202-4302, and to the Office of Management and Budget, Paperwork Reduction Project (0704-0188), Washington, DC 20503.

1. AGENCY USE ONLY (Leave blank)	2. REPORT DATE	3. REPORT TYPE AND DATES COVERED
	February 1995	Final Technical Report 10/1/91–11/30/94

4. TITLE AND SUBTITLE	5. FUNDING NUMBERS
Large Eddy Simulation of Backward-Facing Stop Flow with Application to Coaxial Jet Combustors	F49620-92-J-0003 AFOSR-TR-95 0659

6. AUTHOR(S)

Professor Parviz Moin

7. PERFORMING ORGANIZATION NAME(S) AND ADDRESS(ES)	8. PERFORMING ORGANIZATION REPORT NUMBER
Stanford University Mechanical Engineering Thermosciences Division Stanford, CA 94305-3030	2-DJA-420

9. SPONSORING/MONITORING AGENCY NAME(S) AND ADDRESS(ES)	10. SPONSORING/MONITORING AGENCY REPORT NUMBER
Air Force Office of Scientific Research Dr. James M. McMichael 110 Duncan Avenue, Suite B115 Bolling AFB, DC 20332-0001 NA	F49620- 92-J-0003

11. SUPPLEMENTARY NOTES

12a. DISTRIBUTION/AVAILABILITY STATEMENT	12b. DISTRIBUTION CODE
Approved for public release. Distribution is unlimited.	

DTIC SELECTED OCT 18, 1995 B

13. ABSTRACT (Maximum 200 words)

Large eddy simulations (LES) have been performed for two massively separated flows: a planar backward-facing step and a coaxial jet combustor. The backward-facing step case was used to develop and validate both the numerical method and the subgrid-scale model. Backward-facing step simulations were performed at Reynolds numbers 5100 and 28000. Both cases agree well with experimental data; the low Reynolds number case is also in excellent agreement with DNS data. Two versions of the dynamic subgrid-scale model as well as the classical Smagorinsky model were tested and little difference was found among them. The coaxial jet combustor simulations were used as a first step to study the flame stability problem known as lean blow-out. The study focused on the entrainment and mixing of fuel and air within the combustion chamber, using a passive scalar tracking technique. Chemical reactions and the effects of heat release were ignored in this initial study. Mean statistics at Reynolds number 38000 are in good agreement with experimental data. A motion picture of the unsteady motion revealed intermittent pockets of fuel-rich fluid crossing the annular air jet and becoming entrained in the recirculation zone. A larger source of entrainment, however, was found to be the upstream redirection of the fuel jet near the instantaneous impingement point on the combustor wall.

DTIC QUALITY INSPECTED 5

14. SUBJECT TERMS		15. NUMBER OF PAGES
large eddy simulation, combustor, reacting flow, turbulence		345
		16. PRICE CODE

17. SECURITY CLASSIFICATION OF REPORT	18. SECURITY CLASSIFICATION OF THIS PAGE	19. SECURITY CLASSIFICATION OF ABSTRACT	20. LIMITATION OF ABSTRACT
unclassified	unclassified	unclassified	

NSN 7540-01-280-5500

Standard Form 298 (Rev. 2-89)

Abstract

Large Eddy Simulation (LES) has received renewed attention recently due to the advent of the dynamic subgrid scale (DM) model in the early nineties. This model represents a completely new idea in that it outlines a procedure from which model parameters can be *calculated during* a simulation rather than specified prior to the simulation. The result is a self-tuning model which requires little or no input, but instead adapts to local, instantaneous flow conditions. The DM model has opened the possibility of applying large eddy simulation to complex flow situations often encountered in engineering applications.

Two slightly different versions of the dynamic subgrid scale model have been evaluated in the present work. One is the original version (DM model), and the other is an updated version, known as the dynamic localization (DLM) model. The latter has a more rigorous mathematical basis than the former. Simulations were also run using the standard Smagorinsky model. All models were tested, compared, and evaluated in turbulent flow over a backward facing step.

Two Reynolds numbers were considered, 5100 and 28000. Results from the low Reynolds number case are in excellent agreement with direct numerical simulation (DNS) and experimental data using either of the three models. The reattachment length is predicted to within a percent of the DNS result. The cost of a typical LES was about 0.5 percent of that of a comparable DNS. The LES used about 1.5 percent of the number of grid points required in the DNS. The DM model, the DLM model, and the Smagorinsky model gave nearly identical results for all parameters evaluated. Results from the high Reynolds number calculation were also in good agreement with available experimental results. Again, all models gave nearly identical results.

Several different grid resolutions were considered. Even though the results were practically grid independent, minor improvements, compared with DNS data, were obtained with refined grids. This verifies convergence towards DNS results with increasing grid resolution.

The second part of this study was concerned with an engineering application of LES. The objective was to use LES to study mixing of fuel and oxidizer in

the combustion chamber of a coaxial jet-combustor, in order to gain insight into a phenomenon known as lean blow-out (LBO).

Mixing of fuel and oxidizer was studied by tracking a passive scalar, however, the effects of chemical reactions and heat release were not taken into account. A new numerical method was developed which allows the governing equations to be solved in cylindrical coordinates without causing severe time-step limitations due to fine azimuthal resolution around the center-line, and fine radial resolution at the walls. The DM model was used to model the subgrid scale stresses, and a dynamic eddy-diffusivity model was used to model the subgrid scale scalar flux in the scalar transport equation.

The Reynolds number was 38000, based on the bulk velocity and diameter of the combustion chamber. The velocity ratio of the oxidizer and fuel jets was 3:1. Mean velocities and Reynolds stresses are in good agreement with experimental data. Animated results clearly show that intermittent pockets of fuel-rich fluid are able to cross the annular air jet, virtually undiluted, to be entrained into the recirculation zone. The results further show that most of the fuel-rich fluid is entrained into the recirculation zone around the instantaneous reattachment point of the flow. Fuel trapped in the recirculation zone is for the most part entrained back into the step shear layer close to the base of the burner, indicating that this is a likely location for a pilot flame (consistent with experimental observations). Furthermore, the fuel concentration in the recirculation zone is highest at the base of the burner, which strengthens the likelihood of finding the pilot flame at this location. The mean concentration of fuel predicted in the recirculation zone is above the lean flammability limit, indicating that the flame would be attached. This is consistent with the fuel-rich inflow condition used.

Acknowledgements

TABLE OF CONTENTS

PART I

Large Eddy Simulation of Turbulent Flow over a Backward Facing Step

PART II

Large Eddy Simulation of Turbulent Confined Coannular Jets

APPENDIX

LIST OF TABLES

PART I

PART II

APPENDIX

LIST OF FIGURES

PART I

PART II

xv

APPENDICES

xviii

NOMENCLATURE

Roman symbols

a_i	$i = 1...5$: Coefficients in the Poisson equation determined from spatial discretization.
A	Operator in the passive scalar equation containing terms treated explicitly.
A_i	Operator in the i-th momentum equation containing terms treated explicitly.
B	Operator in the passive scalar equation containing terms treated implicitly.
B_i	Operator in the i-th momentum equation containing terms treated implicitly.
$\overline{B}_2$	Linearized version of B_2.
C	Model coefficient in the Dynamic subgrid scale model.
C_f	Coefficient of friction.
C_p	Pressure coefficient.
C_B	Mixed model coefficient.
C_S	Model coefficient in the Smagorinsky model.
C_φ	Model coefficient in the Dynamic SGS scalar flux model.
D	Divergence operator.
$\mathbf{e}_x$, $\mathbf{e}_r$, $\mathbf{e}_\theta$	Unit vectors in the axial, radial and azimuthal directions, respectively.
E_{ij}	Residual tensor.
$\overline{f}_{ij}$	Total stress tensor based on the large scale velocity, $\overline{u}_i$.
$\mathbf{F}$	Resolved scalar flux vector.
G	Gradient operator.
$\overline{G}$	Filter function at the grid-filter level.
$\widehat{G}$	Filter function at the test-filter level.
h	Step height.
H	Shape factor, $H = \delta^*/\theta^*$.
k'_m	Modified wave number.
ℓ	First length scale in two part eddy-viscosity model.
ℓ^*	Second length scale in two part eddy-viscosity model.

L_i	Extent of inlet section of computational domain.
L_x	Streamwise extent of computational domain.
L_y	Wall-normal extent of comp. domain (backward facing step).
L_z	Spanwise extent of comp. domain (backward facing step).
$\mathcal{L}_{ij}$	Resolved turbulent stress tensor.
m	Spanwise wave number (used in Poisson equation).
M	Operator containing the implicit part of the momentum eqns.
$\mathbf{n}$	Unit vector normal to a given surface.
$N_x,\ N_y,\ N_z$	Number of grid-cells in the streamwise, wall-normal, and spanwise directions, respectively.
$N_x,\ N_r,\ N_\theta$	Number of grid-cells in the axial, radial, and azimuthal directions, respectively.
p	Pressure divided by density.
$\overline{p}$	Large scale value of p at the grid-filter level.
$\widehat{\overline{p}}$	Large scale value of p at the test-filter level.
q_{ij}	Anisotropic part of the subgrid scale stress tensor at the grid-filter level : $q_{ij} = \tau_{ij} - \frac{1}{3}\tau_{kk}\delta_{ij}$
$\mathbf{q}$	Residual scalar flux vector at the grid-filter level.
Q	Volume flow-rate.
Q_{ij}	Anisotropic part of the subgrid scale stress tensor at the test-filter level : $Q_{ij} = T_{ij} - \frac{1}{3}T_{kk}\delta_{ij}$
$\mathbf{Q}$	Residual scalar flux vector at the test-filter level.
r	Radial coordinate.
r_a	Radius of annular (air) pipe.
r_c	Radius of central (fuel) pipe.
r_m	Radial position at the center of a given computational cell.
r_0	Radius of combustion chamber.
$\mathbf{r}$	Vector containing RHS for momentum equations. The components of $\mathbf{r}$ are : r_1, r_2, and r_3.
R	Pipe radius (periodic pipe-flow calculations).
Re	Reynolds number.
Re_h	Step-height Reynolds number : $Re_h = U_0 h/\nu$.
Re_τ	Reynolds number based on friction velocity, u_τ.
$\overline{s}_{ij}$	Stress tensor based on the large scale velocity field, $\overline{u}_i$.
$\overline{S}_{ij}$	Strain rate tensor based on the large scale velocity field, $\overline{u}_i$.
Sc	Schmidt number.

Sc_t	SGS turbulent Schmidt number : $Sc_t = \nu_t/\alpha_t$.
t	Time.
T_{ij}	Subgrid scale stress tensor at the test-filter level.
u_i	General notation for velocity components :
	Cartesian coordinates : $u_1 = u$, $u_2 = v$, and $u_3 = w$.
	Cylindrical coordinates : $u_1 = u_x$, $u_2 = u_r$, and $u_3 = u_\theta$.
$\hat{u}_i$	Components of the intermediate velocity field.
$\overline{u}_i$	Velocity components filtered at the grid-filter level.
$\overline{\overline{u}}_i$	Velocity components filtered twice at the grid-filter level.
u_i'	Subgrid scale velocity components : $u_i' = u_i - \overline{u}_i$.
u_i''	Fluctuation velocity components : $u_i'' = u_i - U_i$.
$\widehat{\overline{u}}_i$	Velocity components filtered at both the grid-filter and test-filter levels.
u_τ	Friction velocity.
$\mathbf{u}$	Velocity vector.
u, v, w	Cartesian coordinates : Streamwise, wall-normal, and spanwise velocity components, respectively.
u_x, u_r, u_θ	Cylindrical coordinates : Streamwise (axial), radial, and azimuthal velocity components, respectively.
U_a	Part II : Bulk velocity in the annular (air) pipe.
U_b	Bulk velocity (periodic pipe-flow calculations).
U_c	Part II : Bulk velocity in the central (fuel) pipe.
U_{con}	Convective velocity used in the convective boundary cond.
U_{cl}	Centerline velocity (periodic pipe-flow calculations).
U_i	General notation for mean (time-averaged) velocity components :
	Cartesian coordinates : $U_1 = U$, $U_2 = V$, and $U_3 = W$.
	Cylindrical coordinates : $U_1 = U_x$, $U_2 = U_r$, and $U_3 = U_\theta$.
U, V, W	Cartesian coordinates : Mean (time-averaged) components of the velocity vector. (Streamwise, wall-normal, spanwise).
U_x, U_r, U_θ	Cylindrical coordinates : Mean (time-averaged) components of the velocity vector. (Streamwise, radial, azimuthal).
U_0	Part I : Maximum inlet free-stream velocity (reference velocity). Part II : Bulk velocity in the combustion chamber.
x	Cylindrical coordinates : axial coordinate.
x, y, z	Cartesian coordinates : Spatial coordinates in the Streamwise, wall-normal, and spanwise directions, respectively.

x_i	General notation for (non-dimensional) spatial coordinates :
	Cartesian coordinates : $x_1 = x$, $x_2 = y$, and $x_3 = z$.
	Cylindrical coordinates : $x_1 = x$, $x_2 = r$, and $x_3 = \theta$.
x, y, z	Spatial position vectors.
X_R	Reattachment length.

Greek symbols

α	Total diffusivity : $\alpha = \alpha_m + \alpha_t$
α_m	molecular diffusivity.
α_t	Eddy-diffusivity.
α_{ij}	$= -2\widehat{\overline{\Delta}}^2 |\widehat{\overline{S}}|\widehat{\overline{S}}_{ij}$
β_k	Factor in RK time-integration scheme.
β_{ij}	$= -2\overline{\Delta}^2 |\overline{S}|\overline{S}_{ij}$
γ_k	Factor in RK time-integration scheme.
δ_{ij}	Kronecker delta.
δ	Boundary layer thickness.
δ^*	Displacement thickness.
Δ	Filter width.
$\overline{\Delta}$	Filter width at the grid-filter level.
$\overline{\Delta}_i$	Filter width at the grid-filter level in the i-th coordinate dir.
$\widehat{\overline{\Delta}}$	Filter width at the test-filter level
$\widehat{\overline{\Delta}}_i$	Filter width at the test-filter level in the i-th coordinate dir.
Δt	Time-step.
$\Delta x, \Delta y, \Delta z$	Cartesian coordinates. Grid-spacing in the streamwise,
	wall-normal, and spanwise directions, respectively.
$\Delta x, \Delta r, \Delta \theta$	Cylindrical coordinates. Grid-spacing in the axial, radial,
	and azimuthal directions, respectively.
$\Delta x^+, \Delta y^+, \Delta z^+$	Grid spacing in wall-units (streamwise, wall-normal, spanwise).
ϵ_m	Molecular dissipation
ϵ_{SGS}	Subgrid scale dissipation
φ	Passive scalar (concentration of fuel in air)
ϕ	Pseudo-pressure : Pressure plus trace of subgrid scale stress
	tensor at the grid-filter level : $\phi = \overline{p} + \frac{1}{3}\tau_{kk}$.
Φ	Pseudo-pressure : Pressure plus trace of subgrid scale stress
	tensor at the test-filter level : $\Phi = \widehat{\overline{p}} + \frac{1}{3}T_{kk}$.

ω_m	Optimum value for the acceleration parameter in the SOR scheme (at wave number m).
ν	Total viscosity : $\nu = 1/\text{Re} + \nu_t$
ν_m	Molecular viscosity
ν_t	Eddy-viscosity
ν_t^*	Second eddy-viscosity in the two-part subgrid scale model by Schumann.
ρ	Density
τ_{ij}	Subgrid scale stress tensor at the grid-filter level.
τ_w	Shear stress at the wall.
θ	Cylindrical coordinates : Azimuthal coordinate.
θ^*	Momentum thickness.
ζ_k	Factor in RK time-integration scheme.

Abbreviations

ADI	Alternate Direction Implicit
CFD	Computational Fluid Dynamics.
DNS	Direct numerical simulation
ER	Expansion Ratio : $ER = L_y/(L_y - h)$.
LBO	Lean Blow-Out
LDA	Laser Doppler Anemometry
LES	Large-eddy simulation
LU	Lower-Upper
PIV	Particle Image Velocimetry
RHS	Right-Hand-Side
RK	Runge-Kutta
SC	Stability Criterion (related to temporal stability)
SGS	Subgrid Scale
SOR	Successive Over Relaxation
2-D	Two-dimensional
3-D	Three-dimensional

Subscripts/Superscripts

$()_{cl}$	Variable evaluated at the centerline.
$()^k$	Variable evaluated at sub-step k in RK-loop.
$()^n$	Variable evaluated at time-step n.
$()_{rms}$	Root-Mean-Square of a variable. Using u'' as example : $u''_{rms} = (<u''^2>_i)^{1/2}$, where i represents directions over which averaging is employed.
$()^+$	1) Variable given in wall-coordinates : $()^+ = ()u_\tau/\nu$. 2) Variable evaluated at the front face of a control-volume.
$()^-$	Variable evaluated at the back face of a control-volume.
$()^x, ()^r, ()^\theta$	Variable evaluated at a control-volume surface with normal in the x-dir., r-dir., or θ-dir., respectively.

Other Symbols

$<>_i$	The quantity inside the brackets is averaged in the i-th direction, where i can be spatial directions as well as time.

PART I

Large Eddy Simulation of Turbulent Flow

over a

Backward Facing Step

INTRODUCTION

1.1 Motivation & Objectives

In large eddy simulation (LES) only the large energy-containing eddies are computed explicitly, whereas the effect of the unresolved subgrid scales is predicted using a subgrid scale (SGS) model. The main idea behind LES is based on the observation that most of the momentum transport is carried out by the large scale energy-containing eddies, and LES should therefore be less sensitive to modeling assumptions than the Reynolds averaging approach. It is also observed experimentally that small scales tend to be more isotropic than large scales and it should therefore be possible to describe them using simpler, more universal models.

The reason for focusing on large eddy simulation is that even with today's super-computers, direct numerical simulation remains very expensive and is therefore regarded unpractical for engineering applications, limiting its use to fundamental turbulence research. In addition, the commonly used Reynolds averaged technique has faced difficulties in predicting some important complex flows.

Earlier subgrid scale models suffered from the same type of limitations as the commonly used Reynolds averaged models in that they contained parameters which had to be specified prior to a simulation, and required *ad hoc* factors such as wall damping functions. This is a difficult task in complex flow situations where the optimum values of the model parameters tend to be different in different regions of the flow, and may even change as a function of time. The dynamic subgrid scale modeling procedure represents a new approach in which the parameters in the subgrid scale model are determined dynamically as a function of space and time during the simulation according to the instantaneous, local conditions of the flow.

The dynamic subgrid scale (DM) model was initially tested in turbulent channel flow and in flow going through transition (Germano *et al.*, 1991), in compressible and incompressible isotropic turbulence (Moin *et al.*, 1991) and in channel flow with passive scalar transport (Cabot & Moin, 1991). It produced very good results in all these flows. However, at the start of the current study, the model had not yet been properly tested in complex flows, for which it was originally developed. After the initial introduction of the DM model in 1991 the model has undergone analysis and modifications. In particular it was pointed out that the underlying algebra contained a mathematical inconsistency. This led to the development of the dynamic localization (DLM) model, which has a rigorous mathematical basis.

The main objective of this work was:

> *"To implement, and assess the performance of the*
> *dynamic subgrid scale model and the dynamic*
> *localization model in a complex flow".*

The test case chosen was turbulent flow over a backward facing step. The backward facing step is a benchmark flow which has been studied extensively in the past, both numerically and experimentally. There are numerous databases which can be used for comparison and verification of results. The extensive study of the backward facing step is due to the fact that even though the geometry itself is fairly simple it gives rise to a large number of distinctly different flow regimes, including boundary layers, a mixing layer, reattachment, flow reversal and recovery, all in the presence of a strong adverse pressure gradient.

1.2 Survey of Previous Work

Many studies in which large eddy simulation (LES) has been used to study turbulent flow in simple geometries, or with simple boundary conditions, have been performed during the past 25 years. During the recent 5-10 years LES has been applied to increasingly more complex flows, and a few of these studies are summarized below. Special attention is given to work covering LES of turbulent flow over the backward facing step. (For a review of earlier LES work, see Rogallo & Moin, 1984. A review of recent advances in LES is provided by Moin & Jimenéz, 1993, and Moin *et al.*, 1994).

Bardina *et al.* (1983) were the first to suggest using information from the smallest resolved scales in the prediction of the subgrid scale stresses. This led to the development of the scale similarity model and the mixed model. The desired information was extracted by applying the filtering operation twice. Bardina *et al.* (1983) applied this idea with considerable success to homogenous isotropic and rotating turbulent flows, as well as homogenous sheared flows. Bardina's idea was later carried further by Germano *et al.* (1991), who developed the so-called dynamic subgrid scale (DM) model.

Zang *et al.* (1993) combined the mixed model with the DM model thereby creating what was termed the dynamic mixed model. Since the DM model is based on Smagorinsky's parameterization, it too assumes that the principal axes of the SGS stress tensor are aligned with those of the resolved strain rate tensor, a result which is not supported by direct numerical simulation (Bardina *et al.*, 1983). Bardina's model, on the other hand is not constrained by this assumption and was used by Zang *et al.* (1993) as the basic parameterization for the subgrid scale stresses. Zang *et al.* (1993) applied the dynamic mixed model to LES of a lid-driven cavity flow at Reynolds numbers ranging from laminar, through transitional to fully turbulent flow. First and second order statistics show overall good agreement with DNS and experimental data, and according to Zang *et al.* (1993) the agreement is somewhat better than that obtained with the DM model.

Recently Piomelli (1993) used the DM model to calculate turbulent flow in a channel at Reynolds numbers (based on friction velocity and half channel width) ranging from 200 to 2000, thus including Reynolds numbers significantly higher than in previous simulations. The calculations used no-slip conditions at the wall despite the resolution being fairly coarse for the higher Reynolds number cases. The

resolution used for the highest Reynolds number case was $64 \times 81 \times 80$ points in the streamwise, wall-normal and spanwise directions, respectively. The corresponding resolution in wall units was $\Delta x^+ = 244$, $[77 > \Delta y^+ > 1.5]$, and $\Delta z^+ = 40$. An interesting result from the study is that first and second order statistics were predicted accurately despite the fact that the mean spacing of low-speed streaks was calculated to be 310 wall units. This is about three times the commonly accepted value of about 100 wall units.

Friedrich & Arnal (1990) and Arnal & Friedrich (1991, 1992) have analyzed turbulent flow over a backward facing step using the subgrid scale model of Schumann (1975). They also used Smagorinsky's (1963) model for comparison in one of their studies. All studies used a computational domain with an expansion ratio of 2 and a wall at the upper boundary. The inflow boundary condition consisted of planes of data taken from a fully developed turbulent channel calculation. The calculations used uniform grid in all three coordinate directions. Since the wall layers could not be resolved, approximate boundary conditions, similar to those used by Schumann (1975) were employed. The Reynolds number was 165000, based on inlet channel centerline velocity and step height, h. Results from the studies were compared with experimental values obtained by Durst & Schmitt (1985) at Reynolds number 113000, as well as experimental data obtained by Tropea (1982), at Reynolds number 11000.

Friedrich & Arnal (1990) used a grid containing $128 \times 32 \times 32$ points in the streamwise, wall-normal and spanwise directions, respectively. Based on the friction velocity, u_τ, in the inlet section this corresponds to a grid spacing in wall units of $810 \times 405 \times 810$ in the three coordinate directions. The computational domain extended 16 step heights in the streamwise direction and 4 step heights in the spanwise direction, with the inflow being imposed at the corner of the step. Even though the mean streamwise velocity agrees reasonably well with experimental data, the agreement in the mean wall-normal velocity is marginal. Turbulent intensities also show large discrepancies when compared with the experiments.

The reattachment location, X_R, is used extensively for comparison with experimental data. Friedrich & Arnal (1990) report their reattachment location to be at $7.0h$, compared to $8.6h$ (Tropea, 1982) and $8.5h$ (Durst & Schmitt, 1985). Friedrich & Arnal (1990) attribute some of this difference to differences in the state of the flow upstream of the step, in addition to the coarse grid resolution. In addition, Friedrich & Arnal argue that the flow in the experiment by Durst & Schmitt (1985)

was not fully developed before reaching the step. This might explain some of the discrepancies. However, the discrepancies are more likely due to a combination of poor grid resolution, the use of artificial wall-boundary conditions, differences in the flow condition upstream of the step, and problems with the SGS model.

The study was later extended by Arnal & Friedrich (1991) to evaluate the influence of spatial resolution as well as the effect of increasing the extent of the computational domain in the spanwise direction. An inlet section of 4 step heights was also added to the computational domain. The Reynolds number and other parameters were the same as in the previous study (Friedrich & Arnal, 1990). Three uniformly spaced grids were used (covering the full computational domain, including the inlet section): $80 \times 16 \times 16$, $160 \times 32 \times 32$, and $320 \times 48 \times 64$, in the streamwise, wall-normal and spanwise directions, respectively. The predicted reattachment lengths were $7.2h$ for the finest grid, $7.3h$ for the middle grid, and $7.7h$ for the coarse grid. Since the difference in the predicted mean reattachment length for the two finer grids was less than 2 percent, Friedrich & Arnal concluded that the middle grid was adequate, at least for prediction of the mean reattachment length. This grid was the same as that used in the previous study (apart from the inlet section).

Arnal & Friedrich (1991) also investigated the effect of the shape of the grid cells and found that using cubical grid cells rather than cuboid (rectangular 2-D projections) ones gave results in better agreement with experiments. When going from rectangular to cubical grid cells the reattachment length increased from 7.3 to 8.5 step heights. They attributed this to deficiencies in the filtering procedure which involves integration of the variables over control volumes. Arnal & Friedrich (1991) investigated the adequacy of the spanwise extent of the computational domain by running simulations where the spanwise extent was changed from 2 to 8 step heights. Again using the reattachment location as indicator, they found that with a spanwise width of about 4-6 step heights, the results were little affected by the spanwise periodic boundary condition. Le & Moin (1994) investigated the two point correlations in their DNS of the backward facing step at $Re = 5100$ and found that a spanwise width of at least 4 step heights was necessary to minimize the influence of the periodic boundary condition.

Results from the literature (e.g., Blowers, 1973; Castro, 1977; Caruso, 1985) as well as the present study (see later chapters) show that it is important to resolve the flow around the corner of the step in the streamwise as well as wall-normal

direction where large truncation errors associated with the corner singularity may be present. This was not done in any of the studies by Arnal & Friedrich, and might be a possible explanation for the discrepancies reported.

Morinishi & Kobayashi (1990) performed large eddy simulations of turbulent flow over a backward facing step at Reynolds number 46000 (based on step height, h, and inlet velocity). The expansion ratio was 1.5 and the inflow boundary condition consisted of fully developed turbulent channel flow. Approximate boundary conditions, constructed to match the law of the wall, were used at the walls. The grid was uniform in the streamwise direction between the step and $x/h = 15$. After that the streamwise grid was stretched at a rate of 6 percent per point. Both uniform and non-uniform wall-normal grids were used. The computational domain had an inlet section of $2h$ and extended $30h$ downstream of the step. The spanwise extent was only $2h$, which according to the results of Arnal & Friedrich (1991) and Le & Moin (1994) probably was too small. A modified version of the Smagorinsky (1963) model was used for most of the calculations. In this model, C_S is determined as a function of two adjustable parameters. (The model is described in a paper by Yoshizawa, 1989). Morinishi & Kobayashi (1990) used the experimental study of Kim *et al.* (1978) as reference for their calculations. They obtained a reattachment length of $9.2h$ using $230 \times 30 \times 20$ grid points in the streamwise, wall-normal and spanwise directions, respectively. (The wall-normal grid had a uniform grid distribution). When increasing the number of grid points in the wall-normal direction from 30 to 50, switching to a non-uniform distribution, the reattachment location decreased to $7.1h$. The latter agrees well with the reattachment length, $X_R = 7 \pm 1h$, measured by Kim *et al.* (1978). A third calculation performed using Smagorinsky's model, with $C_S = 0.1$, gave a reattachment length of $6.6h$. The difference in the reattachment length in the three cases is correlated to the computed turbulent shear stress immediately downstream of the step. Increasing turbulent shear stress means better mixing in the shear layer which produces a shorter reattachment length. This is consistent with the results of Morinishi & Kobayashi (1990). The fact that the state of the boundary layer at the separation point has a strong influence on the reattachment length was also demonstrated by Isomoto & Honami (1989). Based on an experimental study at Reynolds number 32000, they concluded that the reattachment length decreased with increasing (streamwise) turbulence intensity near the wall at the separation point.

The agreement in the mean velocity profiles between the computational case

giving $X_R = 7.1h$ and experiments is only marginal, which Morinishi & Kobayashi (1990) suggest is due to the experimental flow not being fully developed. There are also significant discrepancies between experiments and calculations in turbulence intensities at most stations downstream of the step. The reasons for the discrepancies are likely a combination of poor grid resolution (notice the significant change obtained in X_R when changing the wall-normal grid), the use of approximate boundary conditions, problems with the subgrid scale model, and a too narrow computational domain. It should be mentioned that Le & Moin found, using DNS, that the flow over a backward facing step does not obey the law of the wall immediately downstream of reattachment. (Their analysis showed that in this region, the velocity profile was shifted significantly below the log law). In fact, a significant recovery length was needed for the flow to reproduce the law of the wall. This means that approximate boundary conditions designed to match the law of the wall may not be appropriate (even in the recovery region) for the backward facing step (or many other complex flows).

Recently, Neto *et al.* (1993) completed what they called a statistical and topological study of turbulent flow over the backward facing step, using both DNS and LES. The subgrid scale model used in the LES study was the structure-function model proposed by Métais & Lesieur (1992). The inflow boundary condition was imposed at the corner of the step, and consisted of a mean velocity profile, $U(y)$, with superimposed random "white noise". Two cases were considered; one with expansion ratio 1.67 and Reynolds number 38000, and the other with expansion ratio 5 and Reynolds number 6000. In the high Reynolds number case the mean velocity profile at the inlet was taken from an experimental investigation by Eaton & Johnston (1980); in the low Reynolds number case a uniform mean velocity profile was assumed. Approximate boundary conditions, based on the law of the wall, were used along the walls. At the low Reynolds number, $130 \times 25 \times 40$ grid-points were used in the streamwise, wall-normal, and spanwise directions, respectively, both for the LES and DNS cases. In the high Reynolds number case two grids were used: $90 \times 16 \times 16$, and $200 \times 30 \times 30$. Both grids were used for LES, but only the coarsest grid was used for DNS. It should also be mentioned that the numerical algorithm is based on a third order upwind biased spatial discretization scheme for the convective terms, which introduces numerical diffusion.

Le & Moin (1994) showed that large errors in the solution occur when an inlet boundary condition, based on random numbers, is imposed at the corner of the

step. They also showed that the law of the wall does not hold in the recovery region which means that approximate boundary conditions designed to reproduce the law of the wall will be inaccurate. Results from the present study verifies that the flow downstream of the step is very sensitive to the conditions upstream of the step, and care should therefore always be taken when designing the inflow boundary condition. Thus it is perhaps not surprising that the results of Neto *et al.*'s (1993) calculations show rather poor agreement with experimental data (Eaton & Johnston, 1980), particularly in quantities like Reynolds stresses and turbulent kinetic energy. Even mean streamwise velocity profiles show significant discrepancies (all cases) when compared with experiments.

Other types of complex flows have also been computed recently using LES. For instance, Breuer & Rodi (1994) used both the Smagorinsky (1963) model and the DM model to study turbulent flow in a square duct and through a 180 deg bend, with square cross-section. Two Reynolds numbers were considered, $Re = 4100$ and $Re = 56690$. Because of the high Reynolds number, approximate boundary conditions were applied at the walls. Periodic boundary conditions were applied in the streamwise direction for the straight duct, whereas the bend was fed the velocity field extracted from a plane of the straight duct. Since the latter flow has no homogenous directions, the well known numerical instability problem associated with the early formulation of the DM model was removed by averaging the model coefficient in time (following the procedure applied by Akselvoll & Moin, 1993). Whereas good agreement with DNS and experimental data was obtained in the low Reynolds number case, only qualitative agreement was obtained in the high Reynolds number case.

Balaras & Benocci (1994) performed a similar calculation of turbulent flow in a square duct using Reynolds numbers, $Re = 4410$ and $Re = 42000$ (based on bulk velocity and hydraulic diameter). An improved approximate wall boundary condition, based on the solution of a simplified model equation for each velocity component in the wall region, was used. The DM model was used to represent the subgrid scale stresses. Mean velocity field and low order statistics compare well with the reference data, and a significant improvement in the results is observed when using the DM model compared with the Smagorinsky model. The improved model used for the wall boundaries was found to be more accurate than other existing models. It is worth mentioning that all calculations were performed on a desktop workstation, requiring less than 15 hours of CPU time.

Several researchers have studied flows in cylindrical geometries using LES. Eggels *et al.* (1994) studied turbulent flow in pipes and Eggels & Nieuwstadt (1993) studied turbulent flow in an axially rotating pipe using the Smagorinsky (1963) model. Fatica *et al.* (1994) used both LES and DNS to study a temporally evolving round jet at low Reynolds number using both the Smagorinsky (1963) model (with $C_S = 0.1$) and the DM model. The Reynolds number was 800, based on the centerline velocity and one-fifth the radius of the jet. Generally good results were obtained using both models.

Yang & Ferziger (1993) used the DM model to do LES of low Reynolds number turbulent flow in a channel with a two-dimensional obstacle mounted on one wall. The wall layers were resolved and the results were compared with LES results obtained using the Smagorinsky model ($C_S = 0.1$) as well as results from a direct numerical simulation. Overall agreement with DNS results was good when using the DM model, and represented an improvement over the standard Smagorinsky model.

Hoffmann & Benocci (1994) used large eddy simulation to calculate a jet issuing from a 2-D slit onto a flat plate. A slightly modified form of the DM model was used to represent the subgrid scale stresses. The modification essentially amounted to using test-filtered variables instead of grid-filtered variables in the equation for the the model parameter, C. The aim was to reduce the time correlation of negative eddy viscosities, in order to avoid numerical instability problems. No comparison with experimental results was performed, however, the main physical features of the flow were correctly predicted.

As is evident from the present summary, LES has gone through a significant development during the past 25 years. This has been made possible partly by the increase in computer power, but also as a result of improved subgrid scale models, of which the DM model is the most promising. In the space permitted only a flavor of the past and current work with LES could be covered. However, there is a large ongoing effort to push LES to the point where it can be used as a tool for predicting flows of engineering interest.

1.3 Accomplishments

Specific accomplishments of this study were as follows:

- Demonstrated that LES, based on either the DM model, the DLM model, or the Smagorinsky model gives results in excellent agreement with DNS and experiments using less than 1 percent of the computer time needed in DNS.

- Demonstrated that the DM model, the DLM model, and the Smagorinsky model give nearly identical results at both Reynolds numbers studied.

- Demonstrated that the total dissipation is the same using the DM model, the DLM model, or the Smagorinsky model, despite the fact that the SGS contribution to dissipation may vary between the models.

- Demonstrated that the SGS contribution to the turbulent shear stress generally is low (less than 10 percent), whereas the SGS model contributes more than 80 percent of the total dissipation.

- Demonstrated the importance of properly resolving the flow around sharp corners whether performing LES or DNS.

- Demonstrated the strong sensitivity of the flow in the downstream region to the condition of the flow upstream of the step.

- Demonstrated that a method, based on random numbers, used to generate inflow turbulence in DNS of the backward facing step is not applicable in low Reynolds number LES.

MATHEMATICAL FORMULATION

The governing equations for large eddy simulation (LES) are obtained by filtering the continuity and Navier-Stokes equations. Section 2.1 describes these equations. Properties of a few commonly used subgrid scale models and the dynamic subgrid scale models are presented in section 2.2. Details of two variations of the dynamic model, the dynamic subgrid scale (DM) model (Germano *et al.*, 1991) and the dynamic localization (DLM) model (Ghosal *et al.*, 1994) are given.

2.1 Governing Equations

The flow is nondimensionlized using the step height, $\tilde{h}$, and inlet free-stream velocity, $\tilde{U}_0$. The non-dimensional quantities are given by:

$$u_i = \tilde{u}_i/\tilde{U}_0, \qquad x_i = \tilde{x}_i/\tilde{h}, \qquad t = \tilde{t}\frac{\tilde{U}_0}{\tilde{h}}, \qquad p = \frac{\tilde{p}}{\tilde{\rho}}\frac{\tilde{h}}{\tilde{U}_0^2}, \qquad \frac{1}{Re} = \frac{\tilde{\nu}_m}{\tilde{h}\tilde{U}_0} \qquad (2.1\text{-}1)$$

In the present work, x or x_1 is used to represent the streamwise direction, y or x_2 the wall-normal direction, and z or x_3 the spanwise direction. The corresponding velocity components are denoted u, v and w or u_1, u_2, and u_3.

The non-dimensional Navier-Stokes and continuity equations are:

$$\frac{\partial u_i}{\partial t} + \frac{\partial u_i u_j}{\partial x_j} = -\frac{\partial p}{\partial x_i} + \frac{1}{Re}\frac{\partial^2 u_i}{\partial x_j \partial x_j} \qquad (2.1\text{-}2)$$

$$\frac{\partial u_i}{\partial x_i} = 0 \qquad (2.1\text{-}3)$$

In large eddy simulation the velocity u_i is decomposed into a large scale component $\overline{u}_i$ and a subgrid scale component u_i':

$$u_i = \overline{u}_i + u_i' \qquad (2.1\text{-}4)$$

The large scale field is defined by filtering:

$$\overline{u}_i(\mathbf{x}) = \int \overline{G}(\mathbf{x}, \mathbf{y})\, u_i(\mathbf{y})\, d\mathbf{y} \qquad (2.1\text{-}5)$$

where the integral is extended over the entire flow field. $G(\mathbf{x}, \mathbf{y})$ is any kernel that serves to damp all spatial fluctuations shorter than some characteristic length, and $\mathbf{x}$, $\mathbf{y}$ are position vectors. In the present work an overline over a symbol is used to indicate a filtered quantity.

The governing equations of large eddy simulation are obtained by applying the filtering operation defined in equation 2.1-5 to equations 2.1-2 and 2.1-3. However, in order to obtain equations 2.1-6 and 2.1-7 it has been assumed that filtering commutes with the differential operators in the equations. Several filters, like the Gaussian filter and the sharp cutoff filter, have been shown to have this property in homogenous flow (see Piomelli *et al.*, 1987; Moin *et al.*, 1978; Moin & Kim, 1982). In LES of turbulent channel flow Piomelli *et al.*, (1987) used the box filter with variable width in the wall-normal direction to account for the variation of the turbulence length scales with distance from the wall. This filter also satisfies the commutivity requirement. For general inhomogenous flows Ghosal & Moin (1993) proposed an alternate definition of the filtering operation for which differentiation and filtering commutes up to an error which is second order in the filter width.

The filtered Navier-Stokes and continuity equations become:

$$\frac{\partial \overline{u}_i}{\partial t} + \frac{\partial \overline{u}_i \overline{u}_j}{\partial x_j} = -\frac{\partial \phi}{\partial x_i} + \frac{1}{Re}\frac{\partial^2 \overline{u}_i}{\partial x_j \partial x_j} - \frac{\partial q_{ij}}{\partial x_j} \qquad (2.1\text{-}6)$$

$$\frac{\partial \overline{u}_i}{\partial x_i} = 0 \qquad (2.1\text{-}7)$$

In equation 2.1-6, q_{ij} represents the anisotropic part of the subgrid scale stress tensor, τ_{ij}. The subgrid scale stress tensor describes the effect of the unresolved

small scales on the resolved scales. In the simplest eddy-viscosity models only the anisotropic part of the tensor is modeled because it is assumed that the subgrid scale stress tensor is proportional to the strain rate tensor $\overline{S}_{ij} = \frac{1}{2}(\partial \overline{u}_i/\partial x_j + \partial \overline{u}_j/\partial x_i)$, which for incompressible flow is trace free. q_{ij} must therefore also be trace free. The trace of the subgrid scale stress tensor, τ_{ij}, is lumped together with the pressure, $\overline{p}$, to give the "pseudo"-pressure ϕ. (For convenience, ϕ is referred to as the pressure throughout this report). q_{ij} and ϕ are defined as:

$$q_{ij} = \tau_{ij} - \frac{1}{3}\tau_{kk}\delta_{ij}$$
$$\phi = \overline{p} + \frac{1}{3}\tau_{kk} \tag{2.1-8}$$

where,

$$\tau_{ij} = \overline{u_i u_j} - \overline{u}_i \overline{u}_j \tag{2.1-9}$$

Equations 2.1-6 and 2.1-7 are the governing equations for large eddy simulation of incompressible flow (with constant molecular viscosity, and no body forces). In order to close the equations a subgrid scale model has to be introduced to represent the subgrid scale stress tensor, τ_{ij} (or q_{ij}). Such models are description in the next section.

2.2 Residual Stress Models

The basic philosophy of large eddy simulation is to explicitly compute the large-scale motions that are resolved on the grid and to model the small scales. Since the momentum transport is carried out by the large-scale energy-containing eddies, LES is presumably less sensitive to modeling assumptions than for instance the Reynolds averaging approach. Also, since small scales tend to be more isotropic than large scales it should be possible to parametrize them with simpler, more universal models than standard Reynolds stress models.

The following three sections describe the models used in the present study. These models are known as dynamic subgrid scale models because parameters appearing in the models are computed as a function of space and time during the simulation. In conventional models such parameters have to be specified prior to the simulation and are usually not allowed to vary in space or time. Since the optimum values of these parameters tend to be different in different flows as well as in different flow regimes, the conventional models are usually not very well suited for flows in complex geometries.

2.2.1 <u>Background</u>

The most commonly used model for the subgrid scale stress tensor is an eddy-viscosity model due to Smagorinsky (1963). One way to derive the model is to assume that production and dissipation of subgrid scale turbulent kinetic energy are in balance. The model is:

$$q_{ij} = -2\nu_t \overline{S}_{ij} \tag{2.2-1}$$

where,

$$\nu_t = C\overline{\Delta}^2 |\overline{S}|, \qquad \overline{S}_{ij} = \frac{1}{2}\left(\frac{\partial \overline{u}_i}{\partial x_j} + \frac{\partial \overline{u}_j}{\partial x_i}\right), \qquad |\overline{S}| = \sqrt{2\overline{S}_{ij}\overline{S}_{ij}} \tag{2.2-2}$$

$\overline{S}_{ij}$ is the strain rate tensor (based on the large scale velocity field), and $\overline{\Delta}$ is a length scale, usually taken to be proportional to a measure of the grid spacing. C is a proportionality factor which in the standard Smagorinsky model usually is denoted by C_S, where C_S is equal to the square root of C.

Equation 2.2-1 is substituted into equation 2.1-6 in order to obtain the final form of the governing equations for large eddy simulation used in the present study:

$$\frac{\partial \overline{u}_i}{\partial t} + \frac{\partial \overline{u}_i \overline{u}_j}{\partial x_j} = -\frac{\partial \phi}{\partial x_i} + \frac{\partial}{\partial x_j}\left\{\nu \frac{\partial \overline{u}_i}{\partial x_j} + \nu \frac{\partial \overline{u}_j}{\partial x_i}\right\} \qquad (2.2\text{-}3)$$

$$\frac{\partial \overline{u}_i}{\partial x_i} = 0 \qquad (2.2\text{-}4)$$

where ν is the total viscosity, equal to the sum of the inverse Reynolds number and the eddy-viscosity, $\nu = 1/Re + \nu_t$.

Smagorinsky model

In the Smagorinsky model C (or C_S) is a tunable parameter that must be specified prior to a simulation. Lilly (1966, 1967) found that if the grid cutoff is within the inertial sub-range in isotropic turbulence, and $\overline{\Delta}$ is equal to the grid size, $C_S = 0.23$. In the presence of mean shear, however, this value was found to cause excessive damping of large-scale fluctuations, and in his simulation of turbulent channel flow, Deardorff (1970) used $C_S = 0.1$. *A priori* tests by McMillan *et al.* (1980) on homogenous turbulence confirmed that C_S decreases with increasing mean strain rate. (*A priori* tests involve directly calculating the SGS stresses from DNS data, and comparing with SGS stresses found by applying a SGS model to the filtered DNS data). Eggels & Nieuwstadt (1993) found that $C_S = 0.08$ gave reasonable results in a large eddy simulation of turbulent flow in an axially rotating pipe.

As is evident from the studies listed, C_S is far from being a universal constant. Another drawback of the Smagorinsky model is the fact that it is incapable of properly taking into account the reduction in length scales near solid walls. Non-uniformity of the computational grid in the wall-normal direction is usually not sufficient to account for the variation of length scales, and empirical correlations are commonly used near walls. Moin & Kim (1982) multiplied $\overline{\Delta}$ by the Van Driest (1956) exponential damping function to account for the reduction in length scales. This method has also been used by other researchers. A similar problem is encountered in simulation of transition to turbulence (e.g. Piomelli *et al.*, 1990). The Smagorinsky model predicts excessive damping of large scale structures during early stages of transition. The problem has been "solved" by using an *ad hoc* procedure involving multiplying the Smagorinsky constant by an intermittency function which

effectively reduces the contribution of the SGS model to zero in the laminar and early transitional part of the flow.

Two part model

In LES of turbulent channel flow Schumann (1975) introduced a two-part eddy-viscosity model in which the subgrid scale stresses are calculated according to:

$$q_{ij} = -2\nu_t(\overline{S}_{ij} - <\overline{S}_{ij}>_{xz}) - 2\nu_t^* <\overline{S}_{ij}>_{xz} \qquad (2.2\text{-}5)$$

where $<>_{xz}$ represents averaging over planes parallel to the walls. The first term in the model is supposed to account for locally isotropic subgrid scale stresses whereas the second term accounts for inhomogeneities due to the non-zero component of the mean shear. Moin & Kim (1982) modeled the first term in equation 2.2-5 using a modified Smagorinsky model:

$$\nu_t = \ell^2 \{2(\overline{S}_{ij} - <\overline{S}_{ij}>_{xz})\,(\overline{S}_{ij} - <\overline{S}_{ij}>_{xz})\}^{1/2}, \qquad \ell = C_S\Delta \qquad (2.2\text{-}6)$$

The length scale ℓ is some measure of the length scales in all directions. For the eddy-viscosity, ν_t^*, Moin & Kim (1982) used:

$$\nu_t^* = \ell^* \{2 <\overline{S}_{ij}>_{xz} <\overline{S}_{ij}>_{xz}\}^{1/2}, \qquad \ell^* = c(D\Delta_3)^2 \qquad (2.2\text{-}7)$$

which in their case was supposed to account for the production of subgrid scale kinetic energy in the viscous sublayer, where the grid resolution (particularly in the spanwise direction) was inadequate. ℓ^* depends on the spanwise grid which was too coarse to resolve important near wall structures.

Bardina model

This model is based on the assumption that the main interaction between the resolved and subgrid scale eddies takes place between the smallest resolved eddies and the largest subgrid scale eddies. A velocity field that is filtered twice will only contain the largest scales of motion and the difference between a filtered velocity field and one that has been filtered twice will therefore contain predominantly intermediate scales of motion. Bardina's scale similarity model is of the form:

$$q_{ij} = C_B(\overline{u}_i\overline{u}_j - \overline{\overline{u}}_i\overline{\overline{u}}_j) \qquad (2.2\text{-}8)$$

However, even though the scale similarity model correlates well with the subgrid scale Reynolds stresses, it does not dissipate energy. The fix to this problem, as introduced by Bardina *et al.* (1983) was to use a linear combination of the scale similarity model and the Smagorinsky model:

$$q_{ij} = C_B(\overline{u}_i \overline{u}_j - \overline{\overline{u}}_i \overline{\overline{u}}_j) - 2\nu_t \overline{S}_{ij} \tag{2.2-9}$$

Bardina *et al.* (1983) tested the mixed model (eqn. 2.2-9) in homogenous isotropic and rotating turbulent flows as well as in homogenous sheared flows and concluded that the combined model performs better than the Smagorinsky model, but the differences were not significant.

2.2.2 The Dynamic Modeling Procedure

This section introduces the main ideas behind the dynamic subgrid scale modeling approach. Two different version of the model are described, the DM model (Germano *et al.*, 1991) and the DLM model (Ghosal *et al.*, 1994). The two models are based on the same basic principles, but the latter has removed a mathematical inconsistency shown to be present in the DM model.

Consider application of two different filters to the equations of motion, the so-called *grid* filter, $\overline{G}$, and *test* filter, $\widehat{G}$. The filter width, $\widehat{\Delta}$, of the test-filter is assumed to be larger than that of the grid-filter, $\overline{\Delta}$. Applying the grid-filter to the Navier-Stokes and continuity equations give equations 2.1-6 and 2.1-7. Filtering equations 2.1-6 and 2.1-7 once more, this time using the test-filter, yields the following set of equations:

$$\frac{\partial \widehat{\overline{u}}_i}{\partial t} + \frac{\partial \widehat{\overline{u}}_i \widehat{\overline{u}}_j}{\partial x_j} = -\frac{\partial \Phi}{\partial x_i} + \frac{1}{Re} \frac{\partial^2 \widehat{\overline{u}}_i}{\partial x_j \partial x_j} - \frac{\partial Q_{ij}}{\partial x_j} \tag{2.2-10}$$

$$\frac{\partial \widehat{\overline{u}}_i}{\partial x_i} = 0 \tag{2.2-11}$$

where,

$$Q_{ij} = T_{ij} - \tfrac{1}{3}T_{kk}\delta_{ij}, \qquad \Phi = \widehat{\overline{p}} + \tfrac{1}{3}T_{kk}$$

T_{ij} is the subgrid scale stress tensor at the test-filter level. The subgrid scale stress tensors at the grid-filter and test-filter levels are given in equation 2.2-12 and 2.2-13, respectively,

$$\tau_{ij} = \overline{u_i u_j} - \overline{u}_i \overline{u}_j \tag{2.2-12}$$

$$T_{ij} = \widehat{\overline{u_i u_j}} - \widehat{\overline{u}}_i \widehat{\overline{u}}_j \tag{2.2-13}$$

It is easily verified that the subgrid scale stresses at the two filtering levels are related to the smallest resolved turbulent stresses, $\mathcal{L}_{ij}$, by the following expression:

$$\mathcal{L}_{ij} = T_{ij} - \widehat{\tau}_{ij} \tag{2.2-14}$$

where,

$$\mathcal{L}_{ij} = \widehat{\overline{u}_i \overline{u}_j} - \widehat{\overline{u}}_i \widehat{\overline{u}}_j \tag{2.2-15}$$

It is then assumed that the subgrid scale stresses corresponding to the two filters are similar, that is, both are parametrized by the same model, which in this case is the Smagorinsky model:

$$q_{ij} = \tau_{ij} - \tfrac{1}{3}\tau_{kk}\delta_{ij} = -2C\overline{\Delta}^2 |\overline{S}|\overline{S}_{ij} \tag{2.2-16}$$

$$Q_{ij} = T_{ij} - \tfrac{1}{3}T_{kk}\delta_{ij} = -2C\widehat{\overline{\Delta}}^2 |\widehat{\overline{S}}|\widehat{\overline{S}}_{ij} \tag{2.2-17}$$

The filtered strain rate tensors are given by:

$$\overline{S}_{ij} = \frac{1}{2}\left(\frac{\partial \overline{u}_i}{\partial x_j} + \frac{\partial \overline{u}_j}{\partial x_i}\right), \qquad |\overline{S}| = (2\overline{S}_{ij}\overline{S}_{ij})^{1/2} \tag{2.2-18}$$

$$\widehat{\overline{S}}_{ij} = \frac{1}{2}\left(\frac{\partial \widehat{\overline{u}}_i}{\partial x_j} + \frac{\partial \widehat{\overline{u}}_j}{\partial x_i}\right), \qquad |\widehat{\overline{S}}| = (2\widehat{\overline{S}}_{ij}\widehat{\overline{S}}_{ij})^{1/2} \tag{2.2-19}$$

Substituting equations 2.2-16 and 2.2-17 into equation 2.2-15 gives the following expression:

$$\mathcal{L}_{ij} - \tfrac{1}{3}\mathcal{L}_{kk}\delta_{ij} = -2\overline{\Delta}^2 \left\{ (\widehat{\overline{\Delta}}/\overline{\Delta})^2 C|\widehat{\overline{S}}|\widehat{\overline{S}}_{ij} - \widehat{C|\overline{S}|\overline{S}_{ij}} \right\} \tag{2.2-20}$$

The only unknown in equation 2.2-20 is the model coefficient, C. The equation can therefore be solved to yield C as a function of space and time.

In closing this section it should be pointed out that it is not necessary to use the Smagorinsky model to parameterize the subgrid scale stresses (q_{ij} and Q_{ij}). The dynamic modeling procedure is general and can be used to determine coefficients introduced in other parameterizations. For alternative parameterizations see for instance Moin (1991) or Ghosal *et al.* (1994).

2.2.3 <u>The Dynamic Subgrid Scale Model</u>

The original version of the dynamic subgrid scale (DM) model (Germano *et al.*, 1991) solved equation 2.2-20 simply by contracting both sides of the equation by the strain rate tensor, $\overline{S}_{ij}$. It was assumed that the model parameter C was a slowly varying function of space, which justified pulling C outside the test-filter operation in the last term of equation 2.2-20. The result is a simple algebraic expression from which C can easily be determined.

$$\mathcal{L}_{ij}\overline{S}_{ij} = -2C\overline{\Delta}^2 M_{kl}\overline{S}_{kl} \tag{2.2-21}$$

where,

$$M_{kl} = (\widehat{\overline{\Delta}}/\overline{\Delta})^2 |\widehat{\overline{S}}|\widehat{\overline{S}}_{kl} - \widehat{|\overline{S}|\overline{S}}_{kl} \tag{2.2-22}$$

A problem with equation 2.2-21 is that the quantity on the right hand side might become zero, which would make C indeterminate or ill-conditioned. Germano *et al.* therefore assumed that for channel flow, C was only a function of the wall-normal coordinate and time. To this end, the average of both sides of equation 2.2-21 was taken over planes parallel to the wall (indicated by $<>_{xz}$) which results in the following solution to equation 2.2-21:

$$C(y,t)\,\overline{\Delta}^2 = -\frac{1}{2}\frac{<\mathcal{L}_{ij}\overline{S}_{ij}>_{xz}}{<M_{kl}\overline{S}_{kl}>_{xz}} \tag{2.2-23}$$

Lilly (1992) used a slightly different approach when solving equation 2.2-20. While still assuming that C was a slowly varying function of space he used the least squares approach for determining C. The resulting expression for C is:

$$C\overline{\Delta}^2 = -\frac{1}{2}\frac{\mathcal{L}_{ij}M_{ij}}{M_{kl}M_{kl}} \tag{2.2-24}$$

where M_{ij} is given in equation 2.2-22. This expression for C is expected to be better behaved than the un-averaged version of equation 2.2-23 because its denominator is positive definite.

One problem with equation 2.2-24 (which, by the way is also present in equation 2.2-23) is that the model parameter, C, may become negative, in which case the eddy-viscosity also becomes negative. Negative eddy-viscosity implies flow of energy from the small scales to the larger resolved scales, a phenomena known as back-scatter. It is know from DNS data (Piomelli *et al.*, 1991) that the forward and reverse cascade of energy in a turbulent flow are typically of the same order of magnitude with a slight excess of the former accounting for the overall transfer of energy from the large to the small scales. The presence of back-scatter is therefore a desirable feature of a subgrid scale model. However, if the total viscosity (i.e. the sum of the molecular viscosity and eddy-viscosity) becomes negative, the numerical solution of equation 2.2-3 become unstable.

The instability can be traced to the observation that C has a large correlation time (Lund *et al.*, 1993). Therefore, once it becomes negative in some region, it remains negative for excessively long periods of time leading to exponential growth of the velocity. For turbulent channel flow the remedy has been, as in equation 2.2-23, to assume that C is only a function of the wall-normal direction and time, and to average the numerator and denominator of equation 2.2-24 over planes parallel to the wall. Turbulent channel flow calculations done as part of this study show that this procedure removes all points of negative total viscosity, thus giving a stable calculation. However, the backward facing step has only one periodic direction (spanwise), and tests show that averaging over only one direction is not sufficient to remove all point of negative total viscosity. In order to avoid numerically unstable solutions, the total viscosity is then artificially set to zero at points where the model returns negative values. Although this procedure admittedly is somewhat *ad hoc*, it is not believed to have had a significant effect on the results since for most of the calculations, only a small percentage of the points had to be manipulated. It is important to note that the eddy-viscosity is still allowed to be negative as long as the total viscosity is zero or positive.

An alternative procedure used by Akselvoll & Moin (1993) averaged equation 2.2-24 in time as well as in the homogenous spanwise direction.

The DM model used in the present calculations is:

$$C\overline{\Delta}^2 = -\frac{1}{2}\frac{<\mathcal{L}_{ij}M_{ij}>_z}{<M_{kl}M_{kl}>_z} \tag{2.2-25}$$

where,

$$\mathcal{L}_{ij} = \widehat{\overline{u_i u_j}} - \widehat{\overline{u}}_i\widehat{\overline{u}}_j$$

$$M_{ij} = (\widehat{\overline{\Delta}}/\overline{\Delta})^2 |\widehat{\overline{S}}|\widehat{\overline{S}}_{ij} - \widehat{|\overline{S}|\overline{S}}_{ij}$$

and $<>_z$ indicates an average taken over the homogenous spanwise direction. After solving equation 2.2-25 and calculating the eddy-viscosity (equation 2.2-2), the *total* viscosity is forced to be zero at any point where the model returns a negative value. Definition of the length scales $\widehat{\overline{\Delta}}$ and $\overline{\Delta}$ is deferred until section 2.2.5.

The DM model, as given in equation 2.2-25, has a few important properties. First of all it can be shown that the model exhibits the proper asymptotic behavior near solid boundaries without the use of damping functions. In addition, C vanishes in laminar flow without the use of *ad hoc* intermittency functions. In a fully resolved turbulent flow, $\mathcal{L}_{ij}$ approaches zero, thus removing the contribution from the subgrid scale model. It is generally accepted that the model cannot provide the proper back-scatter, but the fact remains that points with negative eddy-viscosity (as long as the total viscosity is positive) represent some degree of reverse flow of energy. These are all properties lacking in the models described in section 2.2.1.

It should be pointed out that the assumption that the model coefficient is the same at the grid- and test-filter levels (section 2.2.2) is not necessary. Moin (1991) introduces different coefficients in equations 2.2-16 and 2.2-17 which can be solved for using the least squares technique (now giving five equations in two unknowns).

2.2.4 The Dynamic Localization Model

As mentioned in the previous section, the simple algebraic expression for the model coefficient, C, (equation 2.2-25) was derived assuming that C is a slowly varying function of space. However, as pointed out by Moin (1991), Ghosal *et al.* (1994), and verified as part of the present work, this assumption does not hold. In fact C varies quite dramatically as a function of space which is a reflection of the inadequacy of the Smagorinsky model. Ghosal *et al.* (1994) formulated the solution of equation 2.2-20 without making this assumption.

For the purpose of describing this method lets introduce some simplifying notation and recast equation 2.2-20 in the following form:

$$\mathcal{L}_{ij} - \frac{\delta_{ij}}{3}\mathcal{L}_{kk} = C\alpha_{ij} - \widehat{C\beta}_{ij} \tag{2.2-26}$$

where,

$$\alpha_{ij} = -2\widehat{\overline{\Delta}}^2|\widehat{\overline{S}}|\widehat{\overline{S}}_{ij}, \qquad \beta_{ij} = -2\overline{\Delta}^2|\overline{S}|\overline{S}_{ij} \tag{2.2-27}$$

Ghosal *et al.* (1994) proposed to solve equation 2.2-26 using a global least squares technique, thus minimizing the L_2 norm of the error in the equation simultaneously over the entire domain. A local minimization of the sum of the squares of the residuals, $E_{ij}E_{ij}$, where,

$$E_{ij} = \mathcal{L}_{ij} - \frac{\delta_{ij}}{3}\mathcal{L}_{kk} - C\alpha_{ij} + \widehat{C\beta}_{ij} \tag{2.2-28}$$

does not work since the residual at any given point depends on the value of C at neighboring points in the field. The function C that "best satisfies" the integral equation 2.2-26 is the one that minimizes:

$$\mathcal{F}[C] = \int E_{ij}(\mathbf{x})E_{ij}(\mathbf{x})d\mathbf{x} \tag{2.2-29}$$

where $\mathcal{F}[C]$ is a functional of C and the integral extends over the entire domain. The result of the least squares approach is a set of five independent integral equations from which C can be determined:

$$C(\mathbf{x}) = \int_{\mathbf{y}} \mathcal{K}(\mathbf{x},\mathbf{y})C(\mathbf{y})d\mathbf{y} + f(\mathbf{x}) \tag{2.2-30}$$

where,

$$f(\mathbf{x}) = \frac{1}{\alpha_{kl}(\mathbf{x})\alpha_{kl}(\mathbf{x})}\left[\alpha_{ij}(\mathbf{x})\mathcal{L}_{ij}(\mathbf{x}) - \beta_{ij}(\mathbf{x})\int_{\mathbf{y}}\widehat{G}(\mathbf{y},\mathbf{x})\mathcal{L}_{ij}(\mathbf{y})d\mathbf{y}\right] \tag{2.2-31}$$

$$\mathcal{K}(\mathbf{x},\mathbf{y}) = \frac{1}{\alpha_{kl}(\mathbf{x})\alpha_{kl}(\mathbf{x})}\left[\widehat{G}(\mathbf{x},\mathbf{y})\alpha_{ij}(\mathbf{x})\beta_{ij}(\mathbf{y}) + \widehat{G}(\mathbf{y},\mathbf{x})\alpha_{ij}(\mathbf{y})\beta_{ij}(\mathbf{x})\right.$$

$$\left. - \beta_{ij}(\mathbf{x})\beta_{ij}(\mathbf{y})\int_{\mathbf{z}}\widehat{G}(\mathbf{z},\mathbf{x})\widehat{G}(\mathbf{z},\mathbf{y})d\mathbf{z}\right] \tag{2.2-32}$$

where $\widehat{G}$ is the filter function at the test-filter level and $\mathbf{x}$, $\mathbf{y}$, and $\mathbf{z}$ are position vectors. Equation 2.2-30 is easily recognized as a Fredholm's integral equation of the second kind.

Unfortunately the solution of equation 2.2-30 permits negative values of C, which as in the case of the DM model leads to numerical instability. The instability issue is addressed by imposing a constraint on the solution of equation 2.2-30 requiring C to be positive.

$$C(\mathbf{x}) = \left\{ \int_{\mathbf{y}} \mathcal{K}(\mathbf{x}, \mathbf{y}) C(\mathbf{y}) d\mathbf{y} + f(\mathbf{x}) \right\}_{+} \qquad (2.2\text{-}33)$$

where the operation denoted by the suffix '+' is defined as $x_{+} = \frac{1}{2}(x + |x|)$ for any real number x. In order to facilitate an easy numerical implementation, equation 2.2-33 can be manipulated to yield the following expression:

$$C = \frac{1}{\alpha_{kl}\alpha_{kl}} \left\{ \alpha_{ij}(\mathcal{L}_{ij} + \widehat{C\beta}_{ij}) + \beta_{ij}(\widehat{C\alpha}_{ij} - \widehat{\mathcal{L}}_{ij} - \widehat{\widehat{C\beta}}_{ij}) \right\}_{+} \qquad (2.2\text{-}34)$$

As pointed out in the previous section, negative eddy-viscosity by itself does not cause numerical instability problems unless the total viscosity is negative. The restriction that C has to be positive is therefore more strict than is necessary. The problem can instead be formulated in terms of the eddy-viscosity rather than C, where the eddy-viscosity is restricted to be larger than or equal to the negative of the molecular viscosity. This will allow for a small degree of back-scatter (albeit that it may not be a good physical representation of it). Reformulating the problem (equations 2.2-26 through 2.2-28) in terms of the eddy-viscosity and solving yields an expression of the form:

$$\nu_t - \frac{1}{Re} = \left\{ \frac{\psi_{ij}(\mathcal{L}_{ij} + \widehat{\nu_t\gamma}_{ij})}{\psi_{kl}\psi_{kl}} + \frac{\gamma_{ij}(\widehat{\nu_t\psi}_{ij} - \widehat{\mathcal{L}}_{ij} - \widehat{\widehat{\nu_t\gamma}}_{ij})}{\psi_{kl}\psi_{kl}} - \frac{1}{Re} \right\}_{+} \qquad (2.2\text{-}35)$$

where,

$$\psi_{ij} = -2(\widehat{\overline{\Delta}}/\overline{\Delta})^2(|\widehat{\overline{S}}|/|\overline{S}|)\,\widehat{\overline{S}}_{ij}, \qquad \gamma_{ij} = -2\overline{S}_{ij} \qquad (2.2\text{-}36)$$

Ghosal *et al.* (1994) show that if one imposes the constraint that C can only depend on time when minimizing the functional, $\mathcal{F}[C]$, in equation 2.2-29, the value of C that minimizes the functional is:

$$C(t) = \frac{< \mathcal{L}_{ij} m_{ij} >_{xyz}}{< m_{kl} m_{kl} >_{xyz}} \qquad (2.2\text{-}37)$$

where $m_{ij} = \alpha_{ij} - \widehat{\beta}_{ij}$ and $<>_{xyz}$ indicates an average taken over the three spatial directions. Ghosal *et al.* (1994) show that equation 2.2-37 (with the appropriate averaging) also holds as long as there is at least one homogenous direction in the flow and test-filtering is applied only in the direction(s) of homogeneity. The constraint used when minimizing the functional, $\mathcal{F}[C]$ in the latter case, is that C is only a function of time as well as any coordinate direction where the flow is not homogenous. Assuming that test-filtering is applied only in the spanwise direction, equation 2.2-37 becomes identical to equation 2.2-25. Thus, if the model coefficient, C, is assumed only to be a function of the coordinate directions where the flow is not test-filtered, the analysis used in section 2.2.3 does not involve an inconsistency.

However, for a nonhomogenous flow, the general expression 2.2-34 (or 2.2-35) has to be used. The backward facing step calculations were performed using both the DLM formulation, equation 2.2-35, and the simpler DM model, equation 2.2-25. When using the DLM model, (constraining the total viscosity to be positive), test-filtering was applied only in the streamwise and spanwise directions. The L_2 norm of the error (equation 2.2-28) is then minimized globally, not over the entire domain, but over x-z planes parallel to the wall.

When using the DM model, averaging was applied only in the homogenous, spanwise direction, but test-filtering was done in the streamwise as well as the spanwise direction. From the discussion above it is clear that this procedure does involve some inconsistency, but was employed for much of the same reasons Germano *et al.* (1991) used in their early work.

The DLM model is significantly more costly than the DM model. For the backward facing step calculations, the DLM model required more than twice the CPU time used for the DM model.

2.2.5 <u>Issues Related to Filtering</u>

The filter width at the grid and test-filter levels are denoted by $\overline{\Delta}$ and $\widehat{\overline{\Delta}}$, respectively. Two commonly used definitions for the filter widths are:

$$\overline{\Delta}^3 = \overline{\Delta}_1 \overline{\Delta}_2 \overline{\Delta}_3, \qquad \widehat{\overline{\Delta}}^3 = \widehat{\overline{\Delta}}_1 \widehat{\overline{\Delta}}_2 \widehat{\overline{\Delta}}_3 \qquad (2.2\text{-}38)$$

and

$$\overline{\Delta}^2 = \overline{\Delta}_1^2 + \overline{\Delta}_2^2 + \overline{\Delta}_3^2, \qquad \widehat{\overline{\Delta}}^2 = \widehat{\overline{\Delta}}_1^2 + \widehat{\overline{\Delta}}_2^2 + \widehat{\overline{\Delta}}_3^2 \qquad (2.2\text{-}39)$$

where $\overline{\Delta}_i$ and $\widehat{\overline{\Delta}}_i$ are the filter widths in each coordinate direction, associated with the grid- and test-filters, respectively. Equations 2.2-38 and 2.2-39 assume that filtering is performed in all three coordinate directions. As mentioned in the previous section, test-filtering was done only in the streamwise and spanwise directions for the present calculations. The corresponding definitions for the filter widths then become:

$$\overline{\Delta}^3 = \overline{\Delta}_1 \overline{\Delta}_2 \overline{\Delta}_3, \qquad \widehat{\overline{\Delta}}^3 = \widehat{\overline{\Delta}}_1 \overline{\Delta}_2 \widehat{\overline{\Delta}}_3 \qquad (2.2\text{-}40)$$

and

$$\overline{\Delta}^2 = \overline{\Delta}_1^2 + \overline{\Delta}_2^2 + \overline{\Delta}_3^2, \qquad \widehat{\overline{\Delta}}^2 = \widehat{\overline{\Delta}}_1^2 + \overline{\Delta}_2^2 + \widehat{\overline{\Delta}}_3^2 \qquad (2.2\text{-}41)$$

Both the DM model and the DLM model require one input parameter, namely the ratio $\widehat{\overline{\Delta}}/\overline{\Delta} > 1$. The general guidelines are that if this ratio is too small, i.e. a very narrow "window" is used to sample the resolved scales, the calculated subgrid scale stresses can be contaminated by numerical errors. A large value, on the other hand, implies that information from large scales is used to predict the subgrid scale stresses, a feature which obviously is undesirable.

Germano *et al.* (1991) did calculations of turbulent channel flow (test-filtering only in the streamwise and spanwise directions) using both definitions for the filter widths (equations 2.2-40 and 2.2-41). The grid-filter width, $\overline{\Delta}_i$ was set equal to twice the grid spacing, Δx_i, and the ratio $\zeta = \widehat{\overline{\Delta}}_i / \overline{\Delta}_i$ was taken to be the same in all coordinate directions. Two different values of ζ were examined, $\zeta = 2$ and $\zeta = 4$. The results proved to be insensitive to whether equation 2.2-40 or equation 2.2-41 were used to define the filter widths.

On the other hand, *a priori* tests done using DNS databases for turbulent and transitional channel flow indicated some sensitivity to the value used for the ratio, ζ, however, actual LES done in turbulent channel flow showed hardly any sensitivity to variations in this parameter.

Cabot (1991), proposed the following definitions for the grid- and test-filter widths in the case that no explicit test-filtering is done in the wall-normal direction.

$$\overline{\Delta}^2 = \overline{\Delta}_1 \overline{\Delta}_3, \qquad\qquad \widehat{\overline{\Delta}}^2 = \widehat{\overline{\Delta}}_1 \widehat{\overline{\Delta}}_3 \qquad\qquad (2.2\text{-}42)$$

The eddy-viscosity calculated using either the DM model or the DLM model depends only on the ratio $\widehat{\overline{\Delta}}/\overline{\Delta}$. If all $\widehat{\overline{\Delta}}_i/\overline{\Delta}_i$ are the same, the definitions in equation 2.2-40 yield $\widehat{\overline{\Delta}}/\overline{\Delta} = \zeta^{2/3}$ while using the definitions in equation 2.2-42 give $\widehat{\overline{\Delta}}/\overline{\Delta} = \zeta$. Although the differences are not great, Cabot (1991) concludes that the latter definitions yield somewhat better results in LES of turbulent channel flow.

Definitions 2.2-42 were adopted for all large eddy simulations based on the DM model and the DLM model. Equation 2.2-38, combined with the Van Driest (1956) damping function giving:

$$\overline{\Delta} = \{1 - \exp\left(-y^+/A^+\right)\}(\overline{\Delta}_1\overline{\Delta}_2\overline{\Delta}_3)^{1/3} \qquad\qquad (2.2\text{-}43)$$

was used for the Smagorinsky model. $(A^+ = 25)$. No explicit grid-filtering was done. The grid-filter width, $\overline{\Delta}_i$, was assumed to be equal to the grid spacing, Δx_i. The test-filter width was taken to be twice the grid-filter width (streamwise and spanwise). However, note that the ratio is not exactly 2 (but very close) in the streamwise direction due to the non-uniform grid.

Filtering in physical space corresponds to taking local volume averages. Since the test-filter is applied in planes only, averaging is taken locally in these planes. Test-filtering is performed numerically by applying Simpson's rule of integration. Thus, when filtering in the streamwise direction (assuming uniform grid):

$$\widehat{\overline{u}}(i,j,k) = \frac{1}{6}\overline{u}(i-1,j,k) + \frac{2}{3}\overline{u}(i,j,k) + \frac{1}{6}\overline{u}(i+1,j,k)$$

Similar expressions are used for the $\widehat{\overline{v}}$ and $\widehat{\overline{w}}$ velocities, as well as any other test-filtered quantity. When filtering in planes, $\widehat{\overline{u}}(i,j,k)$ becomes a function of $\overline{u}(i,j,k)$ and its eight closest neighbors.

NUMERICAL METHOD

This chapter describes the numerical method used to solve the governing equations derived in the previous chapter. The geometry of the backward-facing step computed is described in section 3.1. Section 3.2 defines the grid and numerical expressions used for spatial derivatives. The time integration scheme is described in section 3.3 and details of the iterative solver used for the Poisson equation are given in section 3.4. Section 3.5 discusses boundary conditions. Finally, section 3.6 describes how statistical quantities are evaluated.

3.1 Flow Configuration

The computational domain used for the backward facing step is shown in figure 3.1-1. The streamwise extent of the domain is L_x which includes an inlet section of length L_i, upstream of the step. The spanwise extent of the domain is L_z and the vertical height of the domain is L_y. All dimensions are normalized by the step height, h. The coordinate system used is located at the lower corner of the step. Three important parameters are defined based on the geometry in figure 3.1-1. These are the mean reattachment length, X_R, the step-height Reynolds number, $Re_h = U_0 h / \nu$, and the expansion ratio $ER = L_y/(L_y - h)$. U_0 is the mean free-stream velocity at the inlet of the domain.

Two cases have been studied. One at a Reynolds number of 5100 and the other at a Reynolds number of 28000. The geometrical parameters and boundary conditions in the low Reynolds number case were chosen to match those used by Le & Moin (1994) in a DNS of the backward facing step, as well as the experimental setup used by Jovic & Driver (1994). The high Reynolds number calculation was designed to match the experimental setup used by Adams *et al.* (1984).

3.2 Spatial Discretization

The spatial discretization scheme is based on a second order finite volume formulation. This section describes the details of the grid and spatial discretization scheme.

3.2.1 <u>Corner Point</u>

Sharp corners are mathematically singular points for the vorticity and pressure fields. Even though the velocity components are not infinite near the corner, the velocity gradients are discontinuous and the vorticity is therefore singular. In the case of the backward facing step the flow also experiences sharp velocity gradients immediately downstream of the separation corner. According to Castro (1977), Blowers (1973) found that fine grids in the vicinity of sharp corners was critical for obtaining accurate results for laminar flow situations similar to the backward facing step. It was clear that numerical errors arising at the separation corner were convected downstream and had an almost overwhelming effect on the rest of the flow field.

In order to demonstrate the problems associated with sharp corners, lets investigate the following example. The modes of vibration of a membrane with a fixed boundary can be determined by finding eigenvalues and corresponding eigenfunctions of the elliptic equation:

$$\nabla^2 \psi + \lambda \psi = 0 \tag{3.2-1}$$

where $\psi = 0$ on the boundary. The eigenvalues are all real and positive, and the smallest corresponds to the fundamental mode of vibration. This problem was described in detail by Reid & Walsh (1965) and only the main results of the derivation are highlighted here.

If the boundary of the membrane has at some point O a corner of internal angle, π/m, as shown in figure 3.2-1a, then an explicit solution for ψ can be found for points on the membrane close to O. The solution is given by:

$$\psi(r, \theta) = \sum_{i=1}^{\infty} C_i sin(mi\theta) J_{mi}(\sqrt{\lambda} r) \tag{3.2-2}$$

where $J_{mi}()$ is the Bessel function of the first kind and im^{th} order. On expanding the Bessel function the solution becomes:

$$\psi(r,\theta) = a_0 r^m sin(m\theta) + O(r^{2m}) + O(r^{m+2}) \tag{3.2-3}$$

For integer values of m, this is an expansion in integer powers of r, and all derivatives of ψ are continuous and bounded at $r = 0$. Figure 3.2-1b shows a domain, similar to the backward facing step, with several internal angles. All the corners, B, C, D, E, and F are right angles for which $m = 2$. Thus all derivatives of ψ w.r.t. r are continuous and bounded at these corners and the corners will not cause any problems when solving equation 3.2-1 (these corners are not singular). However, the internal angle at point A is $3\pi/2$ corresponding to $m = 2/3$. From equation 3.2-3 it is seen that unless $a_0 = 0$, all derivatives of ψ w.r.t. r go to infinity as $r \to 0$. If we consider a central difference scheme for ψ (using the y-direction as an example), the second derivative can be approximated by:

$$\left(\frac{\partial^2 \psi}{\partial y^2}\right)_{i,j} = \frac{\psi_{i,j+1} - 2\psi_{i,j} + \psi_{i,j-1}}{(\Delta y)^2} - \frac{(\Delta y)^2}{12}\left(\frac{\partial^4 \psi}{\partial y^4}\right)_{i,j} + H.O.T \tag{3.2-4}$$

For the case of $\theta = \pi/2$, y coincides with r and it is clear from equation 3.2-3 and 3.2-4 that the error in the approximation for the second derivative of ψ increases towards the corner. It can also be seen from equation 3.2-4 that the increase in the error as $r \to 0$ can be offset by a decrease in the grid spacing, Δy.

There are several methods available for dealing with the problems arising at sharp corners. The analytical solution very close to the corner has been provided by Moffatt (1964) by making use of the argument that sufficiently near the corner the flow is Stokesian. Thus one can prescribe the analytical solution in the close vicinity of the singular corner and use a numerical approach in the rest of the domain. Reid & Walsh (1965) demonstrate how the problem of finding the modes of vibration for the membrane described above can be solved by using conformal mapping. Conformal mapping removes the singular point from the domain. However, it also introduces non-constant coefficients in the equations and makes the boundaries of the domain curved.

As illustrated in the example above, the problems, or rather errors, associated with the singular corner can be controlled (although not totally removed) by refining

the grid around the corner. This approach was used for all calculations presented in chapter 4 and chapter 5. However, in order to demonstrate the importance of refining the grid around the corner of the backward facing step, calculations were done both with and without streamwise grid refinement. Results from these calculations are summarized in appendix A.1.

3.2.2 <u>Computational Grid</u>

The Navier-Stokes and continuity equations are solved on a rectangular, staggered grid (Harlow & Welsh, 1965). The grid is uniform in the spanwise direction and can be either uniform or stretched in the streamwise and wall-normal directions. For all calculations presented in this report the grid was stretched in the wall-normal direction to resolve the boundary layers along the walls, both in the inlet section and downstream of the step. Since the grid is structured, resolving the boundary layer in the inlet section means that the fine grid is carried downstream of the step, into the shear layer as shown in figure 3.2-2. (Figure 3.2-2 is an example of a grid used to calculate a flow using the no-stress boundary condition at $y = L_y$).

Le & Moin (1994) used a uniform streamwise grid in their DNS calculation of the backward facing step and had no apparent problems related to the singularity at the corner. A uniform grid is preferred from a computational point of view since it simplifies the code and allows for the use of Fourier transform methods in the solution of the Poisson equation for pressure. In addition, the order of accuracy generally drops when going from uniform to non-uniform grids. However, as shown in appendix A.1, with a uniform grid in the streamwise direction the resolution used in the LES calculations of the backward facing step was insufficient to control the error at the singular corner. A non-uniform grid was therefore needed in order to avoid the problems imposed by the corner.

Coordinate transform functions are used to map the uniform grid distributions, $\tilde{x}$ and $\tilde{y}$, onto their non-uniform counterparts, x and y. The functions used in the present calculations are based on combinations of hyperbolic tangent functions. This allows one to control the degree of stretching of the grid as well as the location of the zones with high density of grid points. Two different stretching functions were designed. The first consists of two separate hyperbolic tangent functions which are patched together at $x = 0$ in the streamwise direction, and at $y = h$ in the wall-normal direction, with the constraint that the resulting function as well as its first

derivative be continuous (Le & Moin, 1994). This function was used in all cases to generate the grid in the wall-normal direction.

Due to concerns about possible problems related to the fact that the coordinate transform function is continuous only up to and including its first derivative (at the "patching point"), a second coordinate transform function was tested. It is the sum of two hyperbolic tangent functions, shifted relative to some position, $x = 0$. One of the functions is flipped around the $x = 0$ axis and shifted to the left of the axis. The other function is shifted to the right of the axis. By controlling the degree of stretching for each of the two hyperbolic tangent functions as well as the shift relative to the $x = 0$ axis, a function is generated that compresses the grid gently around the point $x = 0$. This transform function, including all its derivatives, is continuous. It was used to generate the grid in the streamwise direction in all calculations. However, no differences were found between results generated using either transform function.

Figure 3.2-3 shows an example of a typical transform function in the streamwise direction, compressing the grid around the corner of the step ($x = 0$). Likewise, figure 3.2-4 shows a typical transform function for the wall-normal direction with refined grid at the wall in the inlet section ($y = h$) and at the lower wall, ($y = 0$), downstream of the step. (A no-stress boundary condition is used along the upper wall).

3.2.3 Evaluation of Spatial Derivatives

The governing equations are approximated using the second order finite volume approach. Linear interpolation is used to get variables at locations in the grid between the nodes where the variables are defined. The diffusive terms for the u-momentum equation (2-D) are evaluated from:

$$\frac{\delta}{\delta x}\left(\nu\frac{\delta u}{\delta x}\right)\bigg|_{i+\frac{1}{2},j} = \frac{1}{x_{i+1} - x_i}\left\{\left(\nu\frac{\delta u}{\delta x}\right)_{i+1,j} - \left(\nu\frac{\delta u}{\delta x}\right)_{i,j}\right\} \tag{3.2-5}$$

$$\frac{\delta}{\delta y}\left(\nu\frac{\delta u}{\delta y}\right)\bigg|_{i+\frac{1}{2},j} = \frac{1}{y_{j+\frac{1}{2}} - y_{j-\frac{1}{2}}}\left\{\left(\nu\frac{\delta u}{\delta y}\right)_{i+\frac{1}{2},j+\frac{1}{2}} - \left(\nu\frac{\delta u}{\delta y}\right)_{i+\frac{1}{2},j-\frac{1}{2}}\right\} \tag{3.2-6}$$

$$\frac{\delta}{\delta y}\left(\nu\frac{\delta v}{\delta x}\right)\bigg|_{i+\frac{1}{2},j} = \frac{1}{y_{j+\frac{1}{2}} - y_{j-\frac{1}{2}}}\left\{\left(\nu\frac{\delta v}{\delta x}\right)_{i+\frac{1}{2},j+\frac{1}{2}} - \left(\nu\frac{\delta v}{\delta x}\right)_{i+\frac{1}{2},j-\frac{1}{2}}\right\} \tag{3.2-7}$$

where,

$$\left.\frac{\delta u}{\delta x}\right|_{i+1,j} = \frac{u_{i+\frac{3}{2},j} - u_{i+\frac{1}{2},j}}{x_{i+\frac{3}{2}} - x_{i+\frac{1}{2}}}, \tag{3.2-8a}$$

$$\left.\frac{\delta u}{\delta y}\right|_{i+\frac{1}{2},j+\frac{1}{2}} = \frac{u_{i+\frac{1}{2},j+1} - u_{i+\frac{1}{2},j}}{y_{j+1} - y_j}, \tag{3.2-8b}$$

$$\left.\frac{\delta v}{\delta x}\right|_{i+\frac{1}{2},j+\frac{1}{2}} = \frac{v_{i+1,j+\frac{1}{2}} - v_{i,j+\frac{1}{2}}}{x_{i+1} - x_i} \tag{3.2-8c}$$

Similar expressions are used for the diffusive terms in the v- and w-momentum equations. Extension to 3-D is straightforward.

Boundaries

The following comments are for the u-momentum equation, where no special treatment is necessary at the west ($x = -L_i$) and east ($x = L_x - L_i$) boundaries. For a u-momentum control volume located next to the boundary at $y = 0$ (with index $(i + \frac{1}{2}, 1)$), $u_{i+\frac{1}{2},\frac{1}{2}}$ can be found without interpolation and is equal to the boundary value. The flux, $(\delta u/\delta y)_{i+\frac{1}{2},\frac{1}{2}}$ on the other hand will require special attention. A common practice is to use the first-order, one-sided approximation:

$$\left.\frac{\delta u}{\delta y}\right|_{i+\frac{1}{2},\frac{1}{2}} = \frac{u_{i+\frac{1}{2},1} - u_{i+\frac{1}{2},\frac{1}{2}}}{y_1 - y_{\frac{1}{2}}} \tag{3.2-9}$$

However, it can easily be shown that when equation 3.2-9 is substituted back into equation 3.2-6, the approximation for the diffusive term in the wall-normal direction is of $O(1)$. If instead of the using equation 3.2-9, $(\delta u/\delta y)_{i+\frac{1}{2},\frac{1}{2}}$ is approximated using:

$$\left.\frac{\delta u}{\delta y}\right|_{i+\frac{1}{2},\frac{1}{2}} = \frac{h_2 - 3h_1}{h_2(h_1 + h_2)}u_{i+\frac{1}{2},2} + \frac{3}{h_2}u_{i+\frac{1}{2},1} - \frac{4}{(h_1 + h_2)}u_{i+\frac{1}{2},1/2} \tag{3.2-10}$$

where, $\qquad h_1 = y_1 - y_{\frac{1}{2}}, \qquad h_2 = y_2 - y_1$

the overall order for the diffusive term in equation 3.2-6 is $O(\Delta y)$, provided the viscosity is constant. The eddy-viscosity is not constant, but it goes as y^3 near the

wall. Thus equation 3.2-6 is still $O(\Delta y)$ at the wall when using equation 3.2-10 for $(\delta u/\delta y)_{i+\frac{1}{2},\frac{1}{2}}$, even with the variable eddy-viscosity.

Caruso (1985) tested both equation 3.2-9 and equation 3.2-10 in laminar channel flow and found that significant errors occur near the boundaries when using approximation 3.2-9. The first order approximation (3.2-10) gave a numerical solution in good agreement with the exact solution. Similar tests were done as part of this work, both for the backward facing step as well as for a (turbulent) periodic channel. No detectable differences were found in first and second order statistics when using equation 3.2-9 or 3.2-10. This is probably due to the second derivative at the wall being smaller in turbulent than in laminar flow. Nevertheless, equation 3.2-10 was used in all calculations reported here.

Poisson Equation

The Poisson equation for the (pseudo) pressure is given in two dimensions by:

$$\nabla \cdot (\nabla \phi) = f \, \nabla \cdot \hat{\mathbf{u}}, \qquad \text{or} \qquad \frac{\partial^2 \phi}{\partial x \partial x} + \frac{\partial^2 \phi}{\partial y \partial y} = f \, \nabla \cdot \hat{\mathbf{u}} \qquad (3.2\text{-}11)$$

where f is a factor depending on the time integration scheme and $\hat{\mathbf{u}}$ is the intermediate velocity field (see section 3.3.3). The expressions for the second derivatives of the pressure is found by balancing fluxes across the control volume:

$$\frac{\delta}{\delta x}\left(\frac{\delta \phi}{\delta x}\right)\Big|_{i,j} = \frac{1}{x_{i+\frac{1}{2}} - x_{i-\frac{1}{2}}}\left\{\frac{\delta \phi}{\delta x}\Big|_{i+\frac{1}{2},j} - \frac{\delta \phi}{\delta x}\Big|_{i-\frac{1}{2},j}\right\} \qquad (3.2\text{-}12)$$

$$\frac{\delta}{\delta y}\left(\frac{\delta \phi}{\delta y}\right)\Big|_{i,j} = \frac{1}{y_{j+\frac{1}{2}} - y_{j-\frac{1}{2}}}\left\{\frac{\delta \phi}{\delta y}\Big|_{i,j+\frac{1}{2}} - \frac{\delta \phi}{\delta y}\Big|_{i,j-\frac{1}{2}}\right\} \qquad (3.2\text{-}13)$$

where, $\quad \dfrac{\delta \phi}{\delta x}\Big|_{i+\frac{1}{2},j} = \dfrac{\phi_{i+1,j} - \phi_{i,j}}{x_{i+1} - x_i}, \qquad \dfrac{\delta \phi}{\delta y}\Big|_{i,j+\frac{1}{2}} = \dfrac{\phi_{i,j+1} - \phi_{i,j}}{y_{j+1} - y_j}$

Extension to three dimensions is straightforward. Since the normal gradient of the pressure is zero at the boundaries, equations 3.2-12 and 3.2-13 with $(\delta \phi/\delta x)_{i-\frac{1}{2},j} = 0$ and $(\delta \phi/\delta y)_{i,j-\frac{1}{2}} = 0$ represent first order approximations at the vertical and horizontal boundaries, respectively.

3.3 Temporal Discretization

The incompressible Navier-Stokes and continuity equations are integrated in time using the fractional step method. A modified third order Runge-Kutta scheme (Spalart, 1987, Spalart *et al.*, 1991) is used for terms treated explicitly and second order Crank-Nicholson is used for terms treated implicitly.

3.3.1 <u>Implicit Versus Explicit Treatment</u>

Common practice has been to treat all diffusive terms implicitly and all convective terms explicitly. The motivation for treating the diffusive terms implicitly is the severe time-step restriction originating from these terms near solid surfaces where the computational grid is refined. The convective terms do not introduce the same limitations because the velocity components generally are small close to solid surfaces.

Provided all terms in the Navier-Stokes equations are treated explicitly, the following expression is an approximation for the maximum time-step permitted:

$$\Delta t \leq \left\{ \frac{|u|}{\Delta x} + \frac{|v|}{\Delta y} + \frac{|w|}{\Delta z} + 2\nu\left(\frac{1}{\Delta x^2} + \frac{1}{\Delta y^2} + \frac{1}{\Delta z^2}\right) \right\}^{-1} \qquad (3.3\text{-}1)$$

The first three terms on the right-hand-side of equation 3.3-1 are related to the convective terms and the last three terms are related to the diffusive terms. Based on an analysis of a typical 3D flow-field from the DNS data of Le & Moin (1994), the maximum values (order of magnitude) throughout the flow field of each of the terms in the curly bracket on the right-hand-side of equation 3.3-1 are:

$$\Delta t \leq \left\{ \frac{|u|}{\Delta x} + \frac{|v|}{\Delta y} + \frac{|w|}{\Delta z} + \frac{2\nu}{\Delta x^2} + \frac{2\nu}{\Delta y^2} + \frac{2\nu}{\Delta z^2} \right\}^{-1}$$

$$6 \cdot 10^{-2} \qquad 1 \qquad 2 \cdot 10^{-2} \qquad 5 \cdot 10^{-4} \qquad 0.7 \qquad 2 \cdot 10^{-4}$$

The terms have been normalized by the maximum of the six terms in the curly bracket. It is clear that both the convective and diffusive terms in the wall-normal direction are equally important in limiting the time-step, and that both terms are

far more important than any other term. The convective term in the wall-normal direction contributes significantly to limiting the time-step because the fine grid close to the wall in the inlet-section extends into the domain downstream of the step. In the recirculation region the velocity in the wall-normal direction is of order one. The convective term in the wall-normal direction therefore introduces a severe limitation on the time-step. It is desirable, therefore, to treat both convective and diffusive terms with derivatives in the wall-normal direction implicitly.

In the absence of body forces, the Navier-Stokes and continuity equations for incompressible, variable viscosity flow are given by (see eqn. 2.2-3 and 2.2-4):

$$\frac{\partial u_i}{\partial t} = -\frac{\partial \phi}{\partial x_i} - \frac{\partial u_j u_i}{\partial x_j} + \frac{\partial}{\partial x_j}\left[\nu \frac{\partial u_i}{\partial x_j}\right] + \frac{\partial}{\partial x_j}\left[\nu \frac{\partial u_j}{\partial x_i}\right] \tag{3.3-2}$$

$$\frac{\partial u_i}{\partial x_i} = 0 \tag{3.3-3}$$

(In this chapter the overline indicating grid-filtered variables has been dropped for convenience). Let the operators A and B, acting on the velocity vector, represent the terms treated explicitly (third order Runge-Kutta) and implicitly (Crank-Nicholson), respectively. The three step time-advancement scheme (Spalart, 1987, Spalart *et al.*, 1991) can then be expressed as:

$$\frac{u_i^k - u_i^{k-1}}{\Delta t} = \beta_k\left\{B_i^k + B_i^{k-1}\right\} + \gamma_k A_i^{k-1} + \zeta_k A_i^{k-2} - 2\beta_k \frac{\partial \phi^k}{\partial x_i} \tag{3.3-4}$$

$$\frac{\partial u_i^k}{\partial x_i} = 0 \tag{3.3-5}$$

The explicit and implicit operators are give by:

$$A_1 = \left\{\frac{\partial}{\partial x_1}\left[\nu \frac{\partial u_1}{\partial x_1}\right] + \frac{\partial}{\partial x_3}\left[\nu \frac{\partial u_1}{\partial x_3}\right]\right\} + \left\{-\frac{\partial u_1 u_1}{\partial x_1} - \frac{\partial u_1 u_3}{\partial x_3}\right\}$$

$$+ \left\{\frac{\partial}{\partial x_1}\left[\nu \frac{\partial u_1}{\partial x_1}\right] + \frac{\partial}{\partial x_2}\left[\nu \frac{\partial u_2}{\partial x_1}\right] + \frac{\partial}{\partial x_3}\left[\nu \frac{\partial u_3}{\partial x_1}\right]\right\} \tag{3.3-6a}$$

$$A_2 = \left\{ \frac{\partial}{\partial x_1}\left[\nu \frac{\partial u_2}{\partial x_1}\right] + \frac{\partial}{\partial x_3}\left[\nu \frac{\partial u_2}{\partial x_3}\right] \right\} + \left\{ -\frac{\partial u_2 u_1}{\partial x_1} - \frac{\partial u_2 u_3}{\partial x_3} \right\}$$

$$+ \left\{ \frac{\partial}{\partial x_1}\left[\nu \frac{\partial u_1}{\partial x_2}\right] + \frac{\partial}{\partial x_3}\left[\nu \frac{\partial u_3}{\partial x_2}\right] \right\} \qquad (3.3\text{-}6b)$$

$$A_3 = \left\{ \frac{\partial}{\partial x_1}\left[\nu \frac{\partial u_3}{\partial x_1}\right] + \frac{\partial}{\partial x_3}\left[\nu \frac{\partial u_3}{\partial x_3}\right] \right\} + \left\{ -\frac{\partial u_3 u_1}{\partial x_1} - \frac{\partial u_3 u_3}{\partial x_3} \right\}$$

$$+ \left\{ \frac{\partial}{\partial x_1}\left[\nu \frac{\partial u_1}{\partial x_3}\right] + \frac{\partial}{\partial x_2}\left[\nu \frac{\partial u_2}{\partial x_3}\right] + \frac{\partial}{\partial x_3}\left[\nu \frac{\partial u_3}{\partial x_3}\right] \right\} \qquad (3.3\text{-}6c)$$

$$B_1 = -\frac{\partial u_1 u_2}{\partial x_2} + \frac{\partial}{\partial x_2}\left[\nu \frac{\partial u_1}{\partial x_2}\right] \qquad (3.3\text{-}7a)$$

$$B_2 = -\frac{\partial u_2 u_2}{\partial x_2} + 2\frac{\partial}{\partial x_2}\left[\nu \frac{\partial u_2}{\partial x_2}\right] \qquad (3.3\text{-}7b)$$

$$B_3 = -\frac{\partial u_3 u_2}{\partial x_2} + \frac{\partial}{\partial x_2}\left[\nu \frac{\partial u_3}{\partial x_2}\right] \qquad (3.3\text{-}7c)$$

Superscript k ($k = 1, 2, 3$) represents the Runge-Kutta sub-steps such that $u^{k-1} = u^n$ for $k = 1$ and $u^k = u^{n+1}$ for $k = 3$. Superscript n represents the full time-step. The coefficients, β_k, γ_k and ζ_k are selected such that the total time advancement is third order accurate for the explicitly treated terms and second-order accurate for the implicitly treated terms. These coefficients are:

$$\begin{array}{lll} \beta_1 = 4/15, & \beta_2 = 1/15, & \beta_3 = 1/6, \\ \gamma_1 = 8/15, & \gamma_2 = 5/12, & \gamma_3 = 3/4, \\ \zeta_1 = 0, & \zeta_2 = -17/60, & \zeta_3 = -5/12, \end{array}$$

$$\sum_{k=1}^{3} 2\beta_k = \sum_{k=1}^{3} (\gamma_k + \zeta_k) = 1$$

The cross-terms on the right-hand-side of equation 3.3-2 arises because viscosity is a function of space. With the exception of the term $\partial/\partial y(\nu \partial v/\partial y)$, these

terms are all treated explicitly. This is not thought to cause any severe time-step limitations since the minimum grid-spacing in the x- and z-directions are at least an order of magnitude larger than the minimum grid-spacing in the y-direction.

Since all terms in the streamwise and spanwise directions are treated explicitly, the following definition is adopted for the stability criterion (SC) of the time-integration scheme:

$$SC = \Delta t \left\{ \frac{|u|}{\Delta x} + \frac{|w|}{\Delta z} + 4\nu \left(\frac{1}{\Delta x^2} + \frac{1}{\Delta z^2} \right) \right\}_{max} \tag{3.3-8}$$

The stability limit for the third order Runge-Kutta scheme is $\sqrt{3}$. However, since the cross-terms, which are all treated explicitly, are not accounted for in the analysis leading to equation 3.3-8, the practical limit on the time-step is lower. Most of the simulations were run at SC of about 0.7, however, some (high Reynolds number) cases used SC as high as 1.2.

3.3.2 Linearization

It is apparent from equation 3.3-7b that due to implicit treatment of the B-operator the discrete u_2 momentum equation is non-linear in u_2. However, the discrete u_1 and u_3 momentum equations are linear in u_1 and u_3, respectively. Treating the convective terms in one direction (i.e. convective terms with derivatives in the wall-normal direction) with an implicit time integration scheme leads to only one non-linear equation. The benefit of having only one non-linear equation over a set of non-linear equations is obvious. Whereas a set of non-linear equations generally requires a complicated and costly solution technique, having only one non-linear equation greatly simplifies the solution procedure. Equations 3.3-7 show that the u_2 momentum equation is uncoupled from the two other equations (apart from the pressure term which will be dealt with in the next section), whereas solution of the u_1 and u_3 momentum equations depends on the availability of u_2^k. The solution strategy is therefore to linearize the u_2 momentum equation and solve for u_2^k first. The two other equations can then be solved in a straight forward manner.

Linearization of the convective term in $B_2(u_j^k)$ follows from a Taylor series expansion:

$$\frac{\partial u_2^k u_2^k}{\partial x_2} = 2 \frac{\partial u_2^{k-1} u_2^k}{\partial x_2} - \frac{\partial u_2^{k-1} u_2^{k-1}}{\partial x_2} + O(\Delta t^2) \tag{3.3-9}$$

$B_2(u_j^k)$ from equation 3.3-7b can therefore be replaced by equation 3.3-10 while maintaining second order accuracy.

$$\overline{B}_2(u_j^k) = -2\frac{\partial u_2^{k-1}u_2^k}{\partial x_2} + \frac{\partial u_2^{k-1}u_2^{k-1}}{\partial x_2} + 2\frac{\partial}{\partial x_2}\left[\nu\frac{\partial u_2^k}{\partial x_2}\right] \qquad (3.3\text{-}10)$$

3.3.3 Fractional Step Method

The fractional step method developed in this section is based on a formulation first introduced by Chorin (1968) and Temam (1969). Since then several different versions have been developed (e.g. Kim & Moin, 1985, Dukowicz & Dvinsky, 1992, and Perot, 1993). Kim & Moin derived a version in which the Poisson equation was formulated in terms of a "pseudo" pressure, ϕ. Their formulation is based on the assumption that the discrete operators in the equations commute. However, this is not always the case (e.g. commutivity brakes down at solid surfaces) which makes the splitting strictly first order in time. (However, the first order error term thus introduced is weak and will in general decrease the overall order of the method only at very small time-steps). In addition, their method is suitable only when treating linear terms in the momentum equations implicitly. Treating nonlinear terms implicitly gives rise to first order error terms.

The development of the method used in the present calculations follows closely the derivation described by Dukowicz & Dvinsky (1992). This method is second order. The intermediate velocity field is a second order approximation to the divergence free velocity field and special boundary conditions for the intermediate velocity field are therefore not needed.

The starting point is the temporally discretized version of the Navier-Stokes and continuity equations, given here in vector form:

$$\mathbf{u}^k - \beta_k\Delta tM(\mathbf{u}^k) + 2\beta_k\Delta tG(\phi^k - \phi^{k-1}) = \mathbf{r}^{k-1} \qquad (3.3\text{-}11)$$

$$D(\mathbf{u}^k) = 0 \qquad (3.3\text{-}12)$$

where G is the gradient operator and D is the divergence operator. M is an operator, operating on the velocity vector, $\mathbf{u}$. The components of M are:

$$M_1(\mathbf{u}^k) = \left(\frac{\partial}{\partial x_2}\left[\nu\frac{\partial\cdot}{\partial x_2}\right] - \frac{\partial u_2^k\cdot}{\partial x_2}\right)u_1^k, \tag{3.3-13a}$$

$$M_2(\mathbf{u}^k) = 2\left(\frac{\partial}{\partial x_2}\left[\nu\frac{\partial\cdot}{\partial x_2}\right] - \frac{\partial u_2^{k-1}\cdot}{\partial x_2}\right)u_2^k \tag{3.3-13b}$$

$$M_3(\mathbf{u}^k) = \left(\frac{\partial}{\partial x_2}\left[\nu\frac{\partial\cdot}{\partial x_2}\right] - \frac{\partial u_2^k\cdot}{\partial x_2}\right)u_3^k \tag{3.3-13c}$$

The right-hand-side, $\mathbf{r}$, is given by:

$$r_1^{k-1} = u_1^{k-1} + \beta_k\Delta t\left\{\frac{\partial}{\partial x_2}\left[\nu\frac{\partial u_1^{k-1}}{\partial x_2}\right] - \frac{\partial u_1^{k-1}u_2^{k-1}}{\partial x_2}\right\}$$

$$+ \gamma_k\Delta t A_1^{k-1} + \zeta_k\Delta t A_1^{k-2} - 2\beta_k\Delta t\frac{\partial\phi^{k-1}}{\partial x_1} \tag{3.3-14a}$$

$$r_2^{k-1} = u_2^{k-1} + \beta_k\Delta t\left\{2\frac{\partial}{\partial x_2}\left[\nu\frac{\partial u_2^{k-1}}{\partial x_2}\right]\right\}$$

$$+ \gamma_k\Delta t A_2^{k-1} + \zeta_k\Delta t A_2^{k-2} - 2\beta_k\Delta t\frac{\partial\phi^{k-1}}{\partial x_2} \tag{3.3-14b}$$

$$r_3^{k-1} = u_3^{k-1} + \beta_k\Delta t\left\{\frac{\partial}{\partial x_2}\left[\nu\frac{\partial u_3^{k-1}}{\partial x_2}\right] - \frac{\partial u_3^{k-1}u_2^{k-1}}{\partial x_2}\right\}$$

$$+ \gamma_k\Delta t A_3^{k-1} + \zeta_k\Delta t A_3^{k-2} - 2\beta_k\Delta t\frac{\partial\phi^{k-1}}{\partial x_3} \tag{3.3-14c}$$

Note that each of the u_i-momentum equations are linear in u_i^k. Also note that equation 3.3-11 expresses the pressure in the so-called "delta-form". This last point is important in order to make the following approximate factorization second order in time. Equations 3.3-11 and 3.3-12 can be written:

$$\begin{bmatrix} I - \beta_k\Delta t M & 2\beta_k\Delta t G \\ D & 0 \end{bmatrix} \begin{bmatrix} \mathbf{u}^k \\ \phi^k - \phi^{k-1} \end{bmatrix} = \begin{bmatrix} \mathbf{r}^{k-1} \\ 0 \end{bmatrix} \tag{3.3-15}$$

In order to factorize, consider the following approximation to equation 3.3-15:

$$\begin{bmatrix} I - \beta_k \Delta t M & (I - \beta_k \Delta t M) 2 \beta_k \Delta t G \\ D & 0 \end{bmatrix} \begin{bmatrix} \mathbf{u}^k \\ \phi^k - \phi^{k-1} \end{bmatrix} = \begin{bmatrix} \mathbf{r}^{k-1} \\ 0 \end{bmatrix} \qquad (3.3\text{-}16)$$

The approximate system, 3.3-16, can be factored into the block LU decomposition:

$$\begin{bmatrix} I - \beta_k \Delta t M & 0 \\ D & -2\beta_k \Delta t D G \end{bmatrix} \begin{bmatrix} I & 2\beta_k \Delta t G \\ 0 & I \end{bmatrix} \begin{bmatrix} \mathbf{u}^k \\ \phi^k - \phi^{k-1} \end{bmatrix} = \begin{bmatrix} \mathbf{r}^{k-1} \\ 0 \end{bmatrix} \quad (3.3\text{-}17)$$

which can be decomposed into:

$$\begin{bmatrix} I - \beta_k \Delta t M & 0 \\ D & -2\beta_k \Delta t D G \end{bmatrix} \begin{bmatrix} \hat{\mathbf{u}}^k \\ \delta \hat{\phi}^k \end{bmatrix} = \begin{bmatrix} \mathbf{r}^{k-1} \\ 0 \end{bmatrix} \qquad (3.3\text{-}18)$$

$$\begin{bmatrix} I & 2\beta_k \Delta t G \\ 0 & I \end{bmatrix} \begin{bmatrix} \mathbf{u}^k \\ \phi^k - \phi^{k-1} \end{bmatrix} = \begin{bmatrix} \hat{\mathbf{u}}^k \\ \delta \hat{\phi}^k \end{bmatrix} \qquad (3.3\text{-}19)$$

From equation 3.3-19 it follows that $\delta \hat{\phi}^k = \phi^k - \phi^{k-1}$. Thus the system of equations becomes:

$$\hat{\mathbf{u}}^k - \beta_k \Delta t M(\hat{\mathbf{u}}^k) = \mathbf{r}^{k-1} \qquad (3.3\text{-}20)$$

$$\nabla^2(\phi^k - \phi^{k-1}) = \frac{1}{2\beta_k \Delta t} D(\hat{\mathbf{u}}^k) \qquad (3.3\text{-}21)$$

$$\mathbf{u}^k = \hat{\mathbf{u}}^k - 2\beta_k \Delta t G(\phi^k - \phi^{k-1}) \qquad (3.3\text{-}22)$$

The solution procedure is as follows. First solve the momentum equations 3.3-20 for the intermediate velocity field, $\hat{\mathbf{u}}^k$. The divergence of the intermediate velocity field yields the right-hand-side of the Poisson equation, 3.3-21. After solving for ϕ^k, the intermediate velocity field is projected onto a divergence free

velocity field by using equation 3.3-22. From equation 3.3-13 it is clear that the u_2-momentum equation will have to be solved first since its solution does not depend on the other velocity components. However, a problem still arises when solving the u_1- and u_3-momentum equations. Before solving the Poisson equation only the intermediate velocity, $\hat{u}_2^k$ is known. Fortunately, it is easy to show that using $\hat{u}_2^k$ instead of u_2^k in equations 3.3-13a and 3.3-13c preserves second order accuracy. This is because $\hat{\mathbf{u}}^k$ is a second order approximation to $\mathbf{u}^k$, as can be seen from equation 3.3-22. The final set of equations (given in "correct" order) therefore becomes:

$$\left\{1 - 2\beta_k \Delta t \frac{\partial}{\partial x_2}\left[\nu\frac{\partial \cdot}{\partial x_2}\right] + 2\beta_k \Delta t \frac{\partial u_2^{k-1} \cdot}{\partial x_2}\right\}\hat{u}_2^k = r_2^{k-1} \tag{3.3-23a}$$

$$\left\{1 - \beta_k \Delta t \frac{\partial}{\partial x_2}\left[\nu\frac{\partial \cdot}{\partial x_2}\right] + \beta_k \Delta t \frac{\partial \hat{u}_2^k \cdot}{\partial x_2}\right\}\hat{u}_1^k = r_1^{k-1} \tag{3.3-23b}$$

$$\left\{1 - \beta_k \Delta t \frac{\partial}{\partial x_2}\left[\nu\frac{\partial \cdot}{\partial x_2}\right] + \beta_k \Delta t \frac{\partial \hat{u}_2^k \cdot}{\partial x_2}\right\}\hat{u}_3^k = r_3^{k-1} \tag{3.3-23c}$$

$$\frac{\partial(\phi^k - \phi^{k-1})}{\partial x_i \partial x_i} = \frac{1}{2\beta_k \Delta t}\frac{\partial \hat{u}_i^k}{\partial x_i} \tag{3.3-24}$$

$$u_i^k = \hat{u}_i^k - 2\beta_k \Delta t \frac{\partial(\phi^k - \phi^{k-1})}{\partial x_i}, \qquad k = 1, 2, 3 \tag{3.3-25}$$

At the end of the third sub-step, $k = 3$, the solution at full time-step $n + 1$ is: $u^{n+1} = u^k$. For the first sub-step, $k = 1$, we have that $u^{k-1} = u^n$. Note that the coefficient (i.e. ζ_k) in front of the the term containing u^{k-2} (equation 3.3-4) is zero at the first sub-step ($k = 1$).

Boundary conditions at the intermediate sub-steps are found from linear interpolation of the boundary conditions at time t^n and t^{n+1}. Thus:

$$u_i^k = u_i^n + (u_i^{n+1} - u_i^n)\sum_{l=1}^{k} 2\beta_l \tag{3.3-26}$$

A main novelty of the fractional step method developed above is that the intermediate velocity field, $\hat{\mathbf{u}}^k$, is a second order approximation to the solenoidal velocity field, $\mathbf{u}^k$. Thus, the same boundary conditions can be used for the two

velocity fields without loss of accuracy. This was not the case in, for example, the scheme developed by Kim & Moin (1985), where separate boundary conditions had to be developed for the intermediate velocity field.

3.3.4 <u>Verification of Time Accuracy</u>

Second order accuracy of the numerical scheme was confirmed through computations. By substituting equation 3.3-22 into equation 3.3-20 it can be verified that the scheme has a second order error term associated with the velocity vector. However, an interesting point to note is that the pressure is only estimated to first order accuracy. But, as pointed out by Perot (1993), the order of accuracy of the pressure update does not affect the order of accuracy of the velocity field.

In order to verify the order of accuracy of the scheme, a numerical experiment was conducted using the flow over a backward facing step at low Reynolds numbers. (The backward facing step calculations are described in detail in chapter 4). Several simulations were run starting from a fully developed turbulent flow field at time T_1, advancing to time T_2. The number of time-steps used to cover the given time interval was increased from 1 to 4000. The solution obtained using the smallest Δt was interpreted as the "correct solution". The error in the solutions obtained at increasing Δt was formed by calculating the rms of the difference in the solution for a given Δt when compared with the "exact solution". The result of these calculations is shown in figure 3.3-1. The slope of the curves for all velocity components (in log-log coordinates) is 2, which verifies that the velocity field is calculated to second order accuracy. Likewise it is evident that the pressure is only first order accurate.

3.4 Poisson Equation

The Poisson equation for pressure is solved using a combination of a Fourier transform method and an iterative solution procedure. Since the computational grid is uniform in the spanwise direction, combined with the use of periodic boundary conditions, Fourier transforms can be used to reduce the 3-D Poisson equation to a set of uncoupled 2-D equations. Since the computational grid is non-uniform in both the streamwise and wall-normal directions transform methods cannot be applied in these directions and an iterative technique is therefore used to solve the 2-D equations. The Poisson equation, 3.3-21, can be represented by:

$$\nabla^2 \psi = f, \quad \text{where} \quad \psi = \phi^k - \phi^{k-1}, \quad \text{and} \quad f = \frac{1}{2\beta_k \Delta t} D(\hat{\mathbf{u}}^{n+1}) \tag{3.4-1}$$

The discrete form of equation 3.4-1 is:

$$\left(\frac{\delta^2}{\delta x^2} + \frac{\delta^2}{\delta y^2} + \frac{\delta^2}{\delta z^2} \right) \psi_{i,j,k} = f_{i,j,k} \tag{3.4-2}$$

Fourier transforming in the spanwise direction transforms equation 3.4-1 into a set of 2-D, uncoupled, Helmholtz equations:

$$\left(\frac{\delta^2}{\delta x^2} + \frac{\delta^2}{\delta y^2} - k'_m \right) \hat{\psi}_{i,j,m} = \hat{f}_{i,j,m}, \qquad k'_m = \frac{2}{\Delta z^2} \left[1 - \cos\left(\frac{2\pi m}{N_z} \right) \right] \tag{3.4-3}$$

where m is the wave number, N_z is the number of cells and Δz is the grid spacing in the spanwise direction. For a rectangular domain equation 3.4-3 represents a banded, penta-diagonal matrix. For the "L-shaped" domain of the backward facing step the matrix is smaller, due to the fact that the points inside the step are not included in the solution. The presence of the step also introduces two additional diagonals, making the resulting matrix septa-diagonal. However, the structure of the matrix is still such that any element on the diagonal only has at most four neighbors in either the horizontal or vertical directions. This is illustrated in figure 3.4-1 where the open circles show positions with non-zero elements. The iterative solution procedure applies a modified version of an ADI (Alternate Direction Implicit) technique. When employing a non-uniform grid the stiffness of the matrix

becomes more severe as the degree of stretching of the grid increases. Since the ratio $\Delta x_i^{max}/\Delta x_i^{min}$ (no summation over i) is typically of the order of 100 in the wall-normal direction ($i = 2$) and 10 in the streamwise direction ($i = 1$) it is beneficial to treat the wall-normal direction implicitly at all iteration steps. (This was verified through numerical tests). Discretizing equation 3.4-3 gives:

$$a_1\hat{\psi}_{i-1,j,m} + a_2\hat{\psi}_{i+1,j,m} + a_3\hat{\psi}_{i,j-1,m} + a_4\hat{\psi}_{i,j+1,m} + (a_5 - k_m')\hat{\psi}_{i,j,m} = \hat{f}_{i,j,m} \quad (3.4\text{-}4)$$

where a_i, $i = 1...5$, are coefficients determined using the spatial discretization technique described in section 3.2.3. Letting superscript n denote the iteration index, equation 3.4-4 is solved as follows, requiring a tridiagonal inversion for every i-location:

$$a_3\hat{\psi}_{i,j-1,m}^{n+1} + (a_5 - k_m')\hat{\psi}_{i,j,m}^{n+1} + a_4\hat{\psi}_{i,j+1,m}^{n+1} = \hat{f}_{i,j,m} - a_2\hat{\psi}_{i+1,j,m}^{n} - a_1\hat{\psi}_{i-1,j,m}^{n+1} \quad (3.4\text{-}5)$$

In order to improve convergence, the ADI scheme is combined with SOR (Successive Over Relaxation). The solution of equation 3.4-5 is in this case interpreted as an intermediate solution, $\tilde{\psi}_{i,j,m}$. The solution at $n + 1$ is then found from:

$$\hat{\psi}_{i,j,m}^{n+1} = \hat{\psi}_{i,j,m}^{n} + \omega_m(\tilde{\psi}_{i,j,m}^{n+1} - \hat{\psi}_{i,j,m}^{n}) \quad (3.4\text{-}6)$$

The optimum value of the acceleration parameter, ω_m, is a function of the spanwise wave number, m, and is typically in the range from 1.0 to 1.9. For the problem at hand, which has an irregular geometry and non-uniform grid, the optimum value of ω_m cannot be determined analytically. The optimum values of ω_m are instead found empirically.

As can be seen from equation 3.4-5, the matrix becomes more and more diagonally dominant as the modified wave-number (k_m') increases (a_5 is always negative). With increasing diagonal dominance the number of iterations decreases. Thus, the lowest wave-numbers are the hardest to converge. In fact the equation for the zero wave number required an excessive number of iterations for convergence. In those cases a Cray library routine based on LU-decomposition of the full matrix was employed. (Note that in the case of the zero wave number the singularity in the matrix is removed by prescribing the solution at one point in the domain). However, as the

number of iterations decreases (with increasing wave-number), the iterative solver becomes more cost effective than the direct matrix solver. The direct matrix solver was therefore only used for the zero wave number equation, and in some cases for a few of the lowest wave number equations. A drawback of the direct solver is the requirement to store the LU-decomposition. This has to be done for every wave-number and requires large disk space. Keeping the number of wave-numbers treated with the direct solver to a minimum is therefore also desirable for reduced storage requirement.

Treating only the wall-normal direction implicitly, as well as optimizing the convergence parameter in the SOR scheme at the start of each simulation result in a significant reduction in computational time for the Poisson solver. However, a few other time-saving features are also included:

When Fourier transforming a set of real numbers the result will be complex. The resulting 2-D Helmholtz equations will therefore have to be solved for both the real and imaginary part of the complex numbers. However, since the matrix (formed by the coefficients of equation 3.4-4) stays the same and only the right-hand-side of the 2-D Helmholtz equation is different for the real and imaginary part of $\hat{\psi}$, the number of iterations needed to reach convergence is roughly the same for the real and imaginary part of the solution. The real and imaginary part of $\hat{\psi}$ are therefore solved for simultaneously and convergence checked using only the real part of the solution. This reduces the effort spent checking for convergence, thus reducing the overall CPU time. Convergence is checked by calculating and comparing the rms of the error in the entire computational domain to some pre-defined limit, a procedure involving a significant number of operations.

Since the matrix (formed by the coefficients of equation 3.4-4) only depends on the geometry and the grid, the number of iterations used to reach convergence is roughly the same (for each spanwise wave number) from time-step to time-step. The code therefore keeps track of the number of iterations used (for each spanwise wave number) at each time-step and uses this information to decide when to start checking for convergence at the following time-step. This saves about 90 percent of the calls to the routine checking for convergence, compared with checking for convergence after every iteration step.

In the last stage of this work one more feature was implemented in the solution procedure for the Poisson equation, cutting the total cost for the solver by approximately 50 percent. From equation 3.3-21 it is clear that the Poisson equation has to

be solved at every sub-step of the Runge-Kutta scheme. Thus the Poisson equation is solved three times for every full time step. It turns out, however, that it is not necessary to fully converge the Poisson equation at the two intermediate sub-steps in the RK scheme. Only a few iterations are necessary to get a rough approximation for $\phi^k - \phi^{k-1}$. As a result, the intermediate velocity field, $\mathbf{u}^k$ ($k = 1, 2$) does not strictly satisfy continuity, however this proves not to be important for stability. At the last sub-step ($k = 3$) the Poisson equation is converged to the specified limit, and the velocity-field at each full time-step is divergence free. The "disadvantage" of this approach is that the total error in the solution increases, even though second order temporal accuracy is retained. (This was verified though numerical tests). In fact, the effect on the error is the same as if the time-step was increased. (Similar to the numerical scheme developed by Le & Moin, attempts were made to rewrite the scheme developed in section 3.3 to avoid solving the Poisson equation altogether at the intermediate sub-steps. However, this resulted in numerical instability problems).

3.5 Boundary Conditions

No-slip condition is used along all solid walls which includes the lower boundary of the computational domain, as well as the top boundary for the high Reynolds number case. The flow is assumed to be homogenous in the spanwise direction justifying the use of periodic boundary conditions. The following gives a brief description of the inflow and outflow boundary conditions as well as the no-stress condition used at the top boundary in the low Reynolds number case.

3.5.1 <u>Inflow Condition</u>

The method used by Le & Moin (1994) to generate turbulent inflow data consists of specifying a mean velocity profile, $U(y)$, with superimposed random fluctuations, $u_i''(y, z, t)$ at $x = -L_i$. The mean velocity profile is taken from a flat plate turbulent boundary layer calculation (DNS) performed by Spalart (1988). Since the resulting "turbulence" does not contain any structures, an inlet section is required for the flow to recover and develop realistic turbulence. Le & Moin found that for the DNS calculation about 10 step heights ($L_i = 10h$) was necessary for the flow to recover before reaching the step. For the low Reynolds number LES of the backward facing step it was not possible to make the flow recover in the same distance using this method (see appendix A.2 for details). A separate LES was therefore performed of a spatially developing boundary layer, using a fairly fine grid (see chapter 4). The method used to get inflow turbulence for the boundary layer calculation was the same as that employed by Le & Moin for the backward facing step. A plane of data (velocity vector) was saved at every time-step at the streamwise location where the boundary layer had recovered from the random inflow condition (found by comparing the characteristics of the flow to the DNS results of Le & Moin right upstream of the step). After proper interpolation to account for differences in the resolution of the boundary layer and the backward facing step calculations, this information was fed into the LES of the backward facing step. Since the inflow now consists of developed turbulence, a long inlet section is no longer needed and the inflow boundary condition was therefore imposed at $L_i = 0.3h$.

The high Reynolds number LES, on the other hand, was run using the same inflow method as employed by Le & Moin. It turns out that with the reduced

damping at the high Reynolds number, the flow is better able to recover from the random inflow condition imposed at $L_i = 10h$. The inlet mean velocity profile was in this case determined by fitting the log-law thorough the experimental data from Adams *et al.* (1984).

3.5.2 <u>Outflow Condition</u>

Several outflow boundary conditions were applied to an unsteady separated boundary layer by Pauley *et al.* (1988). For unsteady problems, the convective boundary condition:

$$\frac{\partial u_i}{\partial t} + U_{con}\frac{\partial u_i}{\partial x} = 0 \qquad (3.5\text{-}1)$$

was best suited for convecting structures out of the computational domain. The boundary condition at the exit at time-step $n + 1$ is found by integrating equation 3.5-1, using the Explicit Euler time-marching scheme. The discrete equation is given by:

$$u_{i,j,k}^{n+1} = u_{i,j,k}^{n} - \frac{\Delta t U_{con}}{\Delta x}\left(u_{i,j,k}^{n} - u_{i-1,j,k}^{n}\right), \qquad i = N_x \qquad (3.5\text{-}2)$$

The convective velocity is set equal to the mean streamwise velocity integrated across the exit plane, consistent with the approach used by Le & Moin.

It should be pointed out that in statistically steady flows the convective boundary condition forces the exit streamlines to be parallel to the x-axis, with zero mean wall-normal velocity. Thus, equation 3.5-1 may result in a significant domain of influence around the exit boundary unless $<v>_t$ naturally is close to zero. Calculations done by Le & Moin, and also as part of this work, verifies that at the exit boundary of the backward facing step $<v>_t$ is close to zero, and the effect of the outflow boundary condition extends no more than about one step height upstream of the boundary.

3.5.3 <u>No-Stress Condition</u>

As mentioned in section 3.1, geometrical parameters and boundary conditions in the low Reynolds number case were chosen to match those used by Le & Moin (1994) in their DNS, as well as the experimental setup used by Jovic & Driver

(1994). Jovic & Driver's experimental facility consisted of a double expansion with a channel height of $10h$ upstream of the step, giving an expansion ratio of 1.2. The boundary layer thickness on either wall was about $1.2h$. Calculations by Le & Moin indicate that for an expansion ratio less than approximately 1.33, the upper boundary does not interfere with the free shear layer. Thus, in those cases the region around the centerline (of the double expansion) is characterized by potential flow with small velocity gradients. This provides some justification for the use of no-stress boundary condition in the calculation, allowing for simulation of only half of the symmetric domain used in the experiment. The no-stress condition is given mathematically by:

$$v = 0, \qquad \frac{\partial u}{\partial y} = 0, \qquad \frac{\partial w}{\partial y} = 0 \qquad\qquad (3.5\text{-}3)$$

3.6 Evaluation of Statistical Quantities

Statistical quantities are calculated by averaging over time as well as the homogeneous spanwise direction. Statistical samples are collected at every time-step. In all cases statistics are collected only after the flow has reached a statistically steady state. Because a staggered grid is used problems arise when calculating quantities like $<u''v''>_{tz}$ because the velocity components are given at different locations in the grid. Therefore, all quantities are averaged to the center of the computational cells (where scalar quantities are defined) before sampling statistics. Only mean quantities are calculated during execution of the program. Statistical quantities, like rms values, are evaluated in a post-processing routine. Statistics up to (and including) second order were considered in the present study.
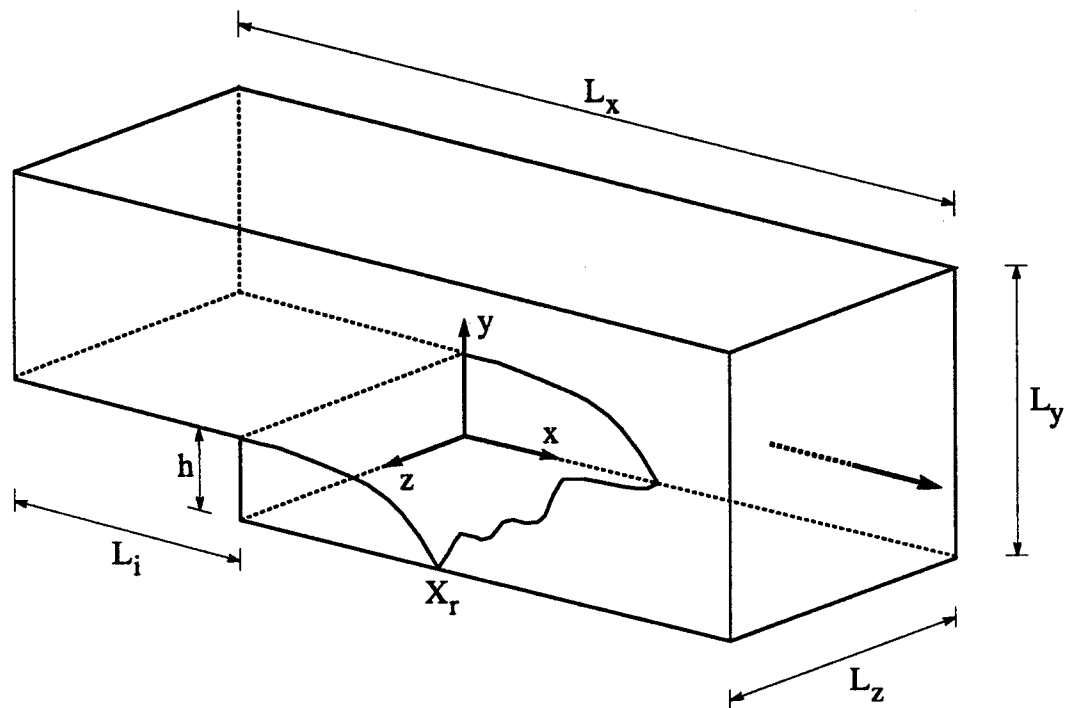
FIGURE **3.1-1**, Computational domain, backward facing step.

(a)

(b)
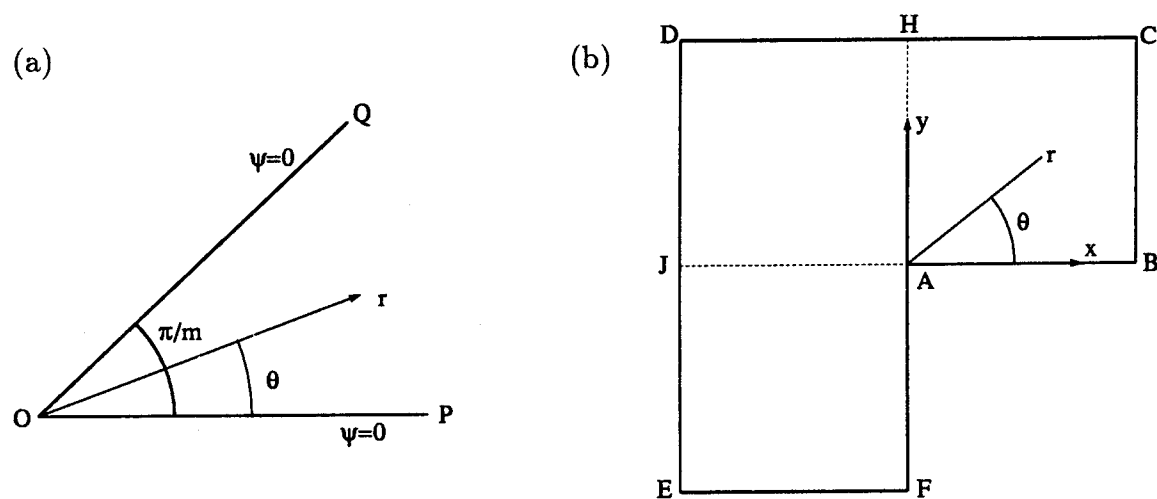
FIGURE **3.2-1**, Problem description, singular corner point example.
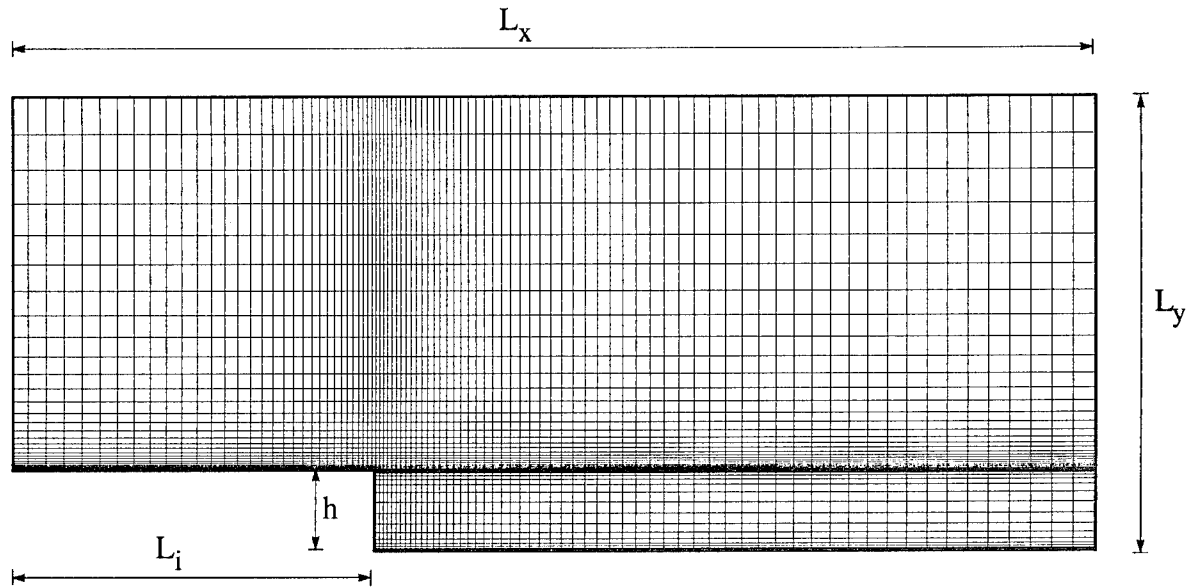
FIGURE **3.2-2**, Example of grid in the streamwise and wall-normal directions.
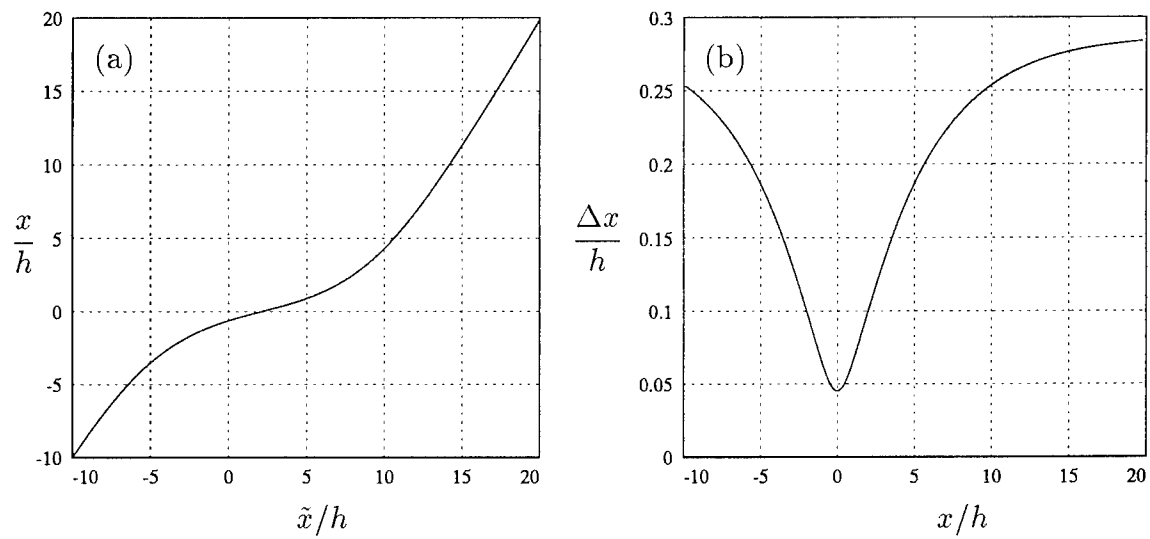
FIGURE **3.2-3**, Stretching function in the streamwise direction.
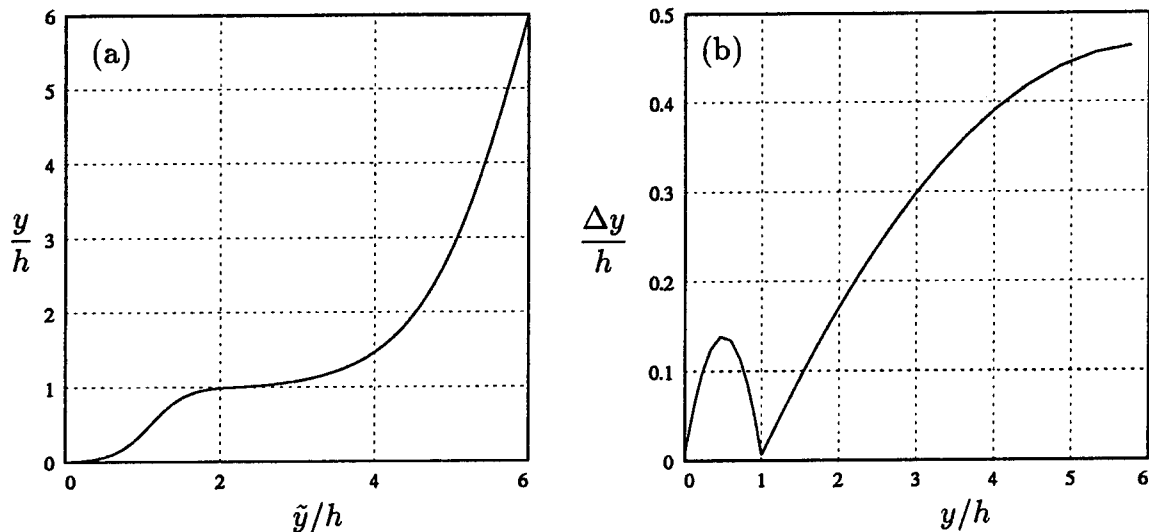
FIGURE **3.2-4**, Stretching function in the wall-normal direction.
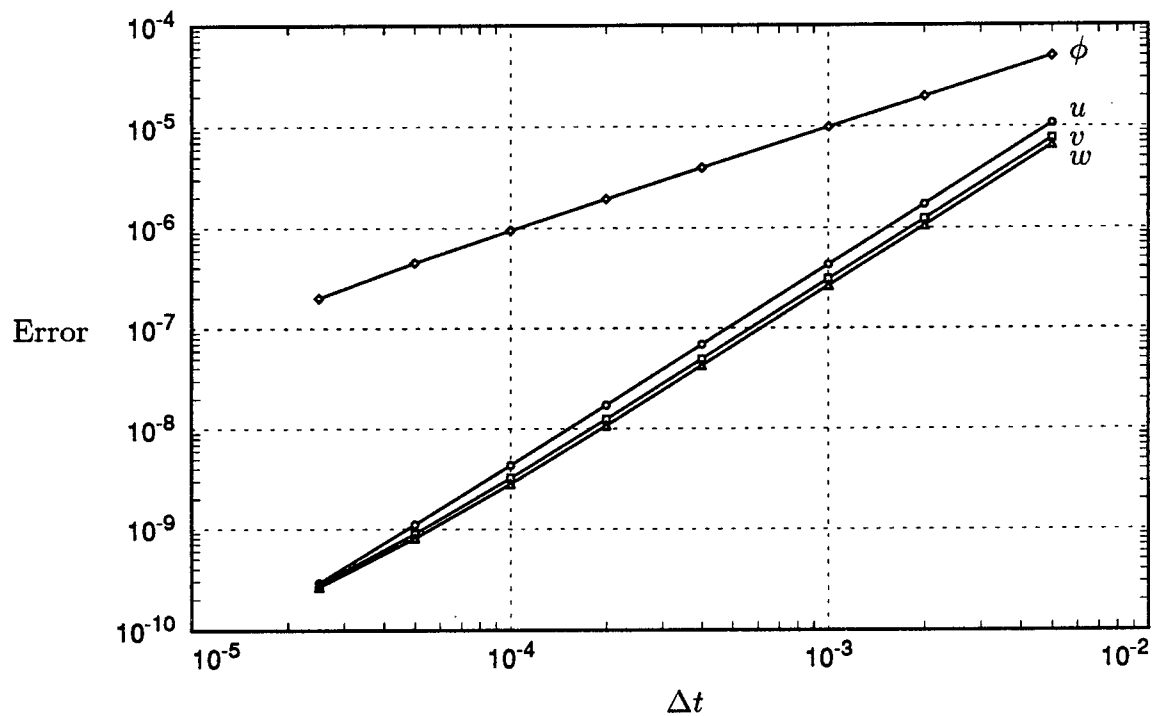
FIGURE **3.3-1**, Temporal accuracy of the numerical scheme.

φ(2,6)
φ(2,7)
φ(2,8)
φ(3,6)
φ(3,7)
φ(3,8)
φ(4,6)
φ(4,7)
φ(4,8)
φ(5,6)
φ(5,7)
φ(5,8)
φ(6,2)
φ(6,3)
φ(6,4)
φ(6,5)
φ(6,6)
φ(6,7)
φ(6,8)
φ(7,2)
φ(7,3)
φ(7,4)
φ(7,5)
φ(7,6)
φ(7,7)
φ(7,8)
φ(8,2)
φ(8,3)
φ(8,4)
φ(8,5)
φ(8,6)
φ(8,7)
φ(8,8)
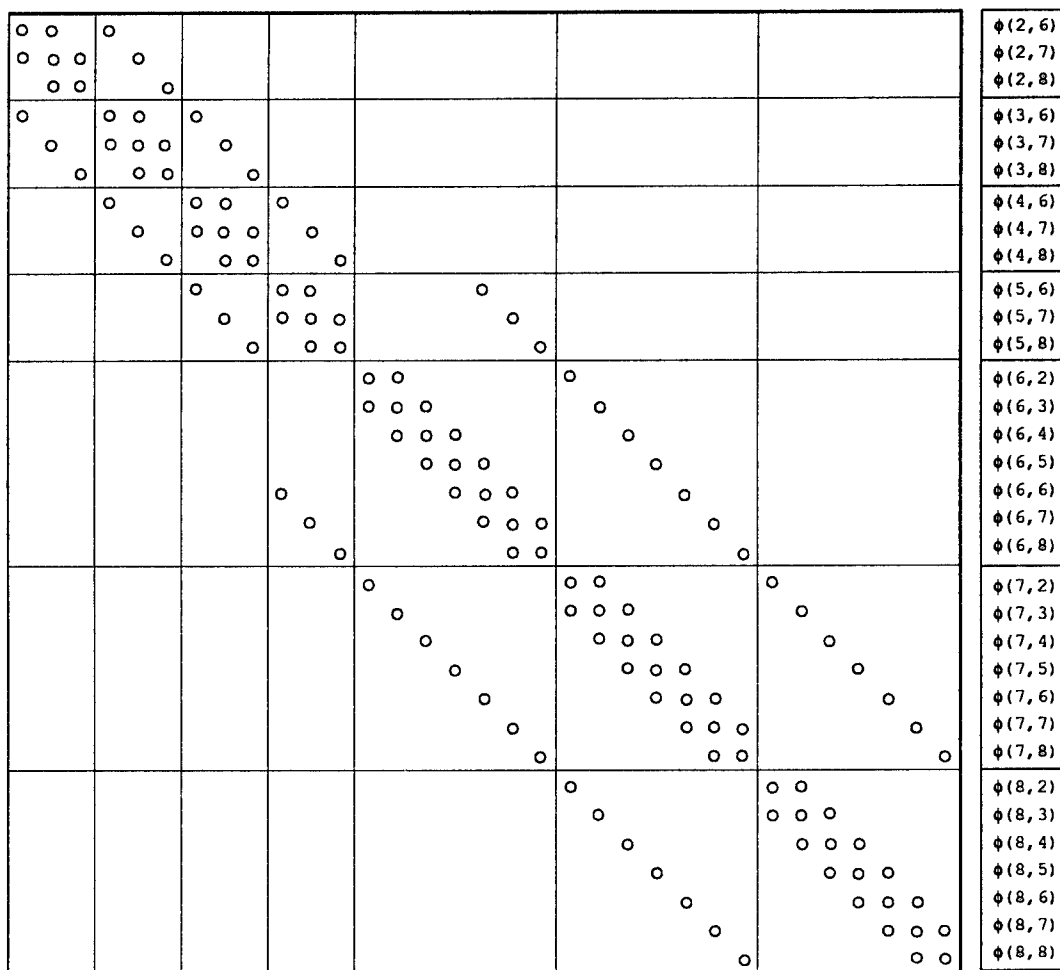
2,8	3,8	4,8	5,8	6,8	7,8	8,8
2,7	3,7	4,7	5,7	6,7	7,7	8,7
2,6	3,6	4,6	5,6	6,6	7,6	8,6
				6,5	7,5	8,5
				6,4	7,4	8,4
				6,3	7,3	8,3
				6,2	7,2	8,2

FIGURE **3.4-1**, Illustration for Poisson Solver.

Chapter 4

RESULTS, LOW REYNOLDS NUMBER CASE

This chapter summarizes the results from the large eddy simulations of turbulent flow over a backward facing step at low Reynolds number. Two studies are used as reference for the large eddy simulations. The first is the direct numerical simulation (DNS) by Le & Moin (1994). The second is an experimental study performed by Jovic & Driver (1994). The experiment, as well as the present large eddy simulations, were designed to match as closely as possible the parameters used in the DNS study. Since Le & Moin have already shown very good agreement between their calculation and the experimental results, the main source of reference for the present study will be the DNS data of Le & Moin. Details of the DNS and the experiments are summarized in section 4.1.

Section 4.2 gives a detailed description of the cases studied. A variety of grid resolutions were studied combined with three different subgrid scale (SGS) models. In addition, one case was run using LES grid resolution, but without a SGS model. A listing of the different cases can be found in section 4.2.3.

Section 4.3 discusses the results obtained at different grid resolutions using the DM model. The main objective is to evaluate the overall performance of the DM model, and to determine its behavior as the resolution changes, i.e. establish convergence towards the DNS results. It is also of importance to determine the minimum grid resolution requirement.

Section 4.4 compares the results from a large eddy simulation using the DM model with similar calculations done using the DLM model (Ghosal *et al.*, 1994) and the Smagorinsky model (1963).

The last section, 4.6, summarizes the performance of the computer code with emphasis on the CPU time associated with solving for the eddy-viscosity using the dynamic subgrid scale modeling approach.

Additional results from large eddy simulations of the backward facing step are included in appendix A. These are mostly from cases computed in the early part of the study that were used to guide the selection of computational parameters in the final calculations. The first large eddy simulations used a uniform distribution of grid points in the streamwise direction. However, it was discovered that it is important to resolve the flow (in the streamwise as well as wall-normal direction) around the corner of the step because of sharp mean gradients and numerical problems associated with the singular corner point. Appendix A.1 shows a comparison of results obtained using uniform versus non-uniform streamwise grids.

As already mentioned in chapter 3, the inflow boundary condition used for the LESs was different than that used for the DNS (Le & Moin). When using the DNS inflow condition in the present calculations, the flow did not recover from the random fluctuations imposed at the inlet. Turbulence stresses, measured at the corner of the step, were significantly under-predicted in large eddy simulations which affected the flow downstream of the expansion. It is apparent that an accurate prediction of the flow downstream of the expansion depends on the ability to have an accurate realization of the flow conditions upstream of the step. Appendix A.2 shows examples of results from the earlier studies using the DNS inflow condition.

4.1 Reference Cases

4.1.1 <u>DNS Case of Le & Moin</u>

The expansion ratio of the computational domain used by Le & Moin was 1.2. Periodic boundary conditions were used in the spanwise direction. No slip condition was used at the lower wall and a no-stress condition at the top boundary. The Reynolds number was 5100 based on step-height, h, and inlet free-stream velocity, U_0. The thickness of the approaching boundary layer was about 1.2 step-heights. A uniform grid was used in the streamwise and spanwise directions and a non-uniform grid was used in the wall-normal direction. The wall-normal stretching function clusters points along the lower wall, both in the inlet section and downstream of the step. A total of $768 \times 192 \times 64$ points were used in the streamwise, wall-normal, and spanwise directions, respectively. The numerical method used by Le & Moin is similar, but not identical, to the method used in the present large eddy simulations. Statistical quantities are calculated by averaging in both the homogenous spanwise direction and time. The total integration time covered more than 320 time units (h/U_0).

4.1.2 <u>Experiments by Jovic & Driver</u>

Jovic & Driver (1994) conducted their experiments in a low speed, suction-driven open-return wind tunnel at NASA Ames Research Center. The experiment was designed to match the geometry and flow conditions used by Le & Moin. The experiment used a double sided expansion with expansion ratio 1.2, the boundary layer thickness on either wall was 1.2 step-heights and the flow at the centerline was therefore essentially undisturbed. The aspect ratio of the tunnel was $L_z/h = 31$. The tunnel side walls were slightly diverged to compensate for the blockage effect due to the boundary layer growth. The boundary layers were tripped approximately $40h$ upstream of the step to ensure that they were fully developed at the point of expansion. The Reynolds number, based on step height and inlet velocity, was 5100. A Laser Doppler velocimeter was used to measure mean velocity and three Reynolds stresses. The coefficient of friction was measured with an Oil-Flow Laser Interferometer.

4.2 Calculation Setup

4.2.1 <u>Geometry</u>

The inflow boundary condition is specified $0.3h$ upstream of the step. The domain extends $20h$ downstream of the step. The height of the domain is $5h$ upstream of the step giving an expansion ratio of 1.2. The spanwise extent of the domain is $4h$.

4.2.2 <u>Boundary Conditions</u>

The inflow boundary condition consists of planes of data, $\mathbf{u}(y, z, t)$, generated by running a separate code calculating a spatially developing boundary layer. Thus, the flow entering the backward facing step domain contains fully developed turbulence, eliminating the need for a long inlet section. The y-z-planes of data from the boundary layer code are stored, and later read by the backward facing step code. The inflow velocity vectors, $\mathbf{u}(y, z, t)$, were generated using one grid resolution, and interpolation was employed in cases where the backstep resolution was different from that used in the boundary layer code.

The boundary layer code is essentially calculating an extended inlet section for the backward facing step. The dimensions of the domain are $25\delta \times 4.2\delta \times 3.3\delta$ in the streamwise, wall-normal and spanwise directions, respectively, where δ is the boundary layer thickness at the inlet of the domain ($\delta = 1.2h$). The inflow boundary condition is the same as that used by Le & Moin in the DNS of the backward facing step. A mean velocity profile (Spalart, 1988) with superimposed random fluctuations is prescribed at the inlet. Because the inflow lacks turbulent structures, the flow goes through a transition before developing normal turbulence. The grid contains $96 \times 31 \times 64$ points in the streamwise, wall-normal and spanwise directions, respectively. The grid in the wall-normal direction is stretched in order to resolve the wall-layer. The grid is uniform in the streamwise and spanwise directions. The DM model (equation 2.2-25) is used to account for the subgrid scale stresses.

Figure 4.2-1 compares the coefficient of friction from the present boundary layer calculation to the coefficient of friction in the inlet section of the backward

facing step DNS of Le & Moin. Also shown is the coefficient of friction obtained by Spalart (1988). It is evident that the flow goes through a transition in the upstream part of the domain before recovering. At $x/h = 10$ the coefficient of friction from the present boundary layer calculation has not yet recovered fully, whereas the DNS of Le & Moin yields an over-prediction (at the step) compared with Spalart's value. The values of the coefficient of friction at $x/h = 10$ are:

Spalart (1988)   : $C_f = 4.834 \cdot 10^{-3}$

Present boundary layer calculation   : $C_f = 4.436 \cdot 10^{-3}$

Le & Moin (1994)   : $C_f = 5.424 \cdot 10^{-3}$

Figure 4.2-2 shows rms profiles at $x/\delta = 8.3$ ($x/h = 10$) from the present boundary layer calculation compared with rms profiles $0.2h$ upstream of the step from the DNS of Le & Moin. Also shown are the rms profiles from Spalart (1988). There is generally good agreement between the profiles.

Based on the excellent agreement between the rms profiles from the boundary layer calculation (taken at $x/\delta = 8.3$) and the rms profiles $0.2h$ upstream of the step from the DNS of Le & Moin, it is deduced that the characteristics of the turbulence in the two cases are similar. Inflow data for the backward facing step calculations was therefore generated by saving y-z-planes of data, taken at $x/\delta = 8.3$, from the developing boundary layer code. This information was later fed into the LES of the backward facing step at $0.3h$, upstream of the step. All backward facing step cases used the same time step (held constant) as that used in the initial boundary layer calculation. This is not strictly necessary, but avoids the additional work of interpolating the inflow data-base in time. Matching the coefficient of friction of Spalart's calculation (or Le & Moin's DNS) was not regarded to be as significant as matching the turbulence statistics. The boundary layer thickness at the corner of the step was approximately $1.2h$, the same as in the DNS of Le & Moin.

4.2.3 Case Definitions

Several simulations of the backward facing step were carried out changing both the grid resolution and the subgrid scale model. As already mentioned, the length of the inlet section used in the LES was only $0.3h$, compared with $10h$ in the DNS study of Le & Moin. Therefore, when comparing the number of grid-points used in the different cases, only the number of points downstream of the step will be

counted in the streamwise direction. The LES cases all used from 6 to 8 points to cover the short inlet section. The DNS case of Le & Moin used 256 uniformly distributed points to cover an extended inlet section.

Table 4.2-1 lists the cases studied. Each case is identified by four characters that will be used throughout this report. The first two characters indicate the subgrid scale model used with DM being the DM model, DL the DLM model, SM the Smagorinsky model, and NM meaning no model. The last two characters indicate the grid used. BA represents the basic resolution. X1 has reduced number of streamwise grid points compared with the basic case, and X2 has more streamwise grid points than the basic case. Y1 and Z1 represent cases with less grid points in the wall-normal and spanwise directions, respectively, compared with the basic resolution. The last case listed in table 4.2-1, DNS, is the DNS of Le & Moin which has been included for comparison.

Case No.	Case ID	Model	N_x	N_y	N_z
1	DMX1	DM	70	48	32
2	DLX1	DLM	70	48	32
3	SMX1	Smagorinsky	70	48	32
4	NMX1	No SGS Model	70	48	32
5	DMBA	DM	112	48	32
6	DMX2	DM	230	48	32
7	DMZ1	DM	112	48	16
8	DMY1	DM	112	29	32
9	DNS	DNS (Le & Moin)	512	192	64

TABLE **4.2-1**, An overview of the cases studied.

The basic resolution is 112 × 48 × 32 points in the streamwise, wall-normal and spanwise directions, respectively. Most of the calculations were, however, run with a reduced number of streamwise grid-points (i.e. 70). In addition, a series of calculations were run using the DM model, but with a systematic change in grid resolution in order to verify that the results converge towards the DNS solution, and also to determine the minimum resolution requirement.

As indicated in table 4.2-1, three different grid resolutions were used in the streamwise direction. The streamwise grid is stretched in order to give a high density of grid points around the corner of the step. The minimum resolution occurs at the corner of the step and is equal to $0.045h$ for all streamwise grids. The uniform streamwise grid spacing used by Le & Moin was $0.039h$. Figure 4.2-3 shows the grid spacing, Δx, as a function of streamwise distance for the three streamwise resolutions (i.e. 70, 112 and 230 points). Figure 4.2-4 shows the wall-normal grid spacing, Δy, versus y/h for the two wall-normal grids used in the present study, as well as for the grid used in the DNS by Le & Moin.

Case No.	Δx^{+}_{min}	Δx^{+}_{max}	Δy^{+}_{min}	Δy^{+}_{max}	Δz^{+}
1-4	8.92	92.9	1.14	91.7	24.7
5	8.92	56.2	1.14	91.7	24.7
6	8.92	24.1	1.14	91.7	24.7
7	8.92	56.2	1.14	91.7	49.4
8	8.92	92.9	2.31	148.3	24.7
9	7.73	7.73	0.23	24.7	12.4

TABLE **4.2-2**, Resolution in wall-coordinates.

The grid resolutions in wall coordinates, given in table 4.2-2, are obtained using the friction velocity at the exit of the computational domain: $u_\tau/U_0 = 3.88 \cdot 10^{-2}$. The minimum streamwise grid-spacing occurs at the corner of the step and the maximum grid-spacing occurs at the exit of the domain.

The initial velocity field was for most of the cases generated by interpolating the final velocity-field from a previous case. After interpolation, the calculation was run for 130 time-units (h/U_0), corresponding to about 5 flow-through times, in order to remove transients resulting from the interpolation. (A flow-through time is defined as the time it takes a fluid particle travelling at the average inlet velocity to pass through the computational domain. For the LES cases one flow-through time corresponds to approximately 25 time-units). Statistics where then sampled at every time-step over a period of 390 time-units (about 15 flow-through times). The time-step, Δt, was kept constant at $0.02h/U_0$.

4.3 Results, DM Model

This chapter describes the results obtained from LESs of the backward facing step using the DM model. Five of the cases listed in table 4.2-1 will be considered. These include the case with basic resolution, DMBA, and each of the cases with reduced resolution in either coordinate direction, DMX1, DMY1 and DMZ1. The last case evaluated is DMX2, which has increased streamwise resolution compared with the basic resolution case, DMBA. Comparison will in all cases be made with the DNS results of Le & Moin.

4.3.1 <u>Characteristics of the Inflow</u>

Figure 4.3-1 shows the turbulence intensities and turbulent shear stress for cases, DMBA, DMX1 and DMX2, compared with DNS (Le & Moin) and results from the boundary-layer code. Figure 4.3-2 gives the same information for the remaining two cases, DMY1 and DMZ1. The wall-normal grid used in the boundary-layer code is identical to the wall-normal grid used in all backward facing step calculations, except DMY1. In the latter case the velocity vector specified at the inlet was interpolated in the wall-normal direction to match the grid of the backward facing step. All backward facing step LES cases used less points spanwise than that used in the boundary layer code. Interpolation of the inflow velocity vector in the spanwise direction was therefore applied in all cases.

From figure 4.3-1 it is seen that the three streamwise grids (DMBA, DMX1, and DMX2) give the same turbulent statistics upstream of the step. However, u''_{rms} has increased and v''_{rms} and w''_{rms} have decreased compared with result from the boundary layer calculation. This is a well known consequence of inadequate grid resolution in numerical simulations of wall bounded flows. The turbulent shear stress on the other hand is unchanged. The change in the turbulence intensities is most likely due to a loss of the smallest scales when interpolating onto the coarser spanwise grid. However, the large scale structures should remain unchanged, and the slight deterioration of the turbulence intensities (caused by the interpolation procedure) is therefore not expected to have a significant influence on the flow downstream of the expansion.

Figure 4.3-2 shows the same trend for cases DMY1 and DMZ1, with the

exception of case DMZ1 (only 16 points spanwise) where the turbulent shear stress has decreased somewhat compared with the boundary layer calculation. But, as will become evident in later sections, this small change does not seem to have a significant impact on the flow conditions downstream of the step.

4.3.2 <u>Coefficient of Friction and Reattachment Length</u>

The coefficient of friction along the lower wall of the domain is defined as:

$$C_f = \frac{\tau_w}{\frac{1}{2}\rho U_0^2}, \qquad \text{or in non-dimensional form :} \qquad C_f = \frac{2}{Re}\left\{\frac{\partial u}{\partial y}\right\}_w$$

where τ_w is the shear stress at the wall and U_0 is the inlet velocity. Figure 4.3-3 shows the coefficient of friction for all five cases, DMBA, DMX1, DMY1, DMZ1 and DMX2, compared with DNS (Le & Moin) and the experimental results from Jovic & Driver. Figure 4.3-4 gives the coefficient of friction for case DMBA in order to include the proper scaling of the vertical axis.

The general impression when studying figure 4.3-3 is that all LES cases agree well with the DNS data except for case DMY1. The latter case shows poor agreement, particularly in the recirculation region (i.e. x/h less than about 6.3). The deviation can most likely be attributed to the use of only 29 wall-normal grid points.

Comparing the three cases with increasing streamwise grid resolution (DMX1, DMBA and DMX2), a slight improvement is observed as the streamwise resolution increases. This is particularly noticeable in the recirculation region. However, note that DMX2 uses more than three times the number of streamwise grid-points used in case DMX1. It can be concluded that the results are close to being independent of the streamwise resolution (to the extent grid independence makes sense in LES) and that convergence towards the DNS data are observed as the streamwise grid is refined.

The last case, DMZ1, with reduced spanwise resolution, also shows overall good agreement with DNS. The quality of this solution is almost as good as DMX1. It is interesting to note that all cases are able to capture the secondary vortex at the lower corner of the step, although it should be noted that the streamwise resolution is fine close to the step in all LES cases.

The reattachment length, X_R, can be found in figure 4.3-3 as the point where the coefficient of friction is zero. The values are summarized in table 4.3-1. Also

included is the deviation from the reattachment length calculated by Le & Moin. A minus sign indicates a shorter reattachment length for the LES compared with DNS. With the exception of DMY1, all resolutions considered give a reattachment length that differs from the DNS value by no more than a couple of percent. The 8.8 percent deviation in the reattachment length for case DMY1 reaffirms the conclusion that the coarsest wall-normal grid is insufficient for the low Reynolds number backstep flow.

	X_R/h	% deviation
Le & Moin	6.28	
Jovic & Driver	6 ± 0.15	
DMX1	6.19	-1.4
DMBA	6.36	1.3
DMX2	6.35	1.1
DMZ1	6.14	-2.2
DMY1	6.83	8.8

TABLE **4.3-1**, Reattachment length for the LES cases.

Based on a comparison of the coefficient of friction and the reattachment length it is evident that the DM model is producing high quality solutions with a minimum number of grid points. In terms of grid resolution the present comparisons indicate that the minimum wall-normal grid is too coarse. However, DMX1, and possibly also DMZ1, show overall good agreement with DNS. Only minor improvements are observed when refining the streamwise or spanwise grids.

4.3.3 Pressure Coefficient

The mean static pressure distribution along the step wall is shown in figure 4.3-5 for case DMBA. A comparison of the five LES cases is given in figure 4.3-6. The pressure coefficient, C_p, is defined as:

$$C_p = \frac{\overline{p} - P_0}{\frac{1}{2}\rho U_0^2}$$

where U_0 is the inlet velocity and P_0 is a reference pressure. When comparing the

DNS and experimental data, Le & Moin used the pressure at $x = -5h$ (upstream of the step) as reference. However, since only a very short inlet section was used in the LES cases, the reference pressure for the DNS and LES comparisons was taken at the corner of the step ($x/h=0$). As with the coefficient of friction, good overall agreement between LES and DNS is observed for all cases but DMY1. The latter case shows a "shift" in the pressure coefficient compared with DNS, similar to the shift observed for the coefficient of friction.

From studying the three cases with increasing streamwise resolution (DMX1, DMBA, and DMX2) it is also evident that the agreement with DNS data gets better as the resolution increases. This is particularly evident in the recovery region (i.e. for x/h larger than about 8). The accuracy of the LES with the coarsest streamwise resolution is most likely adequate for practical engineering purposes. The case with decreased spanwise resolution (DMZ1) shows a larger discrepancy (compared with DNS) in the pressure recovery region than that observed for case DMX1, but the difference is small.

4.3.4 Mean Velocity Profiles

Mean streamwise velocity profiles from cases DMX1, DMBA and DMX2 are compared with DNS data in figure 4.3-7. These are the cases with varying streamwise resolution. Figure 4.3-8 shows the mean streamwise velocity profiles for cases DMY1 and DMZ1. The first six positions, shown in part (a) of the figures, are selected upstream of reattachment (inside the recirculation region), and the last six positions, part (b) of figures, covers the region downstream of reattachment. The corresponding mean wall-normal velocity profiles are shown in figure 4.3-9 for cases DMX1, DMBA and DMX2, and in figure 4.3-10 for cases DMY1 and DMZ1.

Figure 4.3-7 shows a remarkable agreement between LES and DNS results. The LES velocity profiles match the DNS data almost perfectly at all streamwise stations. It is even hard to distinguish between the results from the three LES cases. The profiles at $x/h = 3$ show a slight improvement in the agreement with DNS as the streamwise resolution increases. The same is true at the last four streamwise stations downstream of reattachment. At $x/h = 14$ and $x/h = 16$ in particular, the agreement with DNS is seen to progressively get better as the streamwise resolution increases.

Figure 4.3-9 shows that this conclusion also holds for the mean wall-normal

velocity profiles. While the agreement with DNS seems to be somewhat poorer than for the mean streamwise velocity profiles it should be noted that the mean wall-normal velocity is an order of magnitude smaller than the mean streamwise velocity. Overall, the agreement with DNS data is very good, even for the coarsest streamwise resolution.

Figure 4.3-8 provides a comparison of the mean streamwise velocity between LES and DNS for cases DMY1 and DMZ1. Case DMY1 shows clear deviations from the DNS data, particularly in the near wall region. DMZ1, on the other hand, shows overall good agreement with DNS. The inadequacy of DMY1 become more apparent when examining the mean wall-normal velocity profiles in figure 4.3-10. Poor agreement, compared with DNS, is observed at all, but the last few stations. Case DMZ1 is in better agreement, and considering all streamwise stations, is probably as good as case DMX1, at least downstream of reattachment.

4.3.5 Turbulent Statistics

This section includes profiles of the turbulence intensities and the turbulent shear stress. As explained in chapter 2, only the anisotropic part of the subgrid scale stress tensor is modeled. The isotropic part is lumped together with the pressure in the variable ϕ. Only the resolved part of the turbulence intensities are therefore shown in this section. The subgrid scale part of the turbulent shear stress can on the other hand be calculated from the expression : $\tau_{12} = -2\nu_t \overline{S}_{12}$, and added to the resolved part of the shear stress to give the total turbulent shear stress. The total turbulent shear stress has been used in all comparisons with DNS data.

As will become apparent later in this section, the subgrid scale part of the shear stress is only of the order of a few percent of the total shear stress for the present LES cases. It is therefore reasonable to assume that the subgrid scale part of the turbulence intensities also are small.

Figure 4.3-11 shows the resolved streamwise turbulence intensities downstream of the step for cases DMX1, DMBA and DMX2. The streamwise stations used are the same as those used for the mean velocity profiles (see previous section). The difference between the three LES cases is minimal. The overall agreement with DNS data is good for all streamwise resolutions considered. This is particularly true in the recirculation region. Downstream of reattachment the coarse grid LES

case (DMX1) over-predicts u''_{rms}. However, considering that only a minimal improvement is obtained by tripling the number of streamwise grid-points, the coarse grid solution is adequate.

A comparison of the streamwise turbulence intensity for cases DMY1 and DMZ1 is shown in figure 4.3-12. The agreement with DNS is still fairly good, but DMZ1 seems to over-predict the DNS data close to the wall in the recirculation region, whereas DMY1 over-predicts u''_{rms} downstream of the reattachment. Although the differences are not large, it seems clear that with only 16 points spanwise the grid is too coarse to capture the important near wall-structures of the flow. As already established from comparison of other quantities, the wall-normal resolution in case DMY1 is also too coarse to yield accurate results.

Figure 4.3-13 shows the resolved wall-normal turbulence intensities downstream of the step for cases DMX1, DMBA and DMX2. Again the agreement with DNS data is good for all LES cases. It can be noticed that for x/h larger than about 5, the LES results are lower than the DNS data as the resolution increases. This trend would be expected based on the fact that only the resolved parts of the intensity profiles are included.

Figure 4.3-14 shows the resolved wall-normal turbulence intensities downstream of the step for DMY1 and DMZ1. v''_{rms} is under-predicted below the step in the recirculation region for DMY1. Above the step v''_{rms} is over-predicted. DMZ1 is in good agreement with DNS and the quality of the solution is comparable to that of case DMX1.

The turbulent stress, $<u''v''>_{tz}$, is shown in figure 4.3-15 for cases DMX1, DMBA, and DMX2, and in figure 4.3-16 for cases DMY1 and DMZ1. In figure 4.3-15 the agreement with DNS and LES is very good, particularly in the recirculation region. Downstream of reattachment the coarse grid (DMX1) over-predicts the turbulent shear stress, and there is a clear trend of improved agreement with DNS for increased streamwise resolution. DMY1 and DMZ1 both have problems, particularly in the recirculation region.

Figure 4.3-17 shows the resolved and total turbulent shear stress for case DMX1. It reveals that even for the coarse grid used in case DMX1, the resolved part of the turbulent shear stress is not very different from the total turbulent shear stress. Figure 4.3-18 compares the subgrid scale shear stress, $<\tau_{12}>_{tz}$, for varying streamwise resolution, i.e., cases DMX1, DMBA and DMX2. Figure 4.3-19 shows the same comparison for cases DMZ1 and DMBA. Finally, figure 4.3-20 shows a

measure of the ratio of the subgrid scale shear stress to the resolved turbulent shear stress. The norm, $e(x)$, used to measure the ratio is defined as:

$$e(x) = 100 \times \left\{ \frac{\int_y <\tau_{12}>_{tz}^2 \, dy}{\int_y <u''v''>_{tz}^2 \, dy} \right\}^{1/2} \qquad (4.3\text{-}1)$$

where the integration is carried out over the cross section area of the geometry.

Figure 4.3-18 clearly shows the trend of decreasing SGS model contribution with increasing grid resolution. It it also obvious that the subgrid scale stress is largest in the shear layer just downstream of the step. Downstream of reattachment (i.e for x/h larger than about 7), the subgrid scale stress decreases outside the near wall region. However, close to the wall a peak in the SGS stress indicates boundary layer growth in the recovery region. Figure 4.3-19 shows the same trend with changing spanwise grid resolution. However, contrary to the results in figure 4.3-18, the difference between DMZ1 and DMBA is seen to persist throughout the recovery region.

From figure 4.3-20a it is seen that the subgrid scale stress contributes a maximum of about 8 percent to the total shear stress at $x/h = 1$ (case DMX1). Further downstream of the step the contribution decreases, and is less that 2 percent at $x/h = 16$. This would indicate that the SGS model is most active in the early part of the shear layer. Similar results are also shown for cases DMBA and DMX2. As expected, the contribution from the subgrid scale model decreases with increasing resolution, i.e., the computational grid is able to resolve a larger part of the small scale motion and the dynamic model properly accounts for it. The model contribution to the turbulent shear stress with changing spanwise resolution is shown in figure 4.3-20b. For case DMZ1 the peak value is about 9.5-10 percent, compared with about 6.5 percent for DMBA. In the recovery region the SGS model contribution (case DMZ1) has decreased to 3.5-4 percent. This is about twice the contribution from the SGS model in case DMBA.

Thus, it can be concluded that for the Reynolds number studied, the subgrid scale stresses contribute little to the total turbulent stress. It is also evident that the SGS model correctly predicts a reduction in the SGS stresses as the resolution increases.

4.3.6 <u>Eddy-Viscosity</u>

Figure 4.3-21, shows the effect of changing streamwise resolution (cases DMX1, DMBA and DMX2) on the dynamic eddy-viscosity. The eddy-viscosity has a maximum of roughly 3-3.5 times the molecular viscosity for the coarse grid (DMX1), and a maximum of about 1.5 times the molecular viscosity for the fine grid (DMX2). The eddy-viscosity is seen to attain its highest value in the shear layer, and, as expected, goes to zero at the wall; is rather small close to the step, and increases as the shear layer expands downstream. Most of this effect is probably due to the streamwise grid stretching near the step.

Figure 4.3-22 shows that with changing grid resolution in the wall-normal direction, the eddy-viscosity remains virtually unchanged. However, since test-filtering is applied only in the streamwise and spanwise directions, $C\overline{\Delta}^2$, calculated from equation 2.2-25, should not change significantly when changing the wall-normal resolution. Since the right-hand-side of equation 2.2-25 only contains the ratio of test- to grid-filter widths, it will be insensitive to changes in the wall-normal resolution. Thus, even though $\overline{\Delta}$ changes, the product $C\overline{\Delta}^2$ remains (nearly) unchanged.

Figure 4.3-23 shows the effect of decreasing spanwise resolution on the eddy-viscosity. A very substantial increase in the eddy-viscosity is observed when decreasing the spanwise resolution from 32 to 16 grid-points. The maximum eddy-viscosity is now almost 4.5 times the molecular viscosity.

	% negative $(\nu_t + 1/Re)$	% negative ν_t
DMX1	0.764	11.48
DMBA	0.140	10.47
DMX2	0.046	8.460
DMZ1	1.041	12.83
DMY1	0.189	11.61

TABLE **4.3-2**, Percent of points with negative eddy-viscosity and negative total viscosity (averaged over the homogenous spanwise direction and time).

It can be noticed that the eddy-viscosity goes to zero above roughly $y/h = 4$. Since the DM model vanishes in laminar flow, this indicates a very low, or no turbulent activity in the upper part of the computational domain.

As pointed out in chapter 2, the DM model requires an *ad hoc* "clipping" procedure to remove points of negative total viscosity (sum of eddy-viscosity and molecular viscosity), in order to maintain numerical stability. The number of points with negative total viscosity as well as points with negative eddy-viscosity were counted at each time-step before applying the "clipping" procedure. Table 4.3-2 gives the time averaged values of these measures as percentages of the total number of grid-points in the domain.

It it evident that even for the coarse grids, no more than 1 percent of the grid-points had negative total viscosity at any point in time. The clipping procedure is therefore not thought to have had a noticeable impact on the overall results from the DM model. It should also be pointed out that of the order of 10 percent of the grid-points had negative eddy-viscosity which means that the model does provide for some limited transfer of energy from small to large scales ("back-scatter").

4.3.7 <u>Dissipation</u>

The SGS dissipation can be calculated from : $\epsilon_{SGS} = \nu_t |\overline{S}|^2$, and the molecular dissipation from : $\epsilon_m = |\overline{S}|^2 / Re$. ($|\overline{S}|$ was defined in equation 2.2-2). Figure 4.3-24 shows the ratio of the SGS dissipation to molecular dissipation at several streamwise stations for cases DMX1 and DMBA (different streamwise resolution). Figure 4.3-25 shows the same information for cases DMZ1 and DMBA (different spanwise resolution). $<\epsilon_{SGS}>_{tz} / <\epsilon_m>_{tz}$ is seen to increase with decreasing grid resolution, both in the streamwise and spanwise directions. (The calculations of the dissipation were averaged over only 130 h/U_0, which explains the rather "jagged" appearance of the curves).

Figure 4.3-26 shows the ratio of $<\epsilon_{SGS}>_{tz}$ and $<\epsilon_m>_{tz}$, each quantity averaged over the cross-sectional area of the computational domain, plotted versus streamwise distance. This figure indicates that for DMX1, $<\epsilon_{SGS}>_{tz}$ is almost three times larger than $<\epsilon_m>_{tz}$ at its peak, located at $x/h = 4$-5. Case DMZ1 has a peak value of about 3.5. Notice the similarities between figures 4.3-20 and 4.3-26; Downstream of about $x/h = 8$, cases DMX1 and DMBA yield about the same SGS contribution to both dissipation and shear stress. Differences between the two cases are mostly found upstream of reattachment. However, comparing cases DMZ1 and DMBA, it is clear that the SGS contribution to both dissipation and shear stress is larger for the coarser grid throughout the domain.

4.3.8 <u>Summary</u>

The findings from the DM model simulations can be summarized as follows:

- The DM model yields very accurate results, compared with DNS, using only about 2 percent of the grid-points of a comparable DNS. Even though the finest grid yields the best results, the coarse grid with only one third the streamwise number of grid points as the finest grid gives results with sufficient accuracy for engineering purposes.

- It has been established that the LES results converge toward the DNS solution as the grid is refined. This was particularly evident when studying three cases with increasing streamwise resolution.

- The wall-normal resolution used in case DMY1 is too coarse to yield accurate results. The wall-normal resolution used in all other cases (48 points) seems to be adequate.

- The coarse spanwise grid, DMZ1, yields results in fair agreement with DNS. A minimum of 32 spanwise grid-points are, however, recommended for the present backstep calculations.

- The eddy-viscosity decreases with increasing resolution in directions where explicit test-filtering is applied. However, the eddy-viscosity is virtually unaffected by changes in the grid resolution in directions where no explicit test-filtering is applied.

- For the resolutions studied the maximum eddy-viscosity is of the order of 2 to 4 times the molecular viscosity. The subgrid scale model contributes about 2 to 8 percent of the total turbulent stress, and from 50 to 80 percent of the total dissipation.

- Less that 1 percent of the grid-points have negative total viscosity at any given time-step. Artificially setting the total viscosity to zero at these points is not expected to affect the overall results.

- About 10 percent of the grid-points have negative eddy-viscosity at any given time-step allowing for a limited transfer of energy from small to large scales.

It has been shown that the DM model is capable of accurately predicting turbulent flow over a backward facing step at a low Reynolds number, using only a fraction of the grid-points necessary for DNS. The minimum grid necessary is $70 \times 48 \times 32$ points in the streamwise, wall-normal and spanwise directions, respectively. This is a factor of 60 reduction compared with DNS.

4.4 Comparison of SGS Models

This section shows results from three LES cases, DMX1, DLX1 and SMX1. The only difference between the cases is the subgrid scale model used. The first case, which was also described in the previous section, uses the DM model, the second, DLX1, incorporates the DLM model (Ghosal *et al.*, 1994), and the third, SMX1, uses the standard Smagorinsky model (1963) with $C = 0.01$ (or $C_S = 0.1$), and Van Driest (1956) wall damping.

The grid resolution, as indicated in table 4.2-1, was the same in all cases. The choice of resolution for comparing the subgrid scale models was based on the findings from section 4.3.

4.4.1 C_f, C_p and Reattachment Length

The coefficient of friction from cases DLX1 and SMX1 are compared with the coefficient of friction from case DMX1 in figures, 4.4-1 and 4.4-2, respectively. Although minor differences can be observed, the overall conclusion is that both the DLM model and the Smagorinsky model give results almost identical to that of the DM model.

	X_R/h	% deviation from DNS
DMX1	6.19	-1.4
DLX1	6.12	-2.5
SMX1	6.04	-3.8

TABLE **4.4-1**, Reattachment length for the LES cases.

The same conclusion can be drawn by examining the pressure coefficient, shown in figures 4.4-3 and 4.4-4. Only minor differences can be observed between the different cases, and no claims can be made in favor of any of the models. The reattachment length is given in table 4.4-1. Again, only minor deviations from the DNS results of Le & Moin are observed.

4.4.2 Mean Velocity Profiles

Mean streamwise and wall-normal velocity profiles at several streamwise stations are plotted in figure 4.4-5 and figure 4.4-6, respectively. The mean streamwise velocity profiles are accurately predicted with all three subgrid scale models, at all streamwise stations. The mean wall-normal velocity profiles show only minor differences between the three cases.

4.4.3 Turbulent Statistics

The resolved portion of the streamwise and wall-normal turbulence intensities are shown in figures 4.4-7 and 4.4-8, respectively. As with the mean velocity profiles, all three subgrid scale models give closer to identical results, and all are in close agreement with DNS.

Similar conclusions can be drawn from evaluating the turbulent shear stress, shown in figure 4.4-9. No major differences are found between the three subgrid scale models. All models show an over-prediction of the turbulent shear stress in the region downstream of reattachment.

Figure 4.4-10 shows the subgrid scale part of the turbulent shear stress. The DLM model is seen to give a slightly higher subgrid scale stress than the DM model, but the difference is small. The Smagorinsky model gives a subgrid scale stress of the same order as the two other models. The "kink" observed at $y/h = 1$ is due to refinement of the wall-normal grid around the corner of the step. As is obvious from equation 2.2-43, the definition used for $\overline{\Delta}$ is very sensitive to changes in grid-spacing in either of the coordinate directions. Since the wall-normal grid is very fine around $y/h = 1$, a significant decrease in $\overline{\Delta}$ is observed in this region. (The dynamic models do not have this "problem" since the eddy-viscosity is a function of the *ratio* of test- to grid filter widths).

Figure 4.4-11 shows a measure, $e(x)$, (see equation 4.3-1) of the ratio of SGS shear stress and resolved turbulent shear stress. The DLM model gives a peak (around $x/h = 1$) of about 10 percent compared with about 8 percent for the DM model. Further downstream the contributions from the dynamic models decrease to a few percent. The Smagorinsky model shows a somewhat different trend. The peak in $e(x)$ is about 10 percent, but is located about $0.5h$ downstream of the step. The peak is followed by a sharp drop. A second, local maximum, then follows at about $x/h = 4$. Further downstream the contribution is only a few percent.

4.4.4 <u>Eddy-Viscosity</u>

Eddy-viscosities from the three models are shown in figure 4.4-12 at several streamwise stations. The "kink" in the eddy-viscosity profiles from the Smagorinsky model is clearly discernible and appears for reasons explained in section 4.4.3.

Section 4.3.6 showed that for case DMX1, about 11.5 percent of the points in the computational domain had negative eddy-viscosity (but positive total viscosity) at any given time-step. For case DLX1 the number is 27 percent. Thus the DLM model predicts transfer of energy from small to large scales at more than a quarter of the points in the domain. (Since the model equation has been constrained, the total viscosity is always positive). Thus, even though the DLM model yields higher eddy-viscosity values than the DM model, it also gives a larger transfer of energy from small to large scales.

4.4.5 <u>Dissipation</u>

Figure 4.4-13 shows the ratio of the SGS dissipation to molecular dissipation at several streamwise stations for cases DMX1, DLX1, and SMX1. It is seen that $<\epsilon_{SGS}>_{tz} / <\epsilon_m>_{tz}$ is almost the same at every station for cases DMX1 and DLX1. However, the profiles from SMX1 have the "kink" discussed earlier. The ratio, $<\epsilon_{SGS}>_{tz} / <\epsilon_m>_{tz}$, is a maximum of about 4 for all models.

Figure 4.4-14 shows the total dissipation (SGS dissipation plus molecular dissipation) at the same streamwise stations. Again, the two dynamic models give nearly identical results. Apart from traces of the "kink" at $y/h = 1$, the Smagorinsky model is in good agreement with the two other models.

To better visualize the difference between the three models, figure 4.4-15 shows the ratio of $<\epsilon_{SGS}>_{tz}$ and $<\epsilon_m>_{tz}$, each quantity averaged over the cross-sectional area of the computational domain, plotted versus streamwise distance. Figure 4.4-16 shows the total dissipation averaged over the cross-sectional area and plotted versus streamwise distance.

Figure 4.4-15 shows that the DM model and the DLM model give about the same fraction of SGS dissipation throughout the computational domain. The peak value is about 3 in both cases. In the recovery region the SGS dissipation decreases to about the same level as the molecular dissipation. The contribution from the Smagorinsky model is about the same as from the other models in the recovery

region, but the peak value (upstream of reattachment) is only about 2.2. It is thus interesting to note from figure 4.4-16 that all models give nearly identical total dissipation at all streamwise locations. Lack of SGS dissipation in the Smagorinsky model is made up for by an increase in the molecular dissipation. It should also be noted that the total dissipation in the recovery region is about a factor of four less than the dissipation upstream of reattachment.

4.4.6 <u>Summary</u>

It has been shown that the DM model, the DLM model, and the Smagorinsky model give almost identical results for the backward facing step flow at low Reynolds number. The SGS contribution to the turbulent shear stress is in all cases a maximum of about 8-10 percent. In the recovery region the SGS shear stress is only about 2-3 percent of the resolved turbulent shear stress. However, the Smagorinsky model gives SGS shear stress profiles that are significantly different from those of the dynamic models. All models give the same total dissipation despite the fact that the SGS part of the dissipation is different in the three cases.

4.5 No Model Simulation

This section shows results from a case (NMX1) that was run without a subgrid scale model, using the same grid as that used in DMX1. The objective of the simulation was to get yet another measure of the effect of the subgrid scale model on the flow.

4.5.1 C_f, C_p and Reattachment Length

The coefficient of friction from NMX1 is compared with that from DMX1 and the DNS results of Le & Moin in figure 4.5-1. Discrepancies between NMX1 and DMX1 can be observed, particularly in the recirculation region. The reattachment length is given in table 4.5-1.

	X_R/h	% deviation from DNS
DMX1	6.19	-1.4
NMX1	6.03	-4.0

TABLE **4.5-1**, Reattachment length for the LES cases.

The no-model case is doing a little worse than DMX1 when compared with the reattachment length of the DNS. It is clear that in terms of the coefficient of friction, the subgrid scale model has the largest contribution immediately downstream of the step. From about $x/h = 4$, only minor differences between NMX1 and DMX1 are observed.

The pressure coefficient is shown in figure 4.5-2. It seems that NMX1 yields a better overall agreement, compared with DNS and experiments, than DMX1.

4.5.2 Mean Velocity Profiles

Mean streamwise velocity profiles for cases NMX1 and DMX1 are compared with the DNS data of Le & Moin in figure 4.5-3. Noticeable discrepancies between NMX1 and the DNS data can be observed close to and below the step ($y/h < 1$). Discrepancies between NMX1 and DMX1 (or DNS) can also be observed below about $y/h = 0.5$ in the recovery region.

Figure 4.5-4 shows mean wall-normal velocity profiles at several streamwise locations. In this case it is clear that the no-model case is particularly inaccurate in the recirculation region. However, the agreement improves in the recovery region. This is expected since the subgrid scale model contribution (both in terms of SGS dissipation and turbulent stress) decreases with increasing streamwise distance.

Based on the mean velocity profiles there should be no doubt that the subgrid scale model is affecting the state of the flow, yielding improved agreement with DNS results. It is clear that the model has the largest effect close to the step in the recirculation region. Downstream of reattachment no major differences are seen between NMX1 and DMX1.

4.5.3 Turbulent Statistics

The largest impact of the subgrid scale model can be found by comparing the streamwise and wall-normal turbulence intensities. Figure 4.5-5 reveals large differences in the streamwise turbulence intensities between NMX1 and DMX1. Again the major difference is found in the recirculation region, and just downstream of the reattachment point.

Figure 4.5-6 shows the mean wall-normal turbulence intensity. The difference between NMX1 and DMX1 are largest close to the step and decreases around, and downstream of reattachment. Close to the step the no-model case yields a significant over-prediction of v''_{rms}. However, downstream of reattachment the no-model case agrees better with DNS data than DMX1.

The last quantity considered is the turbulent shear stress, shown in figure 4.5-7. In this case the results from NMX1 and DMX1 are strikingly similar in the recirculation region. Downstream of reattachment, NMX1 is in better agreement with DNS. However, recall from figure 4.3-15 that the turbulent stress was over-predicted downstream of reattachment for DMX1. Upon refining the grid the calculated stress was seen to move close to the DNS results. Thus, the apparently good agreement between NMX1 and DNS downstream of reattachment may be fortuitous and disappear with grid refinement.

4.5.4 <u>Dissipation</u>

It is of interest to compare the total dissipation between the LES and no-model case. (For the no-model case the total dissipation is equal to the molecular dissipation). Figure 4.5-8 shows this quantity averaged over the cross-sectional area of the computational domain, plotted versus streamwise distance. It is clear that the no-model case significantly over-predicts the total dissipation upstream of about $x/h = 3$-3.5. Further downstream an under-prediction is observed.

4.5.5 <u>Summary</u>

From the results presented in the previous sections it is apparent that the subgrid scale model has an appreciable impact on the flow. Several profiles show rather poor agreement with DNS without the subgrid scale model. Activating the DM model improves the agreement with DNS, particularly in the recirculation region.

The results indicate that the turbulence intensities are more sensitive to whether the subgrid scale model is present than the mean velocity components. The case without a subgrid scale model does in general over-predict both u''_{rms} and v''_{rms}. The dissipation is also significantly over-predicted immediately following the step.

4.6 Performance of the Computer Program

As indicated previously, all LES cases were run using a fixed time-step of $\Delta t = 0.02$ time-units (h/U_0). Each case was run 130 time-units (about 5 flow-through times) in order to remove transients resulting from the interpolation process used to generate the initial flow fields. Statistics were then collected over a period of 390 time-units (about 15 flow-through times). This corresponds to a total of 26000 time-steps for each simulation.

A similar calculation was run in order to generate the inflow boundary condition used for the backward facing step calculations. The boundary layer calculation was run at $\Delta t = 0.02$ (matching the time-step for the backward facing step calculations) for a total of 650 time-units. Note that the boundary layer calculation was only run once, generating inflow boundary conditions used by all backward facing step cases.

Case ID	T_1	T_2	T_3
DMX1	0.873	$7.7 \cdot 10^{-6}$	6.30
DLX1	1.138	$1.0 \cdot 10^{-5}$	8.22
SMX1	0.788	$7.0 \cdot 10^{-6}$	5.69
NMX1	0.758	$6.7 \cdot 10^{-6}$	5.47
DMBA	1.220	$6.8 \cdot 10^{-6}$	8.81
DMX2	2.190	$6.1 \cdot 10^{-6}$	15.82
BLAY	0.643	$3.4 \cdot 10^{-6}$	5.72

TABLE **4.6-1**, LES code performance parameters (Cray C-90). T_1 gives CPU time per time step (in seconds), T_2 gives CPU time (seconds) per time-step and node, and T_3 gives total CPU time to run the case (in hours).

Table 4.6-1 gives the performance of the LES code on a Cray C-90 super-computer in terms of CPU time per time-step for a few selected cases. Also given is the total CPU time (hours) spent for the full 520 time units used to get converged statistics. Case, BLAY gives the data for the boundary layer calculation, which was run a total of 32500 time-steps, corresponding to 650 time-units.

The numbers in table 4.6-1 do not take into account the overhead associated with I/O (input/output). With the current structure of the code the overhead was about 20 percent. This could, however, be significantly reduced by restructuring the code.

The overhead associated with the subgrid scale model, i.e. calculating the eddy-viscosity, can be deduced from the data in table 4.6-1. The following is the overhead associated with evaluating the subgrid scale model, compared with the case run without a model:

Smagorinsky model	:	4.0 %
DM model	:	15.2 %
DLM model	:	50.2 %

The large overhead associated with the DLM model is due to the iterative solver needed for the integral equation (see equation 2.2-35). An average of 4.3 iterations were needed per time-step to drop the residual in the integral equation by two orders of magnitude. Tests showed that reducing the residual even further did not alter the results noticeably. Thus, considering the overhead associated with the subgrid scale models, there is a considerable incentive for using the DM model instead of the DLM model.

Le & Moin report that their DNS consumed about 21.8 CPU seconds per time-step. They used a fixed time-step of $\Delta t = 0.0018\ h/U_0$, corresponding to a CFL number of about 1.2. Since the numerical algorithms used in the DNS and LES codes are different, it is impossible to take the difference in the CFL numbers properly into account when comparing the costs. It should also be pointed out that the computational domain of Le & Moin included a significant inlet section upstream of the step, which was not used in the LES cases. Accounting for this difference implies that the DNS code spent about 17.3 CPU seconds per time-step computing the region downstream of the step. Thus, the comparison of costs of LES and DNS assumes that a data-base of inflow data already exists for both cases. In order to cover 520 time-units, the DNS calculation will then require about 1380 CPU hours. (As in the LES cases, the overhead associated with I/O is not included in this number). This means that case DMX1, which was shown to give good results compared with DNS, requires only about 0.5 percent of the CPU time needed for the DNS calculation.
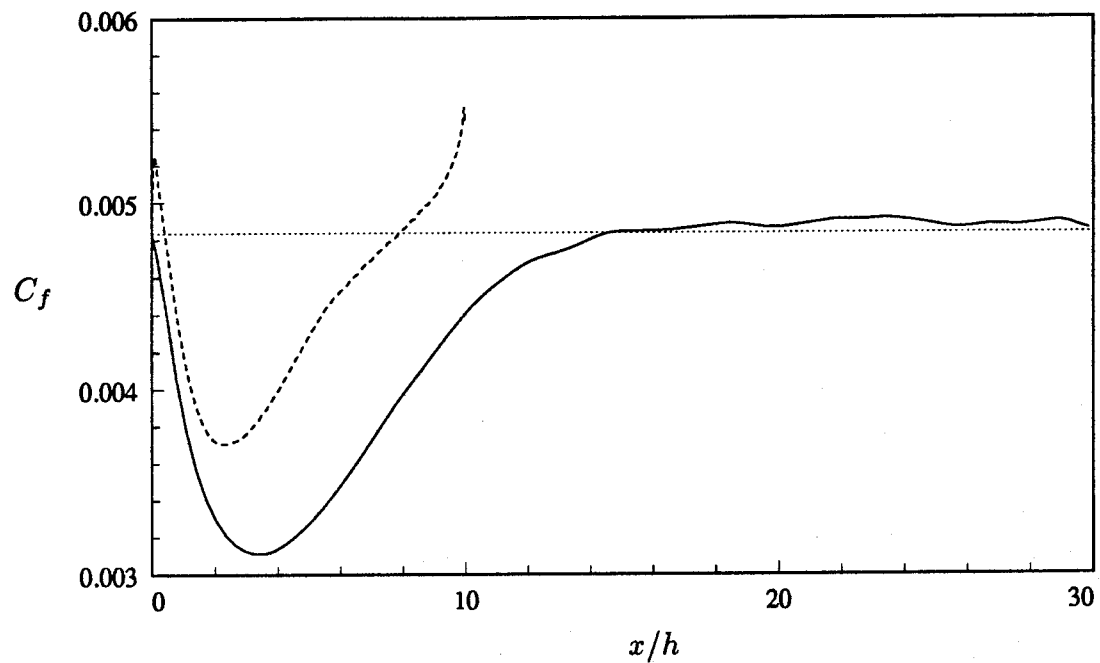
FIGURE **4.2-1**, Coefficient of friction (along the lower wall). ——— : LES of developing boundary layer; ---- : DNS of Le & Moin (upstream of the step); ········ : Spalart (1988).
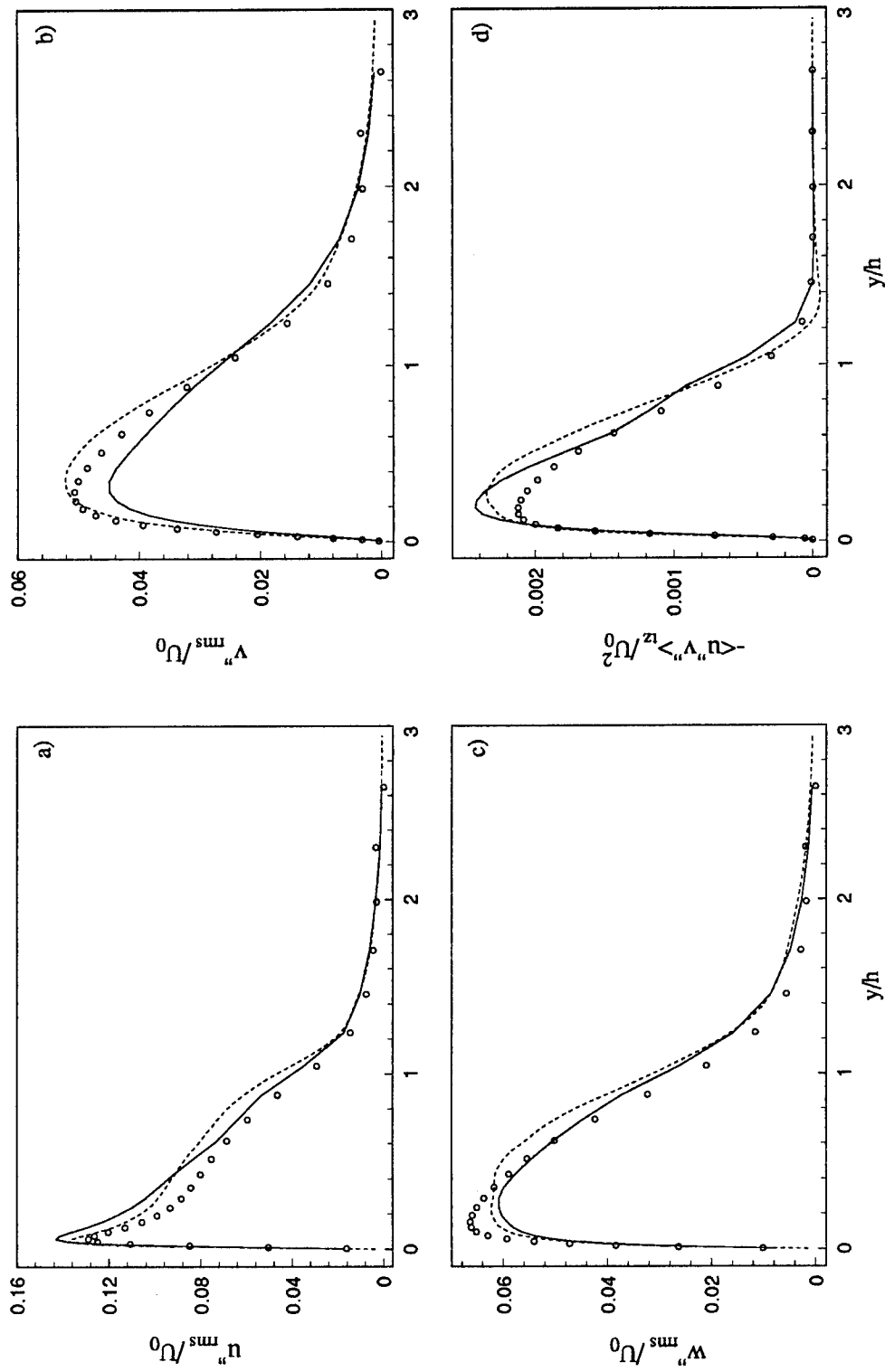
FIGURE **4.2-2**, Turbulent statistics. ———: LES of developing boundary layer ($x/\delta = 8.3$); – – – : DNS of Le & Moin ($x/h = -0.2$); o Spalart (1988). a) u''_{rms}, b) v''_{rms}, c) w''_{rms}, d) Turbulent shear stress (including SGS term).
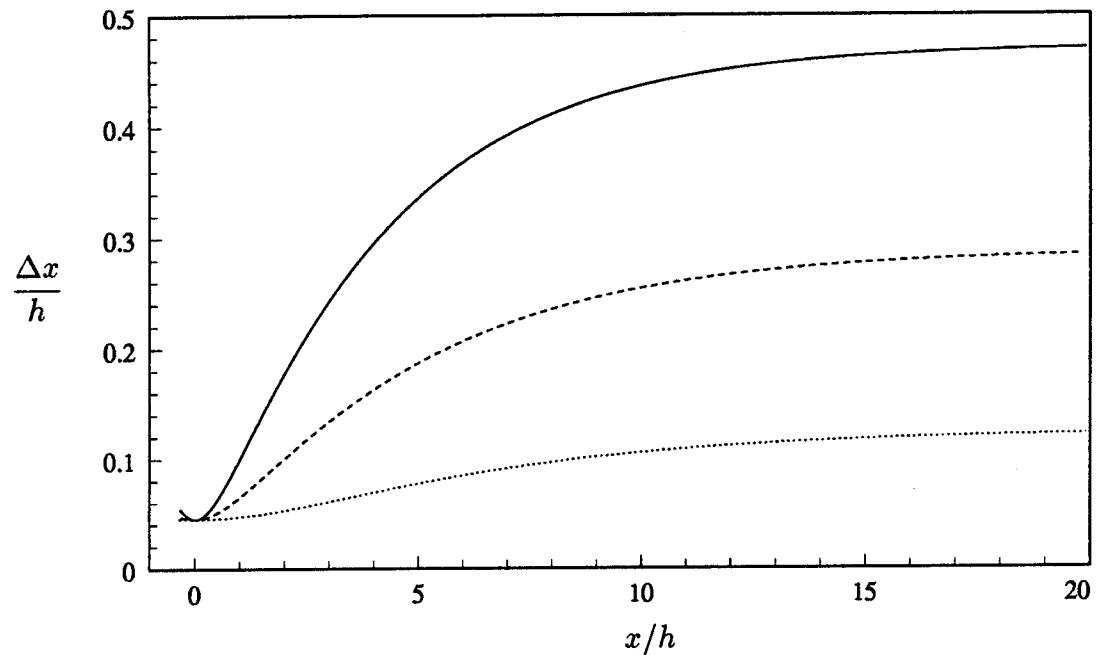
FIGURE **4.2-3**, Streamwise grid spacing versus streamwise distance.

——— : $N_x = 70$;   - - - - : $N_x = 112$;   ········· : $N_x = 230$.
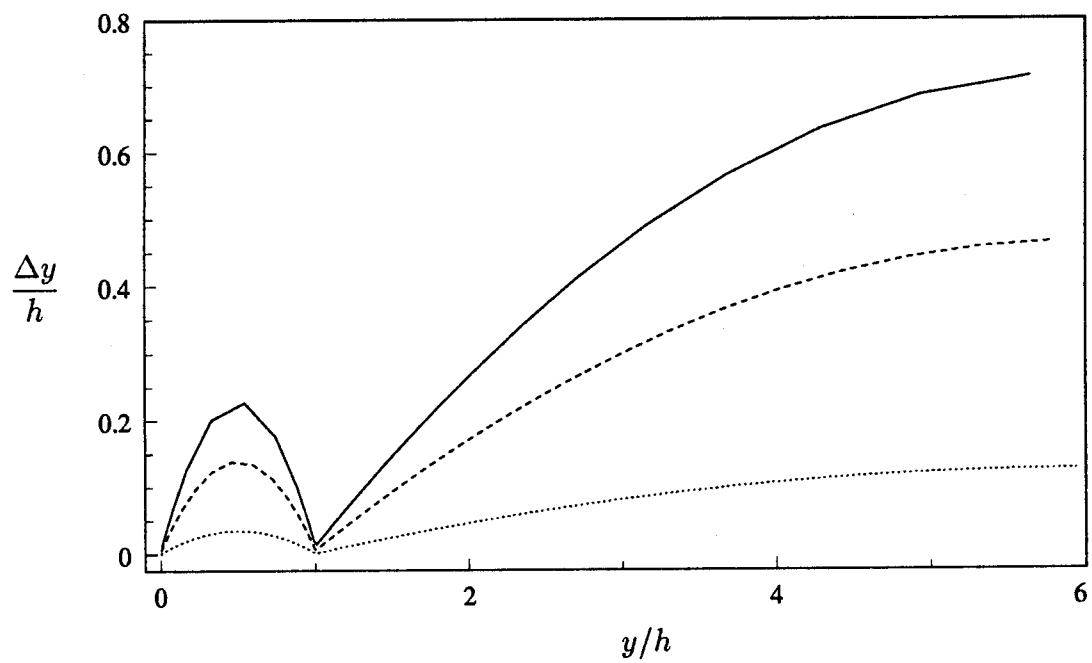
FIGURE **4.2-4**, Wall-normal grid spacing versus wall-normal distance.

——— : $N_y = 29$;   - - - - : $N_y = 48$;   ········· : $N_y = 192$ (Le & Moin).
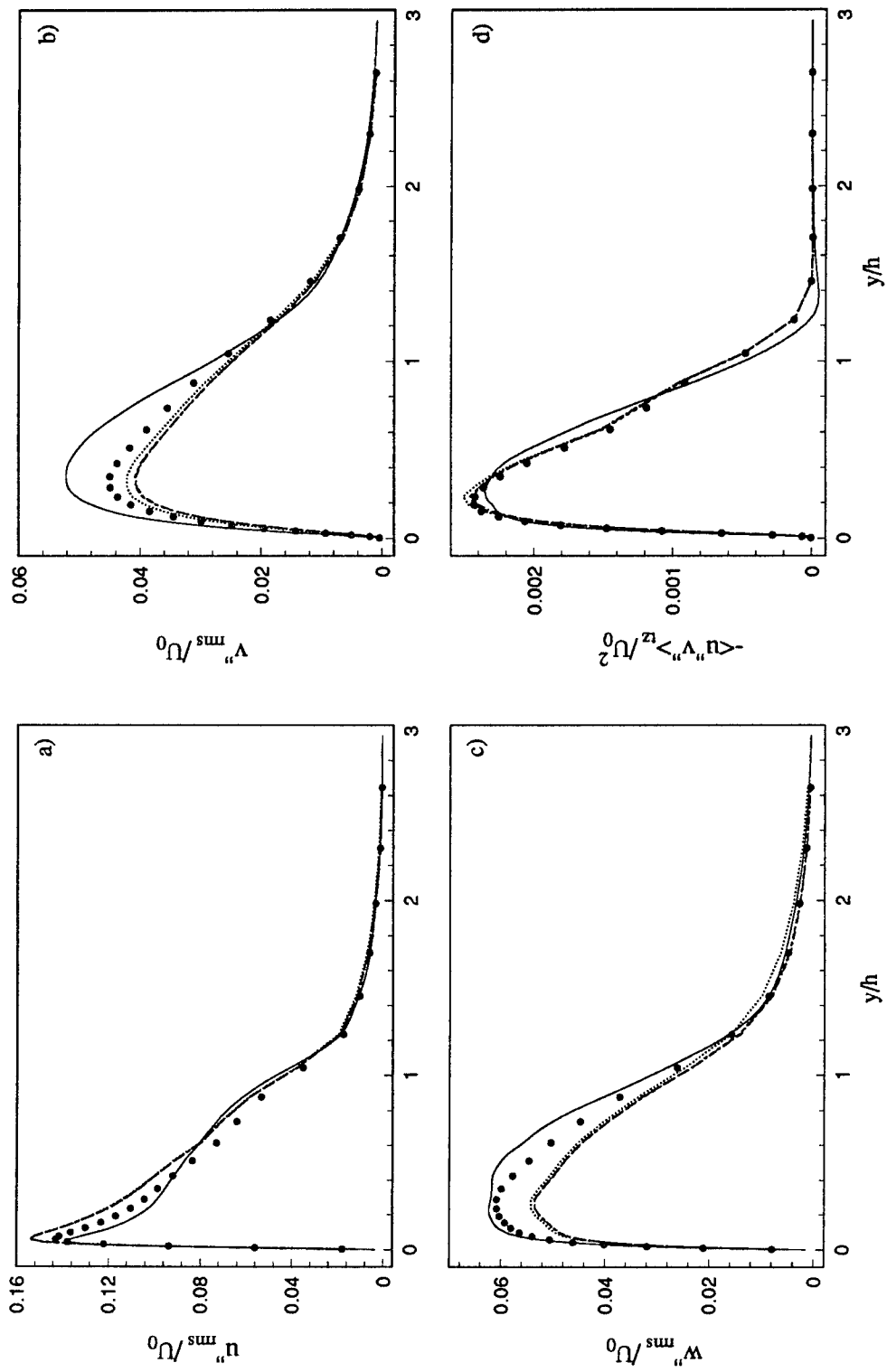
FIGURE **4.3-1**, Turbulent statistics 0.2*h* upstream of the step.   – · – : DMBA;   ······· : DMX1;
— · — : DMX2;   —— : DNS.   ● : LES of developing boundary layer ($x/\delta = 8.3$);   a) u''_{rms},   b) v''_{rms},
c) w''_{rms},   d) Turbulent shear stress (including SGS term).
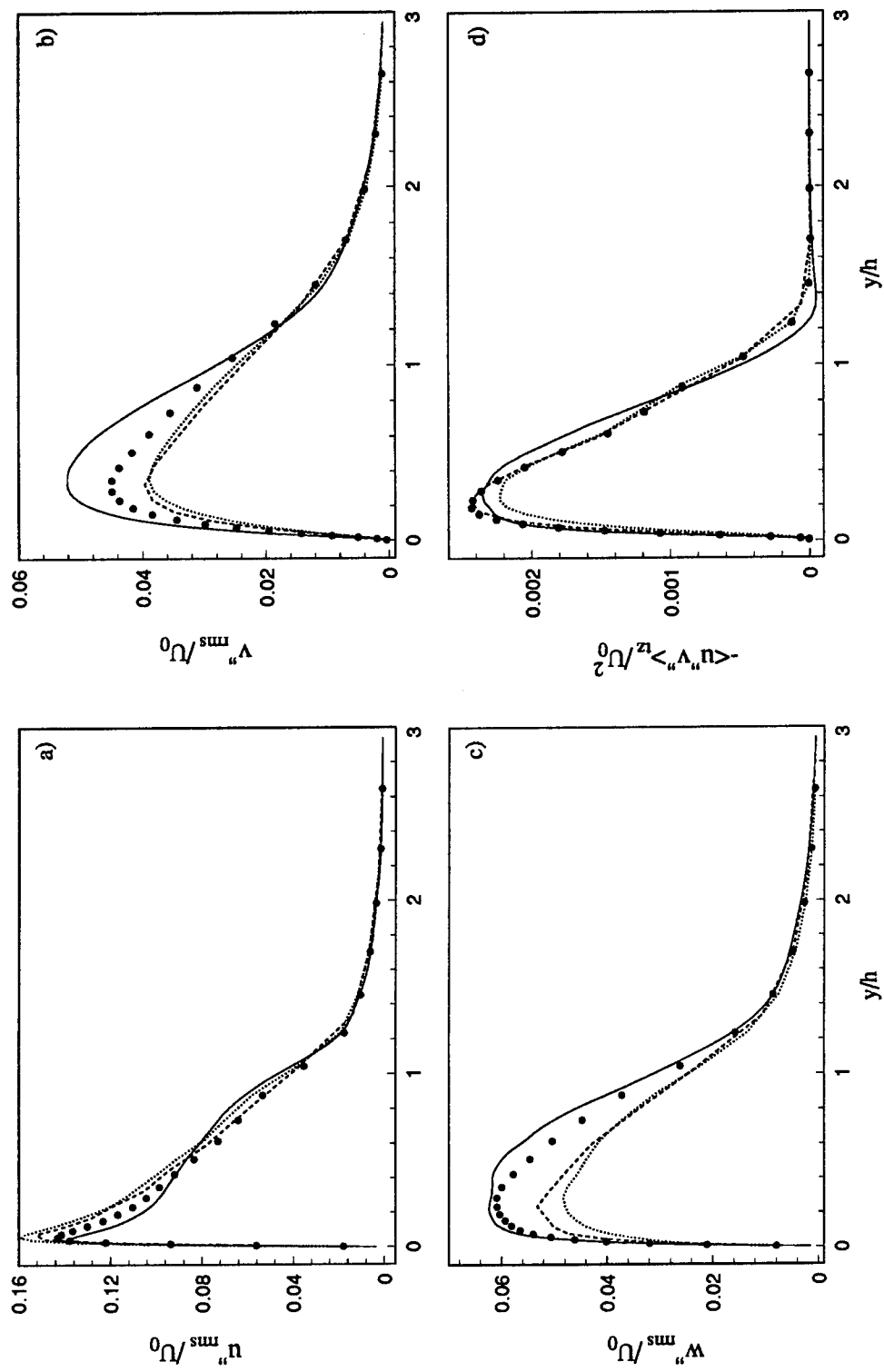
FIGURE **4.3-2**, Turbulent statistics $0.2h$ upstream of the step. $---$: DMY1; $\cdots\cdots$ DMZ1; ——— : DNS. ● : LES of developing boundary layer ($x/\delta = 8.3$); a) u''_{rms}, b) v''_{rms}, c) w''_{rms}, d) Turbulent shear stress (including SGS term).
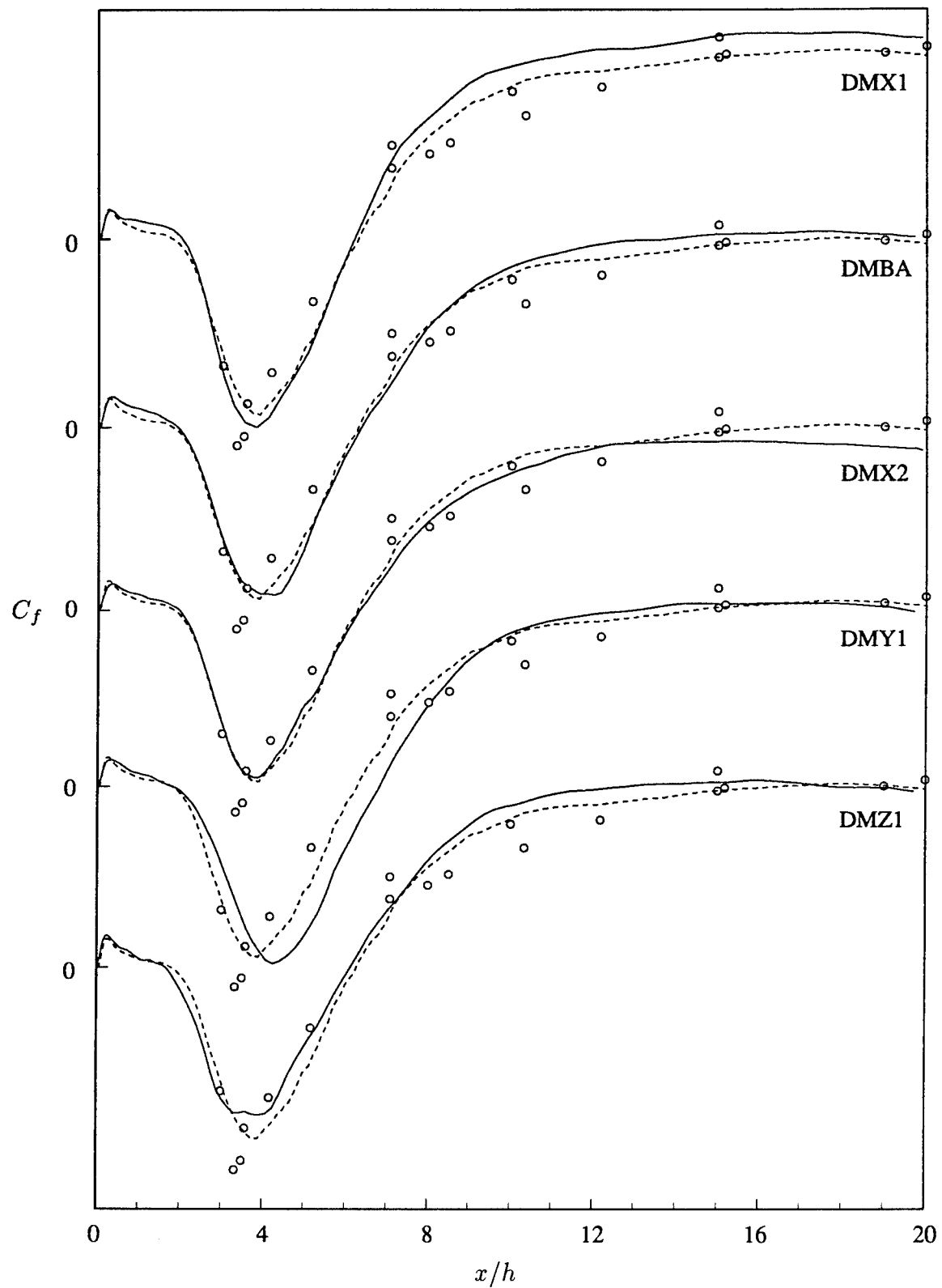
FIGURE **4.3-3**, Coefficient of friction along the lower wall, downstream of the step.
———— : LES; - - - - : DNS (Le & Moin); o : Experiment (Jovic & Driver).
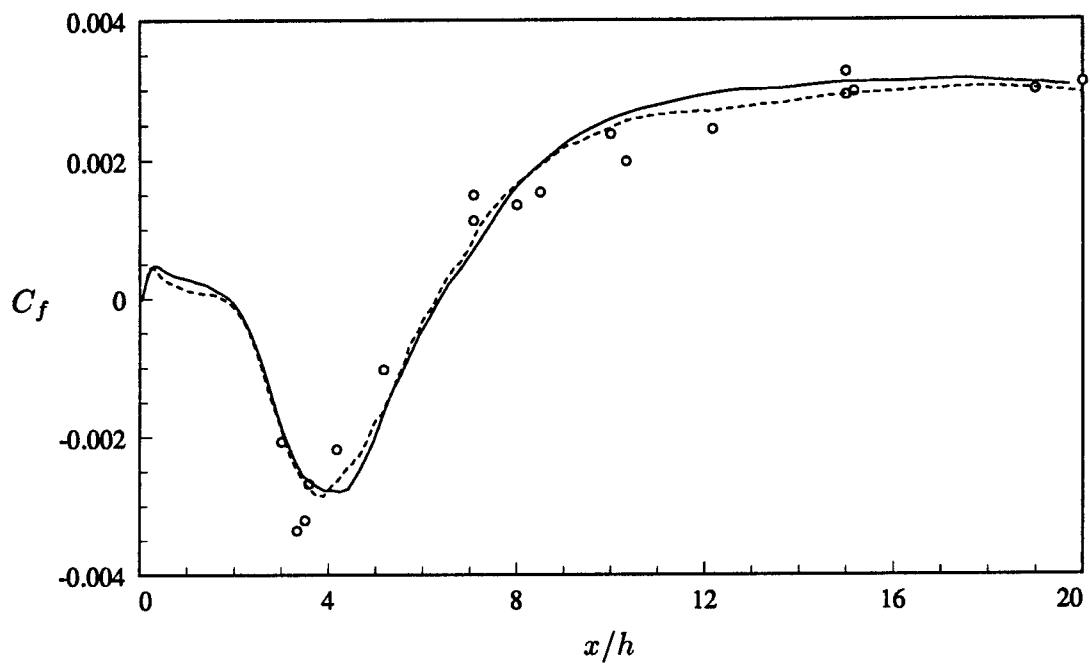
FIGURE **4.3-4**, Coefficient of friction along the lower wall, downstream of the step for case DMBA. ——— : LES; - - - - : DNS (Le & Moin); o : Experiment (Jovic & Driver).
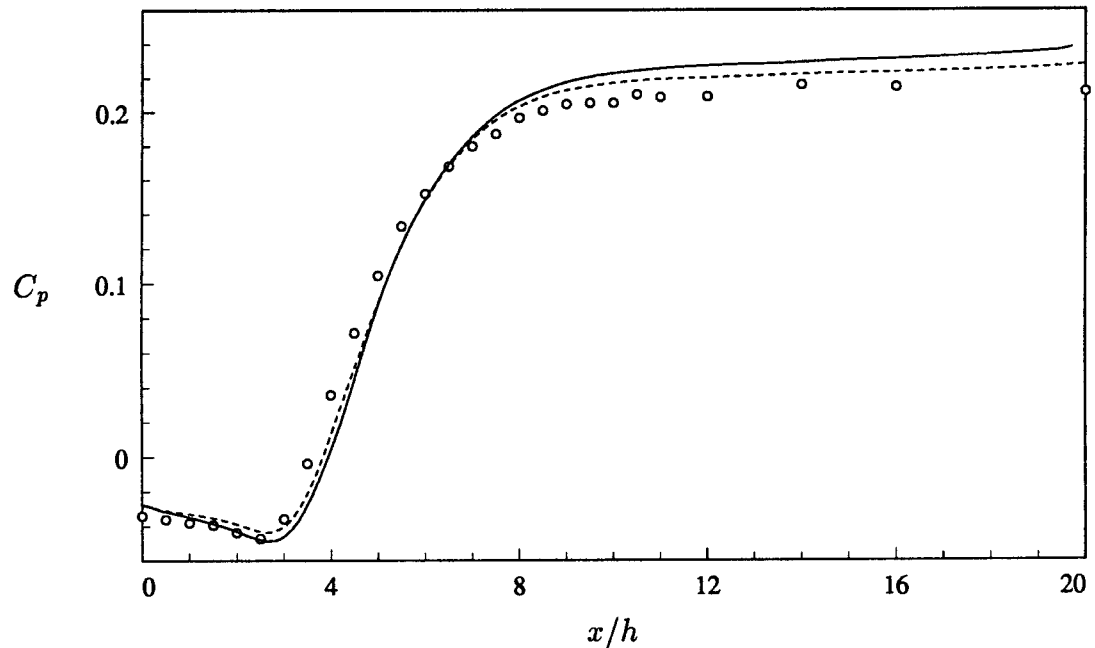
FIGURE **4.3-5**, Pressure coefficient along the lower wall, downstream of the step for case DMBA. ——— : LES; - - - - : DNS (Le & Moin); o : Experiment (Jovic & Driver).
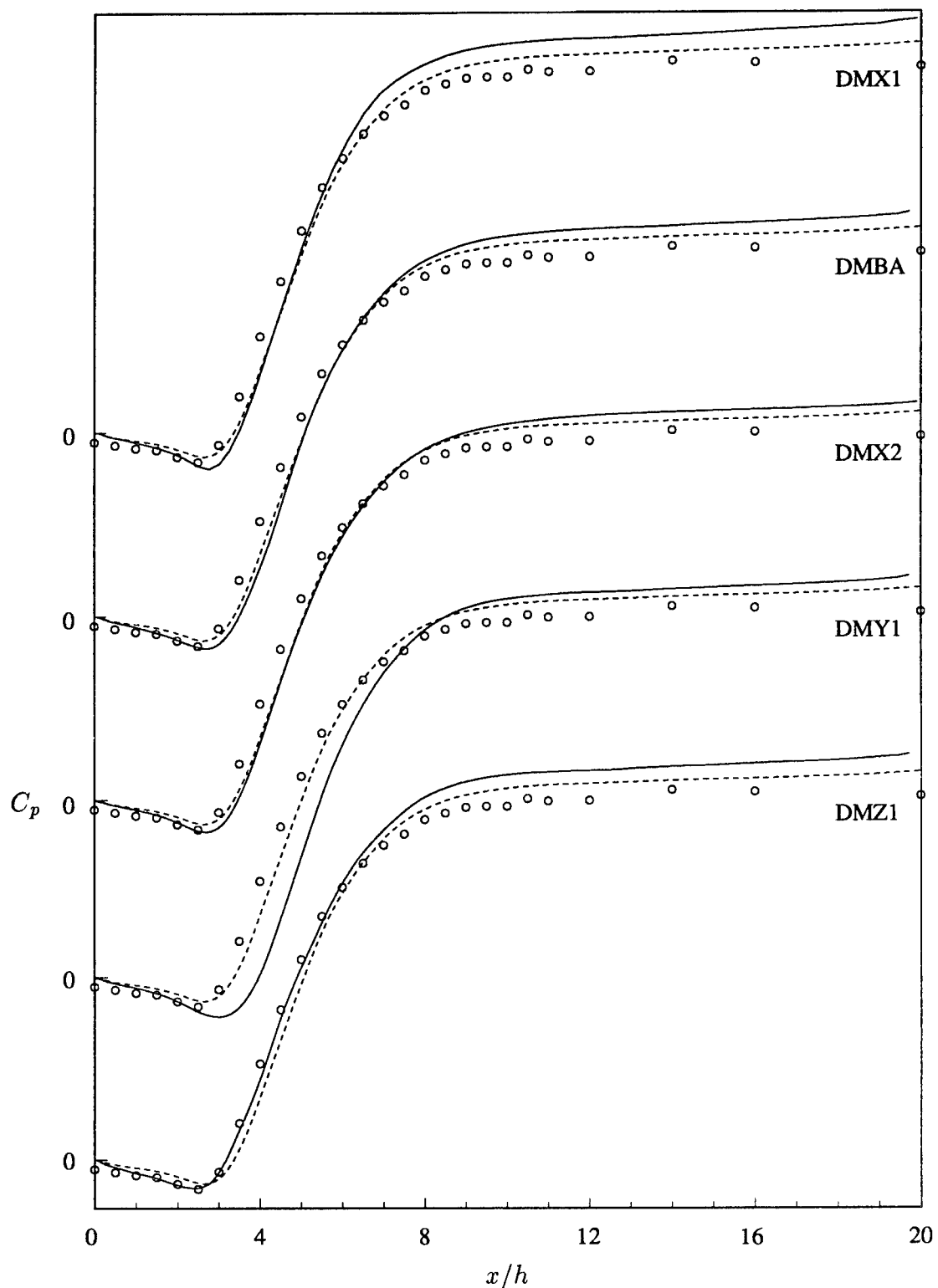
FIGURE **4.3-6**, Pressure coefficient along the lower wall, downstream of the step.
———— : LES;   - - - - : DNS (Le & Moin);   o : Experiment (Jovic & Driver).
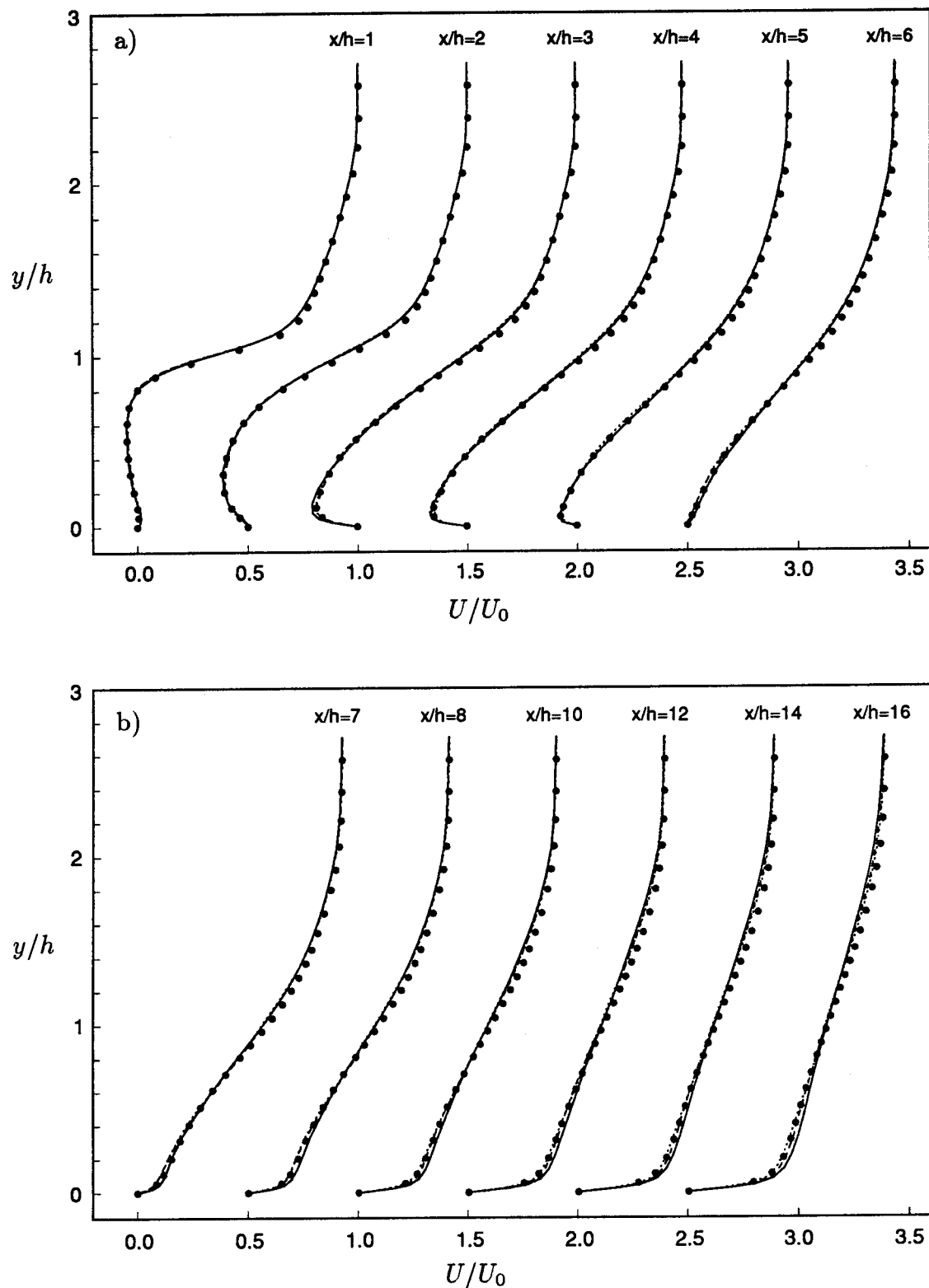
FIGURE **4.3-7**, Mean streamwise velocity profiles. ——— : DMX1;
———— : DMBA; ········ : DMX2; • : DNS. a) $x/h = 1 - 6$, b) $x/h = 7 - 16$.
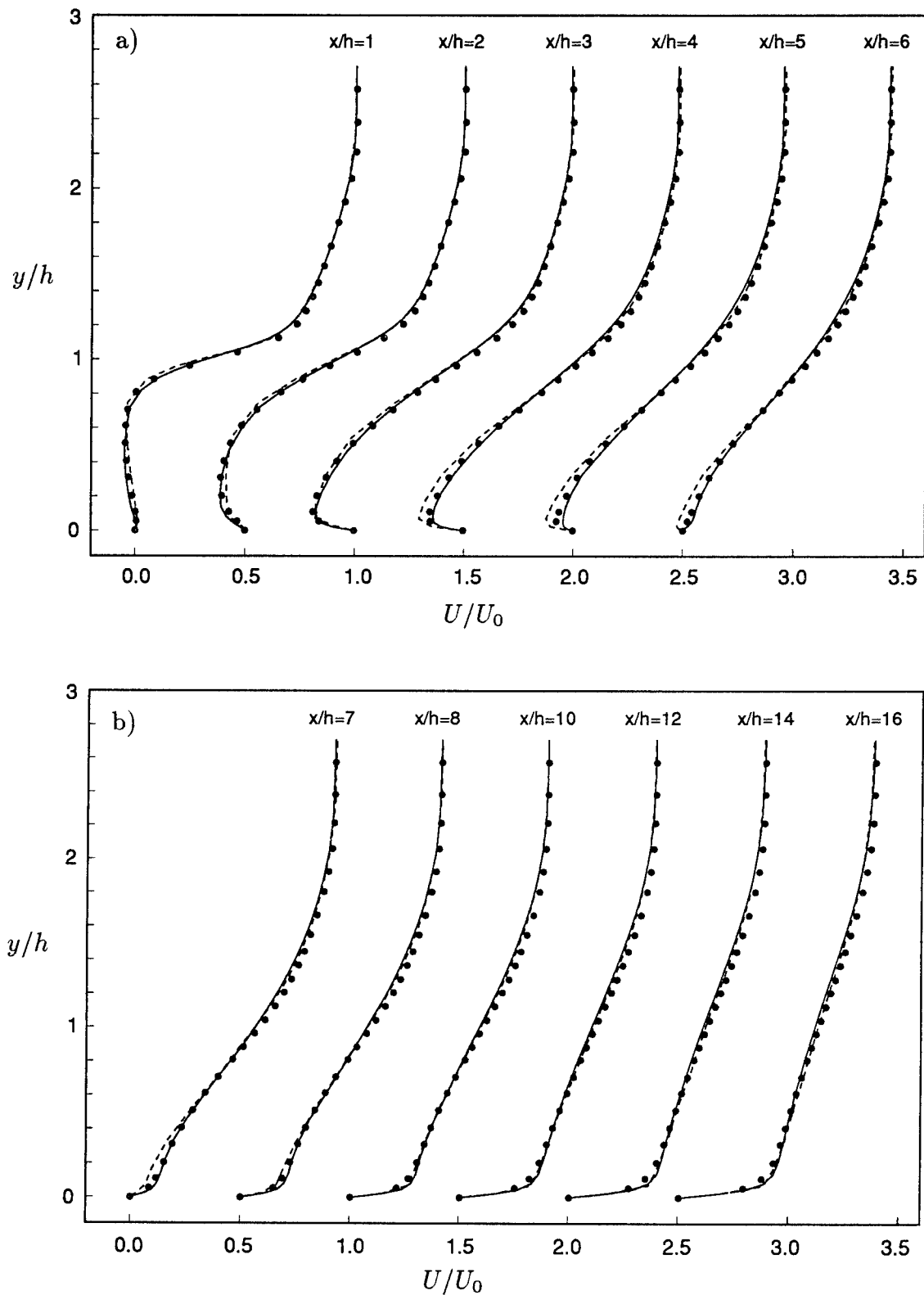
FIGURE **4.3-8**, Mean streamwise velocity profiles. ——— : DMZ1;
---- : DMY1;   ● : DNS.   a) $x/h = 1 - 6$,   b) $x/h = 7 - 16$.
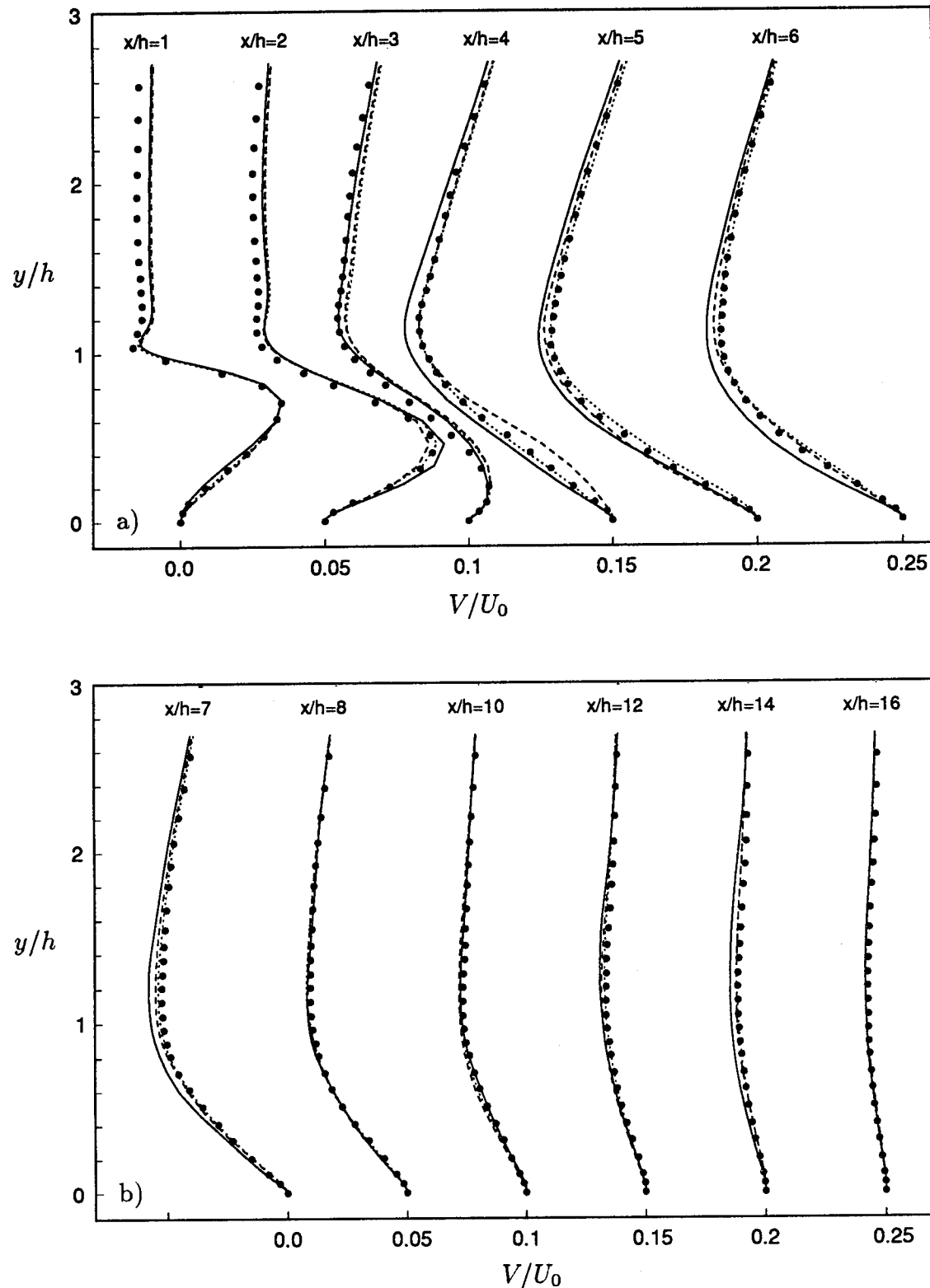
FIGURE **4.3-9**, Mean wall-normal velocity profiles. ——— : DMX1;
---- : DMBA; ········· : DMX2; • : DNS. a) $x/h = 1 - 6$, b) $x/h = 7 - 16$.
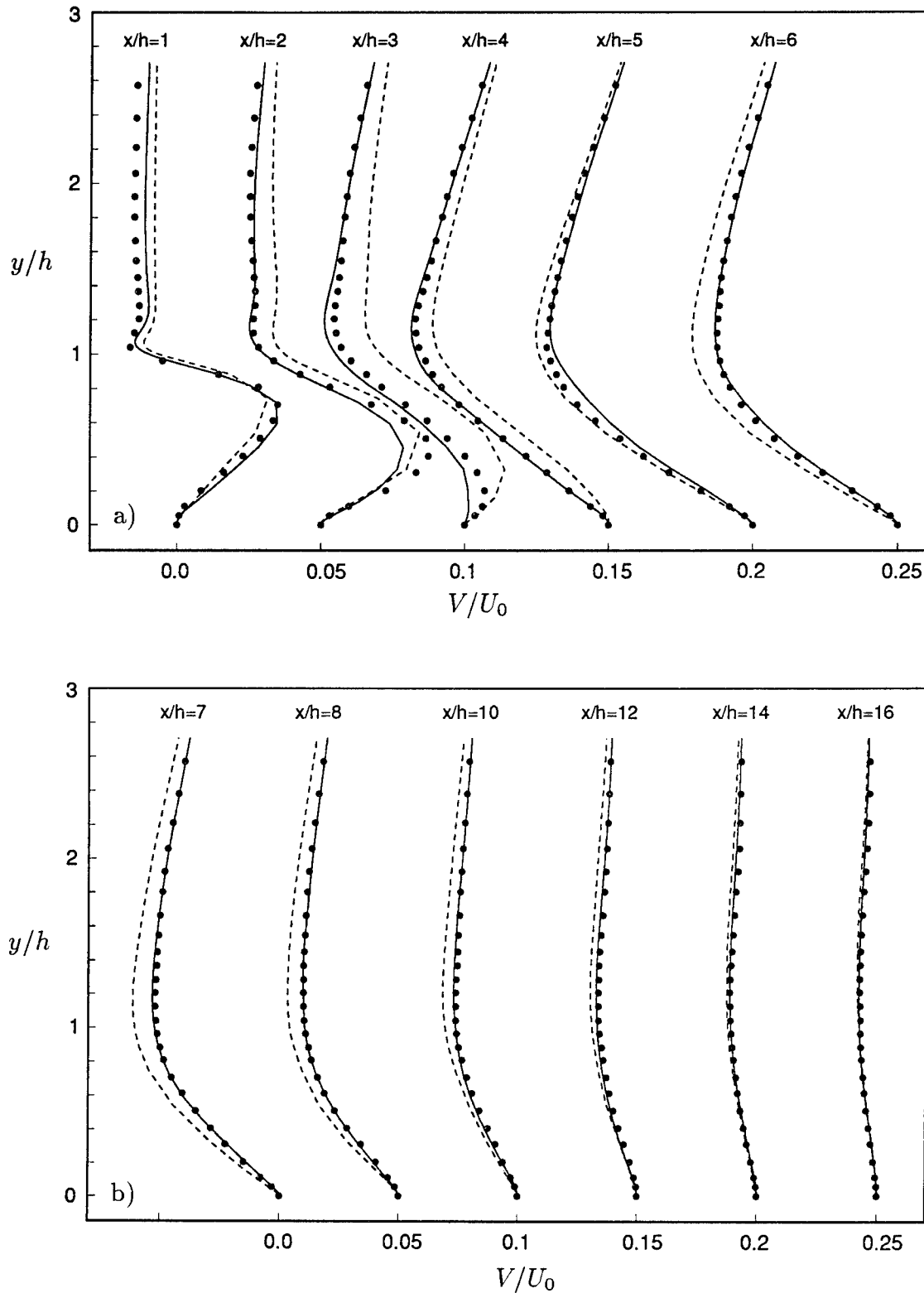
FIGURE **4.3-10**, Mean wall-normal velocity profiles. ——— : DMZ1;
- - - - : DMY1;   • : DNS.   a) $x/h = 1 - 6$,   b) $x/h = 7 - 16$.
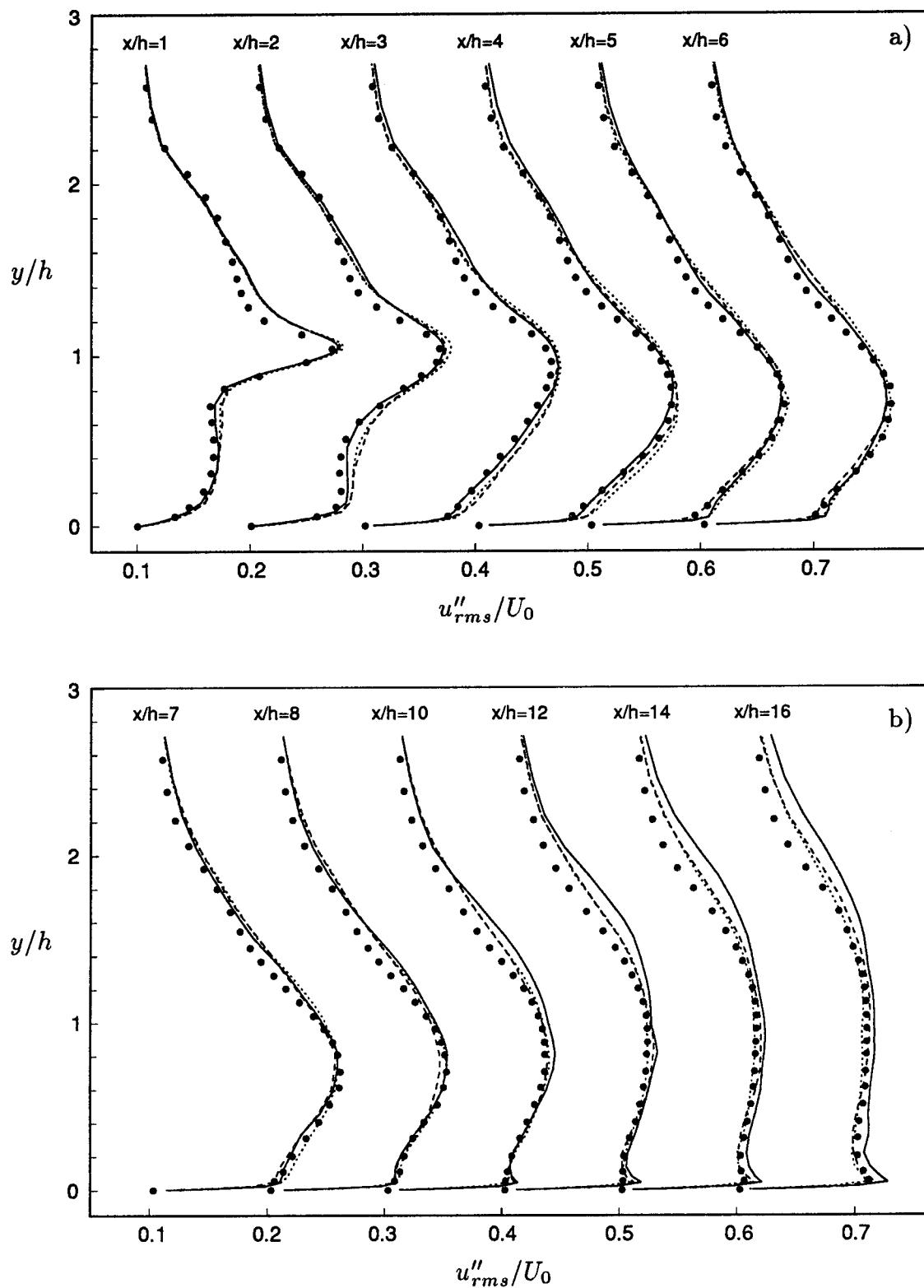
FIGURE **4.3-11**, Resolved streamwise turbulence intensity. ———— : DMX1;
———— : DMBA; ········ : DMX2; • : DNS.   a) $x/h = 1-6$,   b) $x/h = 7-16$.
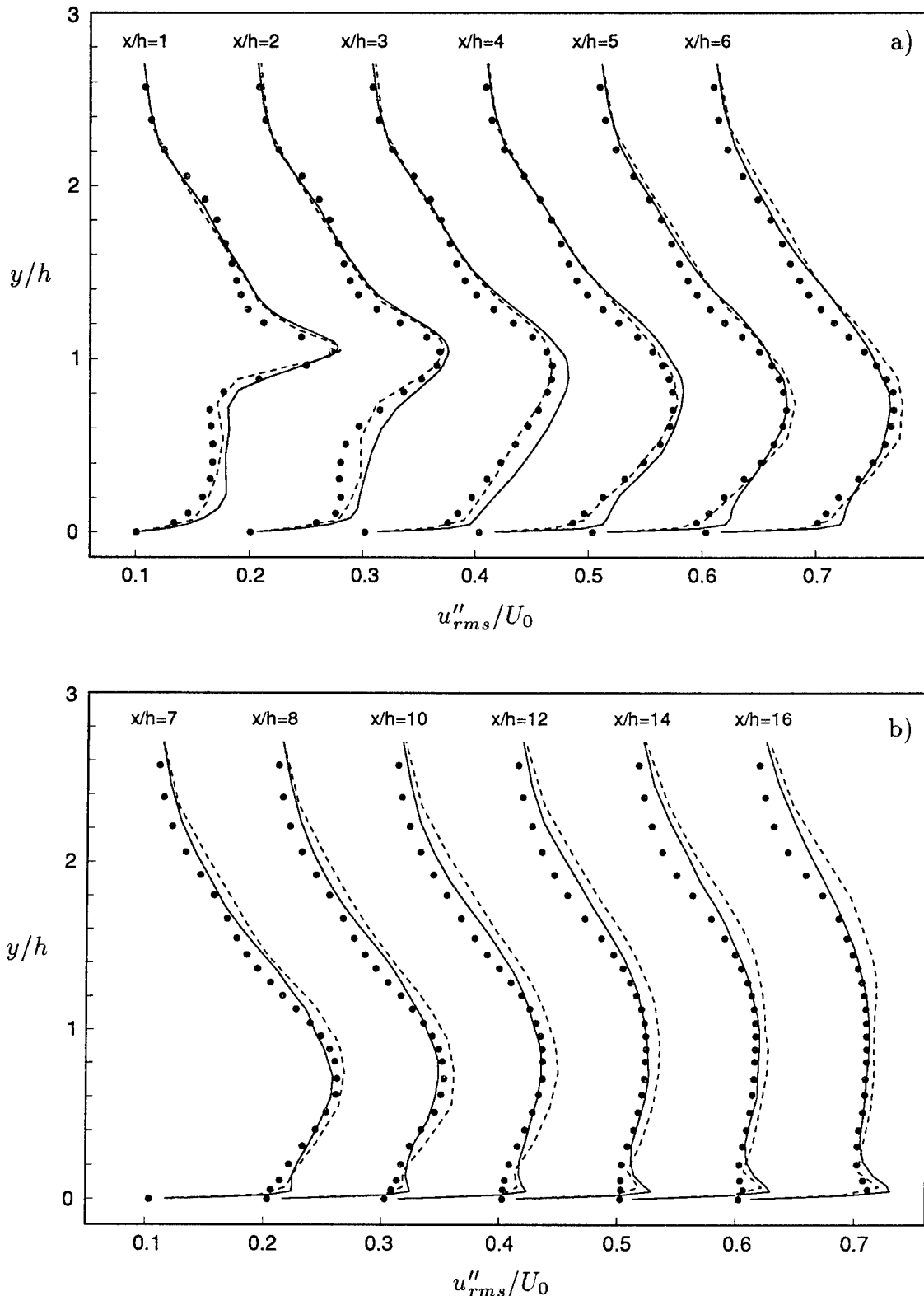
FIGURE **4.3-12**, Resolved streamwise turbulence intensity. ——— : DMZ1;
---- : DMY1;   • : DNS.   a) $x/h = 1 - 6$,   b) $x/h = 7 - 16$.
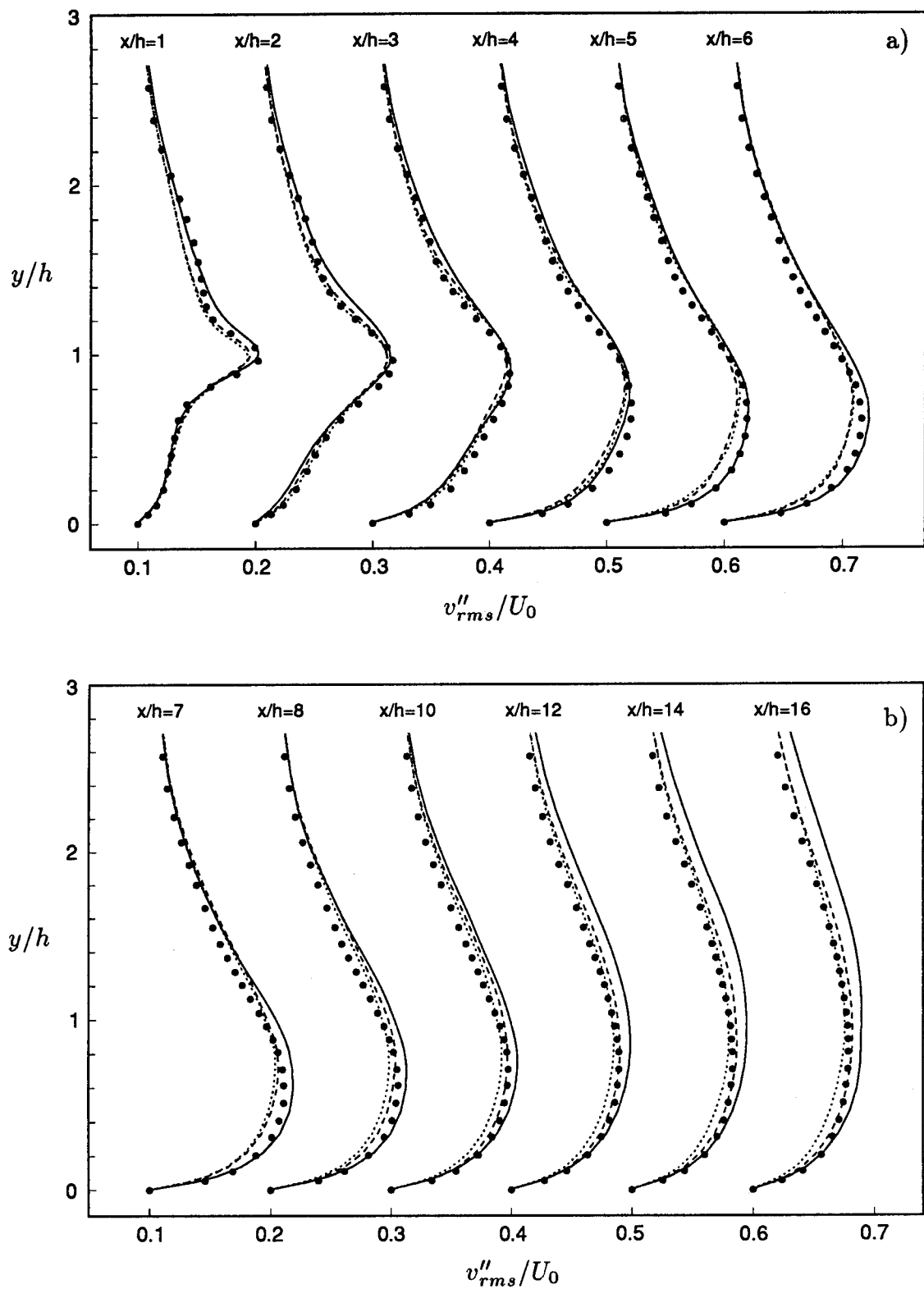
FIGURE **4.3-13**, Resolved wall-normal turbulence intensity.   ——— : DMX1;
– – – – : DMBA;   ········· : DMX2;   ● : DNS.   a) $x/h = 1 - 6$,   b) $x/h = 7 - 16$.
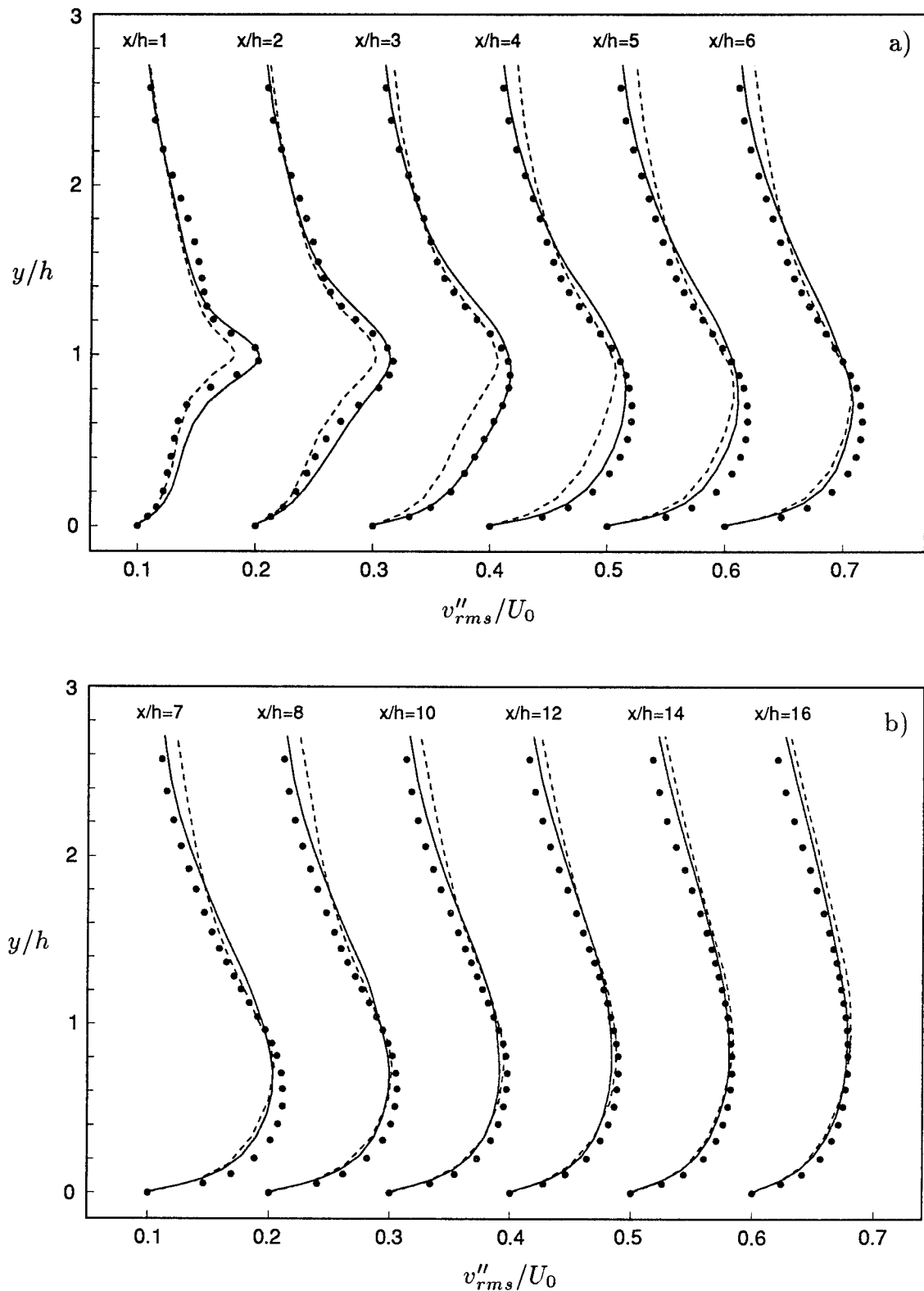
FIGURE **4.3-14**, Resolved wall-normal turbulence intensity. ——— : DMZ1;
---- : DMY1;   ● : DNS.   a) $x/h = 1 - 6$,   b) $x/h = 7 - 16$.
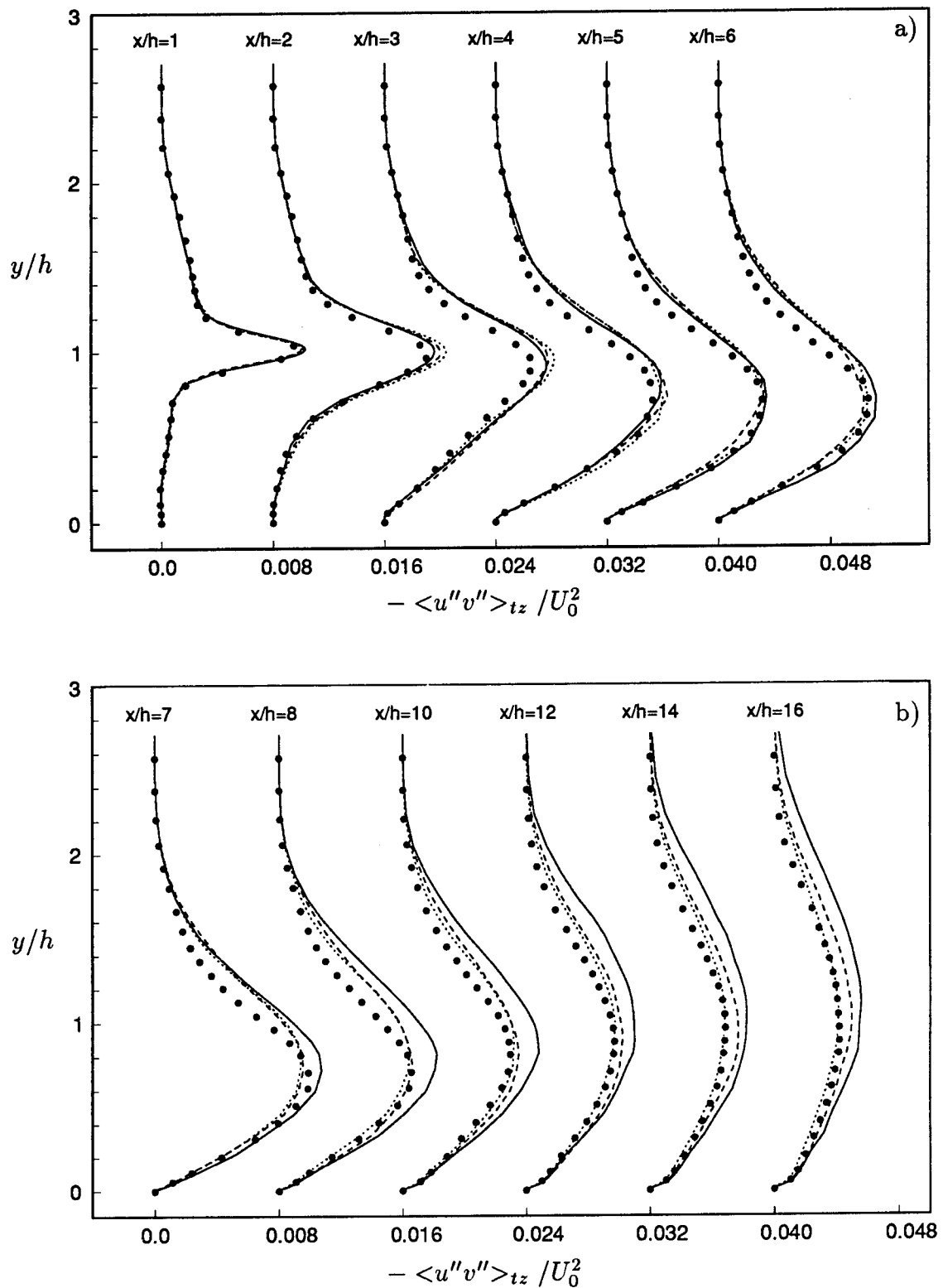
FIGURE **4.3-15**, Turbulent shear stress. ———— : DMX1; ---- : DMBA;
········· : DMX2;   • : DNS.   a) $x/h = 1 - 6$,   b) $x/h = 7 - 16$.
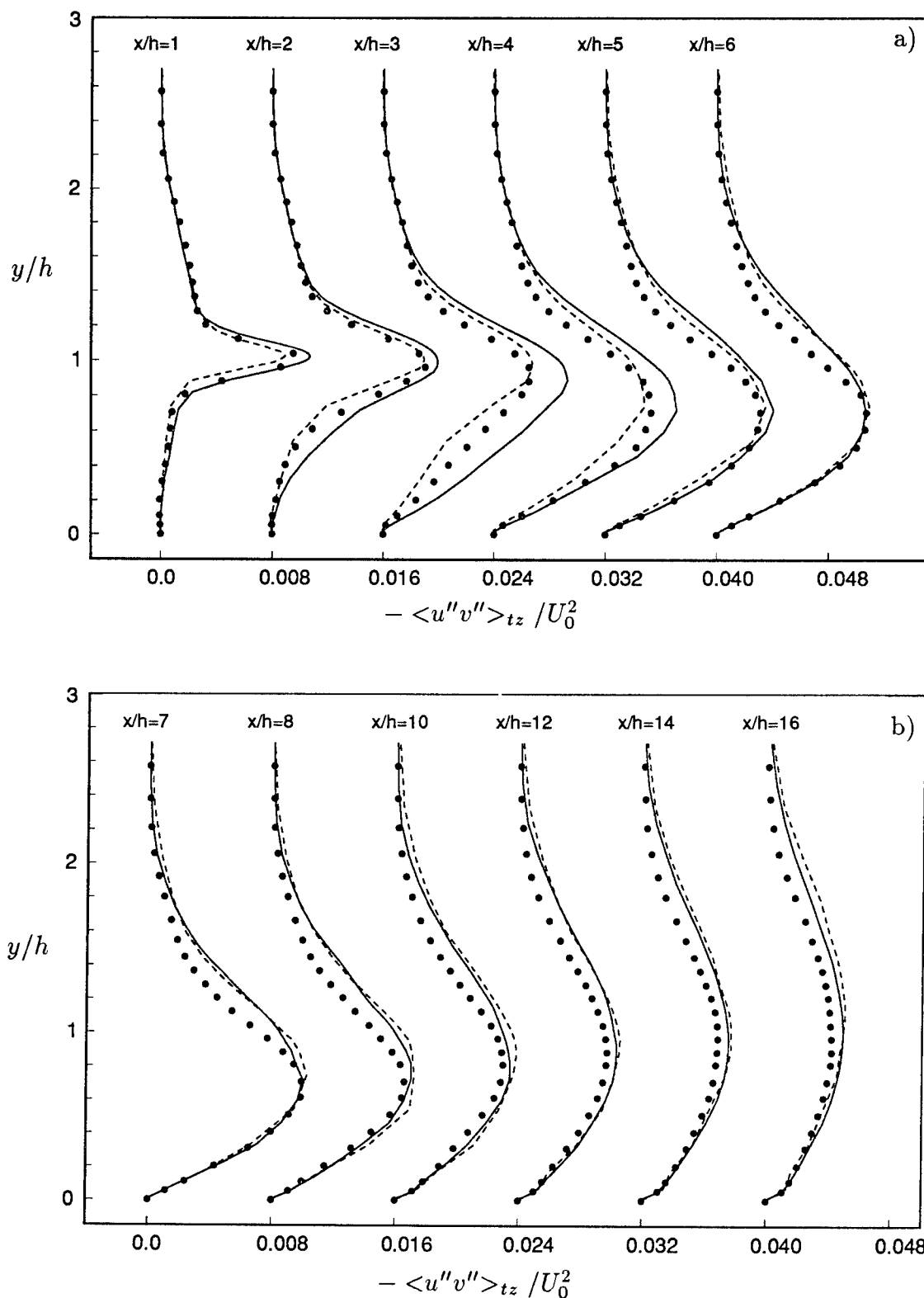
FIGURE **4.3-16**, Turbulent shear stress.   ——— : DMZ1;   – – – – : DMY1;
● : DNS.   a) $x/h = 1 - 6$,   b) $x/h = 7 - 16$.
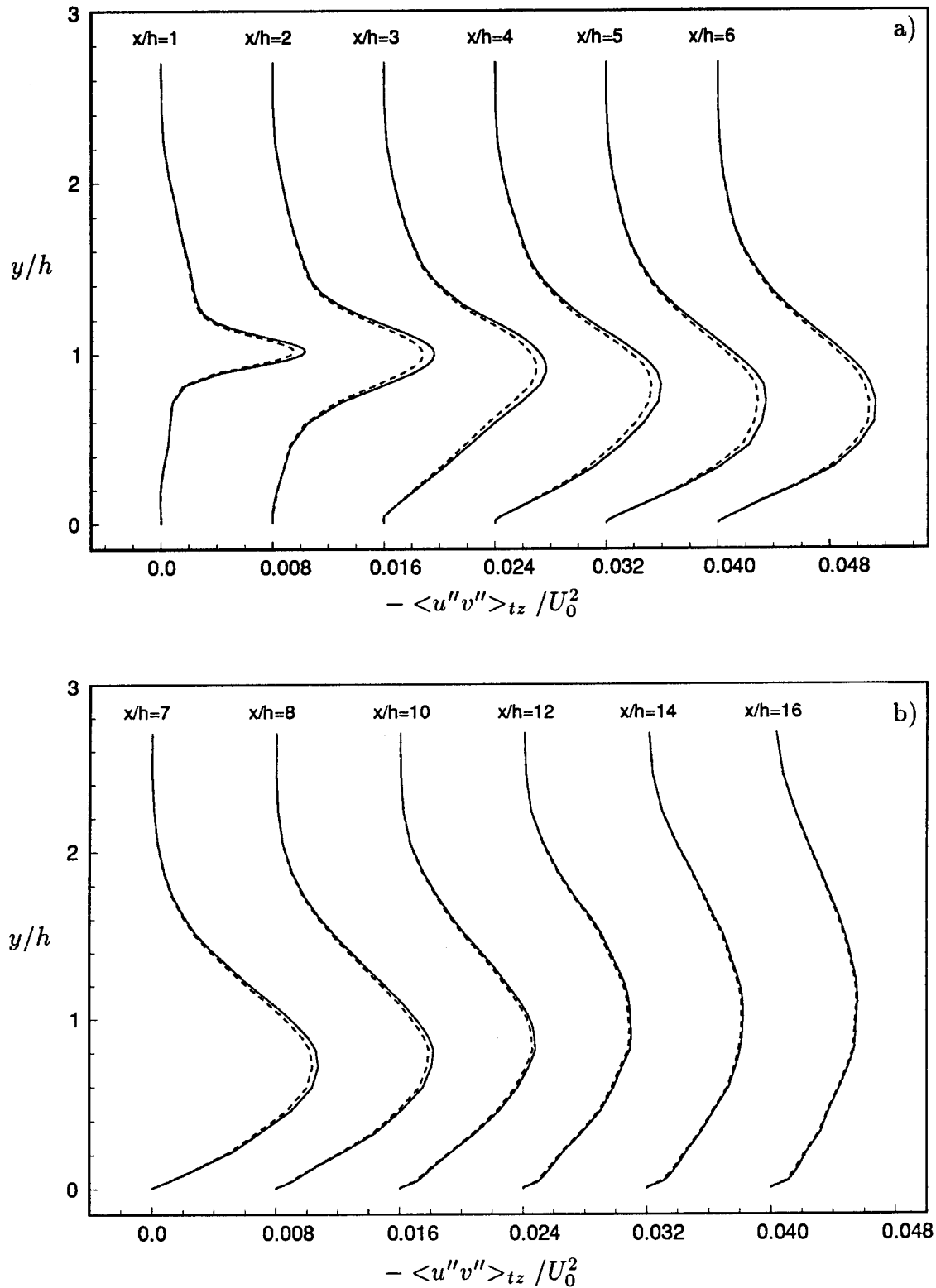
FIGURE **4.3-17**, Resolved turbulent shear stress and total turbulent shear stress for case DMX1. ——— : Total stress; ---- : Resolved Stress. a) $x/h = 1 - 6$, b) $x/h = 7 - 16$.
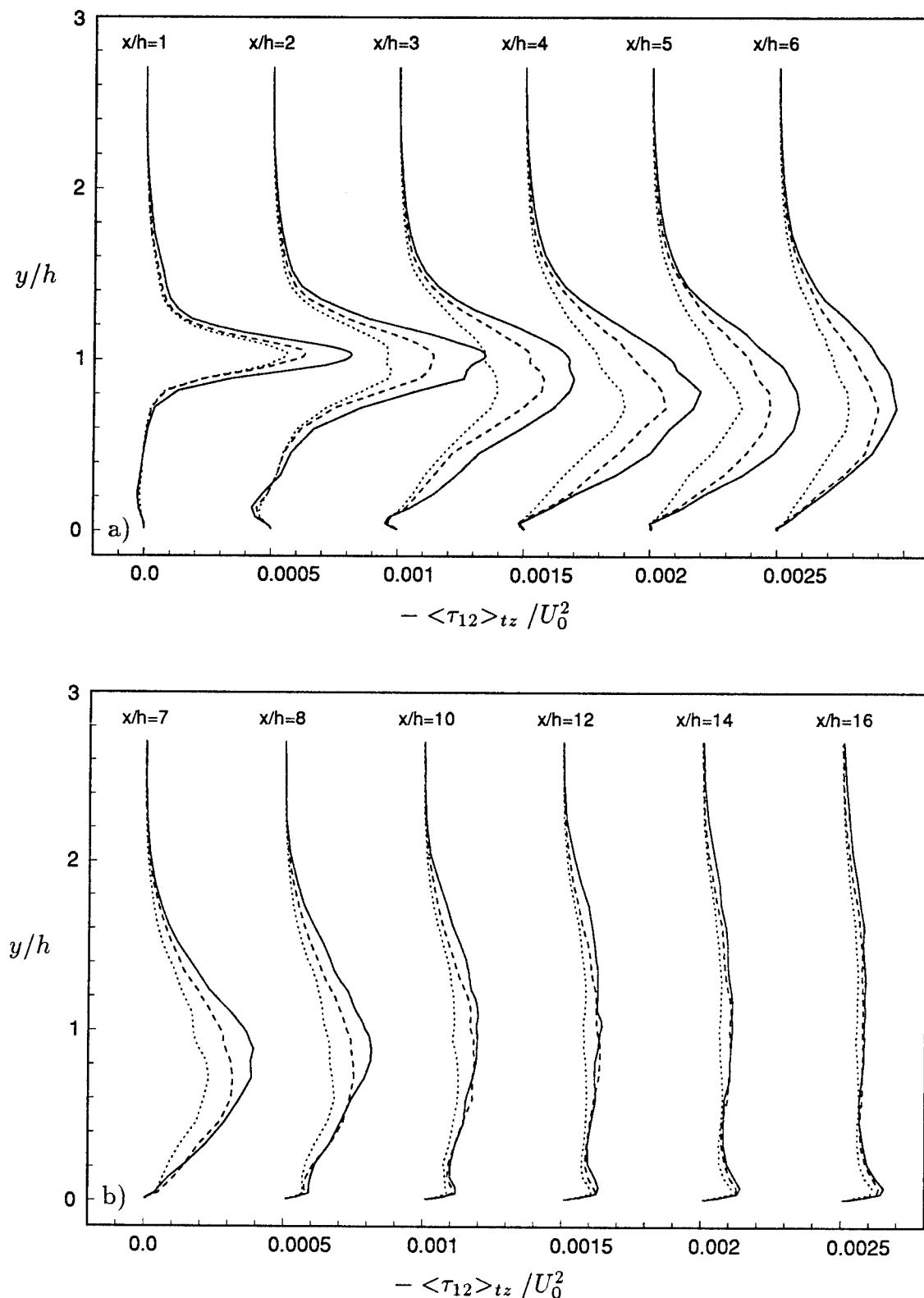
FIGURE **4.3-18**, Subgrid scale shear stress. ——— : DMX1; - - - - : DMBA; ········ : DMX2.   a) $x/h = 1 - 6$,   b) $x/h = 7 - 16$.
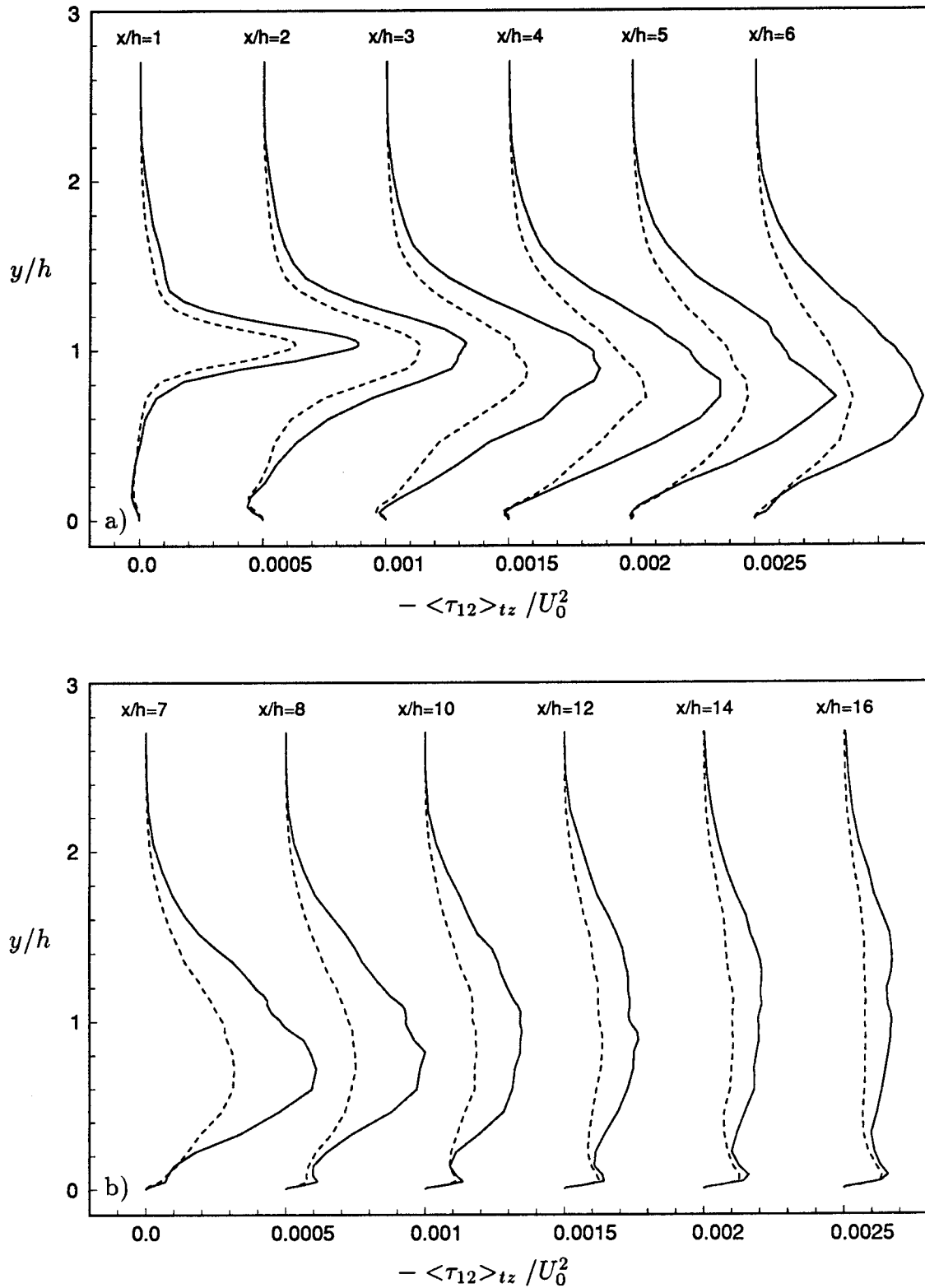
FIGURE **4.3-19**, Subgrid scale shear stress. ———— : DMZ1; ---- : DMBA.
a) $x/h = 1 - 6$, b) $x/h = 7 - 16$.
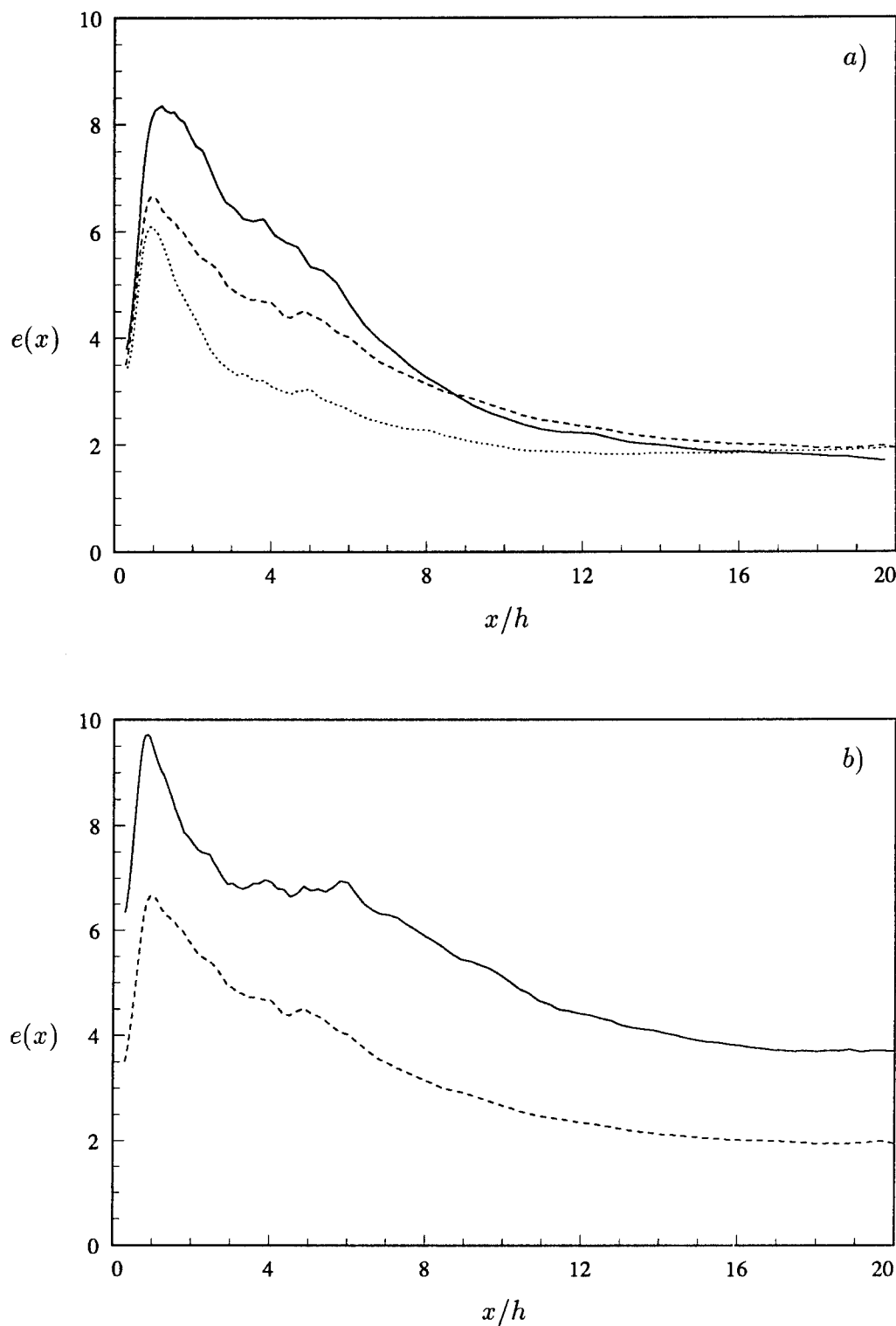
FIGURE **4.3-20**, $e(x)$ (defined in equation 4.3-1) is a measure of the ratio of the SGS shear stress to the resolved turbulent shear stress.   a) ——— : DMX1; ———— : DMBA;   ········ : DMX2.   b) ——— : DMZ1;   ———— : DMBA
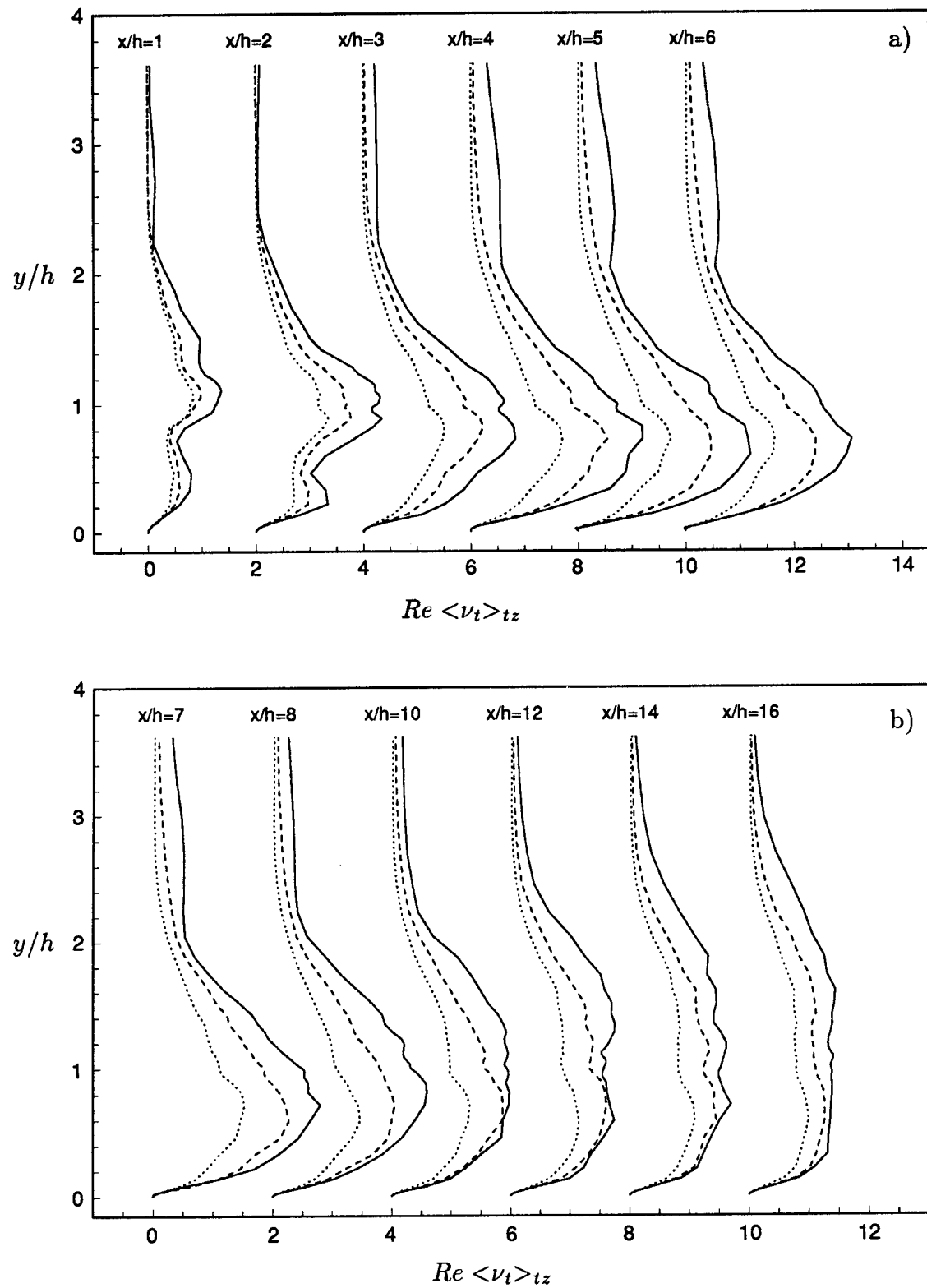
FIGURE **4.3-21**, Ratio of eddy-viscosity to molecular viscosity. ———— : DMX1; ———— : DMBA; ⋯⋯⋯ : DMX2. a) $x/h = 1 - 6$, b) $x/h = 7 - 16$.
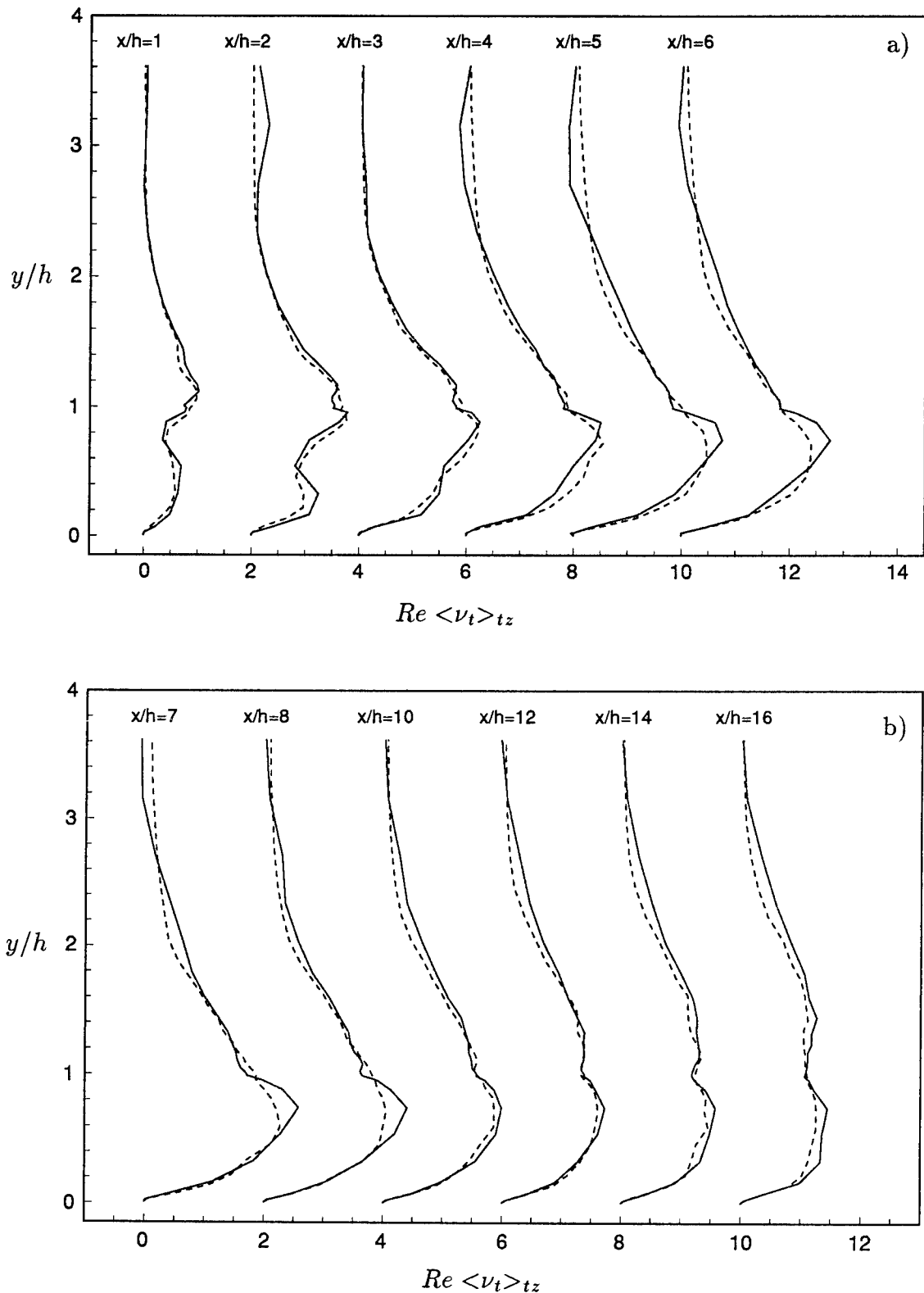
FIGURE **4.3-22**, Ratio of eddy-viscosity to molecular viscosity. ———— : DMY1;
---- : DMBA.   a) $x/h = 1 - 6$,   b) $x/h = 7 - 16$.
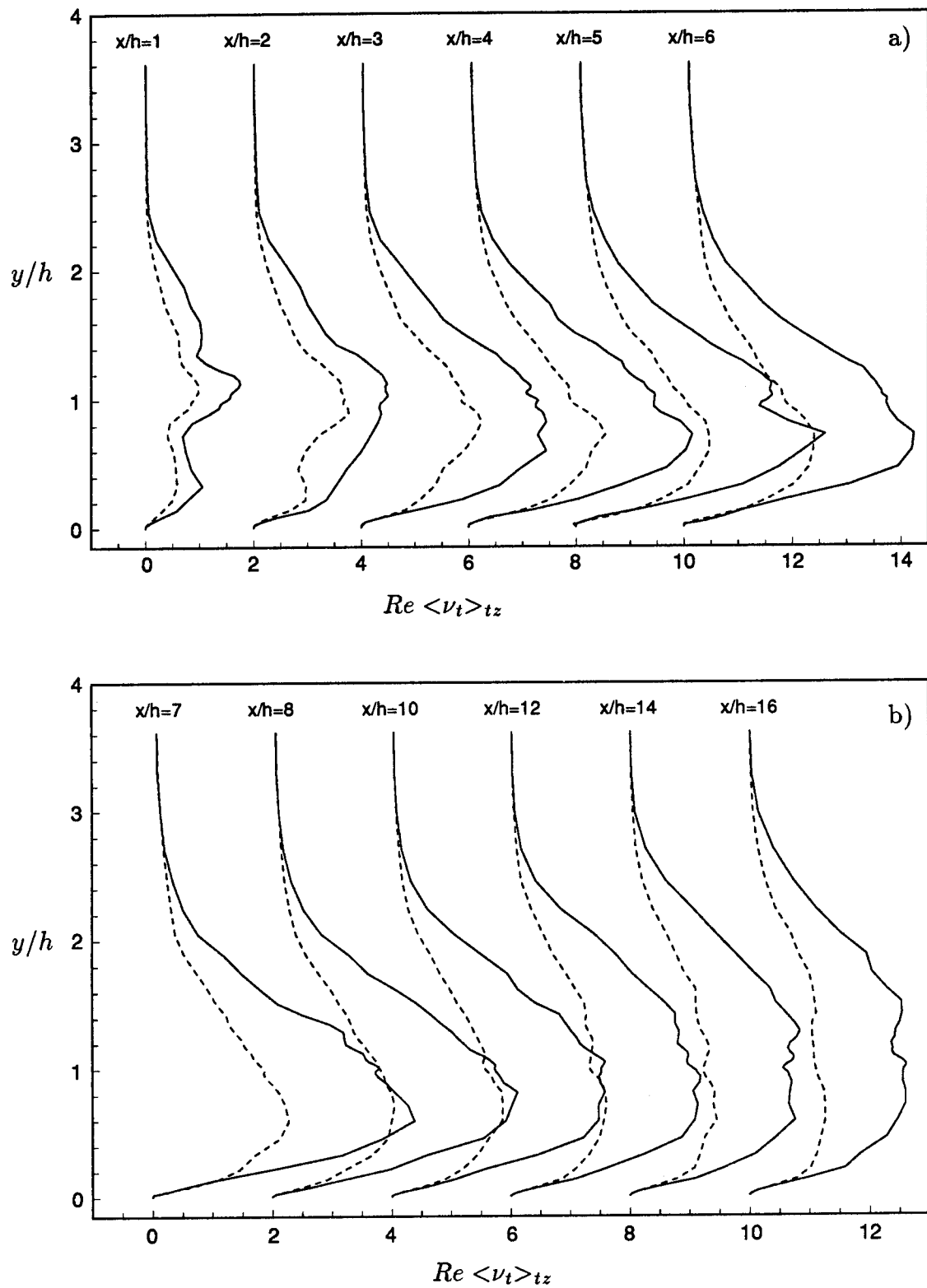
FIGURE **4.3-23**, Ratio of eddy-viscosity to molecular viscosity. ———— : DMZ1; ---- : DMBA.   a) $x/h = 1 - 6$,   b) $x/h = 7 - 16$.
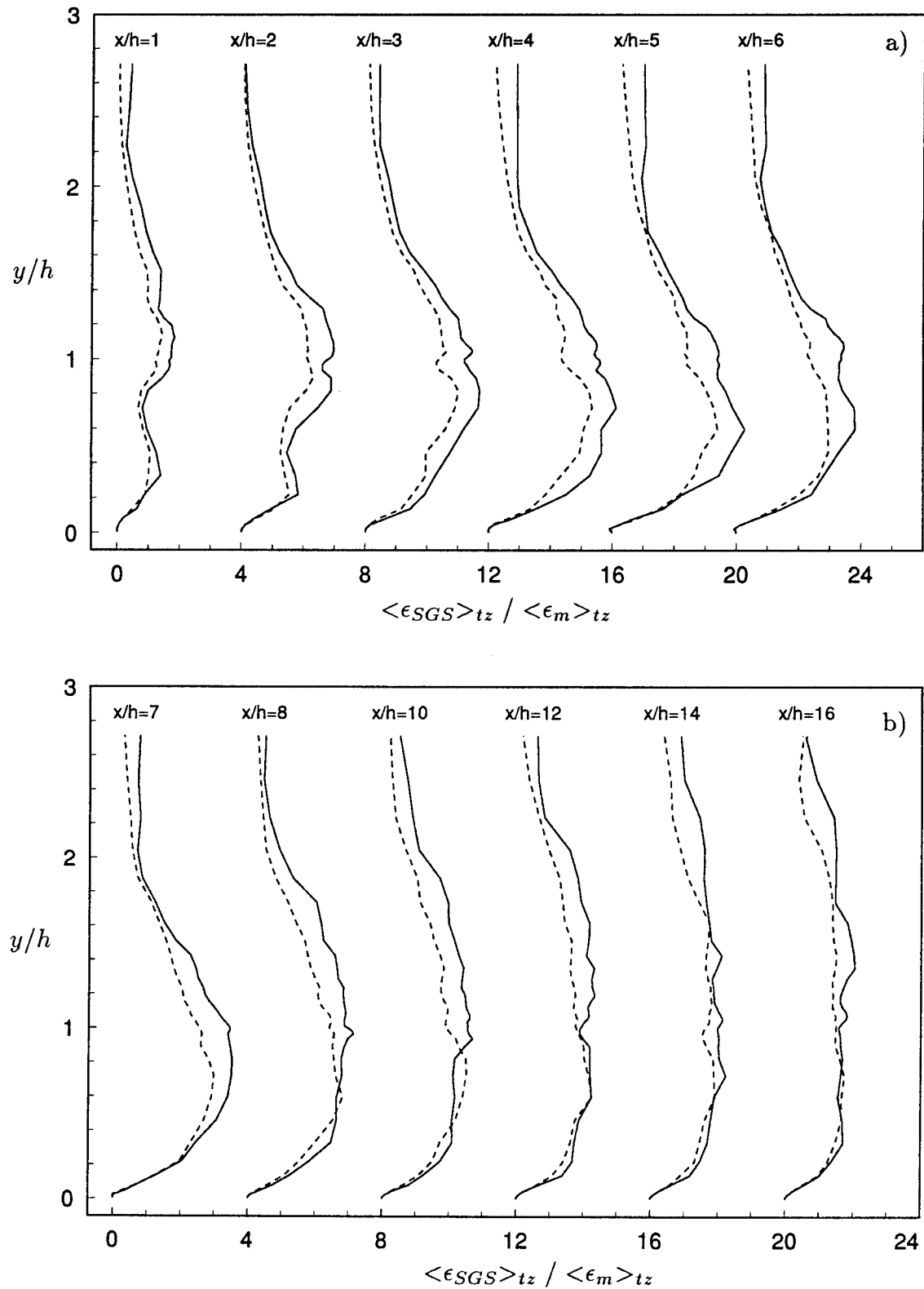
FIGURE **4.3-24**, Ratio of SGS dissipation to molecular dissipation. ———— : DMX1;
---- : DMBA.   a) $x/h = 1 - 6$,   b) $x/h = 7 - 16$.
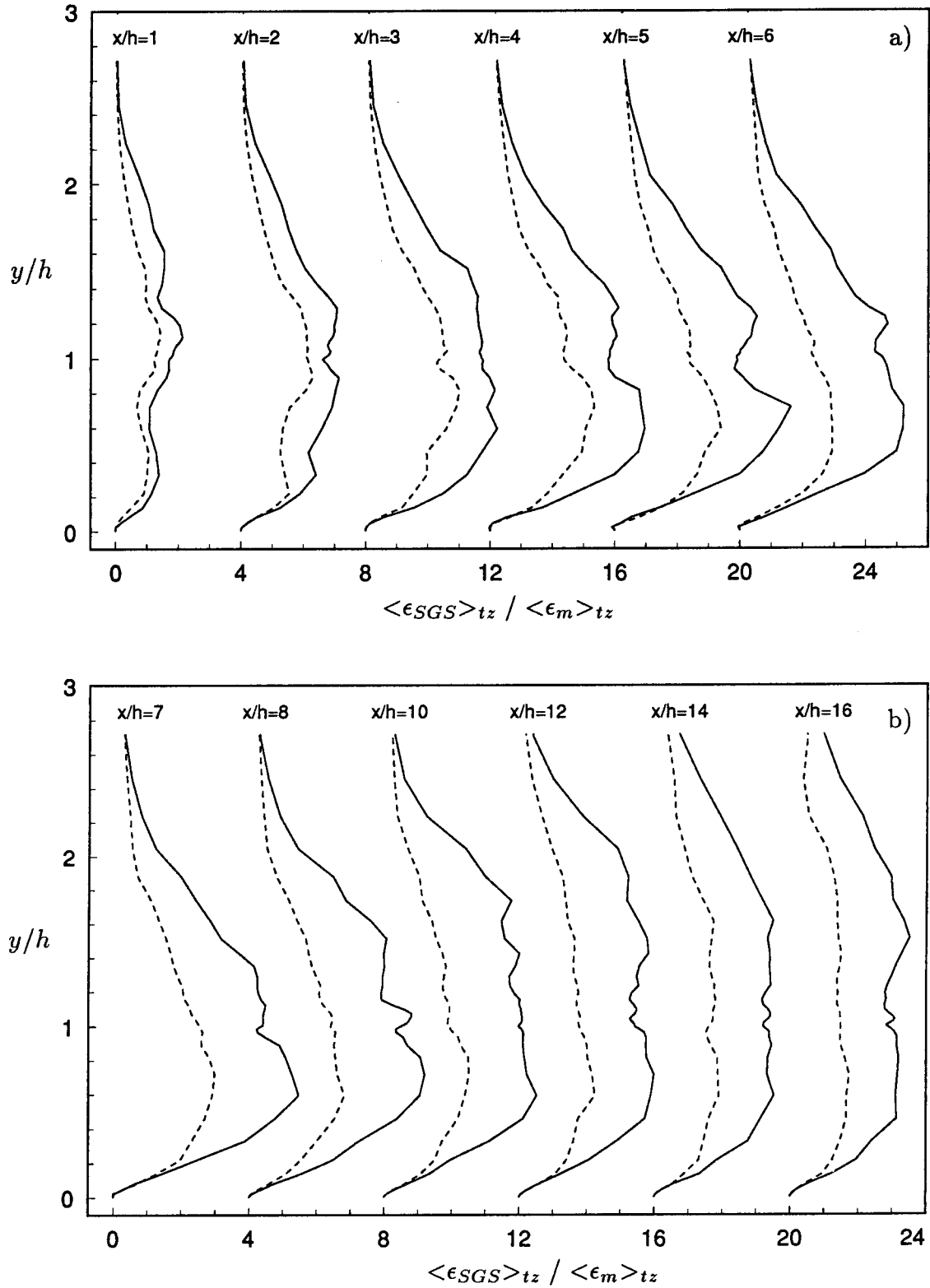
FIGURE **4.3-25**, Ratio of SGS dissipation to molecular dissipation. ———— : DMZ1;
- - - - : DMBA.   a) $x/h = 1 - 6$,   b) $x/h = 7 - 16$.
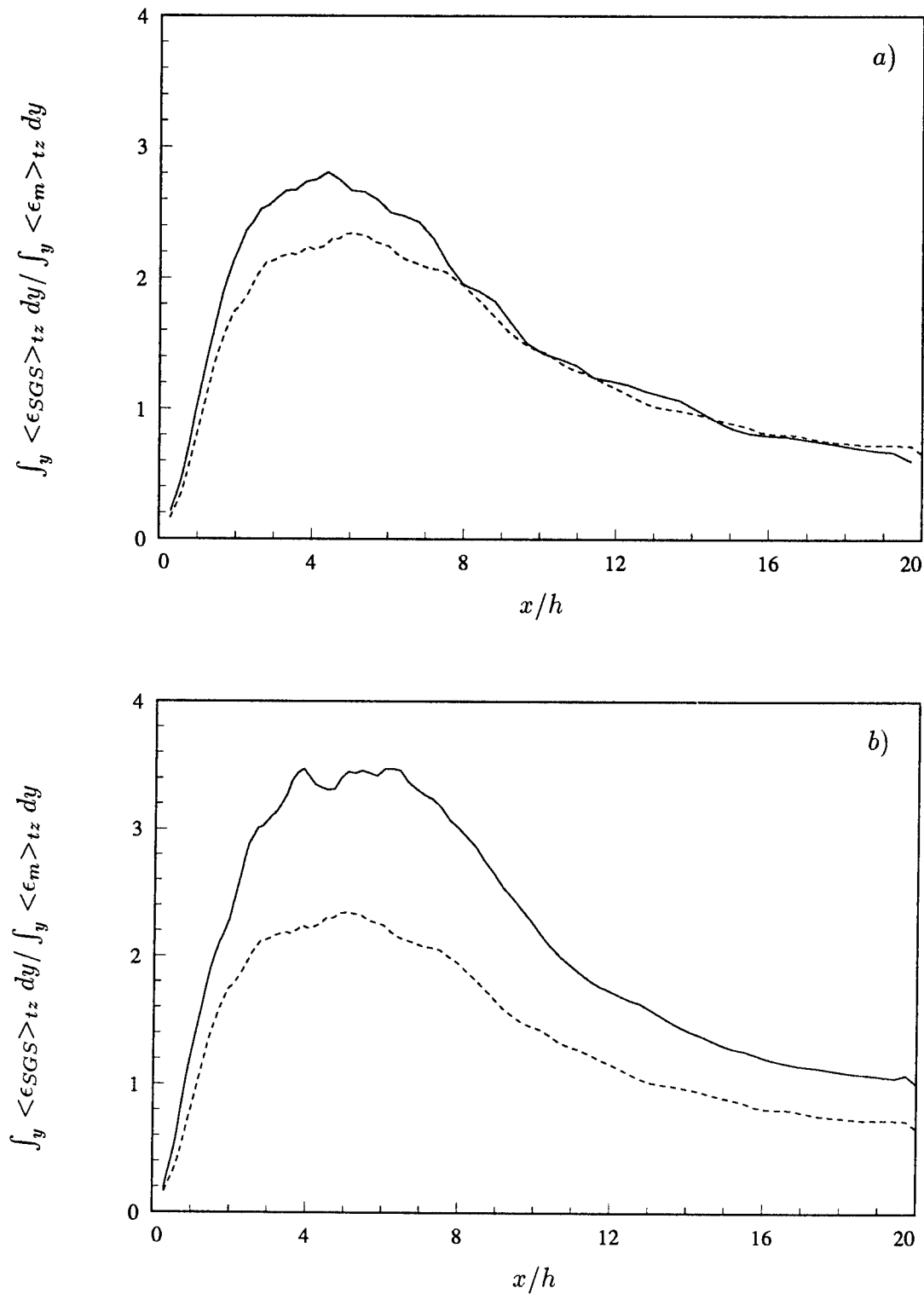
FIGURE **4.3-26**, Ratio of SGS dissipation and Molecular dissipation, both averaged over the cross-sectional area.   a) ——— : DMX1;   - - - - : DMBA;
b)   ——— : DMZ1;   - - - - : DMBA
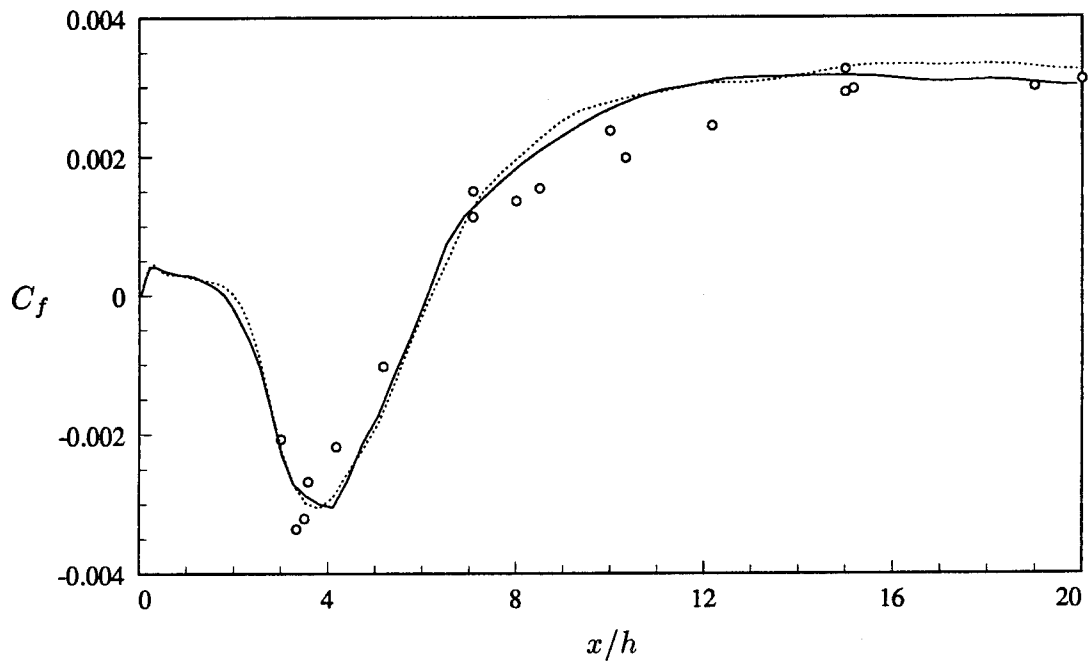
FIGURE **4.4-1**, Coefficient of friction along the lower wall, downstream of the step.
———— : DLX1; ········ : DMX1; o : Experiment (Jovic & Driver).
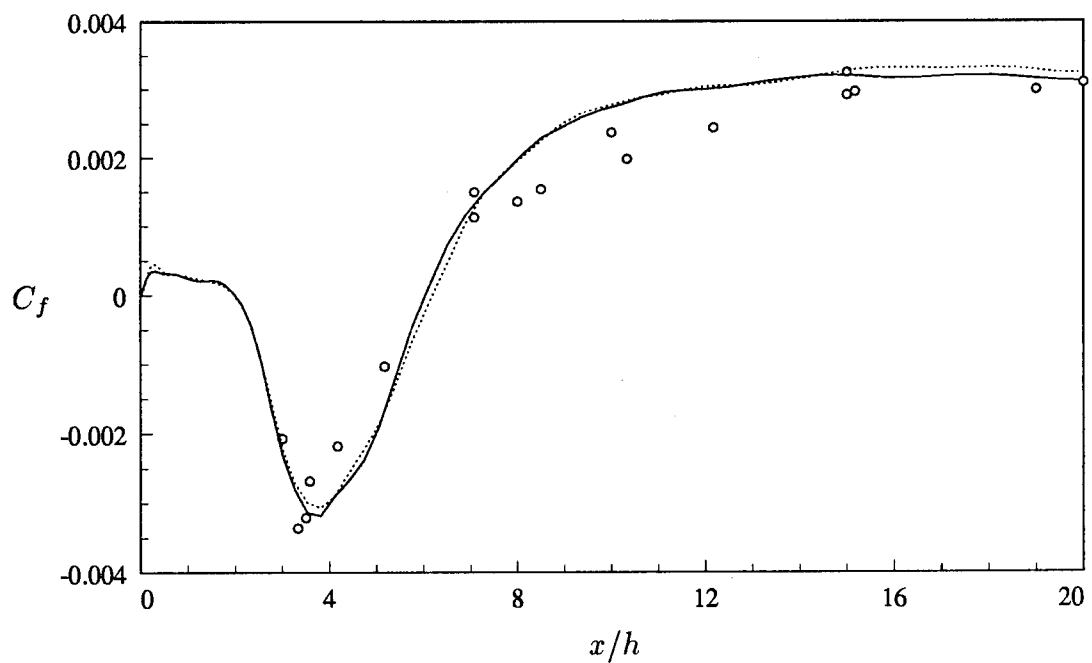
FIGURE **4.4-2**, Coefficient of friction along the lower wall, downstream of the step.
———— : SMX1; ········ : DMX1; o : Experiment (Jovic & Driver).
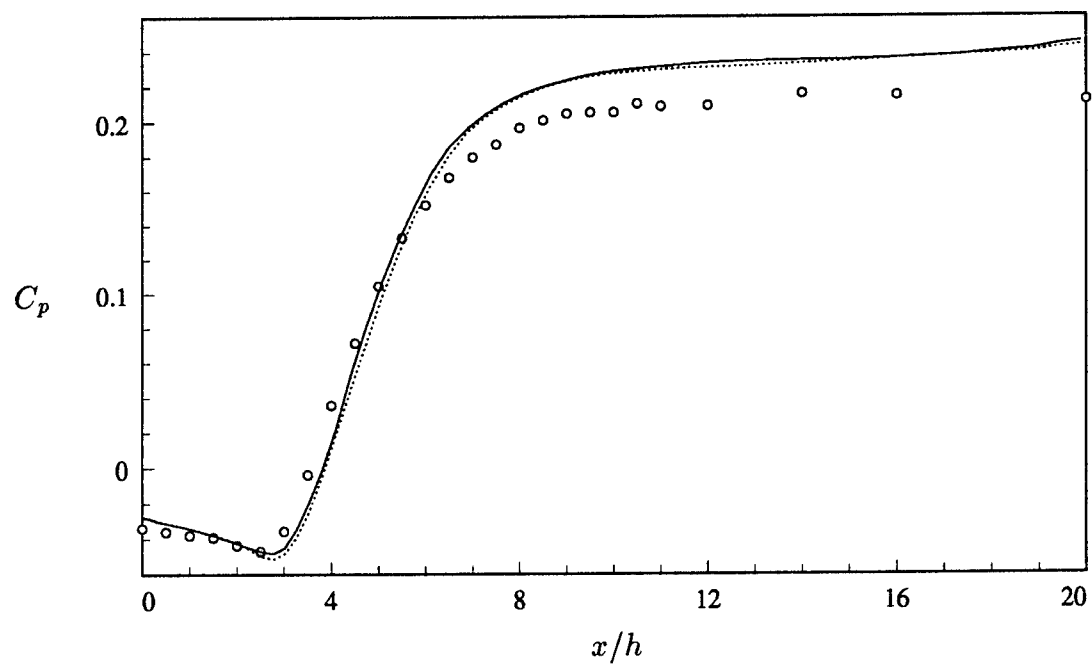
FIGURE **4.4-3**, Pressure coefficient along the lower wall, downstream of the step.
——— : DLX1; ········ : DMX1; o : Experiment (Jovic & Driver).
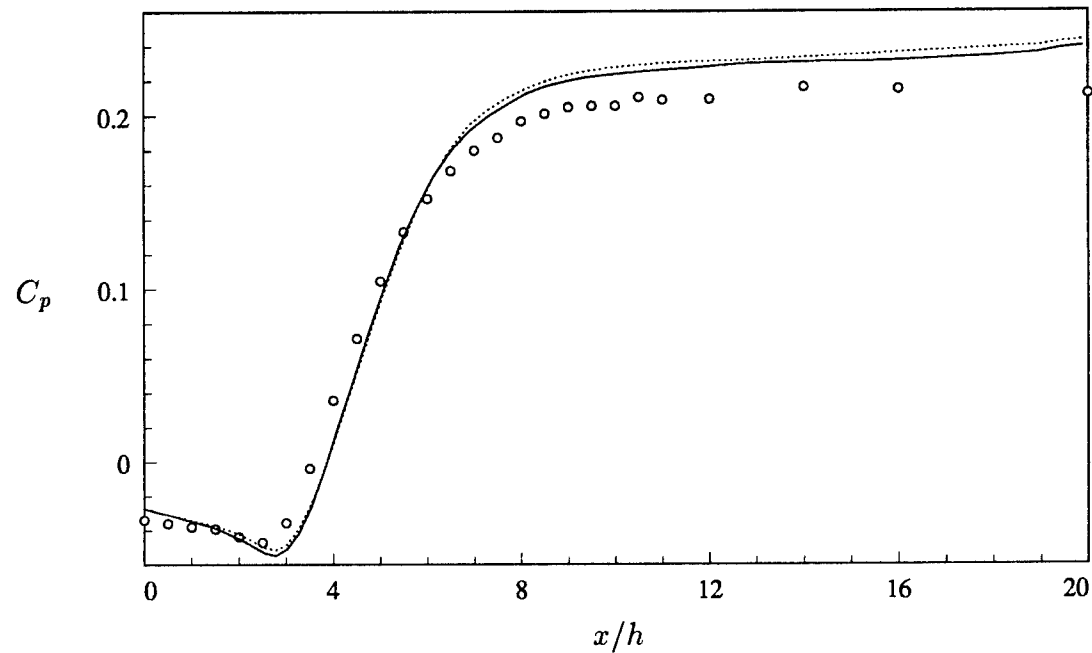
FIGURE **4.4-4**, Pressure coefficient along the lower wall, downstream of the step.
——— : SMX1; ········ : DMX1; o : Experiment (Jovic & Driver).
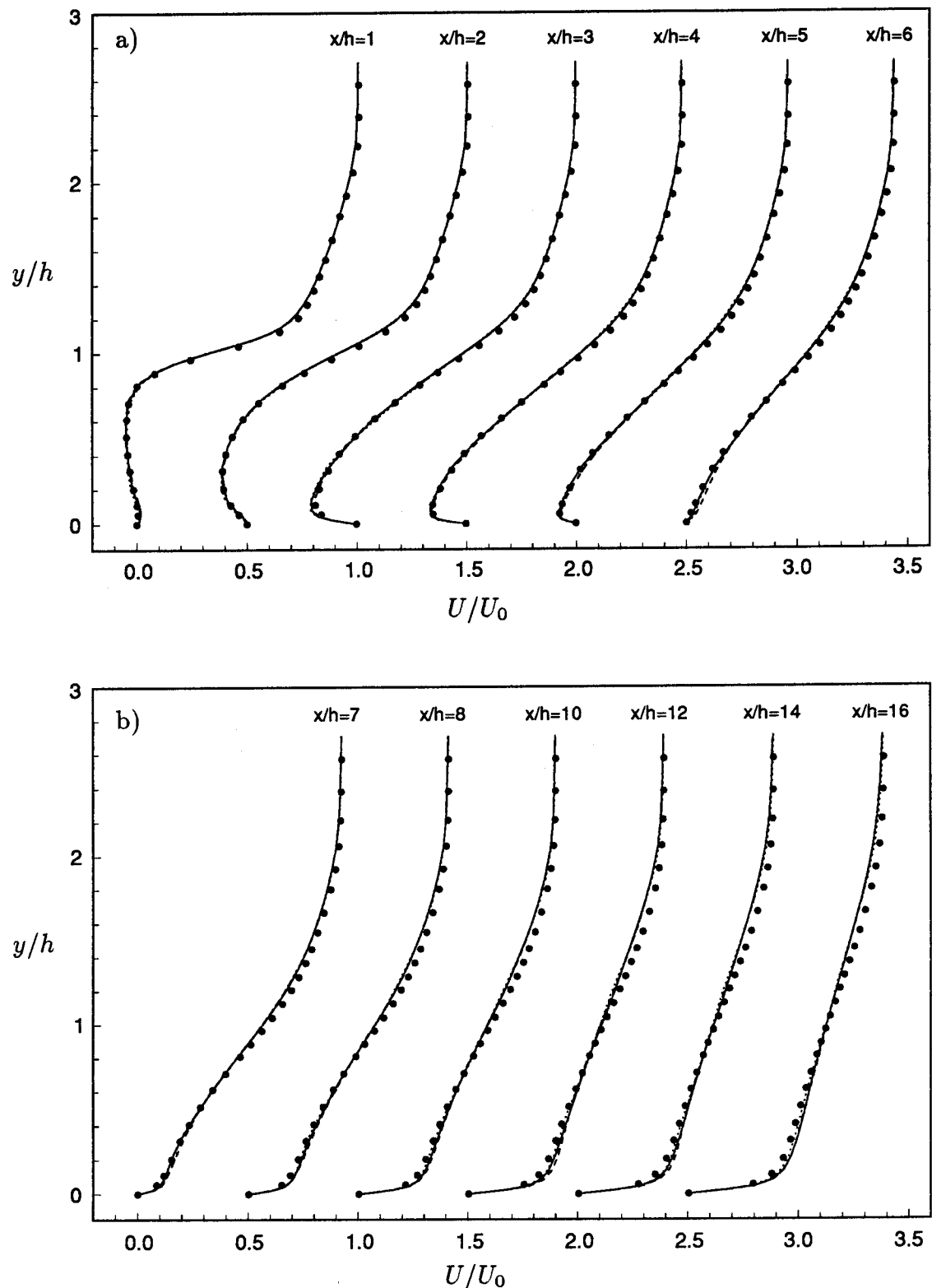
FIGURE **4.4-5**, Mean streamwise velocity profiles. ——— : DMX1;
———— : DLX1; ·········· : SMX1; ● : DNS.   a) $x/h = 1 - 6$,   b) $x/h = 7 - 16$.
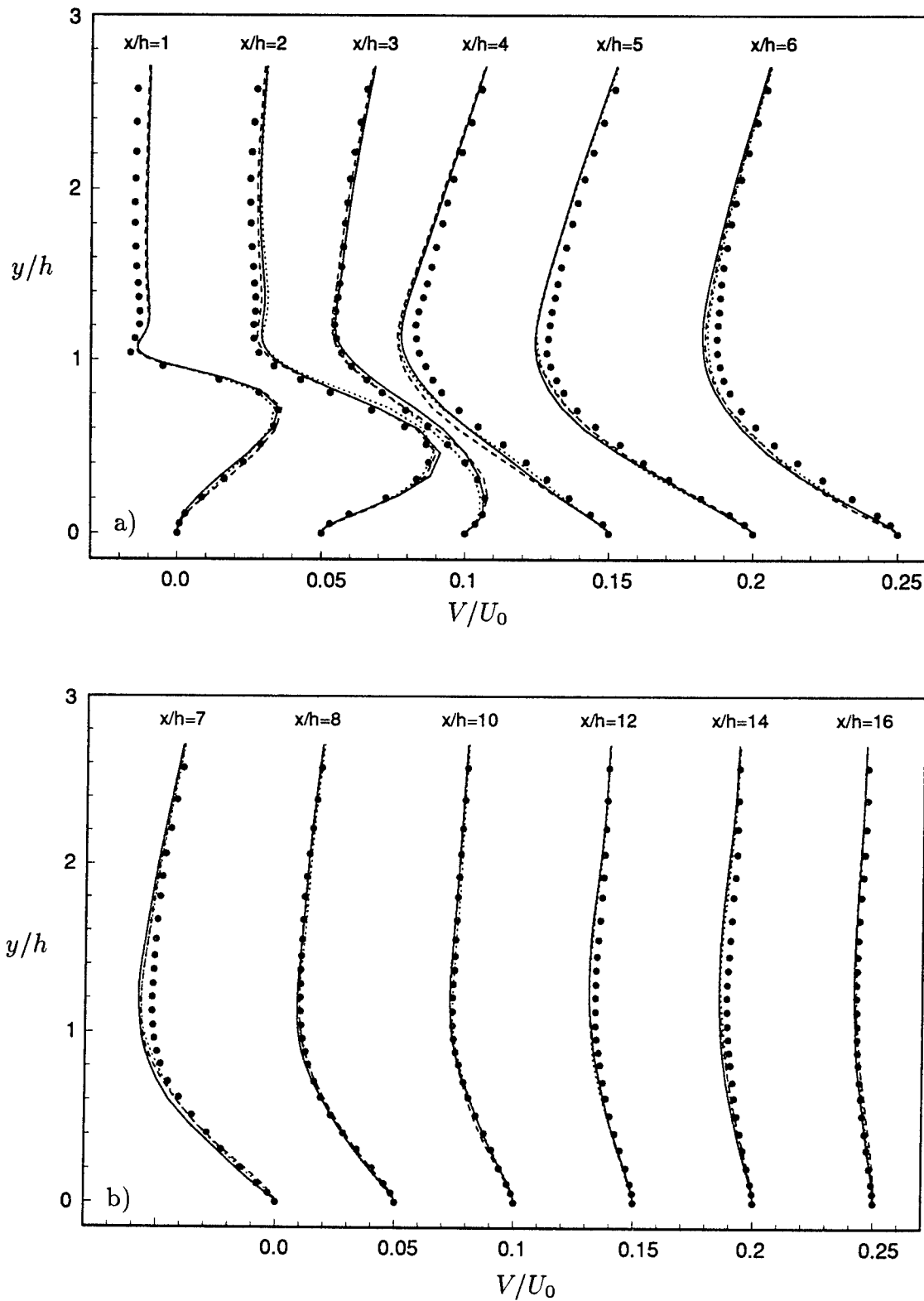
FIGURE **4.4-6**, Mean wall-normal velocity profiles.   ——— : DMX1;
---- : DLX1;   ········ : SMX1;   ● : DNS.   a) $x/h = 1 - 6$,   b) $x/h = 7 - 16$.
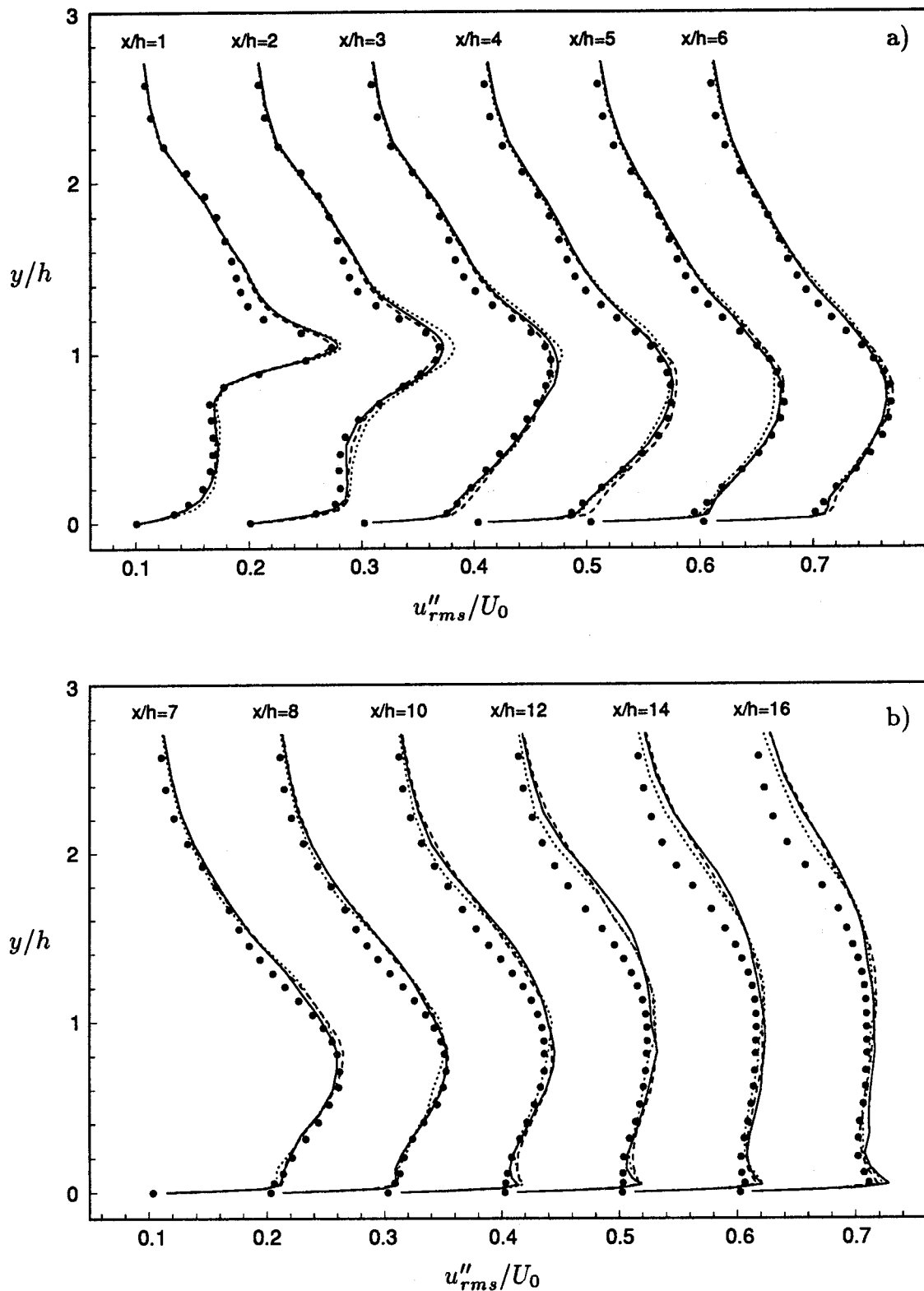
FIGURE **4.4-7**, Resolved streamwise turbulence intensity. ———— : DMX1;
———— : DLX1;   ·········· : SMX1;   • : DNS.   a) $x/h = 1 - 6$,   b) $x/h = 7 - 16$.
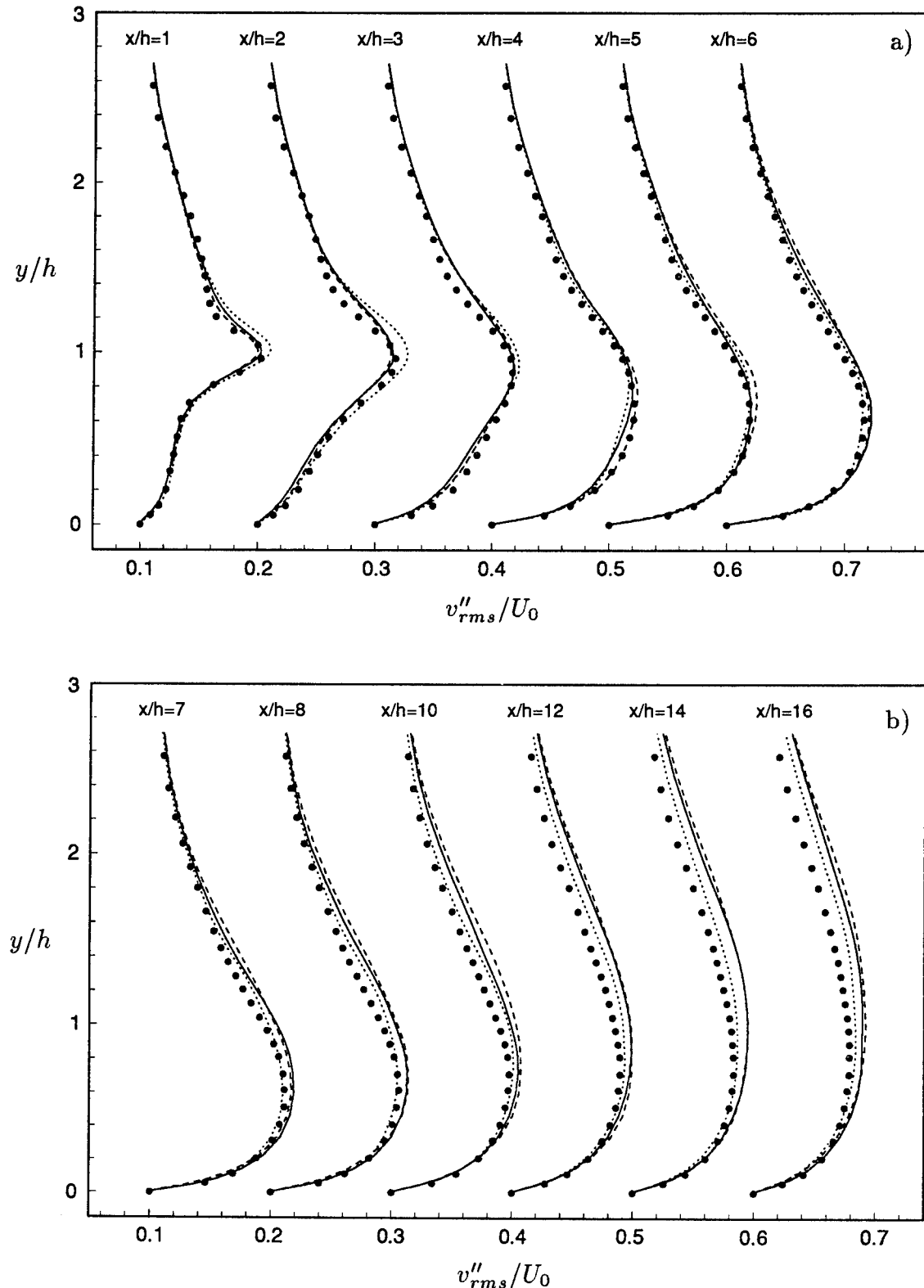
FIGURE **4.4-8**, Resolved wall-normal turbulence intensity.   ——— : DMX1;
———— : DLX1;   ········· : SMX1;   ● : DNS.   a) $x/h = 1 - 6$,   b) $x/h = 7 - 16$.
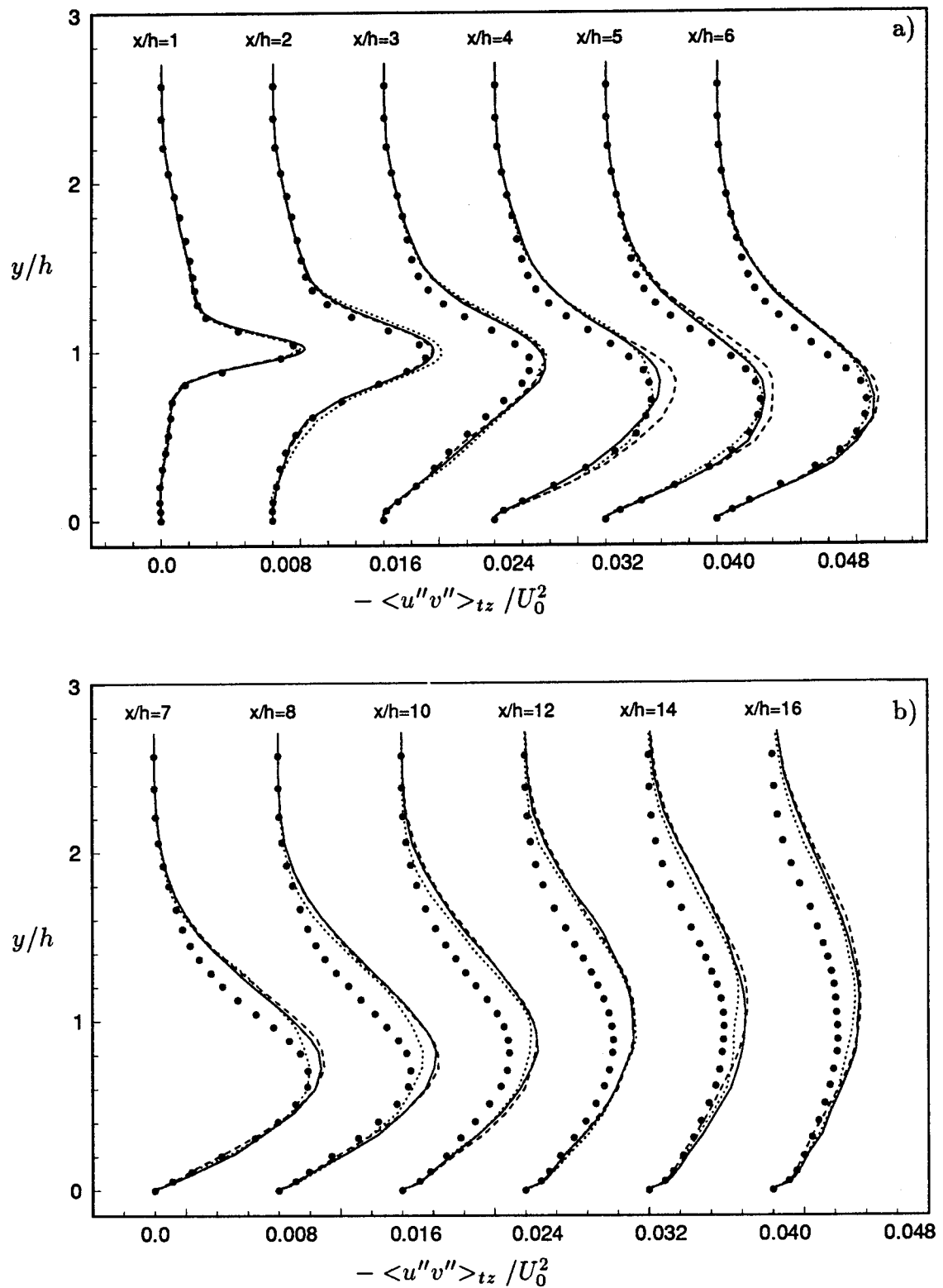
FIGURE **4.4-9**, Turbulent shear stress. ——— : DMX1; ‒‒‒‒ : DLX1; ········ : SMX1; ● : DNS. a) $x/h = 1 - 6$, b) $x/h = 7 - 16$.
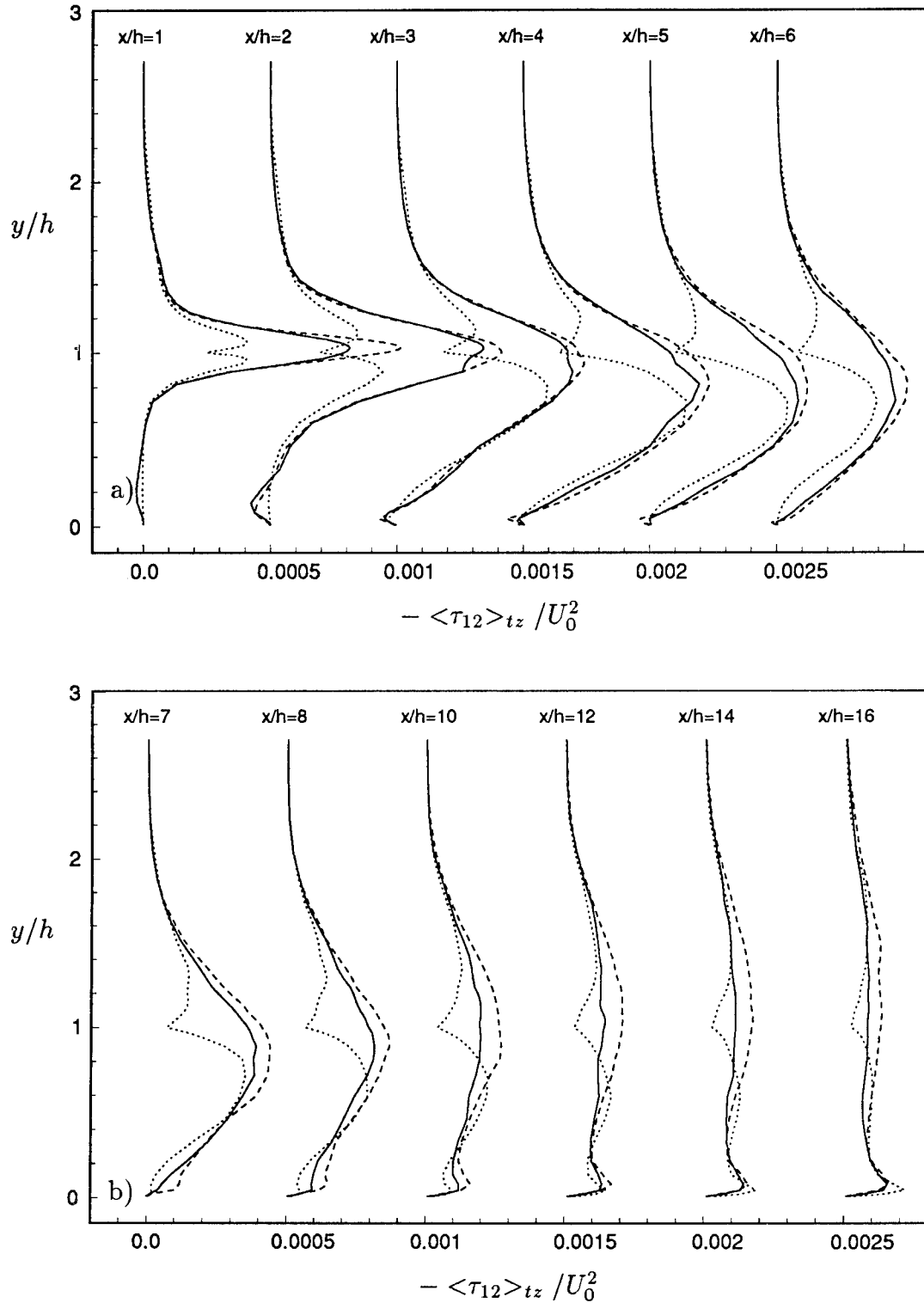
FIGURE **4.4-10**, Subgrid scale shear stress. ——— : DMX1; ———— : DLX1;
········· : SMX1.   a) $x/h = 1 - 6$,   b) $x/h = 7 - 16$.
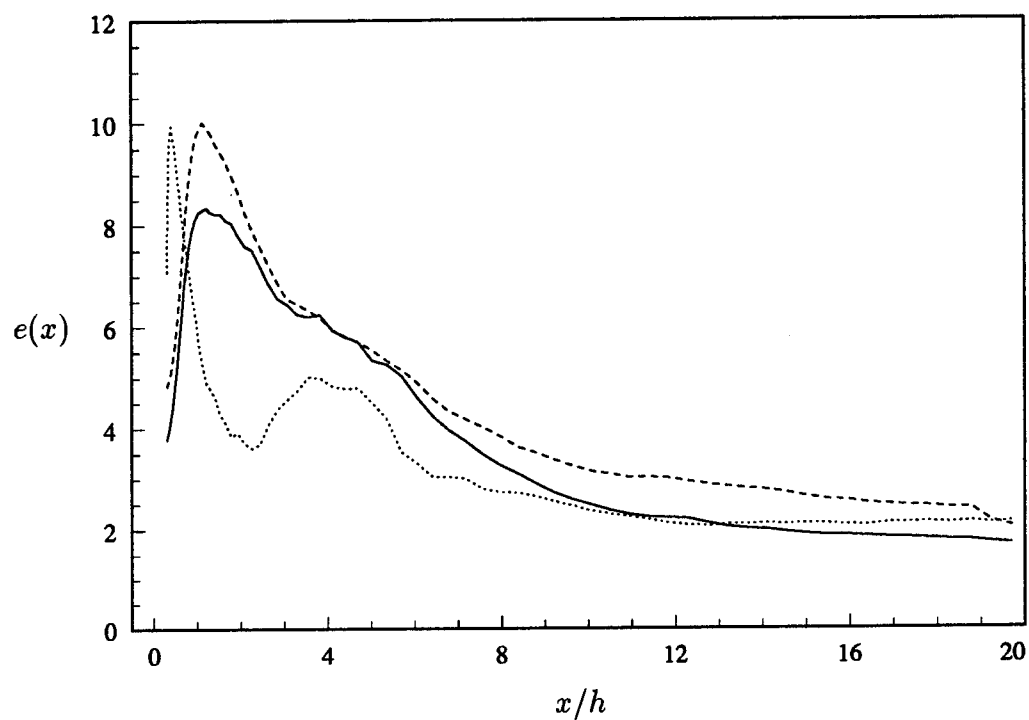
FIGURE **4.4-11**, $e(x)$ (defined in equation 4.3-1) is a measure of the ratio of the SGS shear stress to the resolved turbulent shear stress. ——— : DMX1;
———— : DLX1; ········· : SMX1.
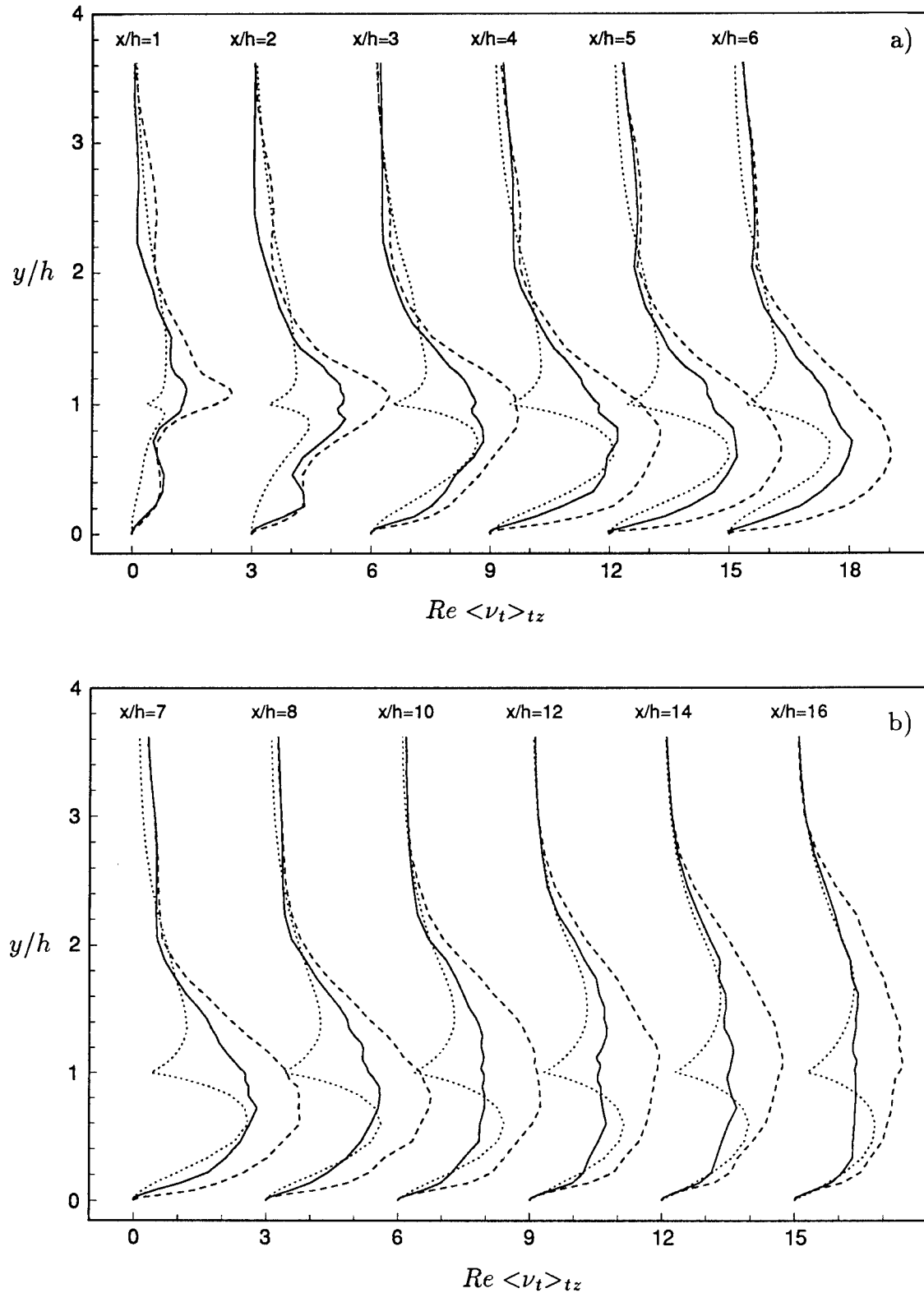
FIGURE **4.4-12**, Ratio of eddy-viscosity to molecular viscosity. ——— : DMX1;
- - - - : DLX1; ········· : SMX1.   a) $x/h = 1 - 6$,   b) $x/h = 7 - 16$.
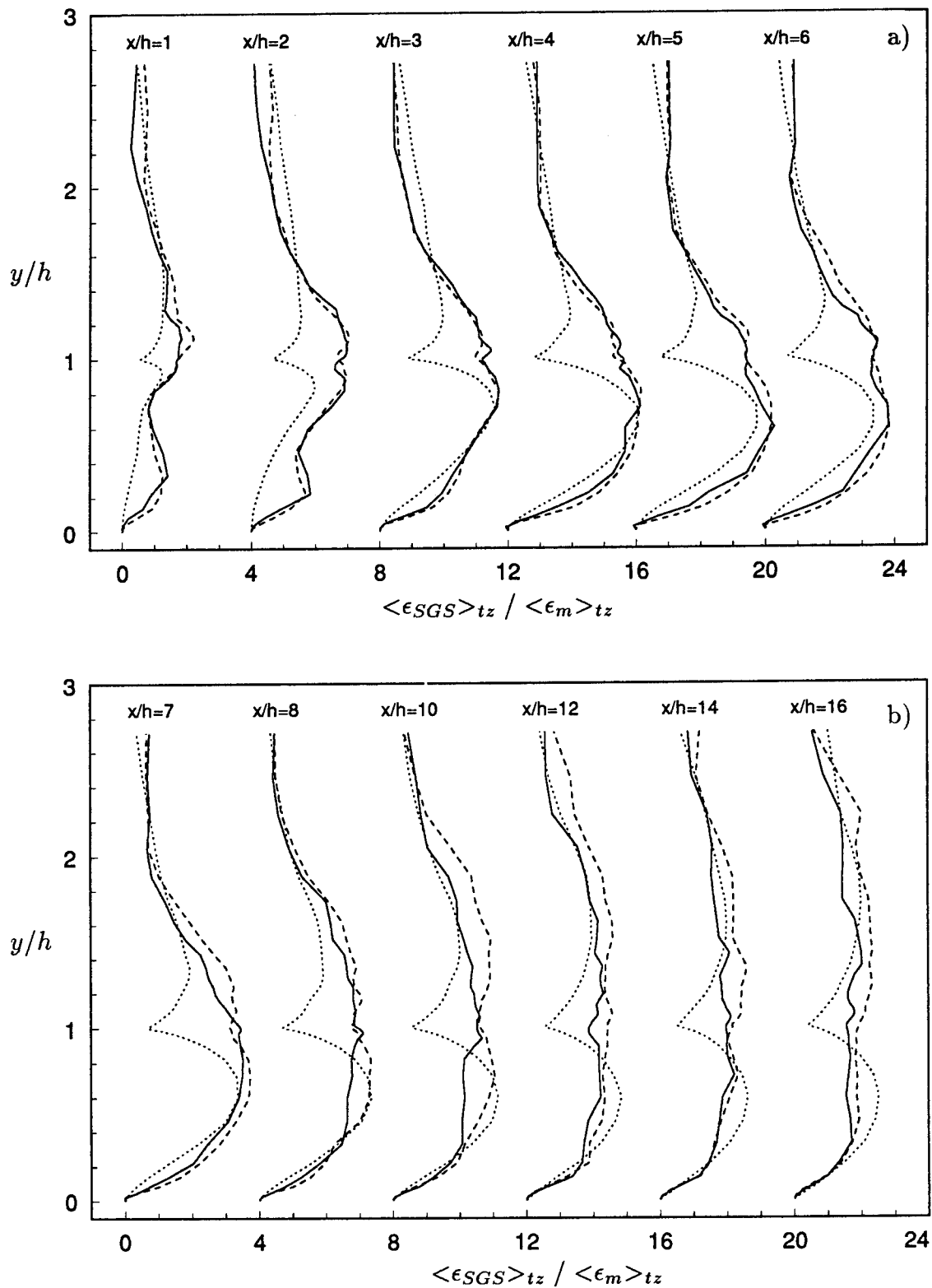
FIGURE **4.4-13**, Ratio of SGS dissipation to molecular dissipation. ———— : DMX1;
———— : DLX1;   ········ : SMX1.   a) $x/h = 1 - 6$,   b) $x/h = 7 - 16$.
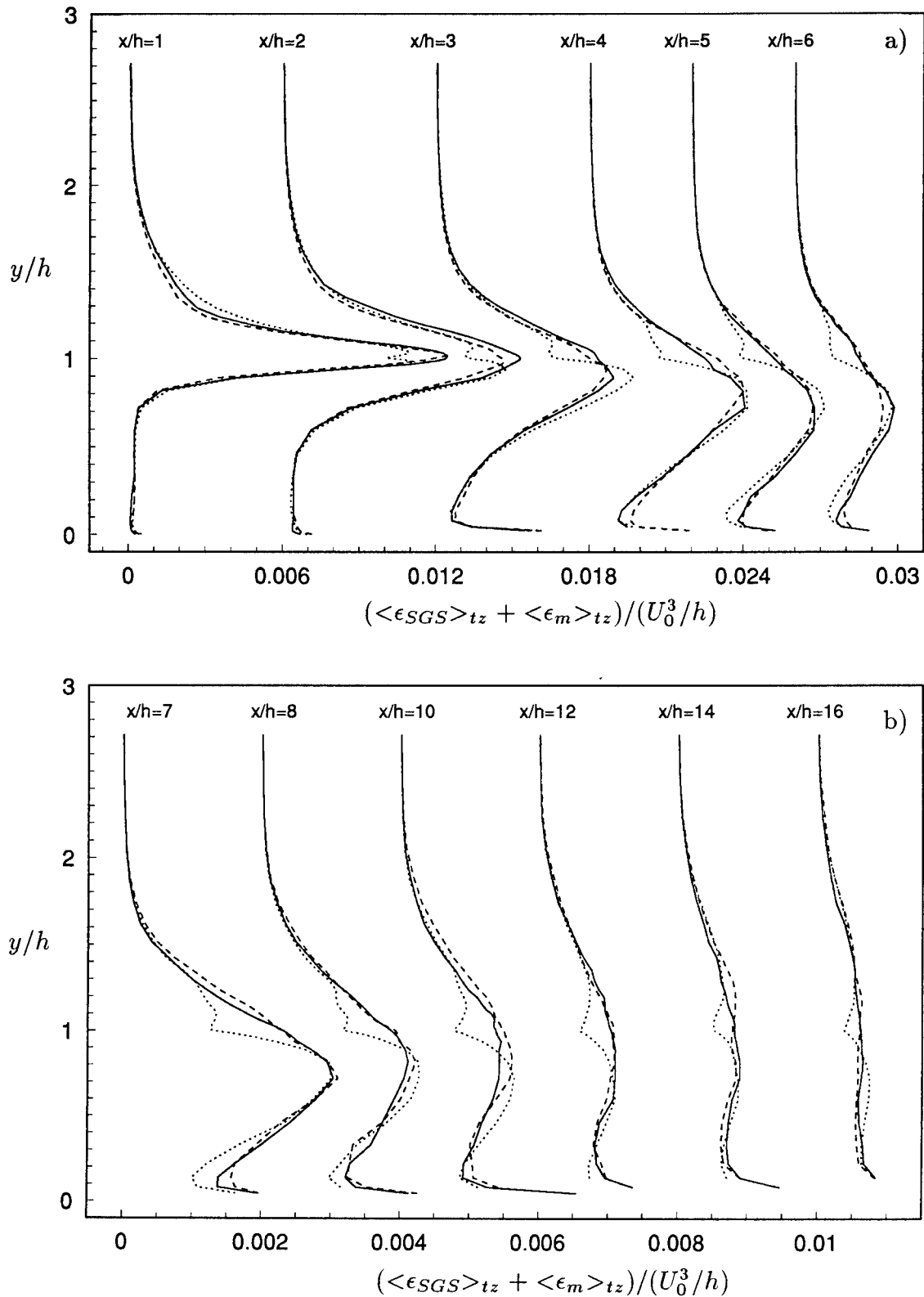
FIGURE **4.4-14**, Sum of SGS dissipation and molecular dissipation. ———— :
DMX1;   - - - - : DLX1;   ········ : SMX1.   a) $x/h = 1 - 6$,   b) $x/h = 7 - 16$.
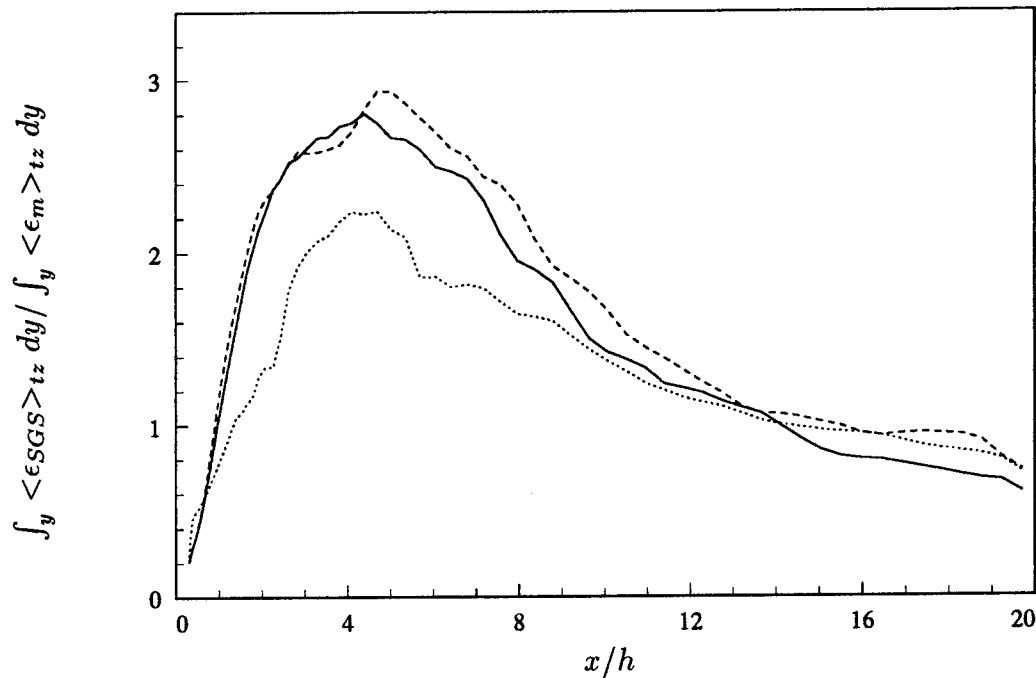
FIGURE **4.4-15**, Ratio of SGS dissipation and Molecular dissipation, both averaged over the cross-sectional area. —— : DMX1; ---- : DLX1; ········ : SMX1.
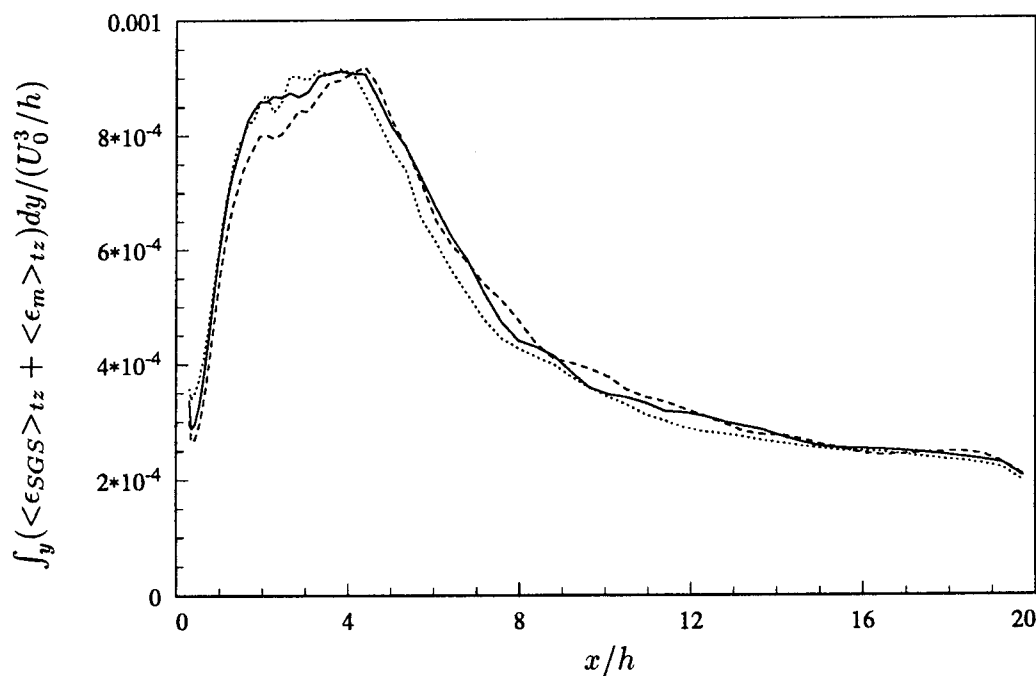
FIGURE **4.4-16**, Sum of SGS dissipation and Molecular dissipation, averaged over the cross-sectional area. —— : DMX1; ---- : DLX1; ········ : SMX1.
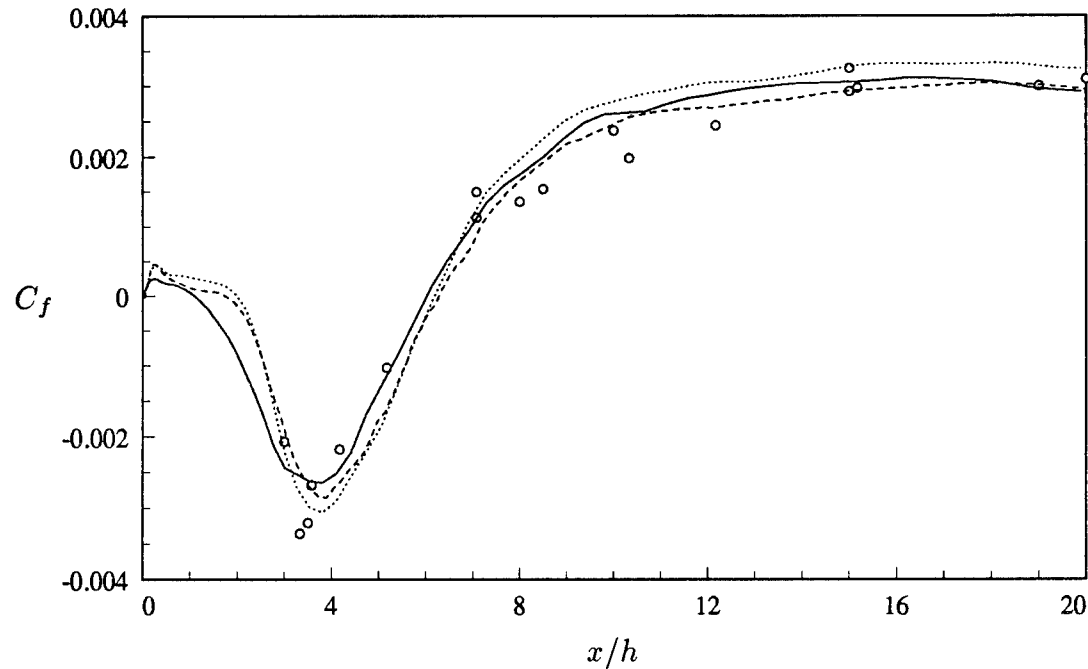
FIGURE **4.5-1**, Coefficient of friction along the lower wall, downstream of the step.
———— : NMX1;   — — — : DNS;   ········ : DMX1;   o : Experiment (Jovic &
Driver).
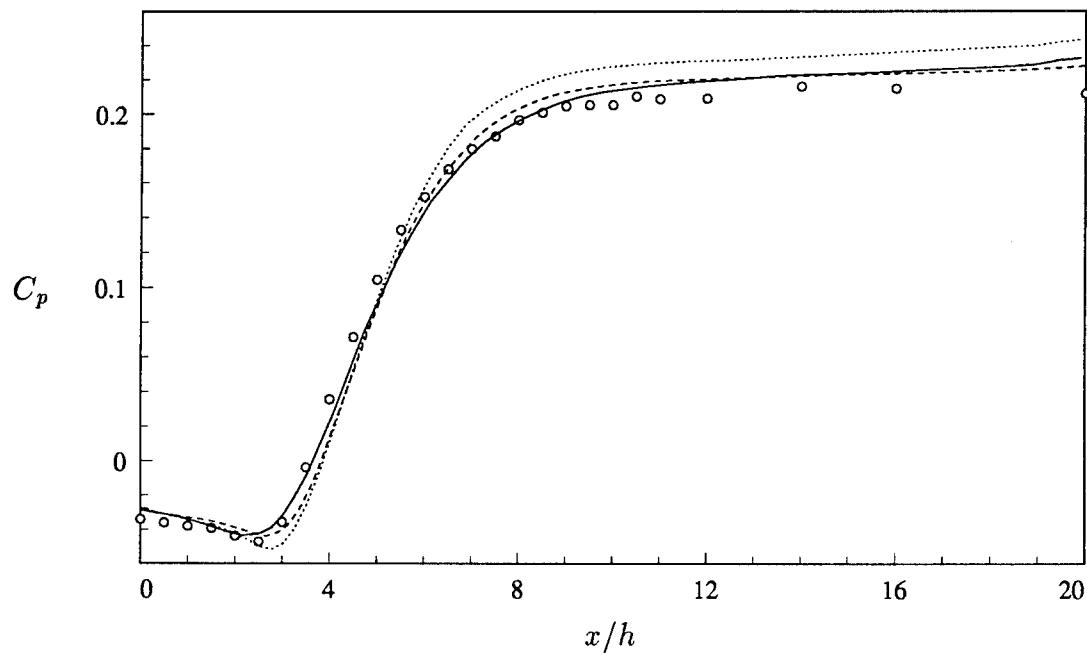
FIGURE **4.5-2**, Pressure coefficient along the lower wall, downstream of the step.
———— : NMX1;   — — — : DNS;   ········ : DMX1;   o : Experiment (Jovic &
Driver).
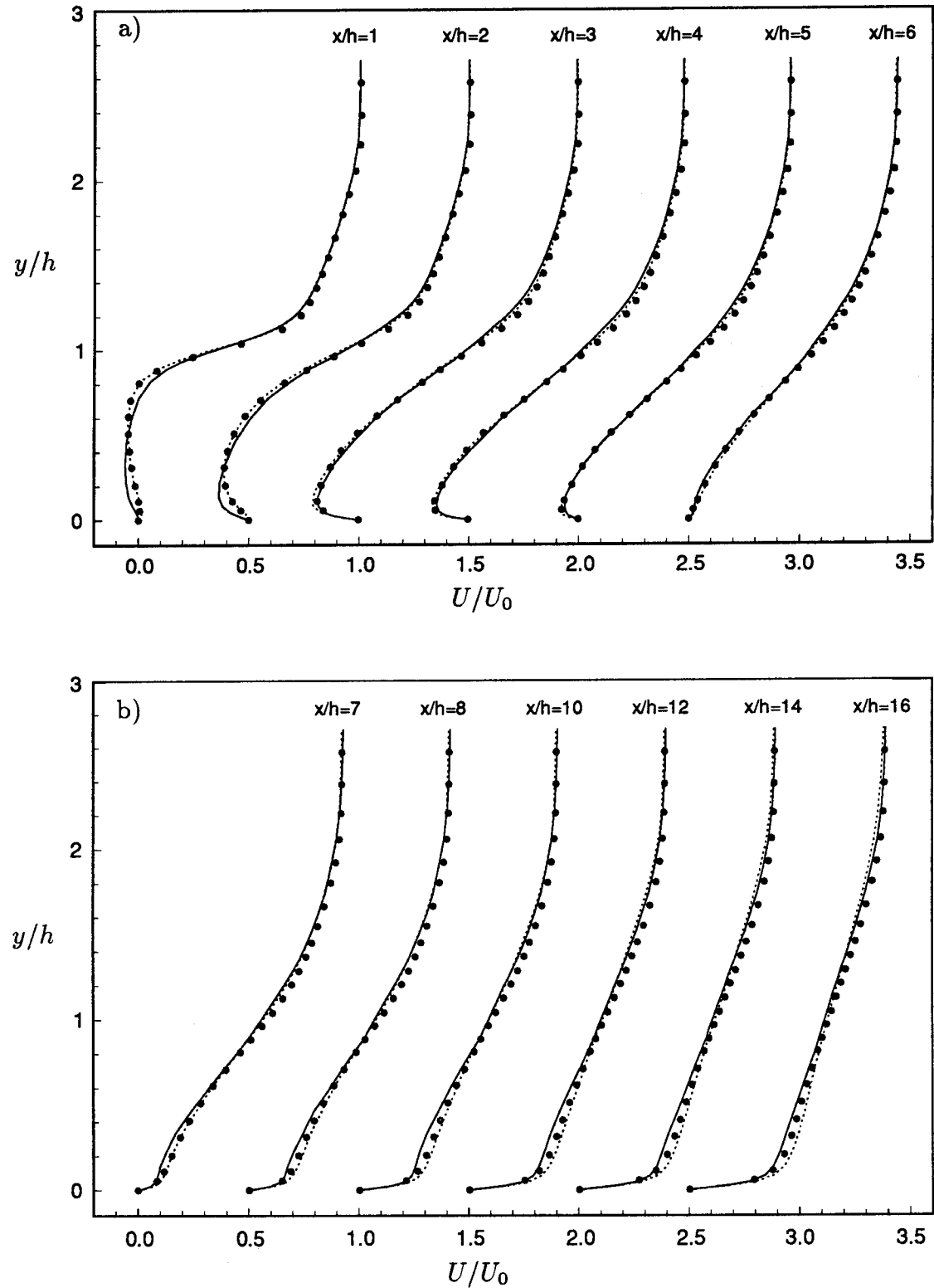
FIGURE **4.5-3**, Mean streamwise velocity profiles. ——— : NMX1;
········ : DMX1; ● : DNS. a) $x/h = 1 - 6$, b) $x/h = 7 - 16$.
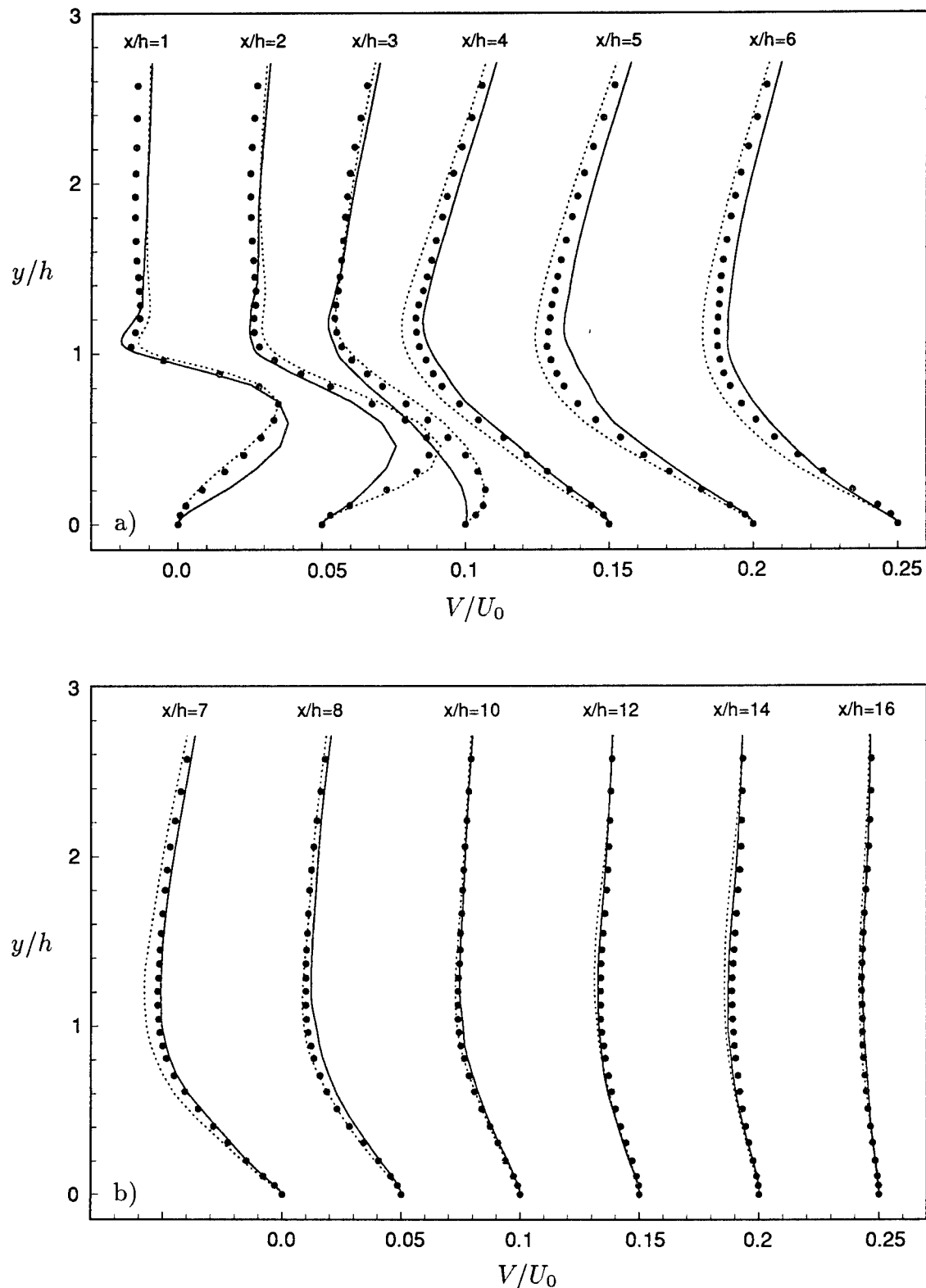
FIGURE **4.5-4**, Mean wall-normal velocity profiles.   ——— : NMX1;
········ : DMX1;   ● : DNS.   a) $x/h = 1 - 6$,   b) $x/h = 7 - 16$.
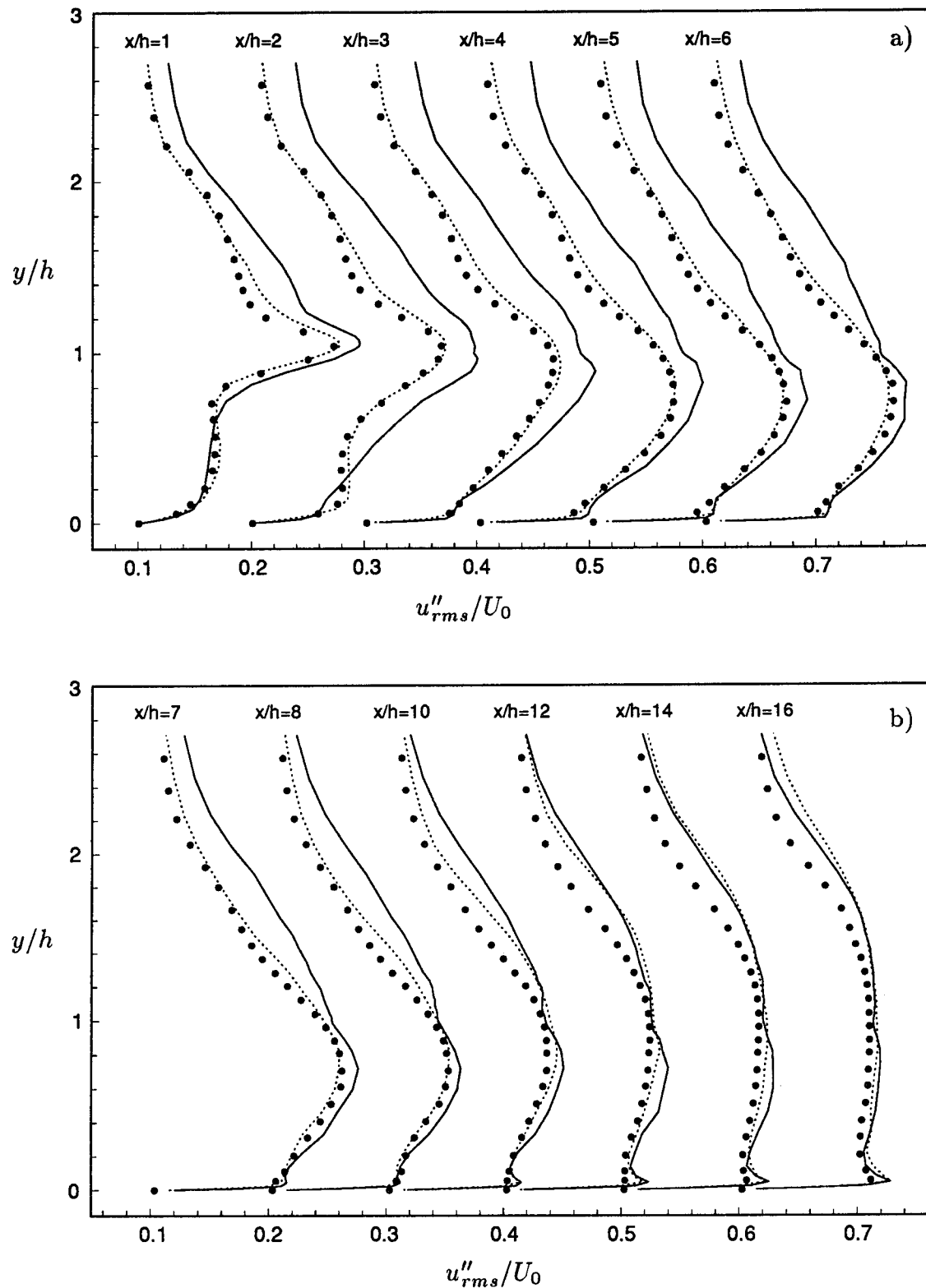
FIGURE **4.5-5**, Resolved streamwise turbulence intensity. ——— : NMX1;
········ : DMX1;   ● : DNS.   a) $x/h = 1 - 6$,   b) $x/h = 7 - 16$.
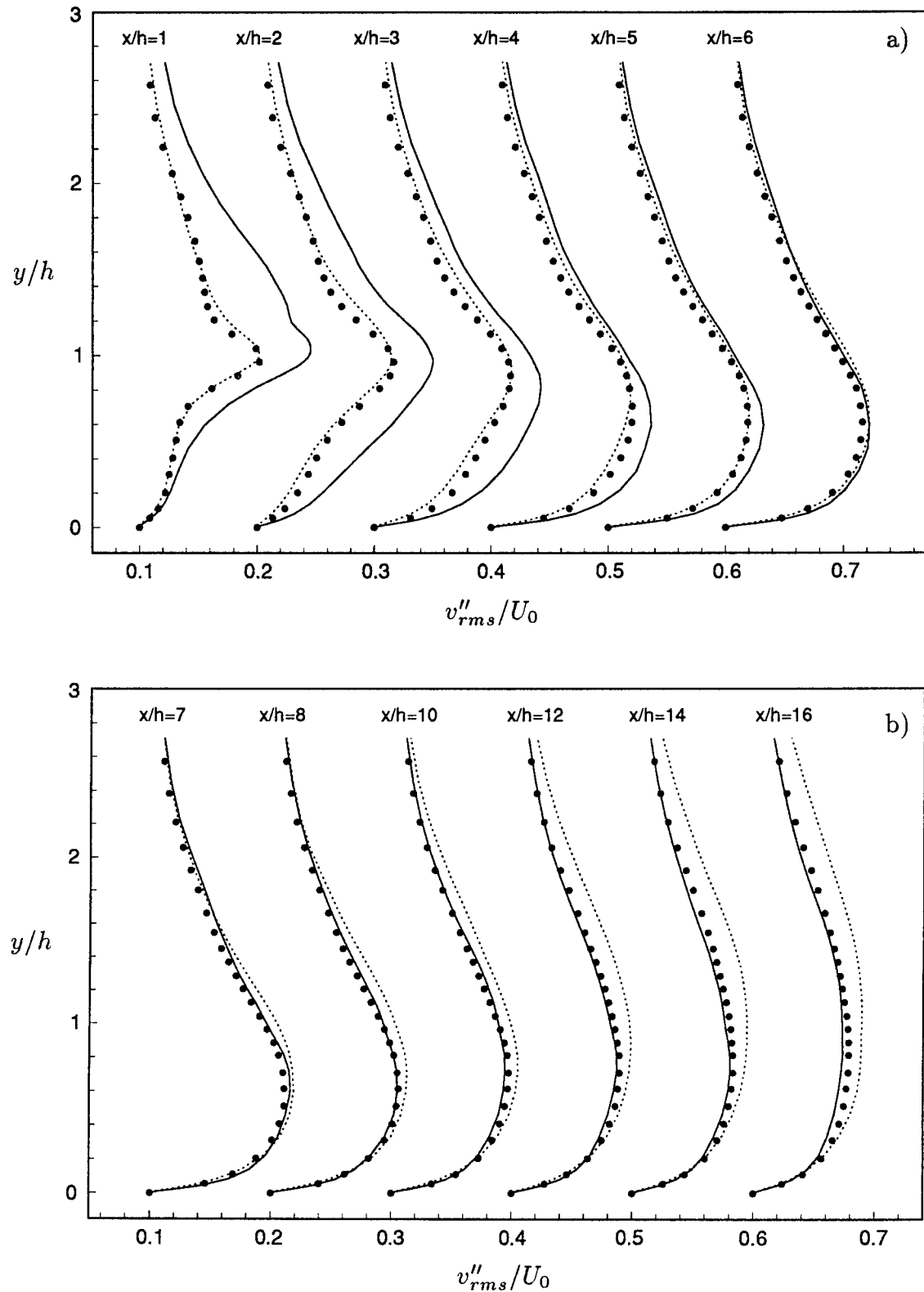
FIGURE **4.5-6**, Resolved wall-normal turbulence intensity. ———— : NMX1;
········ : DMX1;   ● : DNS.   a) $x/h = 1 - 6$,   b) $x/h = 7 - 16$.
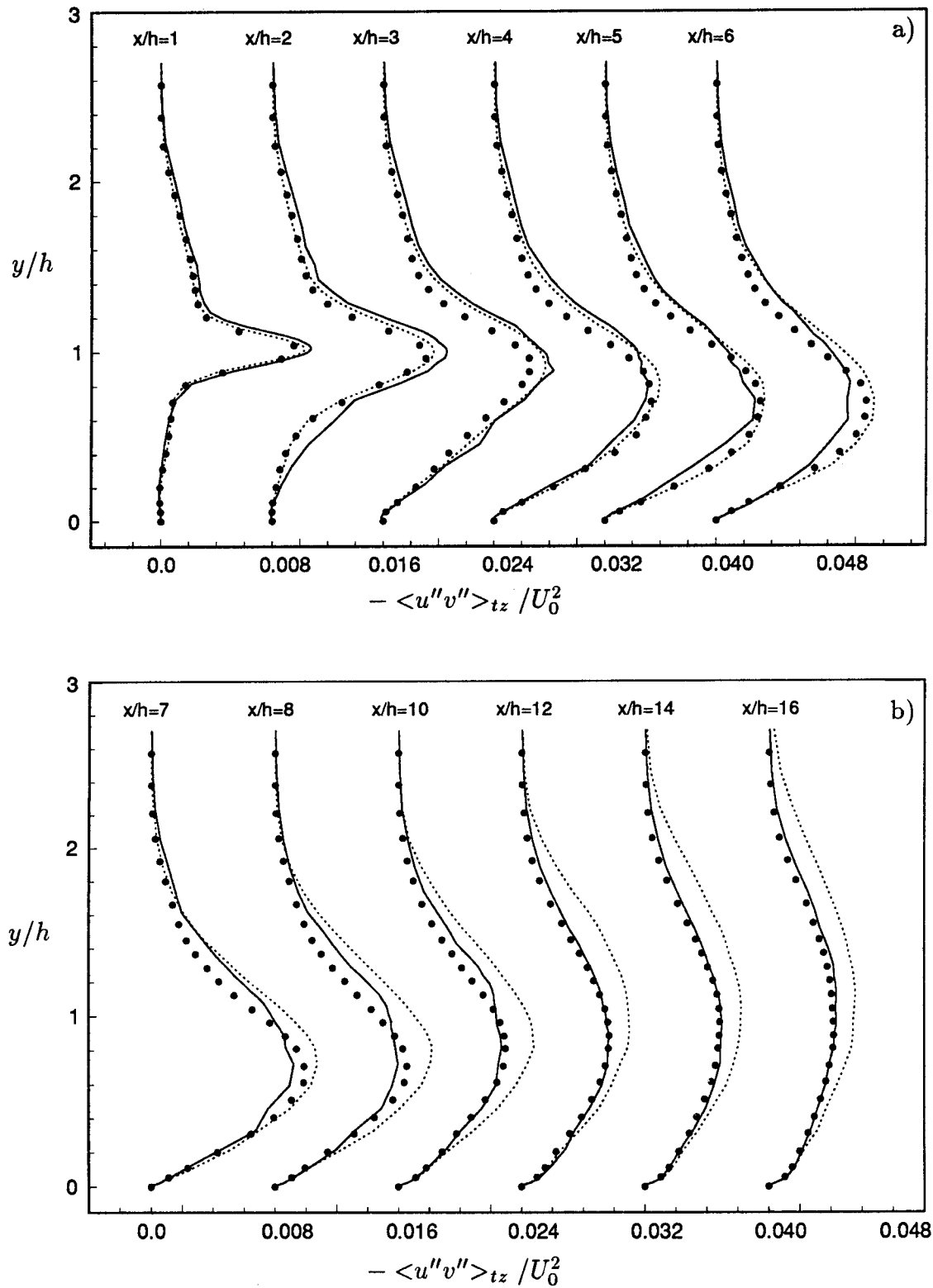
FIGURE 4.5-7, Turbulent shear stress.   ———— : NMX1;   ········ : DMX1;   • : DNS.   a) $x/h = 1 - 6$,   b) $x/h = 7 - 16$.
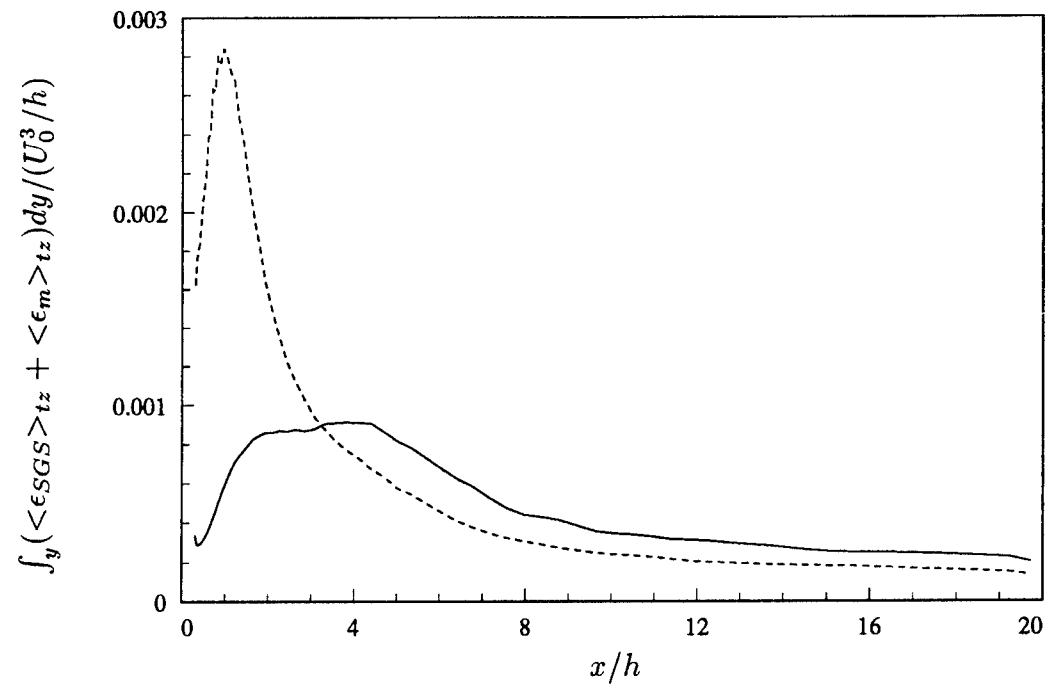
FIGURE **4.5-8**, Sum of SGS dissipation and Molecular dissipation, averaged over the cross-sectional area. ——— : DMX1;   - - - - : NMX1.

<div style="text-align: right;">

Chapter 5

</div>

RESULTS, HIGH REYNOLDS NUMBER CASE

This chapter presents the results from three large eddy simulations of turbulent flow over a backward facing step at Reynolds number, $Re = 28000$. Only one grid resolution was considered, however, both the DM model, the DLM model and the Smagorinsky model were used. This Reynolds number is a factor of 5.5 larger than that used for the simulations described in chapter 4 and falls in the range of engineering interest. It is also outside the range of DNS. Contrary to the low Reynolds number case, a calculation with no subgrid scale model failed to produce meaningful results at $Re = 28000$.

There have been several experimental studies of the backward facing step in the Reynolds number range, 20000 to 45000. Eaton & Johnston (1981) give an excellent review of some of this work. The experimental investigation selected as reference for the present calculations is that of Adams *et al.* (1984).

The objective of the high Reynolds number LES study is to evaluate the performance of the DM model and the DLM model in a complex flow at a Reynolds number of engineering interest.

Section 5.1 gives a brief description of the experimental study by Adams *et al.* Section 5.2 describes the computational domain, including grid resolution and boundary conditions. All results are described in section 5.3, and section 5.4 summarizes the computational costs.

5.1 Reference Case

The experiments of Adams *et al.* (1984) were conducted at Stanford University in a low-speed, open-circuit wind tunnel. The development section upstream of the step was $72h$ long and the side-wall boundary layers were removed using suction boxes placed $12h$ upstream of the step. The last $6h$ of the bottom wall in the development section was covered with a porous plate used for suction or blowing in order to create a boundary layer of any desired thickness. The height of the development section was $4h$, giving an expansion ratio of 1.25. The aspect ratio (spanwise-extent/step-height) of the test section was 11.4.

For the test-case used as reference for the present calculations, the boundary layer thickness at both the step-wall and the upper wall was about $1.2h$. Thus the flow approaching the step consisted of two developing boundary layers with a mostly undisturbed core. Reference pressure and reference velocity were obtained from values $3.3h$ upstream of the step in the potential flow region. The Reynolds number, based on step height, h, and inlet free-stream velocity, U_0, was approximately 28000.

Static pressure measurements were made both on the step-wall and top-wall in the test-section. A Laser Doppler Anemometer was used for measurement of mean and fluctuating components of the streamwise velocity. The coefficient of friction was measured using a pulsed wall probe which allows the magnitude as well as the sign of the skin friction to be obtained.

Profiles of the mean streamwise velocity and streamwise turbulence intensity were measured both upstream and downstream of the step, covering the recirculation region as well as the recovery region. No measurements were made of either the wall-normal turbulence intensity or the turbulent shear stress.

5.2 Calculation Setup

This section gives a full description of the computational setup, including geometry and boundary conditions. Three cases were calculated using the same grid resolution, but different subgrid scale models.

5.2.1 Geometry

The geometry of the computational domain was chosen to match the experimental setup of Adams *et al.* The streamwise extent of the domain is $30h$ which includes an inlet section of length $10h$. The height of the inlet section is $4h$, giving an expansion ratio of 1.25. The top boundary consists of a solid wall. The spanwise extent of the domain is $3h$.

5.2.2 Boundary Conditions

As in the low Reynolds number calculations, the no-slip boundary condition was used along all solid walls. The exit velocity vector was calculated using the convective condition, described in chapter 3. Periodicity was assumed in the spanwise direction.

The inflow boundary condition is essentially the same as that used by Le & Moin in their DNS of the low Reynolds number case. However, the mean inflow velocity profile was found by fitting the log-law through the experimental data of Adams *et al.* (measured $1h$ upstream of the step). The resulting friction velocity at the lower wall is $u_\tau = 0.041$, corresponding to a coefficient of friction of $C_f = 0.0034$. This is the same as that measured by Adams *et al.*

The random phase method, used to generate the fluctuating part of the inflow boundary condition, requires target values for the turbulence intensity profiles. Since only the the streamwise turbulence intensity was measured, the target rms profiles were found by scaling the rms profiles from Spalart's (1988) low Reynolds number boundary layer DNS. The scaling factor was determined as the value that gave the best fit of u''_{rms} to the values measured by Adams *et al.*

As discussed in chapter 4, the random phase method could not be used to generate inflow boundary conditions for the low Reynolds number LES cases, because the flow was not able to recover within the length of the inlet section. However, in

the present case the Reynolds number is significantly higher, yielding less damping in the boundary layer of the inlet section. Figure 5.2-1 shows the coefficient of friction in the inlet section versus streamwise distance, compared with the value measured by Adams *et al.* Results are shown for all LES cases. It can be seen that the flow goes through a transition immediately after entering the domain. This is caused by a lack of turbulent structures in the inflow velocity field. However, in the cases using the DM and the DLM models, the flow starts to recover after a few step heights. At the corner of the step the coefficient of friction has reached about 0.003, which is only about 10 percent off the target value of 0.0034. For comparison, the coefficient of friction from the low Reynolds number case, using the random phase method (appendix A.2), was 20 percent lower than its target value at the corner of the step. The coefficient of friction from the Smagorinsky model shows a much slower recovery.

Unfortunately, apart from the streamwise turbulence intensity, turbulence statistics were not measured by Adams *et al.* Thus, it is difficult to accurately assess the quality of the computed turbulence upstream of the step. (For completeness the computed second order statistics, sampled $0.2h$ upstream of the step, are documented in figure 5.2-2, but with no reference- or target values included).

Despite a faster recovery from the random number inflow boundary condition in the present cases, it should be acknowledged that the inflow method used in the present cases is a potential source of disagreement with the experiment. Calculations, using the inflow method of chapter 4, are therefore currently in progress for the high Reynolds number cases.

5.2.3 Case Definitions

Apart from the SGS model, all parameters were the same in the three LES cases. The grid contained $244 \times 96 \times 96$ points in the streamwise, wall-normal, and spanwise directions, respectively. This includes the 101 streamwise points used to cover the inlet section. Table 5.2-1 gives the grid resolution in wall coordinates, based on the friction velocity at the exit of the domain ($u_\tau/U_0 = 0.028$). The minimum streamwise grid spacing occurs at the corner of the step, whereas the maximum grid spacing occurs at the exit of the computational domain. The grid was stretched in the wall-normal direction, both in the inlet section as well as downstream of the step. Figure 5.2-3 shows the streamwise grid spacing versus

streamwise distance. Figure 5.2-4 gives the same information for the wall-normal direction.

Δx^+_{min}	Δx^+_{max}	Δy^+_{min}	Δy^+_{max}	Δz^+
11.7	186	1.25	155	24.5

TABLE **5.2-1**, Resolution in wall-coordinates.

The initial velocity field for the DM model was obtained by interpolating from a run with a coarser resolution. The two other cases were run later using a restart field from the DM model calculation as initial condition. About 75-100 time units (h/U_0) were used to remove transients from the initial flow fields. Since the total length of the computational domain for the high Reynolds number cases is $30h$, one flow-through time corresponds to about 35 time units. Thus, 2 to 3 flow-through times were used to get rid of transients in the initial fields.

The statistical sampling period used for the DM model was approximately 370 time units. This corresponds to just over 10 flow-through times. The two other cases covered a sampling period of about 250 time units (or 7 flow-through times). For all practical purposes, 250 time units is sufficient to get converged first and second order statistics. The increased sampling time used in DM model is therefore strictly not necessary, but helps smooth some of the statistics, particularly the eddy-viscosity $(<\nu_t>_{tz})$ which proved to be somewhat harder to converge than the other statistical quantities. As in the low-Reynolds number cases, statistics were sampled at each time-step by averaging in time as well as in the homogenous spanwise direction.

5.3 Results

This section contains the results from the large eddy simulations performed of the backward facing step at $Re = 28000$. It should also be mentioned that a case was attempted, using the same grid-resolution as in the LES cases, but without a subgrid scale model. The motivation was as before to generate a basis for evaluating the effect of the subgrid scale models. However, removing the damping provided by the eddy-viscosity led to numerical instabilities. Thus at high Reynolds numbers, the molecular diffusion is insufficient to maintain a stable calculation, and a subgrid scale model contribution is necessary, not only to get good results, but to get any results at all.

5.3.1 Coefficient of Friction and Reattachment Length

The coefficient of friction along the lower wall is shown in figure 5.3-1. Contrary to the low-Reynolds number case, small differences are observed between the two dynamic models. The C_f-curve from the DM model is shifted slightly to the right of the C_f-curve from the DLM model. As in the low Reynolds number case, the Smagorinsky model yields overall good agreement with the two dynamic models.

Good agreement with experimental data is observed upstream of about $x/h = 3$ and around reattachment. The coefficient of friction is under-predicted in the last part of the computational domain, i.e., downstream of about $x/h = 12$. The deviation is most likely due to the grid resolution being too coarse in this region (see table 5.2-1 and figure 5.2-3).

Most noticeable, however, is the significant discrepancy in the recirculation region, around $x/h = 4$. Whereas the minimum value predicted by the experiment is $C_f = -0.9 \cdot 10^{-3}$, the calculations predict a minimum of about $C_f = -1.7 \cdot 10^{-3}$. The reason for the discrepancy is not clear. The calculations may suffer from insufficient grid resolution, however, since only one resolution was explored, conclusions cannot be drawn. In addition, the inflow boundary condition used was found to cause problems in the low Reynolds number case, and might therefore also be a possible source for error in the present case.

With the overall poor agreement between the calculations and the experiment it is not possible to claim that one subgrid scale model yields better results than the

others. The models give nearly identical results, although the difference between them is larger than that observed in the low-Reynolds number cases.

The reattachment lengths from the three calculations are listed in table 5.3-1, together with the deviation, compared with the experimental value of Adams *et al.*

	X_R/h	% deviation
Adams *et al.*	6.7 ± 0.1	
DM model	7.07	5.5
DLM model	6.74	0.6
Smagorinsky model	6.80	1.5

TABLE **5.3-1**, Reattachment length.

The DLM model is seen to give an almost identical reattachment length to that reported by Adams *et al.* The Smagorinsky model gives a 1.5 percent deviation compared with the experiment. The DM model, on the other hand, gives a 5.5 percent deviation, which is outside the uncertainty reported in the experiment. Based on the reattachment length it would therefore seem that both the DLM model and the Smagorinsky model are doing better than the DM model. However, since the calculated reattachment length is tied to the coefficient of friction, which in turn shows poor agreement with the experiment, a firm conclusion about which model is better cannot be drawn based on X_R.

Figure 5.3-2 shows the coefficient of friction along the upper wall of the computational domain. No measurements were taken at this wall, and the results are included for completeness. The rather large difference between the Smagorinsky model and the two dynamic models within the first 3 step heights is due the slower recovery in the inlet section (see figure 5.2-1). Downstream of $x/h = 3$ only minor differences are observed between the three cases. An interesting point to observe is the sharp decrease in C_f at about $x/h = 19$. This is clearly an effect of the outflow boundary condition.

5.3.2 <u>Pressure Coefficient</u>

The pressure coefficient (defined in section 4.3.3) is plotted in figures 5.3-3 and 5.3-4 for the lower and upper walls, respectively. As in the experiment, the reference pressure, P_0, is determined at $3.3h$ upstream of the step, in the core region of the flow. A clear over-prediction by the calculations is observed compared with measured values. However, it should be noted that the pressure is over-predicted even at the corner of the step. Since the flow is going through a transition in the inlet section, recovering from the random inflow conditions, using $x/h = -3.3$ as reference point might not be appropriate.

Figures 5.3-5 and 5.3-6 shows the pressure coefficient along the two walls, using the pressure at the corner of the step as reference. This improves agreement with the experimental values, but C_p is still over-predicted by the calculations. This is the same trend as observed in the low Reynolds number calculations. In those cases it was shown that agreement with the reference data improved with increasing streamwise grid resolution. It is therefore likely that some of the discrepancy is tied to insufficient grid resolution, also in the high Reynolds number cases. In addition, as will become obvious in the next section, the core flow appeared to gain mass through Adams *et al.*'s experimental test section, an effect which is likely caused by side-wall boundary layers developing downstream of the expansion. This would result in a reduced pressure recovery in the experiment, as observed in figures 5.3-5 and 5.3-6.

5.3.3 <u>Mean Velocity Profiles</u>

Mean streamwise velocity profiles are compared at eight locations downstream of the step in figure 5.3-7. Focusing on the calculated profiles first, it is evident that the three subgrid scale models produce nearly identical results. The only difference can be found in the near wall region in the recirculation and reattachment zones. In this region the velocity profiles from the DM model are lagging somewhat behind those from the DLM model, indicating a longer recirculation region in the former case. This is consistent with the differences observed in the coefficient of friction and reattachment length between the two cases. The Smagorinsky model gives results that generally fall between those of the two dynamic models, except at the first measurement station where the Smagorinsky model yields the best agreement with experiments. Even though the differences are small, the DLM model, and possibly

also the Smagorinsky model, give results in better agreement with the experiment than the DM model.

Figure 5.3-7*b* reveals that the calculated velocity profiles are lagging behind the experimental results at the last four streamwise stations. Since the numerical scheme conserves mass it appears that the flow in the experiment is gaining mass at these streamwise stations. This was confirmed by integrating the experimental profiles at the corner of the step and at the last two measurement stations, which shows a 5 percent increase in the mass-flow through the experimental test-section. The speed-up of the flow in the experiment is probably caused by the blocking effect of the side-wall boundary layers. The growth of side-wall boundary layers may be part of the reason for the difference in the pressure coefficient pointed out in the previous section.

5.3.4 Turbulence Statistics

Calculated streamwise turbulence intensity profiles are compared with experimental values in figure 5.3-8. As with the other quantities, only minor differences are observed between the three LES cases. Overall good agreement is also seen between calculated and experimental values. However, at the last three streamwise stations u''_{rms} is over-predicted by the calculations along the upper wall. This result is characteristic of simulations with low grid resolution.

Figure 5.3-9 shows the total turbulent shear stress (resolved plus SGS contribution). No experimental results are available for this quantity and the calculated values are included only to show the similarity in the results from the three subgrid scale models. Apart from the first few measurement stations, the models give almost identical results.

Figure 5.3-10 shows the SGS shear stress, τ_{12}, for the three SGS models. Significant differences are observed between the models. The DLM model yields the highest SGS shear stress in the shear layer coming of the step, however, the Smagorinsky model gives the largest contribution in the boundary layer downstream of reattachment and in the boundary layer along the upper wall. (The "kink" in the profiles from the Smagorinsky model appears for reasons explained in section 4.4.3). The DM model is seen to yield the smallest contribution to the turbulent shear stress at all streamwise stations. However, as shown in figure 5.3-11, the overall contribution from the SGS models to the turbulent shear stress is small in all cases.

Figure 5.3-11 shows that the ratio of the subgrid scale shear stress to resolved turbulent shear stress for the DLM model peaks at about 7.3 percent close to the step, and then drops rapidly to about 1.5-2.5 percent. For the DM model the peak value is about 5.9 percent which decreases to about 0.8-1.8 percent downstream of about $x/h = 3$. The Smagorinsky model has a peak of about 6 percent which decreases to about 2 percent in the recovery region. Thus, it can be concluded that all models provide only a small contribution to the turbulent shear stress.

5.3.5 Eddy-Viscosity

Figure 5.3-12 compares the eddy-viscosities from the three models. There is a noticeable difference in the level of the the eddy-viscosities between the cases. The DM model gives an eddy-viscosity which peaks at about 4 times the molecular viscosity in the recirculation region. The eddy-viscosity from the DLM model is more than a factor of two larger. The eddy-viscosity from the Smagorinsky model falls in between those of the two dynamic models.

As pointed out previously, the eddy-viscosity produced by the DM model had to be clipped to avoid points with negative total viscosity. An average of 2 percent of the points in the computational domain had to be zeroed. The DM model gave negative eddy-viscosity at about 12 percent of the points in the computational domain. The DLM model, on the other hand, gave negative eddy-viscosity at about 31 percent of the points.

5.3.6 Dissipation

Figure 5.3-13 shows the ratio of the SGS dissipation to molecular dissipation at several streamwise stations for all LES cases. It is seen that $<\epsilon_{SGS}>_{tz}$ / $<\epsilon_m>_{tz}$ is almost the same at every station for the DLM model and the Smagorinsky model (apart from the "kink" in the profiles from the Smagorinsky model; discussed in section 4.4.3). However, the DM model yields a value that is up to a factor of two smaller than those from the DLM model and the Smagorinsky model. (The "jagged" appearance of the curves is because the statistics sampling time was significantly shorter for quantities related to dissipation than for other quantities).

Figure 5.3-14 shows the total dissipation (SGS dissipation plus molecular dissipation) at the same streamwise stations. Apart from traces of the "kink" at

$y/h = 1$, the models give roughly the same results. The differences observed are likely due to the statistics sampling time being too short.

To better visualize the difference between the three models, figure 5.3-15 shows the ratio of $<\epsilon_{SGS}>_{tz}$ and $<\epsilon_m>_{tz}$, each quantity averaged over the cross-sectional area of the computational domain, plotted versus streamwise distance. Figure 5.3-16 shows the total dissipation averaged over the cross-sectional area and plotted versus streamwise distance.

Figure 5.3-15 shows that the DLM model and the Smagorinsky model give about the same fraction of SGS dissipation upstream of reattachment. The peak value is about 2.7-2.8 in both cases. The contribution from the DM model peaks at about 2.2. Despite these differences, figure 5.3-16 shows that all models give nearly identical total dissipation at all streamwise locations. As in the low Reynolds number cases, the total dissipation in the recovery region is about a factor of four less than the dissipation upstream of reattachment.

5.3.7 Summary

Both the DM model, the DLM model, and the Smagorinsky model have been used successfully to predict turbulent flow over a backward facings step at $Re = 28000$. There are some discrepancies in the coefficient of friction, but other quantities compare favorably with the experimental data.

The models produce nearly identical results. The subgrid scale model contributes only a few percent of the total turbulent shear stress. However, the eddy-viscosity is from 4 to 8 times higher than the molecular viscosity. The SGS dissipation is as much as 7 times the molecular dissipation using either the DLM model or the Smagorinsky model. The DM model gives a maximum ratio of about 5. However, the total dissipation is the same using either SGS model.

Both dynamic models give negative eddy-viscosity (but positive total viscosity) in sections of the computational domain, thus allowing for some reverse transfer of energy.

5.4 Computer Program Performance

The DM model was run a total of 470 time units at a time-step, Δt of 0.010 h/U_0. This includes about 100 time units used to remove transients from the initial flow field before starting to sample statistics. The corresponding number of time-steps is 47000. The DLM model and the Smagorinsky model were run for 350 time units, including the 100 time units used to remove transients from the initial flow field. Δt in this case was 0.012 h/U_0 giving a total integration time of 29170 time-steps.

Table 5.4-1 gives the CPU time per time-step as well as the total CPU time spent for each calculation. As for the low Reynolds number cases, the numbers in table 5.4-1 do not include overhead associated with I/O (input/output). This overhead was from 5 to 20 percent, depending on the configuration of the external memory of the Cray.

Model	CPU/time-step (s)	# of time-steps	CPU time (h)
DM	10.41	47000	136
DLM	12.15	29170	98
Smagorinsky	9.50	29170	77

TABLE **5.4-1**, Performance of LES code (on a Cray C-90).

It can be noticed that the difference between the computational cost for the two dynamic models is less than that reported in the low Reynolds number case. The main reason for the difference is that the error-tolerance used when converging the integral equation (DLM model) was higher in the present case than that used in the low Reynolds number case. An average of 2.6 iterations were needed in order to drop the residual in the integral equation by a factor of 20 (the low Reynolds number case used 50).
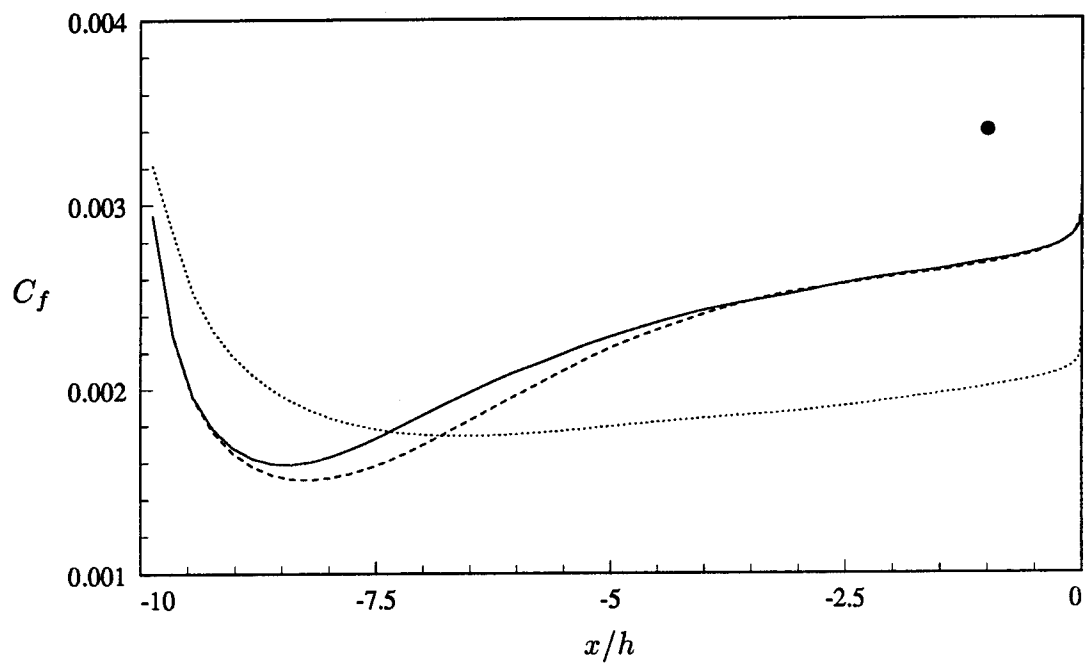
FIGURE **5.2-1**, Coefficient of friction along the lower wall in the inlet section ($Re = 28000$). ——— : DM model; ---- : DLM model; ········ : Smagorinsky model; ● : Adams *et al.* (1984).
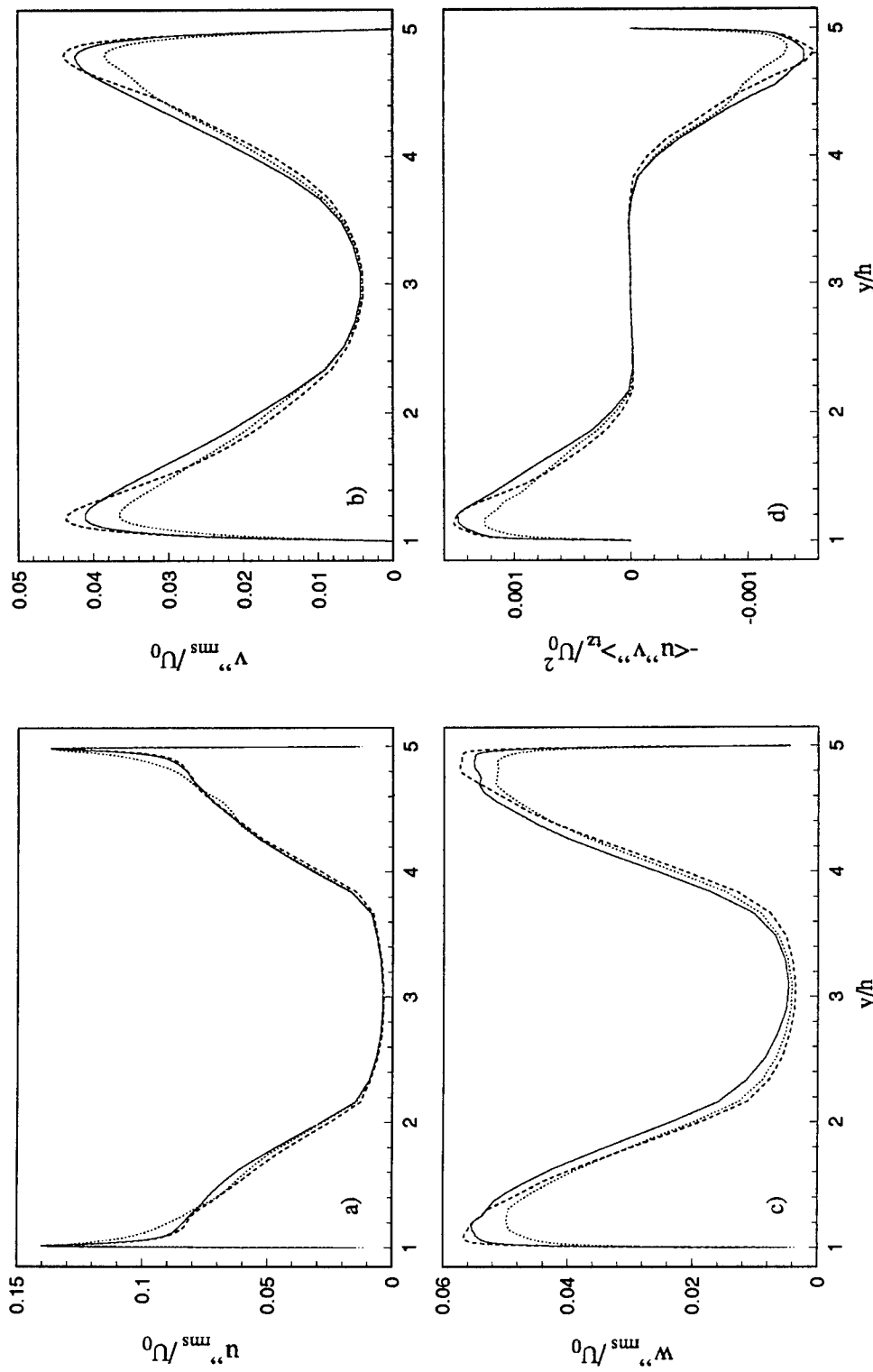
FIGURE **5.2-2**, Turbulent statistics $0.2h$ upstream of the step ($Re = 28000$). ———— : DM model; ———— : DLM model; ········ : Smagorinsky model   a) Streamwise rms fluctuations,   b) Wall-normal rms fluctuations,   c) Spanwise rms fluctuations,   d) Turbulent shear stress (including SGS term).
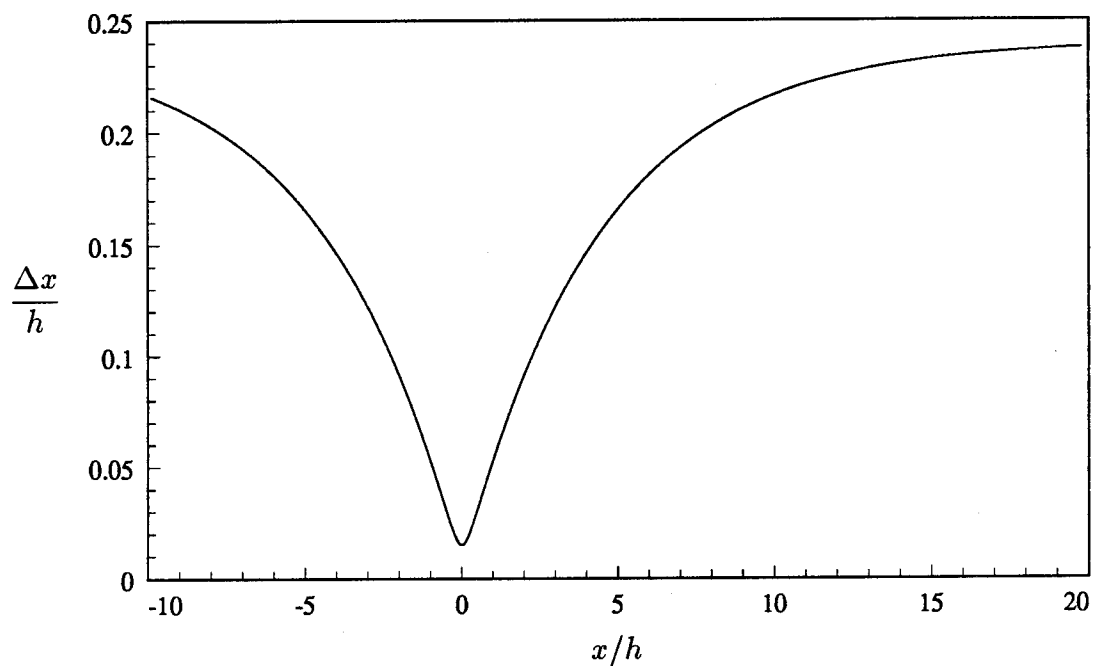
FIGURE **5.2-3**, Streamwise grid spacing versus streamwise distance ($Re = 28000$).
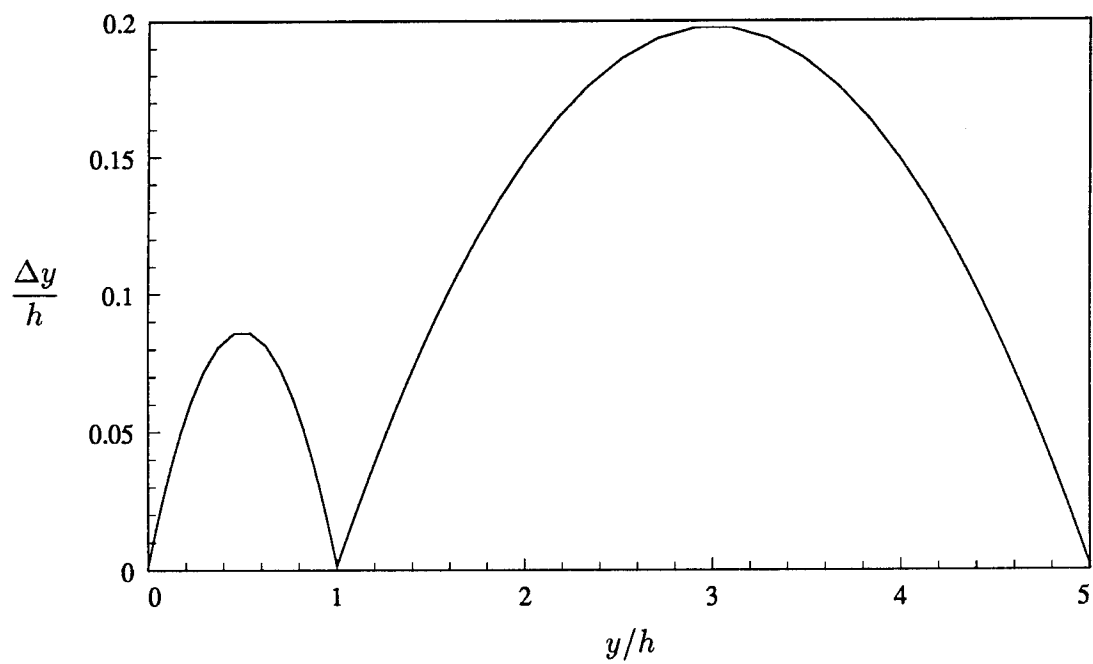
FIGURE **5.2-4**, Wall-normal grid spacing versus wall-normal distance ($Re = 28000$).
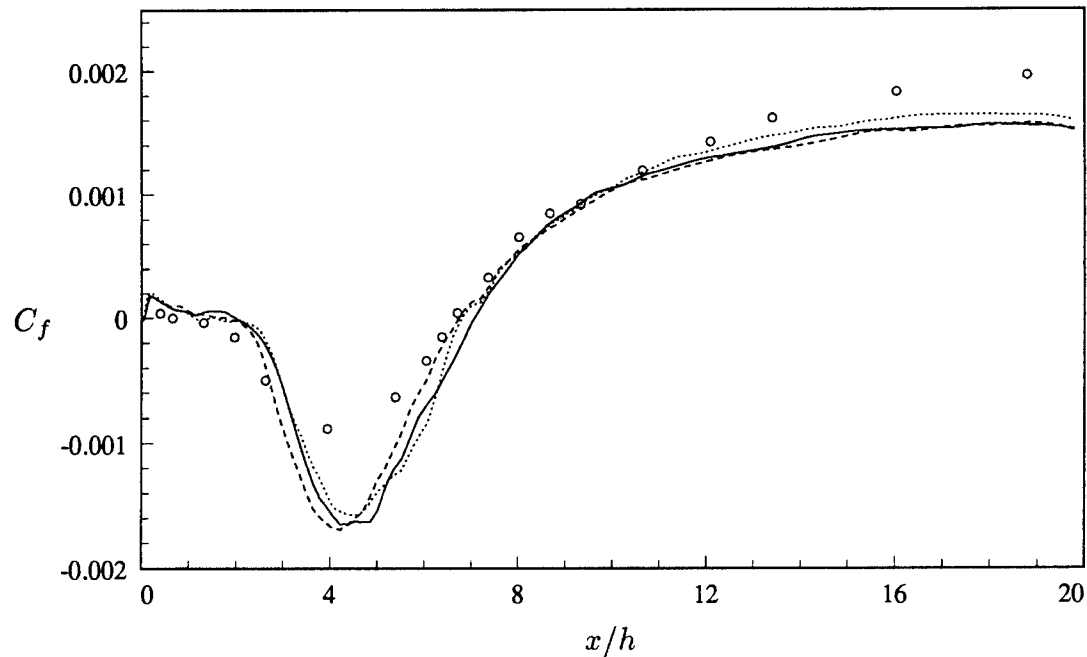
FIGURE **5.3-1**, Coefficient of friction along the lower wall, downstream of the step ($Re = 28000$). ———— : DM model; ——— : DLM model; ········ : Smagorinsky model; o : Experiment (Adams *et al.*).
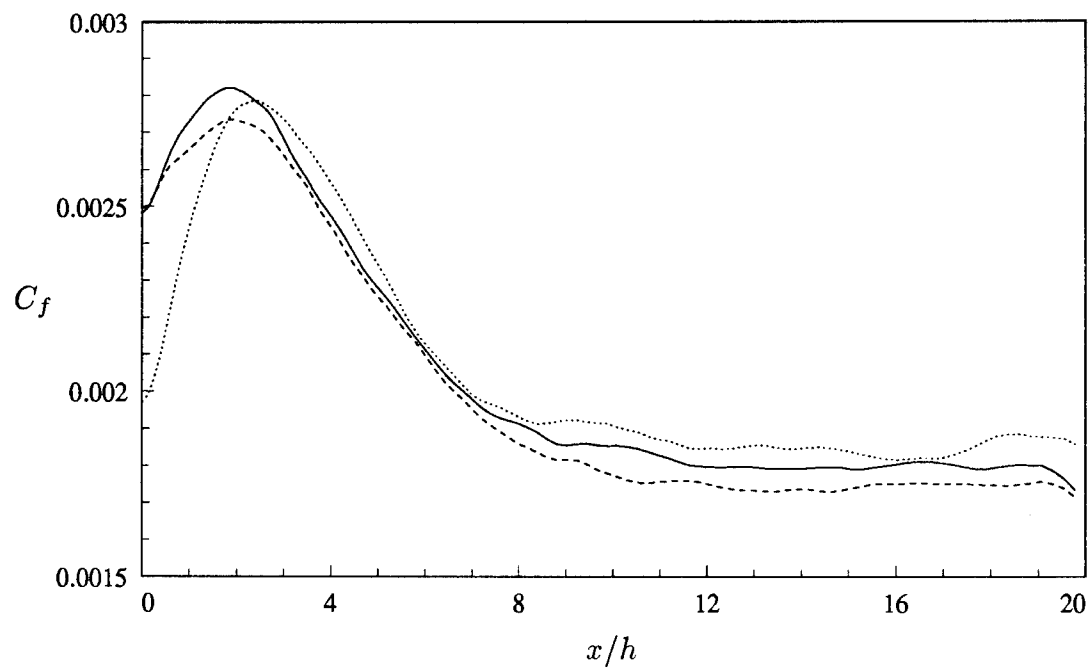
FIGURE **5.3-2**, Coefficient of friction along the upper wall, downstream of the step ($Re = 28000$). ———— : DM model; ——— : DLM model; ········ : Smagorinsky model.
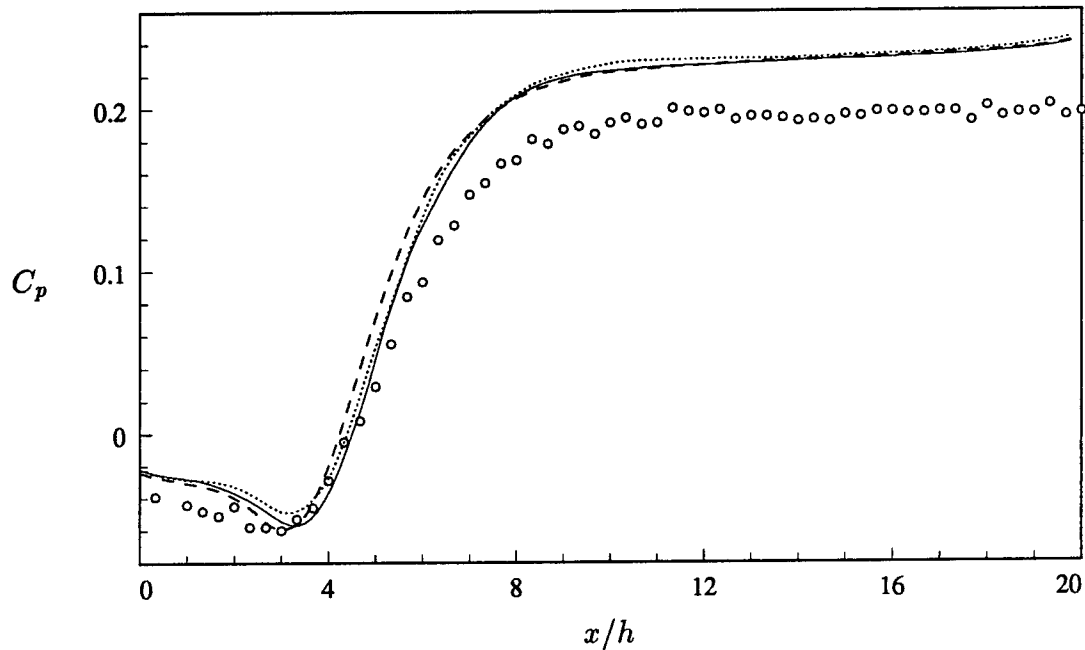
FIGURE **5.3-3**, Pressure coefficient along the lower wall, downstream of the step ($Re = 28000$). Reference point at $x/h = -3.3$. ———— : DM model; ———— : DLM model; ········ : Smagorinsky model; o : Experiment (Adams *et al.*).
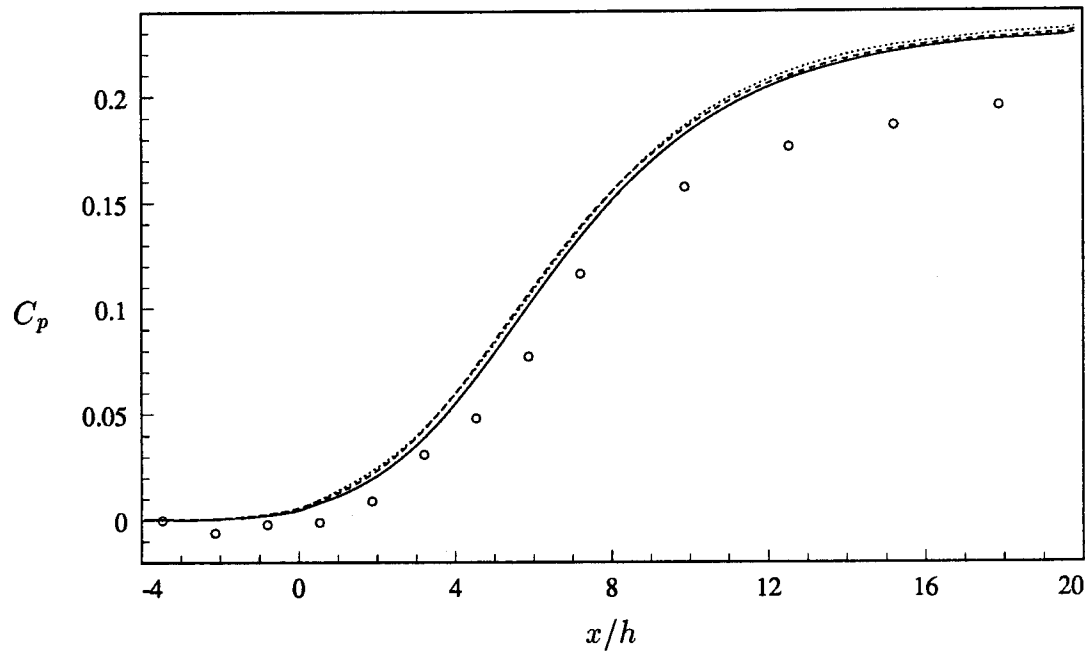
FIGURE **5.3-4**, Pressure coefficient along the upper wall ($Re = 28000$). Reference point at $x/h = -3.3$. ———— : DM model; ———— : DLM model; ········ : Smagorinsky model; o : Experiment (Adams *et al.*).
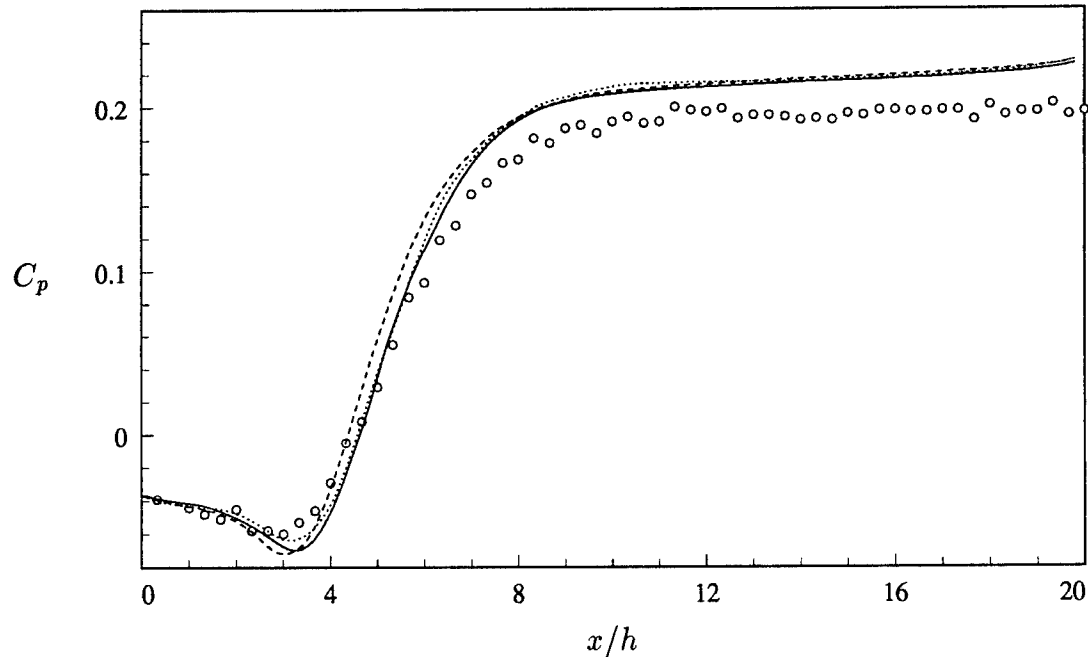
FIGURE **5.3-5**, Pressure coefficient along the lower wall, downstream of the step ($Re = 28000$). Reference point at $x/h = 0$. ———— : DM model;   — — — : DLM model;   ········ : Smagorinsky model;   o : Experiment (Adams *et al.*).
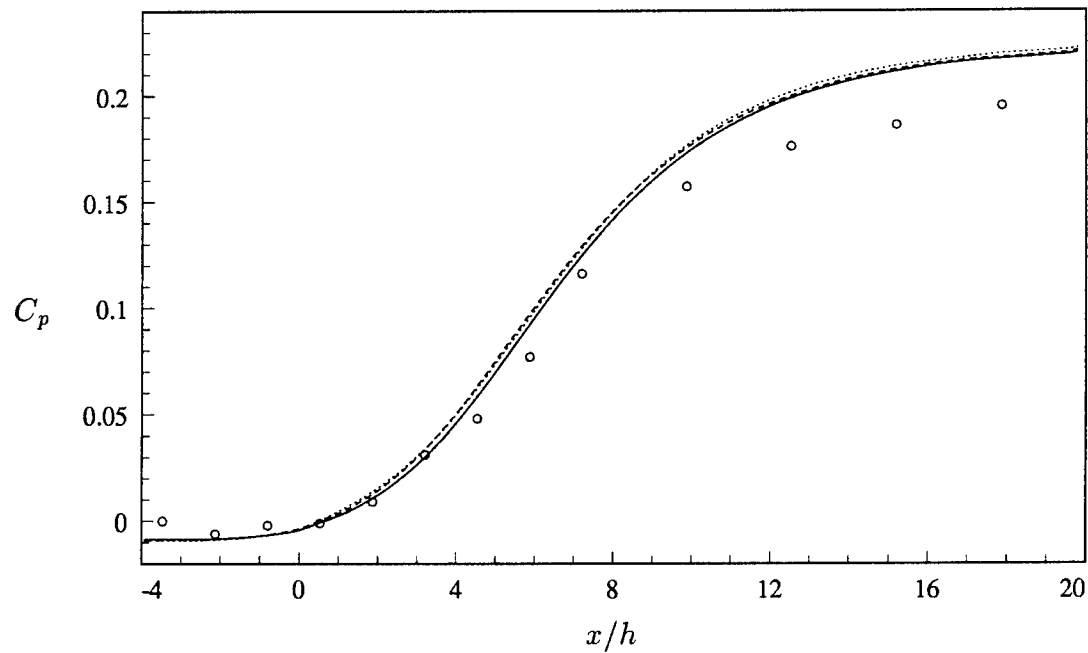
FIGURE **5.3-6**, Pressure coefficient along the upper wall ($Re = 28000$). Reference point at $x/h = 0$.   ———— : DM model;   — — — : DLM model;   ········ : Smagorinsky model;   o : Experiment (Adams *et al.*).
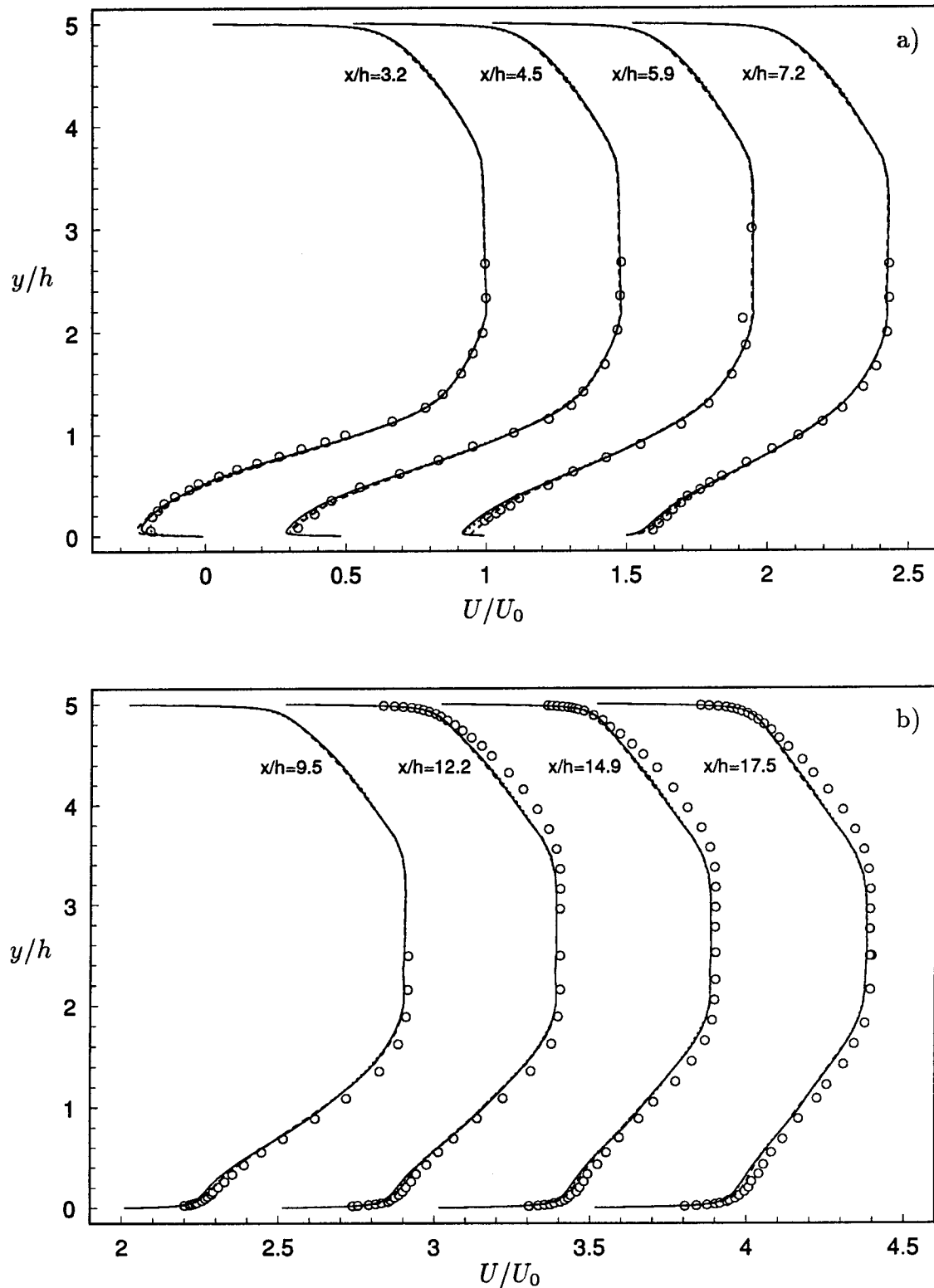
FIGURE **5.3-7**, Mean streamwise velocity profiles ($Re = 28000$). ———— : DM model; ---- : DLM model; ········ : Smagorinsky model; o : Experiment (Adams *et al.*).
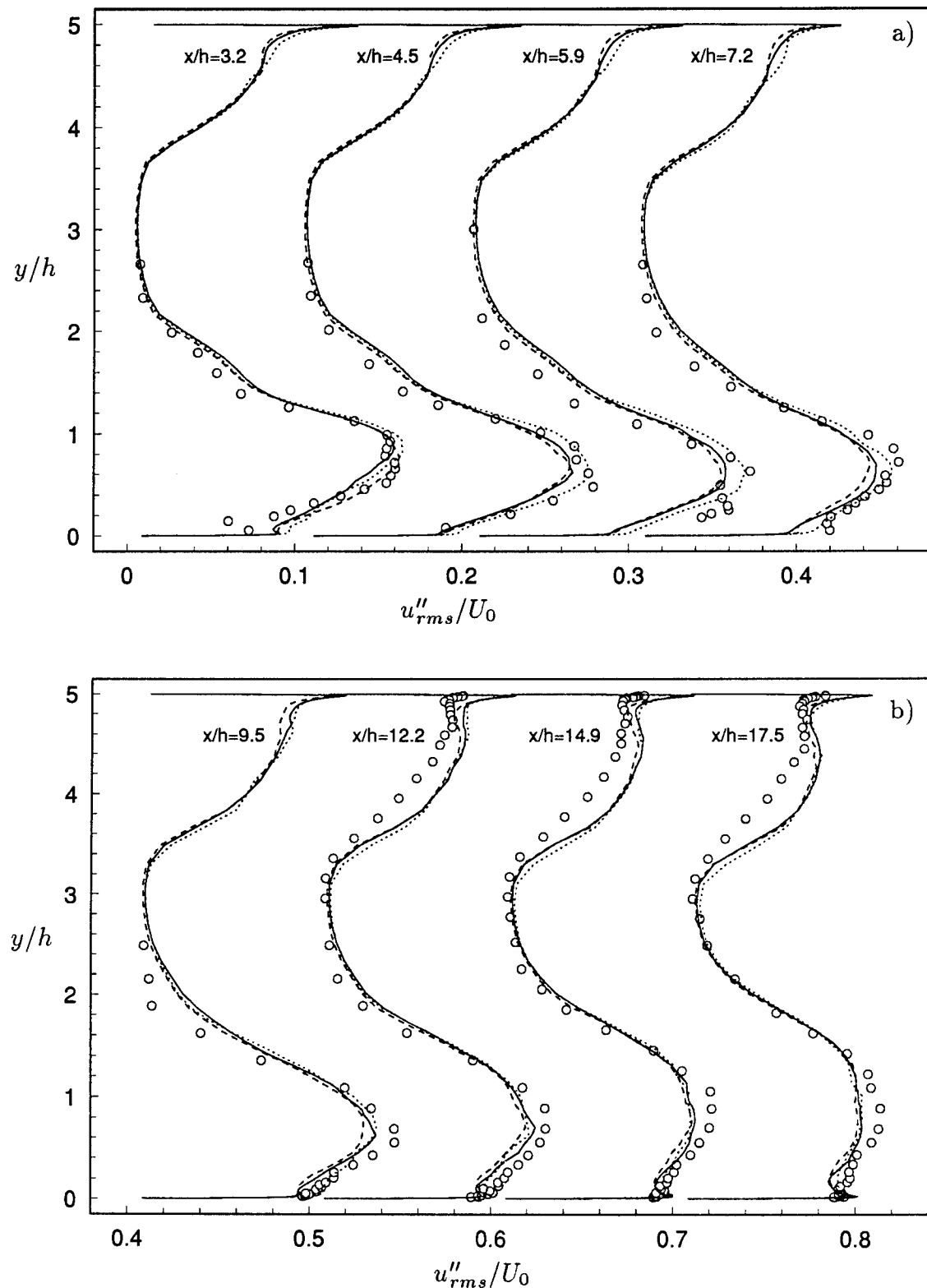
FIGURE **5.3-8**, Resolved streamwise turbulence intensity ($Re = 28000$). ——— : DM model; ———— : DLM model; ········ : Smagorinsky model; o : Experiment (Adams *et al.*).
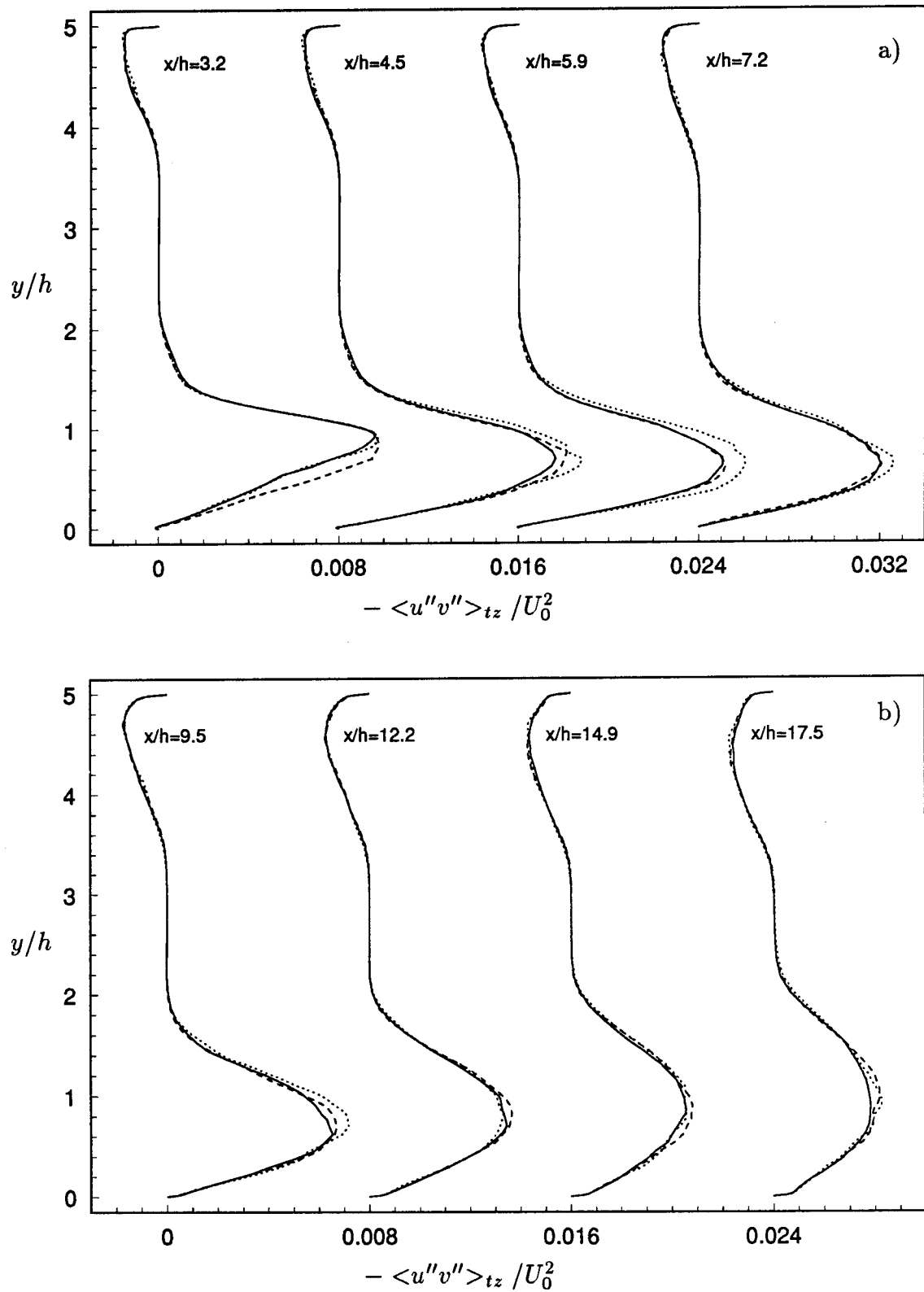
FIGURE **5.3-9**, Turbulent shear stress ($Re = 28000$).   ——— : DM model;
———— : DLM model;   ········ : Smagorinsky model.
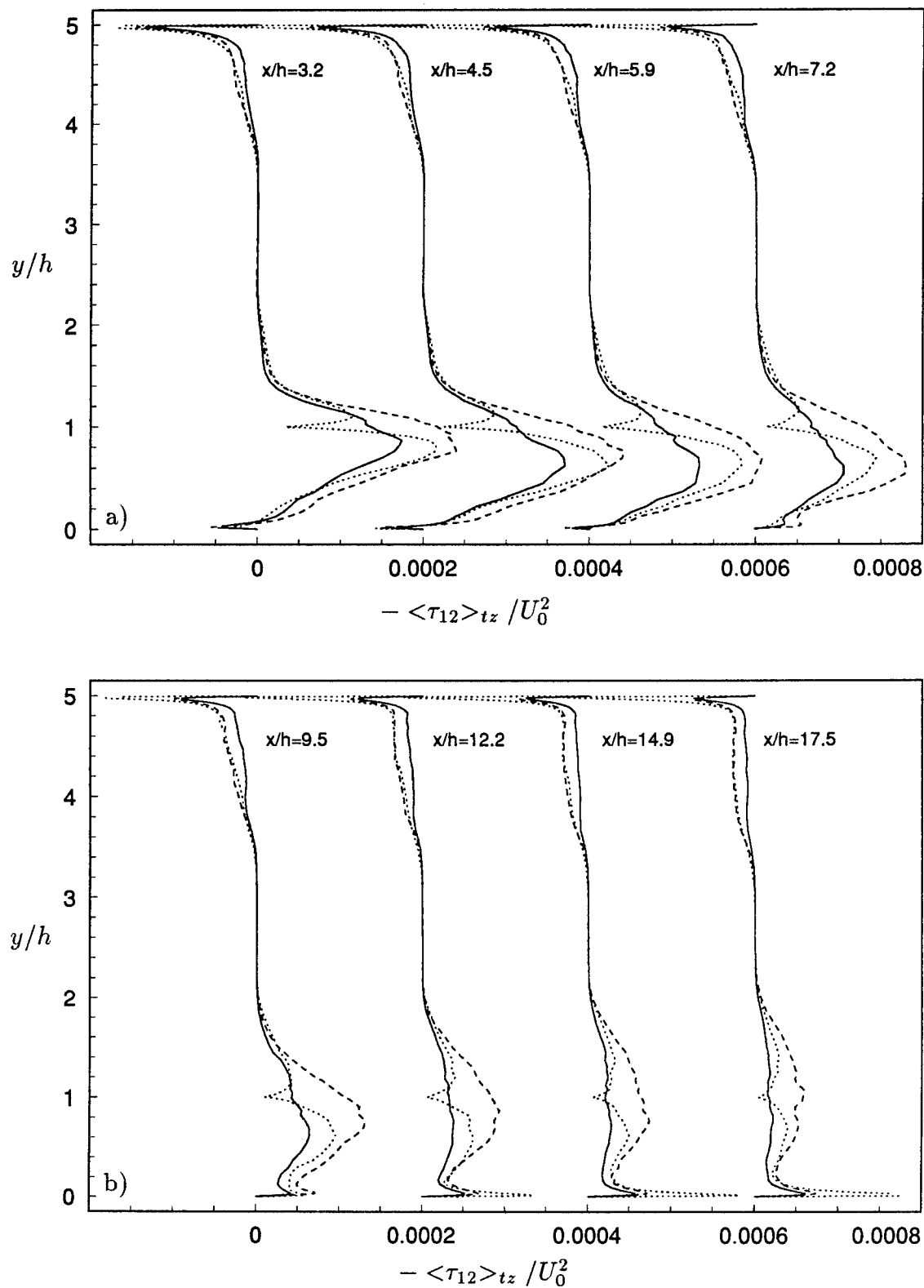
FIGURE **5.3-10**, Subgrid scale shear stress ($Re = 28000$). ——— : DM model; ---- : DLM model; .... : Smagorinsky model.
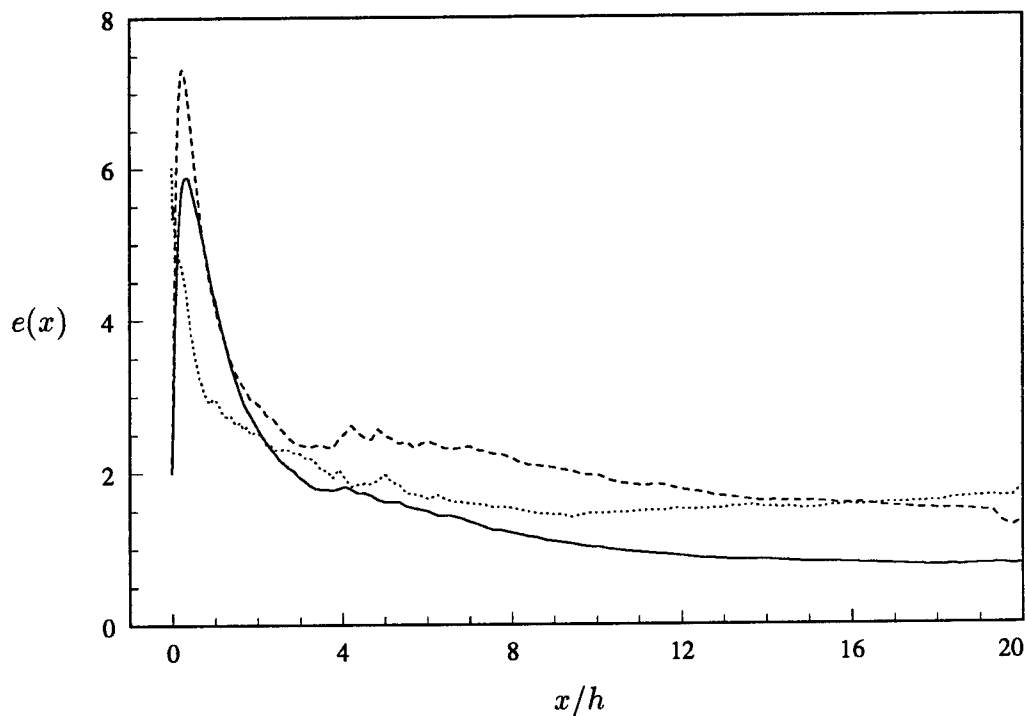
FIGURE **5.3-11**, $e(x)$ (defined in equation 4.3-1) is a measure of the ratio of the SGS shear stress to the resolved turbulent shear stress ($Re = 28000$).

———— : DM model;   − − − − : DLM model;   ········ : Smagorinsky model.
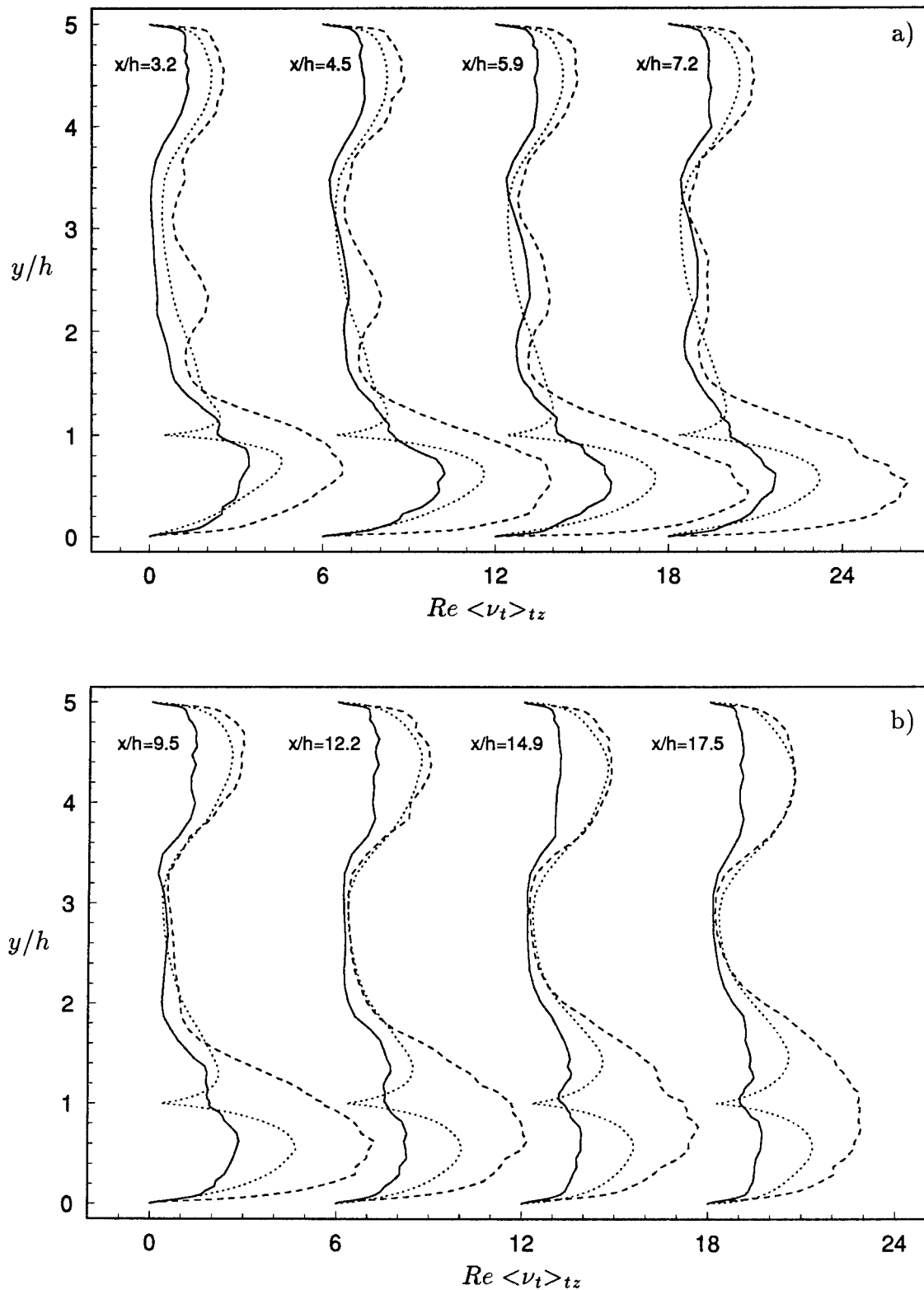
FIGURE **5.3-12**, Ratio of eddy-viscosity to molecular viscosity ($Re = 28000$).
——— : DM model;   – – – – : DLM model;   ········· : Smagorinsky model.
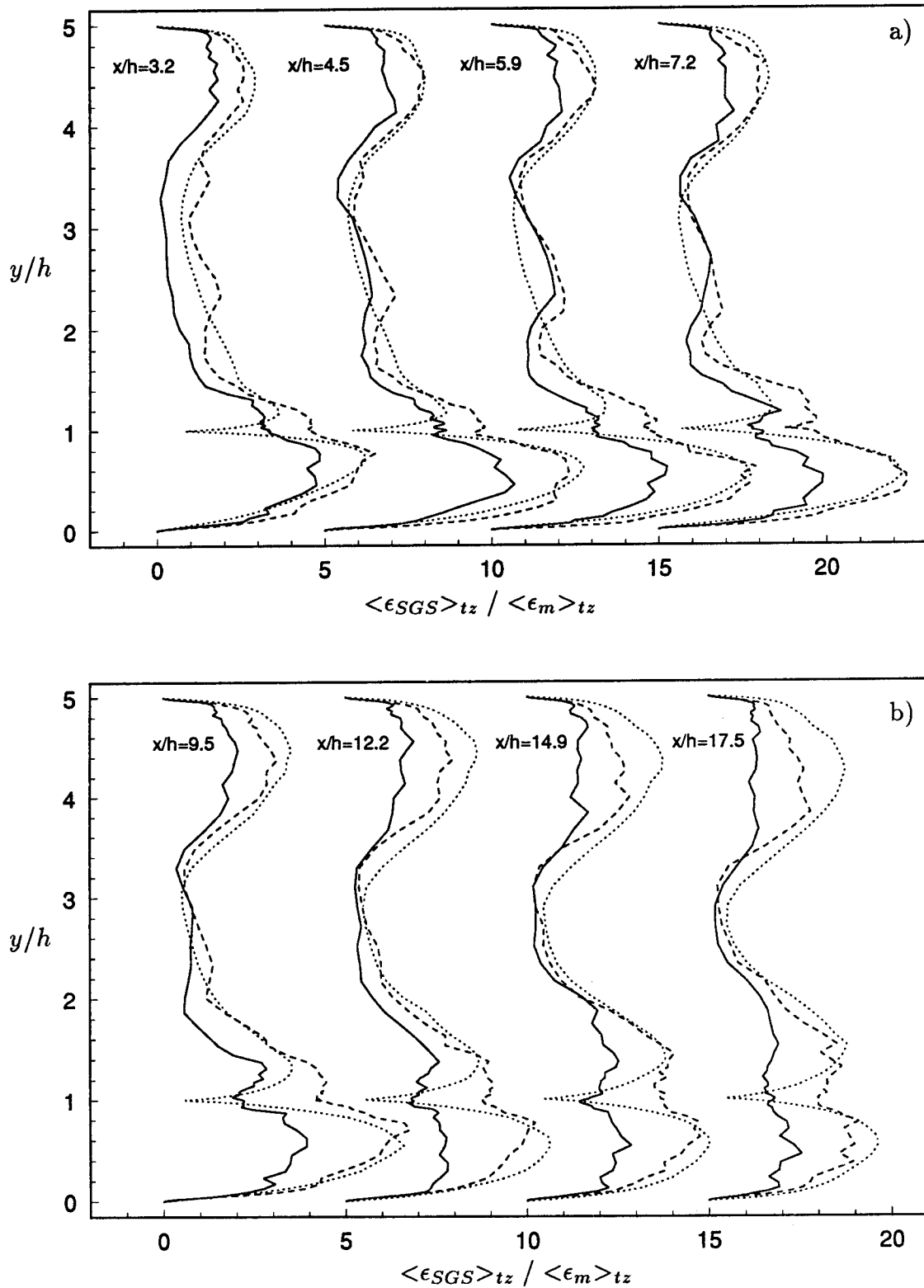
FIGURE **5.3-13**, Ratio of SGS dissipation to molecular dissipation ($Re = 28000$).
——— : DM model; – – – – : DLM model; ········ : Smagorinsky model.
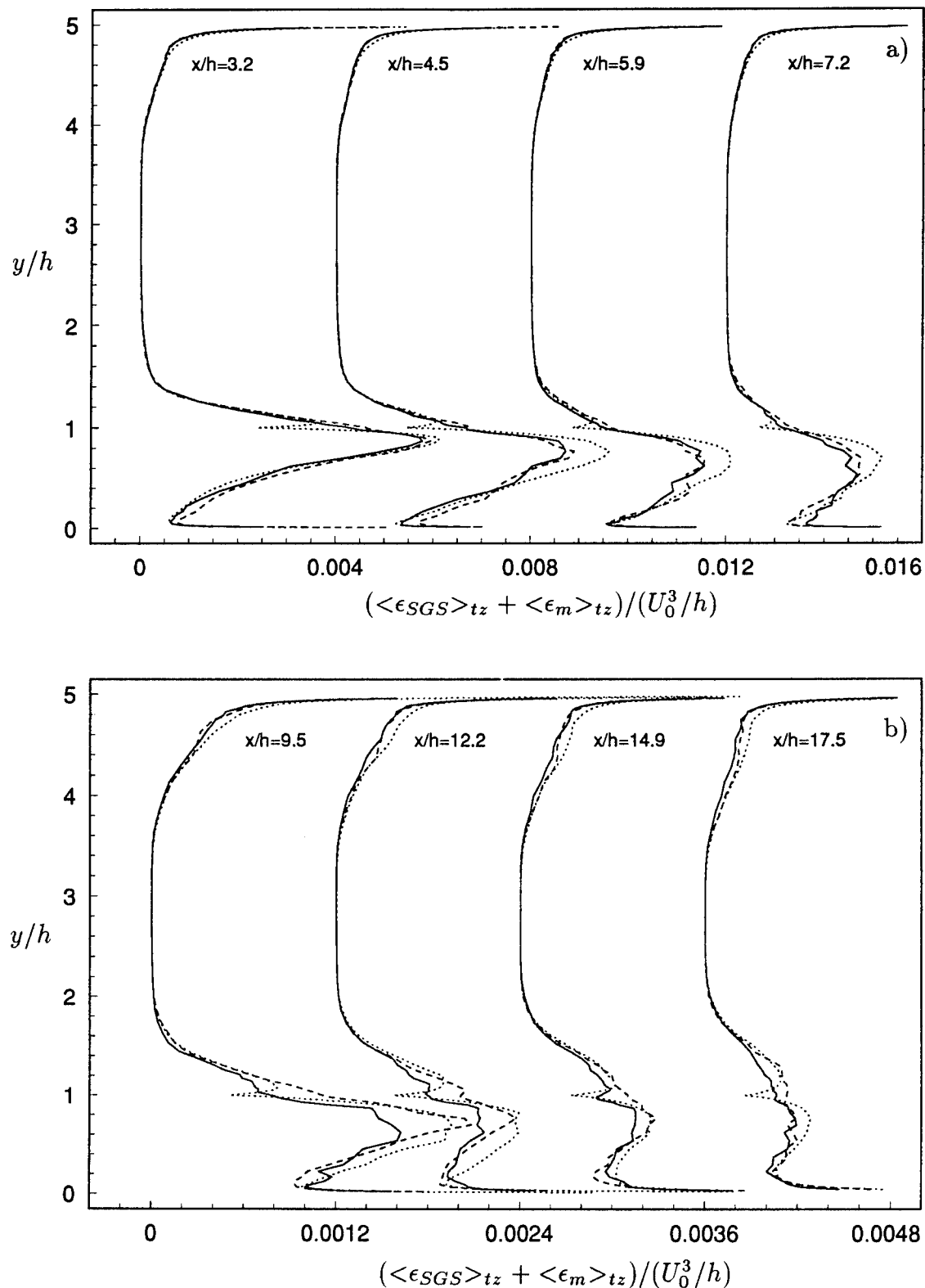
FIGURE **5.3-14**, Sum of SGS dissipation and molecular dissipation ($Re = 28000$).
———— : DM model;   ———— : DLM model;   ········ : Smagorinsky model.
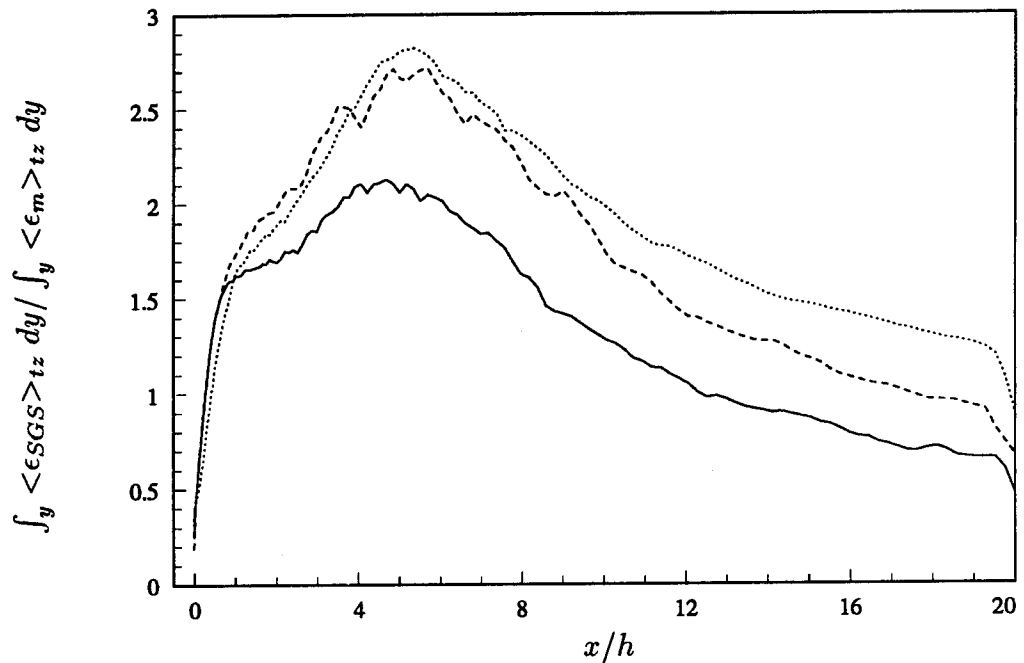
FIGURE **5.3-15**, Ratio of SGS dissipation and Molecular dissipation, both averaged over the cross-sectional area. ———— : DM model;   ———— : DLM model; ········ : Smagorinsky model.
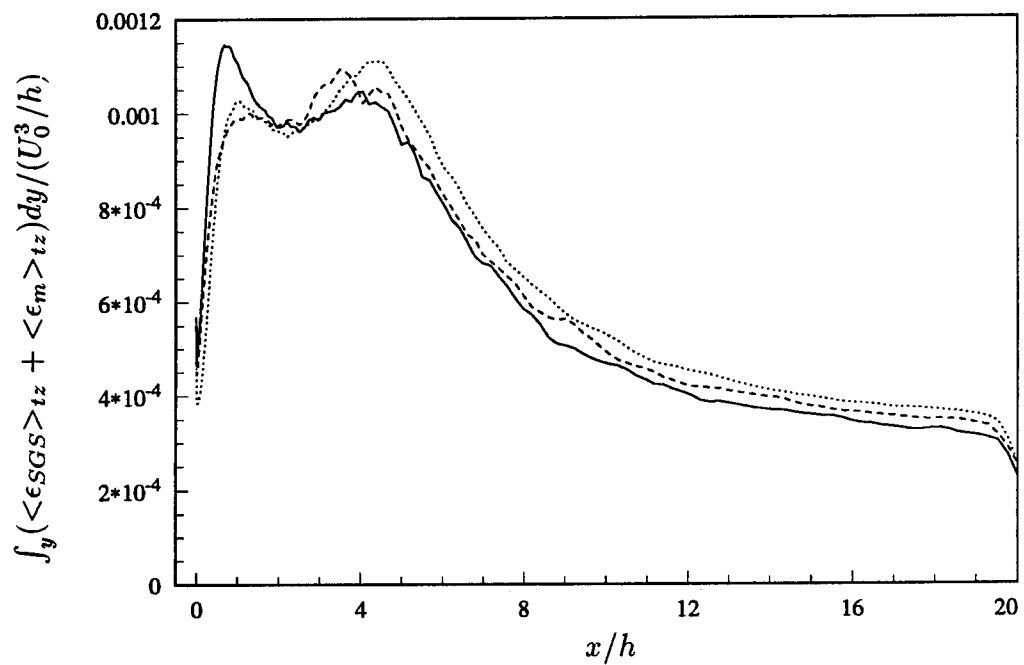
FIGURE **5.3-16**, Sum of SGS dissipation and Molecular dissipation, averaged over the cross-sectional area ($Re = 28000$). ———— : DM model;   ———— : DLM model; ········ : Smagorinsky model.

Chapter 6

CONCLUSIONS

The overall objective of this work was "to implement, test, and assess the performance of the DM model and the DLM model in a complex flow".

DM Model

The DM model was implemented and tested in turbulent flow over a backward facing step at two Reynolds numbers; $Re = 5100$ and $Re = 28000$. Results from the low Reynolds number calculations are in excellent agreement with DNS data for all quantities considered (i.e. first and second order statistics). These results were obtained at roughly 0.5 percent of the computational cost necessary for a corresponding DNS (Le & Moin). Fully converged statistics were obtained in about 6-7 CPU hours on a Cray C-90.

The second set of calculations, at Re=28000, was performed in order to extend the test of the DM model to a Reynolds number of engineering interest. All calculated results were shown to be in good agreement with experimental data, except for the coefficient of friction. Discrepancies were found in the C_f-curve, both in the recirculation region as well as in the recovery region. The reason for the discrepancy remain unclear, but is likely due to problems with the inflow condition or measurement inaccuracies in the recirculation region. The high Reynolds number calculation required about one order of magnitude more grid-points than for the low Reynolds number case.

Several properties of the DM model, previously demonstrated in simpler flows, were shown to hold in the present case. In particular it was shown that the effect of the subgrid scale model decreases as the grid-resolution increases. It was shown that the dynamic eddy-viscosity was insensitive to changes in the grid-resolution in coordinate directions were test-filtering was not applied.

In order to better assess the effect of the subgrid scale model a separate calculation was done using the same grid as that used in a LES, but without the subgrid scale model. Large discrepancies were seen when results from the "no-model" calculations were compared with the DNS or LES. This was particularly apparent in the recirculation region where the SGS turbulent shear stress and dissipation were the largest (indicating the most significant model contribution).

Comparison of SGS models

Calculations were also preformed using the mathematically consistent DLM model and the standard Smagorinsky model (with $C = 0.01$ and Van Driest damping along walls). In the low Reynolds number cases no noticeable differences were found in the results from either model. In the high Reynolds number case, small differences were observed in the results from the three models, with the DLM model and the Smagorinsky model yielding closer agreement with experiments than the DM model. However, the differences were small, particularly when taking the experimental uncertainties into account.

In all cases the SGS model contribution to the turbulent shear stress was a maximum of about 8-10 percent. The peak was located in the recirculation region, close to the step. The peak moved closer to the step with increasing Reynolds number. Downstream of reattachment the SGS shear stress was only a few percent of the resolved turbulent shear stress (all models; both Reynolds numbers).

At the low Reynolds number the ratio of the SGS dissipation to molecular dissipation peaked (towards the end of the recirculation region) at about 4 using either SGS model. This means that up to 80 percent of the total dissipation is supplied by the SGS model. However, at other streamwise stations the SGS model contribution to the dissipation varied between the three models. It is thus interesting to note that the total dissipation was the same at all streamwise stations, using either the DM model, the DLM model, or the Smagorinsky model.

At the high Reynolds number the SGS dissipation was as much as 7 times the molecular dissipation using either the DLM model or the Smagorinsky model. The DM model gave a maximum ratio of abut 5. However, the total dissipation was the same at all streamwise stations, using either SGS model. These results seem to indicate that as long as the total dissipation is predicted correctly, other low order statistical features can be expected to be reasonably predicted as well. The fact that the SGS contribution to the dissipation varied between the models

indicates that the small scales of the flow adapt thus keeping the total dissipation unchanged. The level of the dynamic eddy-viscosity, which varied significantly between the three SGS models, is not an appropriate measure when comparing the effect of the models.

Computational Issues

It was shown to be important to resolve the flow around the corner of the step, both in the streamwise as well as wall-normal direction. The errors generated in the corner region would convect downstream of the step and corrupt the entire solution. It is also important to have a good inflow boundary condition. The flow downstream of the expansion is sensitive to the flow state upstream of the step.

The temporal integration scheme used for the present calculations treated all terms (convective and diffusive) with derivatives in the wall-normal direction implicitly. All other terms were treated explicitly. This is in contrast to the method used by Le & Moin (DNS) which treated all diffusive terms with an implicit scheme and all convective terms with an explicit scheme. The result is a method which allows the maximum time-step to be 3-5 times larger than that permitted by the procedure used by Le & Moin.

A special version of the fractional step method was also developed. The method assures that errors associated with the approximate factorization are of the same order as the errors in the time-integration scheme. In addition, the intermediate velocity field is a second order approximation to the divergence free velocity field which means that special boundary conditions for the intermediate velocity field are not needed.

PART II

Large Eddy Simulation of

Turbulent Confined Coannular Jets

INTRODUCTION

The second part of this report is concerned with large eddy simulations (LES) of the coaxial jet-combustor. This geometry is a natural extension of the backward facing step, and yet far more complex. The coaxial jet-combustor consists of confined coannular jets that discharge into a sudden expansion. The central pipe normally supplies the fuel and the annular pipe supplies the oxidizer (air). This geometry provides a recirculation zone that is similar to those found in modern gas turbine combustors. The recirculation zone established by the step is important because it aids in stabilizing the flame. Figure 1.1-1 shows a sketch of the combustor. A side-view is shown in figure 1.1-2 which also includes some of the important flow- and combustion zones in the device.

When operated in a fuel rich mode the flame is very stable and is anchored in the jet shear layer by a pilot flame attached to the step, near the outer edge of the annular air tube. As the fuel to air ratio decreases, the flame becomes more and more unstable until a point where the entire flame lifts from the base region of the burner and stabilizes further downstream. Reducing the fuel to air ratio even further results in a progressively less stable flame which eventually blows out. This process is known as lean-blow-out (LBO).

1.1 Motivation

A precise understanding of the phenomenon leading to LBO have become more important recently because advancements in gas turbine technology have reduced design tolerances. The ability to accurately predict LBO for combustion chambers is considered important since it is related to combustion stability which is critical to safety and reliability. The problems related to predicting LBO are many. LBO is usually encountered during engine transients and it may therefore be difficult to separate overall system behavior from the combustor characteristics. The

mechanisms of blow-out in one combustor design might therefore be different from those of another design, and even be sensitive to small design changes to the point that manufacturing and assembly tolerances in a system component may be a significant factor. As will become apparent the phenomena of LBO is highly transient and cannot be adequately described by typical time-averaged CFD (computational fluid dynamics) models.

Roquemore *et al.* (1991) investigated the phenomena related to LBO in a combined experimental and computational study in order to gain insight into the characteristics that a model must have for correctly predicting the LBO process. The following is a summary of their findings.

As indicated above, the combustor seems to be operating in two distinct modes: in the fuel rich mode the flame is attached at the face of the combustor, near the edge of the step; in the second mode the flame is stabilized downstream near the end of the recirculation zone established by the step. However, there is a certain degree of intermittency in both these states such that in the fuel rich mode the flame occasionally lifts from the base of the burner, but stays attached most of the time. Likewise, in the fuel lean mode, the flame occasionally flashes back and momentarily attaches to the base of the burner, but stays lifted most of the time. Whether the flame is attached or lifted is believed to be closely related to the amount of fuel and hot combustion products being entrained into the recirculation zone.

When running in a fuel rich mode a region of intense combustion is established in the region where the shear layers between the air- and recirculation zone and the air- and fuel stream merge (a few fuel-pipe diameters downstream of the base of the burner). This combustion zone is being fed directly by fuel coming from the fuel jet. However, this flame is piloted by a weaker flame fed from the the recirculation zone and attached at the outer region of the air-tube, at the base of the burner. It is proposed that unburned fuel and hot combustion products escape through "holes" in the flame into the recirculation zone (as indicated by the arrows in figure 1.1-2). The holes appear to be formed in the braid regions of the vortex trains. Stretching and fast mixing normally occur in the braid regions which might lead to quenching of the flame by finite rate chemistry, thus forming holes in the flame. However, the formation of holes, and consequent escape of fuel and hot combustion products is a highly intermittent process. The fuel concentration in the recirculation zone might therefore at some points in time be too low to support the pilot flame at the base of

the burner and the flame therefore intermittently lifts off. However, the likelihood of this occurring decreases with increasing fuel to air ratio. But as the fuel to air ratio decreases lift-off becomes more frequent to the point where the flame is lifted most of the time.

It is apparent that an understanding of how fuel and hot combustion products are entrained into the recirculation zone is critical in order to understand the processes that makes the flame lift from the base of the burner and eventually blow out. In the case of a lifted flame, knowledge of how much fuel and air are transported into the recirculation zone will help determine whether a flammable fuel to air mixture might exist which could ignite and make the flame flash back and attach at the base of the burner. As indicated by Roquemore *et al.* (1991), it would be instructive to use a cold-flow calculation to examine the characteristics of the recirculation zone for the lifted flame.

Roquemore *et al.* (1991) report that depending on the ratio of fuel to air flow-rates, a small fuel jet recirculation zone is formed at the fuel jet exit. This recirculation zone is similar to that formed behind bluff bodies and is a result of the air flow-rate being much higher than the fuel flow-rate. The high velocity annular air jet expands and entrains surrounding fluid as it enters the combustion chamber. However, the small mass-flow of the fuel jet is not sufficient to satisfy the entrainment requirement of the expanding air jet, and the air-fuel mixture turns back on itself and is entrained back into the air jet much like the flow behind a bluff body. The mixture in this recirculation zone is however too fuel rich to support combustion.

The CFD model used by Roquemore *et al.* (1991) is based on the Reynolds average approach using an isotropic k-ϵ model. The code includes a simple global chemical reaction scheme involving propane, oxygen, water, carbon dioxide and inert nitrogen. Parabolic velocity profiles are specified at the inlet and approximate boundary conditions are used along walls to avoid refinement of the computational grid. All species transport properties (viscosity, thermal conductivity and diffusivity) are assumed to be constant. The CFD code gave results in qualitative agreement with experiments, but were unable to accurately predict the concentration of fuel in the recirculation zone thus failing to predict the attached flame condition. It is also apparent that steady state calculations are unlikely to be able to predict the highly transient phenomenon associated with LBO. Roquemore *et al.* (1991) conclude that the biggest difficulty is to correctly model the processes

responsible for entraining and transporting fuel, products, and heat into and out of the recirculation zone.

The present work uses LES to study the phenomenon of mixing and entrainment of fuel and air in the recirculation zone. The study focuses on fluid flow phenomena and does not involve chemical reactions. The calculations are designed to match an experimental setup used by Johnson & Bennett (1981, 1984). The experiments used water for both the air and fuel jets and were performed to study mixing of the two jets in the combustion chamber. The fuel stream was visualized using dye. The results include mean velocity profiles, mean concentration profiles (fuel in air), turbulence intensities, rms profiles of the concentration, as well as mass transport quantities. Details of the experiment are described later in this report. The experimental data-base is used to verify the accuracy of the present calculation model.

It is apparent that due to the high Reynolds number (38000 based on combustion chamber diameter and bulk velocity), direct numerical simulation (DNS) is unsuitable for the present calculations. In addition, Roquemore *et al.* (1991) have shown that their Reynolds averaged method was incapable of correctly predicting important features of the flow. The current study therefore employs the technique of large eddy simulation in an attempt to understand the processes involved in LBO.

This is believed to be the first study using LES in such a complicated flow. However, a related study was performed by Wagner & Friedrich (1994). They used DNS to calculate turbulent flow in a sudden pipe expansion. This flow is simpler than that of the coaxial jet-combustor in that it contains only one incoming jet and hence only one shear layer.

1.2 Objectives

The objective of the present study is to use the LES technique to calculate mixing of fuel and air in a coaxial jet-combustor in order to aid in understanding the processes leading to LBO. As a first step in a general study, the effects of chemical reactions and variable density are not included.

Statistical quantities from LES are compared with their experimental counterparts. Certain parameters, like the fuel concentration are animated and recorded on video tape in order to aid in analyzing the transient phenomenon involved in the mixing process.
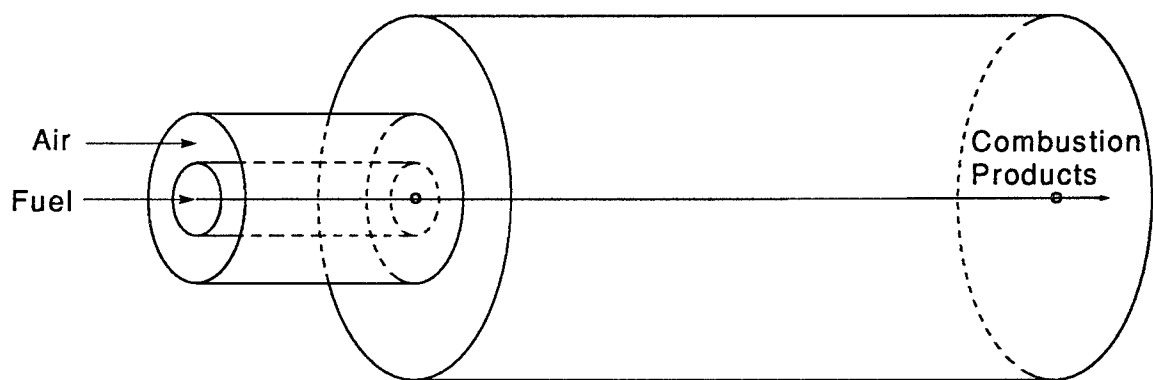
FIGURE **1.1-1**, Coaxial jet-combustor geometry. 3-D view.
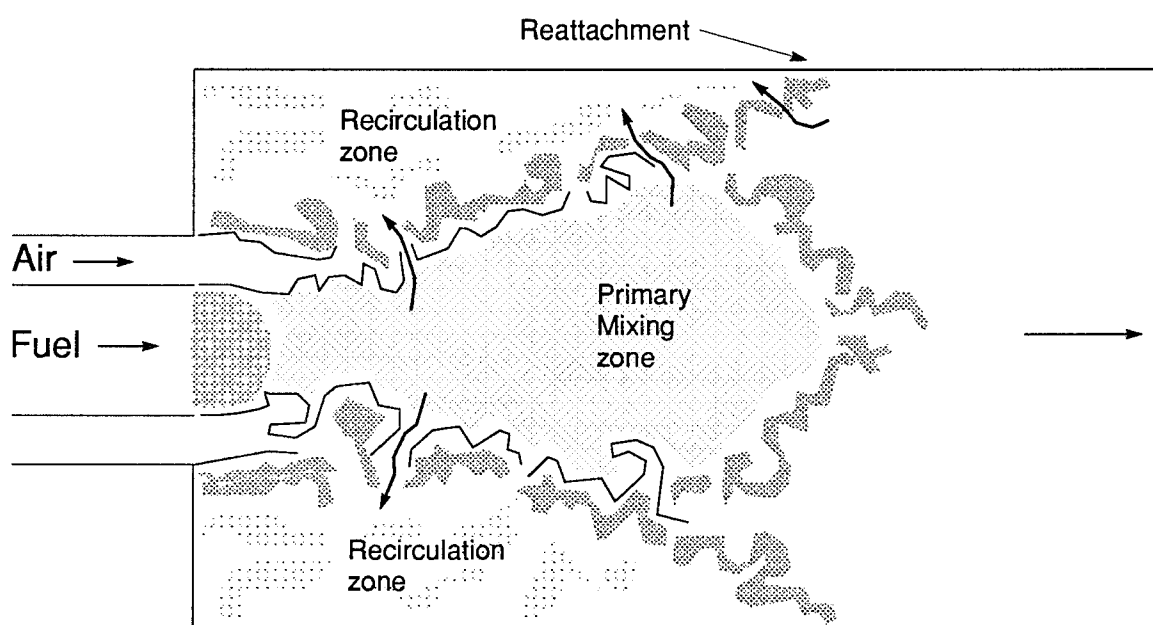
FIGURE **1.1-2**, Coaxial jet-combustor geometry. Side view.

Chapter 2

MATHEMATICAL FORMULATION

The governing equations are the incompressible Navier-Stokes equations and the continuity equation. The only difference from the backward facing step case is that the equations are written in cylindrical instead of Cartesian coordinates. The Navier-Stokes and the continuity equations in cylindrical coordinates are summarized in section 2.1. A detailed description of issues related to cylindrical coordinates is given in appendix B. Similar to the conditions in the experimental facility (Johnson & Bennett), all fluid properties (density and viscosity) are assumed to be the same for the two jets entering the combustion chamber.

Mixing of fuel and air in the coaxial jet-combustor is tracked by solving a passive scalar transport equation, where the scalar represents the mass-fraction of fuel. This equation is described in section 2.2.

2.1 Governing Equations

The governing equations for LES of the backward facing step were developed in Cartesian coordinates in chapter 2, part I. The quantities used to non-dimensionalize the equations in the case of the coaxial jet-combustor are the bulk velocity, U_c, in the central fuel pipe, and the step height, h. (The step height is measured from the outer wall of the annular pipe to the wall of the combustion chamber). Equations 2.1-1 and 2.1-2 are the filtered, non-dimensional Navier-Stokes and continuity equations given in vector form. (An overline indicates a filtered quantity).

$$\frac{\partial \overline{\mathbf{u}}}{\partial t} + \nabla \cdot (\overline{\mathbf{u}} \otimes \overline{\mathbf{u}}) = -\nabla \phi + \nabla \cdot \left\{ \nu \nabla \overline{\mathbf{u}} \right\} + \nabla \cdot \left\{ \nu (\nabla \overline{\mathbf{u}})^T \right\} \qquad (2.1\text{-}1)$$

$$\nabla \cdot \overline{\mathbf{u}} = 0 \qquad (2.1\text{-}2)$$

where ν represents the total viscosity, equal to $\nu_t + 1/Re$. ϕ is the sum of the filtered pressure and the trace of the subgrid scale stress tensor τ_{ij}, i.e. $\phi = \bar{p} + \frac{1}{3}\tau_{kk}$. Note that the dynamic subgrid scale model with

$$q_{ij} = -2\nu_t \overline{S}_{ij} \tag{2.1-3}$$

has been implemented in equation 2.1-1. (q_{ij} is the anisotropic part of the subgrid scale stress tensor, τ_{ij}). The strain rate tensor, $\overline{S}_{ij}$, in cylindrical coordinates is given in equation 2.1-10. Equation 2.1-1 takes the following form when written in cylindrical coordinates (conservative formulation):

$$\frac{\partial \bar{u}_x}{\partial t} = -\frac{\partial \phi}{\partial x} + \frac{\partial}{\partial x}\left(\bar{s}_{xx} - \bar{u}_x \bar{u}_x\right) + \frac{1}{r}\frac{\partial}{\partial r}\left(r\bar{s}_{xr} - r\bar{u}_x \bar{u}_r\right)$$

$$+ \frac{1}{r}\frac{\partial}{\partial \theta}\left(\bar{s}_{x\theta} - \bar{u}_x \bar{u}_\theta\right) \tag{2.1-4a}$$

$$\frac{\partial \bar{u}_r}{\partial t} = -\frac{\partial \phi}{\partial r} + \frac{\partial}{\partial x}\left(\bar{s}_{rx} - \bar{u}_r \bar{u}_x\right) + \frac{1}{r}\frac{\partial}{\partial r}\left(r\bar{s}_{rr} - r\bar{u}_r \bar{u}_r\right)$$

$$+ \frac{1}{r}\frac{\partial}{\partial \theta}\left(\bar{s}_{r\theta} - \bar{u}_r \bar{u}_\theta\right) - \left(\frac{\bar{s}_{\theta\theta}}{r} - \frac{\bar{u}_\theta \bar{u}_\theta}{r}\right) \tag{2.1-4b}$$

$$\frac{\partial \bar{u}_\theta}{\partial t} = -\frac{1}{r}\frac{\partial \phi}{\partial \theta} + \frac{\partial}{\partial x}\left(\bar{s}_{\theta x} - \bar{u}_\theta \bar{u}_x\right) + \frac{1}{r}\frac{\partial}{\partial r}\left(r\bar{s}_{\theta r} - r\bar{u}_\theta \bar{u}_r\right)$$

$$+ \frac{1}{r}\frac{\partial}{\partial \theta}\left(\bar{s}_{\theta\theta} - \bar{u}_\theta \bar{u}_\theta\right) + \left(\frac{\bar{s}_{\theta r}}{r} - \frac{\bar{u}_\theta \bar{u}_r}{r}\right) \tag{2.1-4c}$$

Subscript x is used to denote the axial (or streamwise) direction, r represents the radial direction, and θ represents the azimuthal direction. For convenience, subscripts 1, 2, and 3 are sometimes used to denote the streamwise, radial and azimuthal directions, respectively. The terms in the (symmetric) stress tensor, $\bar{s}_{ij}$, are given by:

$$\bar{s}_{xx} = 2\nu\frac{\partial \bar{u}_x}{\partial x}, \quad \bar{s}_{xr} = \nu\left(\frac{\partial \bar{u}_r}{\partial x} + \frac{\partial \bar{u}_x}{\partial r}\right), \qquad \bar{s}_{x\theta} = \nu\left(\frac{\partial \bar{u}_\theta}{\partial x} + \frac{1}{r}\frac{\partial \bar{u}_x}{\partial \theta}\right)$$

$$\bar{s}_{rr} = 2\nu\frac{\partial \bar{u}_r}{\partial r}, \quad \bar{s}_{r\theta} = \nu\left(\frac{\partial \bar{u}_\theta}{\partial r} + \frac{1}{r}\frac{\partial \bar{u}_r}{\partial \theta} - \frac{\bar{u}_\theta}{r}\right), \quad \bar{s}_{\theta\theta} = 2\nu\left(\frac{1}{r}\frac{\partial \bar{u}_\theta}{\partial \theta} + \frac{\bar{u}_r}{r}\right) \tag{2.1-5}$$

By combining the convective and diffusive fluxes in equation 2.1-4 into a single (symmetric) tensor $\overline{f}_{ij}$, the equation can be simplified as follows:

$$\frac{\partial \overline{u}_x}{\partial t} = -\frac{\partial \phi}{\partial x} + \frac{\partial \overline{f}_{xx}}{\partial x} + \frac{1}{r}\frac{\partial r \overline{f}_{xr}}{\partial r} + \frac{1}{r}\frac{\partial \overline{f}_{x\theta}}{\partial \theta} \tag{2.1-6a}$$

$$\frac{\partial \overline{u}_r}{\partial t} = -\frac{\partial \phi}{\partial r} + \frac{\partial \overline{f}_{rx}}{\partial x} + \frac{1}{r}\frac{\partial r \overline{f}_{rr}}{\partial r} + \frac{1}{r}\frac{\partial \overline{f}_{r\theta}}{\partial \theta} - \frac{\overline{f}_{\theta\theta}}{r} \tag{2.1-6b}$$

$$\frac{\partial \overline{u}_\theta}{\partial t} = -\frac{1}{r}\frac{\partial \phi}{\partial \theta} + \frac{\partial \overline{f}_{\theta x}}{\partial x} + \frac{1}{r}\frac{\partial r \overline{f}_{\theta r}}{\partial r} + \frac{1}{r}\frac{\partial \overline{f}_{\theta\theta}}{\partial \theta} + \frac{\overline{f}_{\theta r}}{r} \tag{2.1-6c}$$

where

$$\overline{f}_{xx} = \overline{s}_{xx} - \overline{u}_x \overline{u}_x, \qquad \overline{f}_{xr} = \overline{s}_{xr} - \overline{u}_x \overline{u}_r, \qquad \overline{f}_{x\theta} = \overline{s}_{x\theta} - \overline{u}_x \overline{u}_\theta,$$

$$\overline{f}_{rr} = \overline{s}_{rr} - \overline{u}_r \overline{u}_r, \qquad \overline{f}_{r\theta} = \overline{s}_{r\theta} - \overline{u}_r \overline{u}_\theta, \qquad \overline{f}_{\theta\theta} = \overline{s}_{\theta\theta} - \overline{u}_\theta \overline{u}_\theta \tag{2.1-7}$$

The continuity equation becomes:

$$\frac{\partial \overline{u}_x}{\partial x} + \frac{1}{r}\frac{\partial (r\overline{u}_r)}{\partial r} + \frac{1}{r}\frac{\partial \overline{u}_\theta}{\partial \theta} = 0 \tag{2.1-8}$$

The DM model is used to represent the subgrid scale stresses in all calculations of the coaxial jet-combustor. The eddy-viscosity is calculated according to:

$$\nu_t = C\overline{\Delta}^2 |\overline{S}|, \qquad C\overline{\Delta}^2 = -\frac{1}{2}\frac{\mathcal{L}_{ij}M_{ij}}{M_{ij}M_{ij}}, \qquad |\overline{S}| = \sqrt{2\overline{S}_{ij}\overline{S}_{ij}}$$

$$\mathcal{L}_{ij} = \widehat{\overline{u}_i \overline{u}_j} - \widehat{\overline{u}}_i \widehat{\overline{u}}_j, \qquad M_{ij} = \left(\widehat{\overline{\Delta}}^2 / \overline{\Delta}^2\right) | \widehat{\overline{S}} | \widehat{\overline{S}}_{ij} - \widehat{| \overline{S} | \overline{S}}_{ij} \tag{2.1-9}$$

The symmetric strain rate tensor, $\overline{S}_{ij}$, in cylindrical coordinates is given by:

$$\overline{S}_{xx} = \frac{\partial \overline{u}_x}{\partial x}, \qquad \overline{S}_{xr} = \frac{1}{2}\left(\frac{\partial \overline{u}_r}{\partial x} + \frac{\partial \overline{u}_x}{\partial r}\right), \qquad \overline{S}_{x\theta} = \frac{1}{2}\left(\frac{\partial \overline{u}_\theta}{\partial x} + \frac{1}{r}\frac{\partial \overline{u}_x}{\partial \theta}\right)$$

$$\overline{S}_{rr} = \frac{\partial \overline{u}_r}{\partial r}, \qquad \overline{S}_{r\theta} = \frac{1}{2}\left(\frac{\partial \overline{u}_\theta}{\partial r} + \frac{1}{r}\frac{\partial \overline{u}_r}{\partial \theta} - \frac{\overline{u}_\theta}{r}\right), \qquad \overline{S}_{\theta\theta} = \left(\frac{1}{r}\frac{\partial \overline{u}_\theta}{\partial \theta} + \frac{\overline{u}_r}{r}\right) \tag{2.1-10}$$

2.2 Passive Scalar Transport

A passive scalar, φ, is used to track mixing of fuel and air in the combustion chamber. φ represents the fuel mass-fraction in the mixture with $\varphi = 1$ being pure fuel, and $\varphi = 0$ being pure air. In vector form the equation governing convection and diffusion of a passive scalar is:

$$\frac{\partial \varphi}{\partial t} = -\nabla \cdot (\mathbf{u}\varphi) + \nabla \cdot (\alpha_m \nabla \varphi) \qquad (2.2\text{-}1)$$

where α_m is the molecular diffusivity. The equation has been non-dimensionalized using the same variables as used in the governing flow equations, i.e. the step height, h, and the bulk velocity, U_c, of the central fuel jet. The convective and diffusive terms in cylindrical coordinates are given by:

$$\nabla \cdot (\varphi \mathbf{u}) = \frac{\partial}{\partial x}(u_x \varphi) + \frac{1}{r}\frac{\partial}{\partial r}(r u_r \varphi) + \frac{1}{r}\frac{\partial}{\partial \theta}(u_\theta \varphi) \qquad (2.2\text{-}2)$$

$$\nabla \cdot (\alpha_m \nabla \varphi) = \frac{\partial}{\partial x}\left(\alpha_m \frac{\partial \varphi}{\partial x}\right) + \frac{1}{r}\frac{\partial}{\partial r}\left(\alpha_m r \frac{\partial \varphi}{\partial r}\right) + \frac{1}{r}\frac{\partial}{\partial \theta}\left(\alpha_m \frac{1}{r}\frac{\partial \varphi}{\partial \theta}\right) \qquad (2.2\text{-}3)$$

Filtering equation 2.2-1 at the grid-filter level yields:

$$\frac{\partial \overline{\varphi}}{\partial t} = -\nabla \cdot (\overline{\mathbf{u}}\,\overline{\varphi}) + \nabla \cdot (\alpha_m \nabla \overline{\varphi} - \mathbf{q}) \qquad (2.2\text{-}4)$$

The vector $\mathbf{q}$ gives the subgrid scale scalar flux. It should not be confused with the tensor q_{ij} used to denote the anisotropic part of the subgrid scale stresses. The subgrid scale scalar flux is given by:

$$\mathbf{q} = \overline{\mathbf{u}\varphi} - \overline{\mathbf{u}}\,\overline{\varphi} \qquad (2.2\text{-}5)$$

The subgrid scale scalar flux represents transport of the scalar φ caused by turbulent scales too small to be resolved on the computational grid. Following the approach of Moin *et al.* (1991), the subgrid scale scalar flux is modeled assuming it is aligned with the scalar gradient vector:

$$\mathbf{q} = -\alpha_t \nabla \overline{\varphi}, \qquad \alpha_t = Sc_t/\nu_t \qquad (2.2\text{-}6)$$

α_t is the eddy-diffusivity, and Sc_t is the SGS turbulent Schmidt number. Substituting equation 2.2-6 into equation 2.2-4, and defining the total diffusivity as the sum of the eddy-diffusivity and the molecular diffusivity ($\alpha = \alpha_t + \alpha_m$) gives the following LES equation for transport of the passive scalar:

$$\frac{\partial \overline{\varphi}}{\partial t} = -\nabla \cdot (\overline{\mathbf{u}} \, \overline{\varphi}) + \nabla \cdot (\alpha \nabla \overline{\varphi}) \qquad (2.2\text{-}7)$$

The eddy-diffusivity is determined following the principles of the dynamic sub-grid scale model (see Moin *et al.*, 1991, for details). The results is that $C_\varphi \overline{\Delta}^2$ can be calculated as a function of space and time according to:

$$C_\varphi \overline{\Delta}^2 = -\frac{< \mathbf{F} \cdot \mathbf{H} >_\theta}{< \mathbf{H} \cdot \mathbf{H} >_\theta} \qquad (2.2\text{-}8)$$

$$\mathbf{H} = (\widehat{\overline{\Delta}}/\overline{\Delta})^2 |\widehat{\overline{S}}| \nabla \widehat{\overline{\varphi}} - \widehat{|\overline{S}| \nabla \overline{\varphi}} \qquad (2.2\text{-}9)$$

$$\mathbf{F} = \widehat{\overline{\varphi} \, \overline{\mathbf{u}}} - \widehat{\overline{\varphi}} \, \widehat{\overline{\mathbf{u}}} \qquad (2.2\text{-}10)$$

and the eddy-diffusivity is found from:

$$\alpha_t = C_\varphi \overline{\Delta}^2 |\overline{S}| \qquad (2.2\text{-}11)$$

As in the expression for the model parameter C (used to get the eddy-viscosity), the numerator and denominator in the expression for C_φ are averaged over directions of flow-homogeneity. (In the case of the coaxial jet-combustor, only the azimuthal direction is homogenous). This means that C_φ will only be a function of the streamwise and radial coordinate (as well as time).

Averaging the numerator and denominator of equation 2.2-8 over the azimuthal direction was not sufficient to avoid points with negative C_φ, and clipping was therefore used to constrain the total diffusivity to be positive. The definitions used for the filter widths, $\overline{\Delta}$ and $\widehat{\overline{\Delta}}$, both for the eddy-viscosity and the eddy-diffusivity are the same as those used for the backward facing step calculations.

NUMERICAL METHOD

This chapter describes the numerical method used for the coaxial jet-combustor. The method is in principle the same as that used for the backward facing step (see chapter 3, part I), but with some important differences. Only the differences will be described here.

Section 3.1 defines the nomenclature associated with the coaxial jet-combustor. Section 3.2 describes the geometry and flow rates, and section 3.3 gives the computational grid. Section 3.4 outlines the spatial discretization scheme, with particular emphasis on the centerline problems faced in axisymmetric geometries.

The temporal integration scheme is essentially identical to the one used for the backward facing step. The only difference is in the selection of terms to treat implicitly. The problem with a cylindrical grid is that in order to get satisfactory azimuthal resolution at the outer wall, the grid becomes unnecessarily fine at the centerline, resulting in a severe time-step restriction. On the other hand, due to refinement of the grid along the walls in the radial direction, diffusive terms pose a severe time-step restriction unless treated implicitly. Section 3.5 describes a new method developed to deal with these problems.

The solution procedure for the Poisson equation for pressure is in principle the same in cylindrical and Cartesian coordinates. However, the coefficients in the equation are different, and the centerline represents an added complexity. Details of the solution procedure in cylindrical coordinates are outlined in section 3.6. Boundary conditions are summarized in section 3.7.

Section 3.8 describes the numerical solution technique used for the passive scalar transport equation. This equation is almost identical to the momentum equations and is thus solved using a nearly identical numerical scheme. However, there are minor differences, particularly in the treatment of the convective terms, which deserve special attention.

3.1 Nomenclature

Figure 3.1-1 identifies the nomenclature used in the remaining chapters of this report. As shown, the *inlet section* of the computational domain consists of the *central pipe* (or fuel pipe), surrounded by the *annular pipe* (or air pipe). The two pipes exit into a larger diameter pipe referred to as the *combustion chamber*. The axial location where the inlet section is attached to the combustion chamber is referred to as the *base of the burner* (or the point of expansion). The intersection between the outer wall of the annular pipe and the base of the burner is referred to as the *corner of the step*. The *outer corner of the step* is the corner created by the intersection of the base of the burner and the wall of the combustion chamber. The shear layer forming between the annular jet and the recirculation zone is referred to as the *step shear layer*. The shear layer between the annular and central jets is referred to as the *fuel-pipe shear layer*.

3.2 Computational Domain and Flow Rates

The computational domain used for the coaxial jet-combustor is shown in figure 3.2-1. (Recall that the device is axisymmetric, as shown in figure 1.1-1). All lengths have been non-dimensionalized using the the step-height, h. A velocity scale is provided by the bulk velocity in the central fuel pipe, U_c. U_a gives the bulk velocity in the annular air pipe and U_0 gives the bulk velocity in the combustion chamber. The radius of the central pipe and the combustion chamber are denoted r_c and r_0, respectively. The outer radius of the annular pipe is denoted r_a. The wall between the central fuel pipe and the annular air pipe is assumed to be infinitely thin.

Figure 3.2-1 indicates that the coordinate system is located at the point of expansion, with $r = 0$ at the centerline. x is used to denote the axial (or streamwise) coordinate, and θ is used to denote the azimuthal coordinate.

The length of the combustion chamber is $19.2h$. The inlet section consists of two concentric pipes separated by a zero thickness wall. The radius of the central pipe is $0.441h$ and the outer radius of the annular pipe is $0.937h$. The radial dimensions are the same as those in the experimental facility of Johnson & Bennett (1981, 1984). Note that the radius of the central pipe corresponds to the radius at the end of the tapered section of the central pipe in the experimental facility (see chapter 4).

Table 3.2-1, below, gives the volumetric flow-rates for the simulations. They were chosen to match as closely as possible the flow-rates used in the experiment by Johnson & Bennett.

	Central	Annular	Comb. Chamber
U_{bulk}/U_c	1.0	3.132	0.600
$Q/(h^2 U_c)$	0.741	6.308	7.049

TABLE **3.2-1**, Bulk velocities and volumetric flow-rates used in the calculations.

The Reynolds number, based on the step height, h, and the bulk velocity in the central fuel pipe, U_c, is 16400. The corresponding value from the experiment was 16310.

3.3 Computational Grid

The following is a description of the computational grid used for the basic case (defined in chapter 5). The basic case used $215 \times 76 \times 128$ grid-points in the axial, radial, and azimuthal directions, respectively. 34 of the 215 axial grid-points were used to cover the inlet section (upstream of the expansion). The axial grid is compressed around the point of expansion and stretched on either side. The radial grid is stretched in order to cluster grid-points along all solid walls, both upstream and downstream of the expansion. Figure 3.3-1 shows the grid spacing, Δx, versus axial distance. Figure 3.3-2 shows the same information for the radial direction.

The friction velocity in the central pipe, annulus, and combustion chamber, are estimated using the empirical correlation (Kays & Crawford) for fully developed turbulent flow in a smooth pipe:

$$C_f/2 = 0.039 Re^{-0.25} \tag{3.3-1}$$

where the Reynolds number, Re, is based on the bulk velocity and diameter (or the hydraulic diameter in the case of the annulus). The friction velocity is found from $u_\tau = U_{bulk}\sqrt{C_f/2}$. The friction velocities in the different sections, based on C_f from equation 3.3-1, are listed in table 3.3-1.

	Central	Annular	Comb. chamber
Re	14465	46304	38000
C_f	0.00711	0.00532	0.00559
u_τ	0.0596	0.1615	0.0316

TABLE **3.3-1**, Friction velocities based on an empirical correlation.

The resolution, in wall-coordinates, for the central pipe, the annular pipe, and the combustion chamber are listed in table 3.3-2.

Subscripts c, a, and 0, indicate that the quantity is evaluated at the wall of the central pipe, outer wall of annulus, and combustion chamber, respectively. (See also figure 3.2-1 for definitions). Subscript cl indicates a quantity evaluated at the centerline. The radial grid spacing at the wall gives the location for the first u_τ

velocity-point off the wall. (The first u_x and u_θ velocity-points are located at half this distance above the wall). For the central- and annular pipes, the maximum axial grid-spacing occurs at the inlet of the computational domain. For the combustion chamber the maximum axial grid-spacing occurs at the exit of the computational domain. The minimum axial grid-spacing is found at the point of expansion.

	Central	Annular	Comb. chamber
Δx^+_{min}	19.5	52.6	10.4
Δx^+_{max}	51.0	138.3	152.1
Δr^+_c	4.47	12.6	
Δr^+_a		12.6	
Δr^+_0			5.30
$(r\Delta\theta)^+_{cl}$	2.30		1.22
$(r\Delta\theta)^+_c$	23.3	63.1	
$(r\Delta\theta)^+_a$		121.8	
$(r\Delta\theta)^+_0$			49.3

TABLE **3.3-2**, Grid resolution for the basic case (defined in chapter 5) based on u_τ from table 3.3-1.

The radial dimensions, and distribution of grid-points, for the inflow generator (see figure 3.2-1) are the same as those quoted above for the inlet-section of the coaxial jet-combustor. The axial extension is $2.51h$ which is covered by 48 equally spaced grid-points. This gives an axial resolution of $\Delta x^+ = 51.0$ in the central pipe, and $\Delta x^+ = 138.3$ in the annular pipe. A uniform grid of 128 points are used in the azimuthal direction. Radially, 20 grid-points are used in the central pipe (from the centerline to the wall) and 25 grid-points are used in the annular pipe.

3.4 Spatial Discretization

The momentum equations are discretized in space using a second order finite volume formulation. From appendix B it is evident that there are no significant differences between the discrete Navier-Stokes equations expressed in cylindrical versus Cartesian coordinates. However, in cylindrical coordinates the $1/r$ factors in the equations cause difficulties. The following explains how the numerical scheme deals with this particular problem.

Figure 3.4-1 shows the locations of control-volumes for all momentum equations both at and away from the centerline. The momentum equations were given in the previous chapter, but are reproduced here for convenience. The axial (or streamwise) momentum equation is:

$$\frac{\partial u_x}{\partial t} = -\frac{\partial \phi}{\partial x} + \frac{\partial f_{xx}}{\partial x} + \frac{1}{r}\frac{\partial r f_{xr}}{\partial r} + \frac{1}{r}\frac{\partial f_{x\theta}}{\partial \theta} \tag{3.4-1}$$

The two last terms in equation 3.4-1 are potential candidates for trouble due to the $1/r$ factors. However, the radius, r, appearing in front of the derivatives is evaluated at the location of the u_x-velocity points in the grid. (See appendix B.2 for details). From figure 3.4-1 it is apparent that even for the "pie-shaped" control-volume next to the centerline, the u_x-velocity point is located a distance $\Delta r/2$ away from the centerline. Thus, division by zero will never take place. In addition it is seen that the flux, f_{xr}, in the radial direction multiplies the radius (or really the area of the control-volume surface). Thus, assuming that f_{xr} is finite at the centerline, this term is zero due to $r = 0$. The discrete axial momentum equation can therefore be evaluated without any special treatment at the centerline, i.e. without the need to evaluate any quantity at the centerline itself.

The radial momentum equation (equation 3.4-2), on the other hand, causes a slight problem. Again, the equation contains $1/r$ factors, but since the the radius, r, appearing in the $1/r$ terms are evaluated at the locations of the u_r-velocity points, division by zero will not take place.

$$\frac{\partial u_r}{\partial t} = -\frac{\partial \phi}{\partial r} + \frac{\partial f_{rx}}{\partial x} + \frac{1}{r}\frac{\partial r f_{rr}}{\partial r} + \frac{1}{r}\frac{\partial f_{r\theta}}{\partial \theta} - \frac{f_{\theta\theta}}{r} \tag{3.4-2}$$

However, a problem arises with the flux term, f_{rr}, in the radial direction. Since the u_r-control-volume closest to the centerline does not extend all the way to the

centerline, the radial flux will have to be evaluated on both sides (radial direction) of the control-volume. This means that the term:

$$f_{rr} = 2\nu \frac{\partial u_r}{\partial r} - u_r u_r \qquad (3.4\text{-}3)$$

will have to be evaluated at the radial surface closest to the centerline. As is evident from figure 3.4-1, the discrete evaluation of f_{rr} at this surface will require knowledge of u_r at the centerline itself.

The problem is that neither u_r nor u_θ are defined at the centerline. In fact, these quantities can be perceived as being multi-valued at this location. (It should be pointed out that the centerline problem arises due to the cylindrical coordinate system. The flow-field itself is not singular at the centerline. Also note that the problem is only present in u_r and u_θ. Scalar quantities as well as the axial velocity, u_x, are well defined and can be evaluated at the centerline without difficulties).

Eggels (1994) tested a few different approaches for dealing with the centerline problem. These included extrapolating u_r from $r \geq \Delta r$ to get u_r and therefore also the convective flux at the control-volume surface closest to the centerline. The diffusive flux was determined using a one-sided differencing stencil, including points at $r \geq \Delta r$, preserving second-order accuracy. In another variant the u_r control-volume was extended to the centerline, giving it a pie-shaped form, thus eliminating the need for knowing the flux at one surface of the control-volume. This method was, however, found to give increased rms fluctuations near the centerline and was therefore judged to be unsuitable.

The method found to give best results involved determining an "artificial" value for u_r at the centerline. This method was also employed in the present work. At the centerline the radial velocity component is assumed to be multi-valued and is at each point found by linear interpolation across the centerline. This means that the radial velocity component at two points located opposite one another (180° apart) at the centerline will be the same, except for having opposite signs. (Conceptually it might be easiest to think of the centerline in this method as a circle of small, but finite radius $\epsilon << \Delta r$). Results from tests done calculating turbulent flow in a cylindrical pipe, using this method (see appendix C), showed good agreement with experimental and computational results from the literature. Thus, the method was used in all coaxial jet-combustor calculations.

The azimuthal momentum equation is given in equation 3.4-4. Again, since r in the $1/r$ factors in the equation is not evaluated at the centerline itself, division by zero will not take place. As in the axial momentum equation, the flux, $f_{\theta r}$, in the radial direction at the centerline multiplies zero and the term drops out of the equation, assuming $f_{\theta r}$ is finite.

$$\frac{\partial u_\theta}{\partial t} = -\frac{1}{r}\frac{\partial \phi}{\partial \theta} + \frac{\partial f_{\theta x}}{\partial x} + \frac{1}{r}\frac{\partial r f_{\theta r}}{\partial r} + \frac{1}{r}\frac{\partial f_{\theta\theta}}{\partial \theta} + \frac{f_{\theta r}}{r} \qquad (3.4\text{-}4)$$

The problem in this case, however, arises because some of the terms involved in calculating the fluxes, $f_{\theta\theta}$ and $f_{\theta r}$ at the control-volume surface with normal in the azimuthal direction will require u_r and u_θ at the centerline (see appendix B.2 for details). As with the radial momentum-equation, these values are determined using linear interpolation across the centerline.

3.5 Temporal Discretization

A modified third order Runge-Kutta scheme (Spalart, 1987, Spalart *et al.*, 1991) is used for terms treated explicitly and second order Crank-Nicholson is used for the terms treated implicitly. The fractional step method, described in details in section 3.3.3, part I, is used to remove the implicit pressure dependence in the momentum-equations.

The special problems that arise with cylindrical coordinates can be illustrated by examining the computational grid, displayed in figure 3.5-1. The grid is stretched in the radial direction in order to resolve the boundary layers along all walls, including the walls of the central- and annular pipes of the inlet section. The fine radial grid which is necessary to resolve the boundary layers in the inlet section extends downstream into the combustion chamber. Since large radial velocities are expected in this region, it is desirable to treat all convective terms with derivatives in the radial direction implicitly. Diffusive terms with derivatives in the radial direction will also have to be treated implicitly. This problem is identical to the problem described for the backward facing step.

Thus, it seems desirable to treat all terms with derivatives in the radial direction with an implicit time-integration scheme (similar to what was done for the backward facing step). However, there is an additional problem with the cylindrical geometry. In order to get acceptable azimuthal resolution at the outer wall, the azimuthal resolution around the centerline becomes unnecessarily fine. Since the azimuthal convection velocity may be significant around the centerline it is clear that all terms (convective and diffusive) with derivatives in the azimuthal direction should be treated implicitly in order to avoid imposing a severe restriction on the time-step.

The two requirements combined implies that one should treat all convective and diffusive terms with derivatives in both the radial and azimuthal directions with an implicit time-integration scheme. However, this would lead to a set of coupled non-linear equations which requires a costly solution procedure (often involving iterations or approximate factorization techniques).

The approach used to integrate the Navier-Stokes equations in the present study circumvents the need to solve a coupled set of non-linear equations by dividing the computational domain into two separate parts. The first part is the so-called

"core-region" which includes the centerline, and extends to a given radius, r_{core}. The rest of the domain is denoted the "outer-region". The idea is to treat all terms with derivatives in the azimuthal direction implicitly in the core-region. All other terms in this region are treated explicitly. In the outer-region terms with derivatives in the radial direction are treated implicitly. All other terms are treated explicitly.

In the core-region, the azimuthal momentum equation will be non-linear since the convective terms with derivatives in the azimuthal direction are treated implicitly. The axial and radial momentum equations remain linear in u_x and u_r, respectively. The azimuthal momentum equation is therefore linearized and solved first to yield u_θ^k. This solution is then used when integrating the other two equations. (The form of the linear and non-linear operators, A and B, needed in equation 3.3-4, part I, is described in appendix B.3). In the outer-region, the solution procedure is similar, except that the radial momentum equation has to be linearized and solved prior to solving the axial and azimuthal momentum equations.

The interface between the core-region and outer-region should be located somewhere in the range, $0 < r_{core} < r_c$. This will assure that all zones with a fine radial grid fall in the outer-region. The interface itself is treated such that overall second order temporal accuracy is retained. In order to validate this method, it was applied to DNS and LES of turbulent pipe-flow. The results from these calculations are compared with experimental and computational results from the literature in appendix C.

The following is a more detailed description of the solution procedure. The first step involves integrating the momentum equations in the core-region. The core-region is shown as the shaded area in figure 3.5-2. For the axial and azimuthal momentum equations, integration includes all points marked by solid symbols, up to and including the points with radial index $j = J$. The radial momentum equation, on the other hand, can only be integrated up to and including points with radial index $j = J - 1$, as seen by studying the coefficients a_k, b_k, and c_k in equation 3.5-1b. (Equation 3.5-1 shows the general form of the discrete momentum equations in the core-region). The coefficients a_k, b_k, and c_k are the elements of the diagonals of the tri-diagonal matrix formed on the left-hand-side of the equations.

u_x momentum equation ($j \leq J$):

$$a_k u_{i,j,k-1}^k + b_k u_{i,j,k}^k + c_k u_{i,j,k+1}^k = RHS_{i,j,k}^{k-1} \qquad (3.5\text{-}1a)$$

where, the functional dependence of the coefficients are:

$$a_k = a_k(w_{i+1,j,k-1}^k, w_{i,j,k-1}^k)$$

$$b_k = b_k(w_{i+1,j,k-1}^k, w_{i,j,k-1}^k, w_{i+1,j,k}^k, w_{i,j,k}^k)$$

$$c_k = c_k(w_{i+1,j,k}^k, w_{i,j,k}^k)$$

u_r momentum equation ($j \leq J-1$):

$$a_k v_{i,j,k-1}^k + b_k v_{i,j,k}^k + c_k v_{i,j,k+1}^k = RHS_{i,j,k}^{k-1} \qquad (3.5\text{-}1b)$$

where

$$a_k = a_k(w_{i,j+1,k-1}^k, w_{i,j,k-1}^k)$$

$$b_k = b_k(w_{i,j+1,k-1}^k, w_{i,j,k-1}^k, w_{i,j+1,k}^k, w_{i,j,k}^k)$$

$$c_k = c_k(w_{i,j+1,k}^k, w_{i,j,k}^k)$$

u_θ momentum equation ($j \leq J$):

$$a_k w_{i,j,k-1}^k + b_k w_{i,j,k}^k + c_k w_{i,j,k+1}^k = RHS_{i,j,k}^{k-1} \qquad (3.5\text{-}1c)$$

where

$$a_k = a_k(w_{i,j,k-1}^{k-1}, w_{i,j,k}^{k-1})$$

$$b_k = b_k(w_{i,j,k-1}^{k-1}, w_{i,j,k+1}^{k-1})$$

$$c_k = c_k(w_{i,j,k+1}^{k-1}, w_{i,j,k}^{k-1})$$

(In equations 3.5-1 and 3.5-2, u, v, and w are used to denote the axial, radial and azimuthal velocity components, respectively). The subscripts (i, j, k) give the nodal position at which the velocity components and the right-hand-side, RHS, are evaluated. The right-hand-side contains only known information (i.e. from substep $k-1$).

As explained above the azimuthal momentum equation has to be inverted first. Equation 3.5-1c shows that the coefficients, a_k, b_k, and c_k, only depend on information from the previous sub-step (k-1) (due to linearization) and the azimuthal momentum equation can therefore be integrated up to and including points with radial coordinate $j = J$. It is further seen that evaluation of a_k, b_k,

and c_k for the axial momentum equation will require u_θ^k $(= w^k)$ up to an including radial location $j = J$, which is now available.

The "problem" arises in the radial momentum equation where it is seen from equation 3.5-1b that the coefficients a_k, b_k, and c_k, depend on u_θ^k up to an including radial location $j + 1$. The radial momentum equation can therefore only be solved at points with radial location up to and including $j = J - 1$ (in the core-region).

The outer-region contains all points not included in the core-region. Thus, the axial and azimuthal momentum equations are integrated from $j = J + 1$ to the wall, and the radial momentum equation is integrated from $j = J$ to the wall. Since all terms with derivatives in the radial direction are treated implicitly in the outer-region, the general form of the discrete momentum equations in this region become:

u_x momentum equation $(j \geq J + 1)$:

$$a_j u_{i,j-1,k}^k + b_j u_{i,j,k}^k + c_j u_{i,j+1,k}^k = RHS_{i,j,k}^{k-1} \tag{3.5-2a}$$

where

$$a_j = a_j(v_{i+1,j-1,k}^k, v_{i,j-1,k}^k)$$
$$b_j = b_j(v_{i+1,j-1,k}^k, v_{i,j-1,k}^k, v_{i+1,j,k}^k, v_{i,j,k}^k)$$
$$c_j = c_j(v_{i+1,j,k}^k, v_{i,j,k}^k)$$

u_r momentum equation $(j \geq J)$:

$$a_j v_{i,j-1,k}^k + b_j v_{i,j,k}^k + c_j v_{i,j+1,k}^k = RHS_{i,j,k}^{k-1} \tag{3.5-2b}$$

where

$$a_j = a_j(v_{i,j-1,k}^{k-1}, v_{i,j,k}^{k-1})$$
$$b_j = b_j(v_{i,j-1,k}^{k-1}, v_{i,j,k}^{k-1}, v_{i,j+1,k}^{k-1})$$
$$c_j = c_j(v_{i,j+1,k}^{k-1}, v_{i,j,k}^{k-1})$$

u_θ momentum equation $(j \geq J + 1)$:

$$a_j w_{i,j-1,k}^k + b_j w_{i,j,k}^k + c_j w_{i,j+1,k}^k = RHS_{i,j,k}^{k-1} \tag{3.5-2c}$$

where

$$a_j = a_j(v_{i,j-1,k+1}^k, v_{i,j-1,k}^k)$$
$$b_j = b_j(v_{i,j-1,k+1}^k, v_{i,j-1,k}^k, v_{i,j,k+1}^k, v_{i,j,k}^k)$$
$$c_j = c_j(v_{i,j,k+1}^k, v_{i,j,k}^k)$$

In this case the radial momentum equation (equation 3.5-2b) will have to solved first to yield u_r^k. After solving equation 3.5-2b, u_r^k is known in the entire domain and the the coefficients a_k, b_k, and c_k in the two other momentum equations can easily be calculated.

Solution of equation 3.5-2 will, however, require some sort of boundary condition at $j = J$ (axial and azimuthal momentum equations) and $j = J - 1$ (radial momentum equation). But, since equation 3.5-1 has been solved first, u_x^k, u_r^k and u_θ^k are already known at their respective boundaries ($j = J$ for u_x and u_θ, and $j = J - 1$ for u_r) and can be used as boundary condition when solving equation 3.5-2. It is easily verified that this preserves second order temporal accuracy.

Since different terms are treated with implicit and explicit time-integration schemes in the core- and outer-regions, the definition used for calculating the stability criterion will also be different in the two regions. As in the definition used in part I (equation 3.3-8), only terms treated explicitly are taken into account when calculating the stability criterion (SC). The definitions adopted in the cylindrical case are:

Core-region :
$$SC = \Delta t \left\{ \frac{|u_x|}{\Delta x} + \frac{|u_r|}{\Delta r} + 4\nu \left(\frac{1}{\Delta x^2} + \frac{1}{\Delta r^2} \right) \right\}_{max} \tag{3.5-3}$$

Outer-region :
$$SC = \Delta t \left\{ \frac{|u_x|}{\Delta x} + \frac{|u_\theta|}{r\Delta \theta} + 4\nu \left(\frac{1}{\Delta x^2} + \frac{1}{(r\Delta \theta)^2} \right) \right\}_{max} \tag{3.5-4}$$

The basic case (defined in chapter 5) was run at a fixed time-step of 0.0025 h/U_c. The corresponding value of the stability criterion, SC, (found in the outer-region for this particular grid) was about 0.9. The calculation was run for 3 flow-through times (90 time-units) in order to remove transients resulting from interpolation of the initial flow-field. Statistics were then sampled over a period of 6 flow-through times (180 time-units). (A flow-through time is defined to be 30 time-units, corresponding roughly to the time it takes a fluid particle to travel through the combustion chamber at $U_0 = 0.6$).

3.6 Poisson Equation

As in the backward facing step calculations, continuity is enforced by solving a Poisson equation for pressure. Since the same time-integration scheme is used, the Poisson equation takes the form of equation 3.3-21, part I:

$$\nabla^2 \psi^k = \frac{1}{2\beta_k \Delta t} D(\hat{\mathbf{u}}^k), \qquad \psi^k = \phi^k - \phi^{k-1} \qquad (3.6\text{-}1)$$

where D is the divergence operator, and $\hat{\mathbf{u}}^k$ is the intermediate velocity field resulting from solving the momentum equations. β_k is a factor associated with the Runge-Kutta time-integration scheme (defined in section 3.3.1, part I). In cylindrical coordinates this equation can be expressed as:

$$\frac{\partial}{\partial x}\left(\frac{\partial \psi^k}{\partial x}\right) + \frac{1}{r}\frac{\partial}{\partial r}\left(r\frac{\partial \psi^k}{\partial r}\right) + \frac{1}{r}\frac{\partial}{\partial \theta}\left(\frac{1}{r}\frac{\partial \psi^k}{\partial \theta}\right) = \frac{1}{2\beta_k \Delta t}\left\{\frac{\partial \hat{u}_x^k}{\partial x} + \frac{1}{r}\frac{\partial r\hat{u}_r^k}{\partial r} + \frac{1}{r}\frac{\partial \hat{u}_\theta^k}{\partial \theta}\right\}$$

$$(3.6\text{-}2)$$

The solution procedure is identical to that used for the backward facing step. Equation 3.6-2 is first Fourier transformed in the azimuthal direction to give a set of uncoupled Helmholtz equations. These equations are then solved using the iterative technique outlined in section 3.4, part I.

It is easily verified that the centerline causes no added complexity in the present case. The control-volumes for pressure coincide with the control-volumes for the axial velocity component, when viewed in the r-θ-plane. From figure 3.4-1 it is seen that the control-volume closest to the centerline is pie-shaped, with zero area at the centerline itself. Thus, assuming that the flux at this surface is finite, it need not be calculated since it multiplies zero. As with the momentum equations, the radius, r, in the $1/r$ factors in equation 3.6-2 is evaluated at the center of the control-volume and is therefore never zero (in the discrete equation). Thus, even though the pressure at the centerline is well defined, it is never needed, and therefore not calculated.

3.7 Boundary Conditions

No-slip boundary conditions are used along all solid walls. Periodic condition is applied in the azimuthal direction. As in the backward facing step calculations of part I, convective outflow boundary conditions are used. As indicated in part I this condition will create errors in the solution around the exit of the domain. However, the domain of influence for the backward facing step was limited to about 1 step height. Analysis of results from the coaxial jet-combustor calculations indicates a domain of influence of similar extent. Thus, the solution upstream of about $x/h = 18$ is not significantly affected by the outflow boundary condition.

The inflow boundary condition consists of fully developed turbulent flow calculated in a separate periodic pipeflow section, with radial dimensions identical to those of the inlet section of the coaxial jet-combustor. The "inflow generator" is shown schematically in figure 3.2-1. The radial and azimuthal grids used in the inflow generator are identical to those in the inlet section of the coaxial jet-combustor. The axial grid is uniform with spacing equal to the axial grid-spacing at the inlet of the computational domain of the coaxial jet-combustor.

The inflow generator is linked into the coaxial jet-combustor code as a separate subroutine. The two codes are therefore run in parallel thus avoiding interpolation in time when transferring a plane of velocity vectors from the inflow generator to the inlet of the coaxial jet-combustor. Also, there is no need to store the inflow velocity vectors on file, which significantly reduces storage requirements and increases the flexibility of the simulations.

3.8 Passive Scalar Transport Equation

A passive scalar transport equation is used to calculate the fuel mass-fraction in the fuel/air mixture. The equation contains convective and diffusive terms, but no sources or sinks. It is given by:

$$\frac{\partial \overline{\varphi}}{\partial t} = -\nabla \cdot (\overline{\mathbf{u}}\,\overline{\varphi}) + \nabla \cdot (\alpha \nabla \overline{\varphi}) \tag{3.8-1}$$

where α is the total diffusivity (equal to the sum of the molecular- and eddy-diffusivity). The convective and diffusive terms are given by:

$$\nabla \cdot (\overline{\varphi}\,\overline{\mathbf{u}}) = \frac{\partial}{\partial x}(\overline{u}_x \overline{\varphi}) + \frac{1}{r}\frac{\partial}{\partial r}(r\overline{u}_r \overline{\varphi}) + \frac{1}{r}\frac{\partial}{\partial \theta}(\overline{u}_\theta \overline{\varphi}) \tag{3.8-2}$$

$$\nabla \cdot (\alpha \nabla \overline{\varphi}) = \frac{\partial}{\partial x}\left(\alpha \frac{\partial \overline{\varphi}}{\partial x}\right) + \frac{1}{r}\frac{\partial}{\partial r}\left(\alpha r \frac{\partial \overline{\varphi}}{\partial r}\right) + \frac{1}{r}\frac{\partial}{\partial \theta}\left(\alpha \frac{1}{r}\frac{\partial \overline{\varphi}}{\partial \theta}\right) \tag{3.8-3}$$

3.8.1 Spatial Discretization

The standard second order control-volume formulation leads to the equivalent of discrete central differencing formulas for both the convective and diffusive terms. At high Reynolds numbers, central differencing applied to convective terms might lead to instabilities, usually observed as spatial point-to-point oscillations. The instability is usually triggered by boundary conditions or stretching of the computational grid. It is sustained and amplified in the scalar equation because of the absence of a pressure like term and insufficient physical diffusion. As an example, the instability is never observed in calculation of turbulent channel flow when using periodic boundary conditions and a uniform grid. However, the use of inflow-outflow boundary conditions, or stretching the grid, will likely trigger the instability.

A common fix to the problem is to use upwind, or upwind biased schemes, which reduces or removes the instability by adding numerical diffusion. The method used in the present calculations is an upwind biased scheme, known as the QUICK (Quadratic Upstream Interpolation for Convective Kinematics) scheme (Leonard, 1979, 1988). The fluxes at the control-volume faces are determined by quadratically

interpolating the solution from the two adjacent, upwind grid points and the one adjacent downwind point of each face. With reference to the (Cartesian) grid in figure 3.8-1, the value of the scalar at the east surface of the control-volume is:

$$\varphi_e = \begin{cases} -\frac{1}{8}\varphi_{i-1} + \frac{3}{4}\varphi_i + \frac{3}{8}\varphi_{i+1}, & \text{if } u_e > 0 \\[2ex] -\frac{1}{8}\varphi_{i+2} + \frac{3}{4}\varphi_{i+1} + \frac{3}{8}\varphi_i, & \text{if } u_e < 0 \end{cases} \tag{3.8-4}$$

The fact that the upwind biased scheme introduces numerical diffusion is easily seen by rearranging equation 3.8-4:

$$\varphi_e = \begin{cases} \frac{1}{2}(\varphi_i + \varphi_{i+1}) - \frac{1}{8}(\varphi_{i-1} - 2\varphi_i + \varphi_{i+1}), & \text{if } u_e > 0 \\[2ex] \frac{1}{2}(\varphi_i + \varphi_{i+1}) - \frac{1}{8}(\varphi_i - 2\varphi_{i+1} + \varphi_{i+2}), & \text{if } u_e < 0 \end{cases} \tag{3.8-5}$$

The convective flux at the east surface of the control-volume can be calculated according to:

$$f_e = \frac{u_e}{2}(\varphi_i + \varphi_{i+1}) - \left\{ \frac{u_e + |u_e|}{2} \right\} \frac{1}{8}(\varphi_{i-1} - 2\varphi_i + \varphi_{i+1})$$

$$- \left\{ \frac{u_e - |u_e|}{2} \right\} \frac{1}{8}(\varphi_i - 2\varphi_{i+1} + \varphi_{i+2}) \tag{3.8-6}$$

Similar expressions apply to the other surfaces of the control volume. It should be mentioned that the previous development applies to uniform grids, but the idea is easily extended to nonuniform grids. The upwind biased QUICK scheme is second order accurate, but has a third (and higher) order diffusive error term(s).

3.8.2 <u>Temporal Discretization</u>

The temporal integration scheme used for the passive scalar equation is similar to that used for the momentum equations. Third order Runge-Kutta is used for the explicitly treated terms and second order Crank-Nicholson is used for the implicitly treated terms. Since the passive scalar equation is similar to the momentum equations, the same arguments used for the momentum equations applies when determining which terms to treat implicitly. Thus, the computational domain is split into two parts, the core-region and the outer-region.

All terms with derivatives in the azimuthal direction are treated implicitly in the core-region, and all terms with derivatives in the radial direction are treated implicitly in the outer-region. The discrete equation is given by (where the bar over the symbols has been dropped for simplicity):

$$\frac{\varphi^k - \varphi^{k-1}}{\Delta t} = \beta_k B(\varphi^k, \mathbf{u}^{n+1}) + \beta_k B(\varphi^{k-1}, \mathbf{u}^{n+1})$$

$$+ \gamma_k A(\varphi^{k-1}, \mathbf{u}^{n+1}) + \zeta_k A(\varphi^{k-2}, \mathbf{u}^{n+1}) \qquad (3.8\text{-}7)$$

Since the momentum equations are solved prior to solving for the scalar, φ, the velocity vector $\mathbf{u}^{n+1}$ at full time-step $n + 1$ is known, and is used as input in the passive scalar transport equation. ($\mathbf{u}^{n+1}$ is used for all Runge-Kutta sub-steps in the passive scalar transport equation). The explicit operator A, and implicit operator B, are given by:

Core-Region:

$$A = \frac{\partial}{\partial x}(u_x \varphi) + \frac{1}{r}\frac{\partial}{\partial r}(r u_r \varphi) + \frac{\partial}{\partial x}\left(\alpha \frac{\partial \varphi}{\partial x}\right) + \frac{1}{r}\frac{\partial}{\partial r}\left(\alpha r \frac{\partial \varphi}{\partial r}\right) \qquad (3.8\text{-}8)$$

$$B = \frac{1}{r}\frac{\partial}{\partial \theta}(u_\theta \varphi) + \frac{1}{r}\frac{\partial}{\partial \theta}\left(\alpha \frac{1}{r}\frac{\partial \varphi}{\partial \theta}\right) \qquad (3.8\text{-}9)$$

Outer-Region:

$$A = \frac{\partial}{\partial x}(u_x \varphi) + \frac{1}{r}\frac{\partial}{\partial \theta}(u_\theta \varphi) + \frac{\partial}{\partial x}\left(\alpha \frac{\partial \varphi}{\partial x}\right) + \frac{1}{r}\frac{\partial}{\partial \theta}\left(\alpha \frac{1}{r}\frac{\partial \varphi}{\partial \theta}\right) \qquad (3.8\text{-}10)$$

$$B = \frac{1}{r}\frac{\partial}{\partial r}(r u_r \varphi) + \frac{1}{r}\frac{\partial}{\partial r}\left(\alpha r \frac{\partial \varphi}{\partial r}\right) \qquad (3.8\text{-}11)$$

3.8.3 <u>Boundary Conditions</u>

Periodic boundary condition is used in the azimuthal direction. The outflow boundary condition is the same convective condition as used for the momentum equations. Neumann condition (gradient of the scalar normal to a surface is zero) is enforced along all horizontal and vertical walls. The inflow boundary condition is determined using a Dirichlet condition: the scalar is set to 1 in the central fuel pipe, and 0 in the annular air pipe.

3.8.4 <u>Centerline</u>

As with the Poisson equation for pressure (see section 3.6), the centerline does not cause any problems for the passive scalar equation. This is easily verified by studying the control-volumes in figure 3.4-1. Since the control-volume for the passive scalar coincides with that of the pressure (which again is the same as that of the u_x momentum equation in the r-θ-plane), the area of the control-volume adjacent to the centerline is zero. There is therefore no need to evaluate the flux in the radial direction at the centerline (assuming that it is finite). Also, any r, appearing in $1/r$ factors, is evaluated at the center of the control-volume which means that division by zero will never take place. Thus, the value of the scalar is never needed, and therefore never calculated, at the centerline itself.

Outer Corner of the Step

Corner of the Step

Recirculation Zone

Reattachment Point

Annular / Air pipe

Step Shear Layer

Central / Fuel pipe

Fuel-Pipe Shear Layer

Combustion Chamber

Inlet Section

Recirculation Zone

Base of burner / Point of expansion / Step
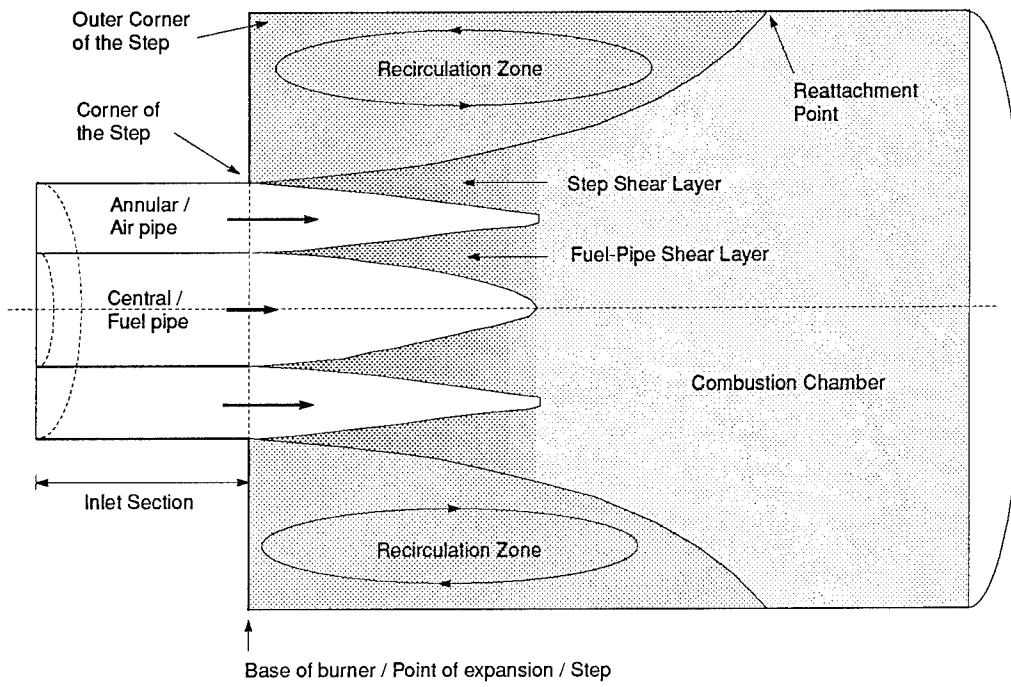
FIGURE **3.1-1**, Sketch of the computational domain identifying the notation used in the text.
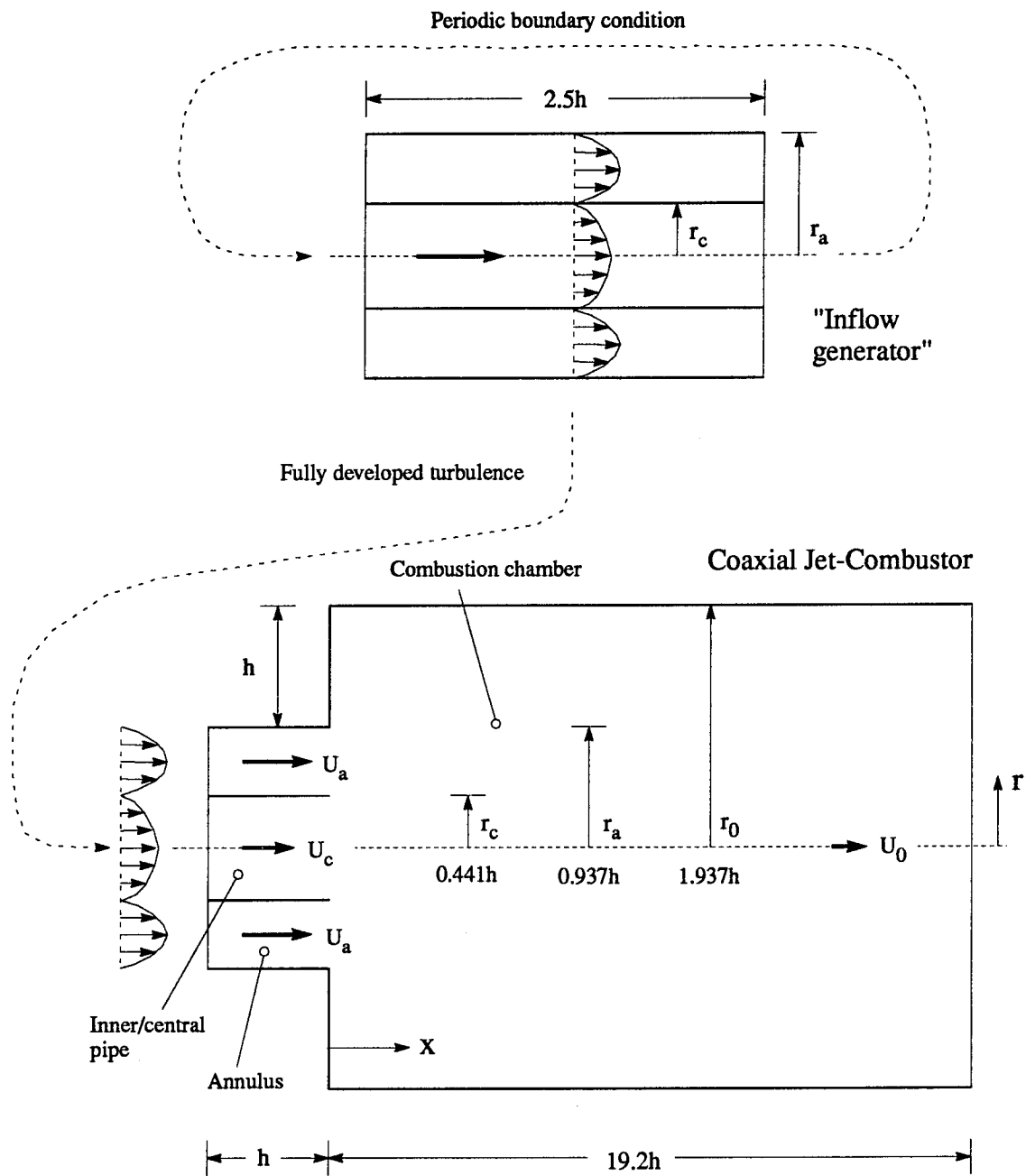
FIGURE **3.2-1**, Computational domain for the coaxial jet-combustor. Also shown is the periodic pipeflow section used to generate the inflow data.
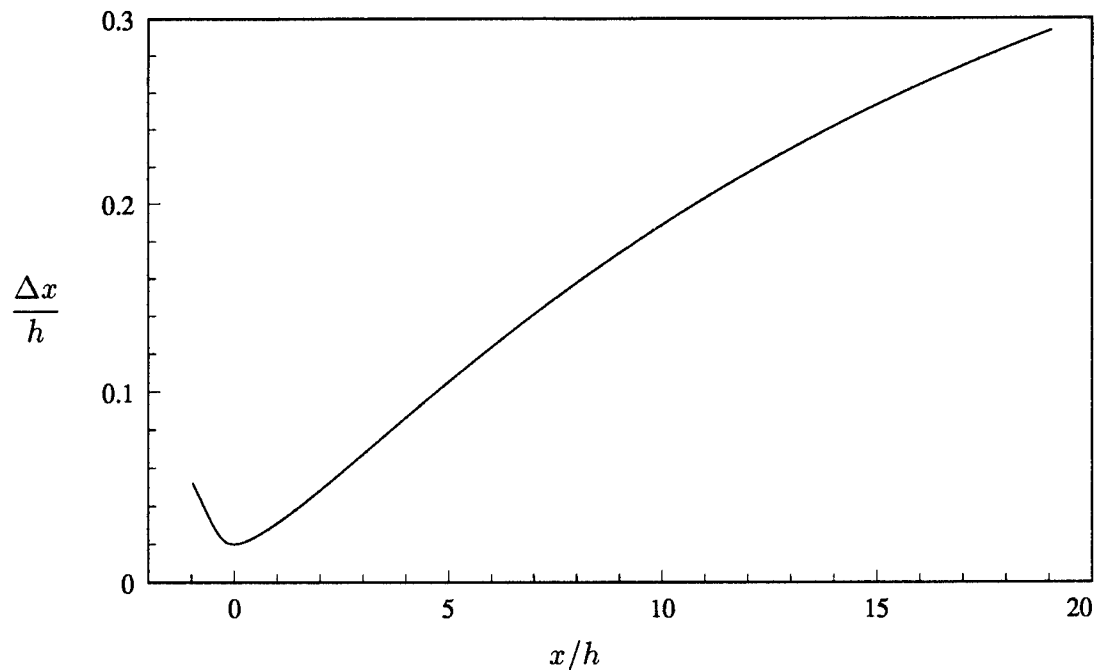
FIGURE **3.3-1**, Axial grid spacing versus axial distance for the basic case.
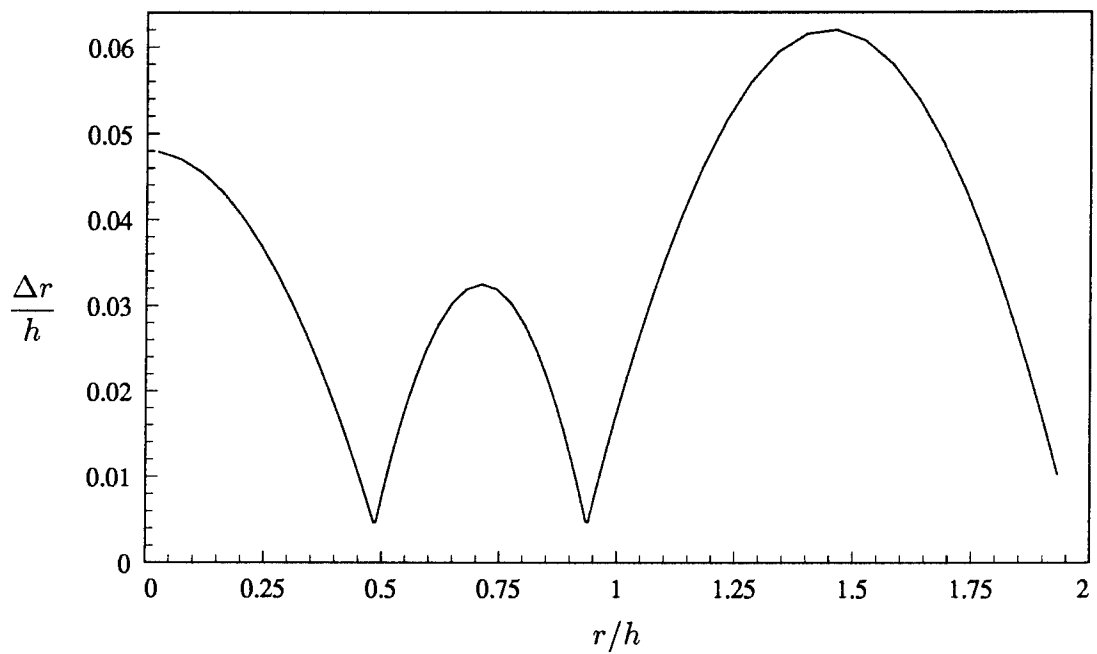
FIGURE **3.3-2**, Radial grid spacing versus radial distance for the basic case.
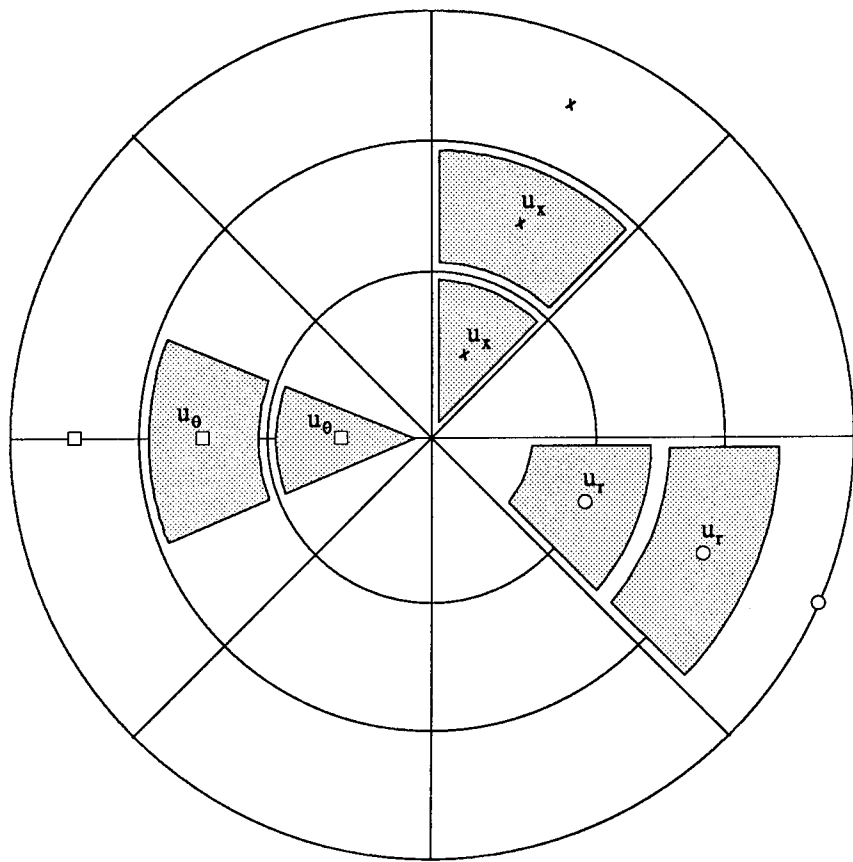
FIGURE **3.4-1**, Control-volume locations in cylindrical coordinates on a staggered grid.
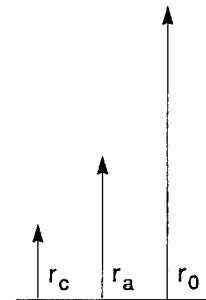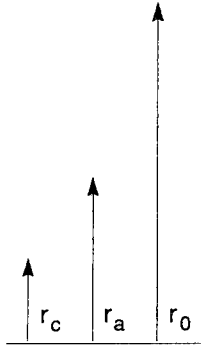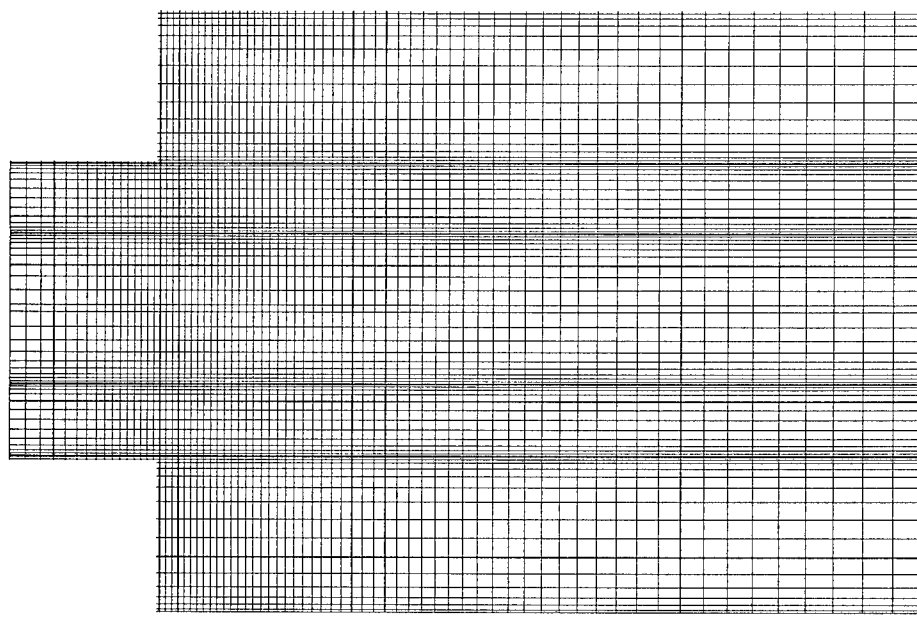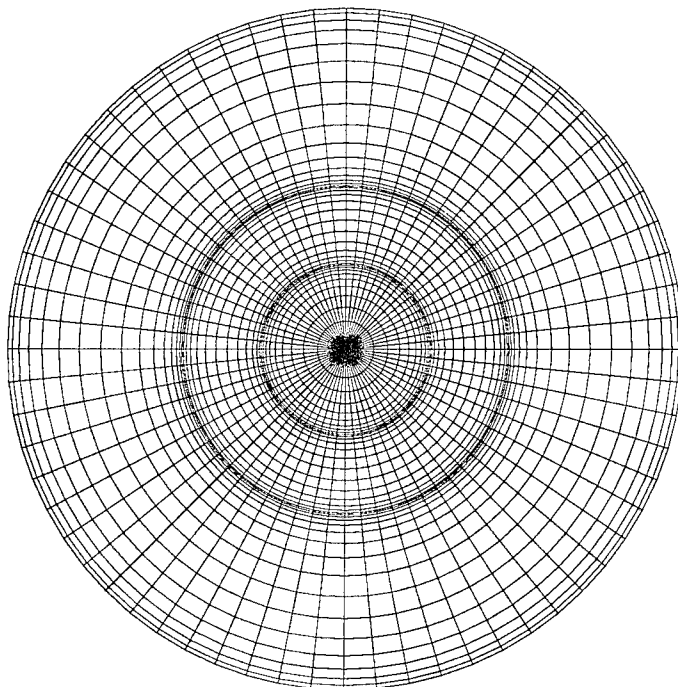
FIGURE **3.5-1**, Example of computational grid. (This particular grid has fewer points than that used in the calculations, but the distribution of points is similar).
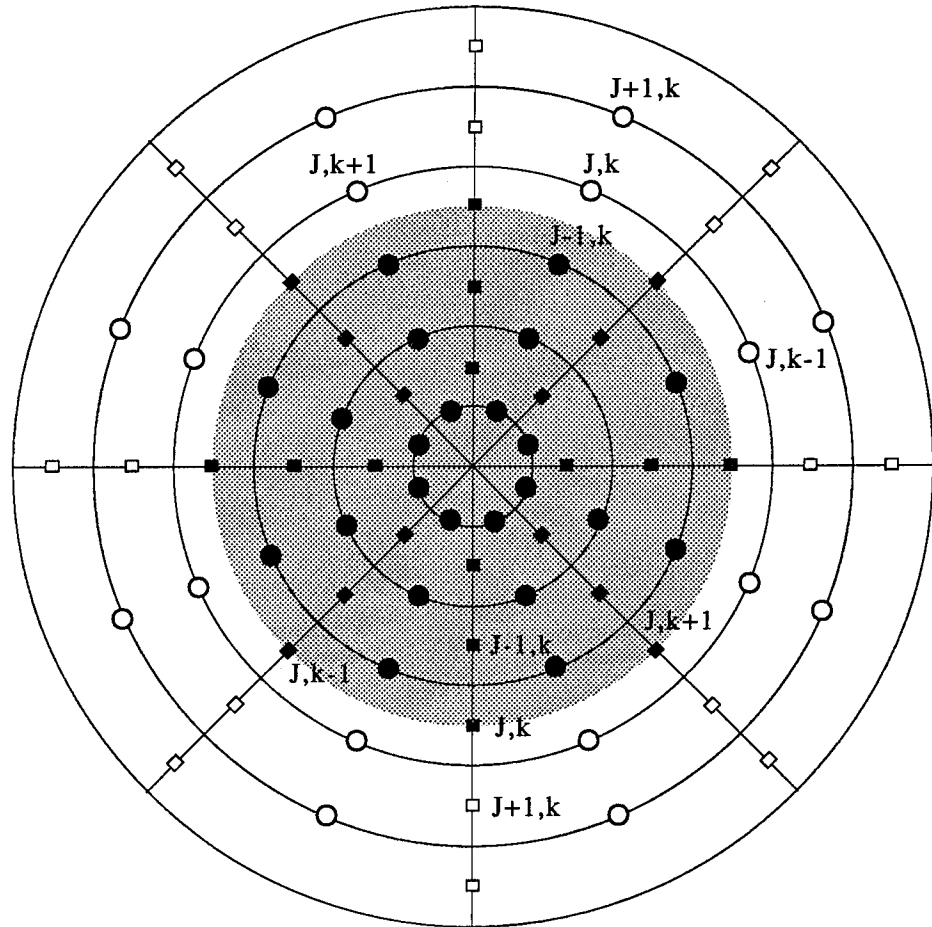
FIGURE **3.5-2**, Illustration of computational domain. Shaded area is the "core-region", which is surrounded by the "outer-region".   o : u_r;   □ : u_θ
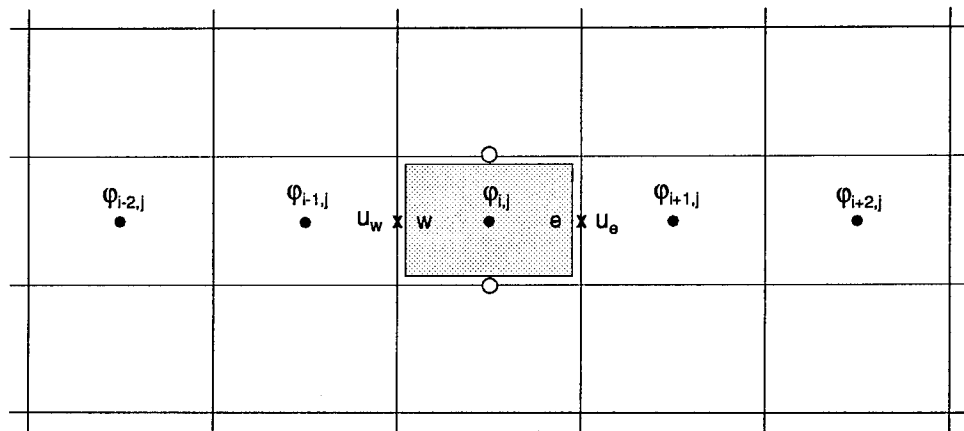
FIGURE **3.8-1**, Illustration for the QUICK upwind biased differencing scheme.

REFERENCE CASE

The computational setup (described in the chapter 3) was designed to match as closely as possible the experimental setup used by Johnson & Bennett (1981, 1984). The experimental setup is described below.

Johnson & Bennett performed a series of experiments studying the mixing of coaxial jets discharging in an expanded duct. The objective of the study was to obtain data that could be used for evaluation and improvement of turbulent transport models, used for combustor flow modeling. The study used laser velocimeter (LV) and laser induced fluorescence (LIF) techniques to measure velocities and concentration. Visualization techniques were used to qualitatively determine the time dependent characteristics of the flow as well as the scale and structure of the turbulent eddies.

Axial, radial and azimuthal velocities, and turbulent momentum and scalar transport rates were measured in x-r and r-θ planes and were used to determine mean values, rms values, skewness and kurtosis.

A sketch of the experimental test-section is shown in figure 4-1. The step-height, h, is defined as the distance between the outer wall of the annular pipe and the wall of the test-section. The working fluid for the experiment was water at a temperature of approximately $20^\circ C$. The kinematic viscosity of water at $20^\circ C$ is $1.004 \cdot 10^{-6} m^2/s$ (pg. 545, Olson).

The test section consisted of a $122mm$ inside diameter by $1m$ long, thin-wall glass tube mounted in an optical box. The flat-faced optical box surrounding the circular test section was filled with water, and was necessary in order to decrease the optical distortion obtained through water-glass-air interfaces when conducting flow visualization and optical experiments in circular tubes.

The inlet plenum for the annular duct contained three perforated plates to produce approximately uniform flow and a honeycomb section to remove swirl from

the flow. No flow straightening devices were used for the central pipe which was approximately $25mm$ in diameter and was fed through a pipe/hose combination with the same diameter and a total length of over $300mm$.

For tests with fluorescein dye, the dye was added to the central jet (fuel) in a mixing chamber located a short distance upstream of a metering valve used to set the central jet flow-rate. Uniform flow of dye was obtained by metering dye through a micrometering valve with large pressure drop compared with other pressure drops in the system. This ensured a uniform concentration of dye in the central jet fluid.

	Central	Annular	test-section
Area $[m^2]$	$0.7354 \cdot 10^{-3}$	$1.9986 \cdot 10^{-3}$	$11.6898 \cdot 10^{-3}$
Area $[h^2]$	0.7412	2.0142	11.7812
U-bulk $[m/s]$	0.52	1.66	0.318
U-bulk $[U_c]$	1.0	3.192	0.612
Q $[m^3/s]$	$0.3912 \cdot 10^{-3}$	$3.331 \cdot 10^{-3}$	$3.722 \cdot 10^{-3}$
Q $[h^2 U_c]$	0.758	6.456	7.214

TABLE **4-1**, Flow variables specified in the experiments. h is the step height, and U_c is the bulk velocity in the central jet.

The cross sectional area of the central pipe, annulus and test-section are listed in table 4-1, both in m^2 and normalized by the step-height, h. The radius of the central pipe is taken to be that at the end of the tapered section (see figure 4-1). Also included in table 4-1 are the bulk velocities and volume-flow rates reported by Johnson & Bennett. These parameters are given both in dimensional and non-dimensional forms. For the purpose of comparing the computational results to the measurements, the measured data were non-dimensionalized using the central pipe bulk velocity, $U_c = 0.52m/s$, and the step height, $h = 31.5mm$. The Reynolds number was 16310, based on the step height and the central pipe bulk velocity. (This corresponds to a Reynolds number of 38600, based on the bulk velocity and diameter of the combustion chamber).

Small differences between the experimental and computational (table 3.2-1) flow-rates can be observed. Small discrepancies are also found when calculating the experimental bulk velocities from the quoted volume flow-rates, or visa versa.

However, there appears to be a more serious inconsistency in the experimental database of Johnston & Bennett. From table 4-1 it is seen that the bulk velocity ratio of the two incoming jets was about 3.2 (corresponding to a peak velocity ratio of about 3). However, as will become apparent in chapter 5, the axial velocity profile measured by Johnston & Bennett at $x/h = 0.41$ seems to indicate that the ratio of the peak velocities in the profiles was closer to 2. It is unlikely that the entrainment of air into the fuel stream was large enough to drop the velocity ratio from 3 to 2 within the first 0.41 step heights after the expansion. (Particularly since the ratio of the measured peak velocities stays about 2 also at the second and third measurement stations, i.e., at $x/h = 1.62$ and $x/h = 3.24$).

Appendix D.3 presents a discussion of the problems apparently associated with the experimental data. This includes results from a simulation in which the ratio of the air- to fuel flow-rates was changed to give a bulk velocity ratio of 2.2 (corresponding to a peak velocity ratio of 2). These results clearly fit the experimental data better in the first part of the combustion chamber, indicating that the flow-rates used in the experiments were not as quoted by Johnston & Bennett.

Station	Distance [mm]	Distance [h]
1	13	0.41
2	51	1.62
3	102	3.24
4	152	4.83
5	203	6.44
6	254	8.06
7	305	9.68

TABLE **4-2**, Axial measurement stations.

However, the results of appendix D.3 are inconclusive in terms of determining the flow-rates actually used in the experiment. It was therefore decided to use the flow-rates quoted by Johnston & Bennett. The analysis and comparison with experimental data in chapter 5 is based on the assumption that the experiment used the flow-rates quoted.

Axial measurement stations were set up at seven locations downstream of the expansion. At each station, measurements were taken at one or several of four

azimuthal locations, spaced 90° apart. The measurement stations are listed in table 4-2. In the present work different symbols are used when plotting experimental results measured in different runs or at different azimuthal stations, but no distinction is made between these when comparing the experimental results to those of the calculations.

It should be pointed out that Johnson & Bennett made no measurements in either the central- or annular pipe in the inlet section thus making a comparison of the flow conditions upstream of the expansion impossible. The section feeding the central pipe of the test-facility consisted of a pipe/hose combination of length $24r_c$. It is questionable whether this was sufficient to ensure fully developed flow at the exit of the pipe in the combustion chamber. In addition it is probable that the tapering at the end of the central pipe has an effect on the flow, although it is impossible to quantify it without reproducing the exact geometry in the simulations.

The length of the annular inlet section was not quoted by Johnson & Bennett. But since it contained three perforated plates (at unspecified locations) and a honeycomb section, it is unlikely that the annular flow was fully developed at the point of expansion into the combustion chamber. Since it is not possible to determine the state of the flow in the experiment, either in the central- or annular pipe, the calculations were performed assuming fully developed turbulent flow.
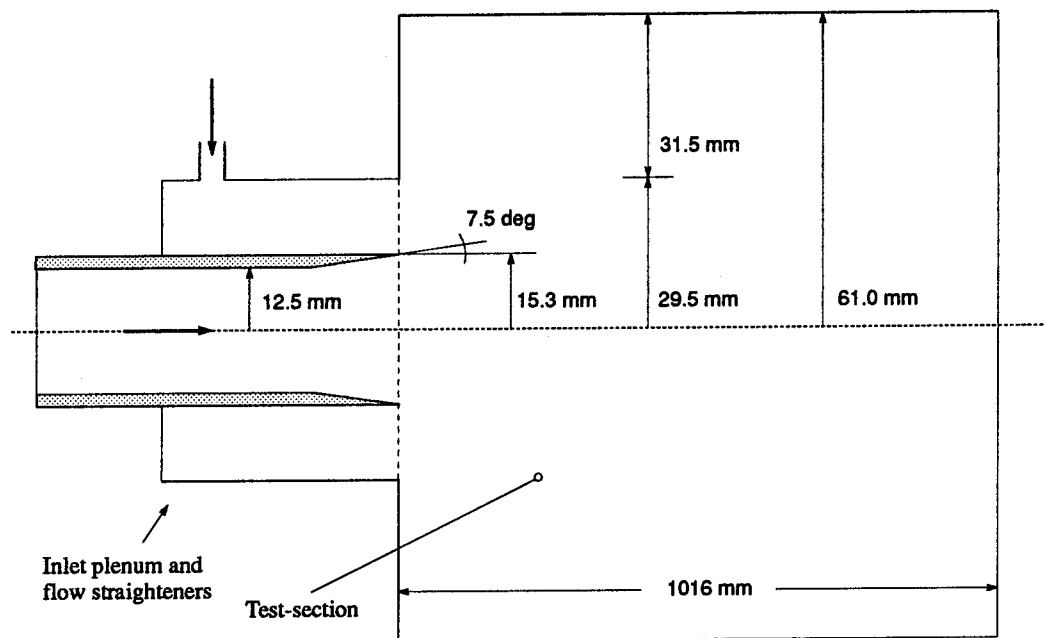
FIGURE **4-1**, Sketch of the experimental setup used by Johnson & Bennett.

Chapter 5

RESULTS

This chapter describes the results from large eddy simulations done to study turbulent mixing in a coaxial jet-combustor. All calculations are "cold-flow" calculations; that is, the effect of chemical reactions has not been taken into account. As pointed out by Roquemore *et al.* (1991) it seems appropriate to use cold-flow calculations to examine the characteristics of the recirculation zone when the flame is in a lifted state. However, at fuel rich conditions, with the flame attached to the base of the burner, this assumption poses more severe restrictions on the analysis and interpretation of the results.

Two main calculations, referred to as the *animation* case and the *basic* case, and several preliminary calculations were performed. The preliminary calculations, discussed in appendix D.1, were necessary in order to assess grid resolution requirements. Apart from grid resolution, and in some cases the length of the inlet section, all parameters used in the different computational cases were the same.

The purpose of the *basic* case was to generate a statistically averaged database in order to evaluate the characteristic features of the flow and scalar distribution in the combustion chamber, with particular emphasis on the recirculation zone. This data-set was also used to validate the simulation results against the experimental data.

The *animation* case was set up to study the transient behavior of the mixing process. Results from this calculation were animated and recorded on video-tape. Appendix D.2 describes the details of this calculation. The animation case used a coarser grid than that used for the basic case. This was done simply to keep the size of the database manageable. However, as is shown in appendix D.2, the turbulent statistics from the animation case agree reasonably well with those from the better resolved basic case, and the qualitative (transient) behavior of the flow captured on video-tape is not thought to have suffered from the coarser grid-resolution.

– 202 –

A thorough comparison of experimental results (Johnson & Bennett) and computational results from the basic case is presented in section 5.1. This includes mean velocity profiles and turbulent stresses. Also shown are the eddy-viscosity and SGS turbulent Schmidt number profiles.

Section 5.2 focuses on an analysis of results from the basic case and the animation case in order to investigate the mixing process and entrainment of fuel into the recirculation zone. Steady state results from the basic case are used to determine the fuel mass-fraction in the recirculation zone. Contour plots of the mean velocity components are used to evaluate where significant entrainment of fuel into the recirculation zone might occur. These plots are also helpful in determining where fluid from the recirculation zone is likely to be entrained into the step shear layer. A study of the animated results are used to shed light on instantaneous characteristics of the mixing process. In particular it is of importance to determine whether fuel-rich pockets of fluid are able to cross the annular air stream to be entrained in the recirculation zone.

Section 5.3, gives a summary of the computer-resources used for the calculations.

5.1 Code Verification

This section contains a detailed comparison of statistical results from the basic case with the experimental results of Johnson & Bennett (1981). Quantities compared include mean velocity profiles, turbulence intensities, turbulent shear stress, and mean fuel mass-fraction profiles. Also shown are profiles of the eddy-viscosity and SGS turbulent Schmidt number which assist in an evaluation of the effect of the subgrid scale models.

5.1.1 <u>Characteristics of the Inflow</u>

As mentioned in chapter 4 the experiments by Johnson & Bennett did not include any measurements of the flow in either the central fuel pipe or the annular air pipe. Thus, a comparison between the computational and experimental flow condition upstream of the expansion is not possible. This section presents some statistical quantities calculated in the "inflow generator" (see figure 3.2-1) in order to document the condition of the flow used as inflow boundary condition for the coaxial jet-combustor.

	Central	Annular (iw)	Annular (ow)
Re	14465	46304	46304
C_f (e)	0.00711	0.00532	0.00532
C_f (c)	0.00672	0.00486	0.00344
u_τ (e)	0.0596	0.1615	0.1615
u_τ (c)	0.0580	0.1543	0.1300
Re_τ (e)	475	597	597
Re_τ (c)	462	571	481

TABLE **5.1-1**, Statistical quantities from the inflow generator. (c): computational, (e): empirical (see table 3.3-1), (iw): inner wall, (ow): outer wall.

Table 5.1-1 lists the friction velocity and coefficient of friction from the calculations. These are compared with the empirically calculated values from table 3.3-1. The Reynolds number in the central pipe is based on the bulk-velocity and

diameter of the pipe, whereas the bulk-velocity and hydraulic diameter is used for the annular pipe. The coefficient of friction is normalized by the bulk velocity. Also given is the friction velocity Reynolds number, Re_τ, which for the central pipe is based on the pipe-radius, and for the annular pipe is based on half the distance between the two walls.

Good agreement is observed between computational and empirical values for the central pipe. However, appreciable discrepancies are present in the results from the annular pipe, particularly at the outer wall. Most of the discrepancies can be attributed to the azimuthal resolution (or rather lack of azimuthal resolution) at the outer wall. From table 3.3-2 it is seen that whereas $(r\Delta\theta)^+ = 23$ at the wall of the central pipe, the resolution increases to $(r\Delta\theta)^+ = 122$ at the outer wall of the annular pipe.

Figure 5.1-1 shows the mean axial velocity profiles from the central- and annular pipes, plotted in wall-coordinates. Figure 5.1-2 shows the mean axial velocity profiles normalized by the central pipe bulk velocity, U_c. From figure 5.1-1 it is seen that the velocity profile in the central pipe is in good agreement with the log-law. However, the velocity profiles at the walls of the annular pipe show clear signs of resolution problems. Particularly at the outer wall where $(r\Delta\theta)^+ = 122$ a significant overshoot is observed compared with the log-law.

Figures 5.1-3 and 5.1-4 show the axial and radial turbulence intensities, respectively, plotted in wall-coordinates. (Each data-set has been normalized by the friction velocity calculated at the respective wall, given in table 5.1-1). The peak of the $(u_x'')_{rms}$ profile is clearly over-predicted at both walls of the annular pipe, a result attributable to a lack of azimuthal resolution (and possibly also lack of axial resolution). Similarly, $(u_r'')_{rms}$ is clearly under-predicted in the annular pipe. The results are similar to results found in large eddy simulations of turbulent channel flow when the spanwise grid is too coarse.

Thus, it seems clear that the flow in the annular pipe is under-resolved. However, the flow statistics in the central pipe look reasonable. The grid-resolution studies summarized in appendix D.1 indicate that the effect of the inlet grid resolution on the flow downstream of the expansion is small.

5.1.2 Mean Velocity Profiles

Mean axial velocity profiles are shown at six axial measurement stations, ranging from $x/h = 0.41$ to $x/h = 8.06$, in figure 5.1-5. As pointed out previously, Johnson and Bennett made several measurements for the same flow condition. During each run they made measurements at one to four azimuthal locations (at each axial measurement station), spaced 90° apart. These measurements are represented by different symbols in the following figures, however, no effort is made to distinguish between measurements taken in different runs or at different azimuthal locations when comparing with the computational results.

Overall agreement between experiments and calculation is seen to be good at most measurement stations. However, closest to the expansion, particularly at $x/h = 0.41$, a fairly significant difference is observed between computational and experimental results. It seems as though the flow-rate in the central jet was higher in the experiments than in the calculation and conversely in the annular air jet. Integration of the mean velocity profiles from the calculation and experiments does however reveal that the total flow-rate (in the combustion chamber) was the same in all cases.

The reason for the discrepancy is not obvious. Johnson & Bennett made no measurements in the inlet section of the experimental facility thus making it impossible to compare the upstream flow conditions. However, the flow-rates used in the calculation, both in the central and annular pipes, match the flow-rates quoted by Johnson & Bennett. It would therefore seem that the fuel stream in the experiments entrains a larger amount of air immediately downstream of the expansion, than that of the calculation, making the central part of the flow speed up and the annular jet slow down. However, as pointed out in chapter 4 there is some evidence to suggest that the flow-rates in the experiments were not as quoted in the report by Johnson & Bennett. If this is the case it would explain some of the differences observed at the first axial measurement stations. (See appendix D.3 for an analysis of the effect of changing fuel to air ratio).

However, assuming the flow-rates are correct, the discrepancy is most likely caused by differences in the inflow in the experiment and the calculation. Recall that the central pipe used in the experiments had a tapered exit whereas an infinitely thin wall was assumed in the calculation. In addition, and perhaps most importantly,

the flow in the experiment, particularly in the annulus, was most likely far from developed at the point of expansion.

The difference between experiments and calculation is still present at $x/h = 1.62$, but has almost vanished at the third measurement station, $x/h = 3.24$. Further downstream only minor differences are observed between experiments and calculation. In particular it is seen that the calculated velocity profiles lead those of the experiments in the central region of the flow, and lag in the outer part (i.e. for r/h larger than about 0.7). This effect is most clearly seen at $x/h = 6.44$.

Radial velocity

Figure 5.1-6 shows mean radial velocity profiles downstream of the expansion. In this case it is more difficult to assess the agreement between experiments and calculation due to the rather large scatter in the experimental data. At the first measurement station it is nevertheless interesting to note that despite the scatter in the experimental data, the experiments seem to predict a larger negative radial velocity in the region $0.3 < r/h < 0.8$ than that predicted by the calculation. This means that the radial flow-rate towards the centerline was larger in the experiments than in the calculation, a result which is consistent with the larger axial velocity measured in the experiments in this region (see figure 5.1-5).

Further downstream (in particular at $x/h = 3.24$ and $x/h = 4.83$) it is seen that even though the qualitative agreement between experiments and calculation is fair, the experiments predict larger peaks, both positive and negative, in the profiles compared with those of the calculation. The agreement between experiments and calculation improves further downstream. However, it is clear that with the large scatter present in the experimental results, a detailed comparison is not possible. But the calculated velocity profiles for the most part fall within the rather large margin of error associated with the experimental data.

Azimuthal velocity

Since the flow was designed to be swirl free, the mean value of the azimuthal velocity component should be zero. However, it turns out that this quantity was not exactly zero in the experiments by Johnson & Bennett. They attribute this to the fact that it was difficult to (experimentally) obtain a completely swirl-free flow. Figure 5.1-7 shows the magnitude of the mean azimuthal velocity component measured by Johnson & Bennett. Also shown in figure 5.1-7 are the mean

azimuthal velocity profiles from the calculation. Since there is no swirl present in the calculation U_θ should be zero. The fact that it is not is a result of the insufficient statistical sample used in the calculation. Increasing the statistical sample would reduce U_θ further, but experience shows that convergence is slow. Since U_θ is already very small (compared with $(u'_\theta)_{rms}$, even at $x/h = 1.62$), the results are regarded as adequately converged.

5.1.3 <u>Turbulence Intensities</u>

Resolved turbulence intensities from the calculation are compared with corresponding experimental results at six axial locations ranging from $x/h = 0.41$ to $x/h = 8.06$. Recall that only the resolved part of the turbulence intensities are shown.

Figure 5.1-8 shows the axial turbulence intensity, $(u''_x)_{rms}$. Although the qualitative agreement between experimental and computational results is good, the calculation tends to over-predict $(u''_x)_{rms}$ at almost all axial stations. It should be noticed once again that there is a rather significant scatter in the experimental data.

The tendency to over-predict $(u''_x)_{rms}$ is consistent with similar results from large eddy simulations of turbulent channel flows using coarse grids. However, the grid resolution studies presented in appendix D.1 indicate that the resolution used in the present case (basic case) was sufficient to obtain (approximately) grid independent results. The question left unanswered is how the results would be affected when the grid is refined in more than one direction at a time.

Another, more likely, source for the discrepancy is related to the significant over-prediction of $(u''_x)_{rms}$ in the annular flow in the inlet section (see figure 5.1-3). The problem with $(u''_x)_{rms}$ being too high in the annular inlet section carries downstream into the combustion chamber as seen from figure 5.1-8.

However, it should also be remembered that the flow in the inlet section of the experimental facility, particularly in the annular pipe, was not fully developed. Even if the grid resolution had been sufficient to give good quality fully developed inflow turbulence, there is no guarantee that comparison with experimental data would have been much better.

The agreement between experimental and computational results is seen to be better for the radial turbulence intensity, shown in figure 5.1-9. As with other

quantities there is a significant scatter in the experimental data. At $x/h = 3.24$ and $x/h = 4.83$ the calculation over-predicts $(u_r'')_{rms}$ in the central region and under-predicts $(u_r'')_{rms}$ in the outer part of the flow, compared with experiments. Despite these differences the qualitative agreement between experiments and calculation is still quite good.

Figure 5.1-10 shows the profiles of the azimuthal turbulence intensity. As with $(u_x'')_{rms}$ and $(u_r'')_{rms}$, the agreement between the experiment and calculation is good. Particularly at the first two measurement stations. Further downstream the calculation over-predicts $(u_\theta'')_{rms}$ in the central region (near the centerline) and under-predicts $(u_\theta'')_{rms}$ in the outer region. This is similar to the behavior of $(u_r'')_{rms}$. Agreement with the experiment improves, at least in the central region, with increasing axial distance.

5.1.4 Turbulent Shear Stress and Eddy-Viscosity

Turbulent shear stress profiles from the experiment and the calculation are compared in figure 5.1-11. The calculated turbulent shear stress includes the sub-grid scale contribution. As with other quantities the qualitative agreement between experimental and computational results is good, although there are some quantitative differences in the profiles. In particular the slope of the shear stress curve (in the range $x/h = 0.5$-1.0) is predicted to be somewhat steeper compared with the experimental data. In addition, at the first three measurement stations the peaks in the computed profiles are somewhat higher than the corresponding peaks in the experimental data. However, as seen with other quantities, the agreement between experiments and calculation gets better with increasing axial distance.

Since the present calculation is a large eddy simulation it is of interest to assess the contribution of the subgrid scale model to the turbulent shear stress. Figure 5.1-12 shows a measure of the ratio of the subgrid scale shear stress to the resolved turbulent shear stress versus axial distance. The norm, $e(x)$, used to measure the ratio is defined as:

$$e(x) = 100 \times \left\{ \frac{\int_0^{r_0} (<\tau_{12}>_{t\theta})^2 \, dS}{\int_0^{r_0} (<u_x'' u_r''>_{t\theta})^2 \, dS} \right\}^{1/2} \tag{5.1-1}$$

The integration is carried out over the cross section area. Figure 5.1-12 shows that $e(x)$ is high at the corner of the step and then drops sharply with increasing axial

distance. The subgrid scale contribution to the total shear stress is about 18 percent at the corner of the step, but drops to only 2 percent 4 step heights downstream of the expansion.

In the same context it is also of interest to examine the ratio of the eddy-viscosity to the molecular viscosity. This is done in figure 5.1-13. The increase in the peak of the eddy-viscosity with increasing axial distance is probably due to the coarsening of the axial grid away from the corner of the step. The peak value of the ratio of eddy-viscosity to molecular viscosity is about 13-14. For comparison, the maximum value of this ratio was about 4 for the high Reynolds number backward facing step calculation (using the DM model) reported in chapter 5, part I.

As explained in chapter 2, part I, the total viscosity had to be clipped to zero at points where the total viscosity became negative, in order to avoid numerical instability problems. On average about 2 percent of the points in the computational domain had to be manipulated. This is the same percentage as for the high Reynolds number backward facing step calculations, and is believed to be small enough not to cause any adverse effect on the results. The dynamic subgrid scale model returned negative eddy-viscosity (but positive total viscosity) at an average of 7 percent of the grid-points.

5.1.5 Passive Scalar

Figure 5.1-14 shows the mean fuel mass-fraction at six stations downstream of the expansion, compared with experimental data from Johnson & Bennett.

At the first two stations excellent agreement between experimental and calculated results is observed. At $x/h = 3.24$ the agreement remains good between $r/h = 0.25$ and the outer wall, however, the calculation under-predicts the fuel mass-fraction in the core region of the flow. The same trend is seen at $x/h = 4.83$, where the "problem region" extends to about $r/h = 0.4$. Further downstream the agreement between experiments and computation improves.

It is speculated that discrepancies in the core region at the third and fourth measurement stations is related to lack of grid resolution. This is a region with rather large axial gradients in the scalar, combined with a coarse axial grid resolution, which generally increase numerical truncation errors. Also, appendix D.2 shows a significant increase in the mismatch with decreasing grid resolution (by comparing the basic and the animation case).

Figure 5.1-15 shows profiles of the SGS turbulent Schmidt number, $Sc_t = <\nu_t>_{t\theta} / <\alpha_t>_{t\theta}$. The SGS turbulent Schmidt number is more or less constant away from the wall downstream of about $x/h = 2$. At the wall Sc_t drops to zero, indicating that the eddy-viscosity goes to zero faster than the eddy-diffusivity. However, there is a rather large region in the range from $r/h = 0.7$-1.8 where Sc_t is almost constant, and about 0.3-0.4. For comparison, Eidson (1985) found that $Sc_t = 0.4$ gave the best results in LES of turbulent channel flow using standard eddy-viscosity models. *A priori* tests by Moin *et al.* (1991), using the dynamic subgrid scale model gave a SGS turbulent Prandtl number of about 0.4 for isotropic homogenous turbulence, and 0.5 in turbulent channel flow, away from the wall. The present calculation therefore gives a SGS turbulent Schmidt number (Prandtl number) similar to that found by other researchers.

5.2 Flow Analysis

This section focuses on an analysis of the statistically averaged- as well as the animated results, in order to address the issues of mixing and fuel entrainment into the recirculation zone.

Mean flow field characteristics are presented in section 5.2.1 and are used to evaluate the flow field and entrainment characteristics of the recirculation zone. Section 5.2.2 focuses on an analysis of the instantaneous pressure- and passive scalar fields in order to visualize important large scale structures. Section 5.2.3 offers an analysis of the fuel mass-fraction distribution in the combustion chamber aimed at evaluating whether a combustible mixture can exists in the recirculation zone. This is combined with a description of animated results which sheds some light on instantaneous characteristics of the mixing and entrainment processes.

5.2.1 <u>Analysis of the Mean Flow Field</u>

The reattachment location, defined as the point where the wall-normal gradient of the axial velocity (at the wall) changes sign, is found to be $X_R/h = 9.4$. A second reattachment point is found at $x/h = 1.0$, indicating that there is a secondary, counter rotating, vortex located in the outer corner of the step. This is confirmed in figure 5.2-1 which shows a contour map of the axial and radial velocity components.

Figure 5.2-1a shows the mean axial velocity. Notice that the contour lines are only shown up to $U_x/U_c = 2.5$. The mean axial velocity ranges from about -0.47 to a maximum of 3.46, with the maximum being located at the center of the the annular pipe. The largest negative velocity is found close to the wall in the recirculation zone.

Figure 5.2-2, shows an enlarged contour map of the region of negative mean axial velocity. It is apparent that the largest backflow occurs very close to the wall. This was also confirmed by the animated results. The animation sequence, showing a contour map of the fuel mass-fraction, showed fuel-rich fluid intermittently moving towards the base of the burner in what seems to be a narrow "belt", very close to the wall. It seems that only a small part of this fluid is entrained into the adjacent shear layer along the way. Most of the fuel-rich fluid came close to the base of the burner before being entrained into the step shear layer.

The vertical vectors shown along the zero axial velocity line represent the

relative magnitude and direction of the mean radial velocity along this line. It is seen that the fluid inside the recirculation zone, moving towards the base of the burner, experiences increased momentum toward the centerline as it gets closer to the base of the burner. In fact, the largest (negative) radial velocity along the zero axial velocity line occurs close to the base of the burner. Entrainment of (fuel-rich) fluid from the recirculation zone into the step shear layer can therefore be expected to be largest at this point. (This was also confirmed by the animated results). The implication is that a pilot flame is likely to be located at the base of the burner, consistent with the observations of Roquemore *et al.*

Figure 5.2-1b shows a contour map of the mean radial velocity component. The minimum and maximum values of U_r/U_c are about -0.17 and 0.12, respectively. Notice that a negative value means that U_r is directed towards the centerline. It is evident that air from the annular pipe is moving towards the centerline for the first 5-6 step heights following the expansion. Further downstream the radial velocity is positive indicating that fluid is moving towards the wall of the combustion chamber. Fluid from the recirculation zone is moving towards the centerline upstream of about $x/h = 4$-5. This fluid is being entrained into the step shear layer. Also notice the small region of positive U_r in the outer corner of the step. This clearly shows the existence of a secondary, counter-rotating vortex.

The point where both the axial and radial velocity components are zero (termed the "vortex center" by Roquemore *et al.*) is indicated by an open circle in figure 5.2-2. The vortex center is seen to be located at about $x/h = 4.5$. Based on the magnitude of the radial velocity vectors it seems that the largest entrainment of fluid into the recirculation zone occurs roughly from about $x/h = 6$ to $x/h = 9$. This was in fact observed to be the case also in the animation. No fuel-rich fluid was seen to cross the annular air stream upstream of the vortex center. Even though isolated pockets of fuel-rich fluid were able to cross around the vortex center, the largest entrainment of fuel into the recirculation zone seemed to occur around the instantaneous reattachment point.

Figure 5.2-3 shows the mean streamlines. The contour values indicated on the plot represent the fraction of the total mass flow-rate passing between the streamlines. The streamlines extending from the central fuel pipe can be seen to converge towards the centerline up to about $x/h = 6$-7, consistent with a negative radial velocity in this region. The center of the closed streamlines in the recirculation zone coincides with the vortex center, identified above. The figure shows that the

average mass-flow in the recirculation zone is about 24 percent of the total mass-flow supplied at the inlet.

Figure 5.2-4 shows the two local peaks (resulting from expansion of the two jets) in the velocity profile downstream of the expansion. (The peak resulting from the central jet is just the centerline velocity). The centerline velocity is seen to slow down slightly after expansion, up to about $x/h = 2$-2.5. Then a sharp increase in the centerline velocity is observed, indicating a significant entrainment of air from the annular stream. This is consistent with figure 5.2-1b which shows that the mean radial velocity is negative in the region from about $x/h = 2$ to $x/h = 6$. This region is clearly characterized by strong mixing. Consequently, a flame (under fuel rich conditions) is likely to be located in this region. In fact, Roquemore *at al.* observed that under fuel rich conditions a zone of intense mixing and combustion was found to start at about two fuel-pipe diameters downstream of the expansion. This corresponds roughly to $x/h = 2$ in the present calculations. The reason for the strong mixing is likely that the shear layers from the fuel pipe and step intersect at about $x/h = 2$ which is accompanied by merging of vortices shed from the corner of the step (step shear layer) and the central pipe (fuel pipe shear layer).

The peak velocity caused by the annular jet is seen to decrease following the expansion indicating a spreading of the jet throughout the combustion chamber. However, the rate of spreading is slow during the first two step heights and then increases sharply as the two shear layers intersect, thus significantly enhancing the mixing. Downstream of about $x/h = 7$ the two jets seem to be completely mixed with the peak value of the velocity profile being the centerline velocity.

5.2.2 Flow Structures

Figure 5.2-5 shows an instantaneous snapshot of the pressure field in one x-r plane and three cross sections (r-θ planes). Downstream of the expansion, up to about $x/h = 2$, the figure reveals organized structures being shed, both from the corner of the step and from the end of the central pipe. The structures are seen to grow in size with increasing axial distance. Between $x/h = 2$ and $x/h = 3$ the structures from the two shear layers merge, and downstream of about $x/h = 3$-4 the clearly identifiable organized structures have all but disappeared.

To better visualize the shear layers, figures 5.2-6 and 5.2-7 focus on the first 7 step heights of the combustion chamber. Part a) of each figure shows contours

of instantaneous pressure in a x-r plane. A narrow interval of contour values has been chosen which is very useful for identifying individual structures. Each of the enclosed surfaces in figures 5.2-6a and 5.2-7a represent vortical structures. Part b) of the figures show instantaneous contours of the passive scalar in a band chosen to highlight the fuel-pipe shear layer in figure 5.2-6b and the step shear layer in figure 5.2-7b.

The pressure contours in figure 5.2-6 (or figure 5.2-7) clearly show individual ring-type vortical structures being shed, both from the step and from the central pipe. The structures are seen to grow with increasing axial distance, caused by pairing of individual vortices. Between $x/h = 2$ and $x/h = 3$ the simple organized structures seen upstream have more or less disappeared, indicating a merging of vortices from the two shear layers. This lack of coherence is a result of the flow being highly turbulent. The axial convection velocity of the vortices is a strong function of the azimuthal position. The vortex rings therefore undergo axial stretching which rapidly breaks azimuthal coherence.

An interesting feature of figure 5.2-6b is that it clearly shows the characteristic roll up of vortices in the early part of the fuel-pipe shear layer. The rollers in figure 5.2-6b can be seen to correspond to the structures traced by the pressure contours in figure 5.2-6a. Figure 5.2-6b also indicates that the "potential core" of the central fuel jet has disappeared about 3 step heights downstream of the expansion. At this point the vortices shed from the fuel-pipe have grown to enclose the centerline of the flow. This is consistent with figure 5.2-5 which showed disappearance of coherent structures downstream of about $x/h = 3$.

Figure 5.2-7b shows contours of the passive scalar chosen to identify the step shear layer. Again the characteristic roll up of vortices is observed in the initial part of the shear layer. A correspondence of structures identified in figures 5.2-7a and 5.2-7b is also apparent. Figure 5.2-7b indicates that the shear layers originating from the step and from the central pipe merge between $x/h = 2$ and $x/h = 3$, thus creating larger structures, identified in the pressure contour plot of figure 5.2-7a (or 5.2-6a).

The convection of vortical structures downstream is most easily seen in figure 5.2-8, which shows a time sequence of contours of instantaneous pressure fluctuations. The plot was generated by subtracting the mean pressure from instantaneous pressure fields. The resulting pressure field was then averaged in the azimuthal direction. This serves to identify any large scale structure that is more or less coherent

in the azimuthal direction. (Note that each figure only shows half of the domain, i.e. from the centerline to the outer wall). Figure 5.2-8 shows that there are indeed large scale structures convected downstream in the combustion chamber. However, the structures tend not to be very coherent. None of the structures in figure 5.2-8 seem to survive past about $x/h = 4$.

One of the animations made from the calculations shows iso-surfaces of low pressure regions, similar to the pictures in figure 5.2-8 (except that no azimuthal averaging was used). There are vortices being shed both from the corner of the step and the end of the central pipe. However, they tend to break up after traveling a few step-heights into the combustion chamber. From figure 5.2-8 the convection velocity of the vortical structures is estimated to be about $1.6U_c$.

To summarize, vortices shed from the step and the fuel-pipe show characteristic roll up patterns as they merge and grow inside the combustion chamber. At about $x/h = 2$-3 the two shear layers intersect, creating a region of intense mixing. Downstream of about $x/h = 3$ the "potential core" of the central jet disappears and the remaining large scale structures show little coherence. Roquemore *et al.* also found that the intersection of the two shear layers takes place about 2 step heights downstream of the expansion, which was identified as a region of intense mixing and combustion. The present calculations are therefore in agreement with experimental observations.

5.2.3 <u>Mass Transport</u>

As explained previously, one of the most important issues related to LBO is the process by which fuel and hot combustion products are entrained into the recirculation zone. An evaluation of the fuel mass-fraction present in the recirculation zone will further determine whether a combustible mixture can exist, which in turn will indicate whether the flame can be expected to be lifted or attached.

Figure 5.2-9 shows a contour plot of the mean mass-fraction of fuel in the combustion chamber. Contour values are plotted in the range $\varphi = 0.01$-0.20. (Higher fuel mass-fraction exists only in the core region of the flow, downstream of the fuel-pipe). Figure 5.2-10 includes several contour plots of the fuel mass-fraction, each limited to a narrow interval of contour values. The purpose is to more clearly outline regions of different fuel mass-fraction in the recirculation zone of the combustion chamber.

First, it is seen that downstream of about $x/h = 14$ the fuel and air appear to be completely mixed. After complete mixing has taken place the fuel mass-fraction should be uniform and equal to the fuel mass-fraction of the fluid entering the combustor, which in the present case is 0.105. Figure 5.2-9 shows that the fuel mass-fraction near the exit of the combustor is in the range 0.10 and 0.11, which agrees with the expected level.

The reattachment point was found to be $X_R/h = 9.4$ (see section 5.2.1). Figure 5.2-9 reveals that the fuel mass-fraction decreases from about 0.07 at the reattachment point to a minimum of about 0.035 when approaching the base of the burner through the recirculation zone. A slight increase in the fuel mass-fraction is found in the outer corner of the combustor, immediately downstream of the expansion point. This region coincides with the location of a secondary, counter-rotating vortex shown earlier.

Roquemore *et al.* did combustion experiments in the coaxial jet-combustor using gaseous propane as fuel and air as oxidizer. The air flow-rate was held fixed at 1000 l/min, and the fuel flow-rate was varied between 30 and 63 l/min. The corresponding fuel equivalence ratio ranged between 0.78 and 1.55. A mixture with a fuel equivalence ratio above 1 is considered fuel rich.

The mass- (or volume) fraction of fuel used in the present calculation is 0.105. Comparing with Roquemore *et al.*'s experimental condition this corresponds to a fuel rich mixture (assuming the fuel is propane). The flame is therefore expected to be attached to the base of the burner. According to Roquemore *et al.* the stoichiometric fuel to air ratio (by mass) for a propane-air mixture is 0.0638, corresponding to a fuel mass-fraction of 0.060. The corresponding lean flammability limit is 0.0309. From figure 5.2-10 it is evident that the fuel mass-fraction is between 0.035 and 0.04 in a major part of the recirculation zone. Since this is above the lean flammability limit the calculation indicates the possibility for (or likelihood of) an attached flame.

However, other factors are also important to determine whether or not the mixture will ignite. Most important, in addition to having the proper fuel concentration, is the amount of hot combustion products present, which will determine if the temperature in the recirculation zone is high enough to ignite the combustible mixture. This is, however, an issue that cold flow calculations cannot address.

As explained in appendix D.2, contour plots of the fuel mass-fraction were animated over a period covering more than 5 flow-through times. An analysis of

the animation indicates that most of the fuel is not able to penetrate the annular air stream and is carried all the way to the reattachment point (which instantaneously varies between $x/h = 7$ and $x/h = 11$) before being entrained into the recirculation zone. This process seems to take place when large pockets of fuel hit the wall and are split, with a part moving upstream, into the recirculation zone, and a part continuing downstream. However, intermittent pockets of fuel are able to escape through the annular air stream and reach the recirculation zone as far upstream as $x/h = 4$-5. It is perhaps interesting to note that this "boundary" coincides with the location of the vortex center, identified in section 5.2.1.

Another interesting point revealed by the animation is that pockets of nearly pure air are able to penetrate the recirculation zone at intermittent time periods, thus temporarily diluting the concentration of fuel in this region. This might temporarily reduce the concentration of fuel in the recirculation zone below the lean flammability limit, thus making the flame (assumed to be attached) momentarily lift off. This phenomenon was observed by Roquemore *et al.* That is, even at fuel rich conditions, the flame would occasionally lift off for short moments, but stay attached most of the time.

The fact that fuel is able to escape through the annular air stream, into the recirculation zone, is consistent with the hypothesis formulated by Roquemore *et al.* They speculated that unburned fuel and hot combustion products escape through "holes" in the flame to be entrained into the recirculation zone. (Holes in the flame are most likely formed in the braid regions of vortex trains where stretching and fast mixing occur). The present calculations verify that in the absence of chemical reactions, fuel-rich pockets of fluid are indeed able to cross the annular air jet without being significantly diluted. However, when adding chemical reactions, the fuel also has to avoid being consumed in the flame, a phenomena which cannot be addressed in the present cold-flow calculations.

The animation further indicates that the fuel mass-fraction inside the recirculation zone is highest close to the wall where fluid seems to be traveling rapidly backwards toward the base of the combustion chamber. Some of the fuel-rich mixture is being entrained into the annular air stream along the way, but most seems to be carried all the way back to the base of the burner. This observation is supported by the findings from section 5.2.1 where it was established that in the mean, the maximum reversed axial velocity was found very close to the wall. Section 5.2.1 also showed that the radial velocity along the zero axial velocity line increased from

the vortex center towards the base of the burner, and in fact reached its peak close to the corner of the step (see figure 5.2-2). Thus entrainment of fluid from the recirculation zone into the step shear layer is likely to be largest near the base of the burner. This indicates why the pilot flame, observed by Roquemore *et al.*, is likely to attach to the base of the burner.

During the time-period covered by the animation, the concentration of fuel in the recirculation zone was highest in the region $0 < x/h < 1$, i.e. close to the base of the burner. This is likely due to the secondary, counter rotating, vortex in the corner of the step trapping fuel-rich fluid, thus building up the concentration of fuel at the outer corner of the step.

All quantities animated illustrate the highly unsteady, three-dimensional behavior of the flow. An example is given in figure 5.2-11 which shows an instantaneous snapshot of the fuel mass-fraction in one x-r plane and three r-θ planes. Even though similarities with the mean fuel mass-fraction of figure 5.2-9 is apparent, the flow is highly unsteady. Thus the present, fully 3-D, calculation is certain to be not only more accurate, but also more revealing than calculations performed using standard Reynolds averaging techniques.

Upon concluding this section it should once again be stressed that the present calculations did not account for chemical reactions and heat release. The results from the above analysis are therefore only indicative of the behavior of the flow in the presence of a flame. To illustrate this fact it can be noted that Roquemore *et al.* found that the calculated reattachment length decreased by more than a factor of 2 when chemical reactions were added to their CFD model. Shortening of the recirculation zone is believed to be caused by the large volumetric expansion of the heated gases.

5.2.4 Instantaneous Axial Velocity

The last topic discussed in this section is not really related to the analysis of mixing and entrainment characteristics of the flow, but serves more to show a few characteristic features of the calculation. Figure 5.2-12 shows an instantaneous snapshot of the axial velocity in one x-r plane and three r-θ planes. The effect of increasing azimuthal resolution towards the centerline is clearly identified in the cross-sectional view at $x/h = 4$. Away from the centerline only large scale structures can be identified. Around the centerline, with DNS resolution in the

azimuthal direction, a wealth of small scales are apparent. However, there are no indications that the flow is under-resolved in any part of the domain (sometimes characterized by diamond shaped contours).

Figure 5.2-12 also serves to indicate the unsteadiness of the flow. It can in particular be noticed that there are regions of positive axial velocity inside the recirculation zone both at $x/h = 1$ and $x/h = 4$.

5.3 Computer Program Performance

The following is a summary of the performance of the computer code used for the coaxial jet-combustor calculations. The performance parameters quoted are based on the basic case which, as stated previously, used $215 \times 76 \times 128$ grid-points.

With the grid of the basic case, the code ran at a sustained rate of about 470-500 Mflops on a Cray C-90 super-computer. The Mflop-rate on the Cray computers generally decreases with decreasing vector length, and the performance would therefore be lower for a smaller grid. Since the present performance is already very high, only minor improvements are expected with increased grid-size. The code used an average of 13.9 CPU seconds per time-step. With a total number of 2,077,920 active grid-points (i.e. including boundary points, but excluding points with $r > r_a$ in the inlet-section) this translates to:

$$6.67 \cdot 10^{-6} \text{ CPU seconds/time-step/node}$$

The 13.9 CPU seconds spent per time-step can be broken up into the following parts:

Navier-Stokes equations	:	42.1	%
Pressure solver	:	12.6	%
SGS models for ν_t and α_t	:	17.2	%
Passive scalar transport equation	:	18.5	%
Inflow boundary condition	:	9.6	%
Sum	:	100.0	%

The subgrid scale model routines, solving for ν_t and α_t, are highly integrated, and α_t is found at virtually no extra cost compared with solving for ν_t alone. This is due to the fact that most of the time spent calculating ν_t and α_t is consumed by evaluating and filtering the strain-rate tensor, (needed for both parameters). It can be noted that 9.6 percent of the time is spent evolving the flow in the inflow-generator.

The code is written to fit within the core memory limitations of the computer. However, in order to minimize the memory requirement several variables share memory, which means that variables are temporarily stored on SSD-files (Solid State Device) when not in use. The access time for SSD files is minimal and this is

therefore a very efficient way of reducing core memory requirements for the code. For the grid used in the basic case the core-memory requirement was about 19 MW (Mega-Words). About 41 MW of file-space was needed for the SSD-files and about 13 MW was needed for the restart and solution files (accessed outside the time-loop in the code).

The code was run at a fixed time-step of $\Delta t = 0.0025 \, h/U_c$. The corresponding value of the stability criteria, SC, was about 0.9. With $\Delta t = 0.0025 \, h/U_c$ a total of 12000 time-steps were needed to cover one flow-through time (defined as the average time a fluid particle takes to traverse the computational domain). Thus, approximately 45 CPU hours were needed to cover one flow-through time. As mentioned previously, the calculation was run for three flow-through times in order to remove transients in the initial velocity field (resulting from the interpolation procedure). Statistics were then sampled over a period of 6 flow-through times. Thus, the entire simulation required a little more than 400 CPU hours (Cray C-90) to complete.
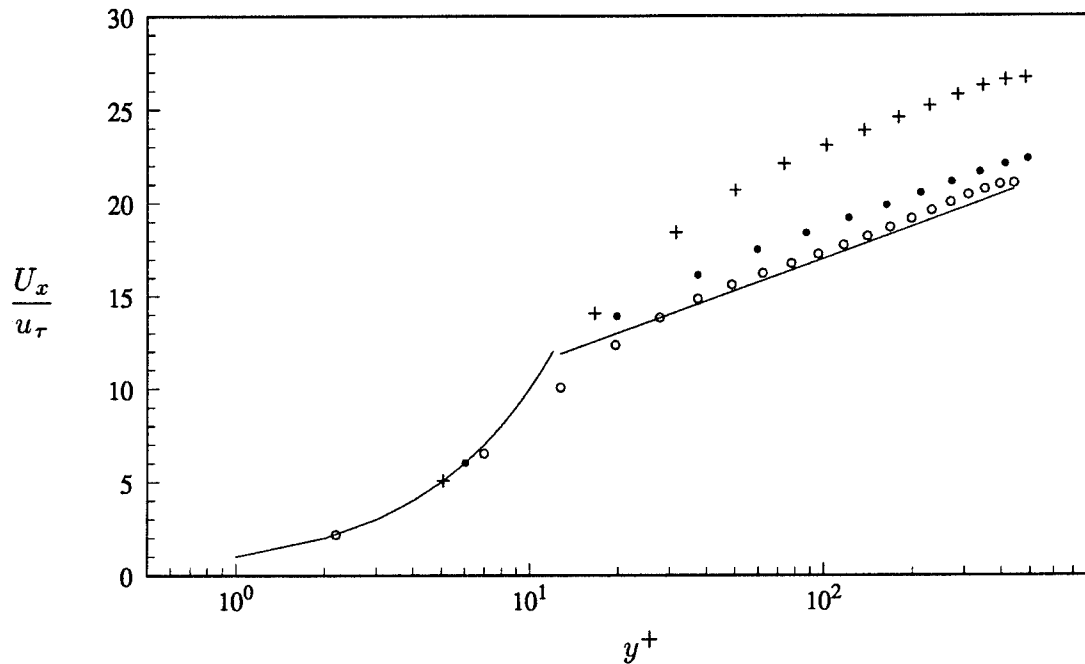
FIGURE **5.1-1**, Mean axial velocity profiles in the "inflow generator". o : Central pipe; • : Inner wall of annulus; + : Outer wall of annulus; ——— : Log-law; $u^+ = 2.44\ln(y^+) + 5.5$
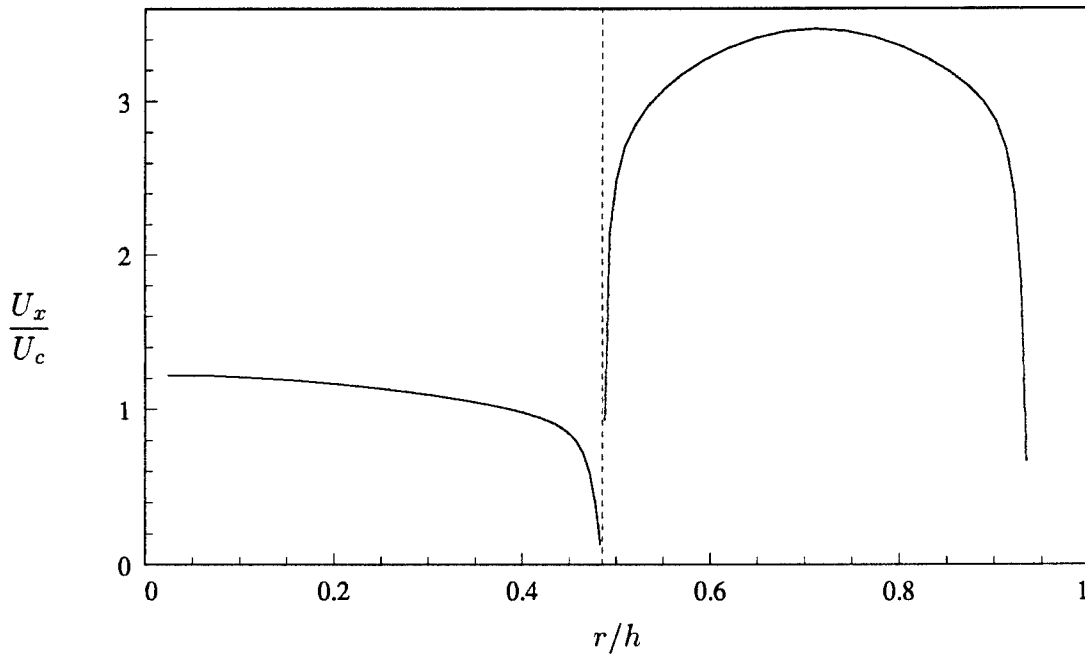
FIGURE **5.1-2**, Mean axial velocity profile in the "inflow generator". The dashed line indicates the position of the central pipe wall.
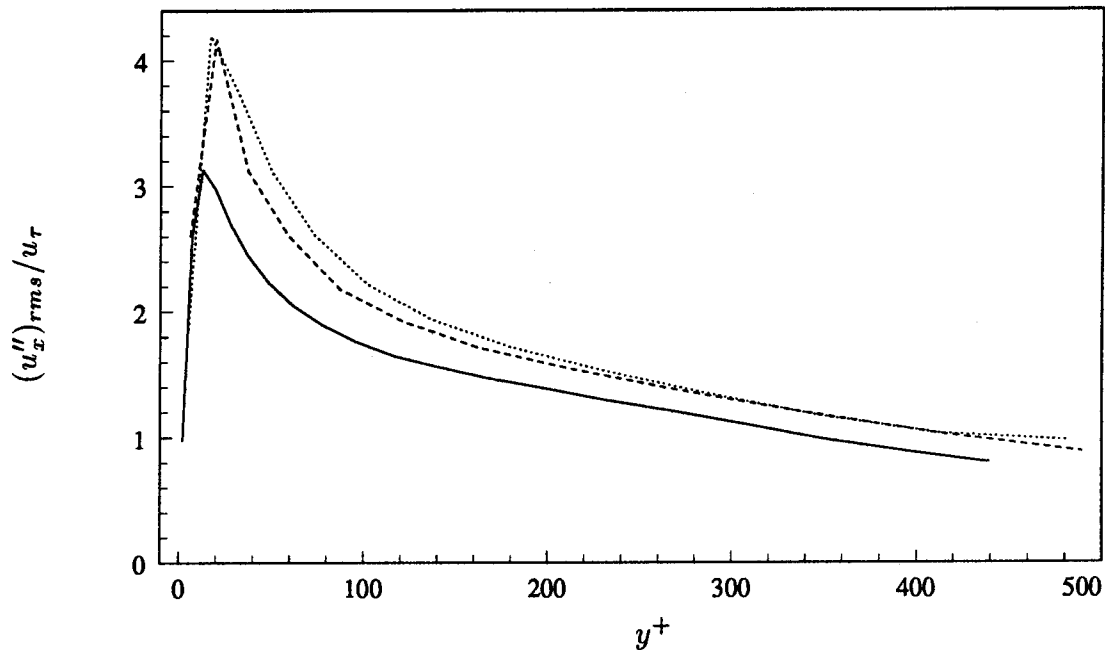
FIGURE **5.1-3**, Resolved axial turbulence intensity. From the "inflow generator".
———— : Central pipe; – – – – : Inner wall of annulus; ········ : Outer wall of
annulus.
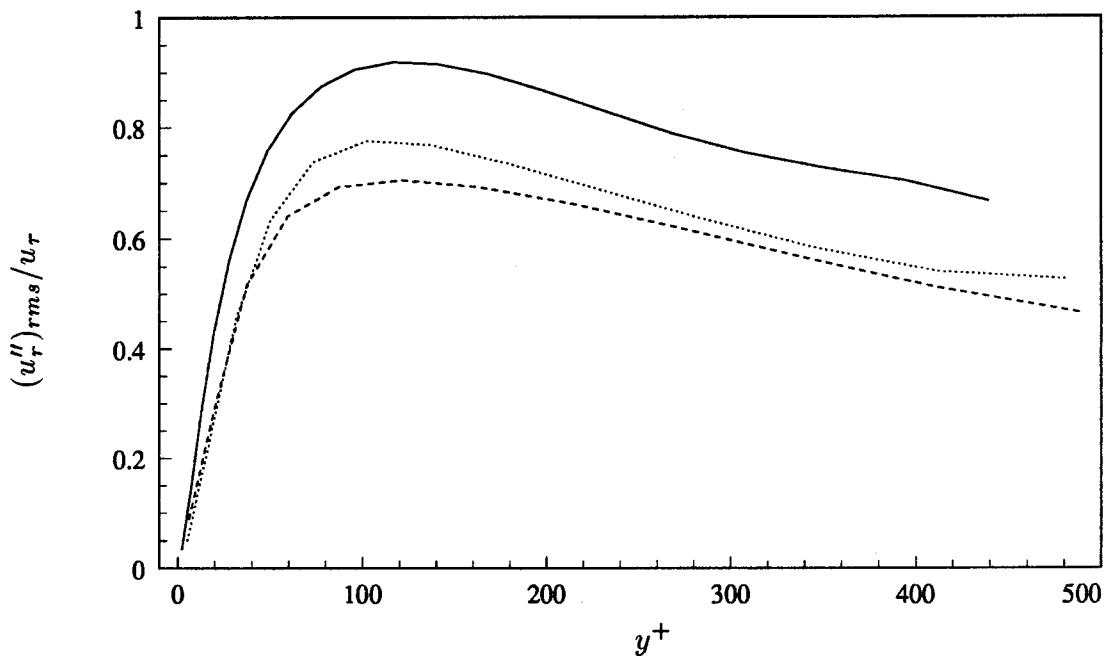
FIGURE **5.1-4**, Resolved radial turbulence intensity. From the "inflow generator".
———— : Central pipe; – – – – : Inner wall of annulus; ········ : Outer wall of
annulus.
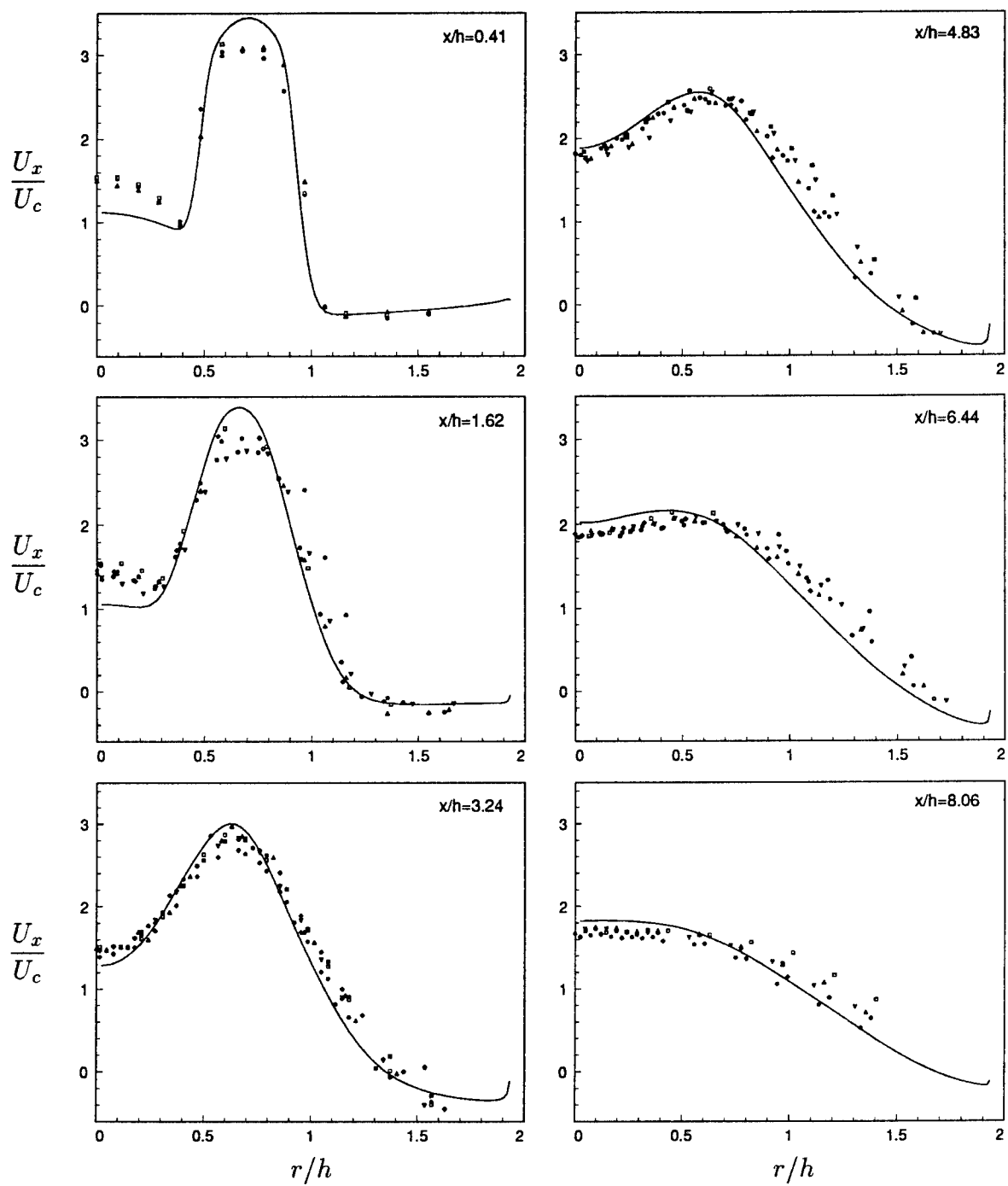
FIGURE **5.1-5**, Mean axial velocity. ———— : Basic case;   All Symbols : Experiments by Johnson & Bennett.
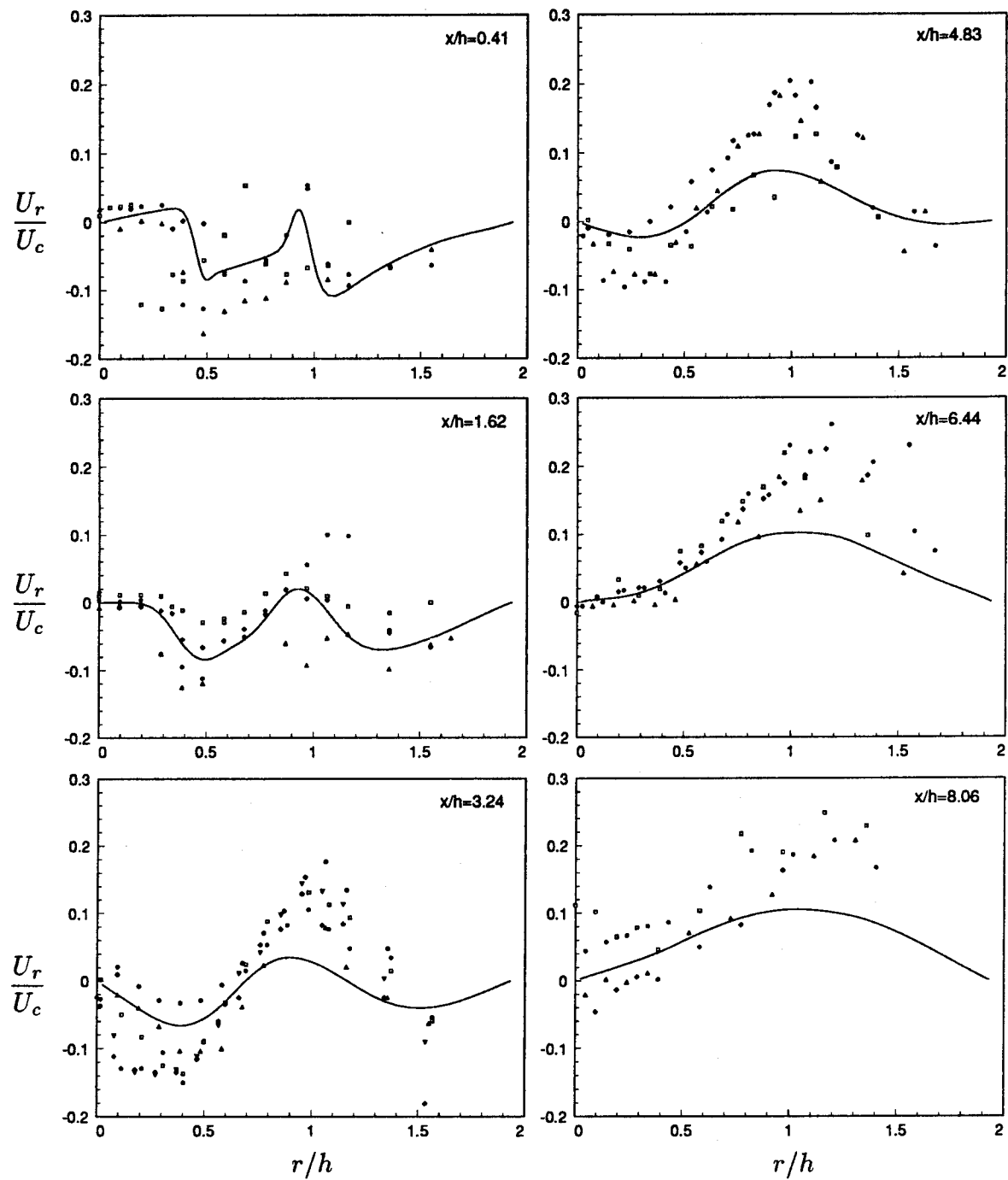
FIGURE **5.1-6**, Mean radial velocity.　　——— : Basic case;　　All Symbols : Experiments by Johnson & Bennett.
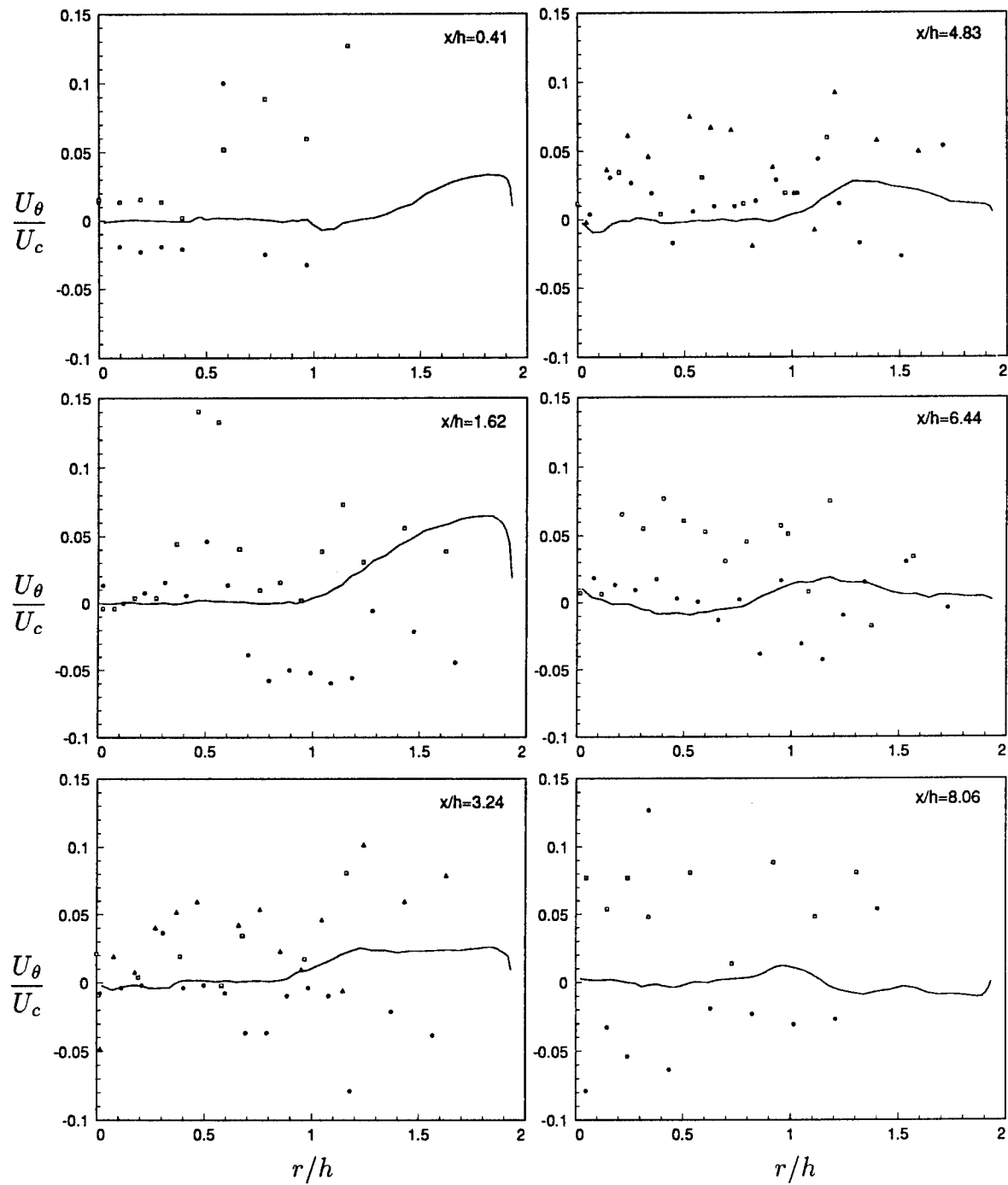
FIGURE **5.1-7**, Mean azimuthal velocity.   —— : Basic case;   All Symbols :
Experiments by Johnson & Bennett.
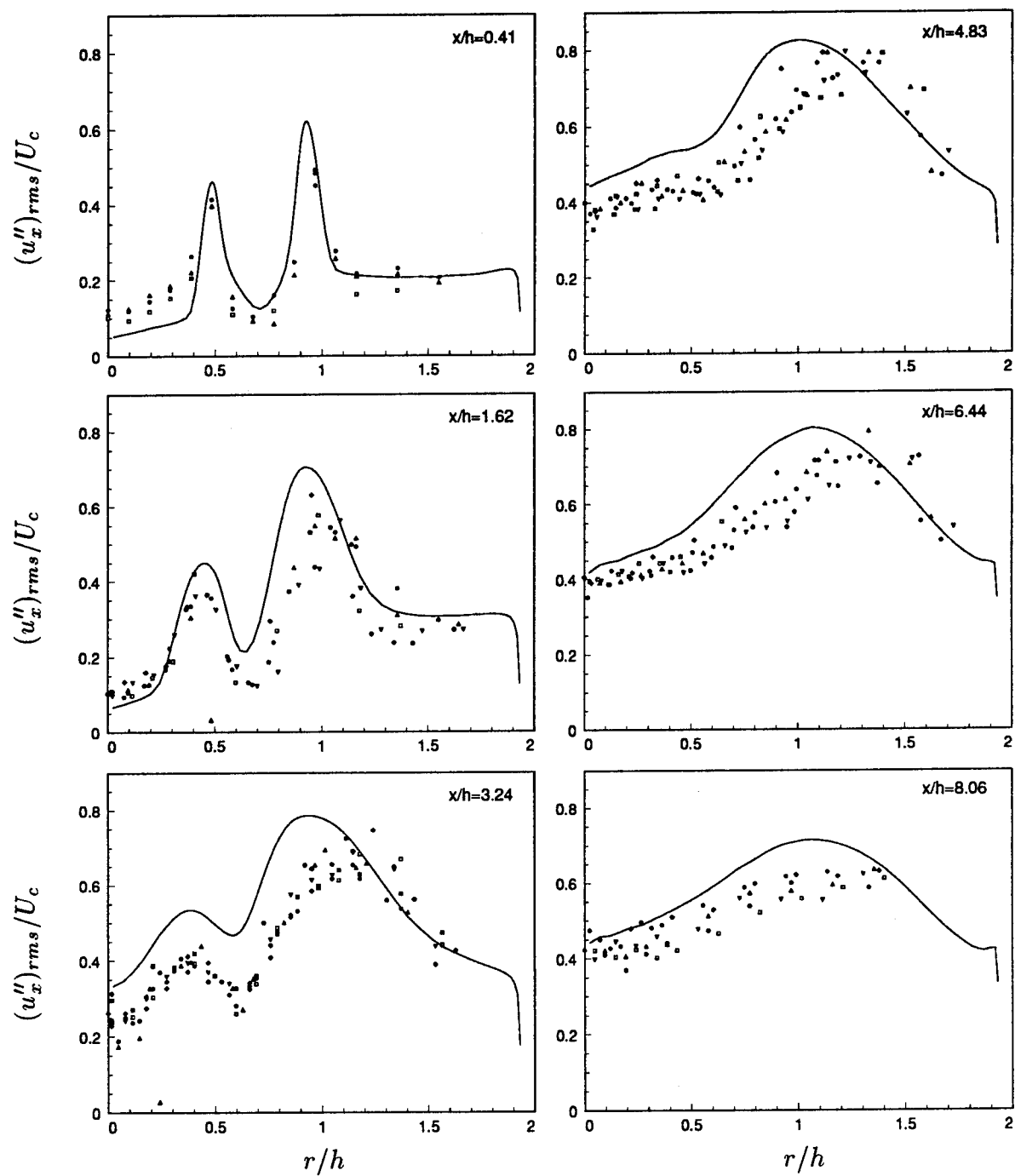
FIGURE **5.1-8**, Resolved axial turbulence intensity.   ——— : Basic case;   All Symbols : Experiments by Johnson & Bennett.
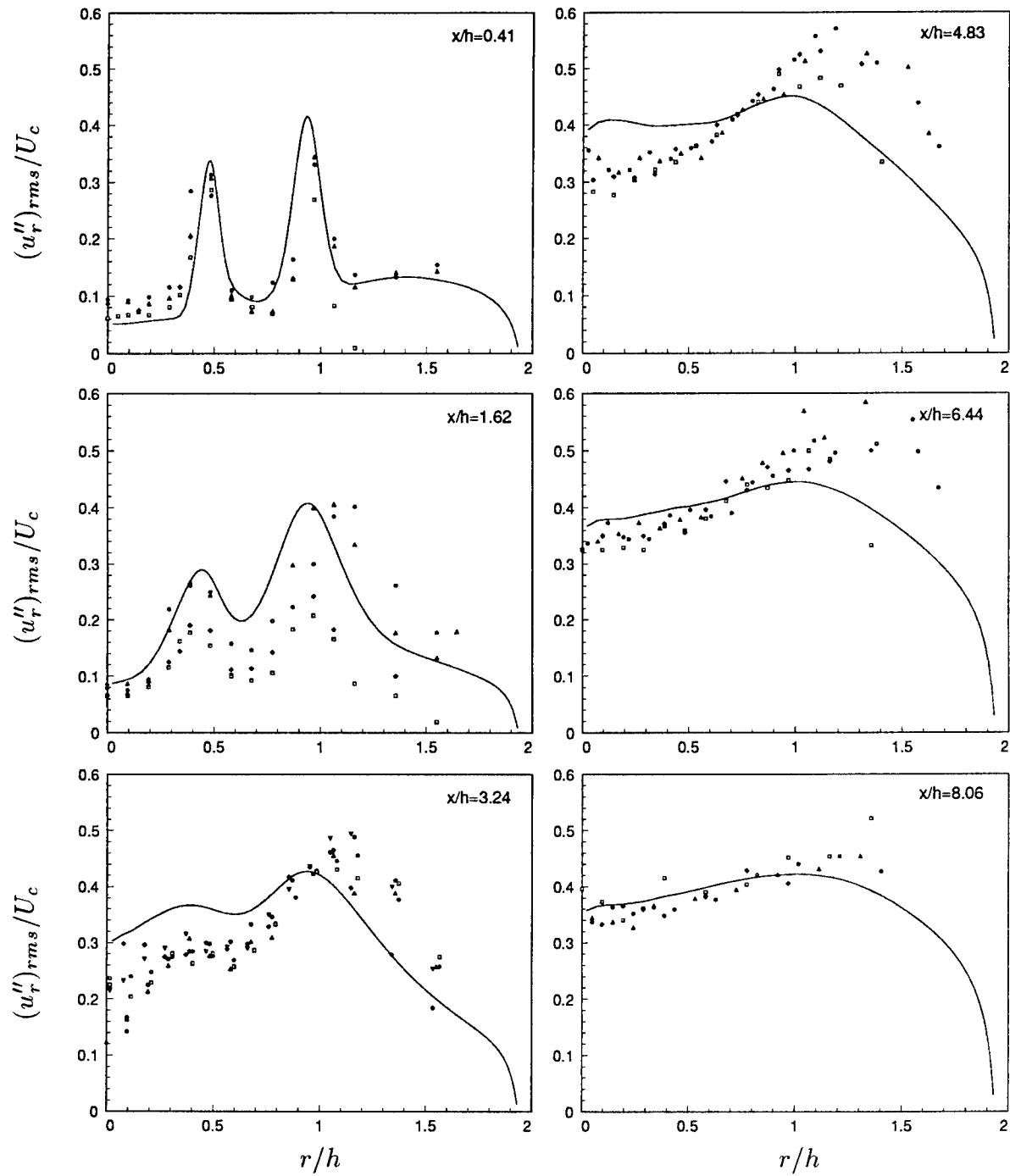
FIGURE **5.1-9**, Resolved radial turbulence intensity.   ——— : Basic case;   All Symbols : Experiments by Johnson & Bennett.
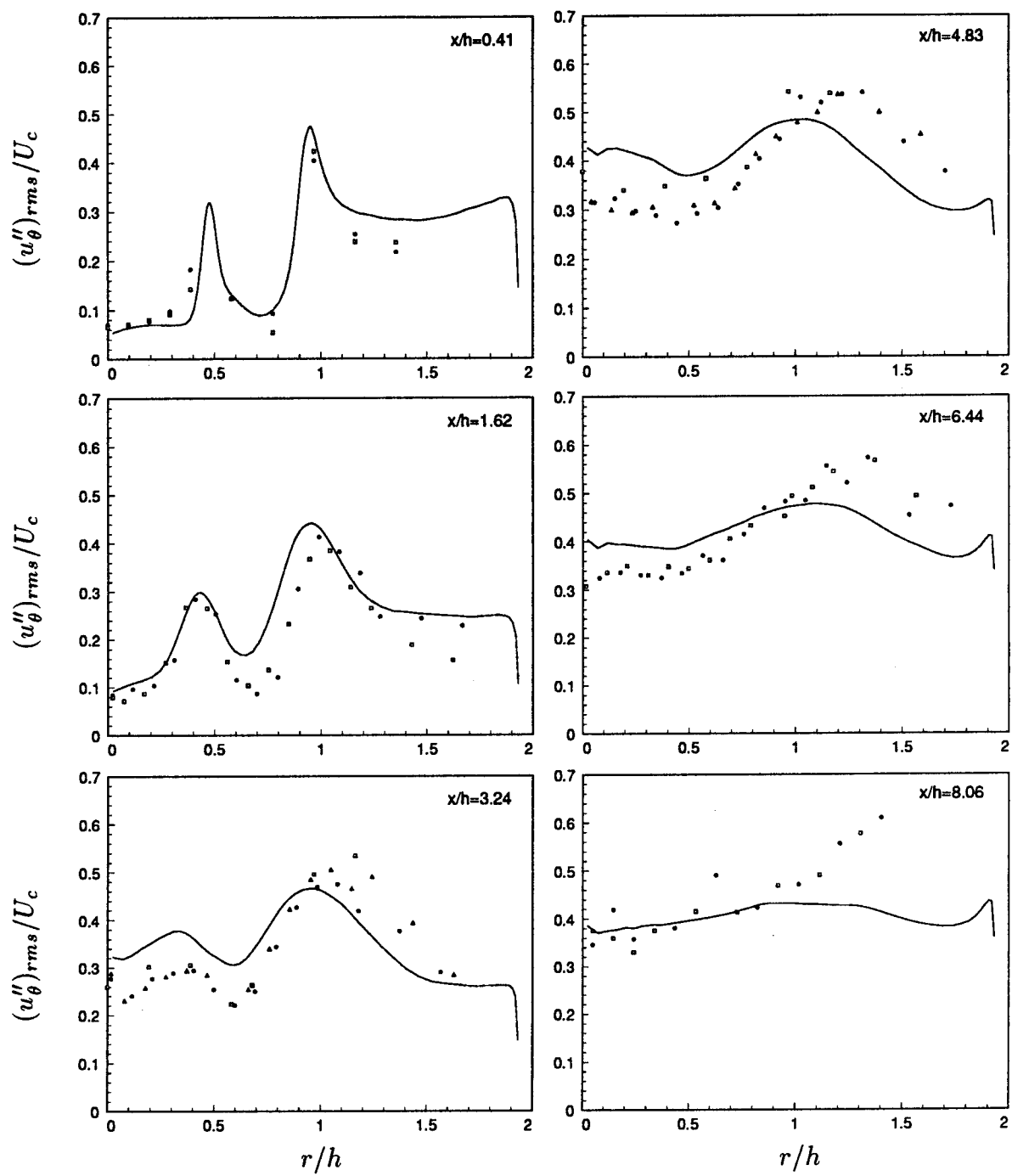
FIGURE **5.1-10**, Resolved azimuthal turbulence intensity. ———— : Basic case;
All Symbols : Experiments by Johnson & Bennett.
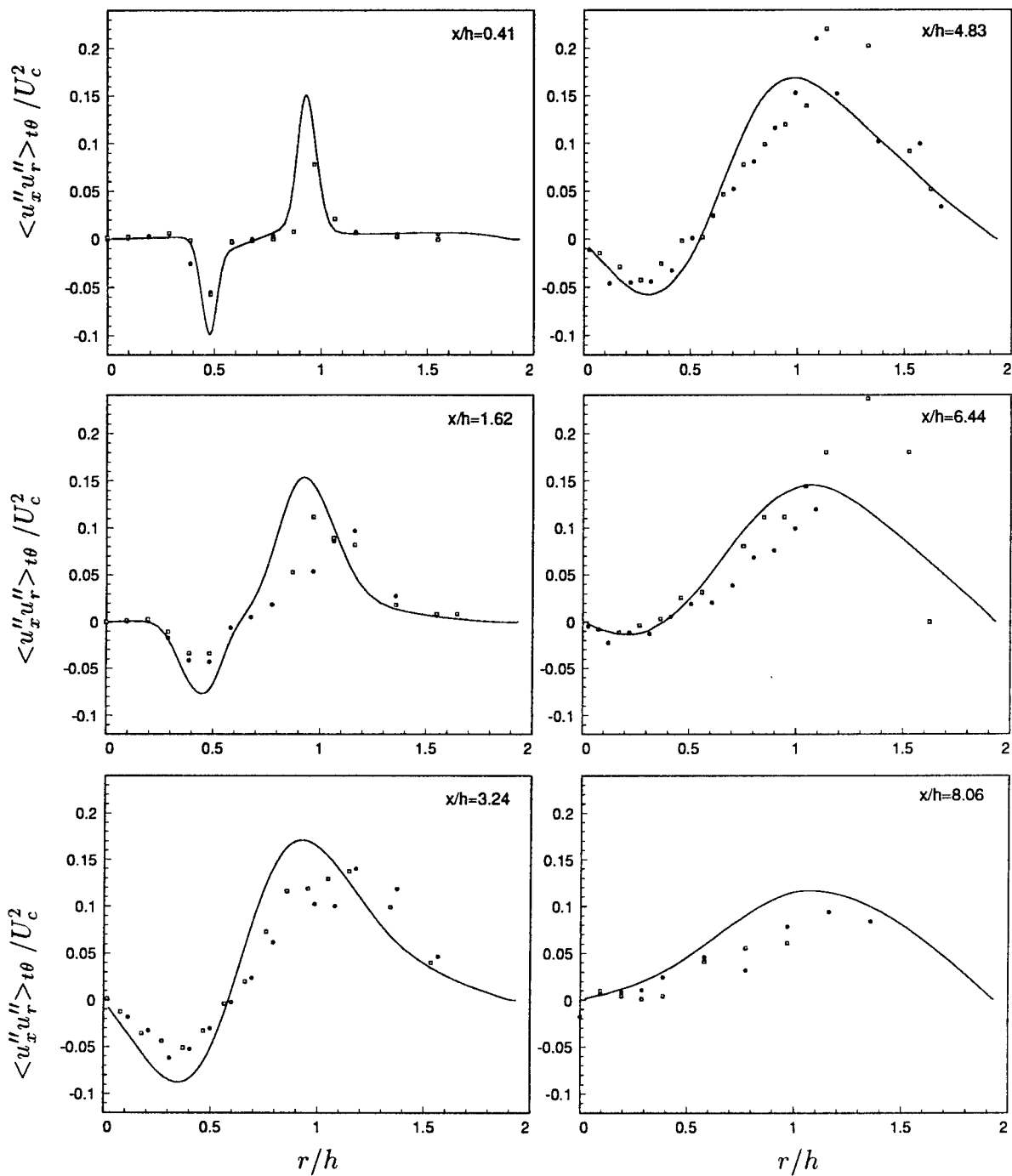
FIGURE **5.1-11**, Turbulent shear stress (incl. SGS model term). ———— : Basic case;   All Symbols : Experiments by Johnson & Bennett.
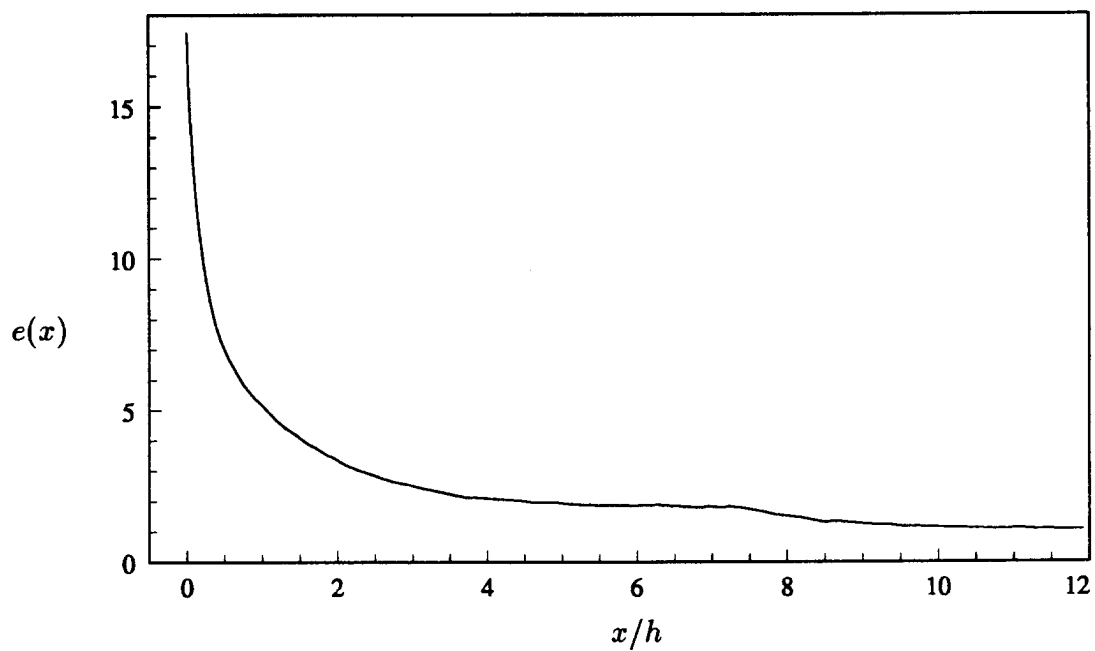
FIGURE **5.1-12**, $e(x)$ (defined in equation 5.1-1) represents the ratio (in percent) of the SGS shear stress to the resolved turbulent shear stress.
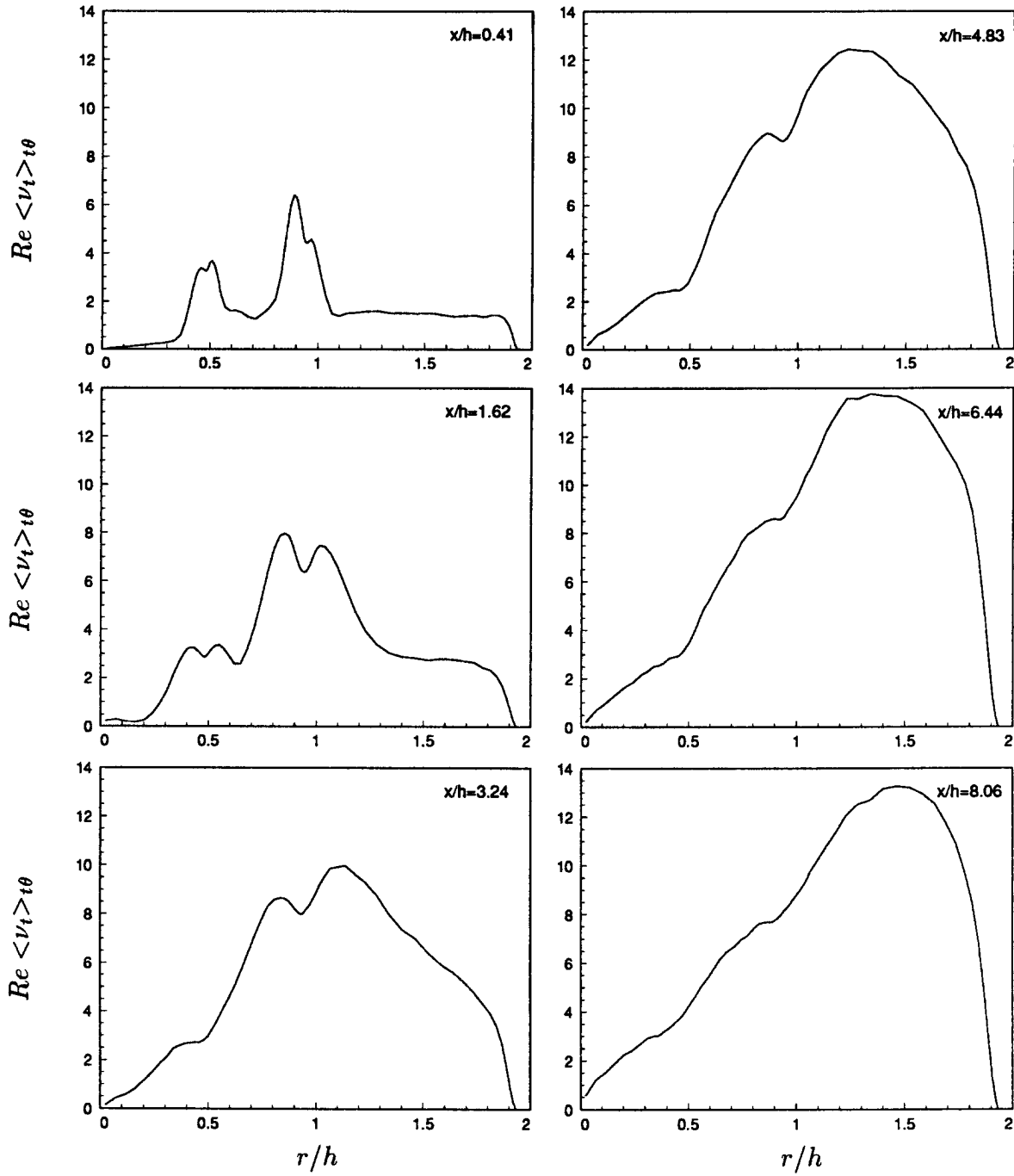
FIGURE **5.1-13**, Ratio of eddy-viscosity to molecular viscosity.
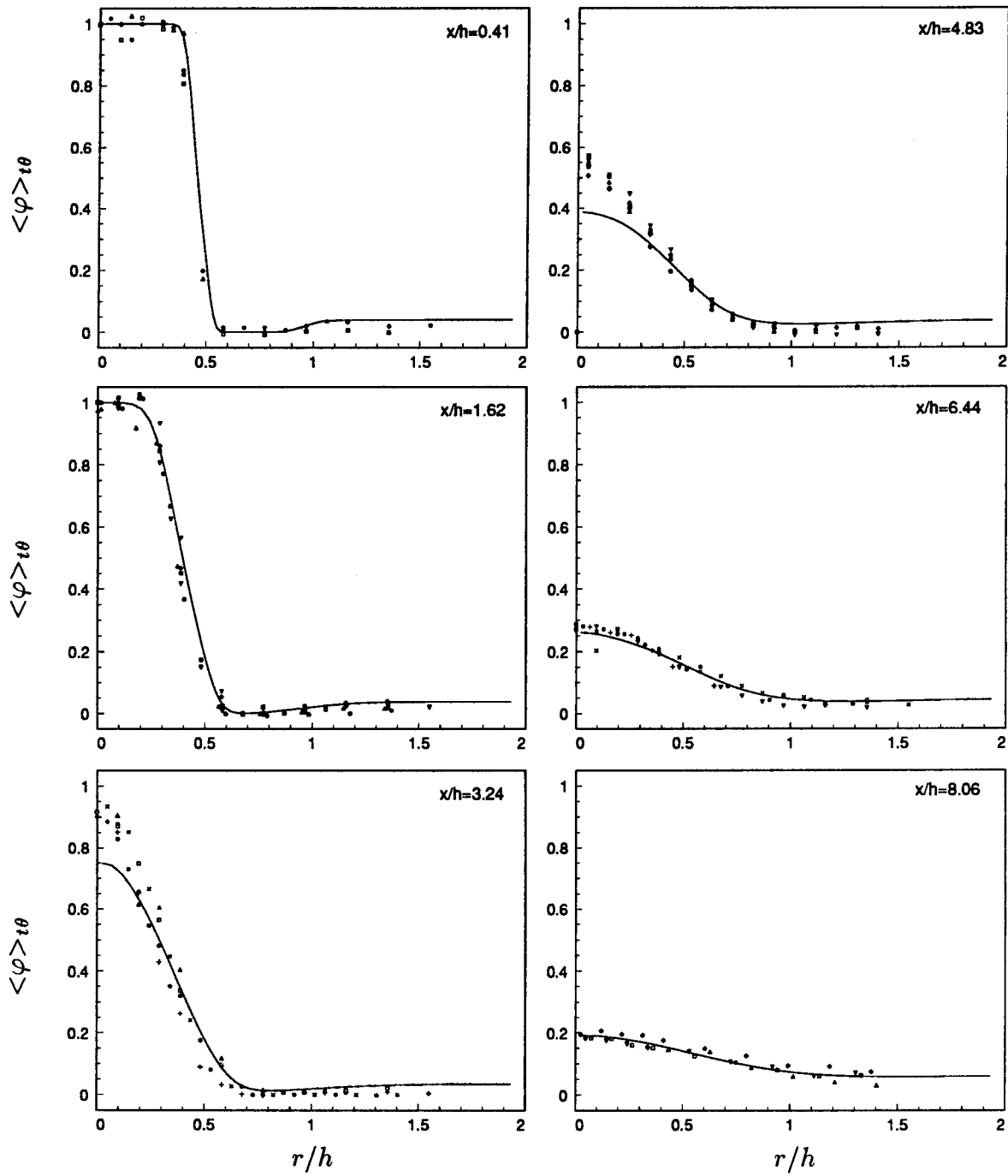
FIGURE **5.1-14**, Mean value of passive scalar. ———— : Basic case; All Symbols: Experiments by Johnson & Bennett.
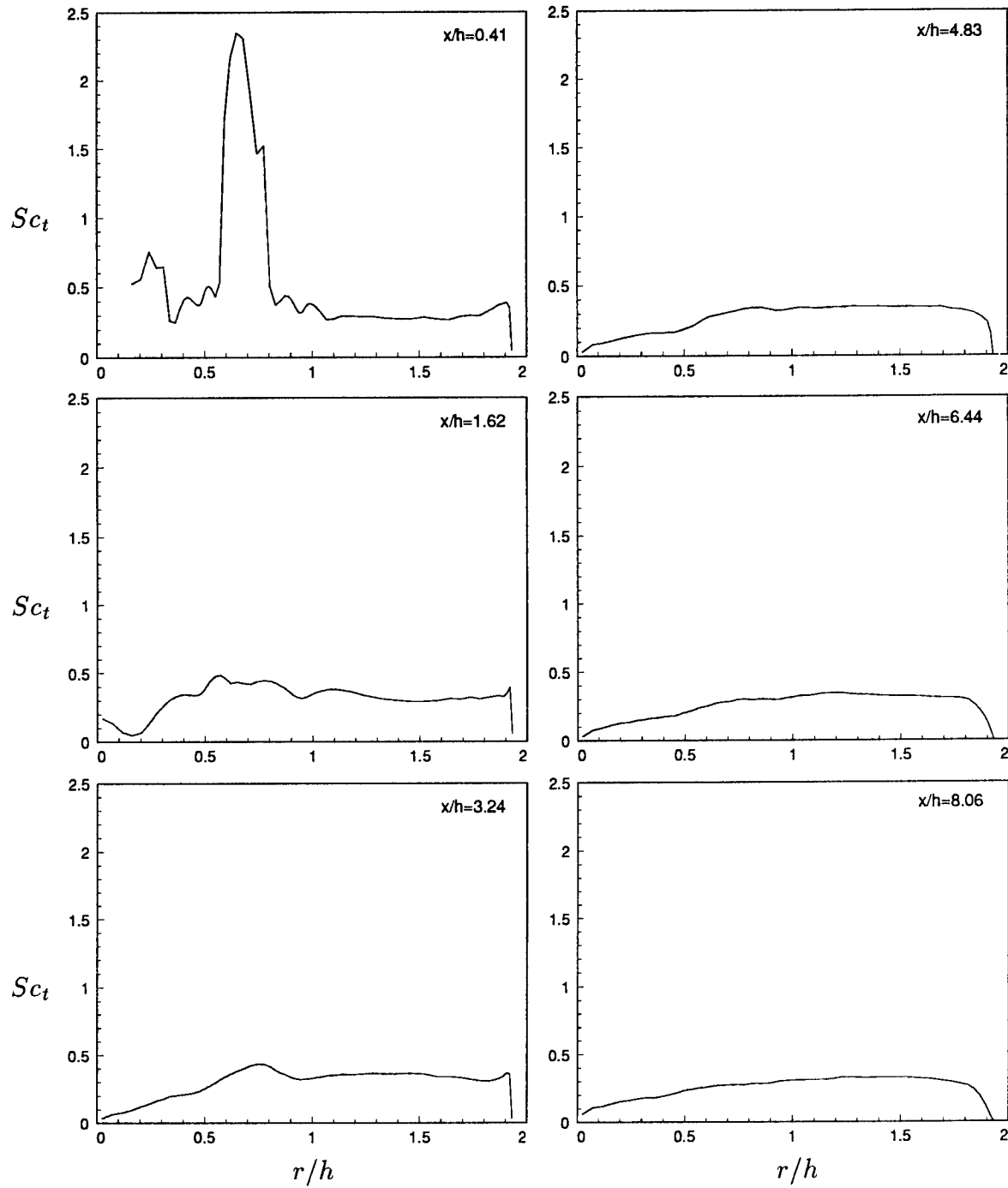
FIGURE **5.1-15**, SGS turbulent Schmidt number.
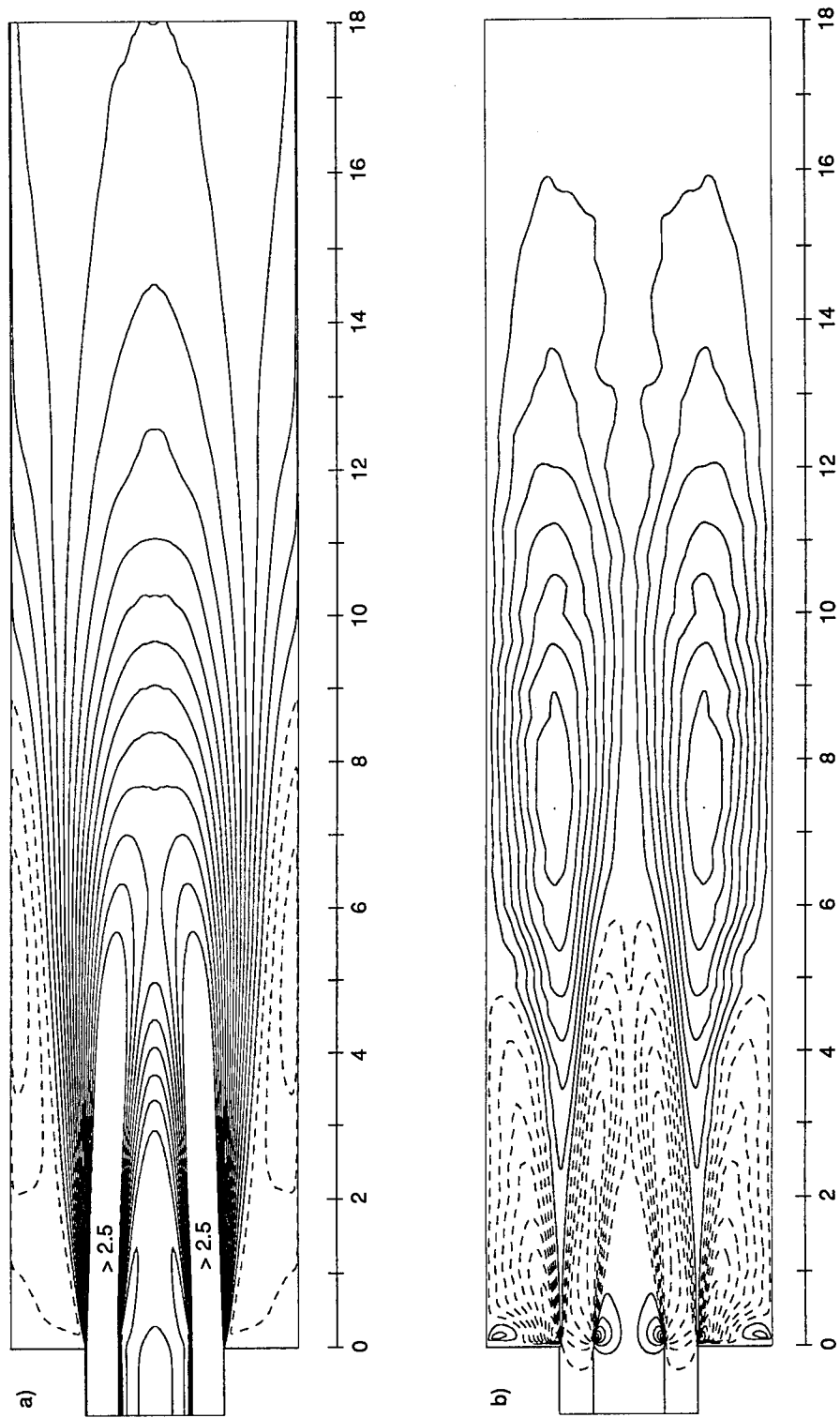
FIGURE **5.2-1**, Contour plots of the mean velocity components. Dashed lines denote negative values, solid lines denote positive values. a) Axial Velocity, U_x/U_c. Range : -0.47 - 3.46. Contour levels shown between -0.5 and 2.5 at intervals of 0.15. b) Radial Velocity, U_r/U_c. Range : -0.17 - 0.12. Contour levels shown between -0.17 and 0.12 at intervals of 0.0145.
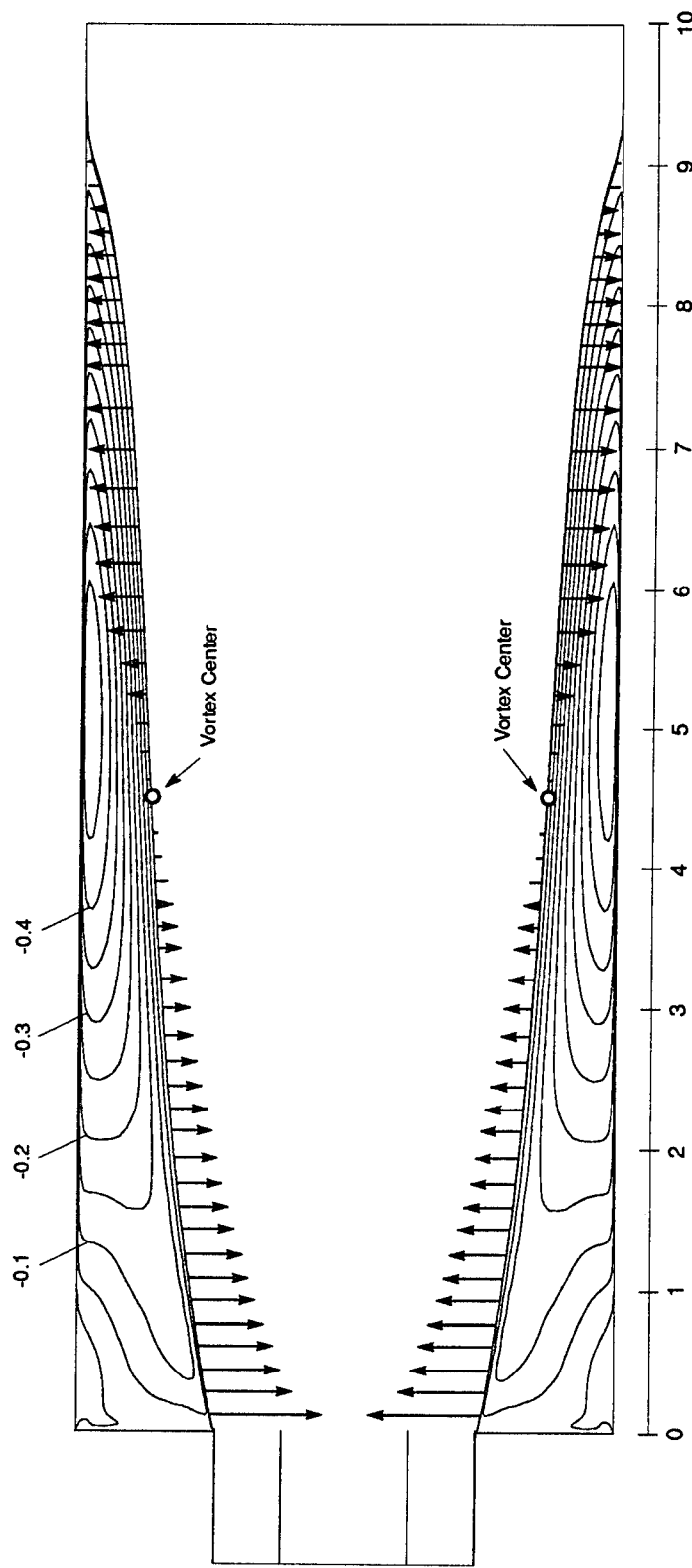
FIGURE **5.2-2**, Contour plot of the negative part of the mean axial velocity component. Contour levels shown between -0.5 and 0.0 at intervals of 0.05. The vectors along the line of zero axial velocity represent the relative magnitude (and direction) of the mean radial velocity component along this line.
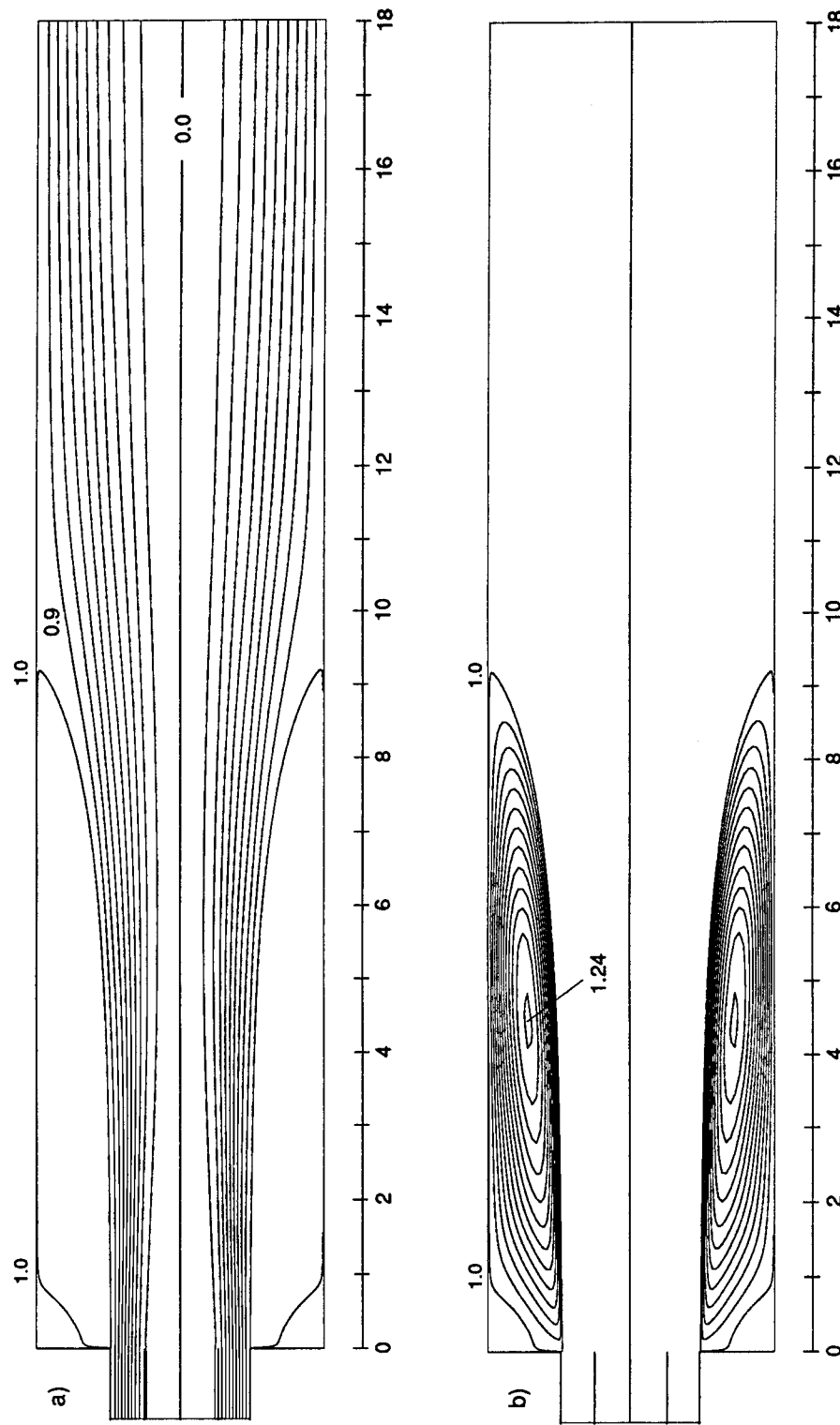
FIGURE **5.2-3**, Streamlines. The values have been normalized by the total mass flow-rate. The contour levels thus give the fraction of the total mass flow-rate passing between the contour lines.   a) Contour levels from 0.0 to 1.0 at intervals of 0.1.   b) Contour levels from 1.0 to 1.24 at intervals of 0.02.
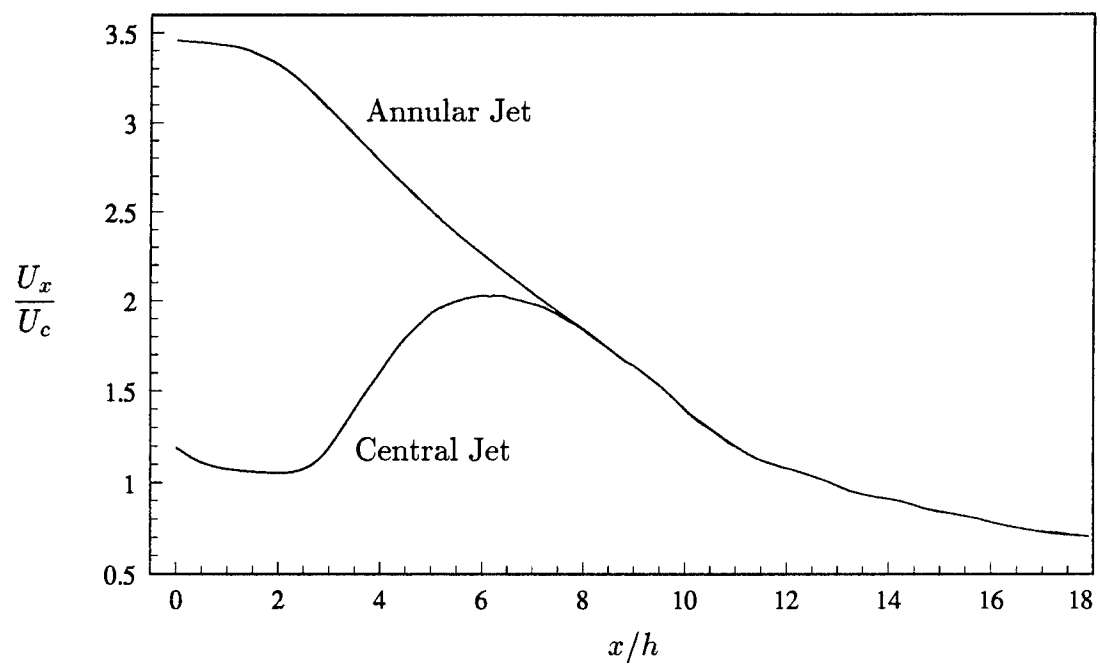
FIGURE **5.2-4**, Values of the two peaks in the velocity profiles downstream of the step (caused by expansion of the central and annular jets).
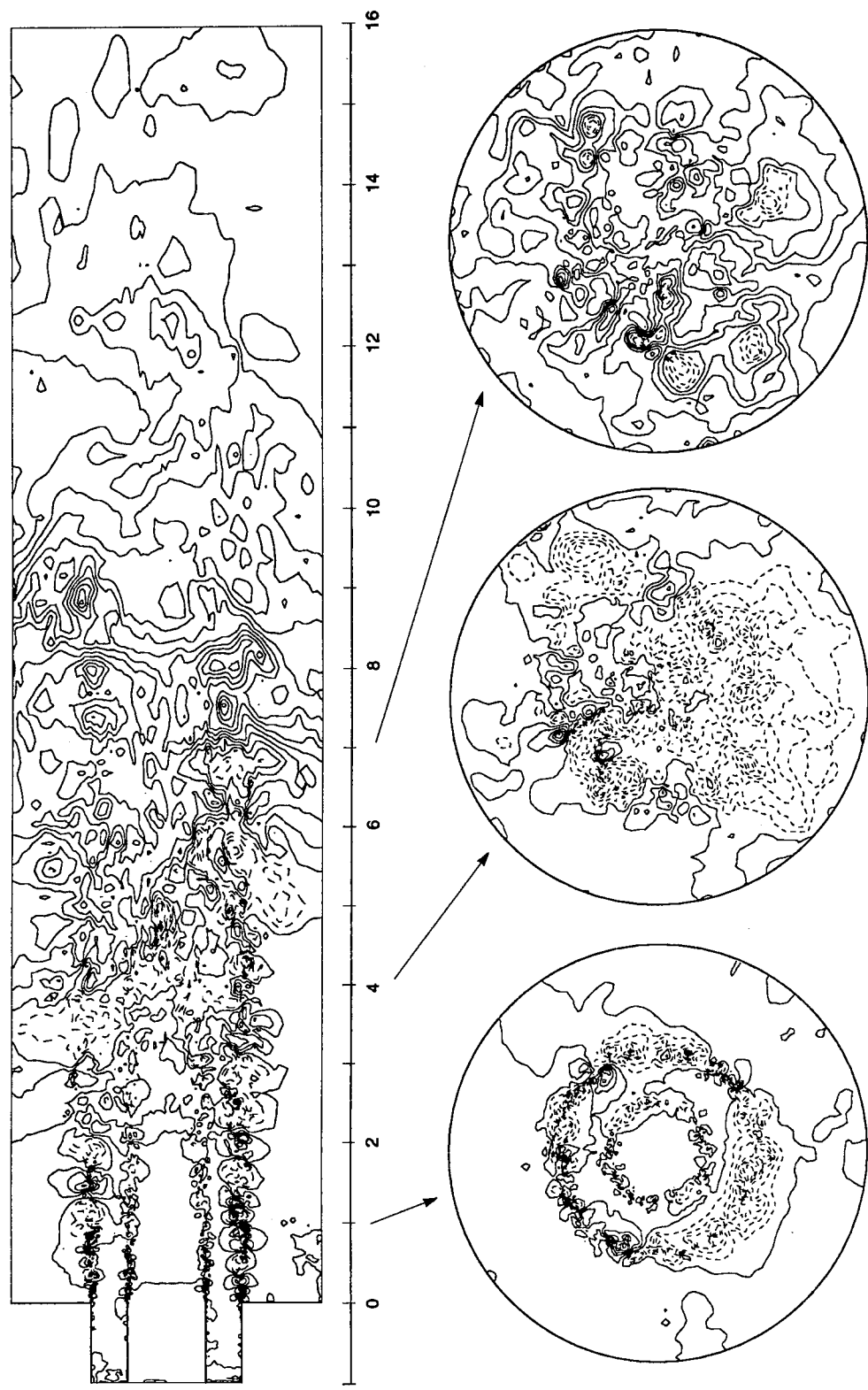
FIGURE **5.2-5**, Contour plot of an instantaneous pressure field. Dashed lines denote negative values, solid lines denote positive values. Contour levels shown between -1.0 and 1.6 at intervals of 0.13.

a)

b)
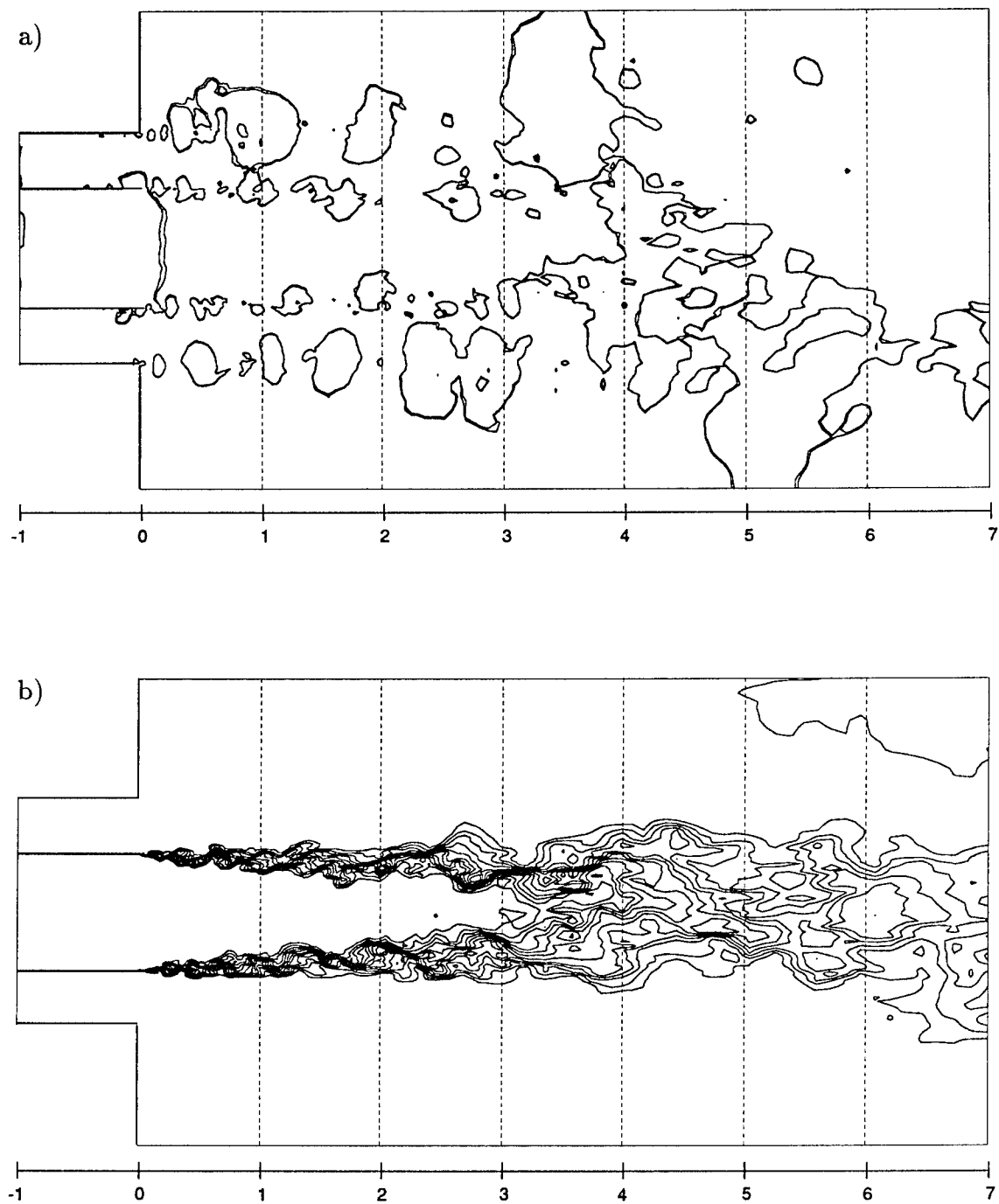
FIGURE **5.2-6**, Visualization of the shear layer between the central and annular jets.   a) Contours of instantaneous pressure. Contour levels: 0.02 to 0.04 at steps of 0.01.   b) Contours of instantaneous fuel mass-fraction. Contour levels: 0.06 to 0.94 at steps of 0.08.
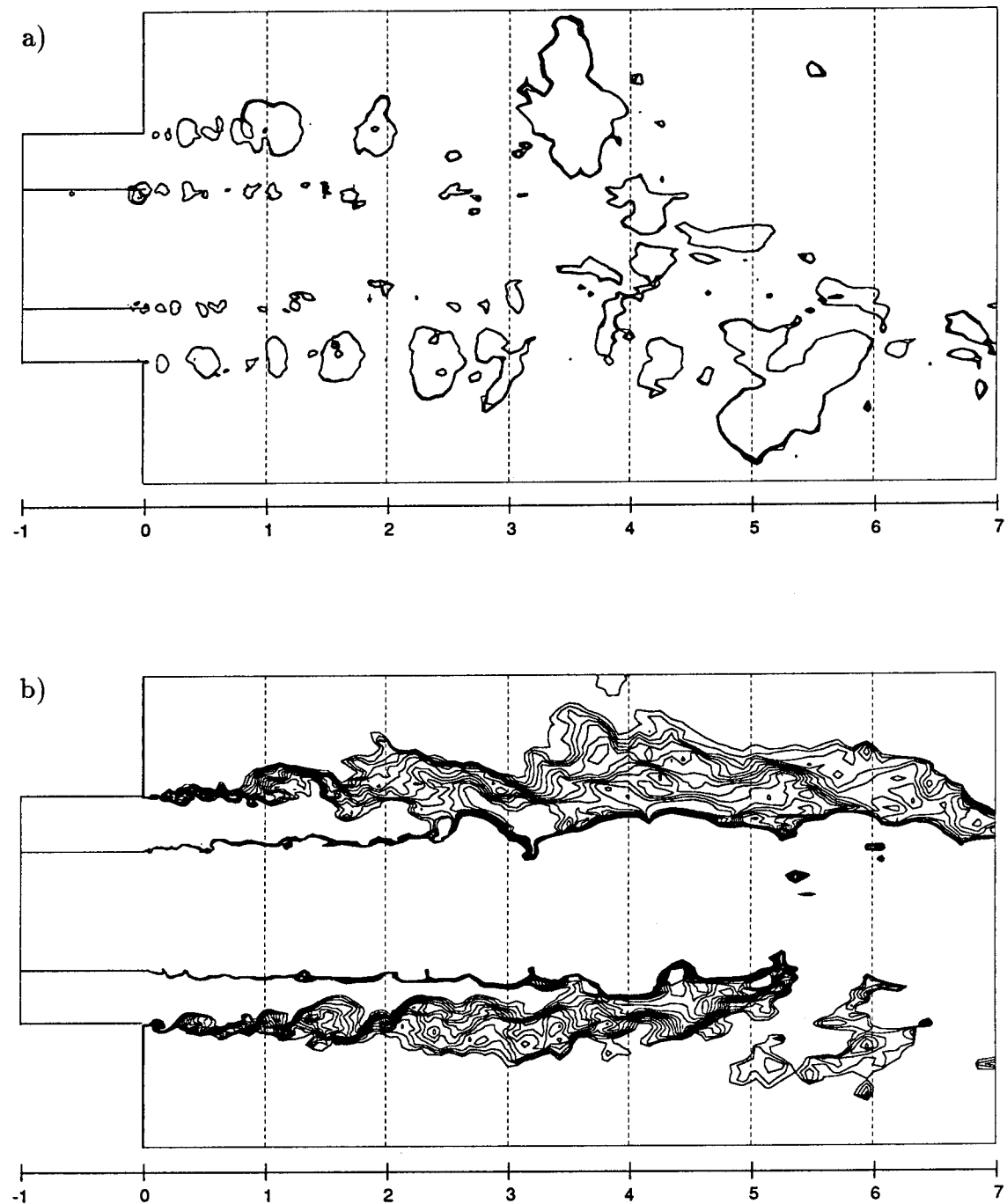
FIGURE **5.2-7**, Visualization of the shear layer between the annular jet and the recirculation zone.   a) Contours of instantaneous pressure. Contour levels: -0.074 to -0.05 at steps of 0.006.   b) Contours of instantaneous fuel mass-fraction. Contour levels: 0.005 to 0.031 at steps of 0.002.
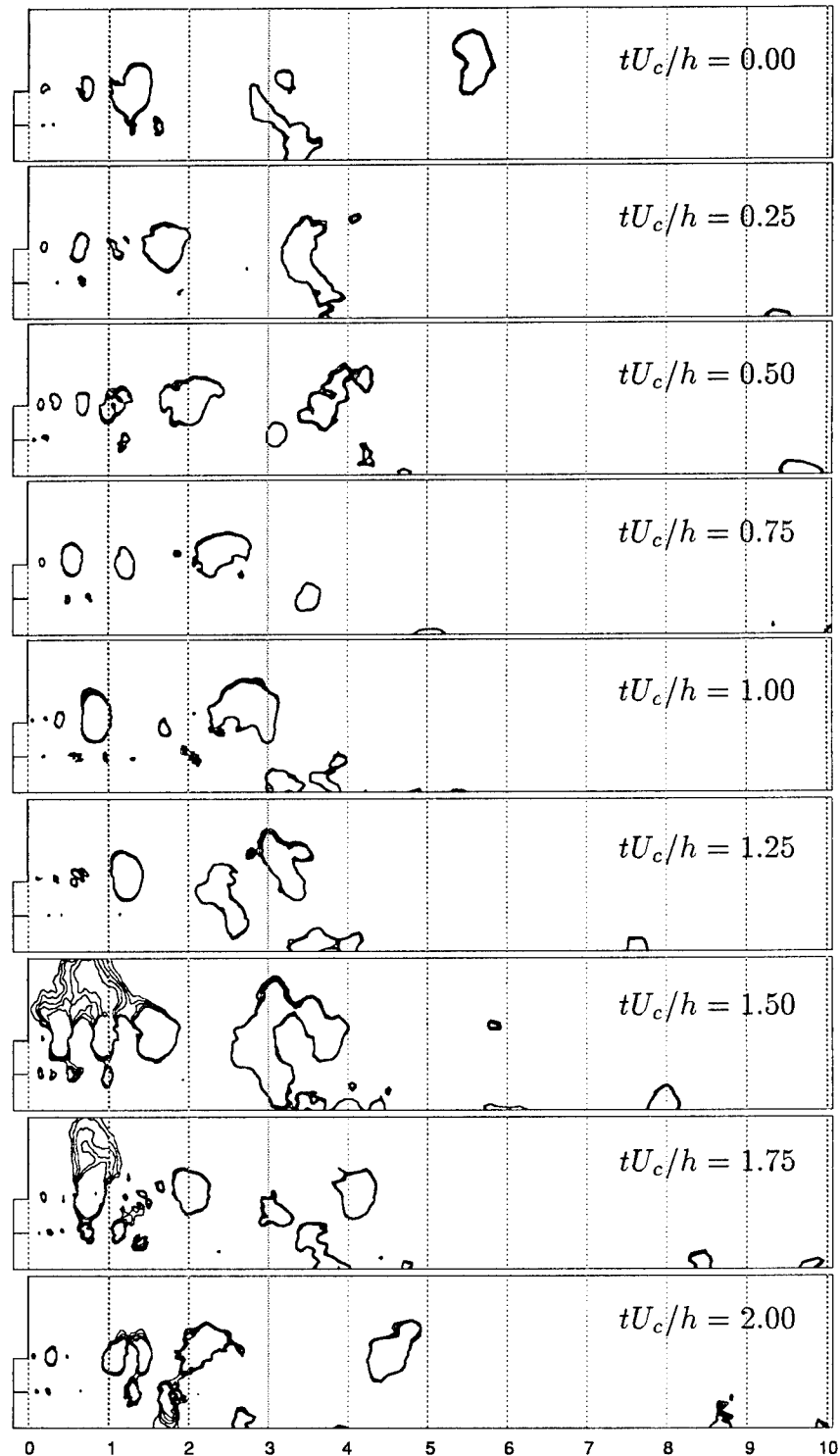
FIGURE **5.2-8**, Contours of instantaneous pressure fluctuations, averaged in the azimuthal direction. The radial direction spans from $r = 0$ to $r = r_0$. Contour levels: -0.06 to -0.04 at steps of 0.004.
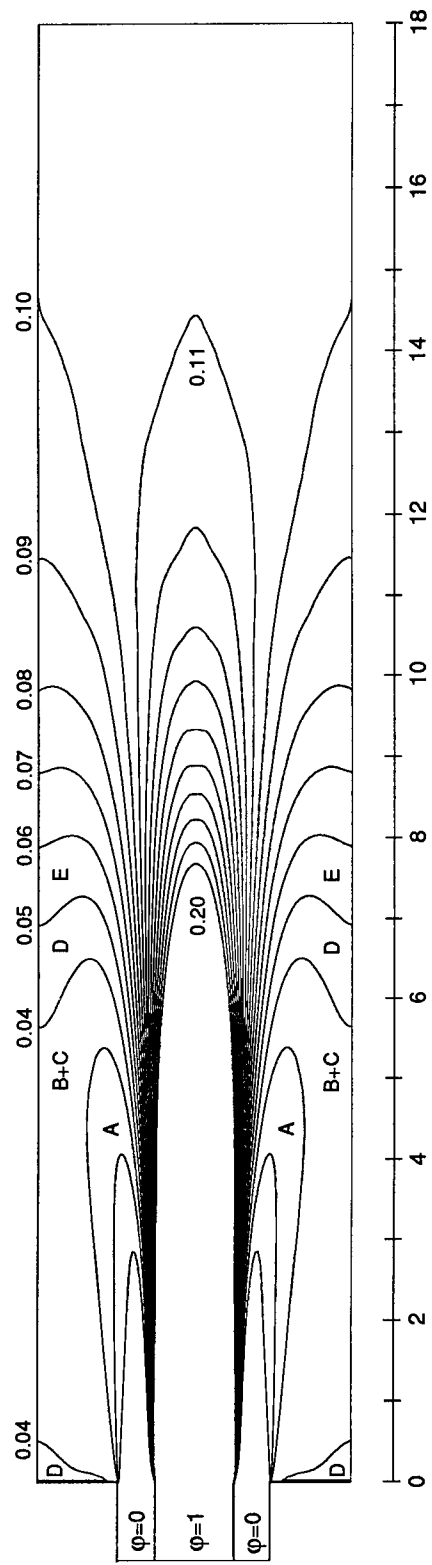
FIGURE **5.2-9**, Contour lines of the mean fuel mass-fraction. The contour values range from $\varphi = 0.01$ to $\varphi = 0.2$ in steps of $\Delta\varphi = 0.01$. The concentration level is higher (up to a maximum of 1) in the core of the flow, immediately downstream of the step. Each of the zones marked with capital letters have been plotted separately in figure 6.3-25.
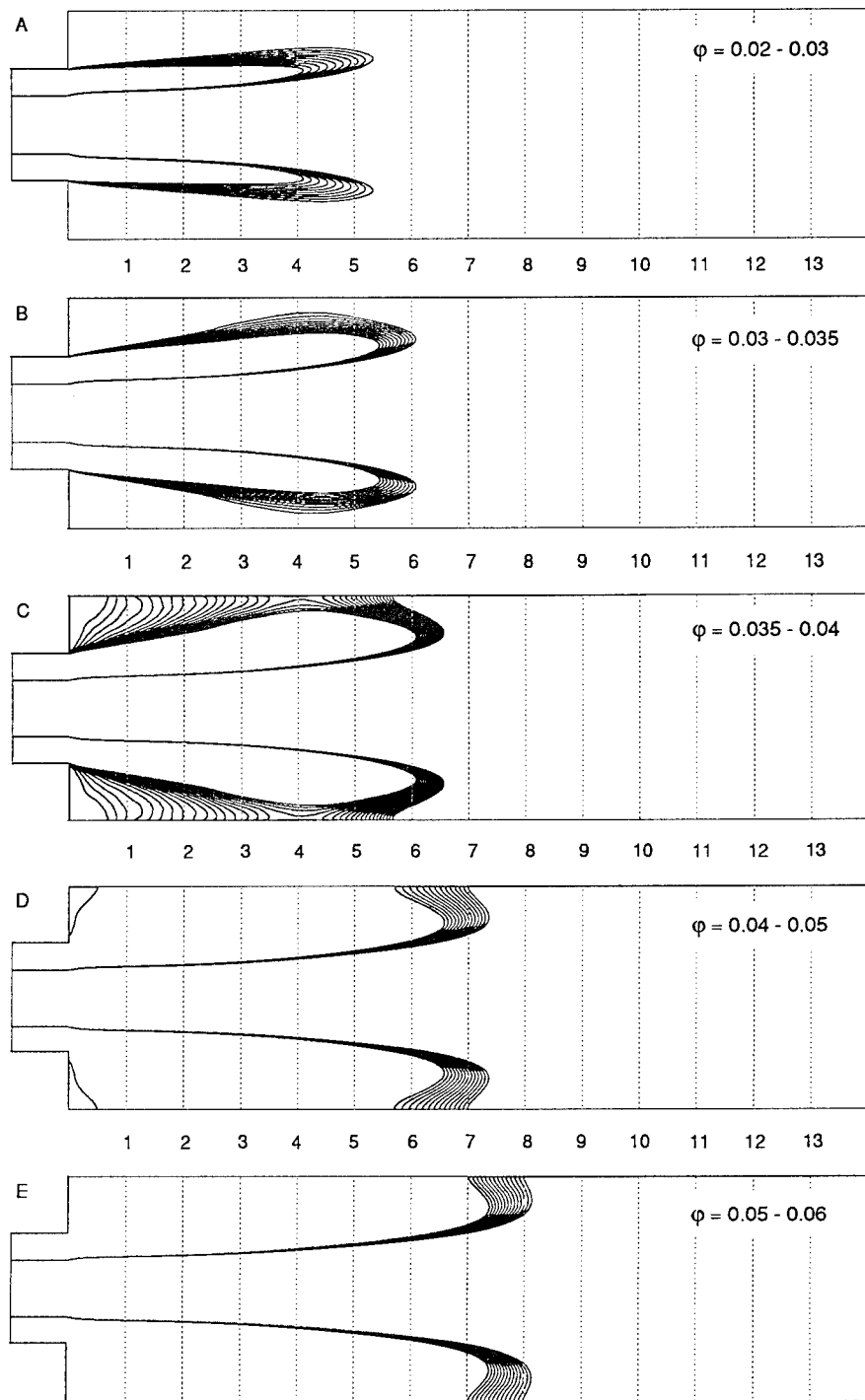
FIGURE **5.2-10**, Average fuel mass-fraction in the recirculation zone. Each of the figures show contour-lines within a narrow interval, as specified in the upper right corner of the figures.
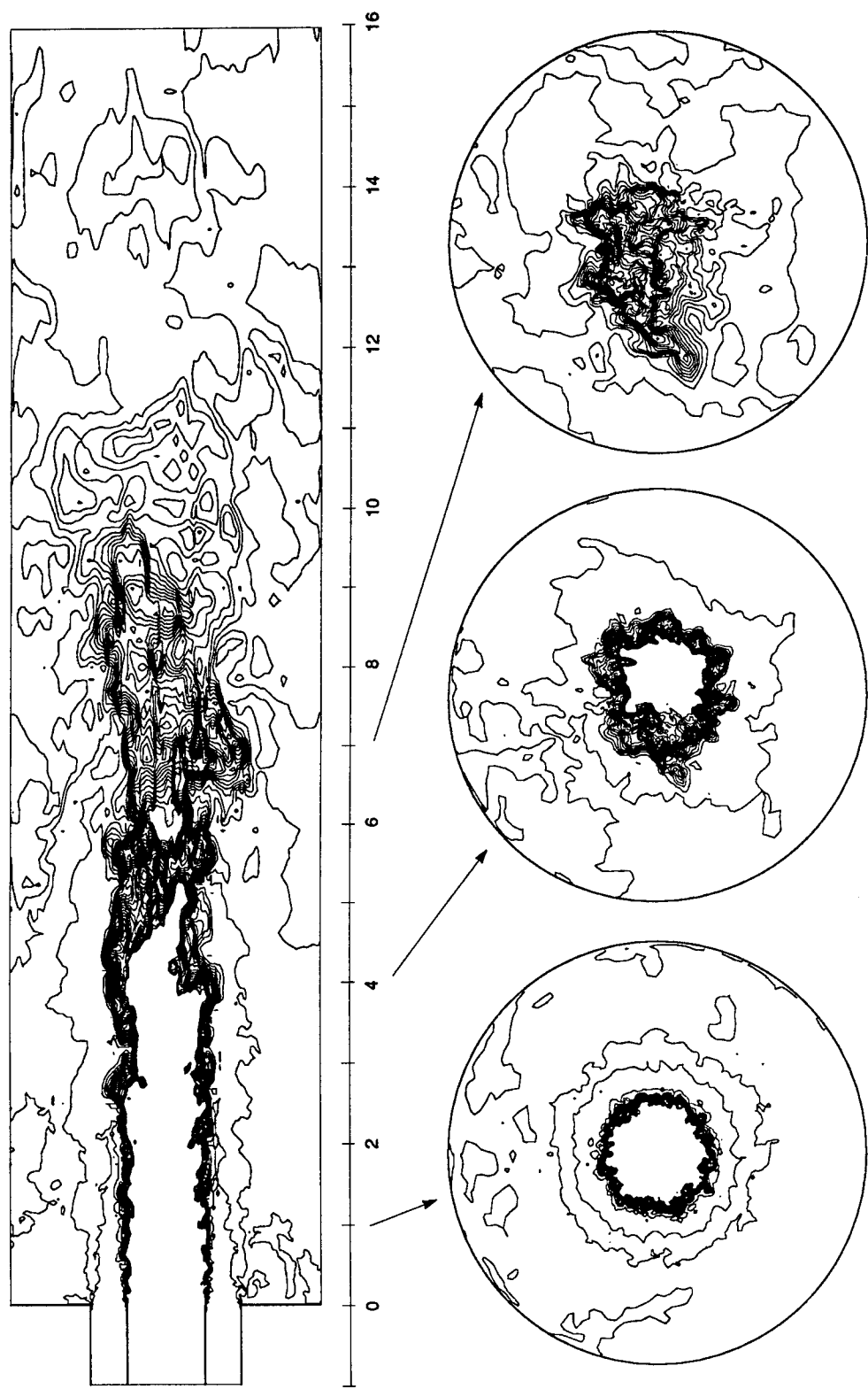
FIGURE **5.2-11**, Contour plot of an instantaneous scalar field. Contour levels shown between 0.0 and 0.4 at intervals of 0.02.
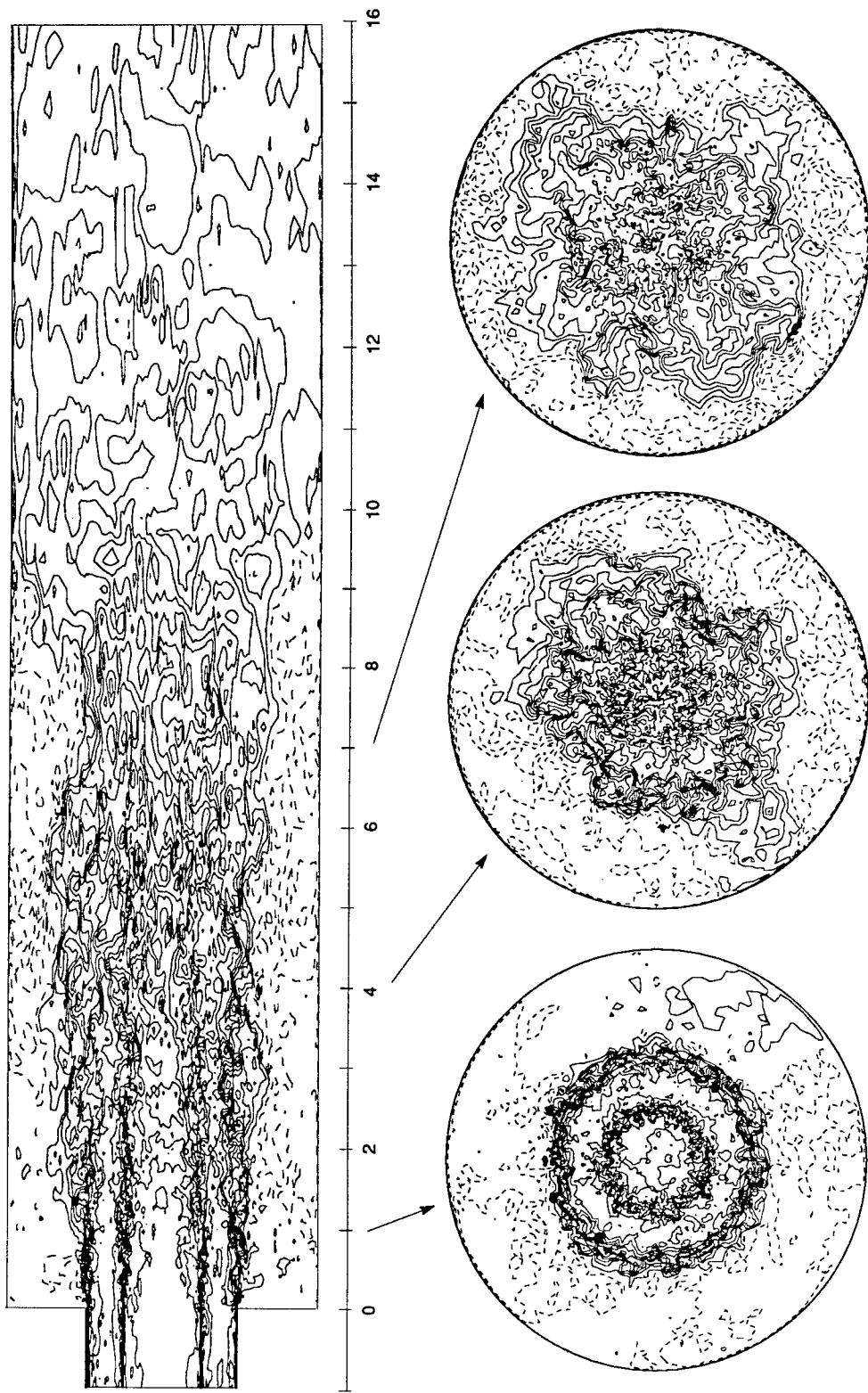
FIGURE **5.2-12**, Contour plot of an instantaneous axial velocity field. Dashed lines denote negative values, solid lines denote positive values. Contour levels shown between -1.2 and 4.0 at intervals of 0.371.

Chapter 6

CONCLUSIONS

The purpose of the present calculations was to use large eddy simulation to study mixing in a coaxial jet combustor in order to provide information that could lead to a better understanding of the phenomenon leading to lean blow-out (LBO). The calculations are interesting in themselves as large eddy simulations of a complex flow which is of engineering interest. They represent perhaps the most challenging test of the dynamic subgrid scale model to date, both in terms of predicting subgrid scale momentum transport and subgrid scale mass transport.

The calculations did not include chemical reactions, a simplification that limits the direct applicability of the results in terms of analysing the LBO phenomena. However, since LBO is strongly related to the mixing and entrainment characteristics of the jets and the recirculation zone, the calculations represent a necessary first step in the analysis of LBO. It should also be mentioned that the present calculations are the first fully time-dependent calculations of the mixing process taking place in a coaxial jet-combustor.

Comparisons of mean quantities with corresponding experimental results of Johnson & Bennett show overall very good agreement in almost all quantities. Some discrepancies do exist, but they are most likely due to problems with matching the (unknown) inflow condition used in the experiments.

In addition to correctly predicting the flow-field, the calculations accurately predict the fuel mass-fraction in the combustion chamber. A scalar transport version of the dynamic subgrid scale model was used to account for subgrid scale mass transport and the calculations provide credence to this model. The turbulent subgrid scale Schmidt number was of the order of 0.3-0.4 in most of the combustion chamber, with the exception of a short region immediately downstream of the expansion.

The mean radial velocity distribution in the combustion chamber suggests that the largest entrainment of fluid into the recirculation zone takes place close to the reattachment point, which was found to be located 9.4 step heights downstream of the expansion. This finding is supported by the animated results which show that most of the fuel is carried all the way to the reattachment point (which instantaneously varies roughly in the range $x/h = 7$-11) before being entrained into the recirculation zone. However, there is also intermittent transport of pockets of fuel into the recirculation zone from about 4 step heights downstream of the expansion. These pockets traverse the annular air stream without being significantly diluted before reaching the recirculation zone. This result supports the possibility that pockets of unburnt fuel can escape through the flame to be entrained into the recirculation zone, as suggested by Roquemore *et al.* No fuel-rich pockets were seen traversing the annular air stream upstream of about $x/h = 4$. This location coincides roughly with the vortex center in the recirculation zone, located at $x/h = 4.5$. (The vortex center is identified as the point where the mean axial and radial velocity components are both zero). The mean radial velocity component is directed towards the centerline upstream of the vortex center and towards the wall of the combustion chamber downstream of the vortex center.

The mean axial back-flow in the recirculation zone is found to be highest close to the wall. This is consistent with observations from the animation which shows that fuel-rich fluid is moving rapidly towards the base of the burner, in a "belt" or layer, very close to the wall. Only a small portion of fuel-rich fluid is being entrained into the adjacent shear layer along the way. The animation shows that most of the fuel-rich fluid is transported almost to the base of the burner before being entrained into the step shear layer. This finding is supported by the mean radial velocity distribution which shows that the radial velocity (along the zero axial velocity line) has its (negative) maximum very close to the base of the burner. This indicates that strong entrainment of fluid from the recirculation zone into the step shear layer occurs near the base of the burner. This in turn leads to the conclusion that a pilot flame, fed from the recirculation zone, is likely to be located near (or be attached to) the base of the burner, consistent with observations of Roquemore *et al.*

Both animated and mean results indicate that the fuel mass-fraction in the recirculation zone is highest in a small region around the outer corner of the step. This coincides with the location of a small counter rotating vortex which seems to

trap fuel-rich fluid, thus increasing the fuel mass-fraction at this point. The counter rotating vortex is located directly beneath the point with highest entrainment rate of fluid from the recirculation zone into the step shear layer. This strengthens the likelihood that a pilot flame might be found at the base of the burner.

An examination of large scale flow structures shows that the step- and fuel pipe shear layers merge about 2-3 step heights downstream of the expansion creating a zone of intense mixing. This is consistent with experimental results of Roquemore *et al.* which showed a region of intense combustion starting about 2 step heights downstream of the expansion.

By studying instantaneous snapshots of the fuel mass-fraction the characteristic roll up of vortices shed from both the fuel pipe and the corner of the step are identified in the early part of the shear layers. However, the structures are not very coherent and it is difficult to identify individual vortex rings. Any coherence in the structures seems to break down after the two shear layers have merged.

The animation also helps to understand why, as observed by Roquemore *et al.*, a lifted flame occasionally would flash back and attach to the base of the burner, and an attached flame occasionally would lift off. The animation reveals that entrainment of fuel into the recirculation zone is a highly unsteady and intermittent process. In fact, the animation shows that occasional pockets of air from the annular stream would be entrained into the recirculation zone as well, thus temporarily diluting the concentration of fuel. Assuming that the flame is attached, the sudden reduction in fuel mass-fraction might quench the pilot flame thus making the flame temporarily lift off from the base of the burner. Likewise, if one assumes that the flame is in a lifted state, a pocket of fuel-rich fluid crossing the annular air stream could temporarily increase the fuel mass-fraction above the lean flammability limit, thus making the flame flash back and attach to the base of the burner.

The fuel to air ratio used in the present calculation corresponds to a fuel-rich condition, provided the fuel is propane. The average concentration of fuel calculated in the recirculation zone is above the lean flammability limit for a propane-air mixture, indicating that the flame would be attached.

FUTURE WORK

All calculations done as part of this study were cold flow calculations. However, it is important to include computations of the chemical reactions associated with the combustion process in order to be able to more accurately address the issue of lean blow-out (LBO). Calculation of the combustion process will significantly increase the complexity and cost of an LES. Additional differential equations must be included for reaction species, compressible or variable density formulations are required to account for the expansion due to heat release, and a model is needed to simulate the chemical reactions taking place at scales smaller than the grid size.

As a first step one may simulate the combustion process by including a simple one-step chemical reaction, assuming infinite reaction rate and neglecting the effect of heat release. This would improve the usefulness of the simulation in that it would provide an opportunity to evaluate the amount of combustion product, in addition to unburnt fuel, entrained into the recirculation zone. The presence of hot combustion products is crucial in determining whether a combustible mixture will actually ignite.

Swirl has been shown to greatly enhance the mixing of fuel and air, and to promote flame stability (Lilley, 1977). Non-reacting swirling jets have been found to have increased growth rates, entrainment rates and rates of decay when compared with non-swirling jets. Reacting swirling jets experience differences in flame shape, size, stability and combustion intensity depending on the amount of swirl imparted on the flow. The physical mechanisms responsible for this increased performance are not completely understood, however, and numerical simulations should be able to elucidate these processes. Swirl can be added to the calculations by including an azimuthal body force in the air jet annulus. The swirl number can be controlled by the magnitude of the body force relative to the streamwise pressure gradient.

In addition to swirl, the use of periodic forcing to excite natural instability modes has been shown to enhance mixing of fuel and air in combustion devices (Wicker and Eaton, 1994). Enhanced mixing is likely to help stabilize the flame and should therefore be studied as a means for preventing LBO. Forcing can be achieved by modulating the mass flows in the fuel and air jets. The forcing can be applied to one stream at a time or simultaneously to both.

APPENDICES

Appendix A

BACKWARD FACING STEP

This appendix focuses on some important issues related to LES of turbulent flow over a backward facing step not covered in the main sections of this report.

Section A.1 demonstrates the problems resulting from using a uniform streamwise grid. If the resolution around the corner of the step (both in the streamwise- and wall-normal direction) is not sufficiently fine, the numerical scheme produces large truncation errors in this region that are convected downstream and ultimately corrupt the solution.

Section A.2 is aimed at showing the importance of having good inflow turbulent boundary conditions. This also serves to show that flow parameters measured downstream of the step are very sensitive to the state of the flow upstream of the step.

A.1 Streamwise Grid

Large eddy simulations of the backward facing step were attempted using a uniform streamwise grid distribution. (The wall-normal grid was non-uniform, as described in chapter 4, part I). This approach did however give rise to large truncation errors around the singular corner point which had an overwhelming effect on the flow downstream of the step. (The fact that no such problems were detected in the DNS study of Le & Moin simply means that their uniform streamwise resolution was sufficient to control the numerical errors originating at the corner point).

This section shows results from six large eddy simulations of the backward facing step. The computational domain was the same as that described in chapter 4, part I, except that the inlet section extended $10h$ upstream of the step. All flow parameters were the same as in chapter 4, part I, except for the inflow boundary condition which was the same as that used in the DNS of Le & Moin. (Problems associated with this inflow condition is discussed in appendix A.2).

Case	x-grid	N_x	$(\Delta x/h)_{min}$	$(\Delta x/h)_{max}$
1	Non-Uniform	117	0.045	0.469
2	Non-Uniform	187	0.045	0.284
3	Non-Uniform	372	0.045	0.122
4	Uniform	96	0.312	0.312
5	Uniform	192	0.156	0.156
6	Uniform	384	0.078	0.078

TABLE **A.1-1**, An overview of the cases used to study the effect of uniform versus non-uniform streamwise grid.

The six cases are summarized in table A.1-1, which gives the number of streamwise grid-points as well as the minimum and maximum streamwise grid spacings. The number of streamwise grid-points given in table A.1-1 is the total number of points, including the inlet section. All cases used a stretched grid with 48 grid-points in the wall-normal direction (the same grid as that used in all but one of the cases in chapter 4, part I) and 32 uniformly distributed points in the spanwise

direction. Three different streamwise resolutions were considered ranging from coarse through medium to fine. All cases were run using the DM model (equation 2.2-25). The non-uniform streamwise grid distributions were designed to have a minimum Δx (at the corner) close to that used in the DNS study of Le & Moin (who used a uniform grid with $\Delta x/h = 0.039$). The maximum grid-spacing occurs at the exit of the domain. Figure A.1-1 shows the grid spacing, Δx, as a function of streamwise distance for the three non-uniform streamwise grids.

The results from the simulations are presented using the coefficient of friction, C_f, along the lower wall as example. Figure A.1-2 shows the coefficient of friction downstream of the step for the three cases with uniform streamwise grid. Figure A.1-3 shows a similar plot for the cases with non-uniform streamwise grid.

Since subgrid scale modeling involves assumptions and approximations, one would not expect the results from a large eddy simulation to be fully independent of the grid resolution. However, one would expect the results to converge towards the DNS results as the computational grid is refined. This is clearly the case with the results in figure A.1-3. Only minor changes are observed in the coefficient of friction as the grid is refined. The reattachment length ranges from $6.48h$ for the finest grid ($N_x = 372$) to $6.86h$ for the coarse grid ($N_x = 117$).

Figure A.1-2, on the other hand, reveals dramatic changes in the coefficient of friction as the (uniform) streamwise grid is refined. The reattachment length changes from $4.87h$ for the coarse grid to $6.67h$ for the fine grid, an increase of more than 35 percent. The fact that the coarse grid calculations with uniform streamwise grids have large problems around the corner can be seen from figure A.1-4, which shows a sharp spike in the coefficient of friction at the corner of the step for the coarser resolutions. As the number of grid-points increase the height of the spike decreases, and for the finest grid ($N_x = 384$), the spike has all but vanished. In fact, no significant difference is observed when comparing the coefficient of friction from the two high-resolution cases (see figure A.1-5).

The examples given above confirm that the errors associated with the singular corner point can be controlled by refining the grid around the corner. It is clear that a uniform streamwise grid is inappropriate for LES of turbulent flow over the backward facing step when resolving the wall-layers.

A.2 Inflow Boundary Condition

This section demonstrates the problems experienced in the low Reynolds number large eddy simulations of the backward facing step when the inflow boundary condition is determined using the random number method of Le & Moin. Because the turbulence supplied at the inflow boundary lacks structures, the flow goes through a transition before recovering. Whereas the flow was able to recover within $10h$ in the DNS of Le & Moin, the same was not found to be the case in the large eddy simulations. The resulting effect on the flow downstream of the step is discussed below.

Two LES cases are compared with the DNS results of Le & Moin. The first, which used the random number method of Le & Moin at the inflow boundary, is case 2 from table A.1-1. The second LES case, which involved fully developed turbulence just upstream of the step, is the case labeled DMBA in section 4.1, part I (see table 4.2-1, part I). The only difference between the two LES cases is the inflow boundary condition (and consequently the length of the inlet section).

The transitional zone in the inlet section, caused by using random numbers at the inflow boundary, can be seen in figure A.2-1. The random number inflow boundary condition was designed to match the statistical characteristics of a turbulent boundary layer calculated by Spalart (1988). The coefficient of friction from this calculation is also shown as reference. It is apparent that both the DNS and LES, using the random number inflow boundary condition, go through a transition before starting to recover. However, unlike the DNS, the coefficient of friction in the LES is not able to recover within the length of the inlet section.

Figure A.2-2 shows the turbulence intensities and the turbulent shear stress $0.2h$ upstream of the step for the LES (random number inflow) and the DNS. Also shown are the corresponding values obtained by Spalart (1988). (Recall that only the resolved part of the turbulence intensities are shown for the LES. The turbulent shear stress includes the subgrid scale contribution). Figure A.2-2 reveals an over-prediction in u''_{rms}, and an under-prediction in v''_{rms} and w''_{rms} for the LES compared with the DNS. This is a result generally found in coarse grid large eddy simulations of wall-bounded flows. The turbulent shear stress is also significantly under-predicted by the LES.

The dramatic effect of the inflow condition on the flow characteristics downstream of the step can be seen by comparing the coefficient of friction along the lower wall. This is done in figure A.2-3. The result from the LES with fully developed turbulent inflow shows excellent agreement with the DNS data. The reattachment location predicted by the DNS is $6.28h$. The LES with fully developed turbulent inflow predicts a reattachment length of $6.36h$, which is only about 1 percent off compared with the DNS value. The results from the other LES case show more pronounced discrepancies, particularly in the recirculation region (i.e. x/h less than about 6). The reattachment length calculated is $6.69h$, or 6 percent larger than the DNS value.

Figure A.2-4 shows mean streamwise velocity profiles at five locations upstream of reattachment. It is obvious that the results from the LES using the random number inflow boundary condition compares poorly with the DNS profiles of Le & Moin. The other LES case is in excellent agreement with DNS.

The difference between the two LES cases is even more pronounced in the mean wall-normal velocity profiles, shown in figure A.2-5. Good agreement between the DNS and the LES using fully developed turbulence at the inlet are observed. However the results from the other LES case show poor agreement with DNS.

Based on the results presented it is obvious that it is important to have the correct flow characteristics upstream of the step in order to be able to correctly predict the flow behavior downstream of the expansion. The long inlet section used in the DNS study by Le & Moin insured that the flow had the right characteristics upstream of the expansion, despite a rather long recovery region. However, when using the same inflow boundary condition for low Reynolds number LES, the flow is not able to recover, resulting in significant discrepancies in the solution.
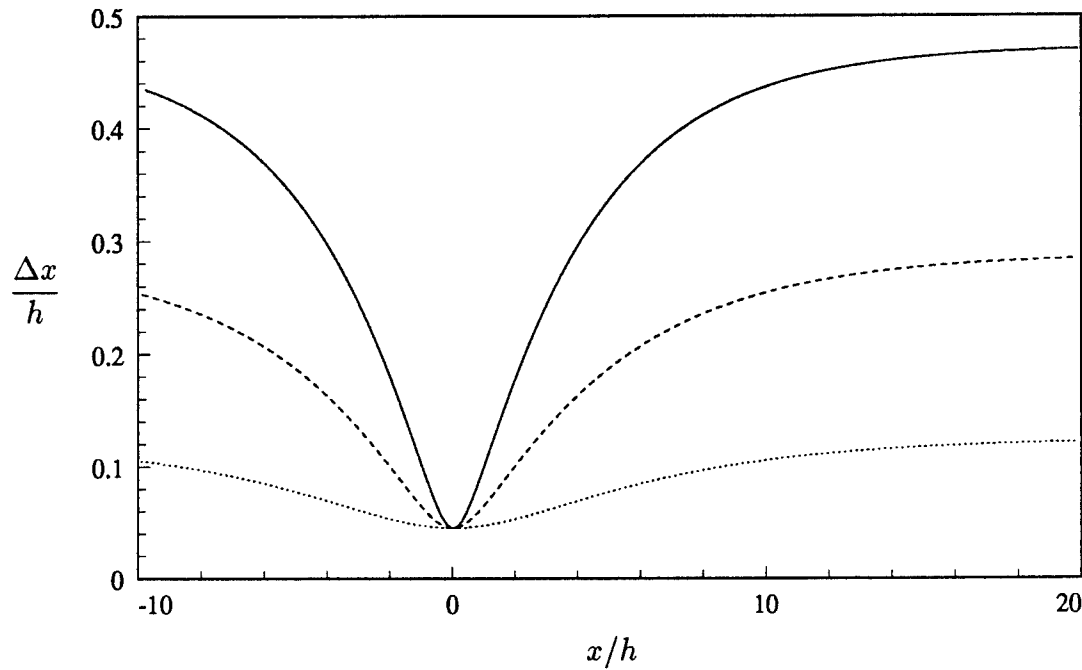
FIGURE **A.1-1**, Streamwise grid spacing versus streamwise distance.

——— : $N_x = 117$;   ---- : $N_x = 187$;   ········ : $N_x = 372$.
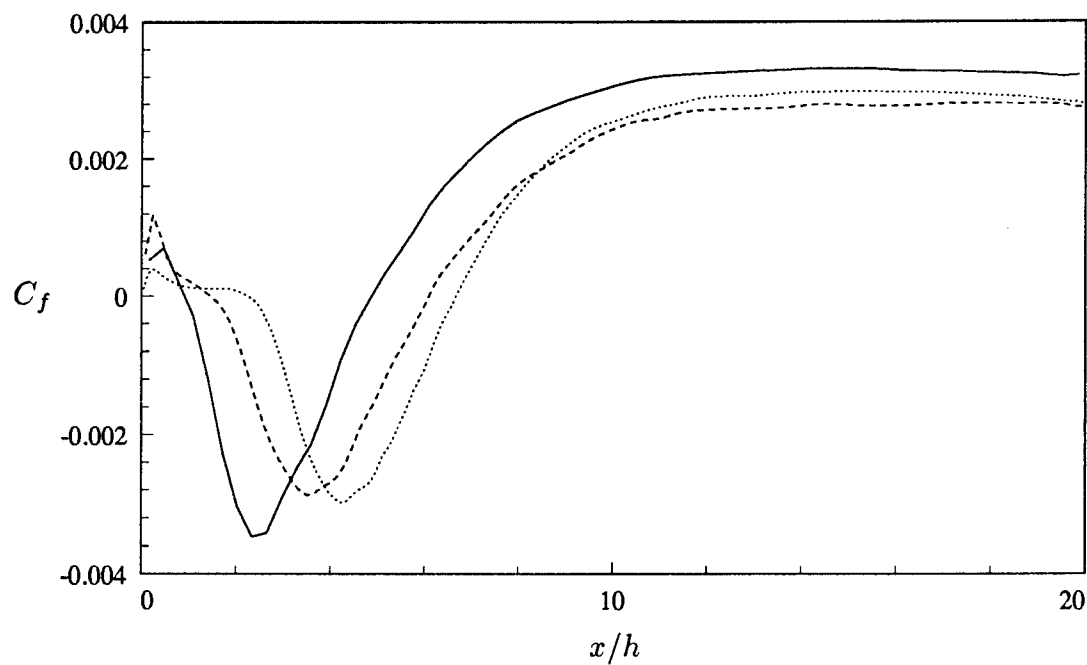

FIGURE **A.1-2**, Coefficient of friction downstream of the step, along the lower wall.
Uniform streamwise grid.   ——— : $N_x = 96$;   ---- : $N_x = 192$;
········ : $N_x = 384$.
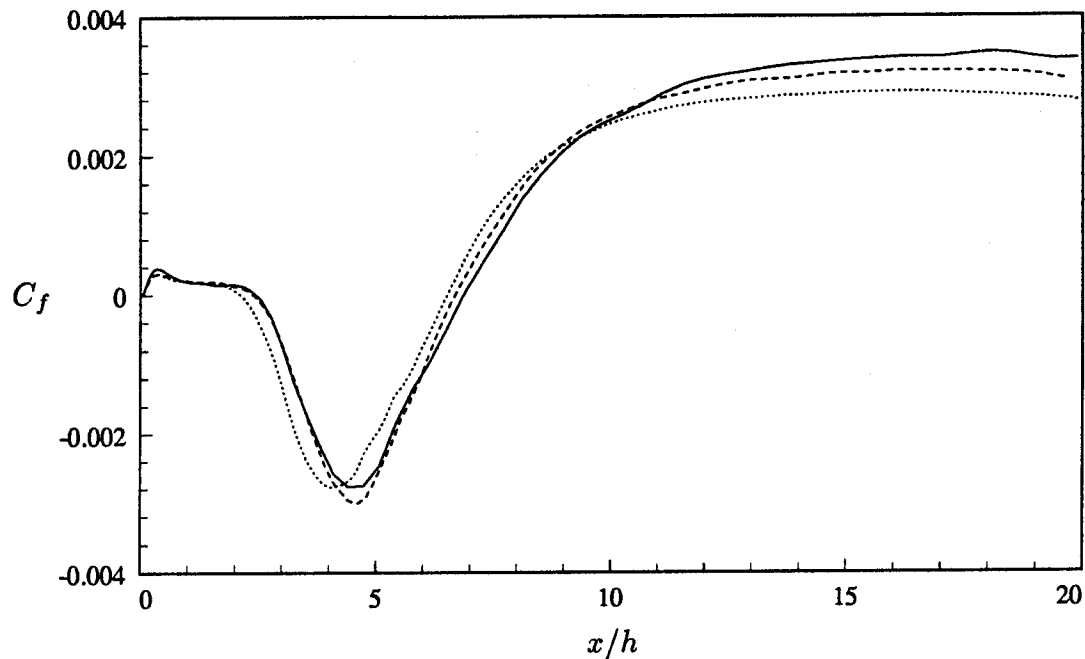
FIGURE **A.1-3**, Coefficient of friction downstream of the step, along the lower wall. Non-uniform streamwise grid. ——— : $N_x = 117$;   - - - - : $N_x = 187$; ········ : $N_x = 372$.
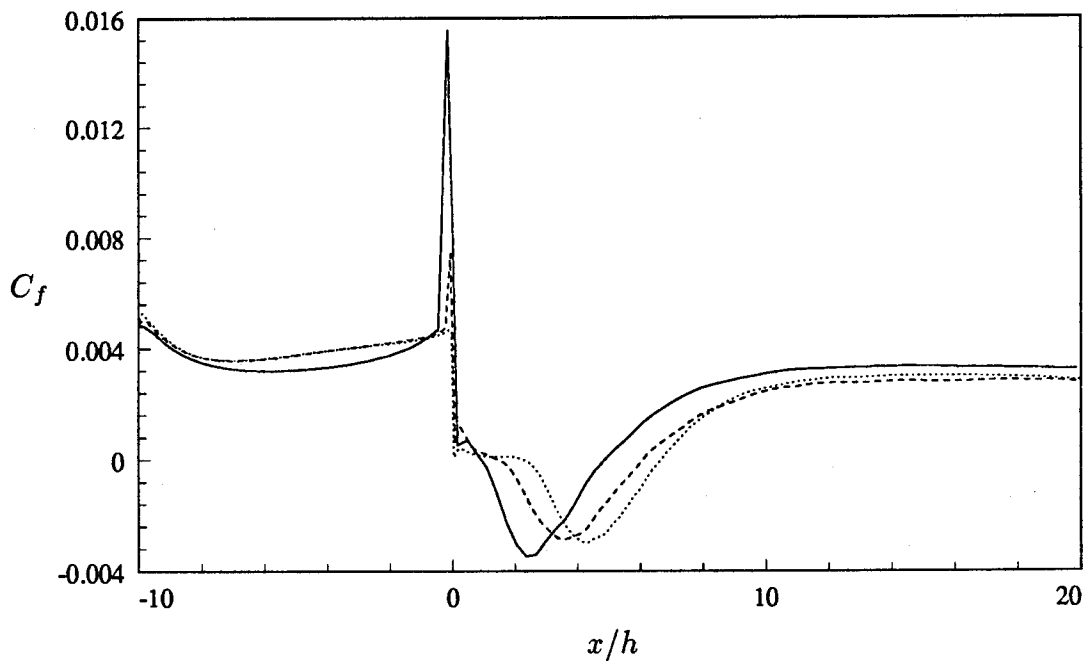

FIGURE **A.1-4**, Coefficient of friction along the lower wall, including the inlet section. Uniform streamwise grid. ——— : $N_x = 96$;   - - - - : $N_x = 192$; ········ : $N_x = 384$.
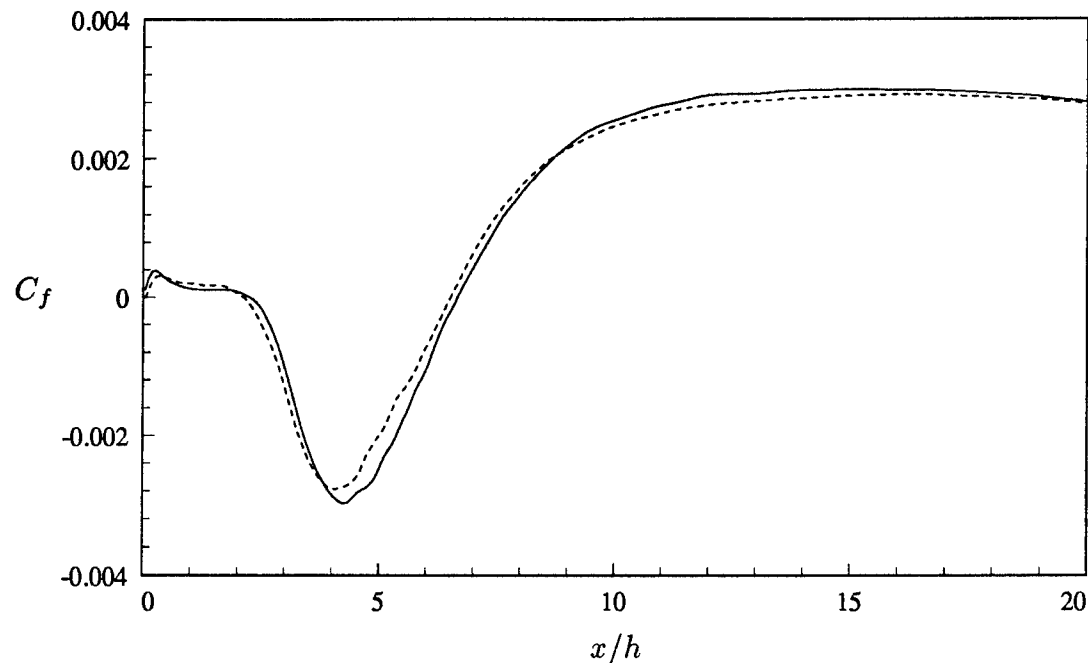
FIGURE **A.1-5**, Coefficient of friction downstream of the step, along the lower wall.
———— : Uniform streamwise grid ($N_x = 372$);   - - - - : Non-uniform streamwise grid ($N_x = 384$).
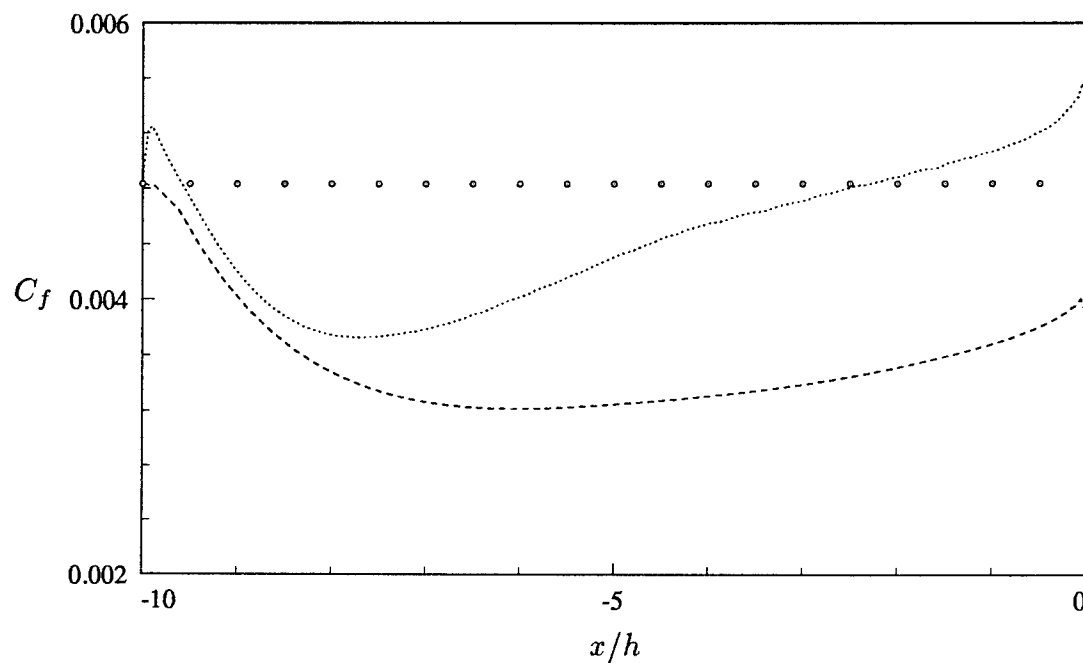

FIGURE **A.2-1**, Coefficient of friction in the inlet section.   - - - - : LES, Random numbers at inlet;   ········ : DNS (Le & Moin);   o : Spalart, 1988 (DNS).
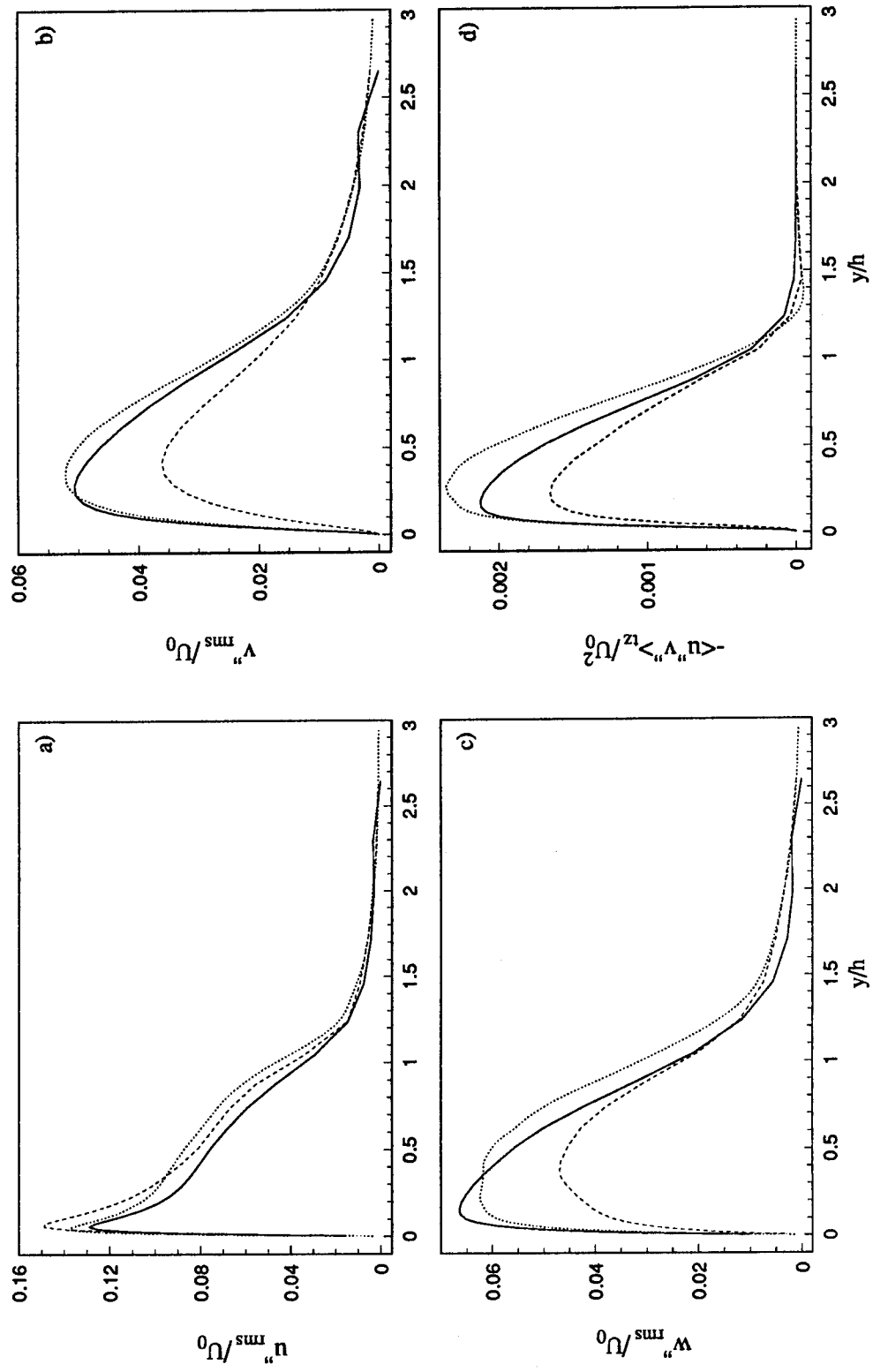
FIGURE **A.2-2**, Turbulent statistics at $x/h = -0.2$. ——— : Spalart, 1988 (DNS); – – – : LES, Random numbers at inlet; ········ : DNS (Le & Moin). a) u''_{rms}, b) v''_{rms}, c) w''_{rms}, d) Turbulent shear stress (including SGS term).
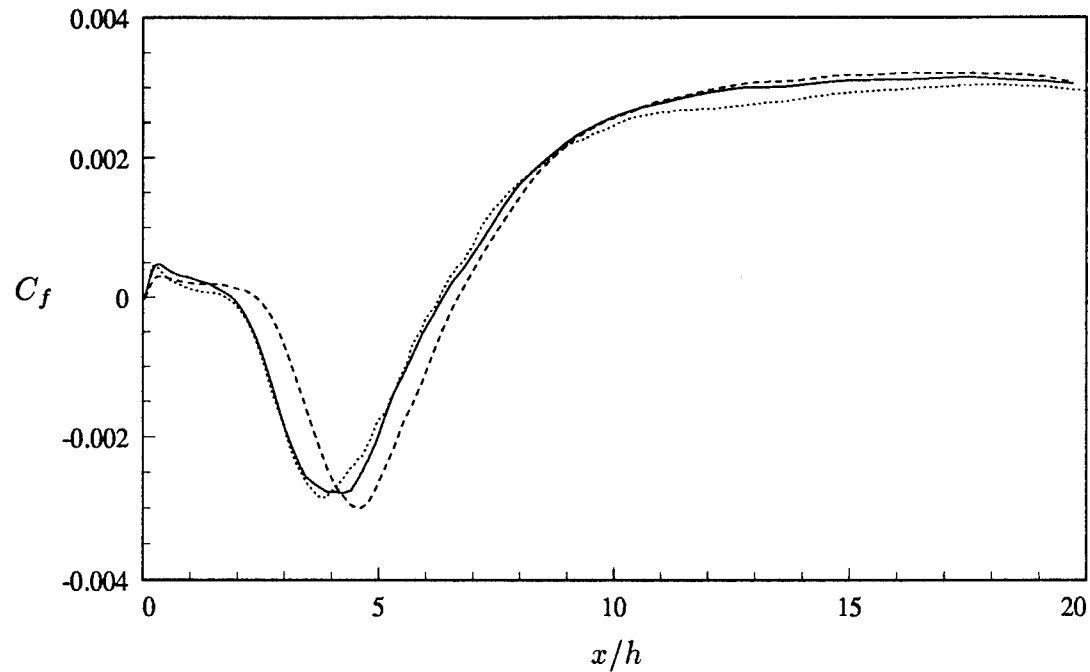
FIGURE **A.2-3**, Coefficient of friction downstream of the step, along the lower wall.
———— : LES, Fully developed turbulence at inlet;   – – – – : LES, Random numbers
at inlet;   ········ DNS (Le & Moin).
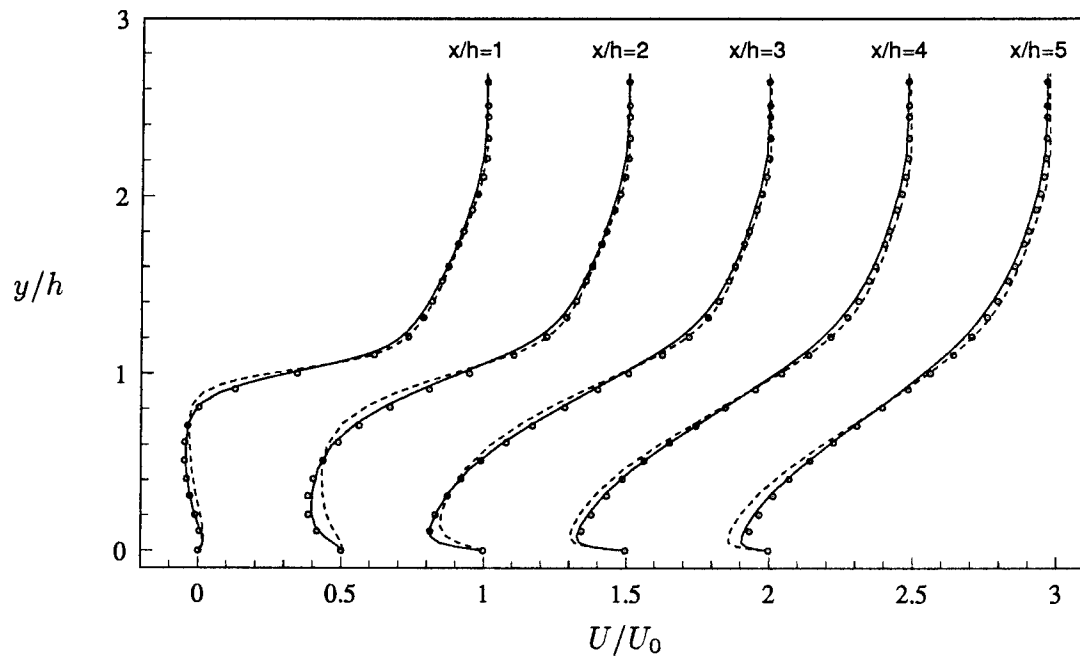
FIGURE **A.2-4**, Mean streamwise velocity profiles in the recirculation region.
———— : LES, Fully developed turbulence at inlet;   – – – – : LES, Random numbers
at inlet;   o : DNS (Le & Moin).

– 263 –
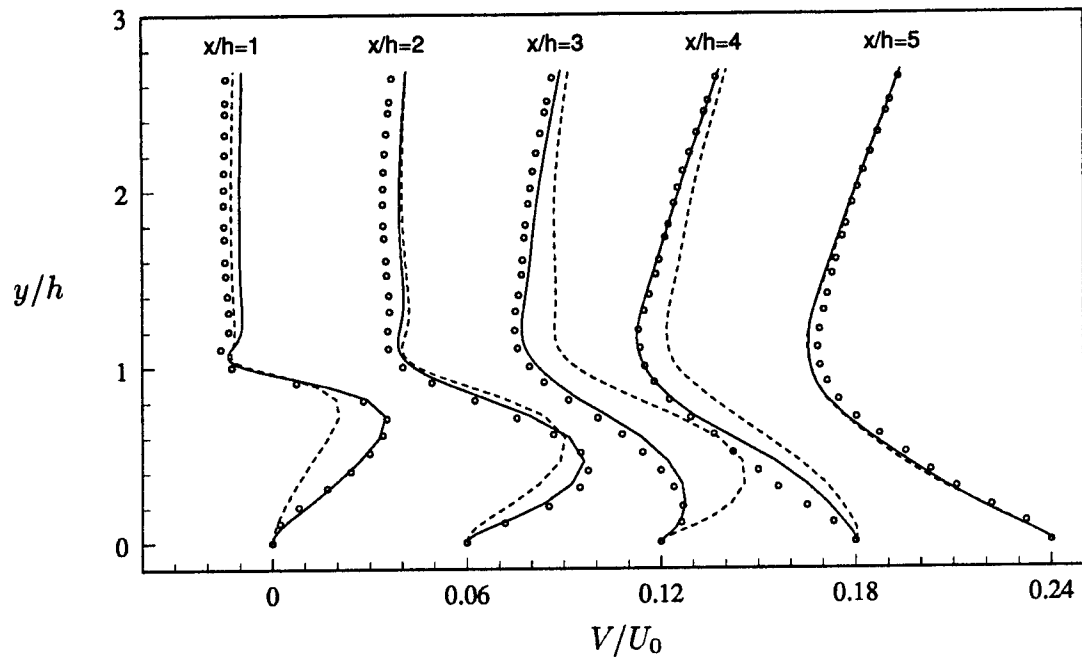
FIGURE **A.2-5**, Mean wall-normal velocity profiles in the recirculation region.
————— : LES, Fully developed turbulence at inlet;   - - - - : LES, Random numbers at inlet;   o : DNS (Le & Moin).

CYLINDRICAL COORDINATES

This appendix summarizes some of the details involved in working with cylindrical coordinates. Section B.1 lists the Navier-Stokes equations. Implementation of the control volume formulation is outlined in section B.2. Section B.3 gives the implicit and explicit operators related to the time-integration scheme.

B.1 Governing Equations

The Navier-Stokes equations in cylindrical coordinates are given in equation B.1-1. The first line in the equations gives the convective terms (in addition to the pressure gradient). The second line gives the diffusive terms and the last line gives the cross-terms. The latter are due to the viscosity being a function of space. If the viscosity was constant continuity would remove these terms.

$$\frac{\partial u_x}{\partial t} = -\frac{\partial \phi}{\partial x} - \left\{ \frac{\partial u_x u_x}{\partial x} + \frac{1}{r}\frac{\partial r u_r u_x}{\partial r} + \frac{1}{r}\frac{\partial u_\theta u_x}{\partial \theta} \right\}$$

$$+ \left\{ \frac{\partial}{\partial x}\left(\nu\frac{\partial u_x}{\partial x}\right) + \frac{1}{r}\frac{\partial}{\partial r}\left(\nu r\frac{\partial u_x}{\partial r}\right) + \frac{1}{r^2}\frac{\partial}{\partial \theta}\left(\nu\frac{\partial u_x}{\partial \theta}\right) \right\}$$

$$+ \left\{ \frac{\partial}{\partial x}\left(\nu\frac{\partial u_x}{\partial x}\right) + \frac{1}{r}\frac{\partial}{\partial r}\left(\nu r\frac{\partial u_r}{\partial x}\right) + \frac{1}{r}\frac{\partial}{\partial \theta}\left(\nu\frac{\partial u_\theta}{\partial x}\right) \right\} \qquad (B.1\text{-}1a)$$

$$\frac{\partial u_r}{\partial t} = -\frac{\partial \phi}{\partial r} - \left\{ \frac{\partial u_x u_r}{\partial x} + \frac{1}{r}\frac{\partial r u_r u_r}{\partial r} + \frac{1}{r}\frac{\partial u_\theta u_r}{\partial \theta} - \frac{u_\theta u_\theta}{r} \right\}$$

$$+ \left\{ \frac{\partial}{\partial x}\left(\nu\frac{\partial u_r}{\partial x}\right) + \frac{1}{r}\frac{\partial}{\partial r}\left(\nu r\frac{\partial u_r}{\partial r}\right) + \frac{1}{r^2}\frac{\partial}{\partial \theta}\left(\nu\frac{\partial u_r}{\partial \theta}\right) - \frac{\nu u_r}{r^2} - \frac{\nu}{r^2}\frac{\partial u_\theta}{\partial \theta} - \frac{1}{r^2}\frac{\partial(\nu u_\theta)}{\partial \theta} \right\}$$

$$+ \left\{ \frac{\partial}{\partial x}\left(\nu\frac{\partial u_x}{\partial r}\right) + \frac{1}{r}\frac{\partial}{\partial r}\left(\nu r\frac{\partial u_r}{\partial r}\right) + \frac{1}{r}\frac{\partial}{\partial \theta}\left(\nu\frac{\partial u_\theta}{\partial r}\right) - \frac{\nu u_r}{r^2} - \frac{\nu}{r^2}\frac{\partial u_\theta}{\partial \theta} \right\} \qquad (B.1\text{-}1b)$$

$$\frac{\partial u_\theta}{\partial t} = -\frac{1}{r}\frac{\partial \phi}{\partial \theta} - \left\{ \frac{\partial u_x u_\theta}{\partial x} + \frac{1}{r}\frac{\partial r u_r u_\theta}{\partial r} + \frac{1}{r}\frac{\partial u_\theta u_\theta}{\partial \theta} + \frac{u_\theta u_r}{r} \right\}$$

$$+ \left\{ \frac{\partial}{\partial x}\left(\nu\frac{\partial u_\theta}{\partial x}\right) + \frac{1}{r}\frac{\partial}{\partial r}\left(\nu r\frac{\partial u_\theta}{\partial r}\right) + \frac{1}{r^2}\frac{\partial}{\partial \theta}\left(\nu\frac{\partial u_\theta}{\partial \theta}\right) - \frac{\nu u_\theta}{r^2} + \frac{\nu}{r^2}\frac{\partial u_r}{\partial \theta} + \frac{1}{r^2}\frac{\partial(\nu u_r)}{\partial \theta} \right\}$$

$$+ \left\{ \frac{\partial}{\partial x}\left(\frac{\nu}{r}\frac{\partial u_x}{\partial \theta}\right) + \frac{1}{r}\frac{\partial}{\partial r}\left(\nu\frac{\partial u_r}{\partial \theta}\right) + \frac{1}{r^2}\frac{\partial}{\partial \theta}\left(\nu\frac{\partial u_\theta}{\partial \theta}\right) - \frac{1}{r}\frac{\partial \nu u_\theta}{\partial r} + \frac{\nu}{r}\frac{\partial u_\theta}{\partial r} + \frac{1}{r^2}\frac{\partial \nu u_r}{\partial \theta} \right\}$$

$$(B.1\text{-}1c)$$

The equations can be rearranged, grouping relevant flux terms, to yield:

$$\frac{\partial u_x}{\partial t} = -\frac{\partial \phi}{\partial x} + \frac{\partial}{\partial x}\left(2\nu\frac{\partial u_x}{\partial x} - u_x u_x\right) + \frac{1}{r}\frac{\partial}{\partial r}\left(r\nu\frac{\partial u_x}{\partial r} + r\nu\frac{\partial u_r}{\partial x} - r u_x u_r\right)$$

$$+ \frac{1}{r}\frac{\partial}{\partial \theta}\left(\frac{\nu}{r}\frac{\partial u_x}{\partial \theta} + \nu\frac{\partial u_\theta}{\partial x} - u_x u_\theta\right) \qquad (B.1\text{-}2a)$$

$$\frac{\partial u_r}{\partial t} = -\frac{\partial \phi}{\partial r} + \frac{\partial}{\partial x}\left(\nu\frac{\partial u_r}{\partial x} + \nu\frac{\partial u_x}{\partial r} - u_r u_x\right) + \frac{1}{r}\frac{\partial}{\partial r}\left(2r\nu\frac{\partial u_r}{\partial r} - r u_r u_r\right)$$

$$+ \frac{1}{r}\frac{\partial}{\partial \theta}\left(\frac{\nu}{r}\frac{\partial u_r}{\partial \theta} + \nu\frac{\partial u_\theta}{\partial r} - \nu\frac{u_\theta}{r} - u_r u_\theta\right)$$

$$- \left(\frac{2\nu}{r^2}\frac{\partial u_\theta}{\partial \theta} + 2\nu\frac{u_r}{r^2} - \frac{u_\theta u_\theta}{r}\right) \qquad (B.1\text{-}2b)$$

$$\frac{\partial u_\theta}{\partial t} = -\frac{1}{r}\frac{\partial \phi}{\partial \theta} + \frac{\partial}{\partial x}\left(\nu\frac{\partial u_\theta}{\partial x} + \frac{\nu}{r}\frac{\partial u_x}{\partial \theta} - u_\theta u_x\right)$$

$$+ \frac{1}{r}\frac{\partial}{\partial r}\left(r\nu\frac{\partial u_\theta}{\partial r} + \nu\frac{\partial u_r}{\partial \theta} - \nu u_\theta - r u_\theta u_r\right)$$

$$+ \frac{1}{r}\frac{\partial}{\partial \theta}\left(2\frac{\nu}{r}\frac{\partial u_\theta}{\partial \theta} + \frac{2\nu u_r}{r} - u_\theta u_\theta\right)$$

$$+ \left(\frac{\nu}{r}\frac{\partial u_\theta}{\partial r} + \frac{\nu}{r^2}\frac{\partial u_r}{\partial \theta} - \frac{\nu u_\theta}{r^2} - \frac{u_\theta u_r}{r}\right) \qquad (B.1\text{-}2c)$$

B.2 Control-Volume Formulation

This section shows how the control volume formulation is applied to the Navier-Stokes equations in cylindrical coordinates. The basis for the evaluation is the Navier-Stokes equations in vector form:

$$\frac{\partial \mathbf{u}}{\partial t} = -\nabla\phi + \nabla \cdot \left\{ \nu\nabla\mathbf{u} + \nu(\nabla\mathbf{u})^T - \mathbf{u} \otimes \mathbf{u} \right\} \qquad (B.2\text{-}1)$$

On a staggered grid the control-volumes used for the three momentum equations do not coincide. However, for the purpose of the following development a "general" control-volume, shown in figure B.2-1, will be used. It is assumed that the control-volume is appropriately surrounding a velocity-node corresponding to the momentum equation being analyzed.

The grid is assumed to be uniform in all three coordinate directions, with spacings Δx, Δr, and $\Delta\theta$. A superscript "+" indicates a quantity evaluate at the front face of the control volume. Correspondingly, a superscript "−" is taken to indicate a quantity evaluate at the back face of the control volume. $\mathbf{n}$ represents an outward unit vector to any given surface of the control-volume. The discrete volume and surface areas of the control-volume are (the subscript indicates the direction of the normal to the surface):

$$\delta V = r_m \Delta x \Delta r \Delta\theta,$$

$$\delta S_x = r_m \Delta r \Delta\theta, \qquad \delta S_r = r\Delta\theta\Delta x, \qquad \delta S_\theta = \Delta r\Delta x \qquad (B.2\text{-}2)$$

where

$$r_m = \tfrac{1}{2}\{r + (r + \Delta r)\} \qquad (B.2\text{-}3)$$

Integrating equation B.2-1 over the infinitesimal control-volume of figure B.2-1 gives:

$$\int_V \frac{\partial \mathbf{u}}{\partial t} dV = -\int_V \nabla\phi \, dV + \int_V \nabla \cdot \left\{ \nu\nabla\mathbf{u} + \nu(\nabla\mathbf{u})^T - \mathbf{u} \otimes \mathbf{u} \right\} dV \qquad (B.2\text{-}4)$$

Invoking Gauss' theorem, and dividing through by the volume, δV gives:

$$\frac{1}{\delta V} \int_V \frac{\partial \mathbf{u}}{\partial t} dV = -\frac{1}{\delta V} \int_V \nabla\phi dV + \frac{1}{\delta V} \int_S \mathbf{n} \cdot \{\nu\nabla\mathbf{u} + \nu(\nabla\mathbf{u})^T - \mathbf{u}\otimes\mathbf{u}\} dS \quad (B.2\text{-}5)$$

The following shows the evaluation of the last integral on the right-hand-side of equation B.2-5 for the three momentum equations given in cylindrical coordinates. A superscript (x, r, or θ) indicates the direction of the normal on the surface where the term is evaluated.

Axial momentum equation

$$\frac{1}{\delta V} \int_S \mathbf{n} \cdot (\mathbf{u}\otimes\mathbf{u}) dS = \left\{ (u_x u_x)^+ - (u_x u_x)^- \right\}^x \frac{1}{\Delta x} \mathbf{e}_x$$

$$+ \left\{ (u_r u_x)^+ r^+ - (u_r u_x)^- r^- \right\}^r \frac{1}{r_m \Delta r} \mathbf{e}_x$$

$$+ \left\{ (u_\theta u_x)^+ - (u_\theta u_x)^- \right\}^\theta \frac{1}{r_m \Delta\theta} \mathbf{e}_x \qquad (B.2\text{-}6)$$

$$\frac{1}{\delta V} \int_S \mathbf{n} \cdot (\nu\nabla\mathbf{u}) dS = \left\{ \left(\nu\frac{\partial u_x}{\partial x}\right)^+ - \left(\nu\frac{\partial u_x}{\partial x}\right)^- \right\}^x \frac{1}{\Delta x} \mathbf{e}_x$$

$$+ \left\{ \left(\nu\frac{\partial u_x}{\partial r}\right)^+ r^+ - \left(\nu\frac{\partial u_x}{\partial r}\right)^- r^- \right\}^r \frac{1}{r_m \Delta r} \mathbf{e}_x$$

$$+ \left\{ \left(\nu\frac{\partial u_x}{\partial\theta}\right)^+ - \left(\nu\frac{\partial u_x}{\partial\theta}\right)^- \right\}^\theta \frac{1}{r_m^2 \Delta\theta} \mathbf{e}_x \qquad (B.2\text{-}7)$$

$$\frac{1}{\delta V} \int_S \mathbf{n} \cdot (\nu\nabla\mathbf{u})^T dS = \left\{ \nu^+\left(\frac{\partial u_x}{\partial x}\right)^+ - \nu^-\left(\frac{\partial u_x}{\partial x}\right)^- \right\}^x \frac{1}{\Delta x} \mathbf{e}_x$$

$$+ \left\{ \nu^+\left(\frac{\partial u_r}{\partial x}\right)^+ r^+ - \nu^-\left(\frac{\partial u_r}{\partial x}\right)^- r^- \right\}^r \frac{1}{r_m \Delta r} \mathbf{e}_x$$

$$+ \left\{ \nu^+\left(\frac{\partial u_\theta}{\partial x}\right)^+ - \nu^-\left(\frac{\partial u_\theta}{\partial x}\right)^- \right\}^\theta \frac{1}{r_m \Delta\theta} \mathbf{e}_x \qquad (B.2\text{-}8)$$

Radial momentum equation

$$\frac{1}{\delta V} \int_S \mathbf{n} \cdot (\mathbf{u} \otimes \mathbf{u}) dS$$

$$= \left\{ (u_x u_r)^+ - (u_x u_r)^- \right\}^x \frac{\mathbf{e}_r}{\Delta x}$$

$$+ \left\{ (u_r u_r)^+ r^+ - (u_r u_r)^- r^- \right\}^r \frac{\mathbf{e}_r}{r_m \Delta r}$$

$$+ \left\{ (u_\theta u_r)^+ - (u_\theta u_r)^- \right\}^\theta \frac{\mathbf{e}_r}{r_m \Delta \theta} - \left\{ (u_\theta u_\theta)^+ + (u_\theta u_\theta)^- \right\}^\theta \frac{\mathbf{e}_r}{2 r_m} \qquad (B.2\text{-}9)$$

$$\frac{1}{\delta V} \int_S \mathbf{n} \cdot (\nu \nabla \mathbf{u}) dS$$

$$= \left\{ \left(\nu \frac{\partial u_r}{\partial x} \right)^+ - \left(\nu \frac{\partial u_r}{\partial x} \right)^- \right\}^x \frac{\mathbf{e}_r}{\Delta x}$$

$$+ \left\{ \left(\nu \frac{\partial u_r}{\partial r} \right)^+ r^+ - \left(\nu \frac{\partial u_r}{\partial r} \right)^- r^- \right\}^r \frac{\mathbf{e}_r}{r_m \Delta r}$$

$$+ \left\{ \left(\nu \frac{\partial u_r}{\partial \theta} \right)^+ - \left(\nu \frac{\partial u_r}{\partial \theta} \right)^- \right\}^\theta \frac{\mathbf{e}_r}{r_m^2 \Delta \theta} - \left\{ (\nu u_\theta)^+ - (\nu u_\theta)^- \right\}^\theta \frac{\mathbf{e}_r}{r_m r \Delta \theta}$$

$$- \left\{ \left(\nu \frac{\partial u_\theta}{\partial \theta} \right)^+ + \left(\nu \frac{\partial u_\theta}{\partial \theta} \right)^- \right\}^\theta \frac{\mathbf{e}_r}{2 r_m^2} - \left\{ (\nu u_r)^+ + (\nu u_r)^- \right\}^\theta \frac{\mathbf{e}_r}{2 r_m r} \qquad (B.2\text{-}10)$$

$$\frac{1}{\delta V} \int_S \mathbf{n} \cdot (\nu \nabla \mathbf{u})^T dS$$

$$= \left\{ \left(\nu \frac{\partial u_x}{\partial r} \right)^+ - \left(\nu \frac{\partial u_x}{\partial r} \right)^- \right\}^x \frac{\mathbf{e}_r}{\Delta x}$$

$$+ \left\{ \left(\nu \frac{\partial u_r}{\partial r} \right)^+ r^+ - \left(\nu \frac{\partial u_r}{\partial r} \right)^- r^- \right\}^r \frac{\mathbf{e}_r}{r_m \Delta r}$$

$$+ \left\{ \left(\nu \frac{\partial u_\theta}{\partial r} \right)^+ - \left(\nu \frac{\partial u_\theta}{\partial r} \right)^- \right\}^\theta \frac{\mathbf{e}_r}{r_m \Delta \theta}$$

$$- \left\{ \left(\nu \frac{\partial u_\theta}{\partial \theta} \right)^+ + \left(\nu \frac{\partial u_\theta}{\partial \theta} \right)^- \right\}^\theta \frac{\mathbf{e}_r}{2 r_m^2} - \left\{ (\nu u_r)^+ + (\nu u_r)^- \right\}^\theta \frac{\mathbf{e}_r}{2 r_m r} \qquad (B.2\text{-}11)$$

Azimuthal momentum equation

$$\frac{1}{\delta V}\int_S \mathbf{n}\cdot(\mathbf{u}\otimes\mathbf{u})dS$$

$$= \left\{(u_x u_\theta)^+ - (u_x u_\theta)^-\right\}^x \frac{\mathbf{e}_\theta}{\Delta x}$$

$$+ \left\{(u_r u_\theta)^+ r^+ - (u_r u_\theta)^- r^-\right\}^r \frac{\mathbf{e}_\theta}{r_m \Delta r}$$

$$+ \left\{(u_\theta u_\theta)^+ - (u_\theta u_\theta)^-\right\}^\theta \frac{\mathbf{e}_\theta}{r_m \Delta \theta} + \left\{(u_\theta u_r)^+ + (u_\theta u_r)^-\right\}^\theta \frac{\mathbf{e}_\theta}{2 r_m} \qquad (B.2\text{-}12)$$

$$\frac{1}{\delta V}\int_S \mathbf{n}\cdot(\nu\nabla\mathbf{u})dS$$

$$= \left\{\left(\nu\frac{\partial u_\theta}{\partial x}\right)^+ - \left(\nu\frac{\partial u_\theta}{\partial x}\right)^-\right\}^x \frac{\mathbf{e}_\theta}{\Delta x}$$

$$+ \left\{\left(\nu\frac{\partial u_\theta}{\partial r}\right)^+ r^+ - \left(\nu\frac{\partial u_\theta}{\partial r}\right)^- r^-\right\}^r \frac{\mathbf{e}_\theta}{r_m \Delta r}$$

$$+ \left\{\left(\nu\frac{\partial u_\theta}{\partial \theta}\right)^+ - \left(\nu\frac{\partial u_\theta}{\partial \theta}\right)^-\right\}^\theta \frac{\mathbf{e}_\theta}{r_m^2 \Delta \theta} + \left\{(\nu u_r)^+ - (\nu u_r)^-\right\}^\theta \frac{\mathbf{e}_\theta}{r_m^2 \Delta \theta}$$

$$+ \left\{\left(\nu\frac{\partial u_r}{\partial \theta}\right)^+ + \left(\nu\frac{\partial u_r}{\partial \theta}\right)^-\right\}^\theta \frac{\mathbf{e}_\theta}{2 r_m^2} - \left\{(\nu u_\theta)^+ + (\nu u_\theta)^-\right\}^\theta \frac{\mathbf{e}_\theta}{2 r_m^2} \qquad (B.2\text{-}13)$$

$$\frac{1}{\delta V}\int_S \mathbf{n}\cdot(\nu\nabla\mathbf{u})^T dS$$

$$= \left\{\left(\nu\frac{\partial u_x}{\partial \theta}\right)^+ - \left(\nu\frac{\partial u_x}{\partial \theta}\right)^-\right\}^x \frac{\mathbf{e}_\theta}{r_m \Delta x}$$

$$+ \left\{\left(\nu\frac{\partial u_r}{\partial \theta}\right)^+ - \left(\nu\frac{\partial u_r}{\partial \theta}\right)^-\right\}^r \frac{\mathbf{e}_\theta}{r_m \Delta r} - \left\{(\nu u_\theta)^+ - (\nu u_\theta)^-\right\}^r \frac{\mathbf{e}_\theta}{r_m \Delta r}$$

$$+ \left\{\left(\nu\frac{\partial u_\theta}{\partial \theta}\right)^+ - \left(\nu\frac{\partial u_\theta}{\partial \theta}\right)^-\right\}^\theta \frac{\mathbf{e}_\theta}{r_m^2 \Delta \theta} + \left\{(\nu u_r)^+ - (\nu u_r)^-\right\}^\theta \frac{\mathbf{e}_\theta}{r_m^2 \Delta \theta}$$

$$+ \left\{\left(\nu\frac{\partial u_\theta}{\partial r}\right)^+ + \left(\nu\frac{\partial u_\theta}{\partial r}\right)^-\right\}^\theta \frac{\mathbf{e}_\theta}{2 r_m} \qquad (B.2\text{-}14)$$

All terms in the axial momentum equation are evaluated according to equations B.2-6, B.2-7, and B.2-8. Likewise, all terms in the radial momentum equation are evaluated according to equations B.2-9, B.2-10, and B.2-11, with one exception. The term:

$$\frac{\nu}{r^2}\frac{\partial u_\theta}{\partial \theta} = \left\{\left(\nu\frac{\partial u_\theta}{\partial \theta}\right)^+ + \left(\nu\frac{\partial u_\theta}{\partial \theta}\right)^-\right\}^\theta \frac{1}{2r_m^2}$$

appearing in both equation B.2-10 and B.2-11, can not be evaluated in this form, unless the differencing stencil is expanded to include four points (as can be seen from figure B.2-2). It is not desirable to expand the differencing stencil, and the conservative evaluation of this particular term is therefore abandoned. Instead the term is evaluated as a source term, at the center of the control-volume.

The same arguments apply to the following two terms from equations B.2-13 and B.2-14:

$$\frac{\nu}{r^2}\frac{\partial u_r}{\partial \theta} = \left\{\left(\nu\frac{\partial u_r}{\partial \theta}\right)^+ + \left(\nu\frac{\partial u_r}{\partial \theta}\right)^-\right\}^\theta \frac{1}{2r_m^2}$$

$$\frac{\nu}{r}\frac{\partial u_\theta}{\partial r} = \left\{\left(\nu\frac{\partial u_\theta}{\partial r}\right)^+ + \left(\nu\frac{\partial u_\theta}{\partial r}\right)^-\right\}^\theta \frac{1}{2r_m}$$

These terms cannot be treated with a conservative formulation without expanding the differencing stencil. The terms are therefore evaluated as source terms. All other terms in the azimuthal momentum equation are treated according to equations B.2-12, B.2-13 and B.2-14.

As on a Cartesian grid, linear interpolation is used to get quantities at locations between naturally occurring grid-nodes. Special treatment at the centerline is described in chapter 3, part II.

B.3 Temporal Integration

The three-step time-advancement scheme (Spalart, 1987, Spalart *et al.*, 1991) used to integrate the momentum equations was presented in section 3.3.1, part I (see specifically equation 3.3-4). This section shows the form of the A (explicit treatment) and B (implicit treatment) operators used in coaxial jet-combustor calculations.

As explained in section 3.3, part II, the computational domain has been divided into two regions, one (core-region) in which all terms with derivatives in the azimuthal direction are treated implicitly, and the other (outer-region) in which all terms with derivatives in the radial direction are treated implicitly. In the core-region the A and B operators are defined as:

$$A_1 = \frac{\partial}{\partial x}\left(2\nu\frac{\partial u_x}{\partial x} - u_x u_x\right) + \frac{1}{r}\frac{\partial}{\partial r}\left(r\nu\frac{\partial u_x}{\partial r} + r\nu\frac{\partial u_r}{\partial x} - ru_x u_r\right)$$

$$+ \frac{1}{r}\frac{\partial}{\partial \theta}\left(\nu\frac{\partial u_\theta}{\partial x}\right) \tag{B.3-1a}$$

$$A_2 = \frac{\partial}{\partial x}\left(\nu\frac{\partial u_r}{\partial x} + \nu\frac{\partial u_x}{\partial r} - u_r u_x\right) + \frac{1}{r}\frac{\partial}{\partial r}\left(2r\nu\frac{\partial u_r}{\partial r} - ru_r u_r\right)$$

$$+ \frac{1}{r}\frac{\partial}{\partial \theta}\left(\nu\frac{\partial u_\theta}{\partial r} - \nu\frac{u_\theta}{r}\right) - \left(\frac{2\nu}{r^2}\frac{\partial u_\theta}{\partial \theta} + 2\nu\frac{u_r}{r^2} - \frac{u_\theta u_\theta}{r}\right) \tag{B.3-1b}$$

$$A_3 = \frac{\partial}{\partial x}\left(\nu\frac{\partial u_\theta}{\partial x} + \frac{\nu}{r}\frac{\partial u_x}{\partial \theta} - u_\theta u_x\right) + \frac{1}{r}\frac{\partial}{\partial r}\left(r\nu\frac{\partial u_\theta}{\partial r} + \nu\frac{\partial u_r}{\partial \theta} - \nu u_\theta - ru_\theta u_r\right)$$

$$+ \frac{1}{r}\frac{\partial}{\partial \theta}\left(\frac{2\nu u_r}{r}\right) + \left(\frac{\nu}{r}\frac{\partial u_\theta}{\partial r} + \frac{\nu}{r^2}\frac{\partial u_r}{\partial \theta} - \frac{\nu u_\theta}{r^2} - \frac{u_\theta u_r}{r}\right) \tag{B.3-1c}$$

$$B_1 = \frac{1}{r}\frac{\partial}{\partial \theta}\left(\frac{\nu}{r}\frac{\partial u_x}{\partial \theta}\right) - \frac{1}{r}\frac{\partial u_x u_\theta}{\partial \theta} \tag{B.3-2a}$$

$$B_2 = \frac{1}{r}\frac{\partial}{\partial \theta}\left(\frac{\nu}{r}\frac{\partial u_r}{\partial \theta}\right) - \frac{1}{r}\frac{\partial u_r u_\theta}{\partial \theta} \tag{B.3-2b}$$

$$B_3 = \frac{1}{r}\frac{\partial}{\partial \theta}\left(2\frac{\nu}{r}\frac{\partial u_\theta}{\partial \theta}\right) - \frac{1}{r}\frac{\partial u_\theta u_\theta}{\partial \theta} \tag{B.3-2c}$$

Similarly the A and B operators in the <u>outer-region</u> are defined as:

$$A_1 = \frac{\partial}{\partial x}\left(2\nu\frac{\partial u_x}{\partial x} - u_x u_x\right) + \frac{1}{r}\frac{\partial}{\partial r}\left(r\nu\frac{\partial u_r}{\partial x}\right)$$

$$+ \frac{1}{r}\frac{\partial}{\partial \theta}\left(\frac{\nu}{r}\frac{\partial u_x}{\partial \theta} + \nu\frac{\partial u_\theta}{\partial x} - u_x u_\theta\right) \tag{B.3-3a}$$

$$A_2 = \frac{\partial}{\partial x}\left(\nu\frac{\partial u_r}{\partial x} + \nu\frac{\partial u_x}{\partial r} - u_r u_x\right)$$

$$+ \frac{1}{r}\frac{\partial}{\partial \theta}\left(\frac{\nu}{r}\frac{\partial u_r}{\partial \theta} + \nu\frac{\partial u_\theta}{\partial r} - \nu\frac{u_\theta}{r} - u_r u_\theta\right)$$

$$- \left(\frac{2\nu}{r^2}\frac{\partial u_\theta}{\partial \theta} + 2\nu\frac{u_r}{r^2} - \frac{u_\theta u_\theta}{r}\right) \tag{B.3-3b}$$

$$A_3 = \frac{\partial}{\partial x}\left(\nu\frac{\partial u_\theta}{\partial x} + \frac{\nu}{r}\frac{\partial u_x}{\partial \theta} - u_\theta u_x\right) + \frac{1}{r}\frac{\partial}{\partial r}\left(\nu\frac{\partial u_r}{\partial \theta} - \nu u_\theta\right)$$

$$+ \frac{1}{r}\frac{\partial}{\partial \theta}\left(2\frac{\nu}{r}\frac{\partial u_\theta}{\partial \theta} + \frac{2\nu u_r}{r} - u_\theta u_\theta\right)$$

$$+ \left(\frac{\nu}{r}\frac{\partial u_\theta}{\partial r} + \frac{\nu}{r^2}\frac{\partial u_r}{\partial \theta} - \frac{\nu u_\theta}{r^2} - \frac{u_\theta u_r}{r}\right) \tag{B.3-3c}$$

$$B_1 = \frac{1}{r}\frac{\partial}{\partial r}\left(r\nu\frac{\partial u_x}{\partial r}\right) - \frac{1}{r}\frac{\partial(r u_x u_r)}{\partial r} \tag{B.3-4a}$$

$$B_2 = \frac{1}{r}\frac{\partial}{\partial r}\left(2r\nu\frac{\partial u_r}{\partial r}\right) - \frac{1}{r}\frac{\partial(r u_r u_r)}{\partial r} \tag{B.3-4b}$$

$$B_3 = \frac{1}{r}\frac{\partial}{\partial r}\left(r\nu\frac{\partial u_\theta}{\partial r}\right) - \frac{1}{r}\frac{\partial(r u_\theta u_r)}{\partial r} \tag{B.3-4c}$$

Subscript 1,2,3 on the symbols for the operators (A, B) indicates the axial, radial and azimuthal equations, respectively.
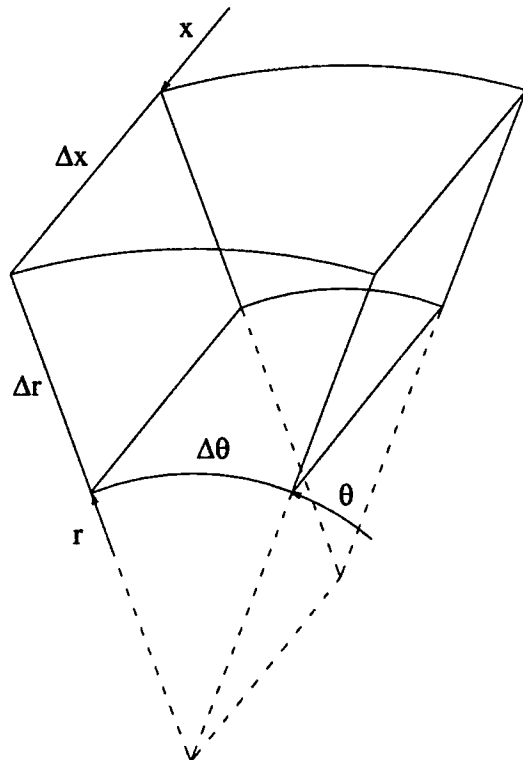
FIGURE **B.2-1**, Grid cell in 3 dimensions, cylindrical coordinates.
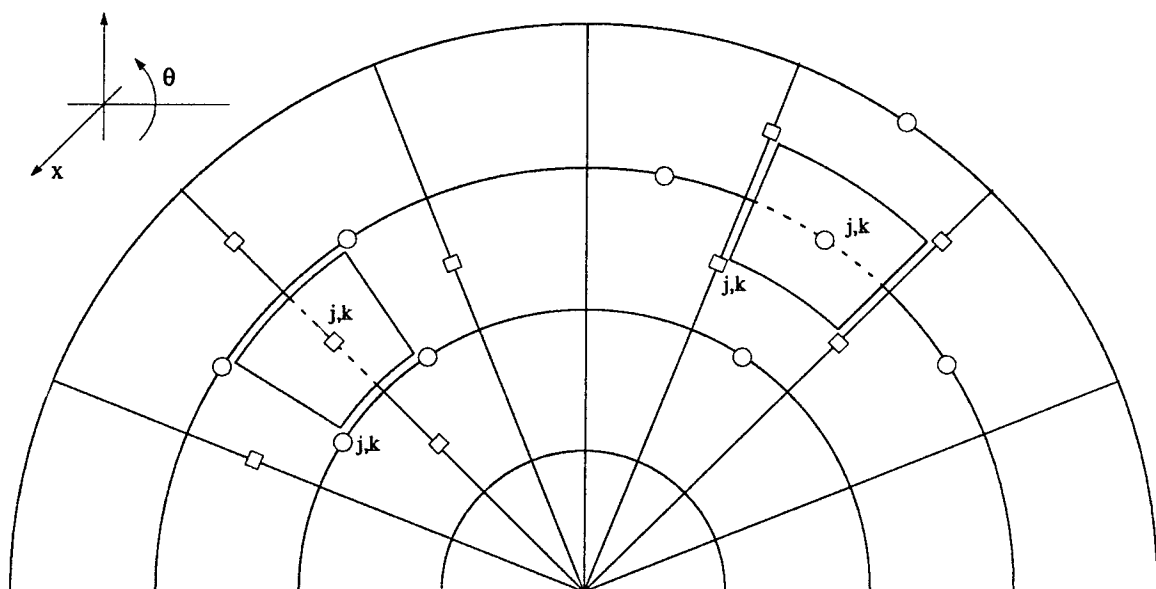
FIGURE **B.2-2**, Staggered grid in cylindrical coordinates.   o : location for u_r, □ : location for u_θ.

TURBULENT PIPE-FLOW

This appendix summarizes the results from a DNS and a LES of turbulent flow in a circular pipe. The Reynolds number was 180 (based on pipe radius and friction velocity), and the results are compared with the experimental results of Westerweel *et al.* (1992) (see also Eggels *et al.*, 1994), and DNS results by Eggels *et al.* (1994).

The objective of the simulations is to validate the numerical method developed for the coaxial jet-combustor calculations, described in chapter 3, part II.

Section C.1 gives a brief description of the two reference cases, and section C.2 describes the computational setup. Results, including mean quantities and second order statistics are described in section C.3, and a few words about the computer program performance are included in section C.4. Section C.5 offers conclusions.

C.1 Reference Cases

C.1.1 <u>Experiments</u>

Measurements (Westerweel *et al.*, 1992) were done near the end of a smooth pipe with radius (R) 63.5 mm, and length $268R$. The Reynolds number was 2725 based on bulk velocity and radius, R. Both laser Doppler anemometry (LDA) and particle image velocimetry (PIV) were used in the experiments. The air flow through the pipe passed a settling chamber, a honeycomb, and a square grid with mesh size of 1 mm and a solidity of about 1, before entering the pipe. The purpose of the grid was to reduce the development length needed to reach a fully developed turbulent state.

C.1.2 <u>Direct Numerical Simulation</u>

The computational domain used by Eggels *et al.* (1994), consisted of a cylindrical pipe of length $10R$. The Reynolds number was 180 (based on radius, R, and friction velocity, u_τ). Periodic boundary conditions were used in the axial and azimuthal directions, and no-slip was used along the wall. The grid had $256 \times 96 \times 128$ points in the axial, radial and azimuthal directions, respectively. The computational grid was uniform in all coordinate directions.

Due to the fine azimuthal grid spacing near the centerline, all terms with derivatives in the azimuthal direction were treated implicitly in the entire computational domain. All other terms were treated explicitly. The implicit time-integration scheme applied second order Crank-Nicholson to the convective terms, and first order implicit Euler to the diffusive terms. The explicit time-integration scheme used second order Leapfrog on the convective terms and first order explicit Euler on the diffusive terms.

Since all terms with radial derivatives were treated explicitly, the maximum allowable time-step (for stability reasons) was restricted by the radial grid-spacing. The radial grid-spacing was $\Delta r^+ = 1.88$ in wall-coordinates, which limited the time-step, Δt, to 0.0004 time-units (R/u_τ).

After reaching a statistically steady state, statistics were collected over a period of 4 time-units at intervals spaced roughly 0.1 time-units apart. In addition, averaging was performed over the homogenous axial- and azimuthal directions.

C.2 Case Descriptions

Two calculations were performed at $Re_\tau = 180$, using the numerical scheme outlined in chapter 3, part II. The first is a DNS, using $256 \times 68 \times 128$ grid-points in the axial, radial, and azimuthal directions, respectively. The second is a LES, using $32 \times 38 \times 64$ grid points. The latter case is based on the DM model. The numerator and denominator in the expression for the model parameter, C, were averaged in the two homogenous directions, leaving C a function of the radial coordinate and time.

The grid was uniform in the streamwise and azimuthal directions, but non-uniform in the radial direction. The grid-spacings in wall-units are listed in table C.2-1 for the two cases (DNS and LES) as well as for the DNS case of Eggels *et al.* (DNS^e).

Case	Δx^+	$(R\Delta\theta)^+$	$(\Delta r\Delta\theta)_{cl}^+$	Δr_{wall}^+	Δr_{cl}^+	Δr_{max}^+
DNS^e	7.03	8.84	0.09	1.88	1.88	1.88
DNS	7.03	8.84	0.13	0.17	2.61	5.94
LES	56.3	17.7	0.42	0.69	4.28	8.87

TABLE **C.2-1**, Grid Resolution in wall-coordinates.

The minimum grid spacing (at the wall) in the radial direction gives the location for the first u_r velocity-point off the wall. The azimuthal grid-spacing at the centerline uses the radial distance to the first u_r velocity-point away from the centerline.

From table C.2-1 it is evident that the radial grids used for the present DNS and LES cases were somewhat refined near the centerline, in addition to a significant refinement at the wall. The radial refinement towards the centerline was found to give a slightly better agreement with the DNS of Eggels *et al.*, compared with a case with no radial grid-refinement. The DNS with no radial grid-refinement at the centerline gave $\Delta r_{max}^+ = \Delta r_{cl}^+ = 8.8$.

As explained in chapter 3, part II, the temporal integration scheme splits the computational domain into two parts; the core-region and the outer region. For

the present pipe calculations, the interface between the two regions was located at $0.5R$.

The DNS was run at a fixed time-step, Δt, of 0.001 time-units, whereas the LES was run with $\Delta t = 0.002$. The DNS was run 11.7 time-units in order to flush out transients resulting from the initial condition. Statistics were then collected at every time-step over a period of 14.1 time-units. The LES was run 43.6 time-units to flush out transients, followed by 41.2 time-units for sampling statistics. Statistics were calculated by averaging in time as well as in the homogenous axial and azimuthal coordinate directions.

C.3 Results

This section shows the results from the DNS and LES done in order to verify the numerical algorithm outlined in chapter 3, part II.

C.3.1 <u>Mean Flow Properties</u>

Several mean flow properties from the present simulations and the reference cases are listed in table C.3-1. Following Eggels *et al.* (1994), the following definitions were adopted for the displacement thickness, δ^*, and the momentum thickness, θ^*:

$$\delta^*(2 - \delta^*) = 2 \int_0^1 r\left(1 - \frac{u_x(r)}{U_{cl}}\right) dr \qquad (C.3\text{-}1)$$

$$\theta^*(2 - \theta^*) = 2 \int_0^1 r\frac{u_x(r)}{U_{cl}}\left(1 - \frac{u_x(r)}{U_{cl}}\right) dr \qquad (C.3\text{-}2)$$

where U_{cl} is the centerline velocity, and all variables have been normalized using the radius, R, and the friction velocity, u_τ. The coefficient of friction given in table C.3-1 is based on the bulk velocity, U_b, and calculated from:

$$C_f = \frac{\tau_w}{\frac{1}{2}\rho U_b^2} \qquad (C.3\text{-}3)$$

From table C.3-1 it follows that the present DNS results agree to within a few tenths of a percent with those of Eggels *et al.* Good agreement with the experimental results of Westerweel *et al.* is also observed. Minor deviations are observed between the LES results and the DNS results. In particular, the coefficient of friction is too low, which explains the higher bulk velocity. The deviations are similar to those found between LES and DNS of turbulent channel flow (when using second order spatial discretization schemes).

The mean velocity profile, normalized by the centerline velocity, U_{cl}, is shown in figure C.3-1. Figure C.3-2 shows the mean velocity profiles plotted in wall coordinates. Excellent agreement between the present DNS results and the two reference cases is observed. The mean velocity profile from the LES, on the other hand, shows a small over-prediction in the log-region.

	LES	DNS	DNS^e	PIV	LDA
Re_τ	180	180	180	183	185.5
U_{cl}	19.15	19.32	19.31	19.38	19.39
U_b	15.11	14.70	14.73	14.88	14.68
U_{cl}/U_b	1.27	1.31	1.31	1.30	1.32
$C_f \cdot 10^3$	8.76	9.25	9.22	9.03	9.28
δ^*	0.112	0.128	0.127	0.124	0.130
θ^*	0.059	0.069	0.068	0.068	0.071
H	1.89	1.85	1.86	1.83	1.83

TABLE **C.3-1**, Mean flow properties. PIV and LDA are measurements from Westerweel *et al.* DNS^e are results from Eggels *et al.* LES and DNS are results from the present calculations.

C.3.2 Turbulence Intensities

Turbulence intensities are shown in figures C.3-3, C.3-4, and C.3-5. (The LES results include the resolved part of the intensities only). An overall excellent agreement is observed between the present DNS and the DNS of Eggels *et al.* The increase in $(u_r'')_{rms}$ from the PIV measurements near the wall is attributed to the data being obscured by noise at small scales. The somewhat high value in $(u_x'')_{rms}$ from the PIV measurements around the peak is by Westerweel *et al.* regarded as a statistical error. Despite these problems the experimental values agree reasonably well with the DNS data.

Discrepancies are, however, observed between the LES results and results from the other cases. It can in particular be noticed that $(u_x'')_{rms}$ is over-predicted, whereas $(u_r'')_{rms}$ and $(u_\theta'')_{rms}$ are under-predicted. This is a well known consequence of inadequate grid resolution in numerical simulations of wall bounded flows.

C.3.3 Turbulent Shear Stress

The turbulent shear stress is shown in figure C.3-6. Only minor difference are observed between the present DNS and the DNS of Eggels *et al.* The turbulent shear stress from the LES, which includes the contribution from the subgrid scale

model, does also show very good agreement when compared with the DNS results.

Figure C.3-7 shows the resolved part of the turbulent shear stress from the LES, compared with the total shear stress. Also shown is the subgrid scale shear stress. It is evident that the subgrid scale contribution to the total shear stress is small, peaking at about 6-7 percent of the resolved shear stress.

Figure C.3-8 shows the ratio of the eddy-viscosity to molecular viscosity as a function of radius. The maximum value is about 0.25.

The total stress balance in the pipe is shown in figure C.3-9. The linearity of the total stress profile is confirmed.

C.4 Computer Program Performance

As pointed out previously, the time-integration method developed in chapter 3, part II, splits the computational domain into two parts, treating different terms in each part with implicit or explicit time-integration schemes. The purpose is to avoid the severe time-step limitations usually encountered in cylindrical geometries due to the fine azimuthal grid around the centerline. At the same time it is important to resolve the wall-layer properly without being penalized unnecessarily in terms of reduced time-step.

The method used by Eggels *et al.* (1994), solved the problem at the centerline by treating all terms with derivatives in the azimuthal direction implicitly. However, this leaves a trade-off between minimum radial resolution and maximum time-step. The radial grid-spacing used by Eggels *et al.*, was $\Delta r^+ = 1.88$. In order to avoid numerical instabilities, the maximum time-step, Δt, was then limited to 0.0004 R/u_τ.

For comparison, the maximum time-step used in the present DNS calculation was 0.001 R/u_τ (a factor of 2.5 higher than that used by Eggels *et al.*), with a minimum radial grid-spacing at the wall of $\Delta r^+ = 0.17$. This is a factor of 10 smaller than the radial grid-spacing used by Eggels *et al.* Since the maximum time-step goes as Δr^2, the radial resolution used in the present case would not have been practical if only terms with derivatives in the azimuthal direction were treated implicitly.

Eggels *et al.* report that their code needed about 5.7 CPU hours per time-unit on a Cray YMP. This would correspond to about 2.6 CPU hours on a Cray C-90. Due to the higher time-step used in the present DNS calculation, we needed only about 1.3 CPU hours per time-unit. For comparison, the LES calculation needed about 0.1 CPU hours per time-unit.

The present DNS, covering a total of 25.8 time-units, required about 34 CPU hours to complete on a Cray C-90. The LES, covering 90 time-units (which probably is an overkill) took 8 CPU hours to complete.

The conclusion is that the numerical method developed in chapter 3, part II is significantly less CPU consuming than the simpler approach used by Eggels *et al.*, yet it allows for more flexibility in terms of radial and azimuthal grid spacings.
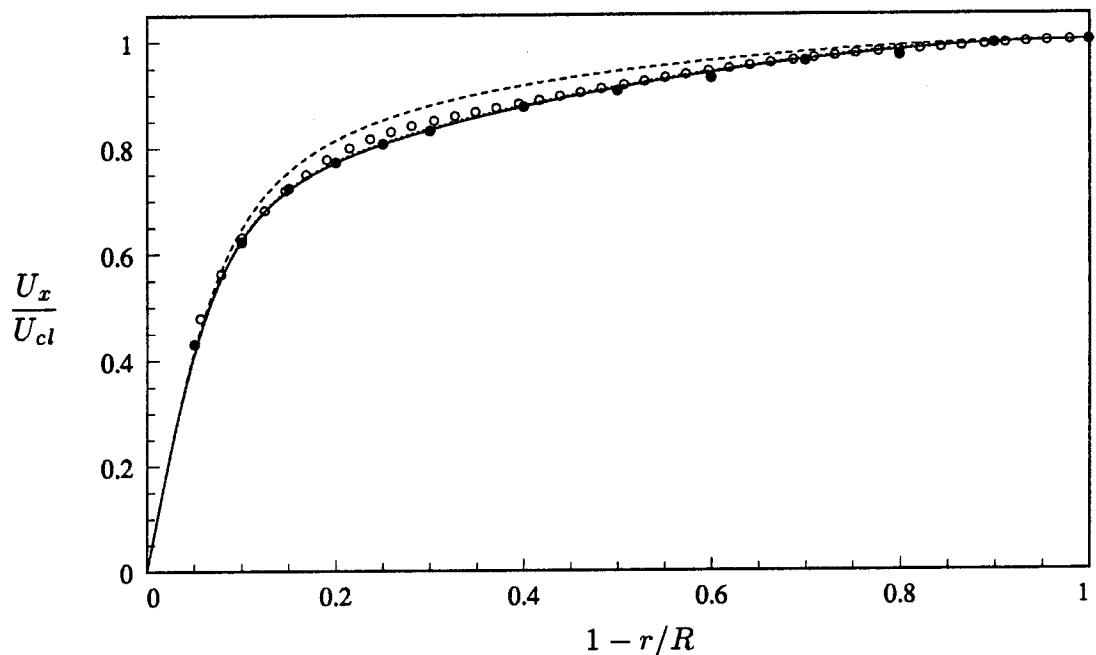
FIGURE **C.3-1**, Mean velocity profile. ——— : DNS; – – – – : LES;
········· : DNS[e]; o : PIV, Westerweel *et al.*; ● : LDA, Westerweel *et al.*
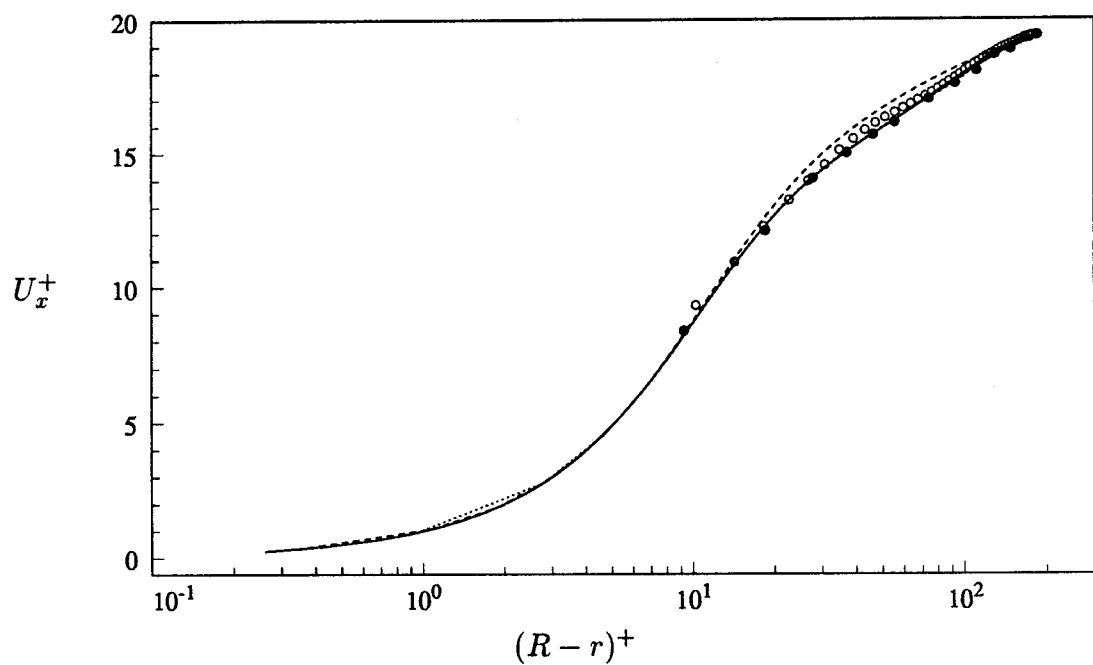
FIGURE **C.3-2**, Mean velocity profile. ——— : DNS; – – – – : LES;
········· : DNS[e]; o : PIV, Westerweel *et al.*; ● : LDA, Westerweel *et al.*
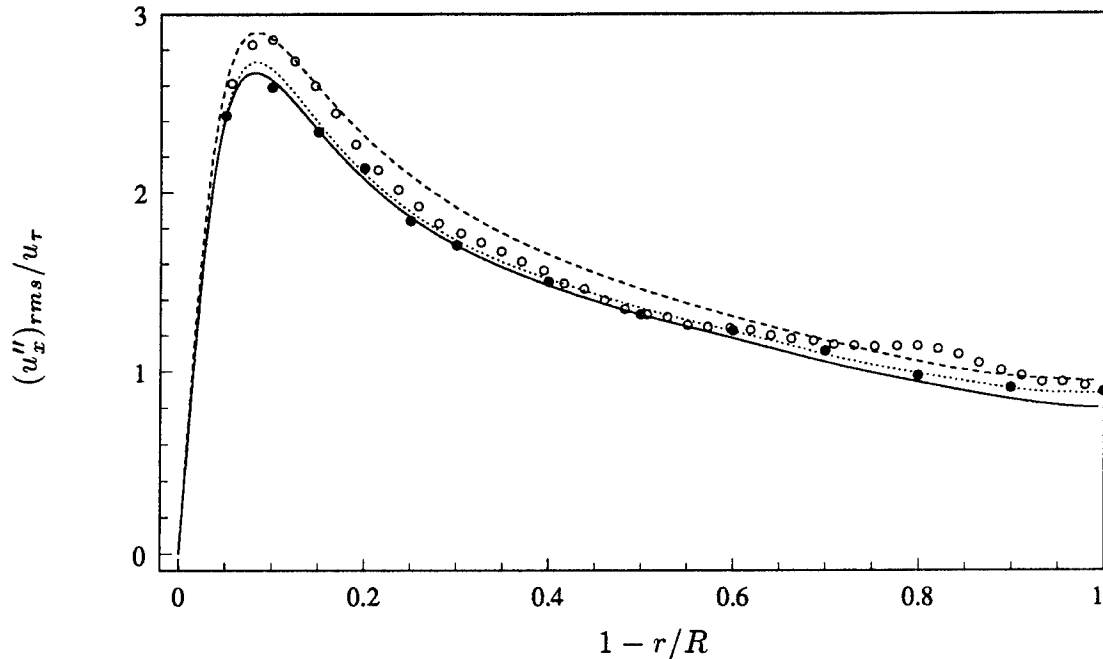
FIGURE **C.3-3**, Axial turbulence intensity. ———— : DNS; ————: LES (resolved part only); ········· : DNS^e; o : PIV, Westerweel *et al.*; • : LDA, Westerweel *et al.*
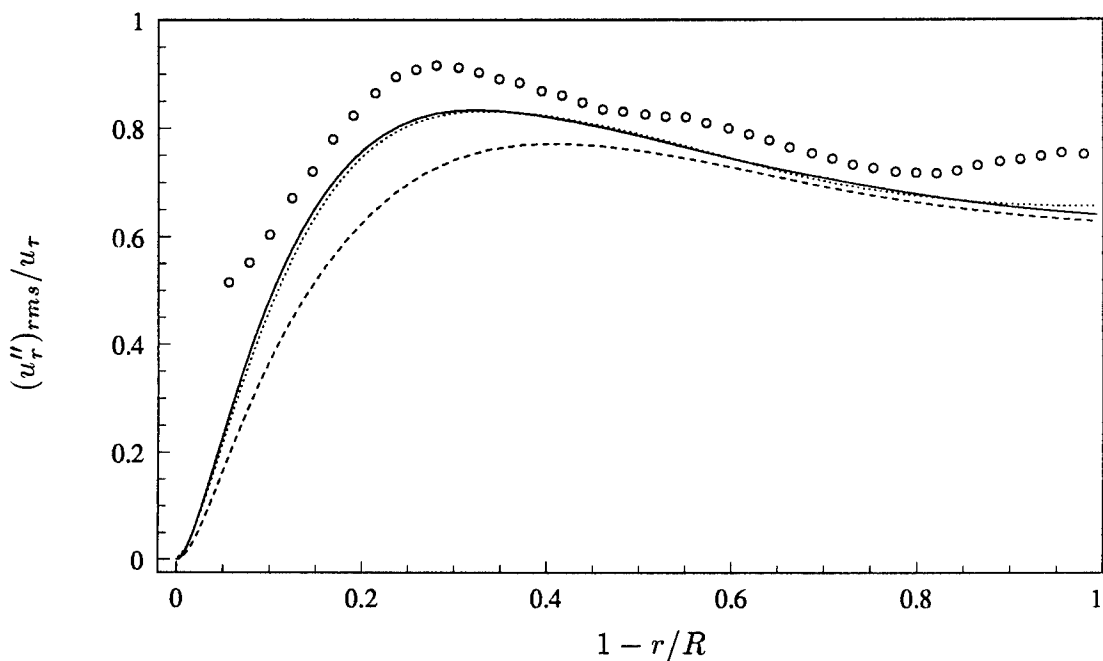

FIGURE **C.3-4**, Radial turbulence intensity. ———— : DNS; ————: LES (resolved part only); ········ : DNS^e; o : PIV, Westerweel *et al.*
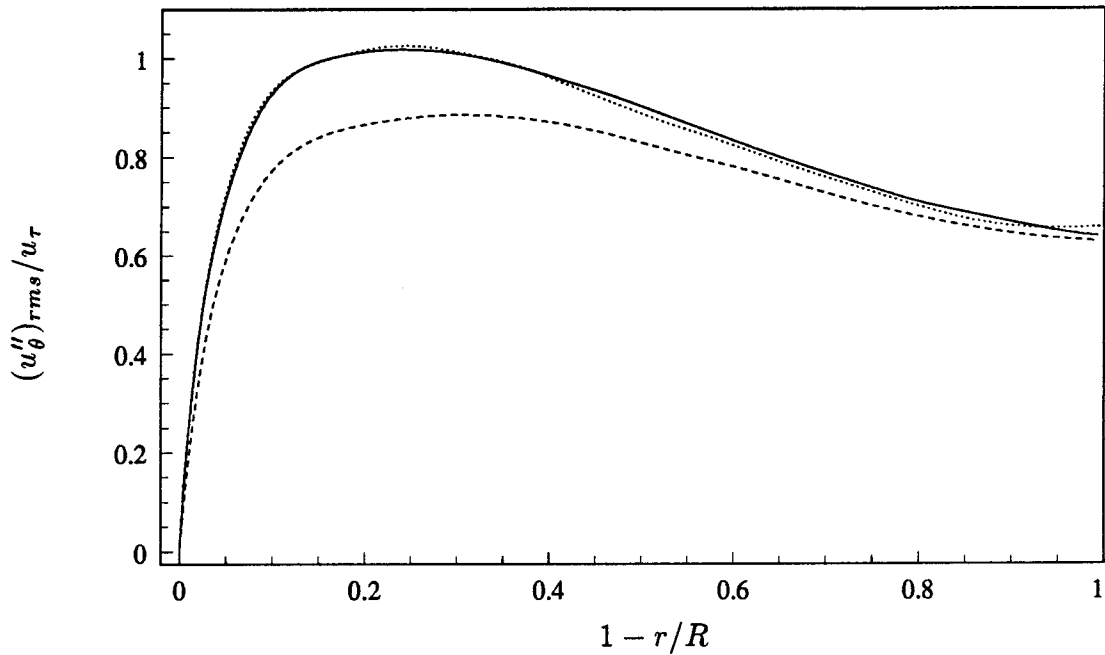
FIGURE **C.3-5**, Azimuthal turbulence intensity. ——— : DNS; ‐‐‐‐ : LES (resolved part only); ········ : DNS^e.
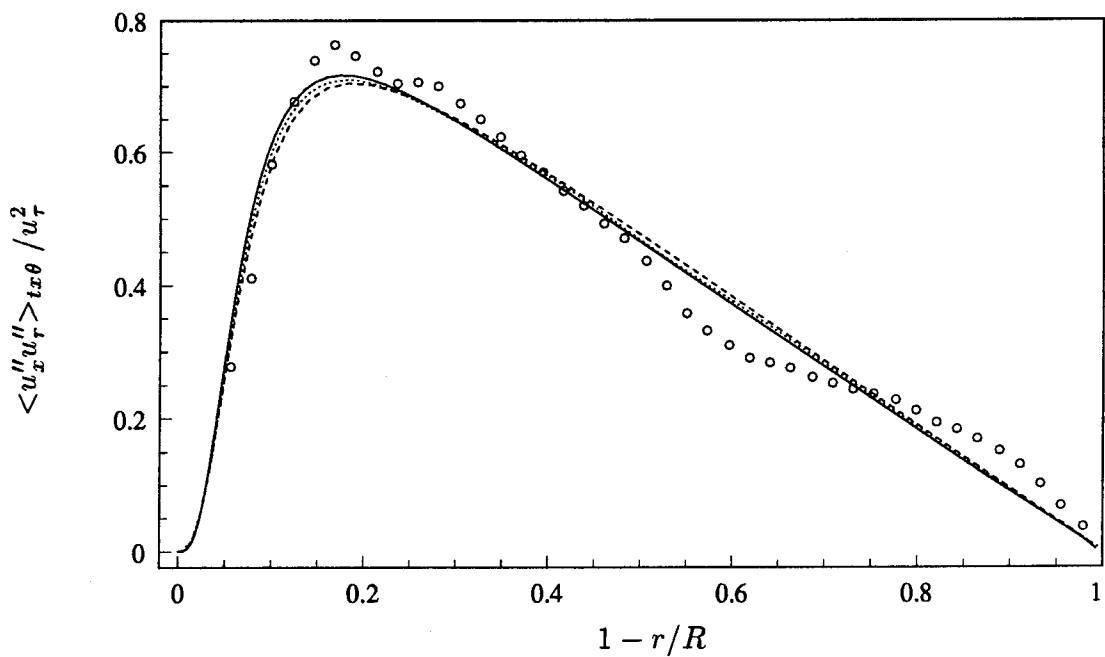
FIGURE **C.3-6**, Turbulent shear stress. ——— : DNS; ‐‐‐‐ : LES (including SGS term); ········ : DNS^e; o : PIV, Westerweel *et al.*
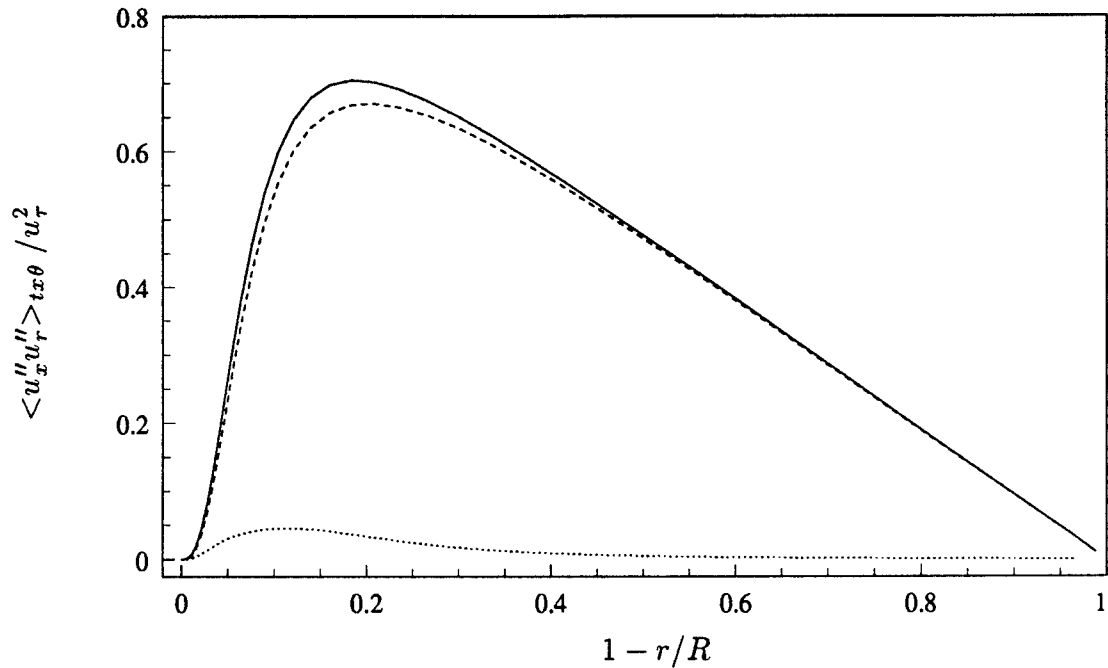
FIGURE **C.3-7**, Turbulent shear stress. ——— : LES, Including SGS model contribution; – – – – : LES, Resolved stress only; ········ : Subgrid scale stress.
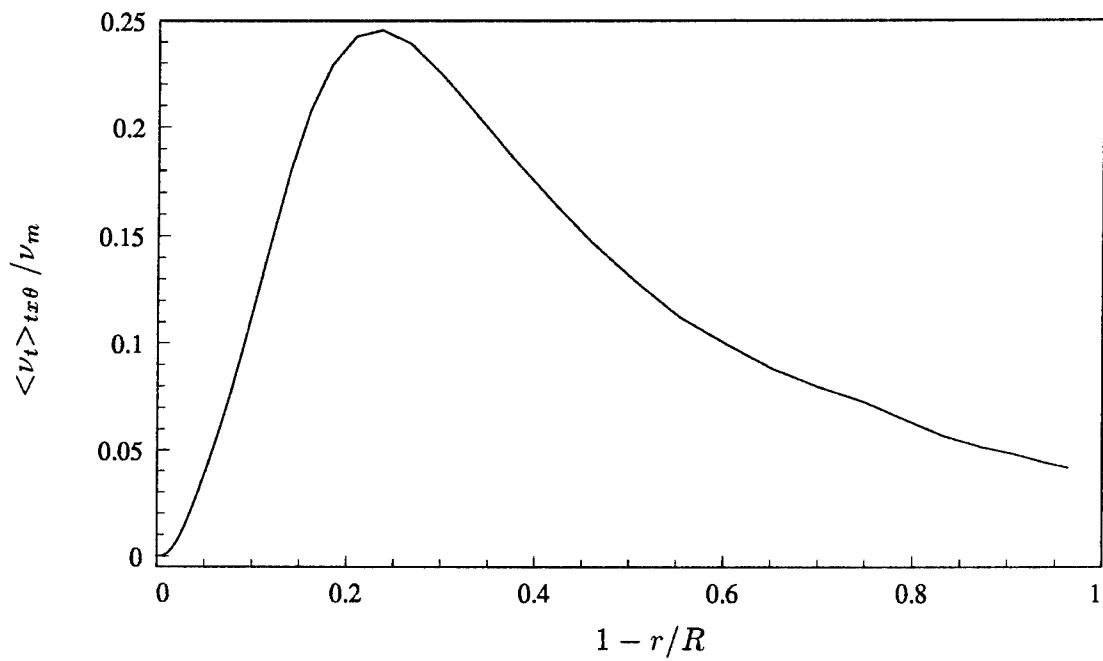

FIGURE **C.3-8**, Ratio of eddy-viscosity to molecular viscosity.
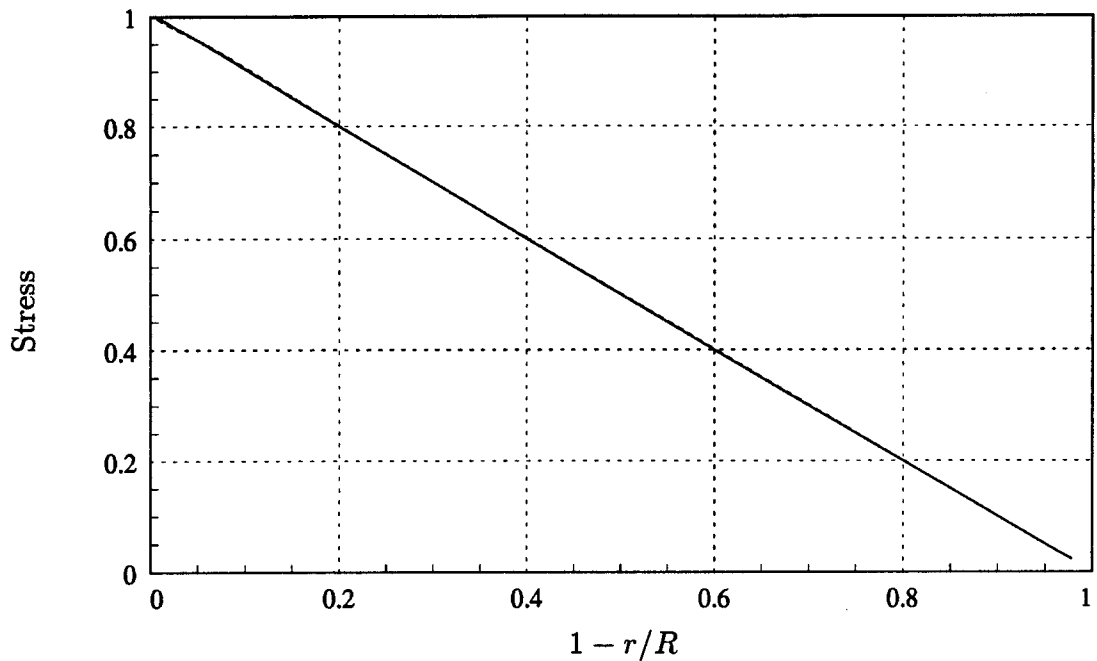
FIGURE **C.3-9**, Total stress balance. ———— : DNS;   - - - - : LES.

COAXIAL JET-COMBUSTOR

This appendix contains three sections related to the contents of chapter 5, part II. Section D.1, includes results from the preliminary calculations performed of the coaxial jet-combustor in order to determine the grid-resolution requirements for the basic case (described in chapter 4, part II). Section D.2 focuses on the case that was labeled the "animation case" in the introduction of chapter 4, part II. Results from this case were animated and recorded on video-tape. Section D.2 includes the computational setup used for the animation case, a description of the contents of the video-tape, and a comparison of statistical quantities with those of the basic case (chapter 5, part II) and experiments (Johnson & Bennett, 1981, 1984).

Section D.3, shows results from a calculation performed using the same grid resolution as the animation case, but with the fuel mass-fraction at the inlet changed in order to give a jet (bulk) velocity ratio of 2.2 (instead of 3.1 which was used in all other cases). The latter case was motivated by the fact that there seems to be an inconsistency in the experimental data of Johnston & Bennett. The volume flow-rates (in the central and annular pipes) quoted in the report gives a velocity ratio of 3.1. Yet, by analysing the measured mean velocity profile at the first measurement station (x/h=0.41) the velocity ratio seems to have been closer to 2.2.

D.1 Preliminary Calculations

This section shows results from preliminary calculations done to determine the grid resolution for the basic case. The grid was varied independently in all three coordinate directions, using three different resolutions in each direction. Thus, a total of seven cases were considered. The length of the inlet section was $1h$ in some cases and $5h$ in others. The length of the downstream region was approximately $20h$ in all cases. All flow parameters were the same as those used in chapter 5, part II.

It should be pointed out that due to excessive computer requirements the statistical sampling period was kept short in all of the preliminary calculations. In most cases statistics were sampled over no more than 30-60 time-units (h/U_c), corresponding to 1-2 flow-through times. For first and second order statistics sampled at the axial stations closest to the point of expansion the short sampling time seemed to be sufficient to get reasonable convergence. However, it is harder to reach a converged state further downstream.

D.1.1 Axial Resolution

Three different axial resolutions were considered, keeping the radial and azimuthal resolutions the same. The inlet section in all cases extended $5h$ upstream of the expansion. The number of grid-points used in each case are given in table D.1-1. N_x gives the total number of grid-points in the axial direction and N_x^{inlet} gives the number of axial points used to cover the (rather long) inlet section. Table D.1-1 also gives an identifying label associated with each case. Figure D.1-1 shows the axial grid-spacing, Δx, versus axial distance, x. The radial grid was the same as that used in the basic case, but the azimuthal grid had only 64 points, compared with 128 points in the basic case.

It should be pointed out that case CX2 is the same as the "animation" case (see appendix D.2). This case was run about 120 time units (4 flow-through times) to remove transients (resulting from interpolation of the initial flow-field) before starting to save frames for the animation, and sample statistics. Statistics were collected over a period of 120 time-units. Thus, the results from case CX2 are statistically well converged. Cases CX1 and CX3, on the other hand, were run

only 37 and 51 time-units, respectively, for gathering statistics following a period of about 30 time-units used to remove transients from the initial flow-fields.

	N_x	N_x^{inlet}	N_r	N_θ
CX1	98	35	76	64
CX2	192	70	76	64
CX3	353	130	76	64

TABLE **D.1-1**, Number of grid-points for the axial resolution-study cases.

Six quantities are used to compare the results from the three calculations. These include mean axial and radial velocities, turbulence intensities in all three coordinate directions, and the turbulent shear stress. The turbulence intensities include only the resolved part of the quantity, whereas the turbulent shear stress includes the SGS model contribution.

Figure D.1-2 shows the mean axial velocity profiles at streamwise stations ranging from $x/h = 0.41$ to $x/h = 8.06$. At the first three stations there seems to be a significant change in the results when going from the coarse to the medium grid (i.e. from case CX1 to case CX2). At the same three stations, the change in going from the medium to the fine grid is negligible. At the last three measurement stations, only minor differences are observed between any of the three cases. The same trend is observed from the mean radial velocity, shown in figure D.1-3. The coarse grid solution really stands out at the first three measurement stations, however, all grids give nearly identical results at the last three stations.

The resolved part of the axial turbulence intensity is shown in figure D.1-4. The differences between the results from the three grids are larger than those observed in the mean velocity profiles. However, the general trend seems to be that there is a significant change in the results when going from the the coarse to the medium grid. The results from the medium and fine grids (cases CX2 and CX3) are, on the other hand, in fair agreement at all stations.

Figure D.1-5, showing the resolved radial turbulence intensity, gives roughly the same trend. At the last four measurement stations no significant differences are observed between the medium and the fine grid. The coarse grid solution is also in close agreement with the solutions from the two finer grids. However, at the first two measurement stations there is a significant change in the results between the

coarse and the medium grid verifying that the coarse grid it too coarse. In the near centerline region there is also a difference between the results from medium grid and the fine grid, indicating that the medium grid is too coarse in this particular region. The azimuthal turbulence intensity, shown in figure D.1-6, leads to the same conclusions.

Based on the turbulence intensities it can be concluded that the coarsest grid is insufficient, mostly because of the poor performance close to the point of expansion. The medium grid is better, but the results improve, compared with experimental data, particularly in the near centerline region, when increasing the resolution from medium to fine. The medium grid seems, however, to be sufficient downstream of about $x/h = 3$.

Figure D.1-7 shows the turbulent shear stress, $<u_x'' u_r''>_{t\theta}$. A significant change in the results is observed when going from the coarse to the medium grid, particularly near the point of expansion. Only minor changes are seen between the medium and the fine grid. At the last few stations all grids give nearly identical results.

D.1.2 Radial Resolution

Three different radial resolutions were considered, keeping the axial and azimuthal resolutions the same. The number of grid-points used in each case is summarized in table D.1-2. The cases are labeled CR1, CR2, and CR3, in order of increasing radial resolution. (Note that case CR2 is the same as the case labeled CX2 in the previous section). The length of the inlet-section was $1h$ in case CR1 and $5h$ for cases CR2 and CR3, which explains the difference in N_x between the three cases. Figure D.1-8a shows the axial grid spacing, Δx, plotted versus axial distance, x, for the two axial grids. It is seen that the two grids are close to identical between $x/h = -1$ and the exit of the domain. Figure D.1-8b shows the radial grid spacing, Δr, versus radial distance, r. The statistics sampling time for cases CR1 and CR3 was about 40 time-units, compared with 120 time-units for case CR2.

Figures D.1-9 and D.1-10 show the mean axial and radial velocity profiles, respectively. It can be seen that changes in the radial resolution have almost no effect on the mean profiles. That is, even the coarsest radial grid would be sufficient.

However, the trend is not as clear when comparing the (resolved) axial turbulence intensity, shown in figure D.1-11. Differences are observed between the results

from the different cases at all streamwise stations. In particular it can be noticed that the coarse grid results (CR1) fall between the results from medium and fine grids at several of the measurement stations.

	N_x	N_x^{inlet}	N_r	N_θ
CR1	151	31	48	64
CR2	192	70	76	64
CR3	192	70	140	64

TABLE **D.1-2**, Number of grid-points for the radial resolution-study cases.

Figures D.1-12 and D.1-13 show the (resolved) radial and azimuthal turbulence intensities, respectively. In both cases only minor differences are observed in the results from the three cases. The same trend is observed in figure D.1-14, showing the turbulent shear stress.

D.1.3 Azimuthal Resolution

Three azimuthal resolutions were considered. The corresponding number of grid-points are listed in table D.1-3. The length of the inlet-section was $5h$ in all cases. The three cases are labeled $C\theta1$, $C\theta2$, and $C\theta3$, in order of increasing azimuthal resolution. Case $C\theta1$ is identical to the case labeled CR2 in section D.1.2 (which is also the same as case CX2 from section D.1.1). Statistics sampling time for cases $C\theta2$ and $C\theta3$ were 30, and 25 time-units, respectively. This is in contrast to the 120 time-units used in case $C\theta1$.

Mean axial velocity profiles are shown in figure D.1-15. For all but the first measurement station it is obvious that the two finest grids give almost identical results, whereas discrepancies are found in the coarse grid case. The same trend is observed in the mean radial velocity profiles, shown in figure D.1-16.

Figure D.1-17 shows the resolved axial turbulence intensities. As with the mean velocity profiles it is clear that the two finest grids, cases $C\theta2$ and $C\theta3$, give close to identical results. (The differences observed around $r/h = 1$ at the two last measurement stations are attributed to the short statistics sampling time). Figures D.1-18 and D.1-19, showing the resolved radial and azimuthal turbulence intensities, respectively, indicate the same trend.

	N_x	N_x^{inlet}	N_r	N_θ
Cθ1	192	70	76	64
Cθ2	192	70	76	128
Cθ3	192	70	76	256

TABLE **D.1-3**, Number of grid-points for the azimuthal resolution-study cases.

Figure D.1-20 shows the turbulent shear stress, $<u_x'' u_r''>_{t\theta}$. It is seen that the results from the medium and the fine grids are almost identical at all measurement stations, whereas the coarse grid is obviously not adequate.

D.1.4 <u>Conclusions</u>

The results presented in section D.1.3 show that 128 azimuthal grid-points are necessary and sufficient to obtain (roughly) grid independent results. However, the conclusions from refining the grid in the the two other directions are not as clear. For the axial direction it was shown that case CX2 (with 192 axial grid-points) was, for the most part, sufficient. However, the radial and azimuthal turbulence intensities show improved agreement with experimental results in the near centerline region, at the first two measurement stations, when the number of axial grid-points was increased from 192 to 353. It would therefore be desirable to use the finest axial grid.

Results from the radial resolution study found that even the coarsest grid (case CR1) gave satisfactory results, compared with the two finer grids, for all quantities but $(u_x'')_{rms}$. The latter quantity, however, gave no clear indication of which grid would be sufficient. This factor taken into account would lead to the conclusion that one should chose the finest grid ($N_r = 140$) in order to be safe.

Thus, the best grid seems to be $353 \times 140 \times 128$ points in the axial, radial, and azimuthal directions, respectively. However, estimates show that this grid would require of the order of 1500 CPU hours (Cray C-90) in order to obtain fully converged statistics, which is not practical. It therefore seems logical to sacrifice some of the accuracy by reducing the radial resolution from 140 to 76 points. After all, all results but $(u_x'')_{rms}$, showed that $N_r = 76$ gave satisfactory results. However, a basic case with $353 \times 76 \times 128$ grid-points would require about 700 CPU hours to complete, which is still rather expensive.

From the axial resolution study it seems apparent that $N_x = 192$ points gave grid independent results, except in the near centerline region at the first two measurement stations. Thus the finest resolution is for the most part not needed. Based on this information a new axial grid was designed for the basic case where the axial stretching function was changed to allow for a finer resolution for a longer distance downstream of the step, while not adding too many points downstream of about $x/h = 2$-3. This combined with cutting the inlet section from $5h$ to $1h$ gave an axial grid with 215 points.

Thus, based on a trade-off between accuracy and cost a grid of $215 \times 76 \times 128$ points (axial, radial, azimuthal) was chosen for the basic case (the results of which are summarized in chapter 5, part II). The estimated CPU time requirement was about 400 hours.

D.2 Animation

This section describes the details of a calculation performed to study the transient behavior of the mixing process in the coaxial jet-combustor. Results from the calculation were animated and recorded on video-tape. Tedious post-processing of the data for the animations was done by Mr. Charles Pierce at Stanford University. The animations were recorded at the NAS visualization Lab at NASA Ames Research Center, and the final editing of the video was performed by Imaging Technology Branch at NASA Ames Research Center. This calculation is referred to as the *animation* case.

D.2.1 <u>Contents of Video-tape</u>

Several quantities were animated and recorded on video-tape. These include contours of the axial velocity and scalar, and iso-surfaces of the scalar and regions of low pressure. Particle trajectories were also calculated using UFAT (Unsteady Flow Analysis Toolkit) (NASA Ames Research Center), and included on the video-tape.

The simulation used for the animation was started from a fully developed turbulent flow-field. Velocity and scalar fields were saved at every 30 time-step starting at initial time, $T = 0$. The time-step was held constant at $\Delta t = 0.0028 \, h/U_c$ which gave a spacing of 0.084 time-units between frames. The calculation was run for a total of 61200 time-steps, saving 2040 frames. The total time-period covered was 171.4 time-units, corresponding to approximately 5.7 flow-through times.

The first animation recorded on the tape shows a contour map of the axial velocity, u_x. The views include one x-r plane and three r-θ planes located at $x/h = 1$, 4, and 7. The animation covers 500 frames, starting at $T = 10.1$, ending at $T = 52$. The recording speed was 15 frames/sec. Total viewing time is about 33 seconds.

The most important quantity recorded is the evolution of the passive scalar field. (The passive scalar represents the fuel mass-fraction, with $\varphi = 0$ being pure air, and $\varphi = 1$ being pure fuel). At time $T < 0$, the value of the scalar is zero everywhere in the computational domain, indicating that there is no fuel present. At time $T = 0$ the scalar is set to 1 at the inflow boundary in the central fuel pipe, indicating the introduction of fuel. At time $T = 121$ (about 4 flow-through times),

the inflow condition for the scalar is abruptly reset to zero in the central fuel pipe, signifying that pure air is now entering through the central pipe (as well as the annular pipe).

Two different techniques were used to animate the scalar field. The first is a contour map which shows one x-r plane and three r-θ planes at $x/h = 1$, 4, and 7. This animation was recorded at two different speeds corresponding to 15 frames per second and 7.5 frames per second. Total viewing time at the fastest speed is about 2 minutes and 20 seconds, covering all 2040 frames. Although the faster recording speed gives the best overall view of the flow, the slower recording speed is better for studying details of the mixing process.

A second scalar animation involves an iso-surface evaluated at $\varphi = 0.2$. The iso-surface is shown in two different views. One is a side-view and top-view, looking at the computational domain along some radial line at $\theta = 0°$ and $\theta = 90°$. The other is a 3-D perspective view looking at the iso-surface from the end of the combustor. This animation covered 500 frames, starting at $T = 52.1$, ending at $T = 94$. Thus the initial introduction and final clearing of fuel from the combustion chamber is not included in this animation. The animation was recorded at 10 frames/sec.

The third animation included on the video-tape shows the trajectories of particles injected in the central fuel pipe as well as in the annular air pipe. The particles are injected about one step-height upstream of the expansion. Particles injected in the fuel pipe are red, whereas particles injected in the air pipe are blue. Particle trajectories were calculated based on the velocity-fields (spaced 0.084 time-units apart) using the Unsteady Flow Analysis Toolkit (UFAT) on the Time Accurate Visualization System (TAVS), at NASA Ames Research Center. The animation covers 880 frames staring at $T = 10.1$, ending at $T = 73.8$. UFAT made three interpolations between every frame from the simulation, giving a total of 2640 recorded frames. The animation was recorded at 30 frames/sec.

The particle trajectories were computed as a function of three spatial coordinates. However, in order to avoid covering the particles injected into the fuel pipe by particles injected into the air pipe, the particle trajectories were projected onto one x-r plane before recording on the video-tape.

The last quantity recorded on the video-tape shows iso-surfaces of low pressure regions. The mean pressure field was calculated during the simulation and later subtracted from the instantaneous pressure fields recorded at every 30 time-step. An iso-value of -0.4 was chosen. Regions of low pressure represent vortex cores and

the animation therefore shows the behavior of large scale structures in the flow. The animation includes two views. The first is a side-view and top-view, looking at the computational domain along some radial line at $\theta = 0°$ and $\theta = 90°$. The second is a 3-D perspective view looking at the iso-surfaces from the end of the combustor. The animation includes 500 frames starting from $T = 10.1$, ending at $T = 52$. This represents a total of about 1.4 flow-through times. The animation was recorded at 10 frames/sec.

D.2.2 <u>Calculation Setup</u>

The computational domain used for the animation case is the same as that used for the basic case, described in chapter 4, part II, except that the length of the inlet section was $5h$. Flow parameters were the same as in the basic case.

The computational grid consisted of $192 \times 76 \times 64$ points in the axial, radial, and azimuthal directions, respectively. 70 axial grid-points were used to cover the inflow section, leaving 122 axial grid-points downstream of the expansion. The axial grid was compressed around the corner of the expansion and stretched on either side. Figure D.2-1 shows the grid spacing, Δx, versus axial distance, x. Figure D.2-2 shows the radial grid spacing, Δr, versus radius, r. The grid was uniform in the azimuthal direction. Based on the friction velocities quoted in table 3.3-1 (part II) the grid-resolution in wall coordinates is as shown in table D.2-1.

Subscripts c, a, and 0, indicate that the quantity is evaluated at the wall of the central pipe, annulus, and combustion chamber, respectively. Subscript cl indicates a quantity evaluated at the centerline. The radial grid spacing at the wall gives the location for the first u_r velocity-point off the lower wall. Likewise, the azimuthal grid-spacing at the centerline uses the radial distance to the first u_r velocity-point away from the centerline. The azimuthal grid-spacings at the walls are based on the radial position of the wall. For the central- and annular pipes, the maximum axial grid-spacing occurs at the inlet of the computational domain. For the combustion chamber the maximum axial grid-spacing occurs at the exit of the computational domain. The minimum axial grid-spacing is in all cases found at the point of expansion. The axial extent of the inflow generator (used to get the inflow boundary condition) was $5.65h$, covered by 32 equally spaced grid-points.

The simulation was started from a flow-field interpolated from a coarser grid. The simulation was then run for 125 time-units (approximately 4 flow-through

times) to remove transients resulting from the interpolation. The time-step was kept fixed at 0.0036 h/U_c. Frames for the animation were generated during the following 171.4 time-units. The time-step during this period was held fixed at 0.0028 h/U_c.

	Central	Annular	Comb. chamber
Δx^+_{min}	19.5	52.6	10.4
Δx^+_{max}	172.6	467.6	209.1
Δr^+_c	4.47	12.6	
Δr^+_a		12.6	
Δr^+_0			5.30
$(r\Delta\theta)^+_{cl}$	4.60		2.44
$(r\Delta\theta)^+_c$	46.6	126.2	
$(r\Delta\theta)^+_a$		243.6	
$(r\Delta\theta)^+_0$			98.6

TABLE **D.2-1**, Grid resolution for the animation case.

D.2.3 Statistical Results

The following is a description of statistical results from the animation case, including mean velocity profiles, turbulence intensities and turbulent shear stress. The profiles are compared with those from the basic case (see chapter 4, part II), as well as the experimental data of Johnson & Bennett. The objective is to document the results from the animation case.

As shown in the previous section the resolution used for the animation case was coarser than that used in the basic case. The radial grid was the same, but the number of azimuthal grid points was 64 in the animation case compared with 128 in the basic case. The number of axial grid-points was 192 in the animation case, compared with 215 in the basic case. However, the inlet section was longer, thus requiring more grid points, and the axial grid-spacing downstream of the expansion was therefore quite a bit coarser for the animation case than for the basic case.

Figure D.2-3 shows mean axial velocity profiles at six measurement stations downstream of the expansion. As expected, there are differences between the

animation case and the basic case, with the latter following the trend of the experimental data better. However, with the scatter of the experimental data taken into account, the results from the animation case look reasonable. The same trend is observed in figure D.2-4 which shows mean radial velocity profiles.

Resolved axial turbulence intensities are shown in figure D.2-5. Differences are observed between the basic case and the animation case at all but one measurement station. The (resolved) radial turbulence intensity (figure D.2-6) shows the same trend. The animation case over-predicts $(u_r'')_{rms}$ at the first three measurement stations and under-predicts $(u_r'')_{rms}$ at the last three measurement stations, compared with the basic case. The resolved azimuthal turbulence intensity is shown in figure D.2-7. As with $(u_x'')_{rms}$ and $(u_r'')_{rms}$, only the qualitative behavior of $(u_\theta'')_{rms}$ is predicted correctly by the animation case.

Figure D.2-8 shows the turbulent shear stress (including the SGS model contribution). The differences between the animation case and the basic case are similar to those observed in the turbulence intensity profiles.

Figure D.2-9 shows the mean value of the scalar, φ. At the first two measurement stations the animation case is doing a fair job in reproducing the experimental results. However, between $x/h = 3.24$ and $x/h = 6.44$, the animation case under-predicts φ in the centerline region. At the last measurement station both computational cases agree well with the experimental results.

D.3 Experimental Inconsistencies

This section describes the results from a case run with a different ratio of air-to fuel flow-rates than that used in the other calculations. The case was motivated by the fact that even though the volume flow-rates quoted by Johnston & Bennett indicate that the (bulk) velocity ratio of the two incoming jets was 3.1, analysis of the measured axial velocity profile at the first measurement station (x/h=0.41) suggests that the (bulk) velocity ratio must have been closer to 2.2. This is illustrated in figure D.3-1 which shows the measured mean axial velocity profile at $x/h = 0.41$, compared with the calculated velocity profile (taken from the basic case). The calculated velocity profile has in this case been normalized by the centerline velocity of the experimental profile.

As explained in chapter 3, part II, the volume flow-rates in the calculations were chosen to match those quoted by Johnston & Bennett. These are shown in table D.3-1, together with the corresponding maximum and bulk velocities calculated in the inlet section (in the basic case).

	Central	Annular	Comb. Chamber
Q - Exp.	0.758	6.456	7.214
Q - Calc.	0.741	6.308	7.049
U_{bulk} - Calc.	1.0	3.132	0.600
U_{cl} - Calc.	1.221	3.467	

TABLE **D.3-1**, Bulk velocities, centerline velocities and volumetric flow-rates. "Exp." gives the flow-rates quoted in the experiment by Johnston & Bennett. "Calc." gives the corresponding values calculated in the basic case.

It is evident from table D.3-1 that the calculations match the flow-rates from the experiments to within a few percent. The ratio of the bulk velocity in the annular pipe to that in the central pipe is seen to be 3.1. (The corresponding ratio using the centerline velocities is about 2.8). Figure D.3-1 shows that the calculated velocity ratio of the two jets is almost unchanged 0.41 step heights downstream of the expansion. However, the experiment seems to indicate that the ratio of the maximum velocities has fallen to about 2. It is unlikely that the entrainment of air

into the fuel stream was large enough during the first 0.41 step-heights to give the drastic reduction in the jet velocity ratio. (Notice in particular (figure D.3-3) that the ratio of the measured peak velocities is about 2 at the first three measurement stations, ranging from $x/h = 0.41$ to $x/h = 3.24$. To have the velocity ratio decrease from 3 to 2 within the first 0.41 step heights, and then stay fixed at 2 for the next 3 step heights seems highly unlikely). One explanation for the decrease in the velocity ratio might be that Johnston & Bennett either misquoted the flow-rates used, or made errors when measuring the flow-rates. However, it seems almost inconceivable that an important parameter like the flow-rate would be subject to such errors.

One piece of evidence to suggest that the volume flow-rates quoted by Johnston & Bennett may actually be correct is shown in figure D.3-2. This figure shows the mass-fraction of fuel, both from measurements and calculations (basic case), at $x/h = 9.68$. Also indicated by horizontal dashed lines is the equilibrium fuel mass-fraction (which is determined by the ratio of the supplied fuel flow-rate to the total flow-rate). Using the flow-rates quoted by Johnston & Bennett give an equilibrium fuel mass-fraction of 0.105. Assuming that Johnston & Bennett misquoted the flow-rates and that the flow-rates where such that the (bulk) velocity ratio of the incoming jets was 2.2 (see the following sections), the equilibrium fuel mass-fraction would be 0.143. From figure D.3-2 it is evident that both the calculated and measured concentration profiles at $x/h = 9.68$ will level off at a value close to 0.105 (not 0.143). This is evidence that the volume flow-rates quoted by Johnston & Bennett are in fact what was used in the experiments.

However, since the results in figure D.3-1 seems to point in another direction a calculation was designed that changed the ratio of the air- to fuel flow-rates to give a ratio of bulk velocities of 2.2 (corresponding to a ratio of the centerline velocities of 2) in order to better match the measured velocity profile at $x/h = 0.41$. The total flow-rate in the combustion chamber was kept unchanged.

D.3.1 <u>Calculation setup</u>

The calculation was performed using the same grid resolution as that used in the animation case. The computational domain was the same, except that the inlet section was reduced from $5h$ to $1h$, in order to reduce the number of axial grid-points. The new case is referred to as the Q2 case. The volume flow-rates and bulk- and centerline velocities for the new case is given in table D.3-2.

The fuel mass-fraction at the inlet is seen to be 0.143 (compared with 0.105 in all previous cases). The Reynolds number, based on bulk velocity, U_0, and diameter, $2r_0$, in the combustion chamber was 38000 (as before). The calculation was run for about 4.5 flow-through times which would yield a reasonable convergence of first and second order statistics.

	Central	Annular	Comb. Chamber
Q	1.008	6.041	7.049
U_{bulk}	1.360	3.000	0.600
U_{max}	1.645	3.317	

TABLE **D.3-2**, Bulk velocities, centerline (or maximum) velocities and volumetric flow-rates from the Q2 case.

D.3.2 Statistical Results

Results from the calculation are compared with results from the animation case since the two cases used the same grid resolution.

The reattachment length calculated in the animation case was about $8.67h$. This compares with $8.71h$ calculated in the Q2 case. Thus the two cases give almost identical reattachment lengths.

Figure D.3-3 shows the mean axial velocity profile at several locations downstream of the expansion. Notice the much better agreement between calculations and experiments at the first two measurement stations with the modification in the incoming flow-rates. At $x/h = 3.24$ and $x/h = 4.83$ the two cases yield very similar profiles, however the results from the Q2 case still seem to agree somewhat better with the experimental data. At the last two measurement stations there are no significant differences between the two computational cases. This is to be expected since the *total* flow-rate is the same in both cases. Figure D.3-4 shows the mean radial velocity profiles. The trend is the same as seen in the mean axial velocity profiles.

The turbulence intensities in the axial, radial and azimuthal directions are shown in figures D.3-5, D.3-6, and D.3-7, respectively. The trend is the same in all figures. There are differences between the two computational cases at the first three

measurement stations with the Q2 case generally agreeing better with experimental results than the animation case. However, the computed *rms* profiles are still over-predicted, compared with the measured values. But, as was shown in section D.2, the level of the *rms* fluctuations generally decreased with increasing grid resolution (see differences between the animation case and the basic case). It is likely that the same would happen if the grid resolution for the Q2 case was increased which would bring the results from the this case in even better agreement with experiments. At the last three measurement stations the differences between the two computational cases are small.

Figure D.3-8 shows the turbulent shear stress (including the SGS model contribution). At the first three measurement stations the Q2 case is seen to yield improved agreement with experiments, compared with the results from the animation case. At the last three measurement stations only minor differences are observed between the two computational cases.

D.3.3 <u>Conclusions</u>

Based on the statistical results from the Q2 case, compared with the results from the animation case, it is clear that the Q2 case agrees significantly better with the experimental results of Johnston & Bennett. This is despite the fact that the flow-rates of fuel and air used in the Q2 case do not match those quoted by Johnston & Bennett. The results from this calculation therefore suggests that Johnston & Bennett either misquoted the flow-rates used, or made errors when measuring the flow-rates.

Figure D.3-2, on the other hand, provides some evidence that Johnston & Bennett used the flow-rates quoted in their report.

Based on the conflicting evidence it is impossible to draw any conclusions about what the actual flow-rates were, except to note that there are unexplainable inconsistencies in the experimental data. It was therefore decided to perform all calculations in the main body of this work using the flow-rates quoted by Johnston & Bennett.

It can be concluded that due to the apparent inconsistencies in the experiments by Johnston & Bennett a different experimental data base should have been chosen to verify the computational results.
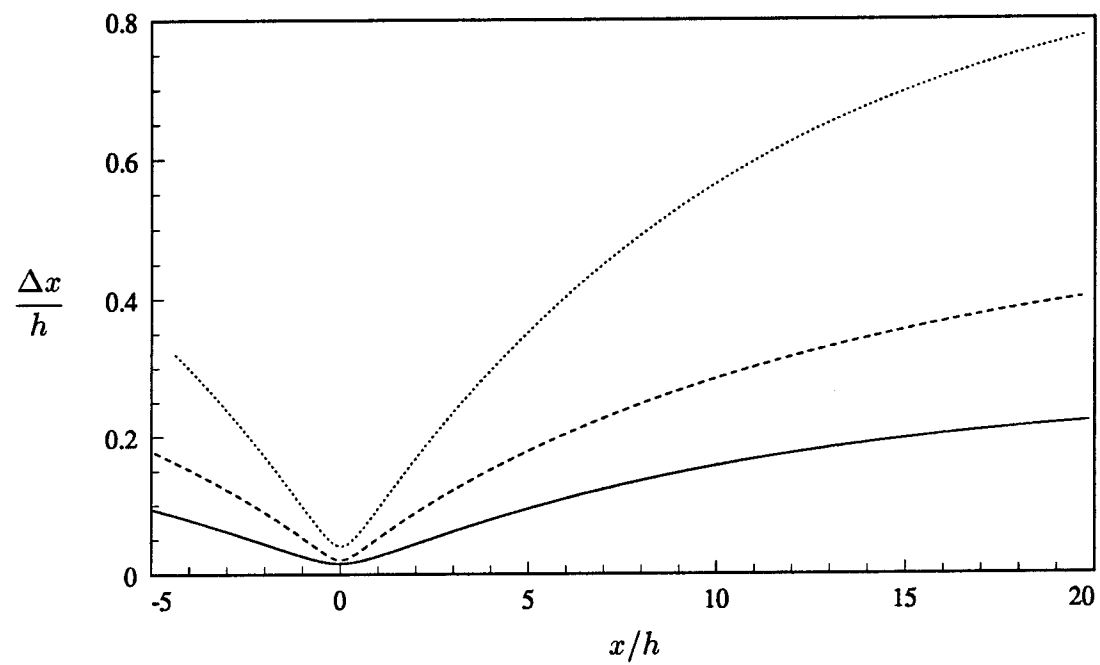
FIGURE **D.1-1**, Axial grid spacing versus axial distance.   ········ : Case CX1 $(N_x = 98)$;   ---- : Case CX2 $(N_x = 192)$;   —— : Case CX3 $(N_x = 353)$.
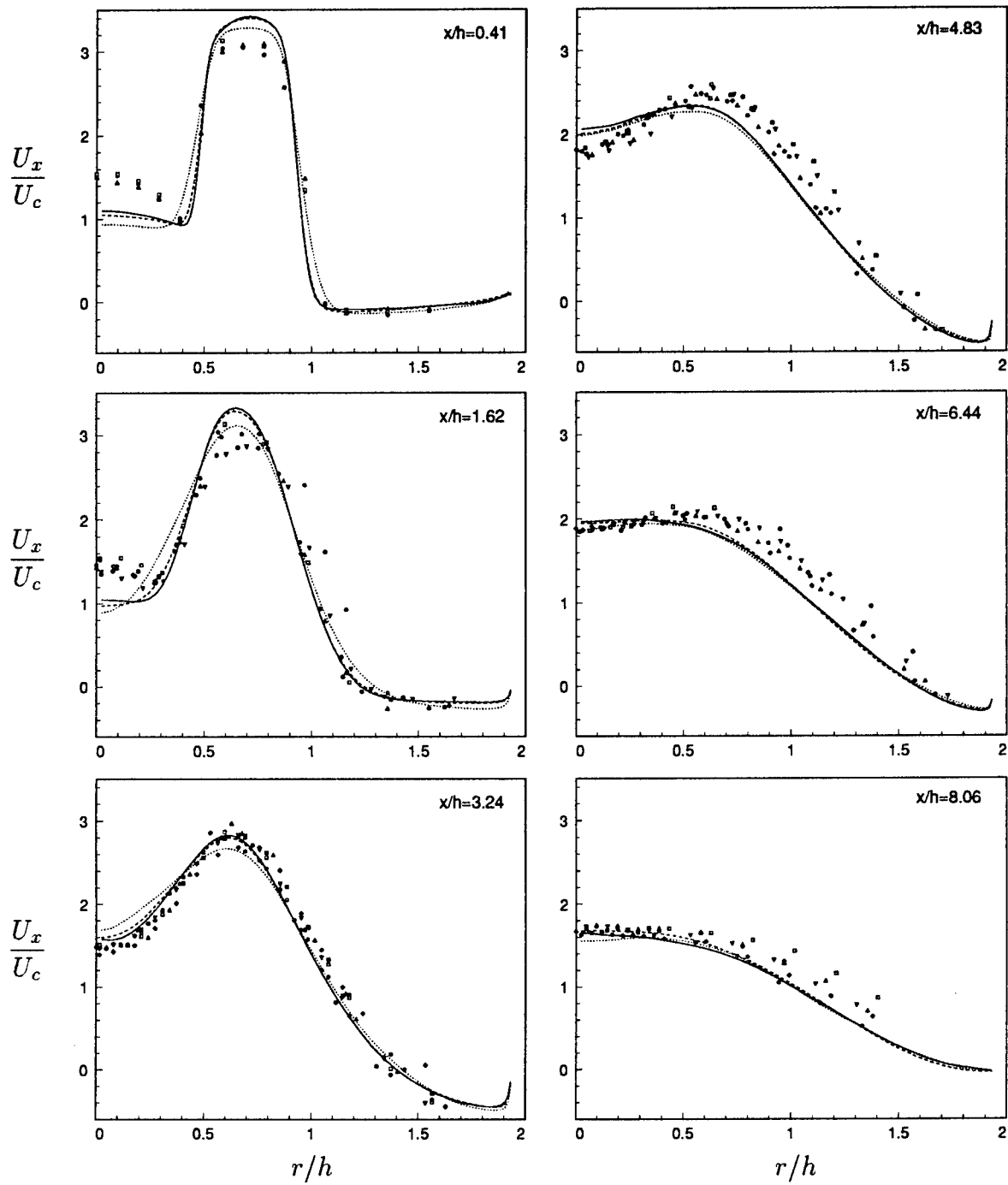
FIGURE **D.1-2**, Mean axial velocity.   ········ : Case CX1 ($N_x = 98$);   ---- : Case CX2 ($N_x = 192$);   —— : Case CX3 ($N_x = 353$);   All Symbols : Experiments by Johnson & Bennett.
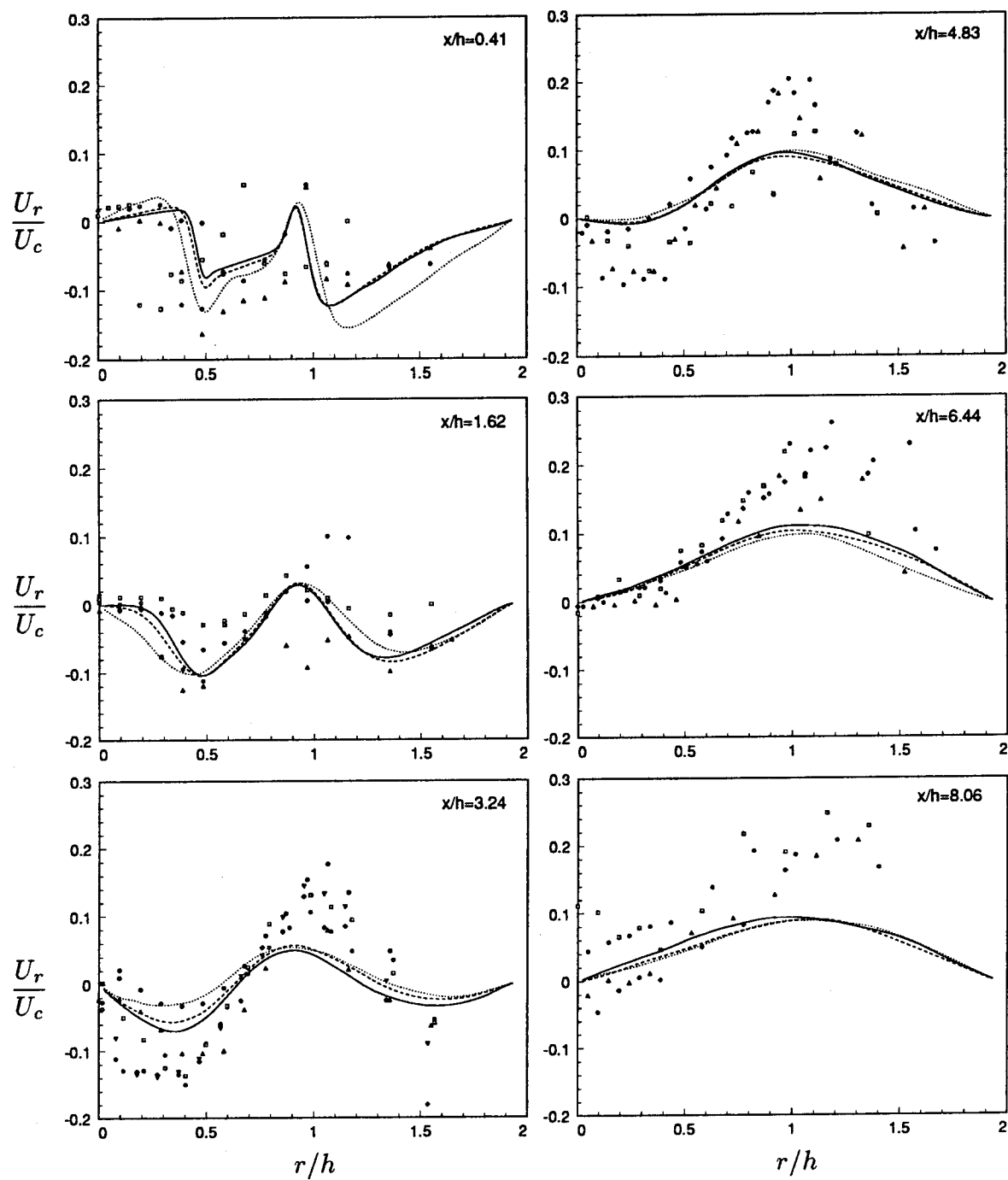
FIGURE **D.1-3**, Mean radial velocity.　········ : Case CX1 ($N_x = 98$);　---- : Case CX2 ($N_x = 192$);　——— : Case CX3 ($N_x = 353$);　All Symbols : Experiments by Johnson & Bennett.
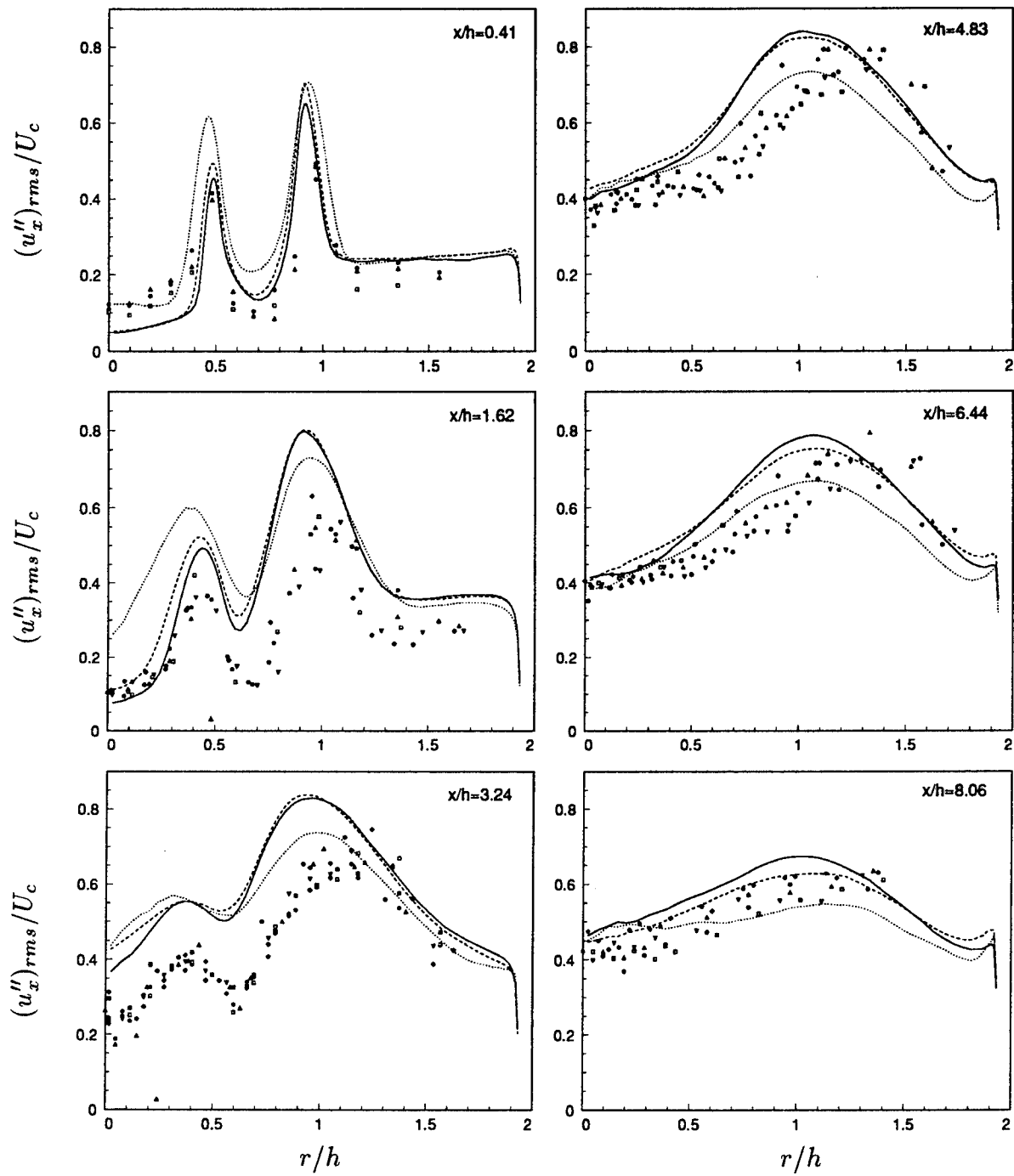
FIGURE **D.1-4**, Resolved axial turbulence intensity.   ⋯⋯ : Case CX1 ($N_x = 98$); ---- : Case CX2 ($N_x = 192$); ——— : Case CX3 ($N_x = 353$);   All Symbols : Experiments by Johnson & Bennett.
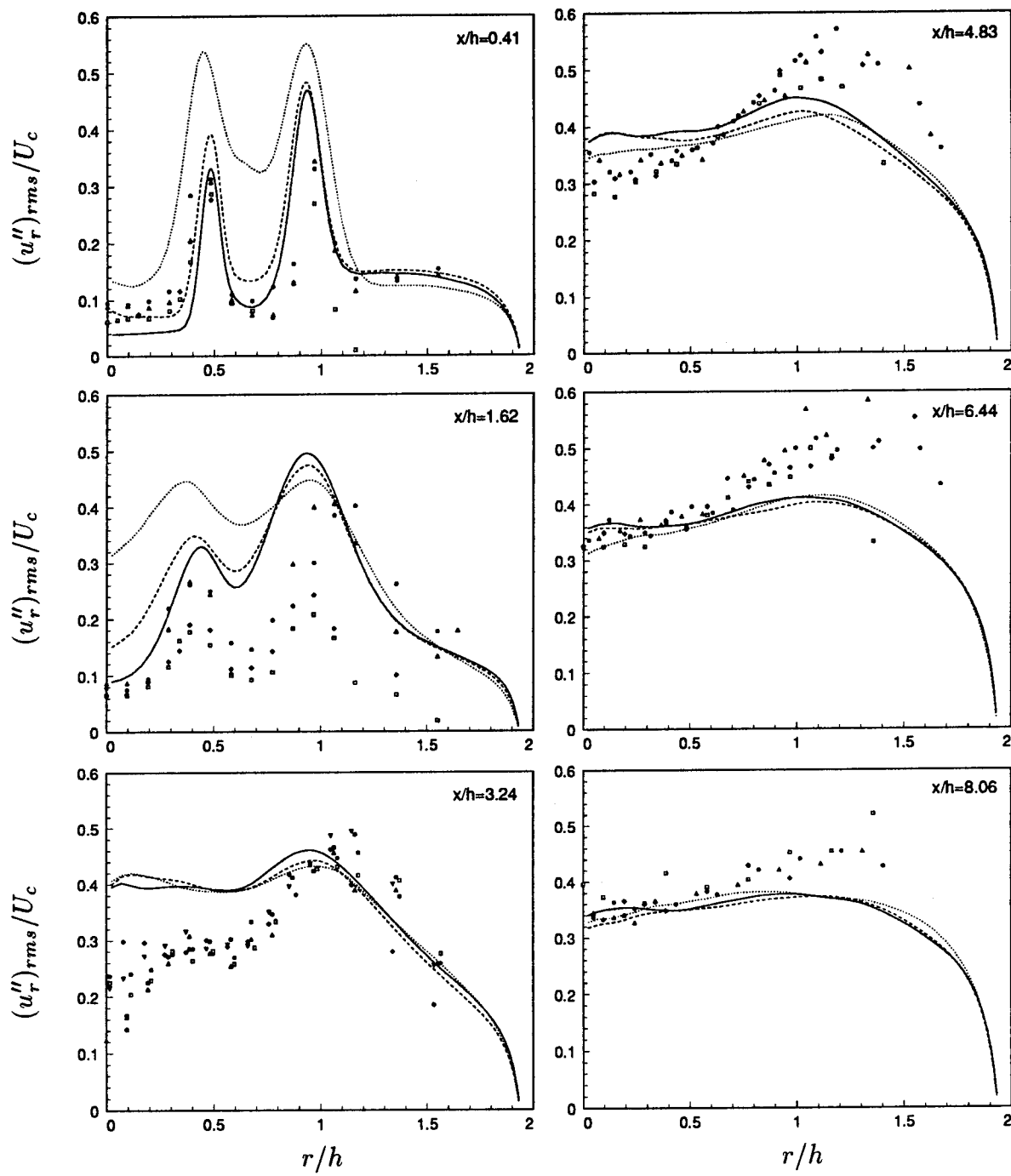
FIGURE **D.1-5**, Resolved radial turbulence intensity.　⋯⋯⋯ : Case CX1 ($N_x = 98$);
---- : Case CX2 ($N_x = 192$);　——— : Case CX3 ($N_x = 353$);　All Symbols :
Experiments by Johnson & Bennett.
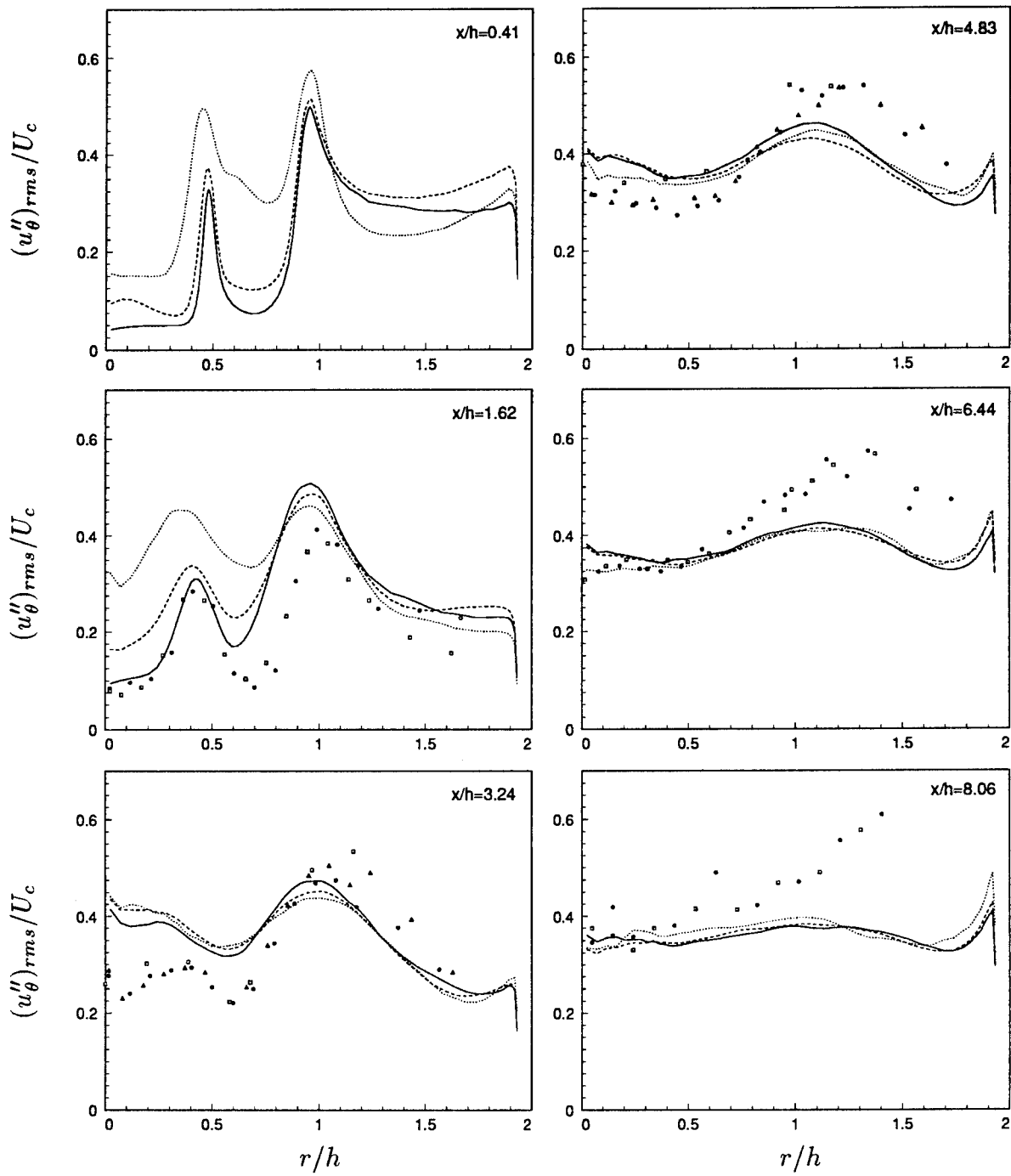
FIGURE **D.1-6**, Resolved azimuthal turbulence intensity.   ⋯⋯⋯ : Case CX1 ($N_x = 98$);   - - - - : Case CX2 ($N_x = 192$);   ——— : Case CX3 ($N_x = 353$); All Symbols : Experiments by Johnson & Bennett.
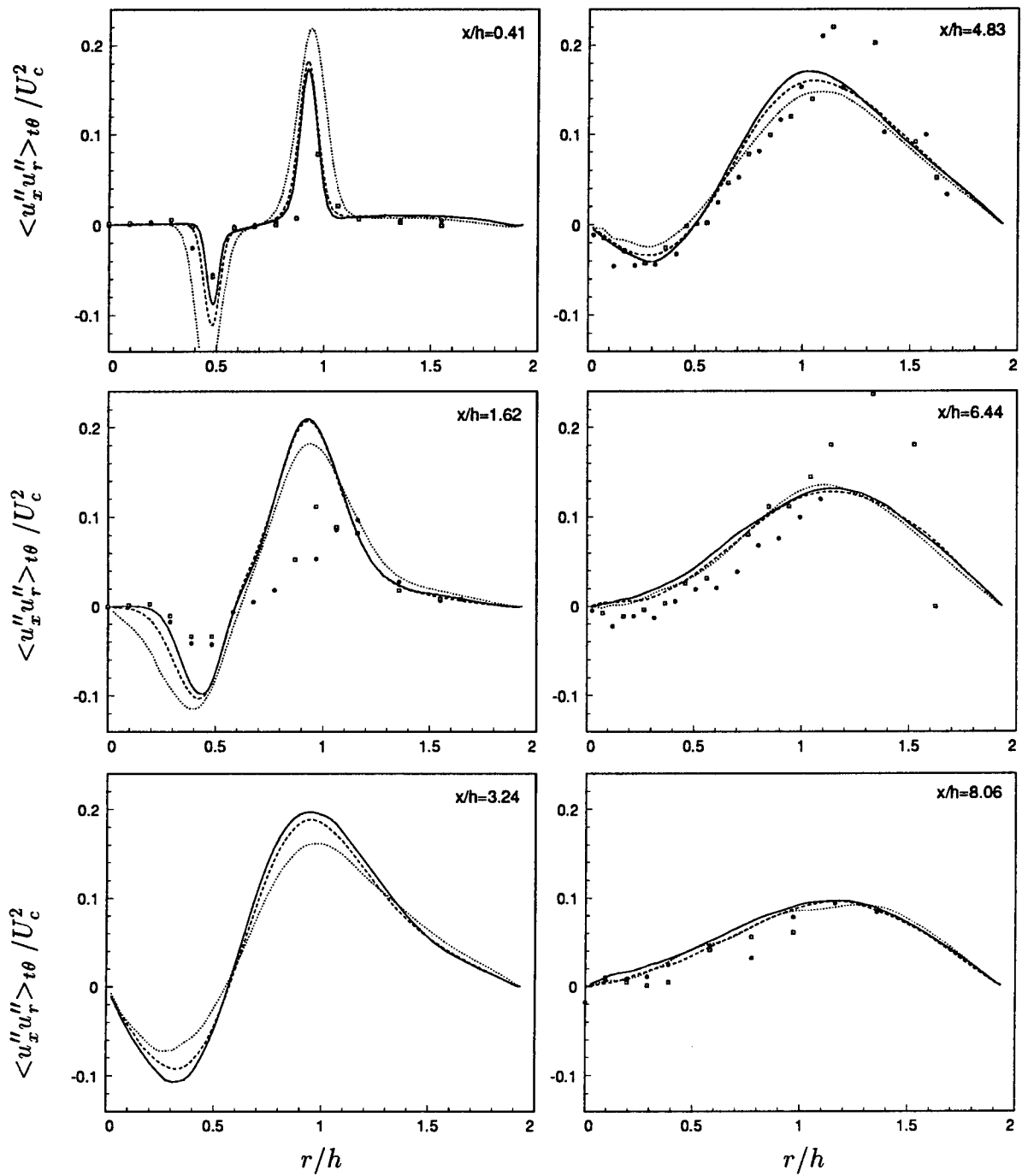
FIGURE **D.1-7**, Turbulent shear stress (incl. SGS model term).   ⋯⋯⋯ : Case CX1 ($N_x = 98$);   - - - - : Case CX2 ($N_x = 192$);   ———— : Case CX3 ($N_x = 353$); All Symbols : Experiments by Johnson & Bennett.
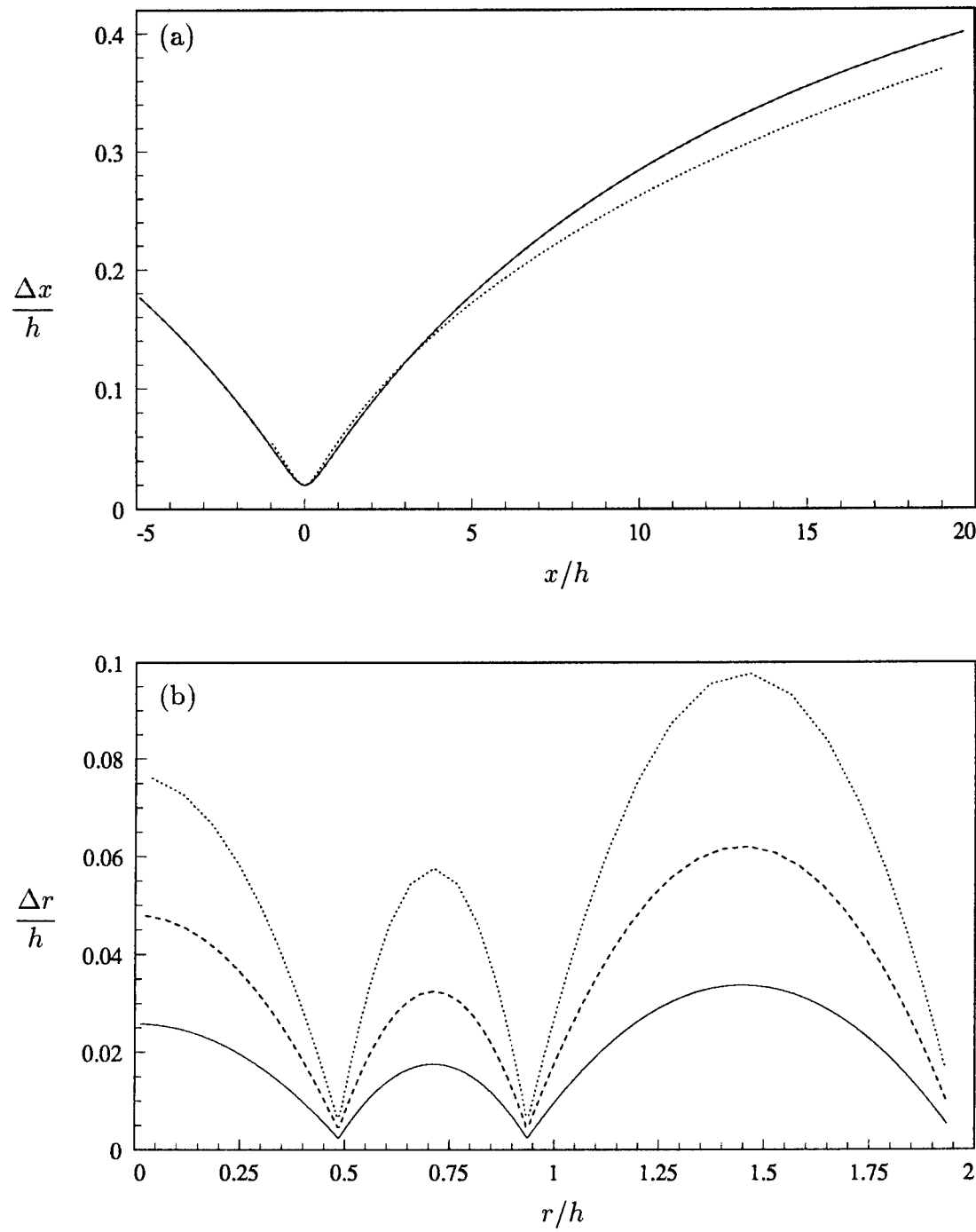
FIGURE **D.1-8**, (a) Axial grid spacing versus axial distance. (b) Radial grid spacing versus radial distance.   ········ : Case CR1 ($N_r = 48$);   ---- : Case CR2 ($N_r = 76$);   —— : Case CR3 ($N_r = 140$).
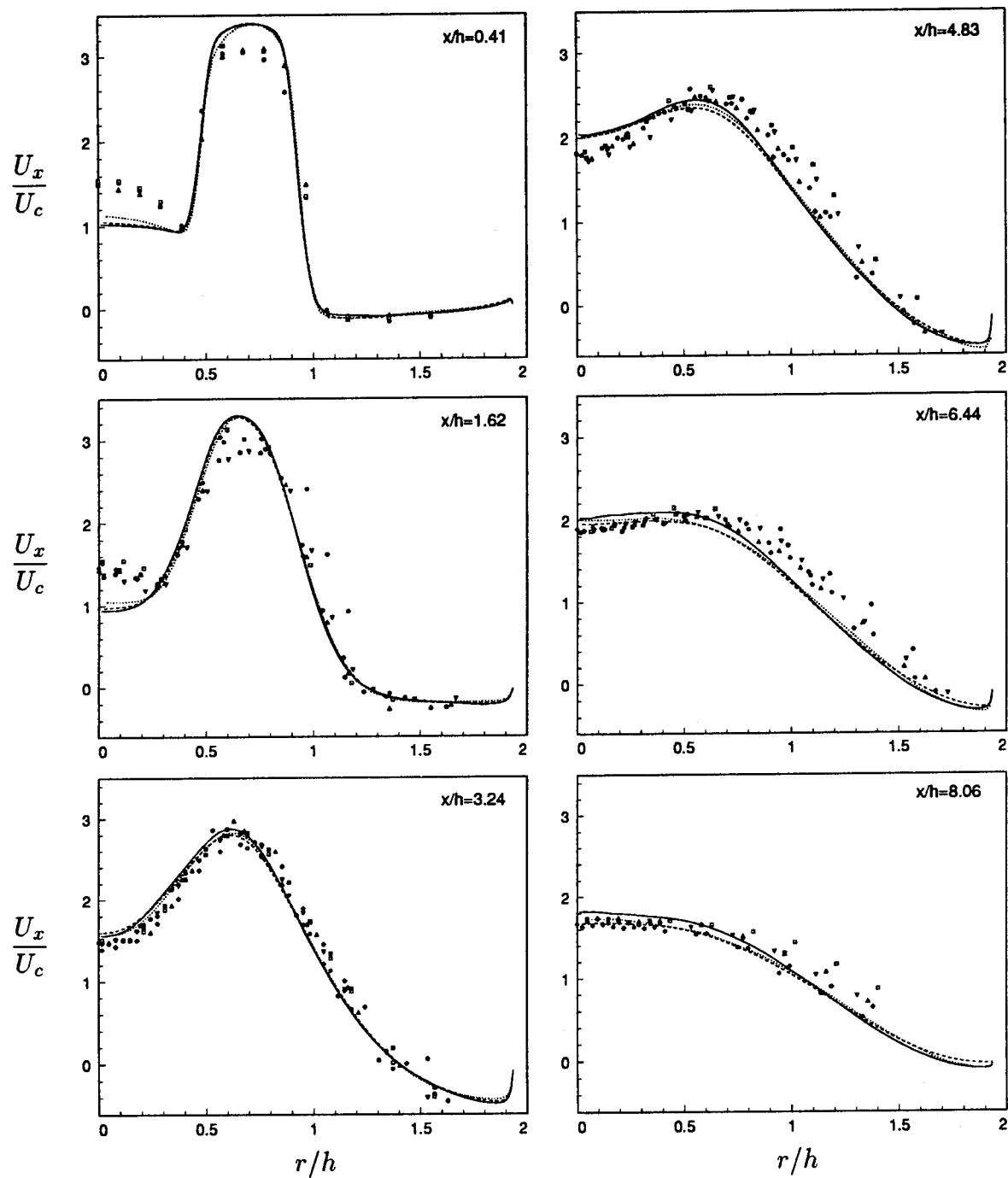
FIGURE **D.1-9**, Mean axial velocity.   .... : Case CR1 ($N_r = 48$);   ---- : Case CR2 ($N_r = 76$);   ——— : Case CR3 ($N_r = 140$);   All Symbols : Experiments by Johnson & Bennett.
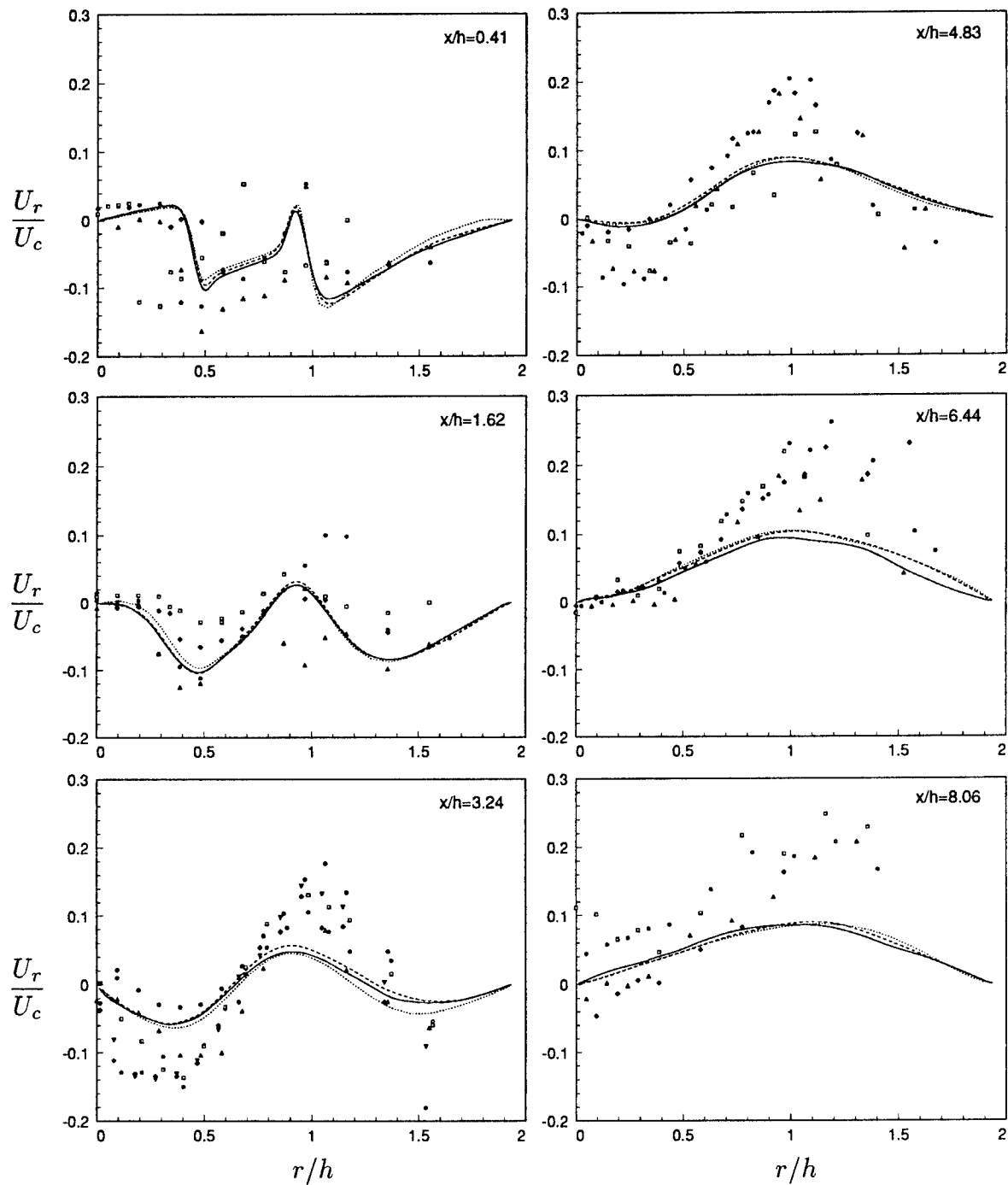
FIGURE **D.1-10**, Mean radial velocity.   ⋯⋯⋯ : Case CR1 ($N_r = 48$);   − − − − :
Case CR2 ($N_r = 76$);   ——— : Case CR3 ($N_r = 140$);   All Symbols : Experiments
by Johnson & Bennett.
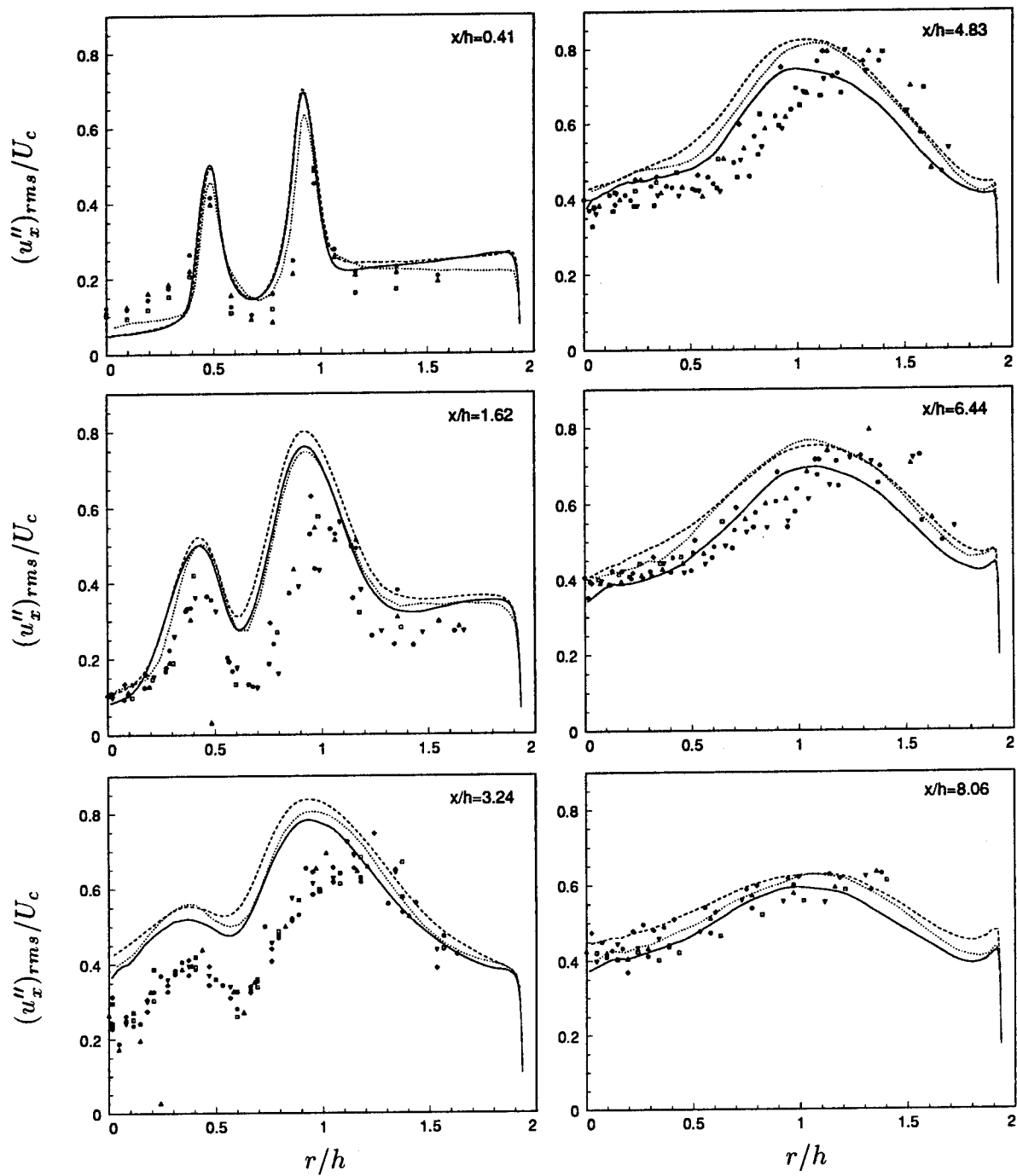
FIGURE **D.1-11**, Resolved axial turbulence intensity.   ········ : Case CR1 ($N_r =$ 48);   ---- : Case CR2 ($N_r = 76$);   ——— : Case CR3 ($N_r = 140$);   All Symbols : Experiments by Johnson & Bennett.
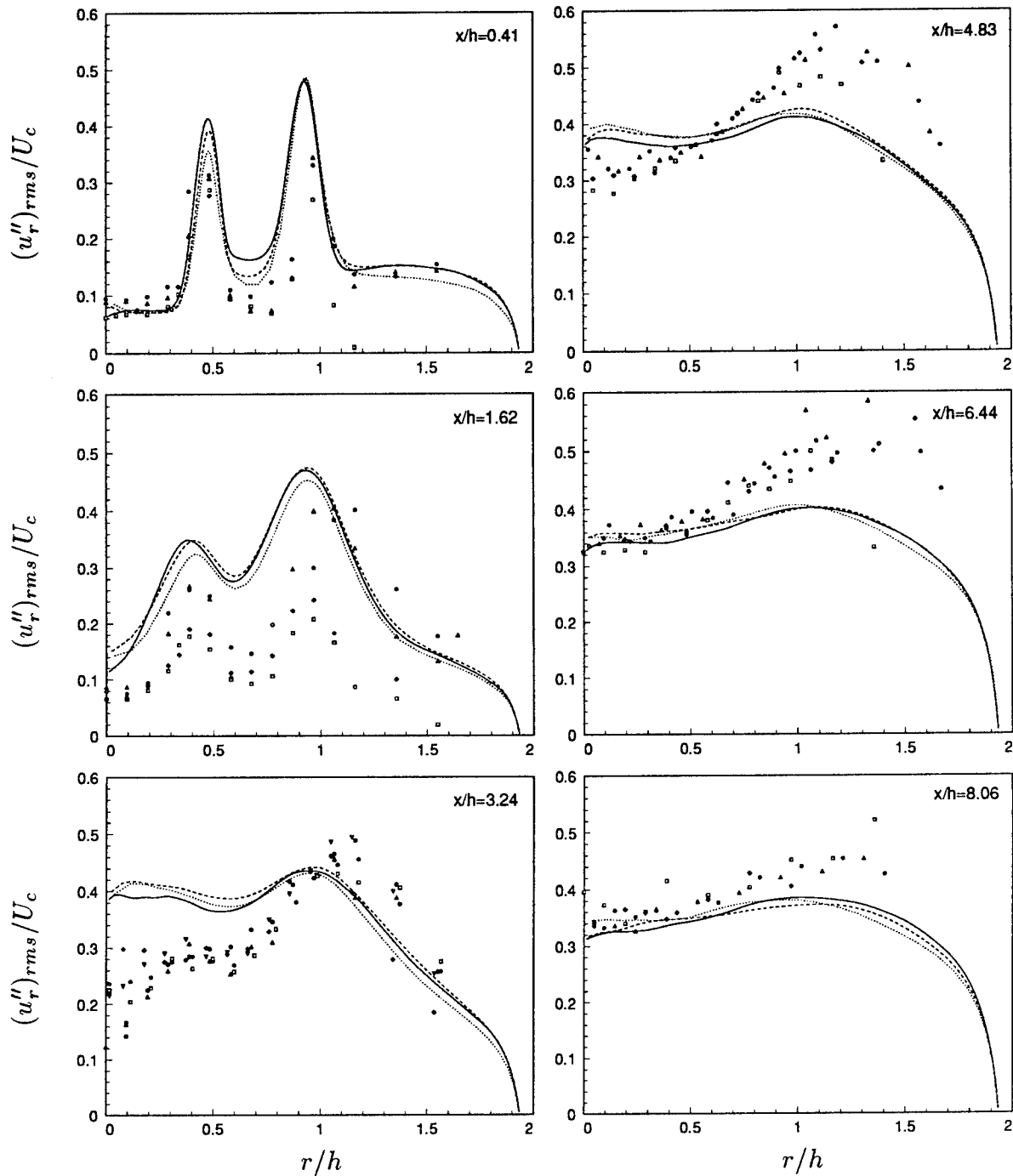
FIGURE **D.1-12**, Resolved radial turbulence intensity.   ········ : Case CR1 ($N_r =$ 48);   ---- : Case CR2 ($N_r = 76$);   ——— : Case CR3 ($N_r = 140$);   All Symbols : Experiments by Johnson & Bennett.
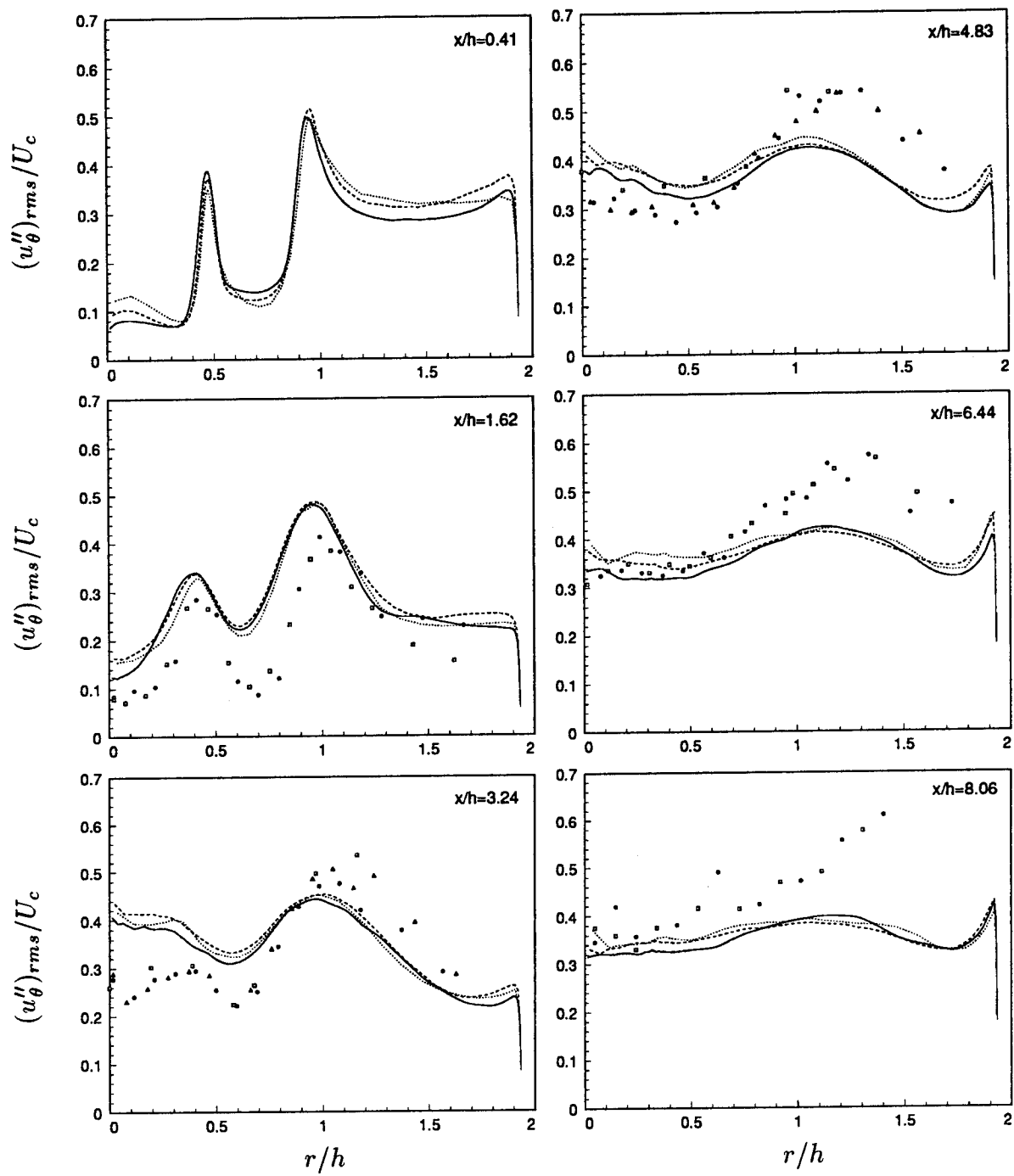
FIGURE **D.1-13**, Resolved azimuthal turbulence intensity.　　⋯⋯⋯ : Case CR1 $(N_r = 48)$;　　---- : Case CR2 $(N_r = 76)$;　　——— : Case CR3 $(N_r = 140)$;　　All Symbols : Experiments by Johnson & Bennett.
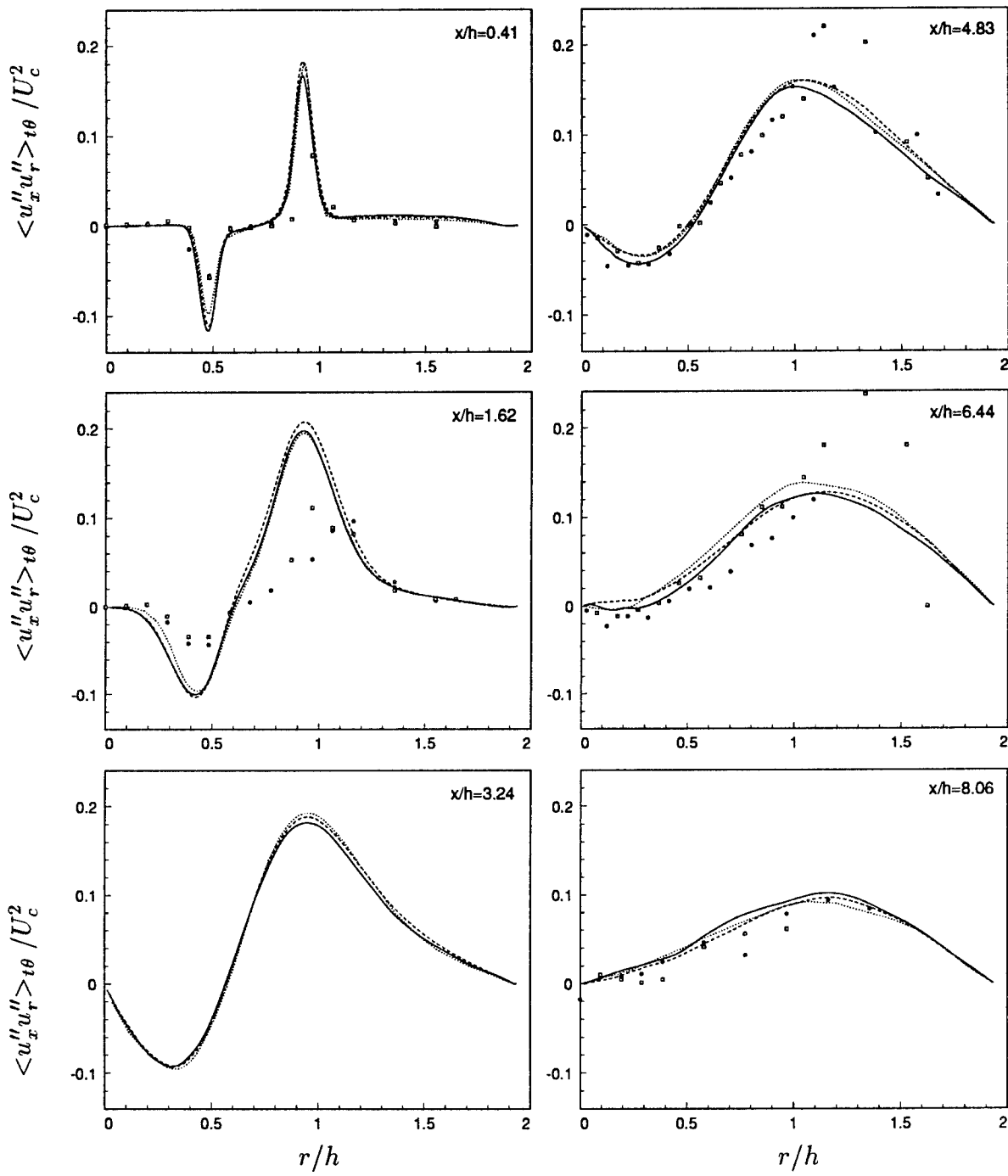
FIGURE **D.1-14**, Turbulent shear stress (incl. SGS model term).   ········ : Case CR1 ($N_r = 48$);   ---- : Case CR2 ($N_r = 76$);   —— : Case CR3 ($N_r = 140$); All Symbols : Experiments by Johnson & Bennett.
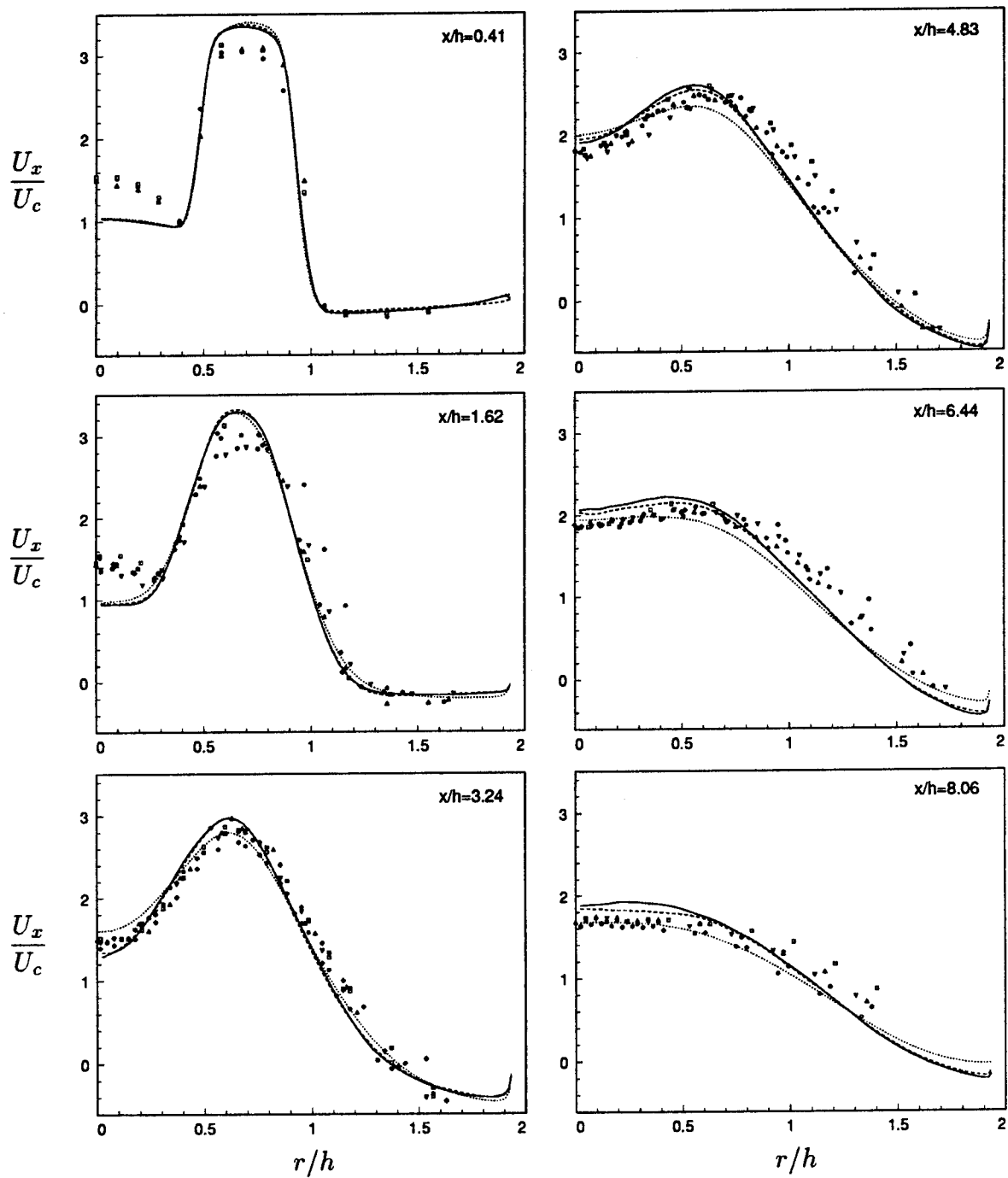
FIGURE **D.1-15**, Mean axial velocity. $\cdots\cdots$: Case $C\theta1$ $(N_\theta = 64)$; $----$: Case $C\theta2$ $(N_\theta = 128)$; $———$: Case $C\theta3$ $(N_\theta = 256)$;   All Symbols : Experiments by Johnson & Bennett.
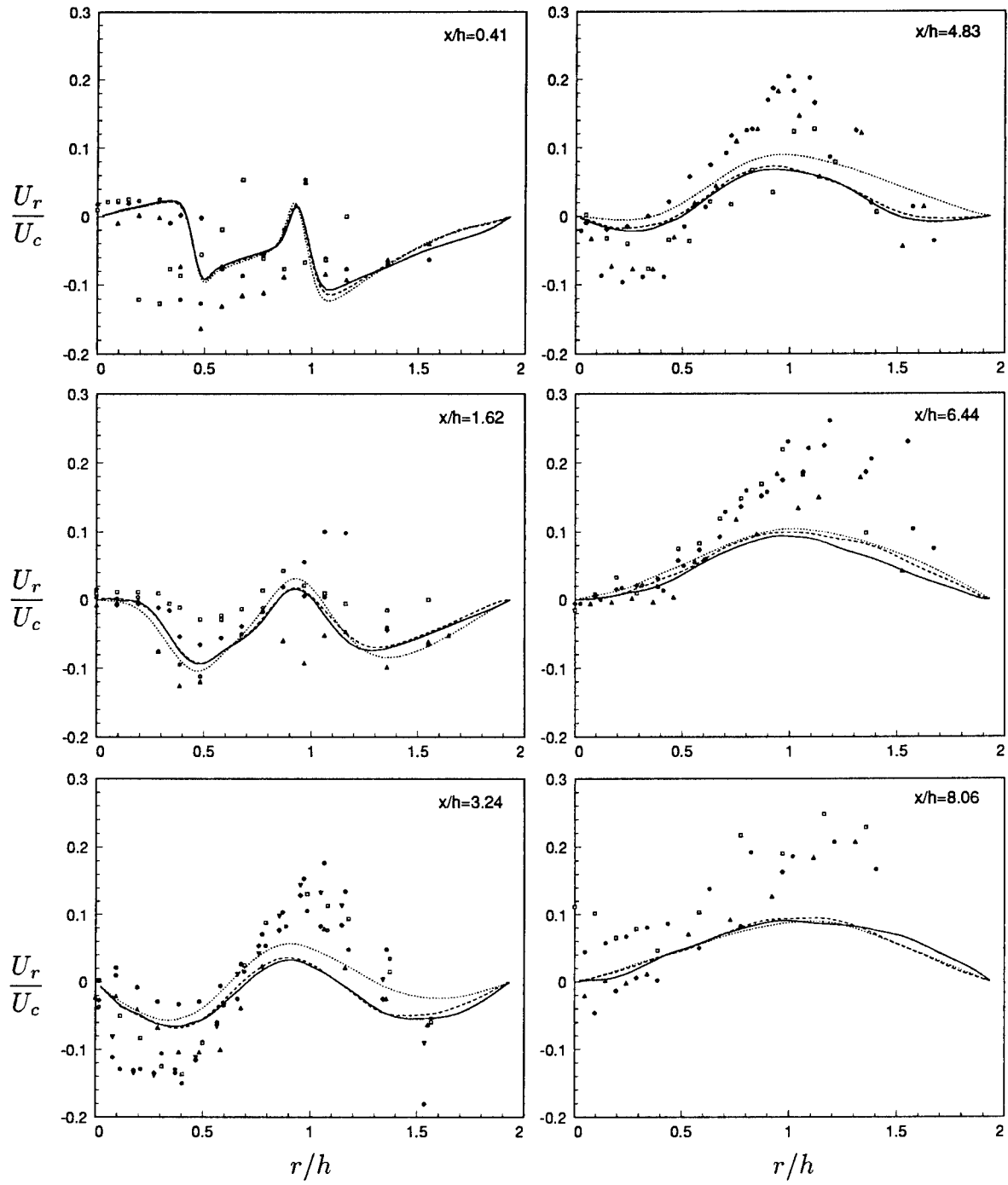
FIGURE **D.1-16**, Mean radial velocity.   ⋯⋯⋯ : Case Cθ1 ($N_\theta = 64$);   ---- : Case Cθ2 ($N_\theta = 128$);   ——— : Case Cθ3 ($N_\theta = 256$);   All Symbols : Experiments by Johnson & Bennett.
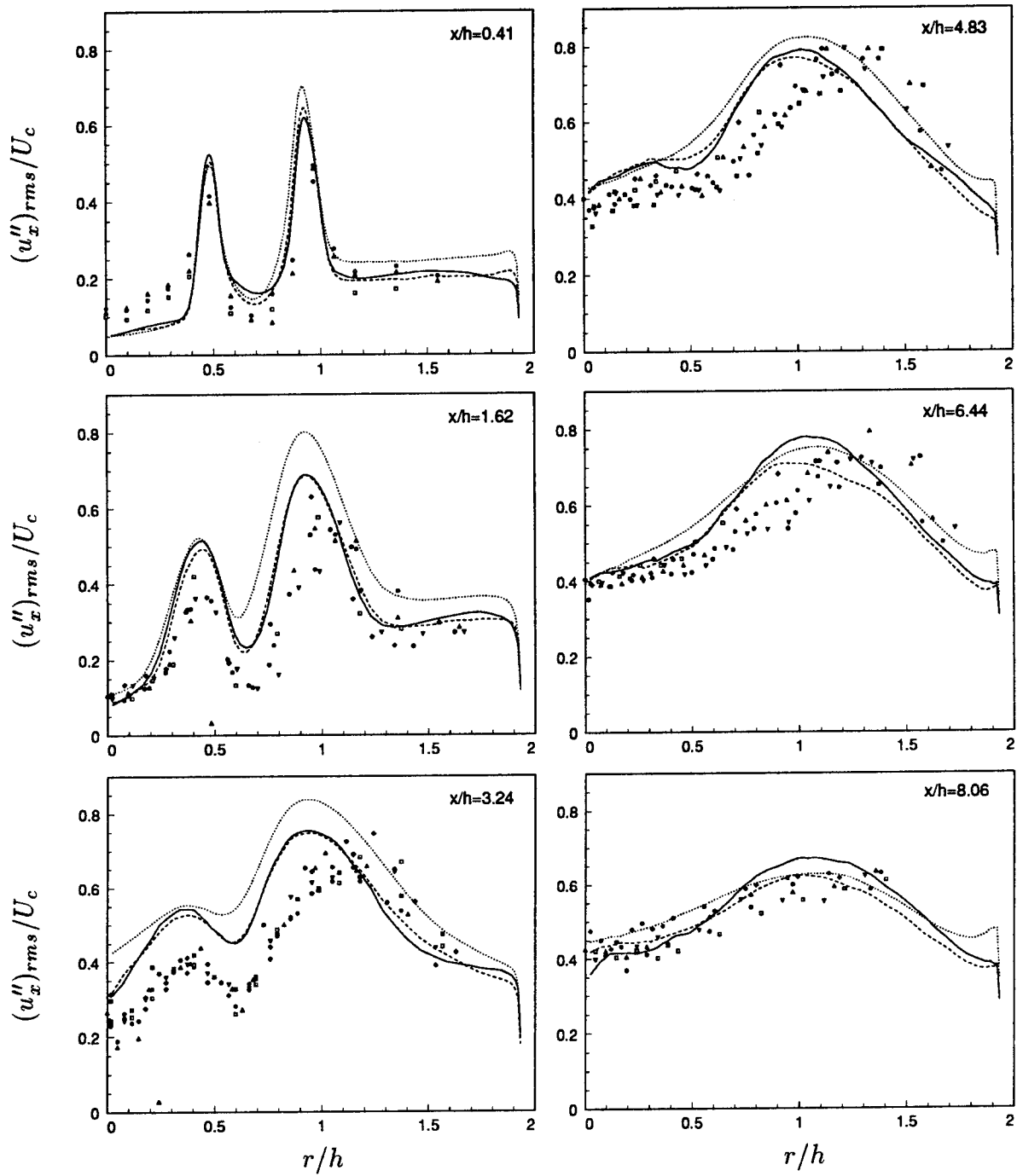
FIGURE **D.1-17**, Resolved axial turbulence intensity.   ⋯⋯ : Case Cθ1 ($N_\theta = 64$);
- - - - : Case Cθ2 ($N_\theta = 128$);   ———— : Case Cθ3 ($N_\theta = 256$);   All Symbols :
Experiments by Johnson & Bennett.
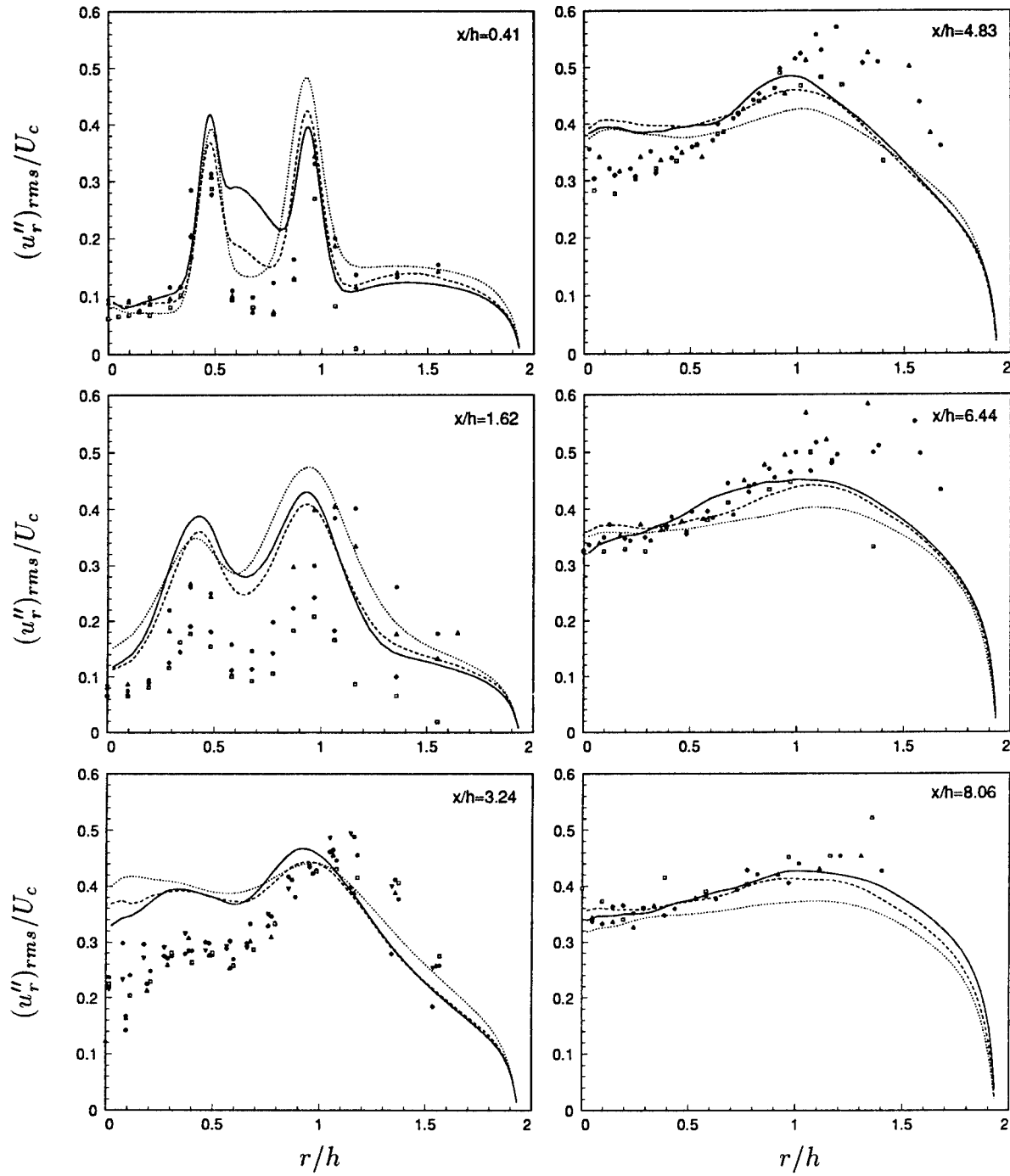
FIGURE **D.1-18**, Resolved radial turbulence intensity.   ⋯⋯⋯ : Case Cθ1 (N_θ = 64);   ---- : Case Cθ2 (N_θ = 128);   ——— : Case Cθ3 (N_θ = 256);   All Symbols : Experiments by Johnson & Bennett.
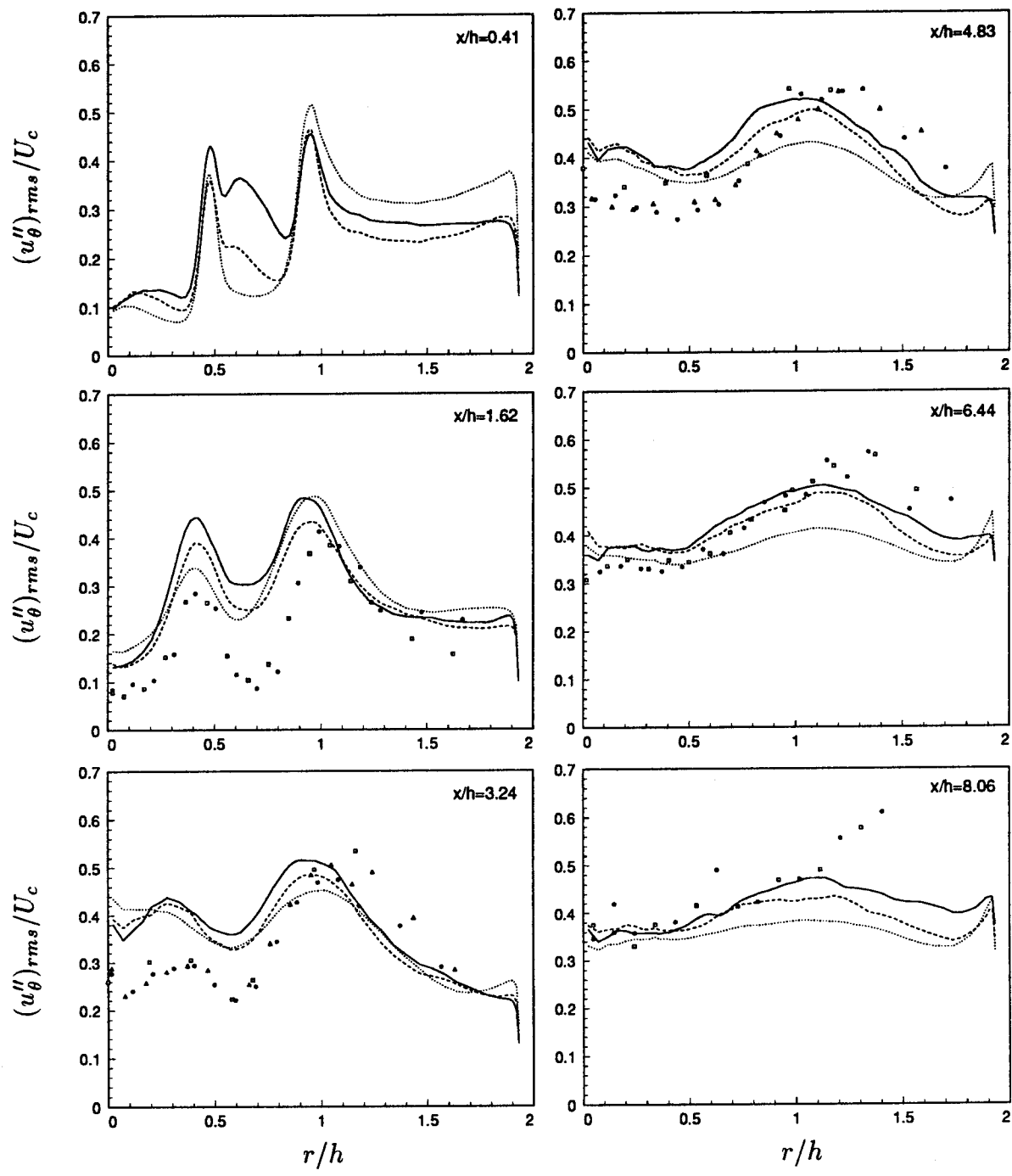
FIGURE **D.1-19**, Resolved azimuthal turbulence intensity.   ········ : Case Cθ1 ($N_\theta = 64$);   ---- : Case Cθ2 ($N_\theta = 128$);   —— : Case Cθ3 ($N_\theta = 256$);   All Symbols : Experiments by Johnson & Bennett.
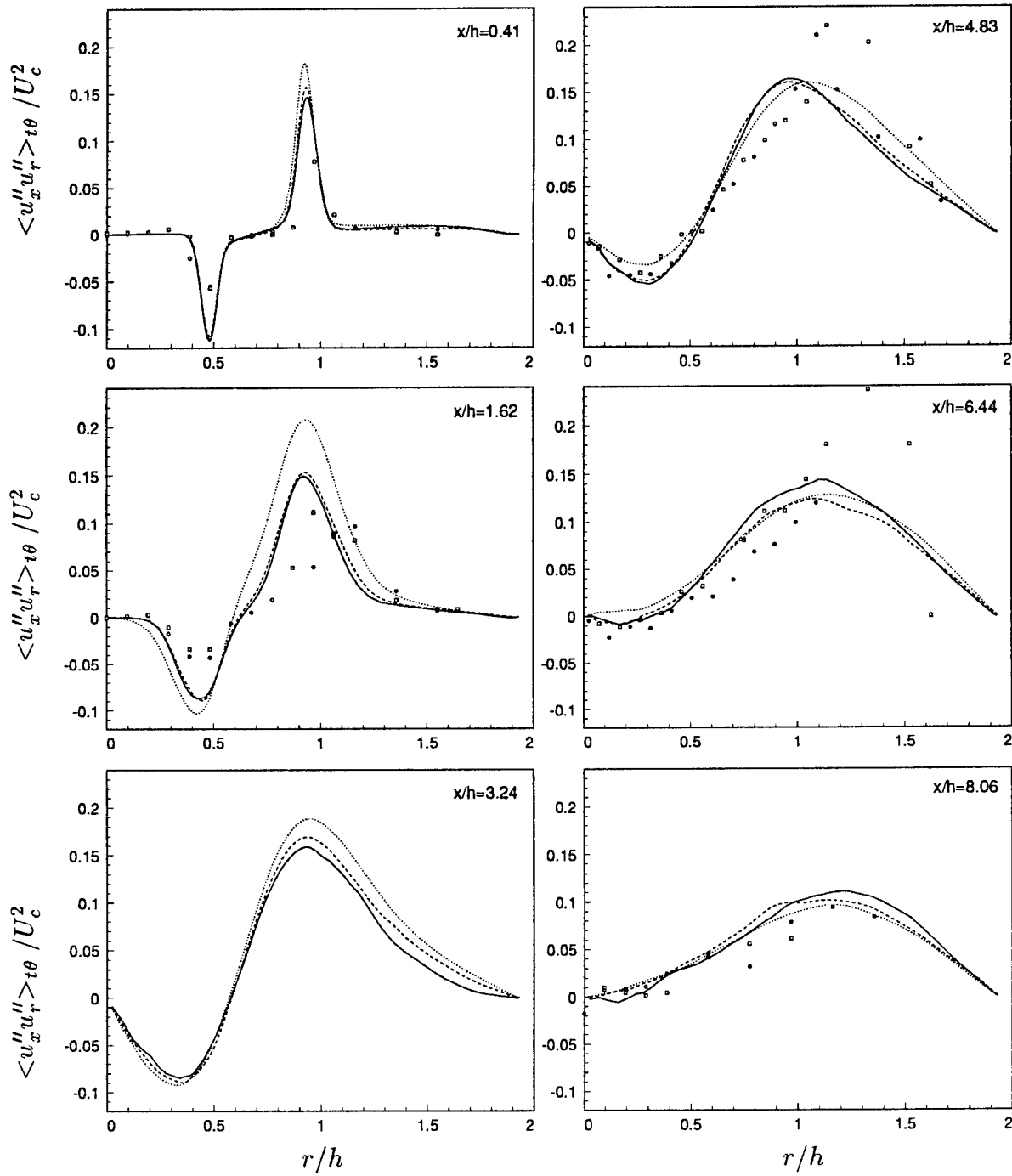
FIGURE **D.1-20**, Turbulent shear stress (incl. SGS model term).   ········ : Case Cθ1 ($N_\theta = 64$);   ‑‑‑‑ : Case Cθ2 ($N_\theta = 128$);   ——— : Case Cθ3 ($N_\theta = 256$); All Symbols : Experiments by Johnson & Bennett.

FIGURE **D.2-1**, Axial grid spacing versus axial distance for the animation case.
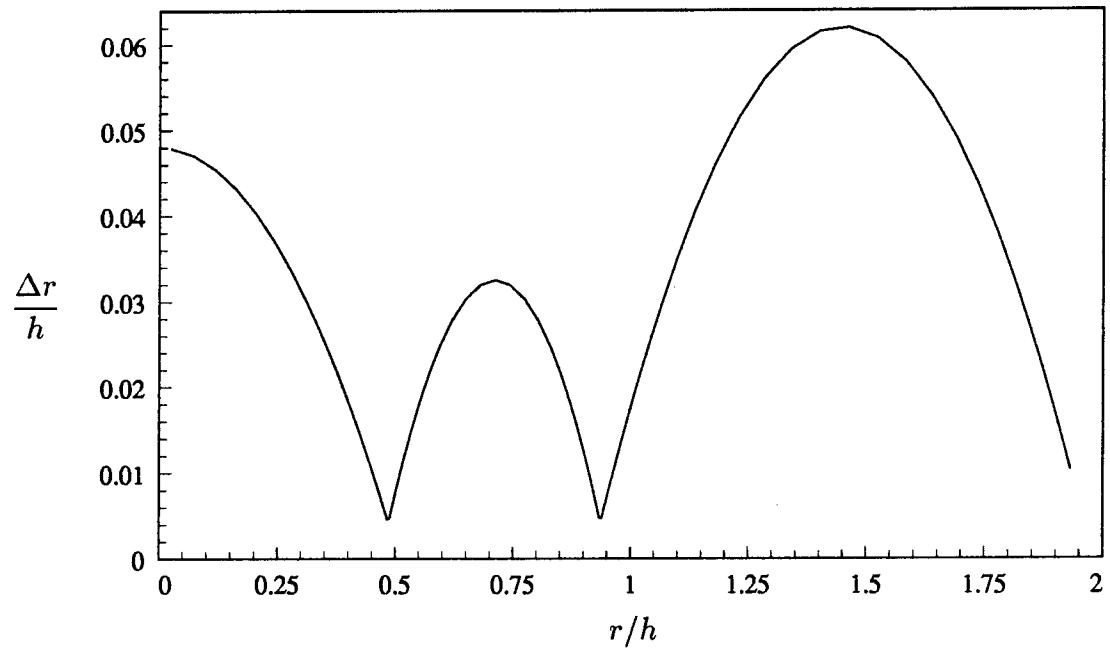
FIGURE **D.2-2**, Radial grid spacing versus radial distance for the animation case.
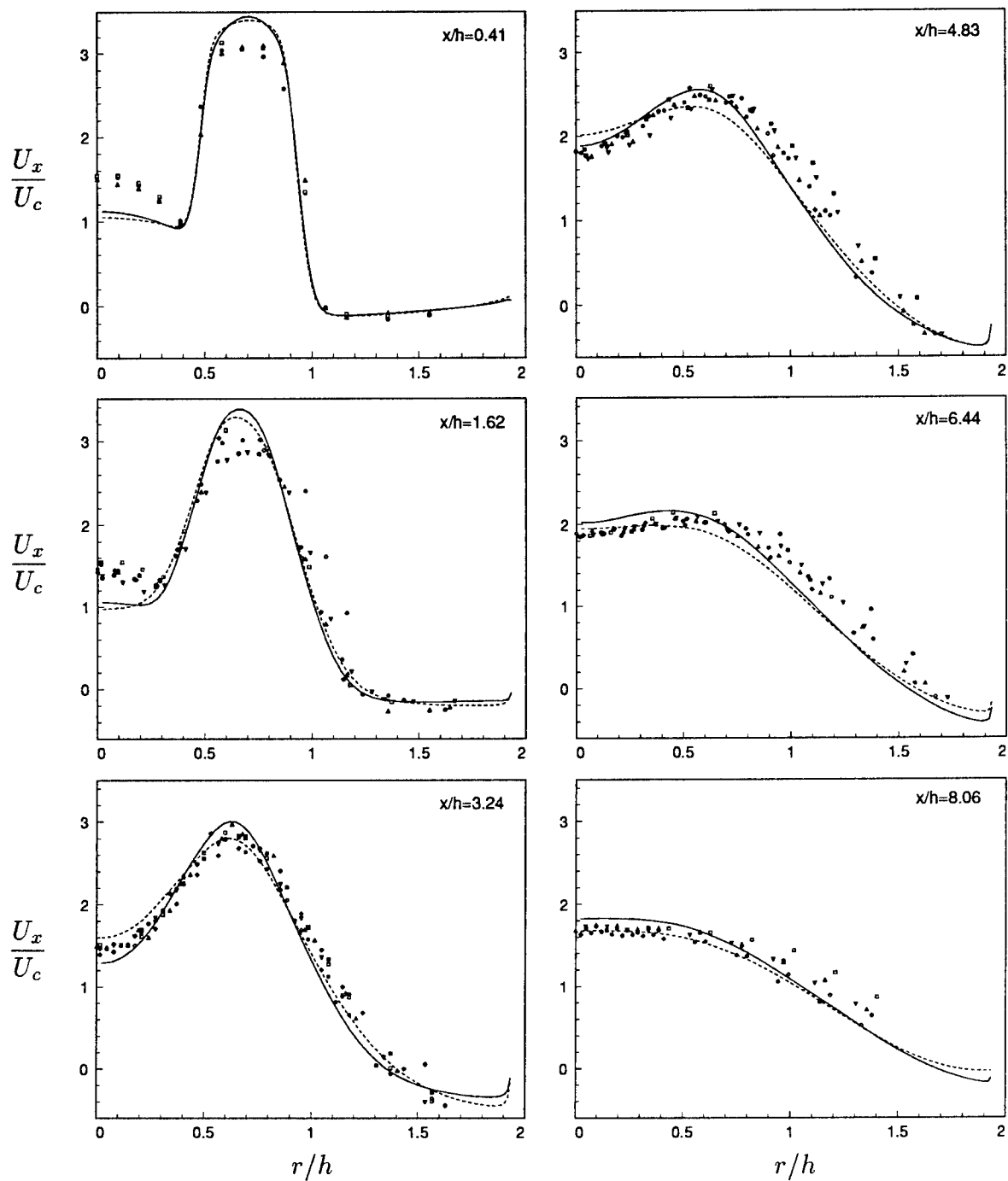
FIGURE **D.2-3**, Mean axial velocity. ———— : Basic case; - - - - : Animation case; All Symbols : Experiments by Johnson & Bennett.
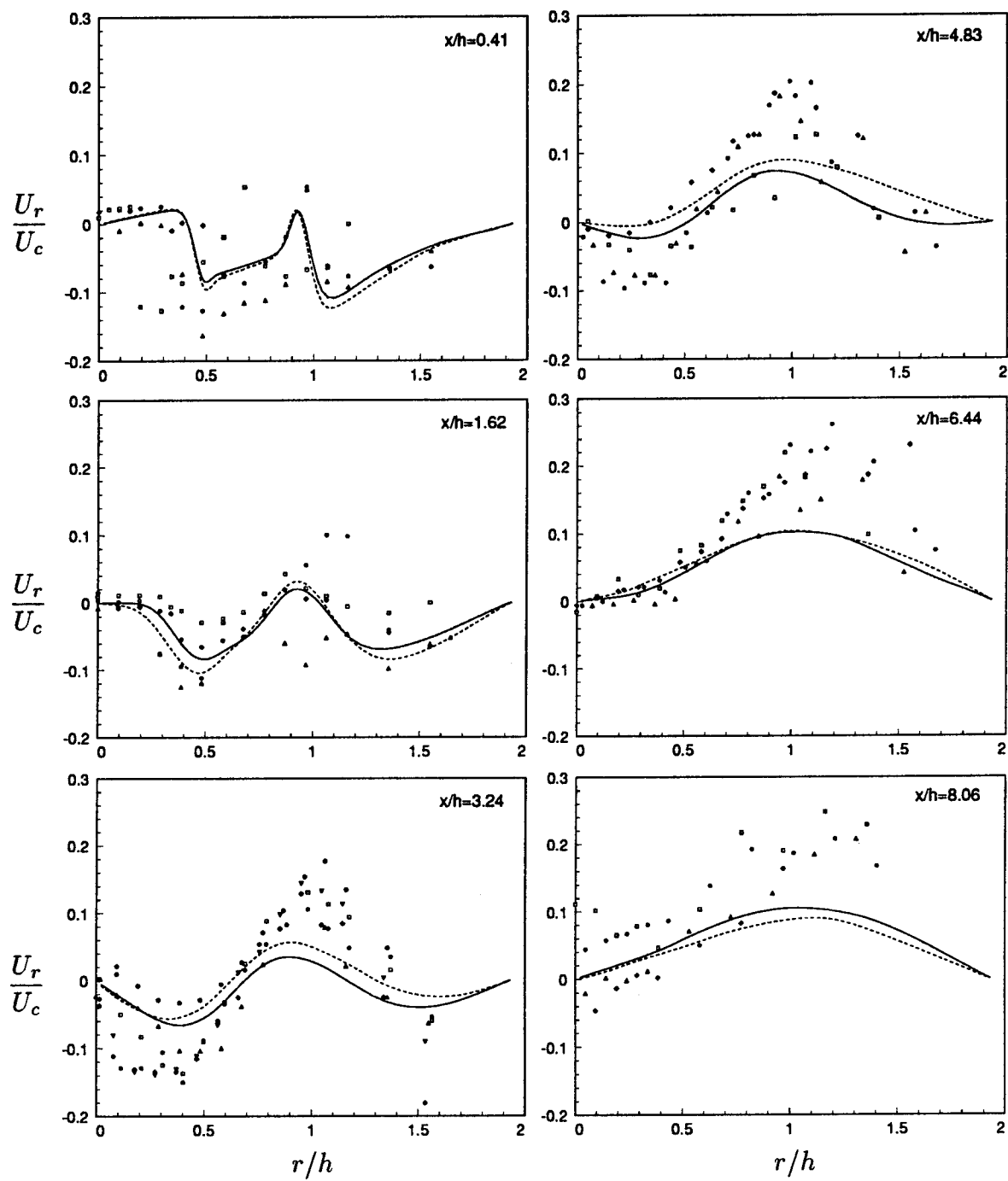
FIGURE **D.2-4**, Mean radial velocity. ———— : Basic case; ---- : Animation case; All Symbols : Experiments by Johnson & Bennett.
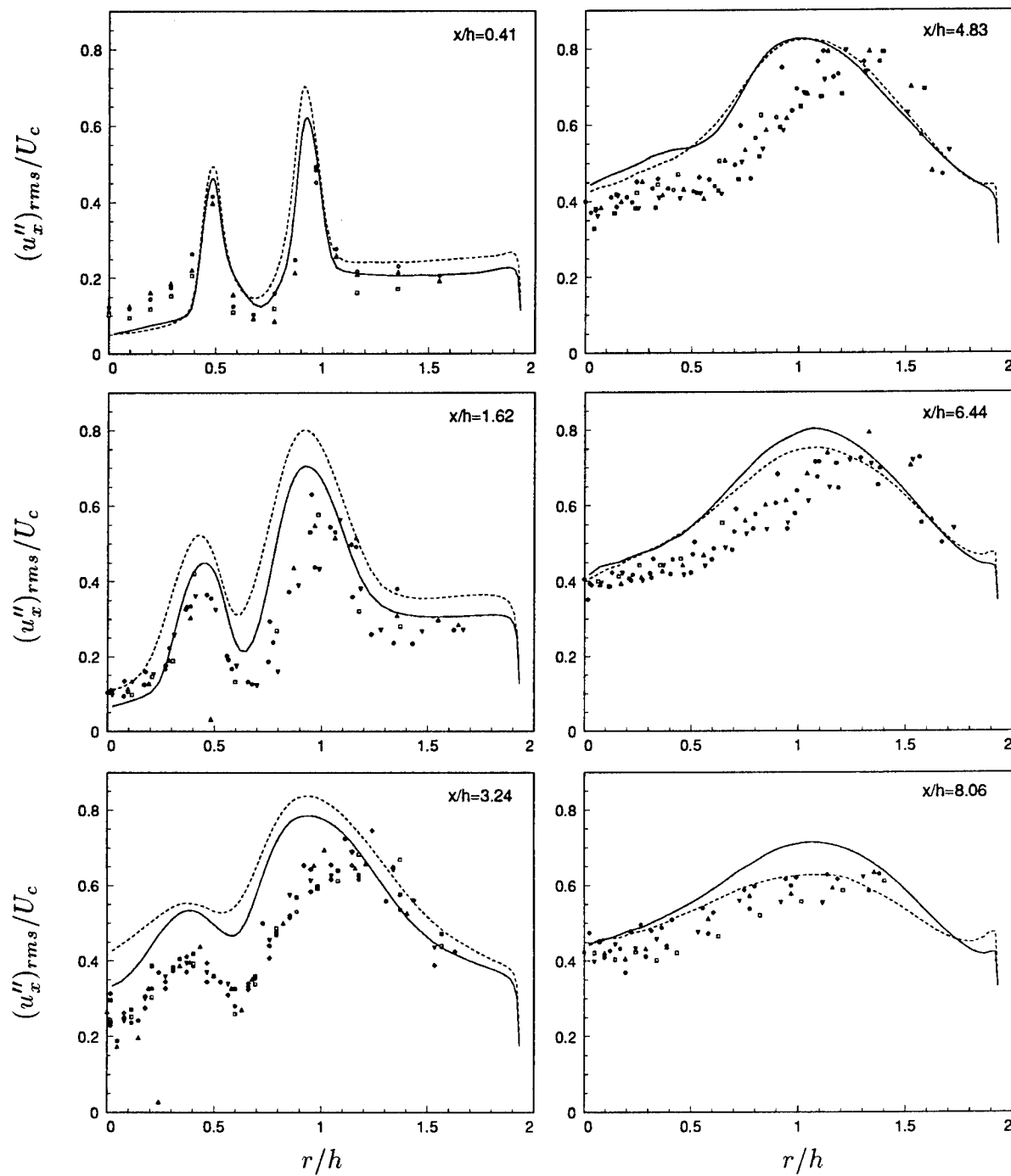
FIGURE **D.2-5**, Resolved axial turbulence intensity. ———— : Basic case;
———— : Animation case;   All Symbols : Experiments by Johnson & Bennett.
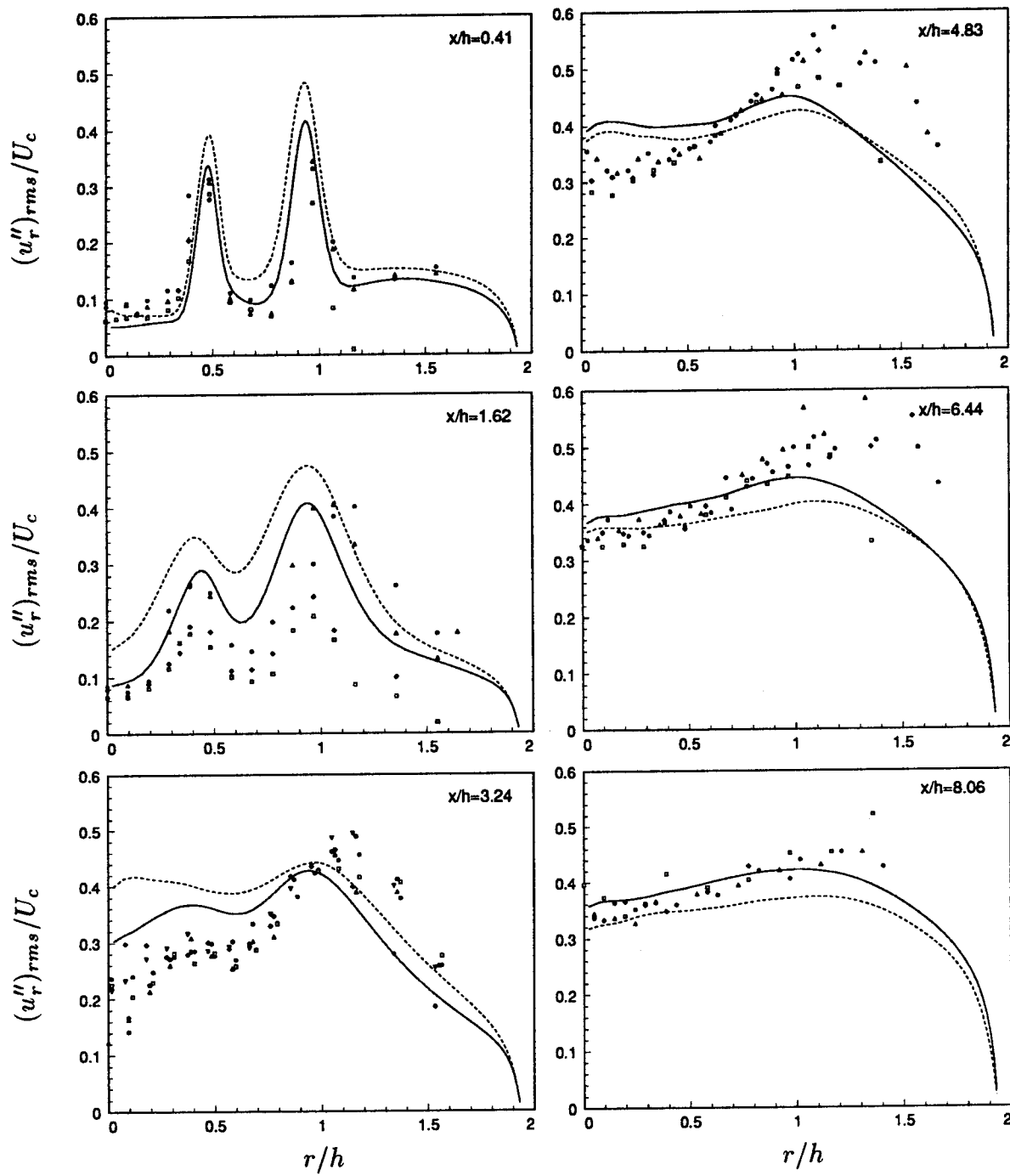
FIGURE **D.2-6**, Resolved radial turbulence intensity.   ——— : Basic case;
———— : Animation case;   All Symbols : Experiments by Johnson & Bennett.
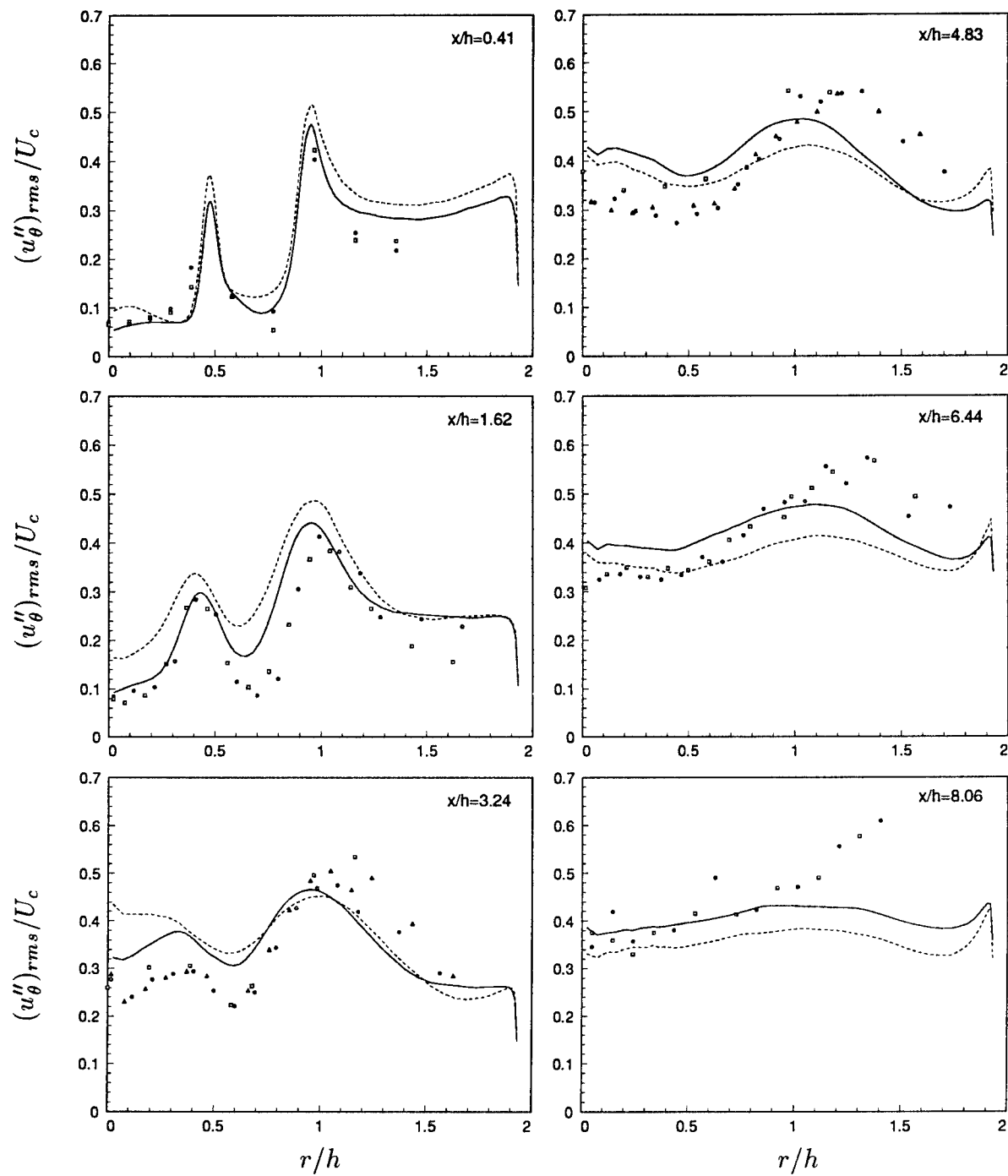
FIGURE **D.2-7**, Resolved azimuthal turbulence intensity. ———— : Basic case; ———— : Animation case; All Symbols : Experiments by Johnson & Bennett.
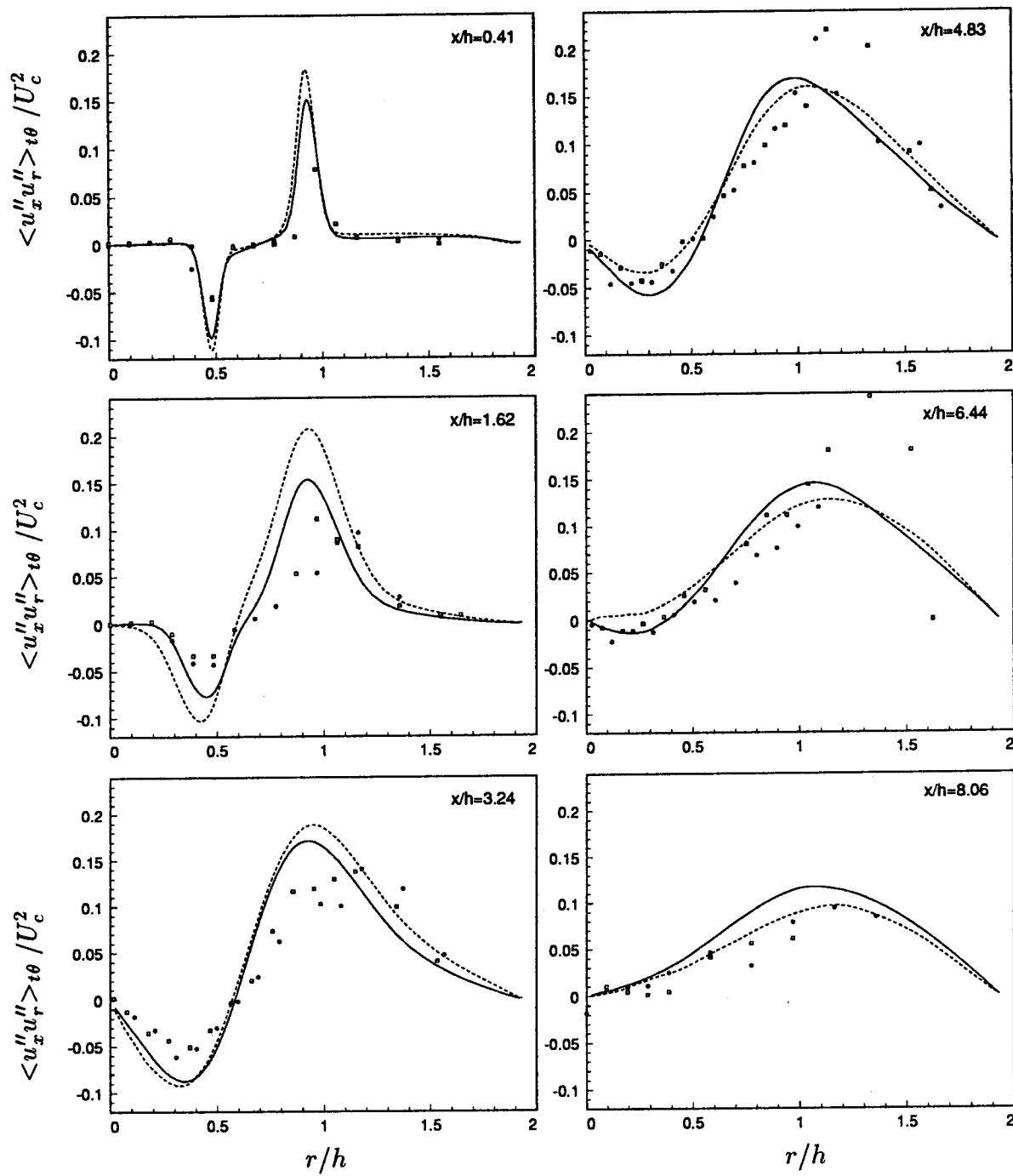
FIGURE **D.2-8**, Turbulent shear stress (incl. SGS model term). ———— : Basic case; ---- : Animation case; All Symbols : Experiments by Johnson & Bennett.
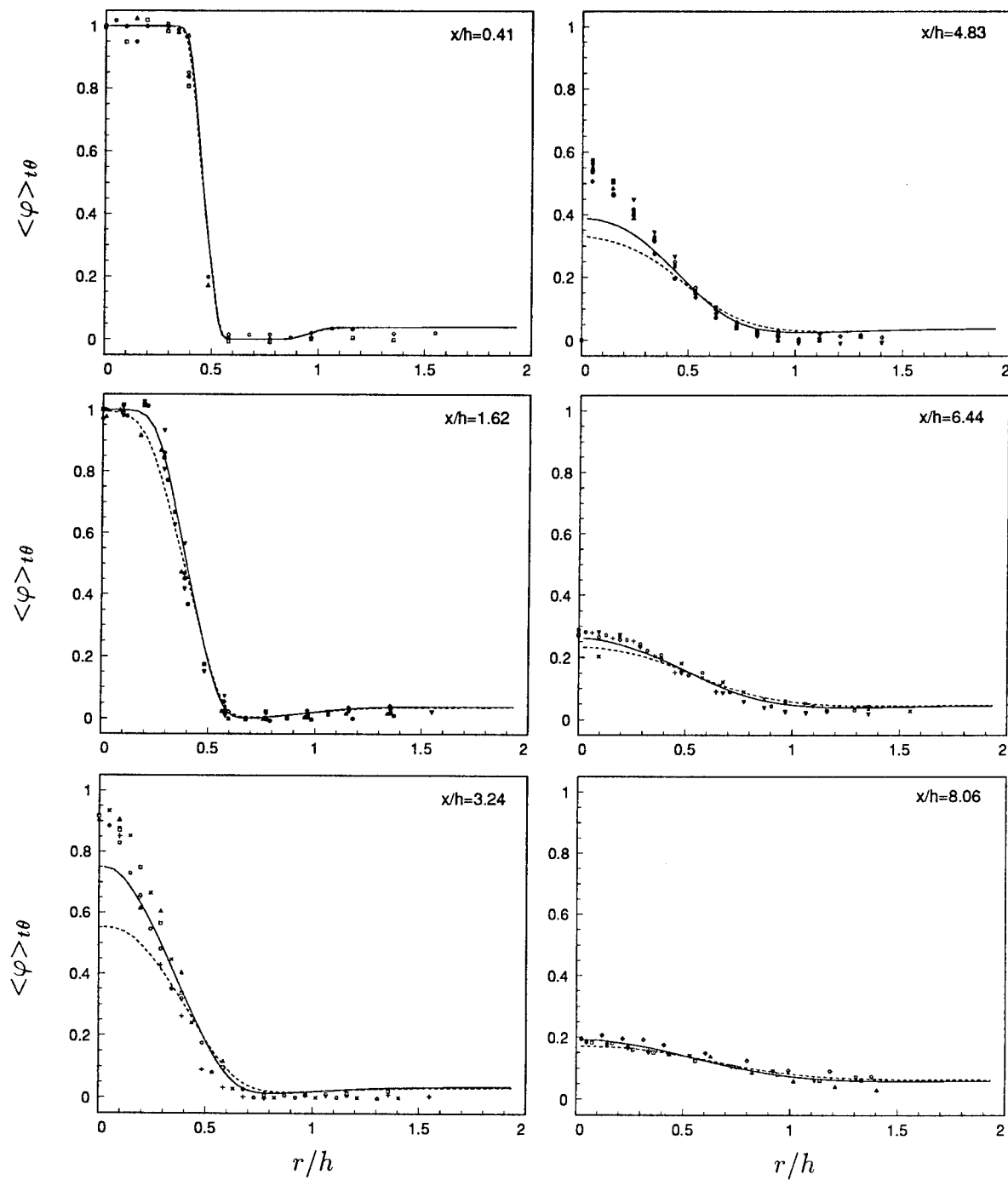
FIGURE **D.2-9**, Mean fuel mass-fraction. ——— : Basic case; - - - - : Animation case; All Symbols : Experiments by Johnson & Bennett.
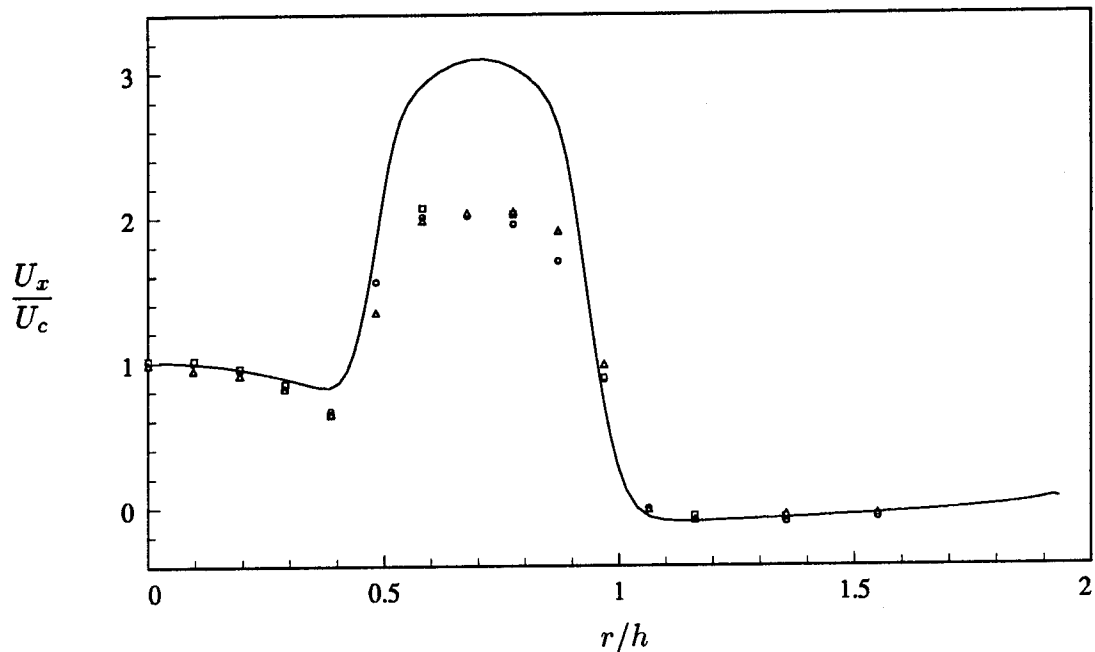
FIGURE **D.3-1**, Mean axial velocity profiles at $x/h = 0.41$. The profiles have been normalized to give the same centerline velocity. ———— : LES (basic case). All symbols : Experiments by Johnston & Bennett.
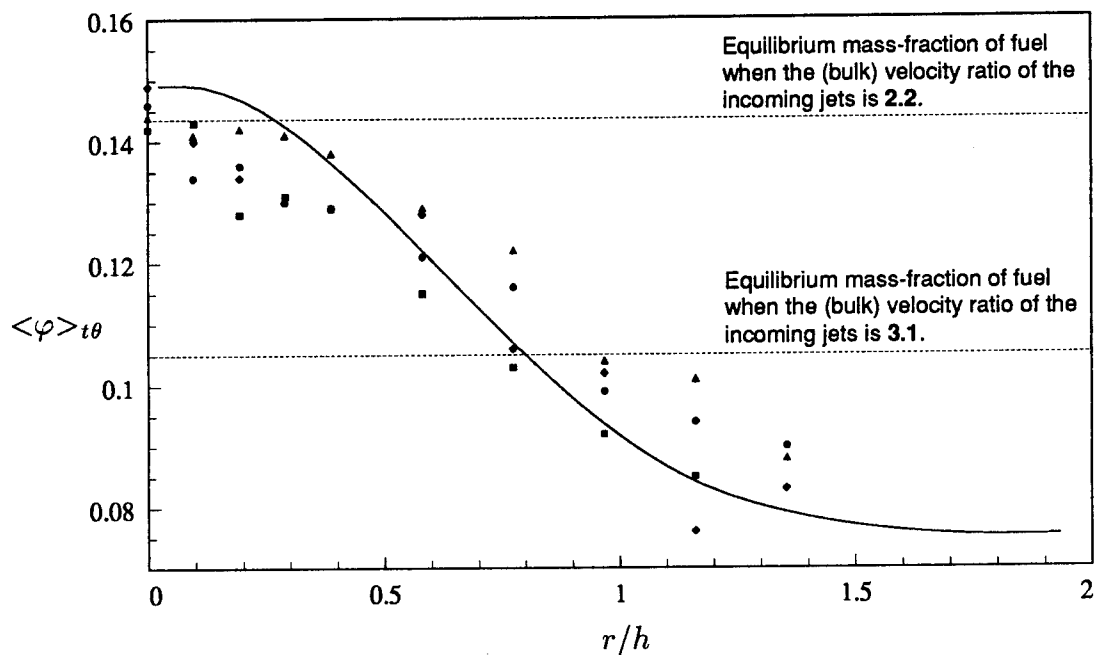

FIGURE **D.3-2**, Mean mass-fraction of fuel at $x/h = 9.68$. ———— : LES (basic case). All symbols : Experiments by Johnston & Bennett.
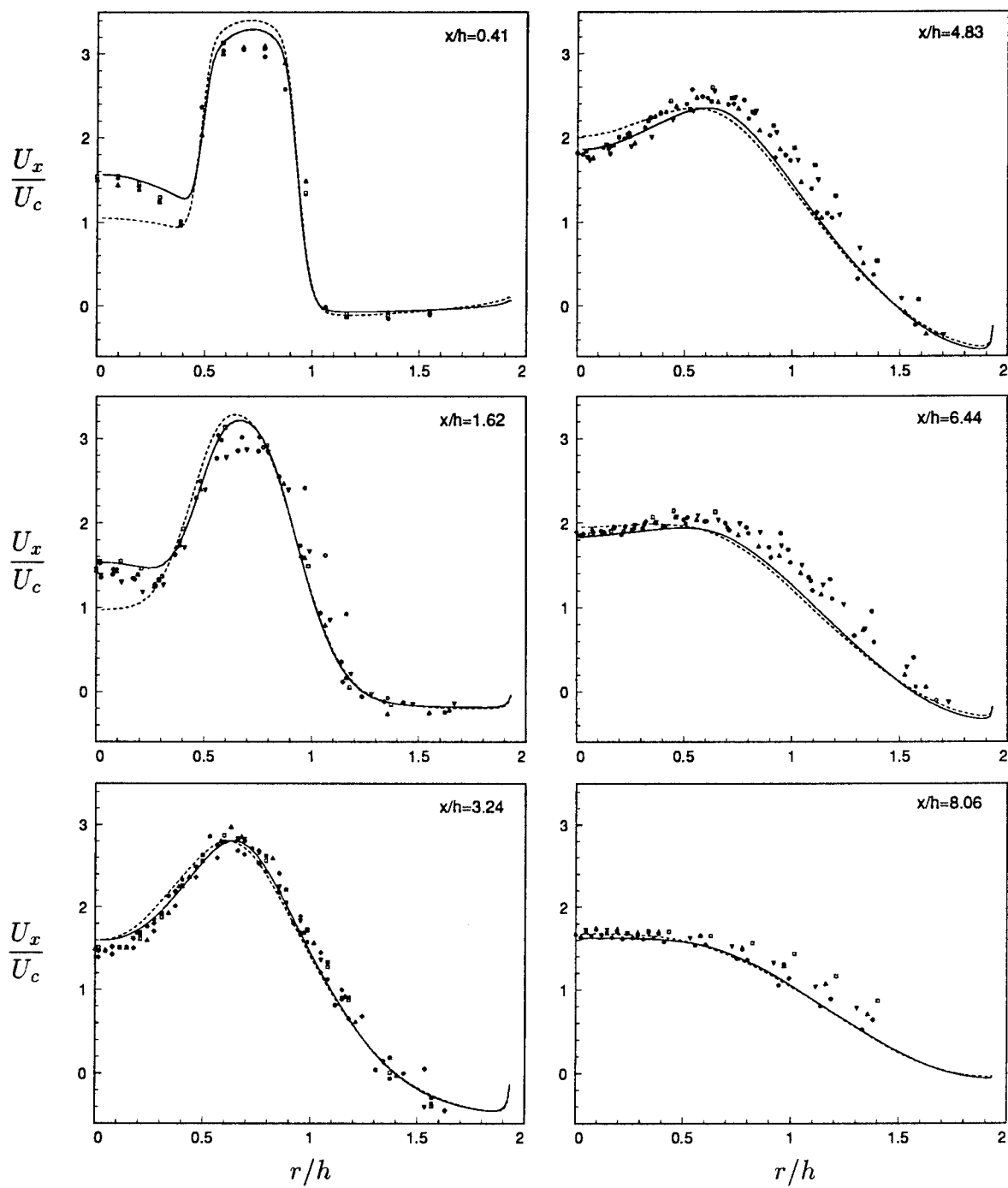
FIGURE **D.3-3**, Mean axial velocity.   ——— : Q2 case, bulk velocity ratio is 2.2;
- - - - : Animation case, bulk velocity ratio is 3.1;   All Symbols : Experiments by
Johnson & Bennett.
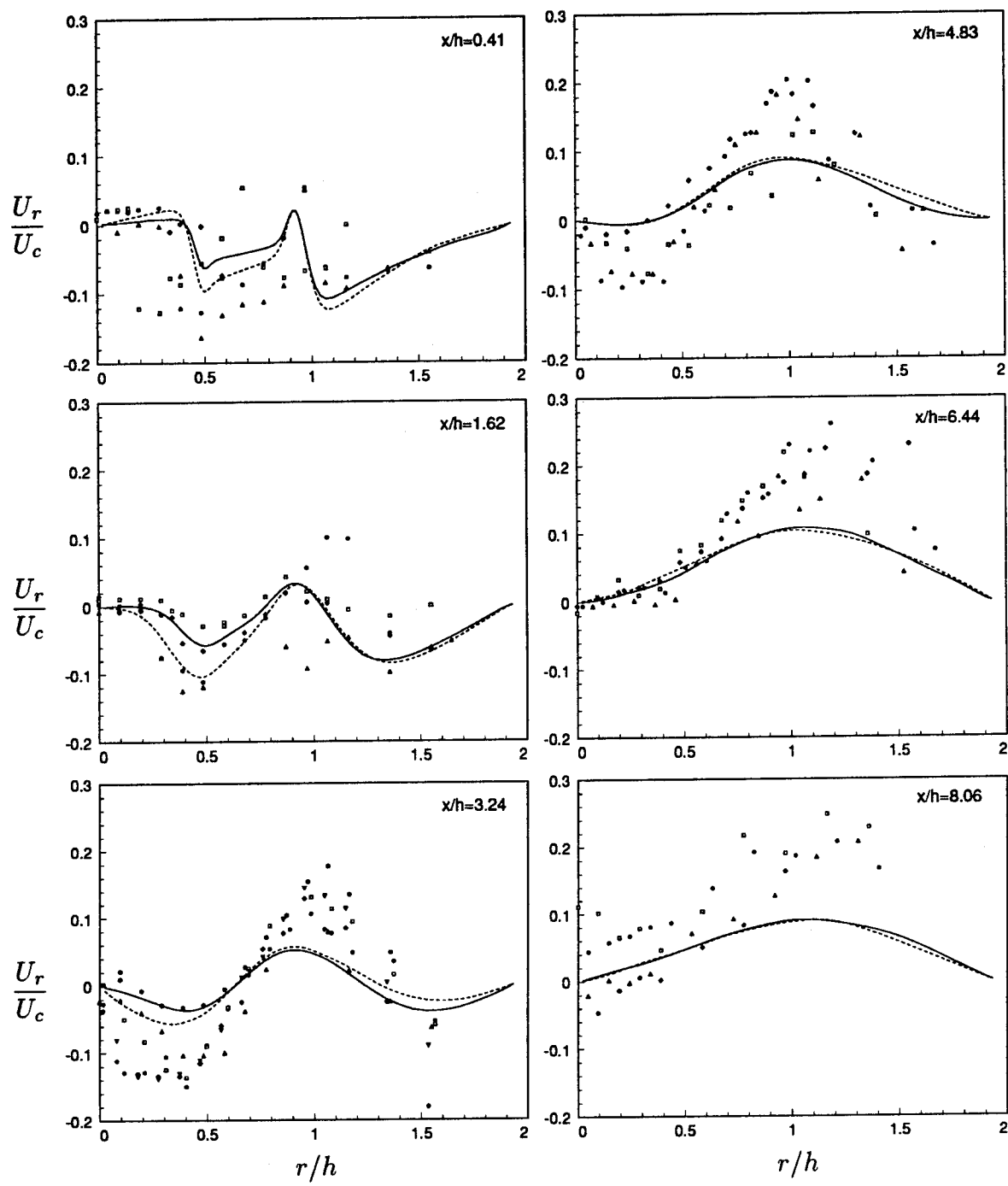
FIGURE **D.3-4**, Mean radial velocity. ———— : Q2 case, bulk velocity ratio is 2.2; ———— : Animation case, bulk velocity ratio is 3.1;   All Symbols : Experiments by Johnson & Bennett.
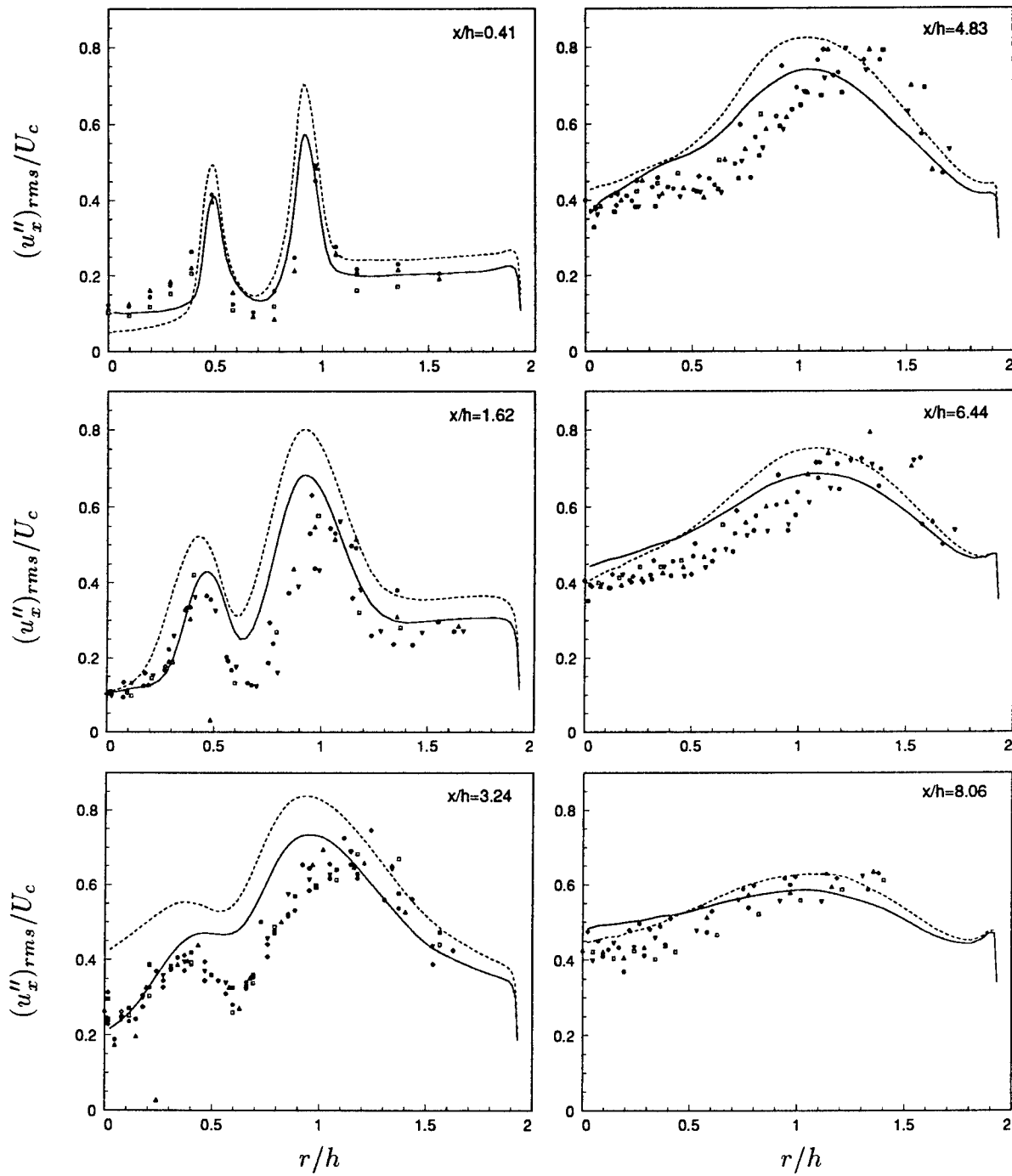
FIGURE **D.3-5**, Resolved axial turbulence intensity.   ———— : Q2 case, bulk velocity ratio is 2.2;   －－－－ : Animation case, bulk velocity ratio is 3.1;   All Symbols : Experiments by Johnson & Bennett.
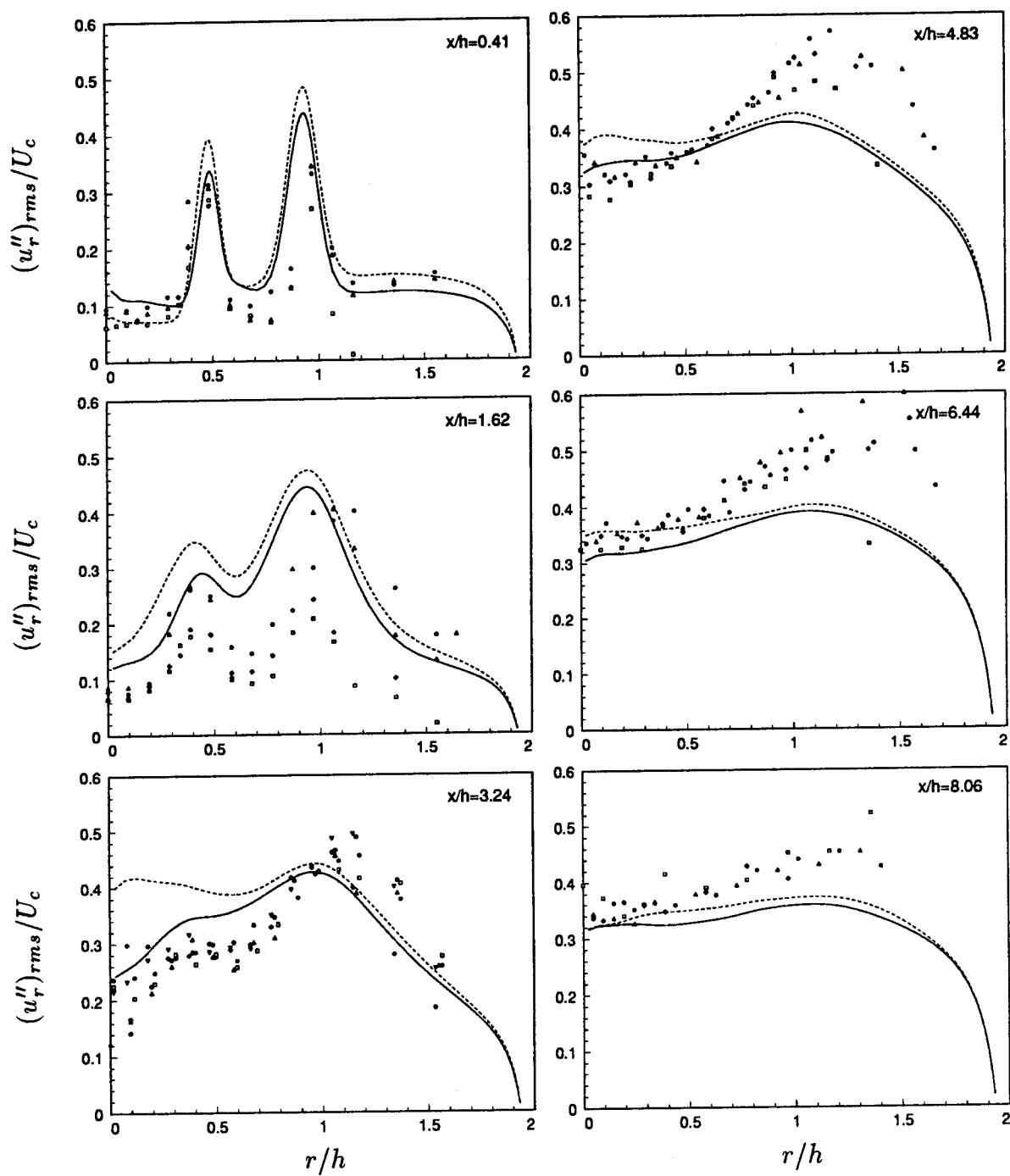
FIGURE **D.3-6**, Resolved radial turbulence intensity.   ——— : Q2 case, bulk velocity ratio is 2.2;   ---- : Animation case, bulk velocity ratio is 3.1;   All Symbols : Experiments by Johnson & Bennett.
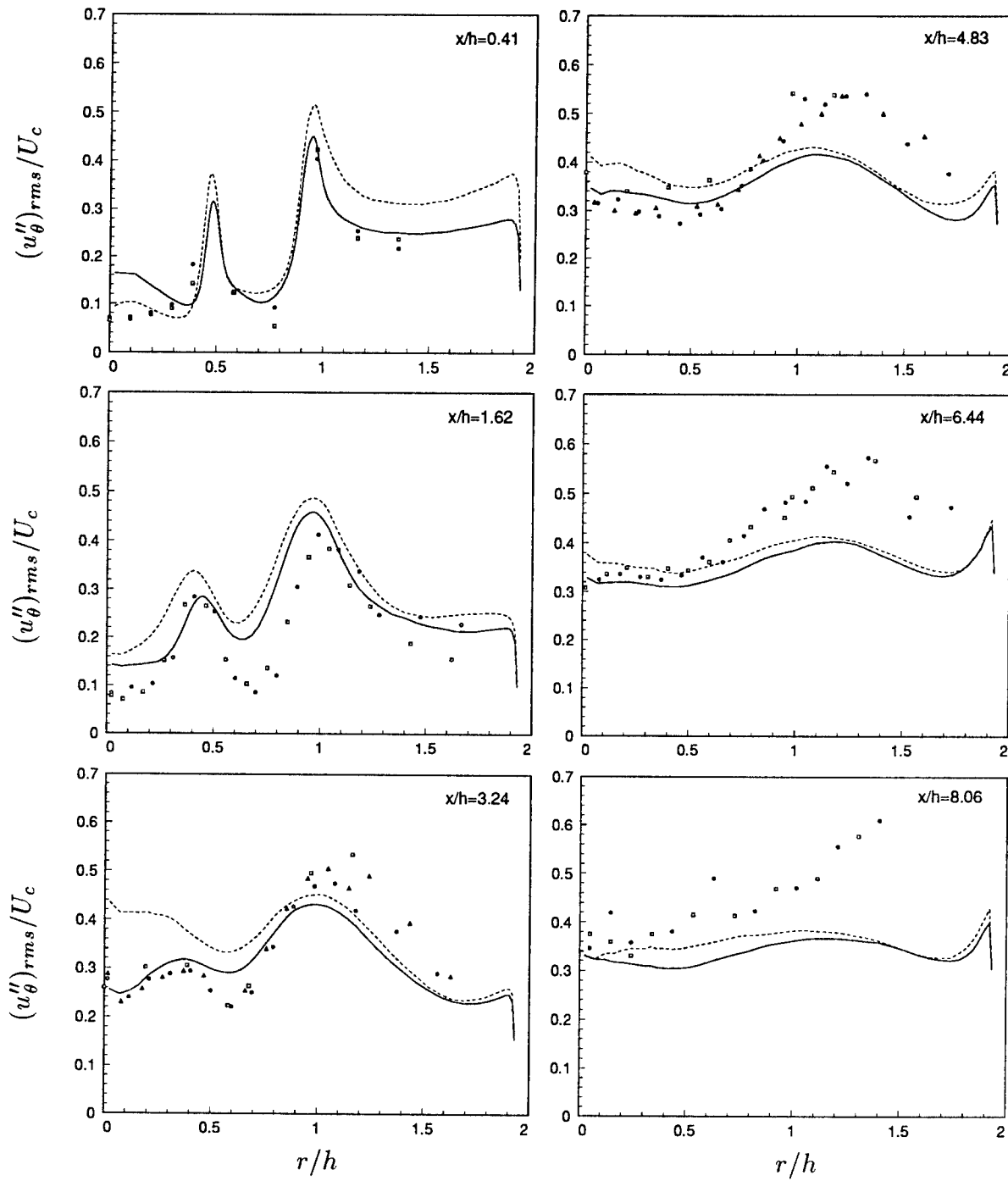
FIGURE **D.3-7**, Resolved azimuthal turbulence intensity.   ——— : Q2 case, bulk velocity ratio is 2.2;   ---- : Animation case, bulk velocity ratio is 3.1;   All Symbols : Experiments by Johnson & Bennett.
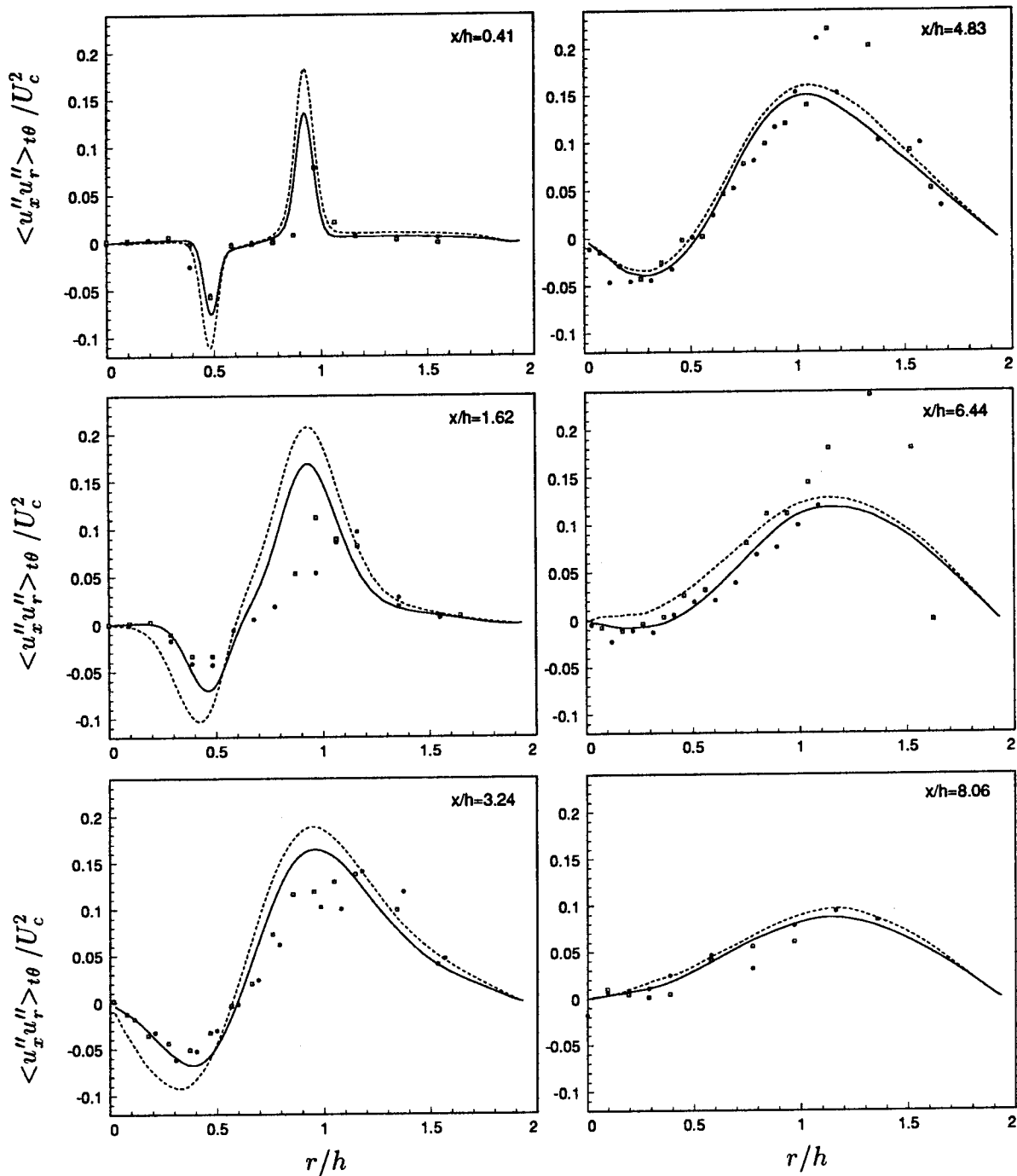
FIGURE **D.3-8**, Turbulent shear stress (incl. SGS model term).   ———— : Q2 case, bulk velocity ratio is 2.2;   - - - - : Animation case, bulk velocity ratio is 3.1;   All Symbols : Experiments by Johnson & Bennett.

References

ADAMS, E. W., JOHNSTON, J. P. & EATON, J. K. (1984) "Experiments on the structure of turbulent reattaching flow". *Report MD-43.* Thermosciences Division, Dep. of Mech. Eng., Stanford University, Stanford, California.

AKSELVOLL, K., AND MOIN, P., (1993) "Large eddy simulation of a backward facing step flow". *2nd International Symposium on Engineering Turbulence Modeling and Measurements.* May 31 - June 2, 1993, Florence, Italy.

ARNAL, M. & FRIEDRICH, R. (1991) "On the effects of spatial resolution and subgrid-scale modeling in large eddy simulation of a recirculating flow". *Proc. of the 9th GAMM-Conf. on Num. Methods in Fluid Mech.* Lausanne.

ARNAL, M. & FRIEDRICH, R. (1992) "Large eddy simulation of a turbulent flow with separation". *Turbulent Shear Flows 8.* Munich, pp. 169-187.

BALARAS, E. & BENOCCI, C. (1994) "Subgrid scale models in finite difference simulations of complex wall bounded flows". *AGARD Symposium on Application of Direct and Large-Eddy Simulation to Transition and Turbulence.* April 18-21, Chania, Crete, Greece.

BARDINA, J., FERZIGER, J. H. & REYNOLDS, W. C. (1983) "Improved turbulence models based on large eddy simulation of homogenous, incompressible, turbulent flows". *Report TF-19.* Thermosciences Division, Dep. of Mech. Eng., Stanford University, Stanford, California.

BLOWERS, R. M. (1973) "The calculation by finite differences of steady two-dimensional laminar flow in a T-junction". *Ph.D Thesis.* University of Surrey.

BREUER, M. & RODI, W. (1994) "Large-eddy simulation of turbulent flow through a straight square duct and a 180 deg Bend". *Proc. of the First ER-COFTAC Workshop on DNS and LES.* Guildford, Surrey, U.K.

CABOT, W. (1991) "Large eddy simulations of passive and buoyant scalars with dynamic subgrid-scale models". *Center for Turbulence Research, Annual Research Briefs, 1991.*

CABOT, W., & MOIN, P. (1991) Large eddy simulation of scalar transport with the dynamic subgrid-scale model. In *Large Eddy Simulation of Complex Engineering and Geophysical Flows,* ed. by B. Galperin, Cambridge University Press.

CARUSO, S. C. (1985) Adaptive grid techniques for elliptic fluid-flow problems". *Ph.D Thesis.* Dep. of Mech. Eng., Stanford University, Stanford, CA, 94305.

CASTRO, I. P. (1977) "Numerical difficulties in the calculation of complex turbulent flows". *Proc. of Penn. Stat Conference on Turbulent Shear Flows.* Academic Press.

CHORIN, A. J. (1968) *Math. Comput.,* **Vol. 22,** 745.

DEARDORFF, J. W. (1970) "A numerical study of three-dimensional turbulent channel flow at large Reynolds numbers". *J. Fluid Mech.* **41,** pp. 453-480.

DUKOWICZ, J. K., & DVINSKY, A. S. (1992) "Approximate factorization as a high order splitting for the implicit incompressible flow equations". *J. Comput. Phys.* **Vol. 102,** No. 2, pp 336-347.

DURST, F. & SCHMITT, F. S. (1985) "Experimental study of high Reynolds number backward-facing step flow". *Proc. 5th Symp. on Turbulent Shear Flows.* Cornell University, Itchaca, NY.

EATON, J. K. & JOHNSTON, J. P. (1980) "Turbulent flow re-attachment: an experimental study of the flow and structure behind a backward-facing step". *Report MD-39.* Dep. of Mech. Eng., Stanford University, Stanford, California.

EATON, J. K. & JOHNSTON, J. P. (1981) "A review of research on subsonic turbulent flow reattachment". *AIAA Journal.* **Vol. 19,** No. 9.

EIDSON, T. M. (1985) "Numerical simulation of the turbulent Rayleigh-Bénard convection using subgrid scale modeling". *J. Fluid Mech.* **Vol. 158,** pp 245-268.

EGGELS, J. G. M. & NIEUWSTADT, F. T. M. (1993) "Large eddy simulation of turbulent flow in an axially rotating pipe". *Ninth Symposium on "Turbulent Shear Flows".* Kyoto, Japan, August 16-18.

EGGELS, J. G. M. (1994) "Direct and large eddy simulation of turbulent flow in a cylindrical pipe geometry". *Thesis, Delft University of Tech.* Delft Univ. Press, 2628 CN Delft, The Netherlands.

EGGELS, J. G. M., UNGER, F., WEISS, M. H., WESTERWEEL, J., ADRIAN, R. J., FRIEDRICH, R. & NIEUWSTADT, F. T. M. (1994) "Fully developed turbulent pipe flow: a comparison between direct numerical simulation and experiment". *J. Fluid Mech.* **Vol 268,** pp. 175-209.

FATICA, M., ORLANDI, P. & VERZICCO, R. (1994) "Direct and large eddy simulation of round jets". *AGARD Symposium on Application of Direct and Large-Eddy Simulation to Transition and Turbulence.* April 18-21, Chania, Crete, Greece.

FRIEDRICH, R. & ARNAL, M. (1990) "Analysing turbulent backward-facing step flow with the lowpass-filtered Navier-Stokes equations". *Journal of Wind Eng. and Industrial Aerodynamics.* **35,** pp. 101-128.

GERMANO, M., PIOMELLI, U., MOIN, P. & CABOT, W. H. (1991) "A dynamic subgrid-scale eddy viscosity model". *Phys. Fluids A.* **Vol. 3,** no. 7.

GHOSAL, S. & MOIN, P. (1993) "The basic equations for the large eddy simulation of turbulent flows in complex geometry". *Center for Turbulence Research, CTR Manuscript 143.* Stanford University, Stanford, CA 94305-3030.

GHOSAL, S., LUND, T. S., MOIN, P. & AKSELVOLL, K. (1994) "A dynamic localization model for large-eddy simulation of turbulent flows". *J. Fluid Mech.* **Vol. 282,** pp 1-27.

HARLOW, F. H. & WELCH, J. E. (1965) "Numerical calculation of time-dependent viscous incompressible flow of fluid with a free surface". *The Physics of Fluids.* **Vol. 8,** no. 12, pp 2182-2189.

HOFFMANN, G. & BENOCCI, C. (1994) "Numerical simulation of spatially-developing planar jets". *AGARD Symposium on Application of Direct and Large-Eddy Simulation to Transition and Turbulence.* April 18-21, Chania, Crete, Greece.

ISOMOTO, K. & HONAMI, S. (1989) "The effect of inlet turbulence intensity on the reattachment process over a backward-facing step". *Journal of Fluids Eng.* **Vol. 111,** pp. 87-92.

JOHNSON, B. V. & BENNETT, J. C. (1981) "Mass and momentum turbulent transport experiments with confined coaxial jets". *NASA Contractor Report NASA CR-165574, UTRC Report R81-915540-9.*

JOHNSON, B. V. & BENNETT, J. C. (1984) "Statistical characteristics of velocity, concentration, mass transport, and momentum transport for coaxial jet mixing in a confined duct". *Journal of eng. for Gas Turbines and Power.* **Vol 106,** pp 121-127.

JOVIC, S. & DRIVER, D. M. (1994) "Backward-facing step measurement at low Reynolds number $Re_h = 5000$". *NASA Technical Memorandum 108807*. Ames Research Center, Moffett Field, California 94035-1000.

KAYS, W. M. & CRAWFORD, M. E. (1980) "Convective heat and mass transfer". Second Edition, McGraw-Hill Book Company.

KIM, J., KLEIN, S. J. & JOHNSTON, J. P. (1978) "Investigation of separation and reattachment of a turbulent shear layer : Flow over a backward-facing step". *Report No. MD-37*. Thermosciences Division, Dept. of Mech Eng., Stanford University.

KIM, J. & MOIN, P. (1985) "Application of a fractional-step method to incompressible Navier-Stokes equations". *J. Comput. Phys.* **Vol. 59,** No. 2, pp 308-323.

LE, H. & MOIN, P. (1994) "Direct numerical simulation of turbulent flow over a backward-facing step". *Report TF-58*. Dep. of Mech. Eng., Stanford University, Stanford, California.

LEONARD, B. P. (1979) "A stable and accurate convective modelling procedure based on quadratic upstream interpolation". *Comp. Meth. in Applied Mech. and Eng.* **Vol 19,** pp. 59-98.

LEONARD, B. P. (1988) "Simple high-accuracy resolution program for convective modelling of discontinuities". *Int. J. for Num. Meth. in Fluids.* **Vol 8,** pp. 1291-1318.

LILLEY, D. G. (1977) "Swirl flows in combustion: A review". *AIAA Journal.* **Vol. 15,** pp 1063-1078.

LILLY, D. K. (1966) "On the application of eddy viscosity concept in the inertial sub-range of turbulence". *NCAR Manuscript No. 123,*. Boulder, Colorado.

LILLY, D. K. (1967) "The representation of small-scale turbulence in numerical simulation experiments". *Proceedings of the IBM Scientific Computing Symposium on Environmental Sciences.* Yorktown Heights, N.Y.

LILLY, D. K. (1992) "A proposed modification of the Germano subgrid-scale closure method". *Phys. Fluids A.* **Vol. 4,** no. 3

LUND, T. S., GHOSAL, S. & MOIN, P. (1993) "Numerical experiments with highly-variable eddy viscosity models". *Engineering applications of large eddy simulations.* ASME Fluid engineering conference, Washington, D.C., June 20-24.

MCMILLAN, O. J., FERZIGER, J. H. & ROGALLO, R.S. (1980) "Tests of new subgrid-scale models in strained turbulence". *AIAA Paper No. 80-1339.*

MÉTAIS, O. & LESIEUR, M. (1992) "Spectral large-eddy simulation of isotropic and stably stratified turbulence". *J. Fluid Mech.* **vol. 239,** pp. 157-194.

MOFFATT, M. K. (1964) "Viscous and resistive eddies near a sharp corner". *J. Fluid Mech.* **Vol. 18,** 1.

MOIN, P., REYNOLDS, W. C. & FERZIGER, J. H. (1978) "Large eddy simulation of incompressible turbulent channel flow". *Report TF-12.* Dep. of Mech. Eng., Stanford University, Stanford, California.

MOIN, P. & KIM, J. (1982) "Numerical investigation of turbulent channel flow". *J. Fluid Mech.* **vol. 118,** pp. 341-377.

MOIN, P. (1991) "A new approach for large eddy simulation of turbulence and scalar transport". *Proc. Monte Veritá Coll. on turbulence, Sept. 9-13, Birkhauser, Bale.*

MOIN, P., SQUIRES, K., CABOT, W. & LEE, S. (1991) "A dynamic subgrid-scale model for compressible turbulence and scalar transport". *Phys. Fluids A.* **Vol. 3,** no. 11.

MOIN, P. & JIMENÉZ, J. (1993) "Large eddy simulation of complex turbulent flows". *AIAA Paper No. 93-3099.* Orlando, Florida, July 6-9.

MOIN, P., CARATI, D., LUND, T. S., GHOSAL, S. & AKSELVOLL, K. (1994) "Developments and applications of dynamic models for large eddy simulation of complex flows". *AGARD Symposium on Application of Direct and Large-Eddy Simulation to Transition and Turbulence.* April 18-21, Chania, Crete, Greece.

MORINISHI, Y. & KOBAYASHI, T. (1990) "Large eddy simulation of backward facing step flow". *International Symposium on Eng. Turbulence Modeling and Measurements".* Dubrovnik, Yugoslavia.

NETO, A. S., GRAND, D., MÉTAIS, O. & LESIEUR, M. (1993) "A numerical investigation of the coherent vortices in turbulence behind a backward facing step". *J. Fluid Mech.* **vol. 256,** pp. 1-25.

OLSON, R. M. (1980) "Essentials of engineering fluid mechanics". *Fourth Edition, Harper & Row, Publishers, New York.*

PAULEY, L. L., MOIN, P. & REYNOLDS, W. C. (1988) "A numerical study of unsteady laminar boundary layer separation". *Report No. TF-34.* Thermosciences Division, Dept. of Mech. Eng., Stanford University.

PEROT, J. B. (1993) "An analysis of the fractional step method". *J. Comput. Phys.* **Vol. 108,** No. 1, pp 51-58.

PIOMELLI, U., FERZIGER, J. H. & MOIN, P. (1987) "Models for large eddy simulations of turbulent channel flows including transpiration". *Report TF-32.* Thermosciences Division, Dep. of Mech. Eng., Stanford University, Stanford, California.

PIOMELLI, U., ZANG, T. A., SPEZIALE, C. G. & HUSSAINI, M. Y. (1990) "On the large-eddy simulation of transitional wall-bounded flows". *Phys. Fluids A.* **Vol. 2,** 257.

PIOMELLI, U., CABOT, W.H., MOIN, P. & LEE, S. (1991) "Subgrid-scale backscatter in turbulent & transitional flows". *Phys. Fluids A.* **Vol. 3,** no. 7, pp. 1766-1771.

PIOMELLI, U. (1993) "High Reynolds number calculations using the dynamic subgrid-scale stress model". *Phys. Fluids A.* **Vol. 5,** no. 6.

REID, J. K. & WALSH J. E. (1965) "An elliptic eigenvalue problem for a reentrant region". *J. Soc. Indust. Appl. Math.* **Vol. 13,** No. 3.

ROGALLO, R. S. & MOIN, P. (1984) "Numerical simulation of turbulent flow". *Ann. Rev. Fluid Mech.* 16:99-137.

ROQUEMORE, W. M., REDDY, V. K., HEDMAN, P. O., POST, M. E., CHEN, T. H., GOSS, L. P., TRUMP, D., VILIMPOC, V. & STURGESS, G.J. (1991) "Experimental and theoretical studies in a gas-fueled research combustor". *AIAA paper 91-0639.* 29th Aerospace Sciences Meeting, Reno, Nevada.

SCHUMANN, U. (1975) "Subgrid scale model for finite difference simulation of turbulent flows in plane channels and annuli". *J. Comput. Phys.* **Vol. 18,** 376-404.

SMAGORINSKY, J. (1963) "General circulation experiments with the primitive equations. I. The basic experiment". *Monthly Weather Review.* **91,** pp. 99-164.

SPALART, P. R. (1987) "Hybrid RKW3 + Crank-Nicholson scheme". *Internal Report*. NASA-Ames Research Center, Moffett Field, CA.

SPALART, P. R. (1988) "Direct simulation of a turbulent boundary layer up to $R_\theta = 1410$". *J. Fluid Mech.* **Vol. 187**, pp. 61-98.

SPALART, P. R., MOSER, R. D. & ROGERS, M. M. (1991) "Spectral methods for the Navier-Stokes equations with one infinite and two periodic directions". *J. Comput. Phys.* **Vol. 96**, 297-324.

TEMAM, R. (1969) *Arch. Rat. Mech. Anal.,* **Vol. 32,** 377.

TROPEA, C (1982) "Die turbulente Strömung in Flachkanälen und offenen Gerinnen". *Dissertation, University of Karlsruhe.*

VAN DRIEST, E. R. (1956) "On turbulent flow near a wall". *J. Aero. Sci.* **23,** pp. 1007-1011.

WAGNER, C. & FRIEDRICH, R. (1994) "Direct numerical simulation of turbulent flow in a sudden pipe expansion". *AGARD Symposium on Application of Direct and Large-Eddy Simulation to Transition and Turbulence.* April 18-21, Chania, Crete, Greece.

WESTERWEEL, J., ADRIAN, R. J., EGGELS, J. G. M. & NIEUWSTADT, F. T. M. (1992) "Measurements with particle image velocimetry on fully developed turbulent pipe flow at low Reynolds number". *Proc. 6th Int. Symp. on Appl. of Laser Techn. to Fluid Mech.* (Lisbon, Portugal) July 20-23.

WICKER, R. B. & EATON, J. K. (1994) "Near field of a coaxial jet with and without axial excitation". *AIAA Journal.* **Vol. 32,** no. 3, pp. 542-546.

YANG, K. S. & FERZIGER, J. H. (1993) "Large-eddy simulation of turbulent obstacle flow using a dynamic subgrid-scale model". *AIAA Journal.* **Vol. 31,** No. 8.

YOSHIZAWA, A. (1989) "Subgrid-scale modeling with a variable length scale". *Phys. Fluids A.* **1,** (7), pp. 1293-1295.

ZANG, Y., STREET, R. L., KOSEFF, R. J. (1993) "A dynamic mixed subgrid-scale model and its application to turbulent recirculating flows". *Phys. Fluids A.* **Vol. 5,** no. 12, pp. 3186-3196.